Unique Luminescence Properties Based on Electronic Structure and Local Environment in Mixed-Anion Compounds

Yuuki KITAGAWA

Table of Contents

Chapter 1
General Introduction

Abstract

Luminescence is indispensable for our daily life. In order to make our lives abundant and advanced, a number of functional luminescent materials have been developed every day. In this chapter, as the general introduction, the mixed-anion phosphors that are focused on as the novel functional materials are overviewed. Although the type of luminescence is determined by the cation species acting as the activator, the luminescence properties depend on the electronic structure and coordination environment, which can be controlled by the coordinating anion species. In the research on luminescent materials, the anion-based material design is a useful strategy. Some studies about the mixed-anion phosphors following these concepts are introduced. The purposes and contents of the studies in this dissertation are briefly explained.

1.1. Introduction of Luminescent Materials

People in the 2020s are surrounded by a variety of *lights*. The environment around us has been drastically changed; in particular, we have witnessed the remarkable development of optoelectronics in the last two decades. Widespread use of light-emitting diodes (LEDs) provides very large high-resolution displays in the city and very bright traffic lights. Inexpensive and mass-produced blue LEDs enable us to enjoy white LEDs for the solid-state lighting device, which is energy-saving and eco-friendly. Tiny, thin, and flexible light-emitting devices, such as micro-LEDs and organic-LED films, play an essential role in brilliant display panels for smartphones and laptops. The development of a light-amplifying system for optical fibers facilitates high-speed data transmission, leading to our better working environments with telework and the Internet of Things (IoT). The state-of-the-art devices utilizing invisible light will be inevitable for the health and safe lives; near-UV light is used for the inactivation of coronavirus or the bacteria elimination [1], and near-infrared (NIR) light is applied to sensing the heat like body temperatures or the molecules included in foods [2]. Lighting applications in the next generation undoubtedly enrich our lives and develop technologies.

There are two types of light-emitting phenomena in solids. One is black-body radiation, whose emission wavelength depends only on temperature. In terms of lighting applications, black-body radiation is not desirable because of its low efficiency with heat emission. *Luminescence* is another light-emitting phenomenon without thermal radiation, which is widely used in a variety of applications, as mentioned in the previous passage. The quantum mechanical illustration of luminescence is provided in Chapter 2. Inorganic luminescent materials, such as phosphors and scintillators, are usually designed by doping a small number of impurity ions (luminescence centers) in inorganic solid-state hosts and forming local energy levels in the host bandgap. Typical luminescence centers in inorganic phosphors are emphasized in the periodic table of elements shown in **Figure 1.1**. Four groups of elements are regarded as the luminescence centers; transition metal (*TM*) ions, lanthanoid (*Ln*) ions, ns^2-type ions, and cluster-type ions with *TM* ions. These luminescence centers are described briefly below;

- Transition metal (*TM*) ions, mainly the first transition series in period four, show luminescence attributed to d-d forbidden transition. Because the Clarke number of these elements is relatively high, they are widely used for functional materials, not only for luminescent materials but also other applications, such as batteries, magnetics, and superconductors. The optical absorption related to *TM* ions has been well-known as a color center of gems and minerals, *e.g., ruby* (Al_2O_3:Cr^{3+}), *sapphire* (Al_2O_3:Fe^{3+},Ti^{3+}), *emerald* ($Be_3Al_2Si_6O_{18}$:Cr^{3+}), and *red beryl* ($Be_3Al_2Si_6O_{18}$:Mn^{3+}) [3]. The optical properties of d-d transition depend on the crystal field strength of incorporated sites by *TM* ions, leading to various luminescence and body colors ranging from the visible to NIR region. Energy levels for electronic transitions are described by the Tanabe-Sugano diagram, depending on Dq/B (Dq: crystal field strength, B: Racah parameter, which is correlated with electrostatic repulsion between electrons). The detailed description is referred to in the textbooks [4,5].

- Luminescence of lanthanoid (*Ln*) ions is widely used in various applications, such as LED lighting [6,7], laser optics [8,9], optical fiber amplification [10–12], and persistent phosphors [13,14]. Considering the natural abundance of elements, lanthanoids are not rare but richer than other noble metals, including Ag, Au, Pd, Ir, and In [15]. Recently, it has been reported that an enormous amount of minerals containing lanthanoids is found in the deep-sea mud taken at the western north pacific ocean around Minamitorishima (Japan) [16,17], leading to further research on lanthanoid-based functional materials in the future. There are two types of radiative electronic transition for *Ln* ions; 4f-4f and 5d-4f transition. The 4f-4f forbidden transition for trivalent *Ln* ions shows very sharp spectral lines in the visible to NIR region. The 4f energy levels for Ln^{3+} ions are shown in **Figure 1.2** (Dieke diagram). The positions of rich energy levels are almost independent of local environments due to shielding of inner 4f orbitals by outer 5s and 5p orbitals, resulting in specific luminescence colors of Ln^{3+} ions. On the other hand, the properties of the 5d-4f transition severely depend on the crystal field around *Ln* ions. The 5d-4f

transition is observed only in specific *Ln* ions, such as Ce^{3+}, Pr^{3+}, Eu^{2+}, and Yb^{2+} ions with relatively low 5d excited levels. The 5d → 4f luminescence is utilized in some commercial phosphors, *e.g.,* $Y_3Al_5O_{12}:Ce^{3+}$ and $CaAlSiN_3:Eu^{2+}$ for white-LEDs, and $SrAl_2O_4:Eu^{2+}$-Dy^{3+} for a persistent phosphor with a long duration over 30 h. The *Ln* ions are important luminescence centers supporting our convenient and advanced lives. Detailed descriptions of the 5d-4f and 4f-4f transitions are provided in sections 2.1.2 and 2.1.3.

- Some heavy metal ions, such as Sn^{2+}, Sb^{3+}, Hg^0, Tl^+, Pb^{2+}, and Bi^{3+}, are regarded as the ns^2-type luminescence center. They show the optical absorption and emission related to the ns^2-nsnp transition. The physical properties of the ns^2-type centers have been investigated in various alkaline halide hosts [18–20]. In particular, broad luminescence bands of non-toxic Bi^{3+} have been studied in many oxides for optical applications [21,22].

- The polyhedra or clusters formed by *TM* ions have the potential to show luminescence by the radiative transition between the molecular orbitals. The *TM* ions in the high oxidation states, such as V^{5+}, W^{6+}, and Mo^{6+}, form TMO_4 tetrahedra, which show efficient luminescence from the charge transfer (CT) states between *TM* d and O 2p orbitals (see section 2.1.4). The uranyl ion $[UO_2]^{2+}$ and the tetracyanoplatinate ion $[Pt(CN)_4]^{2-}$ also show interesting luminescent phenomena related to the CT transition [23–25]. The luminescence properties of these clusters are discussed with the molecular orbital formed in them.

By selecting the optimal centers strategically, many researchers have been working to realize the desirable and promising properties. The luminescence properties of these ions and clusters largely depend on the physical and chemical characters of the ligand field and the electronic structure of host compounds. In many cases, cations play a role of "function," whose properties significantly depend on the coordinating anions. Therefore, it is essential to select not only the optimal cations as the luminescence centers but also anions that can bring about unique features that are not observed in conventional materials.

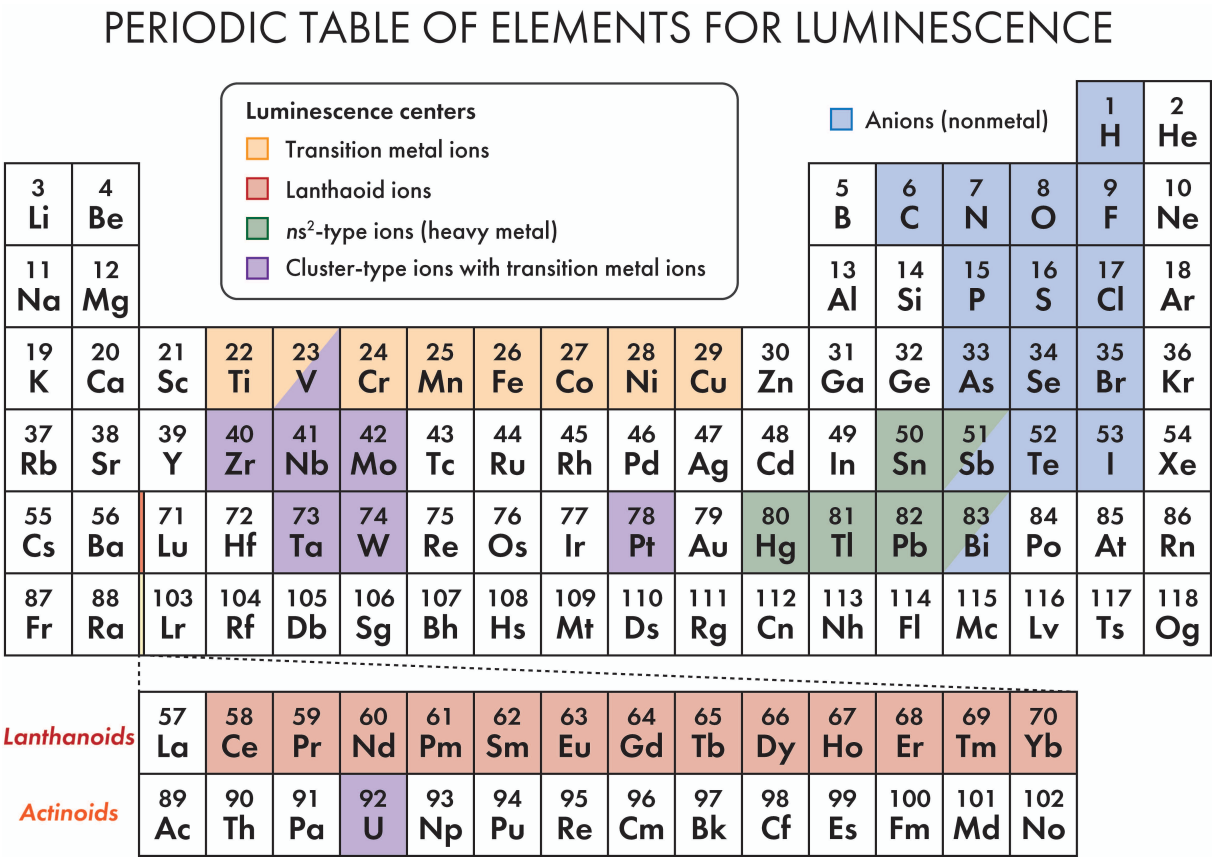

Figure 1.1. Periodic table of elements, emphasizing the four groups of elements that act as luminescence centers in inorganic compounds and the group of nonmetal elements forming anions.

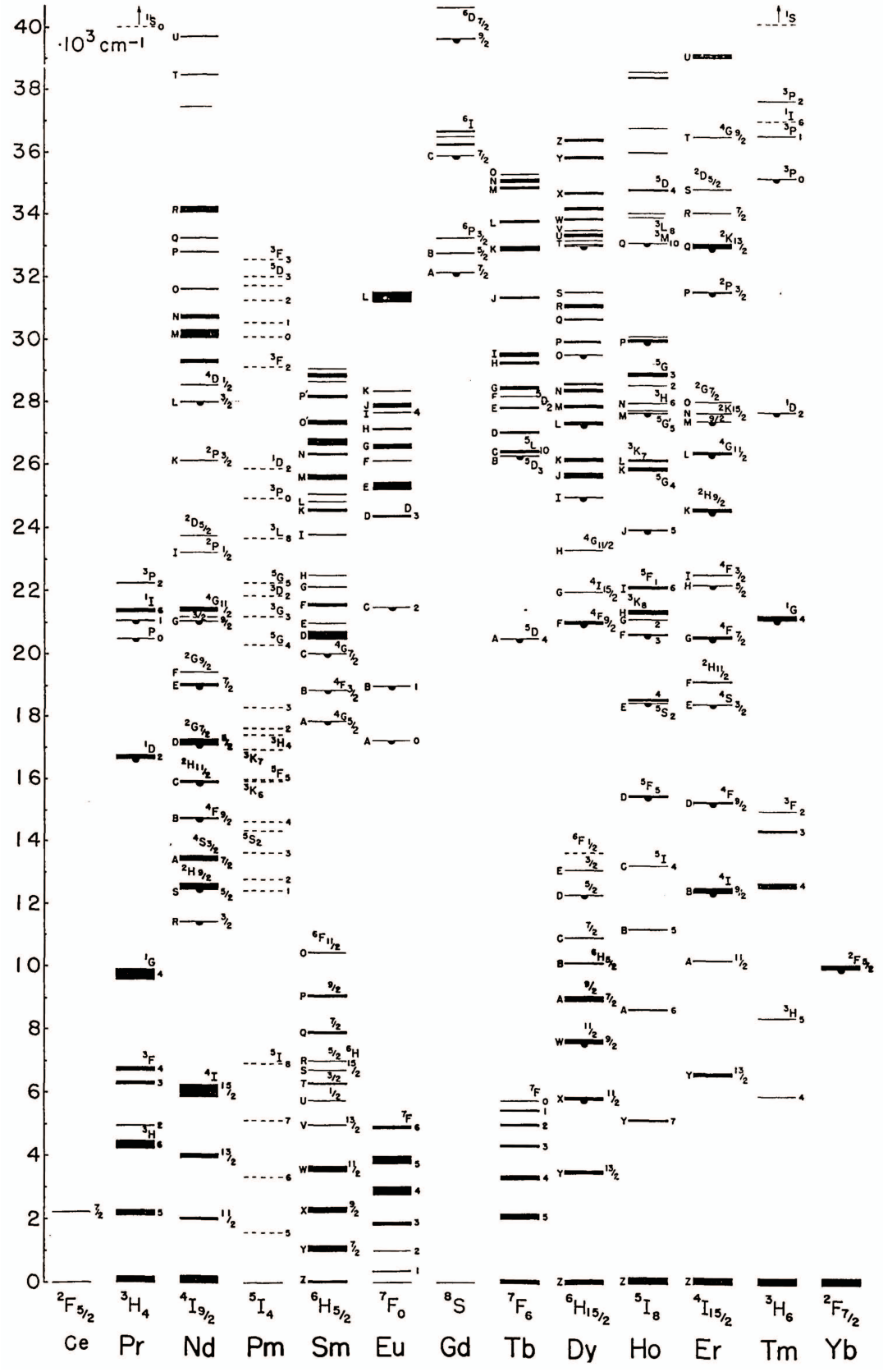

Figure 1.2. Energy levels of the trivalent lanthanoid ions (Ln^{3+}) in the $LaCl_3$ host (Dieke diagram) [26].

1.2. Mixed-Anion-Type Luminescent Materials

For many years, an enormous number of functional solids have been studied for a variety of applications, such as electronic and optical devices, catalysts, batteries, magnetics, and superconductors, to realize our prosperous life. The accumulation of knowledge based on experiments and theoretical calculations brings about deep understandings of the physical properties of "*mono-anion*" compounds, including oxides, halides, nitrides, and sulfides, and contributes to improving these properties. However, now that the crystal structures and morphologies have been already optimized, the material exploration of existing mono-anion compounds stagnates, and the breakthrough for novel functional materials groups is required.

Recently, more and more researchers have focused on the "*mixed-anion*" compounds, which contain two or more kinds of anions in their composition. While the conventional mono-anion compounds can take a variety of structures through cation substitution, the variation of the local structure around cations is restricted because only one type of anion with a negative formal charge forms the coordination polyhedra. For example, in the perovskite-type compounds that are used in various functional materials, the site-symmetry of cation sites, particularly octahedral sites, is not largely affected and distorted. On the other hand, for mixed-anion compounds, one can drastically change the local environments around cations by tuning various parameters, such as the composition ratio of anions and the geometrical positions (*i.e., cis* and *trans*). Because each anion has different nature (formal charge, ionic radius, electronegativity, and dipole polarizability), the unique properties related to mixed-anion compositions are expected.

The basic concepts of functionalization of mixed-anion compounds are summarized in the review article [27]. Eight features are listed as follows: Tuning crystal field splitting (CFS); Bandgap control; Local degree of freedom; Local asymmetry; Bonding differentiation; Anion diffusion and reaction; Dimensional reduction; and Molecular anions. The important concepts for functional luminescent materials and examples in this dissertation are summarized in **Figure 1.3**.

i. **Tuning CFS.** The degenerated d levels of *TM* ions in the free-ion state are dispersed,

and the degree of CFS depends on the crystal field strength of the coordination polyhedron. For instance, in the regular octahedron with O_h symmetry, the d orbitals are split into t_{2g} and e_g orbitals. When one of the six coordinating anions is replaced by another type of anion, some symmetry elements are lost, and the degenerated t_{2g} and e_g levels are resolved, leading to the greater CFS. In the case of oxyhalide-tungstates, the five-fold square pyramid caused by the introduction of bigger Cl^- than O^{2-} shows different optical properties from the oxide-tungstates with six-fold octahedra (Chapter 9).

ii. **Bandgap control.** Unlike mono-anion compounds, it is relatively easy in mixed-anion compounds to control the energy level of the valence band top. Especially in the case of oxynitrides, the valence band top elevates because the valence band is mainly composed of N 2p orbitals. Thus, the Eu^{3+}-doped oxynitrides show the redshifted CT excitation bands due to the elevation of the valence band, resulting in the near-UV excitable Eu^{3+} red luminescence (Chapter 3, 4).

iii. **Local asymmetry.** It is possible to reduce the local symmetry by anion substitution. For instance, O_h symmetry of the regular octahedron is reduced into C_4 symmetry by one-anion substitution and into C_3 symmetry by three-anions substitution. In particular, the 4f-4f transition strength is drastically enhanced by the missing inversion center (Chapter 4).

iv. **Bonding differentiation.** The bonding nature between cation and anion (*i.e.,* ionic vs. covalent) influences the transition strength of specific transitions. The covalent Br^- coordination enhance Eu^{3+} deep-red luminescence at around 700 nm (Chapter 8).

Thus, the mixed-anion compounds are a promising strategy for the development of novel functional luminescent materials. Here, some examples of research on phosphors in various mixed-anion compounds are briefly introduced.

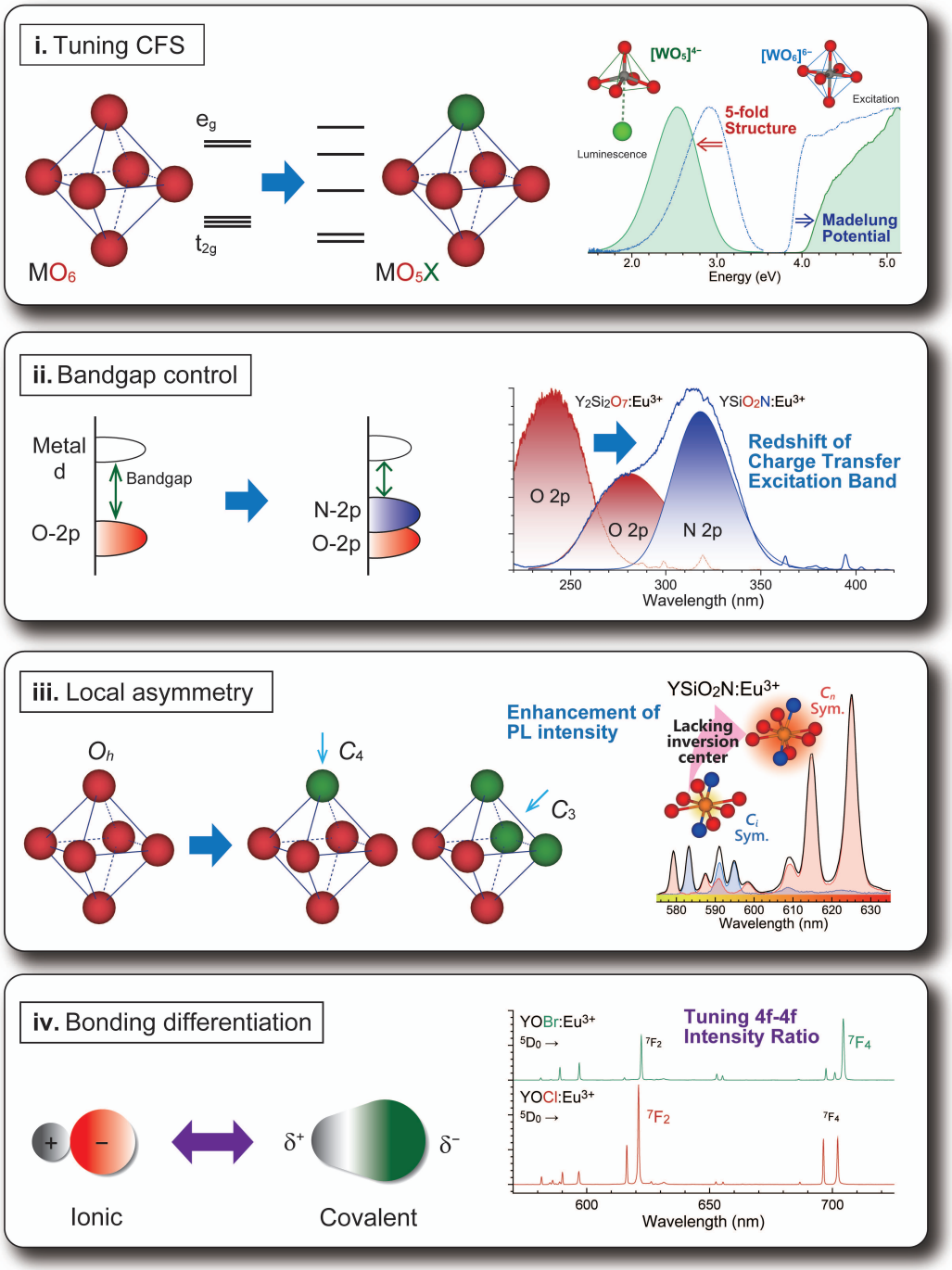

Figure 1.3. Expected features for mixed-anion-type luminescence materials, based on the concepts of functionalization of mixed-anion compounds suggested in the reference [27]. **i.** Extensive tuning of crystal field splitting (CFS). The large CFS brings about a redshift of the luminescence band. **ii.** Non-oxide anion with lower electronegativity (vs. oxide) in semiconductors raises the valence band top and narrows the bandgap. The charge transfer excitation energy for Eu^{3+}-doped materials lowered, depending on the electronegativity of ligands. **iii.** Local coordination asymmetry. The O_h symmetry of the regular octahedron is lost by replacing ligands. Lacking an inversion center enhances the 4f-4f luminescence intensity. **iv.** Covalency and ionicity can be turned to acquire desired functions, leading to variation of line strengths for specific 4f-4f transition.

1.2.1. Oxynitrides

Oxynitrides contain nitrogen and oxygen that are adjacent to each other on the periodic table of elements, in which each anion is in aliovalent N^{3-} and O^{2-} states. Nevertheless, because of the similar ionic radii of N^{3-} and O^{2-} ions, there are many reports on oxynitrides with a similar structure to oxides, accompanied by the proper charge compensation [28]. The more covalent bonding between N^{3-} and metal cations due to the small electronegativity of N leads to a number of stable oxynitrides in the ambient atmosphere. Many oxynitride materials, including α- and β-SiAlON [29–32], are utilized as the host compounds for practical and commercialized phosphors [33]. In order to prevent N desorption, oxynitride compounds are synthesized with a variety of methods, such as not only the conventional solid-state reaction but also the high-pressure synthesis [34–36], topochemical reaction [37], high-temperature ammonolysis [38], and nitridation reaction with solid nitriding agents [39], possibly leading to new functional luminescent materials.

The oxynitride phosphors activated with Ce^{3+} or Eu^{2+} tend to show luminescence with a longer wavelength than many oxide phosphors because of the nephelauxetic effect caused by covalent N^{3-} ions (as explained in detail in section 2.1.2.2). In other words, the higher polarizability the coordinating anions take, the larger the centroid shift of the 5d levels is. Since the polarizability of anions is correlated with the refractive index of the host materials, the materials with a high refractive index can show the largely redshifted Ce^{3+} or Eu^{2+} luminescence. The dipole polarizability of N is larger than that of O [40]. Thus, oxynitrides and nitrides are desirable host materials for LED phosphors with a large redshift of Ce^{3+}/Eu^{2+} luminescence [41].

In terms of the electronic structure, the bandgap of oxynitrides is smaller than that of oxides because the valence band top elevates due to the N 2p orbitals. In particular, the oxynitrides composed of transition metal ions with d^0 or d^{10} electronic configuration have a small bandgap of ~2.0 eV, resulting in a number of studies about visible-light-driven photocatalysts [27,42]. Such a small bandgap for photocatalysts is not suitable for phosphor materials because the localized energy levels of impurity ions are buried in the host bandgap, and the excited states are immediately quenched through the auto-ionization process.

Nevertheless, for other oxynitrides with only main-group or rare-earth elements, some unique luminescence properties of activators are expected by tuning to some extent the relative positions of impurity energy levels with respect to the host conduction and valence bands. The tunable valence band can bring about some unique properties, such as near-UV excitable Eu^{3+} luminescence [43] and Eu^{3+} persistent red luminescence through the hole trapping-detrapping scheme [44].

1.2.2. Oxyhalides

For many years, halides have been studied for phosphor materials due to the wide bandgap and their stabilities. In particular, researchers have focused on alkaline halides to investigate and understand the luminescence phenomena related to impurities and point defects. At the same time, some oxyhalides have been studied because it is not difficult to synthesis them. As examples of oxyhalides for the phosphor host, there are the rare-earth oxyhalide *RE*O*X* (*RE*: rare-earth, *X*: halogen) with the PbClF-type structure (space group: *P*4/*nmm*) [45], the halosilicates of $LaSiO_3Cl$ or $Ca_3SiO_4Cl_2$ [46–48], and the apatite-type halophosphates $Ca_{10}(PO_4)_6F_2$ or $Sr_{10}(PO_4)_6Cl_2$ [46,49]. The red luminescent $K_2Ca(PO_4)F:Eu^{2+}$ (fluorine oxygen ligand phosphor: FOLP) is reported as a practical phosphor [50]. The FOLP:Eu^{2+} with a new monoclinic structure (space group: $P2_1/m$) absorbs not blue but only near-UV light, leading to the quite large Stokes shift of 11130 cm^{-1}. The phosphor-converted LED device consisting of a near-UV LED chip and various phosphors, including FOLP, shows warm-white emission [50].

Halide anions X^- (X = F, Cl, Br, and I) has a smaller formal charge of monovalent −1 than the oxide anion O^{2-}. Cl^-, Br^-, and I^- ions have a smaller electronegativity than O^{2-}, while F^- takes a large electronegativity of 3.98 [51]. Because Cl^-, Br^-, and I^- ions have a large ionic radius [52], it is difficult to replace O^{2-} sites in oxides. Considering the Hard and Soft Acid and Base (HSAB) theory, Br^- and I^- ions, which are soft acids, tend to form bonding with soft bases, possibly resulting in a layered structure. These features in oxyhalides provide unique coordination environments formed by both X^- and O^{2-} ions. The *RE* sites in *RE*O*X* with the PbClF-type structure form the nine-fold monocapped square antiprism with five O^{2-} and four X^- ions [53]. The Y^{3+} sites in $Ba_3Y_2O_5Cl_2$ with the Ruddlesden-Popper phase (n = 2) form the five-fold square

pyramid $[YO_5]^{7-}$ because of the long interatomic distance between Y^{3+} and Cl^- ions [54]. These various coordination polyhedra can affect the 4f-4f and 5d-4f transition of *Ln* ions. The difference in the electronegativity or polarizability of X^- ions can induce the variation of transition strength for the 4f-4f transition [55]. Besides, a series of haloborate glass shows the unique body colors related to trapped X_2 molecules in the glass matrix [56]. Despite the fact that it has been extensively studied, further investigation into the luminescent and optical properties of oxyhalides is still required.

1.2.3. Oxysulfides

Oxysulfides have been utilized as phosphor hosts, leading to some practical materials. The important materials are $Y_2O_2S:Eu^{3+}$ and $La_2O_2S:Eu^{3+}$, which were used as the red phosphors for the cathode-ray tubes and brought about a revolutionary development in color television [57,58]. In recent, Murazaki *et al.* found out that the $Y_2O_2S:Eu^{3+}$-Mg^{2+}-Ti^{4+} phosphor show red persistent luminescence with duration over three hours [59]. For the Eu^{3+}-doped oxysulfides, the CT excitation bands are redshifted and located at the near-UV region of 320–380 nm because of the S 3p orbitals.

There are only a few reports of oxysulfide phosphors except for RE_2O_2S. Compared with oxynitrides, many oxysulfides are chemically unstable and easily react with moisture in the air. Although the O^{2-} and S^{2-} ions are isovalent, the isostructural oxysulfides with oxides cannot be obtained by replacing O^{2-} into S^{2-} ions because of the nonequivalent ionic radii (S^{2-}: 1.84 Å, O^{2-}: 1.38 Å) [52]. Due to their chemical and structural instability, oxysulfides require further material exploration for functional luminescent materials.

1.2.4. Oxyhydrides

In recent years, there has been an increasing number of reports about compounds containing hydride anions H^-. Hydrogen can be a monovalent anion with the same electronic configuration of $1s^2$ as He. For this reason, H is placed on F in the periodic table in Figure 1.1. Note that H undoubtedly is placed on Li in the periodic table of elements defined by IUPAC because H has an electron in the outer 1s orbital. H^- ions have unique features [27]; the size of H^- ions is

extraordinarily flexible because the number of electrons is quite small (only two); the H^- ions without any p orbitals show characteristic chemical bonding nature by preventing the π-bondings between molecular orbitals.

There are many reports about (oxy)hydride-type phosphors, which are introduced in detail in the review article by Kunkel [60]. Although many (oxy)hydrides are unstable in the ambient atmosphere, some are stable. The $Sr_2LiSiO_4H:Eu^{2+}$ phosphor shows the redshifted luminescence, compared with the isostructural oxyfluoride $Sr_2LiSiO_4F:Eu^{2+}$, because of the nephelauxetic effect caused by the covalent H^- ions [61,62]. For the GdHO:Tb^{3+} phosphor, the 5d-4f and CT excitation bands are located at the lower energy side than those for $Gd_2O_3:Tb^{3+}$ [63]. The redshift of the 5d excited states is explained by the nephelauxetic effect, and the redshifted CT band suggests that the contribution of H 1s orbital to the host valence band is more significant than that of O 2p orbitals. There are some reports about not only oxyhydride-type but also halohydride-type phosphors [64,65], and further research is expected in the near future.

1.2.5. Other Non-Oxide Type Compounds

Carbonitridesilicates $RE_2Si_4N_6C$, composed of the covalent $[SiN_3C]$ tetrahedral units, show high Debye temperatures and excellent mechanical and optical properties, which is expected for phosphor applications. In the star-shaped unit $[SiN_3]_4C$, the C^{4-} ions with the sp^3 hybridization bridge four tetrahedra. Although there are some reports about the luminescence properties of Ce^{3+}-doped $RE_2Si_4N_6C$ [66,67], in which the researchers have considered applications for LED phosphors, the quenching temperature is not so high as would be expected from the Debye temperature.

The PbClF-type structure is common for the mixed-anion compounds with monovalent and divalent anions when the cation is a trivalent rare-earth ion. To form this structure, the ratio of the ionic radius among the RE^{3+} ion and anions is important, resulting in the structure of some halochalcogenides. The fluorosulfide α-YFS has the PbClF-type structure, in which the Y^{3+} ions are coordinated by four F^- and five S^{2-} ions. The mixed-anion coordination with ionic F^- and covalent S^{2-} ions is interesting. The Ce^{3+}-doped α-YFS phosphor shows the unique deep-red

luminescence, which is not observed in other Ce^{3+}-doped compounds [68]. This deep-red luminescence is observed even at high temperatures (~500 K), assigned to the Ce^{3+}: 5d-4f transition. For the PbClF-type structure, it is possible to design the structure by inserting fluorite-type blocks in between, as in the case of layered perovskites [69].

There are more and more reports about phosphors containing molecular anions. For example, the $BaCN_2:Eu^{2+}$ phosphor, which includes the cyanamide ions CN_2^{2-}, shows the red luminescence because of the strong crystal field caused by the short Eu-N bonding [70]. Besides, Eu^{2+} luminescence in $BaCN_2$ is sensitive to the induced pressure because of the small bulk modulus [71]. Recently, the mixed-anion phosphor with O^{2-} and CN_2^{2-} ions was reported [72]. The CT excitation band for the $La_2O_2CN_2:Eu^{3+}$ phosphor is redshifted, resulting in the near-UV excitable Eu^{3+} red luminescence.

1.3. Purpose and Outline of This Dissertation

The purpose of this dissertation is to investigate how the unique electronic structure and local environment of various mixed-anion compounds affect the properties of the luminescence centers through spectroscopic measurements, and to characterize the luminescent properties in a complex manner by combining techniques such as crystal structure analysis and first-principle calculations. Ultimately, the goal is to apply them to innovative, world-changing functional luminescent materials.

In Chapter 1, the strategy of the selection of the luminescence centers and inorganic host materials to obtain the desirable luminescent materials is explained. Especially, the recent studies on mixed-anion phosphors are introduced.

In Chapter 2, the theoretical backgrounds, including the physics in the electronic transition between two states and the physical and electronic structures of the inorganic host materials, are overviewed to understand this dissertation.

In Chapter 3, the Eu^{3+}-doped oxynitride phosphor, $YSiO_2N:Eu^{3+}$, was synthesized by the solid-state reaction method, and its luminescence properties were characterized by the Judd-Ofelt analysis. Because of N 2p orbitals, the CT excitation band of the $YSiO_2N:Eu^{3+}$ phosphor

was located at the near-UV region in 300–340 nm, leading to the near-UV excitable Eu^{3+} luminescence peaking at 626 nm. The results of the Judd-Ofelt analysis reveal that the oxynitride coordination [$Eu^{3+}O_6N_2$] drastically enhances the hypersensitive Eu^{3+} luminescence in the $YSiO_2N$ host.

In Chapter 4, the relationship between the luminescence properties of Eu^{3+} ions and the local environments of the Eu^{3+} sites was investigated with site-selective and time-resolved spectroscopy. The single-crystal X-ray and neutron diffraction reveal that the prepared $YSiO_2N$ has the new monoclinic *C*2/*c* structure, in which there are five nonequivalent Y^{3+} sites. In terms of centrosymmetry, the Y^{3+} sites are divided into two groups; C_n sites and C_i sites. The Eu^{3+} luminescence properties in the C_n and C_i sites were characterized, and the results suggest that thermal distortion from centrosymmetry induces the electronic dipole transition, resulting in a shorter luminescence lifetime.

In Chapter 5, the anomalous deep-red to near-infrared luminescence in the $YSiO_2N:Eu^{2+/3+}$ sample was characterized at low temperatures. The X-ray absorption spectroscopy reveals that almost half of Eu ions were in the divalent state in the prepared sample. The detailed spectroscopic results conclude that the anomalous luminescence is attributed to the recombination emission related to the Eu^{2+}-trapped exciton states in the $YSiO_2N$ host.

In Chapter 6, the Ce^{3+}-doped $YSiO_2N$ sample was prepared, and the energy level structure of the Ce^{3+} 5d states is discussed by the characterization of the luminescence properties at 4–600 K. The excitation spectra reveal that the centroid shift and crystal field splitting of Ce^{3+}: 5d levels in the [YO_6N_2] dodecahedra are 2.24 and 1.69 eV, respectively.

In Chapter 7, the vacuum referred binding energy (VRBE) diagram for the $YSiO_2N$ host was constructed by the experimental spectroscopic data, indicating that Sm^{3+} or Tm^{3+} co-doping to the $YSiO_2N:Ce^{3+}$ phosphor can cause the Ce^{3+} persistent luminescence by the electron trapping-detrapping scheme. The persistent luminescence properties of the prepared $YSiO_2N:Ce^{3+}$-Ln^{3+} (*Ln* = Sm, Tm) samples were characterized. The carrier trap distributions of the samples were revealed by the thermoluminescence glow curve analyses with the initial rise method.

In Chapter 8, the Eu^{3+}-doped oxyhalide YO*X* (*X* = Cl, Br) were prepared, and the influence of the oxyhalide coordination on their Eu^{3+} luminescence properties is discussed based on the results of the Judd-Ofelt analysis. The covalent Br^- ions largely affected the Judd-Ofelt intensity parameter Ω_4, resulting in the intense Eu^{3+}: $^5D_0 \rightarrow {}^7F_4$ luminescence at around 700 nm.

In Chapter 9, the CT luminescence of the five-fold square pyramid $[WO_5]^{4-}$ in the oxychloride host $Ca_3WO_5Cl_2$ was characterized, and its luminescence mechanism is discussed by using the energy level diagram obtained by *ab initio* molecular orbital and configuration interaction calculation. The luminescence and absorption energies of the CT transition in the $[WO_5]^{4-}$ were lower and higher, respectively, than that of the $[WO_6]^{6-}$ octahedron in the oxide Ca_3WO_6. The Madelung potential related to Cl^- ions in the lattice shifted the CT states in the $[WO_5]^{4-}$ to the high energy. On the other hand, it is suggested that the large structural relaxation of the excited CT states in the five-fold polyhedron brings about the redshift of luminescence.

In Chapter 10, the new synthesis route of the MgB_4O_7:Ce^{3+}-Li^+ ceramics is proposed for the optically stimulated luminescence dosimetry application. By annealing the magnesium borate glass over 700 ºC, the glass-ceramic MgB_4O_7:Ce^{3+}-Li^+ samples were successfully obtained. The dosimetric properties of the glass-ceramic MgB_4O_7:Ce^{3+}-Li^+ were comparable to the commercial optically stimulated dosimeter Al_2O_3:C.

References

[1] T. Minamikawa, T. Koma, A. Suzuki, T. Mizuno, K. Nagamatsu, H. Arimochi, K. Tsuchiya, K. Matsuoka, T. Yasui, K. Yasutomo, M. Nomaguchi, "Quantitative evaluation of SARS-CoV-2 inactivation using a deep ultraviolet light-emitting diode". *Sci. Rep.* **11** (2021) 5070 (9p).

[2] V. Rajendran, H. Chang, R.-S. Liu, "(INVITED) Recent progress on broadband near-infrared phosphors-converted light emitting diodes for future miniature spectrometers". *Opt. Mater. X.* **1** (2019) 100011 (11p).

[3] K. Nassau, "The Physics and Chemistry of Color". (John Wiley & Sons, New York, 2001)

[4] H. Kamimura, S. Sugano, Y. Tanabe, "Ligand Field Theory and Its Applications". (Shokabo, Takyo, 1969, *in Japanese*)

[5] M.G. Brik, C.-G. Ma, "Theoretical Spectroscopy of Transition Metal and Rare Earth Ions From Free State to Crystal Field". (Jenny Stanford Publishing, Singapore, 2020)

[6] K. Bando, K. Sakano, Y. Noguchi, Y. Shimizu, "Development of High-bright and Pure-white LED Lamps". *J. Light Visual Environ.* **22** (1998) 2–5.

[7] J. Ueda, S. Tanabe, "(INVITED) Review of luminescent properties of Ce^{3+}-doped garnet phosphors: New insight into the effect of crystal and electronic structure". *Opt. Mater. X.* **1** (2019) 100018 (19p).

[8] J.E. Geusic, H.M. Marcos, L.G. Van Uitert, "Laser Oscillations in Nd-Doped Yttrium Aluminum, Yttrium Gallimu and Gadolinium Garnets". *Appl. Phys. Lett.* **4** (1964) 182–184.

[9] J. Hecht, "Short history of laser development". *Organ. Ethic.* **49** (2010) 091002 (23p).

[10] R.J. Mears, L. Reekie, I.M. Jauncey, D.N. Payne, R.J. Mears, "Low-noise erbium-doped fiber amplifier operating at 1.54 μm". *Electron. Lett.* **23** (1987) 1026–1028.

[11] M. Nakazawa, Y. Kimura, K. Suzuki, "Efficient Er^{3+}-doped optical fiber amplifier pumped by a 1.48 μm InGaAsP laser diode". *Appl. Phys. Lett.* **54** (1989) 295–297.

[12] S. Tanabe, "Glass and Rare-Earth Elements: A Personal Perspective". *Int. J. Appl. Glass Sci.* **6** (2015) 305–328.

[13] T. Matsuzawa, Y. Aoki, N. Takeuchi, Y. Murayama, "A New Long Phosphorescent Phosphor with High Brightness, $SrAl_2O_4$:Eu^{2+},Dy^{3+}". *J. Electrochem. Soc.* **143** (1996) 2670–2673.

[14] J. Xu, S. Tanabe, "Persistent luminescence instead of phosphorescence: History, mechanism, and perspective". *J. Lumin.* **205** (2019) 581–620.

[15] G.B. Haxel, J.B. Hedrick, G.J. Orris, "Rare Earth Elements-Critical Resources for High Technology". *U.S. Geological Survey Fact Sheet*. **87** (2002) 02 (4p).

[16] Y. Takaya, K. Yasukawa, T. Kawasaki, K. Fujinaga, J. Ohta, Y. Usui, K. Nakamura, J.-I. Kimura, Q. Chang, M. Hamada, G. Dodbiba, T. Nozaki, K. Iijima, T. Morisawa, T. Kuwahara, Y. Ishida, T. Ichimura, M. Kitazume, T. Fujita, Y. Kato, "The tremendous potential of deep-sea mud as a source of rare-earth elements". *Sci. Rep.* **8** (2018) 5763 (8p).

[17] K. Yasukawa, J. Ohta, T. Miyazaki, B.S. Vaglarov, Q. Chang, K. Ueki, C. Toyama, J.-I. Kimura, E. Tanaka, K. Nakamura, K. Fujinaga, K. Iijima, H. Iwamori, Y. Kato, "Statistic and Isotopic Characterization of Deep-Sea Sediments in the Western North Pacific Ocean: Implications for Genesis of the Sediment Extremely Enriched in Rare Earth Elements". *Geochem. Geophys. Geosyst.* **20** (2019) 3402–3430.

[18] R.W. Pohl, "Electron conductivity and photochemical processes in alkali-halide crystals". *Proc. Phys. Soc. London.* **49** (1937) 3–31.

[19] F. Seitz, "Interpretation of the Properties of Alkali Halide-Thallium Phosphors". *J. Chem. Phys.* **6** (1938) 150–162.

[20] A. Ranfagni, D. Mugnai, M. Bacci, G. Viliani, M.P. Fontana, "The optical properties of thallium-like impurities in alkali-halide crystals". *Adv. Phys.* **32** (1983) 823–905.

[21] M. Back, J. Ueda, J. Xu, K. Asami, L. Amidani, E. Trave, S. Tanabe, "Uncovering the Origin of the Emitting States in Bi^{3+}-Activated $CaMO_3$ (M = Zr, Sn, Ti) Perovskites: Metal-To-Metal Charge Transfer Versus s−p Transitions". *J. Phys. Chem. C.* **123** (2019) 14677–14688.

[22] A. Krasnikov, E. Mihokova, M. Nikl, S. Zazubovich, Y. Zhydachevskyy, "Luminescence Spectroscopy and Origin of Luminescence Centers in Bi-Doped Materials". *Crystals.* **10** (2020) 208 (53p).

[23] C.K. Jørgensen, R. Reisfeld, "Uranyl photophysics". In: *Topics Inorg. Phys. Chem., Structure and Bonding.* 50 (1982) 121–171. (Springer, Heidelberg)

[24] M.L. Moreau-Colin, "Electronic spectra and structural properties of complex tetracyanides of platinum, palladium and nickel" *Structure and Bonding*. 10 (1972) 167–190. (Springer, Heidelberg)

[25] W.M. Yen, S. Shionoya, H. Yamamoto, "PHOSPHOR HANDBOOK". (second ed., CRC Press, Boca Raton, 2007)

[26] G.H. Dieke, H.M. Crosswhite, B. Dunn, "Emission Spectra of the Doubly and Triply Ionized Rare Earths". *J. Opt. Soc. Am*. **51** (1961) 820–827.

[27] H. Kageyama, K. Hayashi, K. Maeda, J.P. Attfield, Z. Hiroi, J.M. Rondinelli, K.R. Poeppelmeier,

"Expanding frontiers in materials chemistry and physics with multiple anions". *Nat. Commun.* **9** (2018) 772 (15p).

[28] H. Kageyama, H. Ogino, T. Hasegawa, "Science of Mixed-Anion Compounds". (Maruzen Publishing, Tokyo, 2021. *in Japanese*)

[29] J.W.H. van Krevel, J.W.T. van Rutten, H. Mandal, H.T. Hintzen, R. Metselaar, "Luminescence properties of terbium-, cerium-, or europium-doped α-sialon materials" *J. Solid State Chem.* **165** (2002) 19–24.

[30] K.H. Jack, "Sialons and related nitrogen ceramics" *J. Mater. Sci.* **11** (1976) 1135–1158.

[31] R.-J. Xie, M. Mitomo, K. Uheda, F.-F. Xu, Y. Akimune, "Preparation and luminescence spectra of calcium- and rare-earth (R = Eu, Tb, and pr)-codoped α-SiAlON ceramics" *J. Am. Ceram. Soc.* **85** (2004) 1229–1234.

[32] R.-J. Xie, N. Hirosaki, H.-L. Li, Y.Q. Li, M. Mitomo, "Synthesis and Photoluminescence Properties of β-sialon:Eu^{2+} ($Si_{6-z}Al_zO_zN_{8-z}$:Eu^{2+}): A Promising Green Oxynitride Phosphor for White Light-Emitting Diodes". *J. Electrochem. Soc.* **154** (2007) J314–J319.

[33] L. Wang, R.-J. Xie, T. Suehiro, T. Takeda, N. Hirosaki, "Down-Conversion Nitride Materials for Solid State Lighting: Recent Advances and Perspectives". *Chem. Rev.* **118** (2018) 1951–2009.

[34] E. Soignard, D. Machon, P.F. McMillan, J. Dong, B. Xu, K. Leinenweber, "Spinel-Structured Gallium Oxynitride (Ga_3O_3N) Synthesis and Characterization: An Experimental and Theoretical Study". *Chem. Mater.* **17** (2005) 5465–5472.

[35] B.J. Adamczyk, D. Poelman, K. Korthout, D. Michalik, T. Pawlik, M. Sopicka-Lizer, "Role of pressure in stabilization of oxynitride phosphor synthesis". *Appl. Phys. A: Mater. Sci. Process.* **127** (2021) 500 (8p).

[36] Q.-Q. Zhu, L. Wang, N. Hirosaki, L.Y. Hao, X. Xu, R.-J. Xie, "Extra-broad band orange-emitting Ce^{3+}-doped $Y_3Si_5N_9O$ phosphor for solid-state lighting: Electronic, crystal structures and luminescence properties". *Chem. Mater.* **28** (2016) 4829–4839.

[37] N. Masuda, Y. Kobayashi, O. Hernandez, T. Bataille, S. Paofai, H. Suzuki, C. Ritter, N. Ichijo, Y. Noda, K. Takegoshi, C. Tassel, T. Yamamoto, H. Kageyama, "Hydride in $BaTiO_{2.5}H_{0.5}$: A Labile Ligand in Solid State Chemistry". *J. Am. Chem. Soc.* **137** (2015) 15315–15321.

[38] S.G. Ebbinghaus, H.-P. Abicht, R. Dronskowski, T. Müller, A. Reller, A. Weidenkaff, "Perovskite-related oxynitrides – Recent developments in synthesis, characterization and investigations of physical properties". *Prog. Solid State Chem.* **37** (2009) 173–205.

[39] T. Sakata, R. Yoshiyuki, R. Okada, S. Urushidani, N. Tarutani, K. Katagiri, K. Inumaru, K. Koyama,

Y. Masubuchi, "Environmentally Benign Synthesis and Color Tuning of Strontium-Tantalum Perovskite Oxynitride and Its Solid Solutions". *Inorg. Chem.* **60** (2021) 4852–4859.

[40] P. Schwerdtfeger, J.K. Nagle, "2018 Table of static dipole polarizabilities of the neutral elements in the periodic table". *Mol. Phys.* **117** (2019) 1200–1225.

[41] M. Mikami, "Computational Chemistry Approach for White LED (Oxy)Nitride Phosphors". *ECS J. Solid State Sci. Technol.* **2** (2013) R3048–R3058.

[42] K. Maeda, K. Domen, "Oxynitride materials for solar water splitting". *MRS Bull.* **36** (2011) 25–31.

[43] Y. Kitagawa, J. Ueda, M.G. Brik, S. Tanabe, "Intense hypersensitive luminescence of Eu^{3+}-doped $YSiO_2N$ oxynitride with near-UV excitation". *Opt. Mater.* **83** (2018) 111–117.

[44] H. Luo, A.J.J. Bos, P. Dorenbos, "Controlled Electron–Hole Trapping and Detrapping Process in $GdAlO_3$ by Valence Band Engineering". *J. Phys. Chem. C.* **120** (2016) 5916–5925.

[45] G. Blasse, A. Bril, "Fluorescence of Eu^{3+}-Activated Lanthanide Oxyhalides LnOX". *J. Chem. Phys.* **46** (1967) 2579–2582.

[46] W.M. Yen, M.J. Weber, "Inorganic Phosphors: Compositions, Preparation and Optical Properties". (CRC Press, Boca Raton, 2004.)

[47] W. Lehmann, T.J. Isaacs, "Lanthanum and Yttrium Halo-Silicate Phosphors". *J. Electrochem. Soc.* **125** (1978) 445–448.

[48] W.L. Wanmaker, J.G. Verriet, "Luminescence of Phosphors with $Ca_3SiO_4Cl_2$". *Philips Res. Repts.* **28** (1973) 80–83.

[49] H.G. Jenkins, A.H. McKeag, P.W. Ranby, "Alkaline Earth Halophosphates and Related Phosphors". *J. Electrochem. Soc.* **96** (1949) 1–12.

[50] H. Daicho, Y. Shinomiya, K. Enomoto, A. Nakano, H. Sawa, S. Matsuishi, H. Hosono, "A novel red-emitting $K_2Ca(PO_4)F:Eu^{2+}$ phosphor with a large Stokes shift". *Chem. Commun.* **54** (2018) 884–887.

[51] A.L. Allred, "Electronegativity values from thermochemical data". *J. Inorg. Nucl. Chem.* **17** (1961) 215–221.

[52] R.D. Shannon, "Revised effective ionic radii and systematic studies of interatomic distances in halides and chalcogenides". *Acta Crystallogr. A.* **32** (1976) 751–767.

[53] F.A. Bannister, "The crystal-structure and optical properties of matlockite (PbFCl)". *Mineral. Mag.* **23** (1934) 587–597.

[54] Y. Iwasa, Y. Su, Y. Tsuchiya, M. Tatsuda, K. Kishio, T. Yanagida, F. Takada, T. Nishio, Y. Tsujimoto, K. Fujii, M. Yashima, H. Ogino, "Synthesis, structure, and luminescence properties of layered oxychloride $Ba_3Y_2O_5Cl_2$". *J. Mater. Chem*. **8** (2020) 17162–17168.

[55] Y. Kitagawa, J. Ueda, K. Arai, H. Kageyama, S. Tanabe, "Difference of Eu^{3+} luminescent properties in YOCl and YOBr oxyhalide hosts". *J. Appl. Phys*. **129** (2021) 183104 (11p).

[56] K. Kusuki, "Luminescence by 4f-4f Transition in Lanthanoid ion-doped Mixed-Anion Compounds". (Master's Thesis in Kyoto University, 2021, *in Japanese*)

[57] O.J. Sovers, T. Yoshioka, "Fluorescence of Trivalent-Europium-Doped Yttrium Oxysulfide". *J. Chem. Phys*. **49** (1968) 4945–4954.

[58] A. Abdel-Kader, M.M. Elkholy, "Cathodoluminescence emission spectra of trivalent europium-doped yttrium oxysulphide". *J. Mater. Sci.* **27** (1992) 2887–2895.

[59] Y. Murazaki, K. Arai, K. Ichinomiya, "New red super long persistence phosphor". *J. Illum. Engng. Inst. Jpn*. **35** (1999) 41–45. (*in Japanese*)

[60] N. Kunkel, T. Wylezich, "Recent Advances in Rare Earth-Doped Hydrides". *Z. Anorg. Allg. Chem*. **645** (2019) 137–145.

[61] F. Gehlhaar, R. Finger, N. Zapp, M. Bertmer, H. Kohlmann, "$LiSr_2SiO_4H$, an Air-Stable Hydride as Host for Eu(II) Luminescence". *Inorg. Chem.* **57** (2018) 11851–11854.

[62] T. Wu, A. Ishikawa, T. Honda, H. Tamatsukuri, K. Ikeda, T. Otomo, S. Matsuishi, "Nephelauxetic effect of the hydride ligand in Sr_2LiSiO_4H as a host material for rare-earth-activated phosphors". *RSC Adv.* **9** (2019) 5282–5287.

[63] J. Ueda, S. Matsuishi, T. Tokunaga, S. Tanabe, "Preparation, electronic structure of gadolinium oxyhydride and low-energy 5d excitation band for green luminescence of doped Tb^{3+} ions". *J. Mater. Chem*. **6** (2018) 7541–7548.

[64] D. Rudolph, T. Wylezich, A.D. Sontakke, A. Meijerink, P. Goldner, P. Netzsch, H.A. Höppe, N. Kunkel, T. Schleid, "Synthesis and optical properties of the Eu^{2+}-doped alkaline-earth metal hydride chlorides $AE_7H_{12}Cl_2$ (*AE* = Ca and Sr)". *J. Lumin*. **209** (2019) 150–155.

[65] A. Mutschke, T. Wylezich, A.D. Sontakke, A. Meijerink, M. Hoelzel, N. Kunkel, "$MCaH_xF_{3-x}$ (M = Rb, Cs): Synthesis, structure, and bright, site-sensitive tunable Eu^{2+} luminescence". *Adv. Opt. Mater.* **9** (2021) 2002052 (10p).

[66] C. Yan, Z. Liu, W. Zhuang, R. Liu, X. Xing, Y. Liu, G. Chen, Y. Li, X. Ma, "$YScSi_4N_6C:Ce^{3+}$ - A Broad Cyan-Emitting Phosphor to Weaken the Cyan Cavity in Full-Spectrum White Light-Emitting Diodes". *Inorg. Chem*. **56** (2017) 11087–11095.

[67] A.C. Duke, M. Hermus, J. Brgoch, "Structure Transformation and Cerium-Substituted Optical Response across the Carbonitridosilicate Solid Solution $(La_{\delta}Y_{1-\delta})_2Si_4N_6C$ (δ = 0-0.5)". *Inorg. Chem.* **57** (2018) 519–527.

[68] Y.-C. Wu, Y.-C. Chen, D.-Y. Wang, C.-S. Lee, C.-C. Sun, T.-M. Chen, "α-(Y,Gd)FS:Ce^{3+}: a novel red-emitting fluorosulfide phosphor for solid-state lighting". *J. Mater. Chem.* **21** (2011) 15163–15166.

[69] S.-N. Chen, T.-M. Chen, "Luminescence and spectroscopic studies of $(Y_{0.99}Ce_{0.01})_3OF_3S_2$: A new orange yellow-emitting oxyfluorosulfide phosphor for LEDs". *J. Chin. Chem. Soc.* **60** (2013) 961–964.

[70] Y. Masubuchi, S. Nishitani, A. Hosono, Y. Kitagawa, J. Ueda, S. Tanabe, H. Yamane, M. Higuchi, S. Kikkawa, "Red-emission over a wide range of wavelengths at various temperatures from tetragonal $BaCN_2$:Eu^{2+}". *J. Mater. Chem.* **6** (2018) 6370–6377.

[71] Y. Masubuchi, S. Nishitani, S. Miyazaki, H. Hua, J. Ueda, M. Higuchi, S. Tanabe, "Large redshift of luminescence from $BaCN_2$:Eu^{2+} red phosphor under high pressure". *Appl. Phys. Express.* **13** (2020) 042009 (3p).

[72] R. Okada, K. Kawanishi, K. Katagiri, K. Inumaru, "Ammonolysis-free synthesis of $La_2O_2CN_2$ by cyanamidation of $La(OH)_3$ using urea, and its photoluminescence properties". *Ceram. Int.* **45** (2019) 9325–9329.

Chapter 2

Theoretical Background

Abstract

In this chapter, the fundamentals of luminescence phenomena discussed in this dissertation are overviewed briefly. First, the optical absorption and emission processes caused by the interaction between matter and light are illustrated from a quantum mechanical point of view. The introduced Fermi's golden rule plays an important role in discussing the transition probability. The 4f-5d and 4f-4f transitions in lanthanoid ions show the characteristic features due to the difference in the nature of 4f and 5d orbitals. Despite the electric dipole forbidden character, the 4f-4f transition takes a high transition probability in the odd-parity field, which is explained by the Judd-Ofelt theory. The luminescence phenomena, related not to the intrinsic transition in lanthanoid ions but to the charge transfer and exciton states, are discussed. As the characters of host materials provide unique luminescence properties, the point groups in crystals and the band structure are illustrated. The local structure around *Ln* ions is characterized by the thirty-two point groups in terms of symmetrical operations. The band structure for the luminescent materials activated with lanthanoid ions is described by the vacuum referred binding energy diagram, which is very useful to predict the luminescence properties and discuss the luminescence mechanisms.

2.1. Theory of Electronic Transition for Luminescence

There are two types of light-emitting phenomena in solids; black-body radiation and luminescence. Whereas black-body radiation is the thermal emission of photons leading to visible to near-infrared emission over a few thousand kelvins, luminescence usually takes place on the solids at ambient temperature, not accompanied by heat emission. Luminescence is observed when excited *centers* (or *activators*) in solids, such as impurity ions, vacancies, and other point defects, are relaxed down into the stable states. In this section, the electronic transition related to luminescence is described with a quantum mechanical illustration. Some important textbooks are referred to for writing this chapter [1–4].

2.1.1. Electronic Transition in Dielectric Materials

2.1.1.1. Optical Electronic Transition

In quantum mechanics, localized electrons in ions or molecules have discrete energy levels. The optical absorption and emission processes in ions/molecules are regarded as the electronic transition between two levels for $|n>$ and $|m>$ states. **Figure 2.1** depicts the optical processes between two levels; absorption and emission. In Figure 2.1a, the transition from the n to m state is induced by absorption of light with the energy of $(E_m - E_n)$. Since the light is quantized as a photon, this energy is denoted as $h\nu_{nm}$. Here, h and ν are the Planck constant and frequency, respectively. The opposite phenomenon of absorption is *stimulated emission*, depicted in Figure 2.1b. For the stimulated emission, the electronic transition is induced by light, resulting in the light intensity that is proportional to the number of electrons in the state $|m>$. It is necessary that the population inversion is formed to obtain intense emission, in which the number of electrons in the excited states is larger than that in the ground states. The population inversion is the basis of light amplification by stimulated emission of radiation (laser). On the other hand, the light emission also takes place without any stimulation, which is *spontaneous emission*. Both stimulated and spontaneous emission processes are characterized by the photon energy of $h\nu_{mn}$.

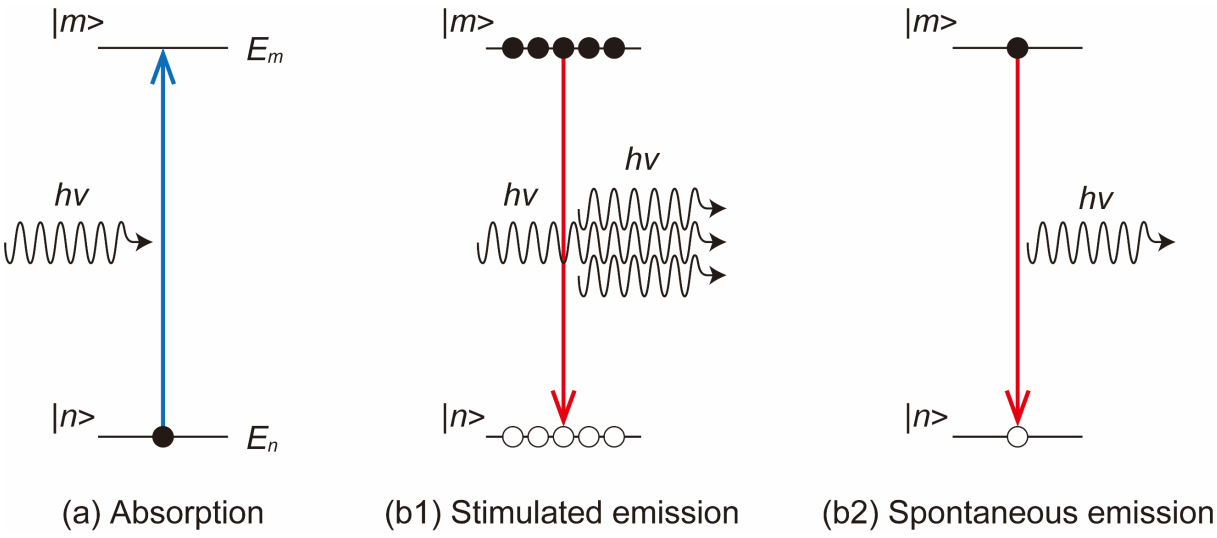

Figure 2.1. Two levels scheme for (a) absorption, (b1) stimulated emission, and (b2) spontaneous emission processes. The black and white circles represent the electrons and holes, respectively.

2.1.1.2. Semi-Classical Theory of Optical Transition

First, the transition probabilities of light absorption and emission are discussed by using a semi-classical model that treats matter quantumly and light classically. The time-dependent Schrödinger equation is as follows;

$$\hat{H}\Psi(\boldsymbol{R},t) = i\hbar\frac{\partial\Psi(\boldsymbol{R},t)}{\partial t}, \tag{2.1}$$

where $\hbar$ is the Dirac constant (= $h/2\pi$). If the Hamiltonian $\hat{H}$ does not depend on time t, the wavefunction of the steady-state m can be divided into temporal and spatial parts and described with the eigenfunction of $|m\rangle \equiv \varphi_m(\boldsymbol{R})$ and the eigenenergy of W_m for the Hamiltonian $\hat{H}_0$;

$$\Psi_m(\boldsymbol{R},t) = \exp\left(\frac{-iW_m t}{\hbar}\right)|m\rangle. \tag{2.2}$$

Here, the effect of the interaction between the dielectric materials and light with an angular frequency ω is introduced as a perturbation term $\hat{H}'$ because the interaction energy is usually very small;

$$\hat{H} = \hat{H}_0 + \hat{H}'. \tag{2.3}$$

The wavefunction $\Psi_m(\boldsymbol{R}, t)$ is no longer the eigenfunction of $\hat{H}$. The interaction between matter and light is usually very small, and then it is treated as a perturbation term. The eigenfunction $\Psi(\boldsymbol{R}, t)$ of $\hat{H}$ is described by a linear combination of eigenfunctions of $\hat{H}_0$ as follows;

$$\Psi(\boldsymbol{R},t)=\sum_n b_n(t)\,\Psi_n(\boldsymbol{R},t). \tag{2.4}$$

Here, $|b_n(t)|^2$ is interpreted as the probability density that electrons are in state n, and the summation of $|b_n(t)|^2$ is unity according to the normalization condition. By applying eqs. 2.3 and 2.4 in eq. 2.1, multiplying $\Psi_m^*(\boldsymbol{R}, t)$ from the left side, and integrating with $\boldsymbol{R}$, the Schrödinger equation is rewritten below;

$$i\hbar\frac{\partial b_m(t)}{\partial t}=\sum_n b_n(t)\,H_{mn}{}'\exp(i\omega_{mn}t)\,, \tag{2.5}$$

where $H_{mn}' = \langle m|\hat{H}|n\rangle$ and $\omega_{mn} = (W_m - W_n)/\hbar$ are given.

When an electric field $\boldsymbol{E}$ is induced to atoms, the interaction energy is expressed as $\sum_i e\boldsymbol{r}_j \cdot \boldsymbol{E}$, where $\boldsymbol{r}_j$ is the coordinate of the j-th electron with respect to the nuclei. Since the wavelength of light is large enough for the size of an atom, the location-dependence of the photoelectric field in an atom can be negligible (so-called *the electric dipole approximation*). The interaction energy caused by light irradiation with the angular frequency ω is given;

$$\hat{H}' = -\widehat{\boldsymbol{M}}\cdot\boldsymbol{E}_0\cos\omega t = -\hat{\mu}E_0\cos\omega t. \tag{2.6}$$

$\widehat{\boldsymbol{M}}=\sum_j e\boldsymbol{r}_j$ is the electric dipole (ED) momentum of an atom, and $\hat{\mu}$ is the magnitude of the component in the electric field direction. One can treat them as quantum mechanical operators, whereas the electric field E_0 is treated as a variable; *i.e.*, matter and light are treated in quantum and classical theories, respectively.

The probability density $|b_n(t)|^2$ depends on time t, indicating that the electron transfer between different states (*i.e.*, transition) takes place. The probability that an electron in state n at time 0 is found in state m at time t under light illumination with constant intensity is discussed. First, the eigenfunction in state m $b_m(t)$ is described by using eqs. 2.5 and 2.6 as follows;

$$b_m(t)=\left(\frac{\boldsymbol{M}_{mn}\cdot\boldsymbol{E}_0}{2\hbar}\right)\left[\frac{e^{i(\omega_{mn}+\omega)t}-1}{\omega_{mn}+\omega}+\frac{e^{i(\omega_{mn}-\omega)t}-1}{\omega_{mn}-\omega}\right]. \tag{2.7}$$

This equation corresponds to Bohr's condition; that is, the first and second terms on the right side correspond to light emission and absorption, respectively. In the case of absorption, the probability density is given by ignoring the first term with $\omega_{mn} \approx \omega$;

$$|b_m(t)|^2 = \frac{|\boldsymbol{M}_{mn} \cdot \boldsymbol{E}_0|^2}{\hbar^2} \frac{\sin^2 \left\{ (\omega_{mn} - \omega)t/2 \right\}}{(\omega_{mn} - \omega)^2}, \tag{2.8}$$

for which the following relationship can be applied,

$$\frac{1}{\pi} \lim_{t \to \infty} \frac{\sin^2 \left\{ (\omega_{mn} - \omega)t/2 \right\}}{(\omega_{mn} - \omega)^2 t/2} = \delta(\omega_0 - \omega), \tag{2.9}$$

and then,

$$|b_m(t)|^2 = \frac{\pi}{2\hbar^2} |\boldsymbol{M}_{mn} \cdot \boldsymbol{E}_0|^2 t \delta(\omega_{mn} - \omega). \tag{2.10}$$

The probability $|b_m(t)|^2$ that electrons are found in state m is proportional to time t. Therefore, the transition probability w_{mn} is given as follows,

$$w_{mn} = \frac{\mathrm{d}|b_m(t)|^2}{\mathrm{d}t} = \frac{\pi}{2\hbar^2} |\boldsymbol{M}_{mn} \cdot \boldsymbol{E}_0|^2 \delta(\omega_{mn} - \omega). \tag{2.11}$$

As expected, the transition probability is proportional to illuminated light intensity. Here, $\delta(\omega_0 - \omega)$ is the delta function, which is zero when ω is not ω_0 and satisfies the following integrals;

$$\begin{aligned} \int \delta(\omega_0 - \omega) \mathrm{d}\omega &= 1, \\ \int F(\omega) \delta(\omega_0 - \omega) \mathrm{d}\omega &= F(\omega_0). \end{aligned} \tag{2.12}$$

The delta function has no width, leading to just a line. As the spectral line usually has a certain width, the spectral shape is expressed by a given function $f(\omega)$ that satisfy the normalized condition; $\int f(\omega) \mathrm{d}\omega = 1$. Besides, the average energy of illuminated light per unit volume is set to ρ_ω. If the matter is dilute and takes the permittivity ε_0, the ρ_ω is calculated to be $\varepsilon_0 |\boldsymbol{E}_0|^2/2$. The transition probability in eq. 2.11 becomes;

$$\begin{aligned} w_{mn} &= \int \frac{\pi |\boldsymbol{M}_{mn}|^2}{6\hbar^2} \frac{2\rho_\omega}{\varepsilon_0} f(\omega_{mn}) \delta(\omega_{mn} - \omega) \mathrm{d}\omega_{mn} \\ &= \frac{\pi |\boldsymbol{M}_{mn}|^2}{3\varepsilon_0 \hbar^2} f(\omega_{mn}) \rho_\omega = B_{mn} f(\omega) \rho_\omega. \end{aligned} \tag{2.13}$$

Here, $|\boldsymbol{M}_{mn} \cdot \boldsymbol{E}_0|^2$ is replaced by $|\boldsymbol{M}_{mn}|^2 |\boldsymbol{E}_0|^2/3$ because $\cos^2\theta$ is 1/3 by averaging over all directions in three-dimensional space. In the same way, the transition probability of induced light emission w_{nm} is also calculated. The probabilities for the $m \leftarrow n$ and $m \rightarrow n$ transition are equal, and the following equation is obtained;

$$B_{nm} = \frac{\pi |\boldsymbol{M}_{nm}|^2}{3\varepsilon_0 \hbar^2} = B_{mn}. \tag{2.14}$$

Note that the n and m states in eq. 2.14 do not degenerate. Taking the degeneracy of the n (g_n-fold) and m (g_m-fold) states into account, eq. 2.14 can be generalized as follows;

$$\begin{aligned} B_{mn} &= \frac{g_m \pi |\boldsymbol{M}_{mn}|^2}{3\varepsilon_0 \hbar^2}, \\ B_{nm} &= \frac{g_n \pi |\boldsymbol{M}_{nm}|^2}{3\varepsilon_0 \hbar^2}. \end{aligned} \tag{2.15}$$

B_{mn} and B_{nm} are *Einstein's B-coefficients* of stimulated emission and optical absorption processes.

In the framework of the semi-classical theory, the spontaneous emission does not appear in eq. 2.7. In order to understand the transition probability of spontaneous emission, one has to consider the thermodynamic equilibrium described by the Boltzmann distribution and the Planck equation. In the Boltzmann statistics, the numbers of electrons in the state n and m, N_n and N_m, are given at a given temperature T with the degeneracy of g_n and g_m, as follows;

$$\frac{N_m}{g_m} = \frac{N_n}{g_n} \exp\left(-\frac{E_m - E_n}{kT}\right), \tag{2.16}$$

where k is the Boltzmann constant. If the thermodynamic equilibrium between two states n and m is maintained, the number of transitioned electrons for the $m \leftarrow n$ transition (absorption) N_{nm} should be equal to the number of those for the $m \rightarrow n$ transition (emission) N_{mn}. In the case of the absorption process, N_{nm} is written by applying eq. 2.13;

$$N_{nm} = N_n W_{nm} = N_n B_{nm} \rho_\omega, \tag{2.17}$$

where $f(\omega)$ is replaced by the delta function. The emission process, on the contrary, can be described by the linear combination of stimulated and spontaneous emission, as follows;

$$N_{mn} = N_m W_{mn} = N_m (B_{mn} \rho_\omega + A_{mn}), \tag{2.18}$$

where A_{mn} is *Einstein's A-coefficient*, which represents spontaneous emission rate of transition. By applying eqs. 2.16–18, ρ_ω is obtained;

$$\rho_\omega = \frac{A_{mm}}{B_{mn}} \frac{1}{\frac{B_{nm}}{B_{mn}} \frac{g_n}{g_m} \exp\left(\frac{E_m - E_n}{kT}\right) - 1}. \tag{2.19}$$

The radiation energy per unit volume ρ_ω is expressed by the Planck's radiation law;

$$\rho_\omega = \frac{\hbar\omega^3}{c^3\pi^2}\frac{1}{\exp\left(\frac{\hbar\omega}{kT}\right)-1}, \tag{2.20}$$

where *h* and *c* are the Planck constant and speed of light, respectively. From eq. 2.19, the following relationships are obtained,

$$\hbar\omega_{mn} = E_m - E_n, \tag{2.21}$$

$$A_{mn} = \frac{\hbar{\omega_{mn}}^3}{c^3\pi^2}B_{mn}. \tag{2.22}$$

Eq. 2.22 indicates that the transition probabilities of optical absorption, stimulated emission, and spontaneous emission are not independent. Therefore, the spontaneous emission rate of the $m \rightarrow n$ transition with the g_n-fold n state is described as follows;

$$A_{mn} = \frac{g_n|\boldsymbol{M}_{mn}|^2{\omega_{mn}}^3}{3\pi\varepsilon_0\hbar c^3}. \tag{2.23}$$

2.1.1.3. Quantum Mechanical Illustration of Optical Transition

In the previous section, the interaction between matter and light is treated within the semi-classical theory. Here, the optical transition is discussed from the quantum mechanical point of view. Prior to the discussion on the transition probabilities, the validity of the ED approximation is examined. By applying a Lagrangian function, the classical hamiltonian for electrons in an electric field is described below;

$$H = \frac{1}{2m}(\boldsymbol{p} + e\boldsymbol{A})^2 - e\phi + V, \tag{2.24}$$

where $\boldsymbol{p}$, $V(\boldsymbol{r}, t)$, $\boldsymbol{A}(\boldsymbol{r}, t)$, and $\phi(\boldsymbol{r}, t)$ are the momentum of electrons, non-electrostatic potential, vector and scalar potentials at positions of electrons, respectively. In eq. 2.24, $\boldsymbol{p}^2/2m$ and $V - e\phi$ are the kinetic energy and potential for electrons, respectively, suggesting that the other part represents the interaction between electrons and the electric field. Thus, eq. 2.24 can be simplified as follows;

$$H = H_0 + H', \tag{2.25}$$

and

$$H' = H_1 + H_2, \tag{2.26}$$

with

$$H_1 = \frac{e}{2m}(\boldsymbol{p}\cdot\boldsymbol{A} + \boldsymbol{A}\cdot\boldsymbol{p}),$$
$$H_2 = \frac{e^2}{2m}\boldsymbol{A}^2. \tag{2.27}$$

H_1 is related to the absorption or emission of electromagnetic waves in the matter, while H_2 is related to the scattering of electromagnetic waves. It is possible to ignore H_2 because the influence of H_2 is usually very small. As applied to quantum theory, the hamiltonian $\hat{H}_1$ is described with the Coulomb gauge $\nabla\cdot\boldsymbol{A} = 0$;

$$\hat{H}_1 = \frac{e}{m}\hat{\boldsymbol{p}}\cdot\hat{\boldsymbol{A}}. \tag{2.28}$$

The operator $\boldsymbol{A}$ can be represented;

$$\hat{\boldsymbol{A}} = \left(\frac{\hbar}{2\varepsilon_0 V\omega}\right)^{\frac{1}{2}}\boldsymbol{e}[\hat{a}\exp\{i(\boldsymbol{k}\cdot\boldsymbol{r}-\omega t)\} + \hat{a}^\dagger\exp\{-i(\boldsymbol{k}\cdot\boldsymbol{r}-\omega t)\}], \tag{2.29}$$

with the following operators of

$$\hat{a} = (2\hbar\omega)^{-\frac{1}{2}}\left(\omega\hat{Q} + i\hat{P}\right),$$
$$\hat{a}^\dagger = (2\hbar\omega)^{-\frac{1}{2}}\left(\omega\hat{Q} - i\hat{P}\right). \tag{2.30}$$

The operators $\hat{Q}$ and $\hat{P}$ are corresponds to the coordinate and momentum of a harmonic oscillator, respectively. Therefore, the hamiltonian $\hat{H}_1$ is described as follows;

$$\hat{H}_1 = \frac{e}{m}\sum_\lambda\left(\frac{\hbar}{2\varepsilon_0 V\omega_\lambda}\right)^{\frac{1}{2}}\hat{\boldsymbol{p}}\cdot\boldsymbol{e}_\lambda[\hat{a}_\lambda\exp\{i(\boldsymbol{k}_\lambda\cdot\boldsymbol{r}-\omega_\lambda t)\} + \hat{a}^\dagger{}_\lambda\exp\{-i(\boldsymbol{k}_\lambda\cdot\boldsymbol{r}-\omega_\lambda t)\}]. \tag{2.31}$$

When the position of a nuclear is set on the coordinate origin, $\boldsymbol{k}\cdot\boldsymbol{r}$ ($\boldsymbol{k}$: wave vector) takes a similar value to ka (a: atomic radius), which is small enough to be compared to unity. Then, the exponential functions are expanded as follows;

$$\hat{\boldsymbol{p}}\exp(\pm i\boldsymbol{k}\cdot\boldsymbol{r}) = \hat{\boldsymbol{p}} \pm i\hat{\boldsymbol{p}}(\boldsymbol{k}\cdot\boldsymbol{r}) + \cdots. \tag{2.32}$$

By applying only the first term on the right side into eq. 2.31, the hamiltonian $\hat{H}_1$ is rewritten as follows;

$$\hat{H}_{\mathrm{E1}} = \frac{e}{m}\sum_\lambda\left(\frac{\hbar}{2\varepsilon_0 V\omega_\lambda}\right)^{\frac{1}{2}}\hat{\boldsymbol{p}}\cdot\boldsymbol{e}_\lambda(\hat{a}_\lambda e^{-i\omega_\lambda t} + \hat{a}^\dagger{}_\lambda e^{i\omega_\lambda t}). \tag{2.33}$$

In order to estimate the transition probability from the *g* to *f* states through this interaction, one

can apply the equation of $\langle f|\hat{\boldsymbol{p}}|g\rangle = \boldsymbol{p}_{fg} = im\omega_{fg}\boldsymbol{r}_{fg}$. Therefore, the transition probability calculated by the hamiltonian $\hat{H}_{\mathrm{E1}}$ is correlated with the ED momentum $\widehat{\boldsymbol{M}} = -e\hat{\boldsymbol{r}}$, whose transition is called *electric dipole* (*ED*) *transition*. Besides, the approximation in which only the first term is extracted in eq. 2.32 is called the *ED approximation*.

When the matrix elements $\langle f|\hat{\boldsymbol{r}}|g\rangle$ are zero between specific states *g* and *f*, one has to consider the second and below terms in eq. 2.32. The transition with non-zero matrix elements $\langle f|\hat{\boldsymbol{r}}|g\rangle$ is called *allowed transition*; in contrast, the transition with zero $\langle f|\hat{\boldsymbol{r}}|g\rangle$ is *forbidden transition*. In the case of the forbidden transition, the second term on the right side of eq. 2.32 yields the hamiltonians for the magnetic dipole and electric quadrupole interactions, leading to *magnetic dipole* (*MD*) *transition* and *electric quadrupole* (*EQ*) *transition*, respectively. As expected by eq. 2.32, the MD and EQ transition intensity is at most $(ka)^2$ times of ED transition intensity, suggesting that the observed spectral lines in the visible range are mainly attributed to the ED transition.

Eqs. 2.26, 27, and 31 indicate that the hamiltonian of the interaction between matter and light $\hat{H}'$ depends on time. Considering the quantized radiation field $\hat{H}_{\mathrm{R}}$, the time-dependent Schrödinger equation is described as follows;

$$\left[\hat{H}_0 + \hat{H}_R + \exp\left(\frac{-i\hat{H}_R t}{\hbar}\right)\hat{H}'(t)\exp\left(\frac{i\hat{H}_R t}{\hbar}\right)\right]\Phi(t) = i\hbar\frac{\partial\Phi(t)}{\partial t}, \tag{2.34}$$

with

$$\hat{H}_R = \sum_{\lambda}\hbar\omega_\lambda\left(\hat{a}_\lambda{}^\dagger\hat{a}_\lambda + \frac{1}{2}\right), \tag{2.35}$$

and

$$\Phi(t) = \exp\left(\frac{-i\hat{H}_R t}{\hbar}\right)\Psi(t), \tag{2.36}$$

where $\Phi(t)$ is a new wavefunction taking the interaction with the radiation field into account. Here, for the hamiltonian $\hat{H}'$, the following relationship holds;

$$\exp\left(\frac{-i\hat{H}_R t}{\hbar}\right)\hat{H}'(t)\exp\left(\frac{i\hat{H}_R t}{\hbar}\right) = \hat{H}'(0). \tag{2.37}$$

Therefore, the hamiltonian for the system is described to be $\hat{H} = \hat{H}_0 + \hat{H}_{\mathrm{R}} + \hat{H}'(0)$, which is independent of time. From now on, the $\hat{H}'(0)$ is denoted by $\hat{H}'$.

Usually, the influence of $\hat{H}'$ is small enough to be treated as a perturbation term. Supposing that the matter is in the state m and the radiative field with λ-degrees of freedom is formed by n_λ electrons, which is denoted by $|m, n_\lambda\rangle \equiv |M\rangle$, the perturbation theory leads to the following equation like eq. 2.5;

$$i\hbar \frac{\partial {b_M}^{(s+1)}}{\partial t} = \sum_N {b_N}^{(t)} {H_{MN}}' \exp(i\omega_{MN} t)\,, \tag{2.38}$$

where the eigenfunction of $\Phi(t)$ is defined by $\sum_N {b_N}^{(t)} |N\rangle$, and the energy difference between the states M and N ($W_M - W_N$) is given by $\hbar\omega_{MN}$. If the system is in the initial state I, the perturbation calculation of an arbitrary order leads to the following equation;

$$w_{MI} = \frac{2\pi}{\hbar} |{H'}_{MI}|^2 \delta(W_M - W_I), \tag{2.39}$$

where w_{MI} is the transition probability of the transition between the initial state I and terminal state M. This equation is called *Fermi's golden rule*, which was finally formularized by not Enrico Fermi but Paul A.M. Dirac. The δ function represents the energy conservation.

The A-coefficient related to spontaneous emission is obtained by quantum mechanical illustration with Fermi's golden rule. In the case of a light emission process from the state e to the state g, the ED approximation gives the following hamiltonian $\hat{H}'$;

$$\hat{H}' = \sum_\lambda i \left(\frac{\hbar\omega_\lambda}{2\varepsilon_0 V}\right)^{\frac{1}{2}} \widehat{\boldsymbol{M}} \cdot e_\lambda \left({\hat{a}_\lambda}^\dagger - \hat{a}_\lambda\right). \tag{2.40}$$

Putting the hamiltonian in eq. 2.40 in the golden rule, the transition probability w_{GE} is described as follows;

$$\begin{aligned} w_{GE} &= \sum_\lambda \frac{2\pi}{\hbar} \left|\left\langle g, n_\lambda + 1 \middle| {\hat{H}'}_\lambda \middle| m, n_\lambda \right\rangle\right|^2 \delta(\hbar\omega_{eg} - \hbar\omega_\lambda) \\ &= \sum_\lambda \frac{\pi\omega_\lambda}{\hbar\varepsilon_0 V} \left|\boldsymbol{M}_{ge} \cdot \boldsymbol{e}\right|^2 (n_\lambda + 1) \delta(\hbar\omega_{eg} - \hbar\omega_\lambda)\,. \end{aligned} \tag{2.41}$$

Here, the transition probability of light emission consists of two parts; one is proportional to the number of electrons in a state n_λ (stimulated emission), and the other is independent of n_λ (spontaneous emission). Unlike the stimulated emission, the spontaneous emission takes place for all modes. The number of degrees of freedom per unit volume between ω and $\omega + \mathrm{d}\omega$ $D(\omega)$

is given as follows;

$$D(\omega) = \frac{\omega^2}{\pi^2 c^3}. \tag{2.42}$$

Therefore, by replacing the summation with the integral, the spontaneous emission rate for the $e \rightarrow m$ ED transition is described as follows;

$$\begin{aligned} A_{ge} &= \int \frac{\pi \omega_{eg}}{\hbar \varepsilon_0 V} \frac{|\boldsymbol{M}_{ge}|^2}{3} \frac{V {\omega_{eg}}^2}{\pi^2 c^3} \delta(\omega_{eg} - \omega) \mathrm{d}\omega \\ &= \frac{|\boldsymbol{M}_{ge}|^2 {\omega_{eg}}^3}{3\pi \varepsilon_0 \hbar c^3}. \end{aligned} \tag{2.43}$$

By considering the degeneracy of the terminal state, the A-coefficient in eq. 2.23 is obtained.

Until now, the matter is treated as being dilute; *i.e.*, the induced and local electric fields in the matter are not distinguished, and the average energy of illuminated light per unit volume ρ_ω is considered to be $\varepsilon_0|\boldsymbol{E}_0|^2/2$. However, especially for dense matter, the local electric field is affected by the polarization of the matter, and the permittivity differs from the vacuum permittivity ε_0. By applying the Lorentz local field $\boldsymbol{E}_{\mathrm{loc}} = (n^2 + 2)\boldsymbol{E}/3$ (n; refractive index), the local field correction terms χ in a dielectric matter with the relative permittivity ε are calculated and summarized in **Table 2.1**. For the oscillator strength f, one does not have to consider the local field correction. In contrast, the A- and B-coefficients for the emission and absorption processes have to be corrected. As the density of states for photons is proportional to n^3, the correction term for the A-coefficient is n^3 times as much as the relevant term for the B-coefficient. Note that the correction term χ for the MD transition is obtained by using $|\boldsymbol{m}\cdot\boldsymbol{B}|^2$ instead of $|\boldsymbol{M}\cdot\boldsymbol{E}|^2$, where $\boldsymbol{m}$ and $\boldsymbol{B}$ are a magnetic momentum and magnetic flux density, respectively. In the order of frequency of light, the permittivity μ is approximated to the vacuum permittivity μ_0, leading to the unnecessity of local field correction for the absorption.

Table 2.1. List of the local field corrections χ for ED and MD transitions

	B-coefficient (absorption) χ^{abs}	A-coefficient (emission) χ^{em}
ED transition	$\dfrac{(n^2+2)^2}{9n^2}$	$\dfrac{n(n^2+2)^2}{9}$
MD transition	1	n^3

2.1.2. 5d-4f Allowed Transition

Lanthanoid (*Ln*) ions in ground states have empty 5d orbitals out of inner 4f orbitals. The electronic transition between these 4f and 5d orbitals is accompanied by optical absorption or emission. Because the 5d and 4f orbitals have the even (gerade) and odd (ungerade) parities, respectively, the 5d-4f transition is allowed, according to Laporte's selection rule. Thus, the luminescence lifetime of the 5d → 4f transition is shorter than those of the 3d → 3d and 4f → 4f forbidden transition; 17–65 ns for Ce^{3+} [5,6] and 0.4–3.3 μs for Eu^{2+} [7,8]. The broad 5d-4f absorption (excitation) and emission bands are caused by the electronic transition from inner 4f to outer 5d orbitals with a large interaction with local environments around *Ln* ions. The luminescence properties depend on the crystal field strength, ligand species, and refractive index of the host materials, as shown in **Figure 2.2**. In this section, the sensitive 5d-4f transition is illustrated by the energy level diagram schemes.

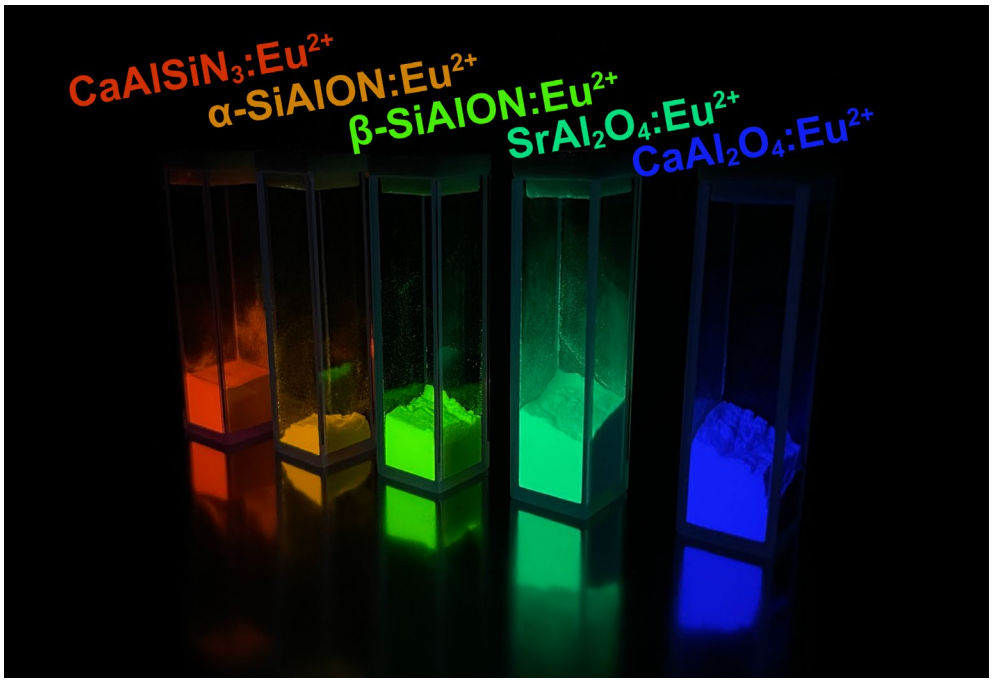

Figure 2.2. Series of Eu^{2+}-doped commercial phosphors under UV illumination, exposing the color tunability of the Eu^{2+}: $4f^6 5d^1 \rightarrow 4f^7$ allowed transition upon changing the local environment around Eu^{2+} ions.

2.1.2.1. Sensitive 5d States to Local Environments

Supposing a *Ln* ion is surrounded by some ligands, the 5d excited states should be influenced by all the ligands arranged in three dimensions around the *Ln* ion. For the sake of brevity, only the interaction between the *Ln* ion and a given ligand is extracted, resulting in a model of a diatomic molecule. The hamiltonian of a molecule, which consists of N nuclei with masses M_α, electrical charges Z_α, coordinates $\boldsymbol{R}_\alpha$ (α = 1–N) and n electrons with coordinates $\boldsymbol{r}_i$ (i = 1–n), is described as follows;

$$\hat{H} = -\frac{\hbar^2}{2m}\sum_{i=1}^{n}\Delta_i - \frac{\hbar^2}{2}\sum_{\alpha=1}^{N}\frac{\Delta_\alpha}{M_\alpha} + \frac{1}{2}\sum_{i=1}^{n}\sum_{j=1}^{n}\frac{e^2}{|\boldsymbol{r}_i - \boldsymbol{r}_j|} + \frac{1}{2}\sum_{\alpha=1}^{N}\sum_{\beta=1}^{N}\frac{Z_\alpha Z_\beta e^2}{|\boldsymbol{R}_\alpha - \boldsymbol{R}_\beta|} - \sum_{\alpha=1}^{N}\sum_{i=1}^{n}\frac{Z_\alpha e^2}{|\boldsymbol{R}_\alpha - \boldsymbol{r}_i|}. \tag{2.44}$$

The first and second terms are the kinetic energy of n electrons and N nuclei. The third and fourth terms describe the potential energy of the Coulomb repulsion between all electrons and nuclei, respectively. The fifth term considers the potential energy of the Coulomb interaction between electrons and nuclei. This hamiltonian is so complex that the Schrödinger equation for a molecule cannot be solved if both coordinates of electrons and nuclei are variable. Therefore, the *adiabatic* (*Born-Oppenheimer*) *approximation* is introduced, assuming that electrons are moving around fixed (or "frozen") nuclei because a nuclear is much heavier than electrons. If the Coulomb potential terms are denoted to be $V(\boldsymbol{r}, \boldsymbol{R})$ for the sake of brevity, the stationary Schrödinger equation for a molecule is written as follows;

$$\left\{-\frac{\hbar^2}{2m}\sum_{i=1}^{n}\Delta_i - \frac{\hbar^2}{2}\sum_{\alpha=1}^{N}\frac{\Delta_\alpha}{M_\alpha} + V(\boldsymbol{r}, \boldsymbol{R})\right\}\Psi(\boldsymbol{r}, \boldsymbol{R}) = E\Psi(\boldsymbol{r}, \boldsymbol{R}), \tag{2.45}$$

where E is the energy eigenvalue, and $\Psi(\boldsymbol{r}, \boldsymbol{R})$ is the corresponding wavefunction. The adiabatic approximation enables us to represent the wavefunction $\Psi(\boldsymbol{r}, \boldsymbol{R})$ as a product of two terms, one of which depends on the nuclear coordinate $\boldsymbol{R}$ only [$\phi(\boldsymbol{R})$], and another one depends on both electron and nuclear coordination $\boldsymbol{r}$ and $\boldsymbol{R}$ [$\Phi(\boldsymbol{r}, \boldsymbol{R})$];

$$\Psi(\boldsymbol{r}, \boldsymbol{R}) = \phi(\boldsymbol{R})\Phi(\boldsymbol{r}, \boldsymbol{R}). \tag{2.46}$$

By introducing this approximation, the movements of electrons and nuclei can be described separately, leading to the adiabatic potential $U_j(\boldsymbol{R})$. Here, a configurational coordinate q_λ is

introduced instead of ***R*** for the movement of nuclei. By expanding the interaction term between electrons and nuclei at around $q_\lambda = 0$ within the perturbation theory and adding the vibrational potential for nuclei of $\sum_\lambda {\omega_\lambda}^2 {q_\lambda}^2 \big/ 2$, the adiabatic potential is described as follows;

$$U_j(q) = W_j + \sum_\lambda \frac{1}{2} {\omega_\lambda}^2 (q_\lambda - \Delta_{ij})^2 \tag{2.47}$$

with

$$W_j = \left\langle j \middle| \hat{H}_e(r) + \hat{H}_{eL}(r,0) \middle| j \right\rangle - \sum_\lambda \frac{1}{2} {\omega_\lambda}^2 {\Delta_{ij}}^2 , \tag{2.48}$$

$$\Delta_{ij} = \frac{\langle j | c_\lambda | j \rangle}{{\omega_\lambda}^2} . \tag{2.49}$$

Here, the hamiltonians $\hat{H}_e$ and $\hat{H}_{eL}$ represent the summation of potential and kinetic energy for electrons and the interaction energy between electrons and nuclei, respectively. Here, the minimum point of the adiabatic potential curve for the ground state is set on the coordinate origin. The adiabatic potentials for the ground and excited states are given as follows;

$$\begin{aligned} U_g(q) &= \sum_\lambda \frac{1}{2} {\omega_\lambda}^2 {q_\lambda}^2 , \\ U_e(q) &= W_e + \sum_\lambda \frac{1}{2} {\omega_\lambda}^2 (q_\lambda - \Delta_\lambda)^2 . \end{aligned} \tag{2.50}$$

By introducing the j-th components of the normalized angular frequency $\xi_{\lambda j}$ that satisfies the orthogonal conditions of $\sum_j \xi_{\lambda j} \xi_{\lambda' j} = \delta_{\lambda\lambda'}$ and $\sum_\lambda \xi_{\lambda i} \xi_{\lambda j} = \delta_{ij}$, the following parameters are obtained;

$$\begin{aligned} Q_i &= \sum_\lambda \omega_\lambda q_\lambda \xi_{\lambda i} , \\ \omega_\lambda q_\lambda &= \sum_i \xi_{\lambda i} Q_i . \end{aligned} \tag{2.51}$$

Here, when Q_1 is c under the condition of $q_\lambda = \Delta_\lambda$, Q_1 is selected as follows;

$$\begin{aligned} cQ_1 &= \sum_\lambda {\omega_\lambda}^2 q_\lambda \Delta_\lambda , \\ c &= \sum_\lambda {\omega_\lambda}^2 {\Delta_\lambda}^2 . \end{aligned} \tag{2.52}$$

Therefore, the adiabatic potentials in eq. 2.50 are given;

$$U_g(Q) = \sum_i \frac{1}{2} {Q_i}^2,$$
$$U_e(Q) = W_0 - cQ_1 + \sum_i \frac{1}{2} {Q_i}^2, \tag{2.53}$$

where $W_0 = W_e + c^2/2$. Two potentials differ only in the interaction mode Q_1. Eq. 2.53 indicates that the shape of the adiabatic potential at around the minimum point can be approximated by the quadratic function.

Figure 2.3 depicts the adiabatic potential curves for the $4f^N$ ground and $4f^{N-1}5d^1$ excited states. This picture is called *the configuration coordinate diagram*, where the *x*-axis represents the configuration coordinate. The R_0 and R_1 indicate the equilibrium position of a *Ln* ion and a ligand and the shift of ligands in the excited state, respectively. The levels labeled by *v* and *v*' are related to the vibrational modes, represented to be $E_v = (v + 1/2)\hbar\omega_p$ ($\hbar\omega_p$; phonon energy). The absorption from the lowest vibrational level with $v = 0$ in the $4f^N$ ground state is considered. On this level, the squared wavefunction $|\Psi|^2$ represents the probability density of electrons, shown in the curve on the initial level. Upon being excited, electrons vertically transition from point A to point B on the $4f^{N-1}5d^1$ excited state. During the electronic transition, the position and momentum of nuclei are unchanged, according to the adiabatic approximation, which is called *the Franck-Condon principle*. The excited electrons relax down along the potential curve without photon emission to the lower vibrational levels. This relaxation is accompanied by the ligands shift because of the interaction between the 5d electron (or 4f holes) and ligands, which is regarded as *the lattice relaxation* (W_{LR}). The relaxed electrons distributed on the excited states cause the radiative transition from point C to D, according to the Franck-Condon principle.

The configurational coordinate diagram provides information about the spectral shapes for the optical transition. Assuming the ED transition with the momentum μ in the electric field direction, the spectral shape function $A(\hbar\omega)$ for the e ← g absorption transition is described as follows;

$$A(\hbar\omega) = \sum_n \sum_m \rho_{gn} \left| \langle \Psi_{em} | \hat{\mu} | \Psi_{gn} \rangle \right|^2 \delta(W_{em} - W_{gn} - \hbar\omega)\,, \tag{2.54}$$

with

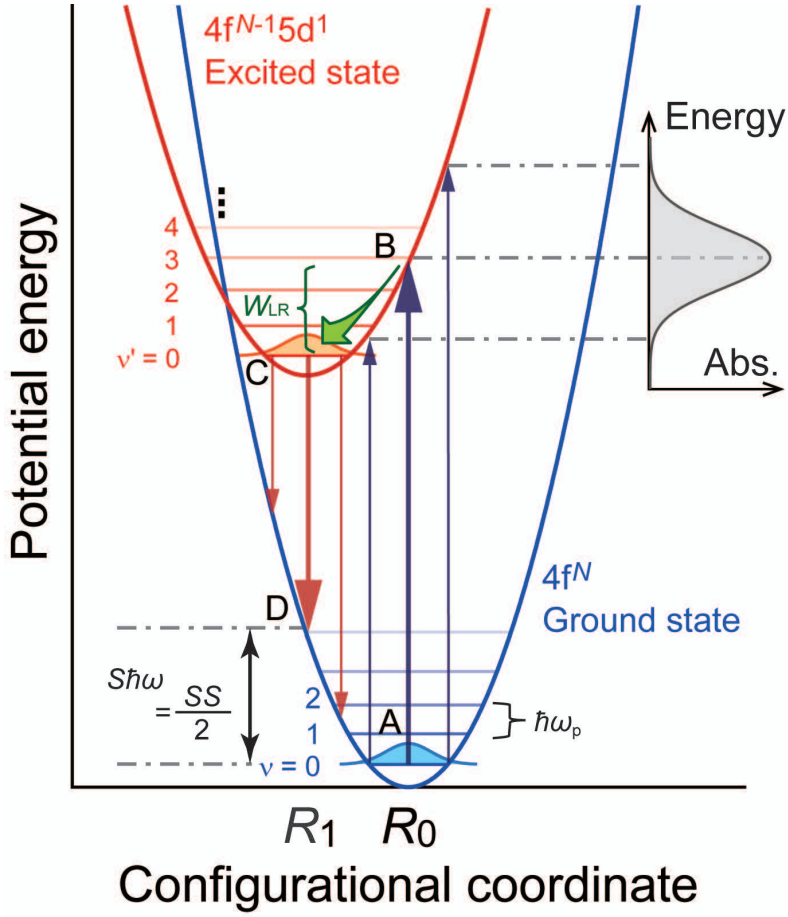

Figure 2.3. Schematic illustration of a configurational coordinate model. The vertical arrows between A–B or C–D indicate the absorption and emission processes.

$$\rho_{gn} = \frac{\exp\left(-{W_{gn}}/{kT}\right)}{\sum_n \exp\left(-{W_{gn}}/{kT}\right)}, \tag{2.55}$$

where ρ_{gn} is the probability that the system is initially in the gn state. The matrix elements for the ED transition from the n-th level in the g state to the m-th level in the e state are given by eq. 2.46;

$$\langle \Psi_{em} | \hat{\mu} | \Psi_{gn} \rangle = \int \phi_{em}{}^{*}(q) \mu_{eg} \phi_{gn}(q)\, \mathrm{d}q, \tag{2.56}$$

with

$$\mu_{eg}(q) = \int \psi_{e}{}^{*}(\boldsymbol{r}, q) \hat{\mu} \psi_{g}(\boldsymbol{r}, q) d\boldsymbol{r}. \tag{2.57}$$

Here, *the Condon approximation* is introduced, which suppose that $\mu_{eg}(q)$ does not depend on q,

indicating that the magnitude of the matrix elements for the ED transition only depends on the overlap integral between $\phi_{em}(q)$ and $\phi_{gn}(q)$. The squared absolute value of this overlap integral is important to determine the spectral shape;

$$F_{mn} = \left|\phi_{em}{}^{*}(q)\phi_{gn}(q)\right|^2, \tag{2.58}$$

which is called *the Franck-Condon factor*. Especially at T = 0 K, $\rho_{gn} = \delta_{n0}$ leads to the following relationship;

$$A(\hbar\omega) = \sum_m F_{m0}\delta(\hbar\omega - W_{00} - m\hbar\omega_{\mathrm{p}}), \tag{2.59}$$

where $W_{00} = W_{e0} - W_{g0}$, and $\hbar\omega_{\mathrm{p}}$ is the phonon energy. **Figure 2.4** illustrates the theoretical spectral shapes of the absorption band at 0 K, indicating that the absorption spectra consist of spectral lines with the increment of $\hbar\omega_{\mathrm{p}}$. The spectral line at 0 in Figure 2.4 is called *the zero phonon line* (*ZPL*), which is not related to any phonons. Each phonon line is characterized by the Lorentzian profile with widths of $\hbar/\tau$, according to the Heisenberg uncertainty principle. Here, *the Huang-Rhys factor S* is introduced by the following relationships;

$$S = \frac{W_{\mathrm{LR}}}{\hbar\omega_{\mathrm{p}}}, \tag{2.60}$$

and

$$F_{m0} = e^{-S}\left(\frac{S^m}{m!}\right). \tag{2.61}$$

The physical meaning of the Huang-Rhys factor *S* is the number of emitted phonons during the lattice relaxation. The twice of W_{LR} or $S\hbar\omega_{\mathrm{p}}$ corresponds to *the Stokes shift* (*SS*), which is defined as the peak difference between the absorption (or excitation) and emission bands.

In Figure 2.4, the *S*-dependence of the absorption band is displayed. If the electron-lattice interaction is very weak (*i.e., S* is almost zero), the ZPL is significant at around n = 0. With S = 5, the ZPL and fine structure related to the n-th phonon lines are still observed. Here, if the phonon energies for the ground and excited states are the same, the emission and absorption (or excitation) spectra appear in a mirror image relationship with the common ZPL. When the *S* value is large enough (S = 20), the width of the absorption band is broad, and the ZPL intensity is weak. The large *S* is interpreted as the large offset R_1, indicating that the movement of the nuclei can be treated in the classical theory according to the correspondence principle, and

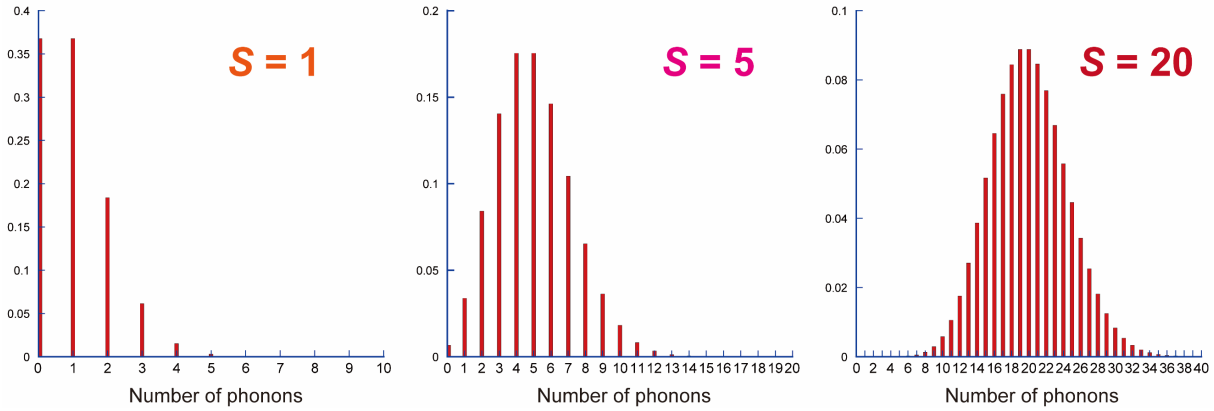

Figure 2.4. Dependence of the absorption band shape on the value of the Huang-Rhys factor *S* at 0 K. The number of phonons generated in the absorption transition is shown along the horizontal axis [7,8].

$|\phi_{em}(q)|$ takes a large value only on the adiabatic potential curve. Therefore, the spectral shape of the absorption band with a large *S* is described by the following equation;

$$A(\hbar\omega) = \frac{|\mu_{eg}|^2}{\sqrt{4\pi kTaW_{\mathrm{LR}}}} \exp\left[-\frac{(W_e + W_{\mathrm{LR}} - \hbar\omega)^2}{4kTW_{\mathrm{LR}}}\right], \tag{2.62}$$

whose shape is characterized by the Gaussian profile. As shown above, the configurational coordinate model is a good approximation to explain the dynamics of excited states and the spectral shape with the large *S* value.

2.1.2.2. Energy Level Structure of 5d Excited States

Considering the radial wavefunction, the 5d orbital is outside the 4f, 5s, and 5p orbitals [9]. Therefore, the 5d-4f transition for a *Ln* ion is largely influenced by the local environments, such as the chemical, structural, and electronic features. **Figure 2.5** shows the schematic illustration of the 4f and 5d energy levels for Ce^{3+}. The $4f^1$ state for Ce^{3+} is split into two levels denoted by $^2F_{5/2}$ and $^2F_{7/2}$ because of the spin-orbit interaction, in which the ground level is labeled by $^2F_{5/2}$. The energy difference between these two levels is about 0.25 eV. In the free ion state, the degenerated Ce^{3+}: $5d^1$ levels are located at 6.35 eV higher than the ground $^2F_{5/2}$ level. When a Ce^{3+} ion is put in a given spherical ligand field, the ligands make the $5d^1$ level to be lowered, which is called *the nephelauxetic effect*. The term "nephelauxetic" means *cloud-expanding* in Greek. The electrons of ligands reduce the effective positive charge of the Ce^{3+} nuclear, leading to the electron cloud expansion of 5d orbitals. The degree of the energy shift is the centroid shift

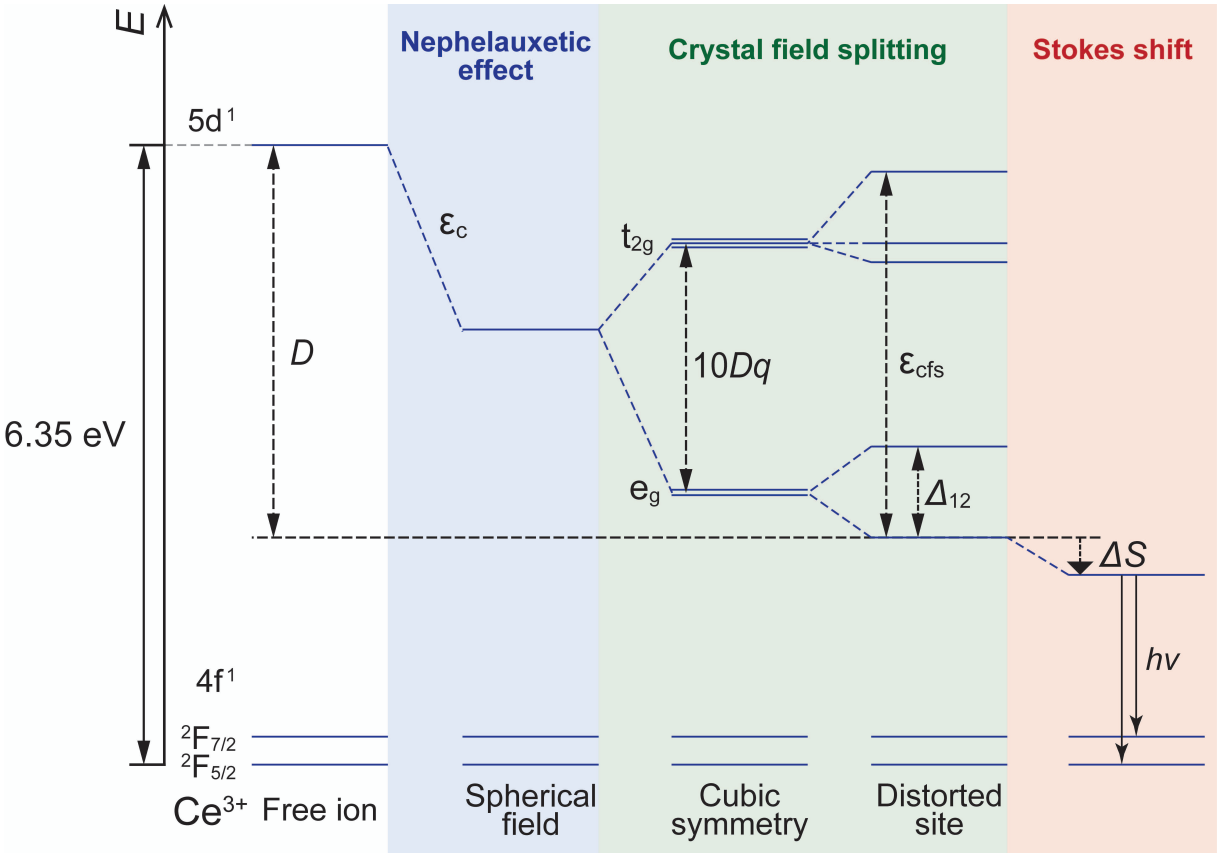

Figure 2.5. Energy level structure of Ce^{3+} showing the depression D of the lowest 5d level with respect to the free ion energy of Ce^{3+} (6.35 eV).

ε_c. The ε_c value depends on the following nephelauxetic series by Jørgensen [10,11];

$$F^- < O^{2-} < Cl^- < N^{3-} < Br^- < I^- < S^{2-} < Se^{2-},$$

which corresponds to the order of decreasing electronegativity of corresponding elements [12].

While the nephelauxetic effect is isotropic, the crystal field with a given symmetry brings about the anisotropic effect on the 5d levels, resulting in the split 5d levels. In the cubic site with O_h symmetry, the degenerated 5d levels are resolved into two, which are the lower two-fold e_g and higher three-fold t_{2g} levels, due to the interaction between the ligands and 5d orbitals. The crystal field splitting $10Dq$ is given as the energy difference between the e_g and t_{2g} levels. In the distorted sites, the degenerated 5d levels are finally resolved into five $5d_1$–$5d_5$ levels. The energy differences between $5d_1$–$5d_5$ and $5d_1$–$5d_2$ are designated as ε_{cfs} and Δ_{12}, respectively, which are important for discussion on Ce^{3+} luminescence. The centroid energy of the 5d levels is given by a simple arithmetical mean and corresponds to the value of $(6.35 - \varepsilon_c)$ eV. The redshift of the

Ce^{3+}: $5d_1$ level is called depression *D*, depending on the compositional and structural features of host compounds. In order to obtain the desirable luminescent properties of the 5d-4f transition, one has to design the phosphor materials with suitable *D* values.

2.1.3. 4f-4f Forbidden Transition

2.1.3.1. Characteristics of Lanthanoid Ions

Following the Pauli exclusion principle, lanthanoid ions can take a variety of electronic configurations because of the unfiled 4f orbitals. The energy level diagram for Ln^{3+} ions (Dieke diagram) is shown in Figure 1.2, where each state is denoted by *the Russell-Saunders notation* $^{2S+1}L_J$. Here, *L*, 2*S* + 1, and *J* are the total orbital angular momentum, spin multiplicity (*S*: the total spin angular momentum), and total angular momentum, respectively. The values of $L = 0$, 1, 2, 3, 4, 5, 6, 7, 8 are used to be designated by the capital letters of S, P, D, F, G, H, I, K, and L. The total angular momentum *J* takes the 2*S* +1 values of $(L + S)$, $(L + S - 1)$, …, and $|L - S|$. Since the *L* and *S* are good quantum numbers for light elements, the state is described only by the ^{2S+1}L term, called *the Russell-Saunders* (*RS*) *coupling scheme* (or *LS-coupling scheme*). However, the *L* and *S* are no longer good quantum numbers for Ln^{3+} ions, leading to the "*mixing*" between adjacent ^{2S+1}L terms. Thus, the $^{2S+1}L_J$ multiplets are introduced to take the influence of the non-negligible spin-orbit interaction into account.

The 4f-4f luminescence is caused by the radiative transition between the "rich" levels labeled by the multiplet $^{2S+1}L_J$. The inner 4f orbital hardly interacts with the ligand field, leading to the sharp spectral shape for the 4f-4f transition (*i.e.,* with the small Huang-Rhys factor *S*). Because the transition energy between two levels is almost independent of the local environment, one can roughly apply the Diele diagram for all the Ln^{3+}-based luminescent materials. The 4f-4f luminescence is the electronic transition between the state with the same parity (ungerade), resulting in the ED forbidden and MD allowed transition by considering the matrix elements for each transition. Nevertheless, intense ED luminescence is observed in a variety of Ln^{3+}-based phosphors. This is due to the mixing of the even-parity in 4f orbitals, which is explained by the Judd-Ofelt theory. The ED transition in Ln^{3+} is called "*induced*" ED transition. The quantum mechanical illustration of the induced ED transition is provided in the following section.

2.1.3.2. Judd-Ofelt Theory

The transition probability of the 4f-4f transition is described by the Judd-Ofelt theory [13–15], which was independently proposed by Brian R. Judd and George S. Ofelt in 1962 and summarized later. This theory provides a theoretical explanation of the optical strength of the electronic transition between the $4f^N$ energy levels for trivalent lanthanoid ions Ln^{3+}. Here, the optical strength of the 4f-4f transition is overviewed with the fundamental quantum mechanics. The hamiltonian of the 4f electrons are described as follows;

$$\hat{H} = \hat{H}_0 + \hat{H}_{\mathrm{SO}} + \hat{V}_{crys}, \tag{2.63}$$

with

$$\hat{H}_0 = -\sum_{i=1}^{N} \frac{\hbar^2 {\nabla_i}^2}{2m} - \sum_{i=1}^{N} \frac{z^* e^2}{r_i} + \sum_{i>j}^{N} \frac{e^2}{r_{ij}}, \tag{2.63}$$

$$\hat{H}_{\mathrm{SO}} = \sum_{i=1}^{N} \xi\,(\boldsymbol{r}_i)(\boldsymbol{s}_i \cdot \boldsymbol{l}_i). \tag{2.64}$$

The hamiltonian $\hat{H}_0$ is represented by the linear combination of the kinetic energy and the electrostatic potential of 4f electrons. On the other hand, the hamiltonian $\hat{H}_{\mathrm{SO}}$ is derived from the spin-orbit interaction, which is ignored within the RS coupling scheme. As the spin-orbit interaction coefficient ξ is proportional to the fourth power of atomic number, the $\hat{H}_{\mathrm{SO}}$ term is not negligible for 4f electrons. As mentioned above, the ^{2S+1}L terms for Ln^{3+} ion split up, indicating that the total orbital angular momentum L and total spin angular momentum S are no longer good quantum numbers. Because the contributions of $\hat{H}_0$ and $\hat{H}_{\mathrm{SO}}$ are comparable, *the intermediate coupling scheme* is applied to describe the interaction related to 4f electrons. A state of a Ln^{3+} ion with $4f^N$ electron(s) is expressed by a linear combination of RS states as follows;

$$|4f^N[\alpha SL]J\rangle = \sum_{\alpha' S' L'} a_J(\alpha SL{:}\,\alpha' S' L')\,|4f^N \alpha' S' L' J'\rangle, \tag{2.65}$$

where α is a quantum number that distinguishes the states with the same $^{2S+1}L_J$ term. For example, $^5G_2$ states of Eu^{3+} in a free-ion state are located at 26269 and 38616 cm^{-1} with respect to the $^7F_0$ ground state [16], which should be identified. The letters in the bracket are not good quantum numbers.

Considering the Laporte selection rule, the 4f-4f electronic transition is forbidden because

the matrix elements with an ED moment are zero. However, when Ln^{3+} ions are incorporated at a given non-centrosymmetric local environment in solids or liquids, the ED transition gets to be partly allowed. Even though Ln^{3+} ions are in a centrosymmetric field, the coupling with lattice vibration (*i.e.,* phonons) in odd-parity can induce the ED transition of Ln^{3+}. Therefore, the Ln^{3+} intense 4f-4f luminescence related to the ED transition is usually observed in a variety of luminescent materials. In eq. 2.63, the potential of electrons related to the crystal field around a Ln^{3+} ion is represented as follows;

$$\hat{V}_{\mathrm{crys}} = \sum_i \sum_j \frac{-eQ_j}{|\boldsymbol{r}_i - \boldsymbol{R}_j|}, \tag{2.66}$$

where $\boldsymbol{r}_i$ and $\boldsymbol{R}_j$ are the coordinates of the i-th electron and j-th ion with a point charge Q_j, respectively. The vector $\boldsymbol{R}_j(R_j, \theta_j, \varphi_j)$ is described in the polar coordinates system. Considering $\boldsymbol{r}_i < \boldsymbol{R}_j$ and Θ_{ij} defining the angle between $\boldsymbol{r}_i$ and $\boldsymbol{R}_j$, eq. 2.66 is described with the formula related to the Legendre polynomial $P_k(\cos\Theta_{ij})$;

$$\hat{V}_{\mathrm{crys}} = \sum_i \sum_{t,p} {r_i}^2 A_{tp} {C_p}^{(t)}(\theta_i, \varphi_i) = \sum_{t,p} A_{tp} {D_p}^{(t)}, \tag{2.67}$$

with

$$ {C_p}^{(t)}(\theta_i, \varphi_i) = \left(\frac{4\pi}{2t+1}\right)^{\frac{1}{2}} Y_{tp}(\theta, \varphi), \tag{2.68}$$

$$A_{tp} = \left(\frac{4\pi}{2t+1}\right)^{\frac{1}{2}} \sum_j \frac{-eQ_j}{{\boldsymbol{R}_j}^{t+1}} {Y_{tp}}^*(\theta_j, \varphi_j), \tag{2.69}$$

$$ {D_p}^{(t)} = \sum_i {r_i}^t {C_p}^{(t)}(\theta_i, \varphi_i). \tag{2.70}$$

Here, Y_{tp} and ${Y_{tp}}^*$ are the spherical harmonics and their conjugates, respectively. The A_{tp} is called the crystal field parameter. The product of A_{tp} and $\langle r_i \rangle$, which is a radial wavefunction, is denoted as B_t^p, which is also called the crystal field parameter in some literature. In the case of Ln^{3+}, the crystal field potential $\hat{V}_{\mathrm{crys}}$ is usually very small with respect to the hamiltonians $\hat{H}_0$ and $\hat{H}_{\mathrm{SO}}$. This is because the inner 4f orbitals are shielded by the outer 5s and 5p orbitals. Therefore, the $\hat{V}_{\mathrm{crys}}$ term can be treated as a perturbation. Considering the $\hat{V}_{\mathrm{crys}}$ term, the total angular momentum J is neither no longer a good quantum number. The states are designated by the irreducible representations (irreps) of the point group for the local structure.

The energy level splitting of the degenerated $2J + 1$ levels in a free-ion state is observed, which is *the crystal field* (*Stark*) *splitting*. The degree of the Stark splitting depends on the J value and the symmetry of the local structure. Depending on whether J is an integer or a half-integer, the maximum number of the Stark sublevels is $(2J + 1)$ or $(J + 1/2)$. This is due to *the Kramers degeneracy*, in which Ln^{3+} energy levels with an odd number of electrons degenerate at least two-fold. By considering the number of the Stark sublevels, one can roughly assign the symmetry of a local structure.

Here, the ED transition between two states φ_a and φ_b with $4f^N$ electronic configuration is considered, under an assumption that a Ln^{3+} ion is located at a given non-centrosymmetric local field. The hamiltonian is represented by eq. 2.63. The crystal field potential for odd-parity V_{odd} is treated as a perturbation term as follows;

$$\begin{aligned} |\varphi_a\rangle &= |a\rangle + \sum_c |c\rangle \frac{\langle c|V_{\mathrm{odd}}|a\rangle}{W_a - W_c}, \\ |\varphi_b\rangle &= |b\rangle + \sum_c |c\rangle \frac{\langle c|V_{\mathrm{odd}}|b\rangle}{W_b - W_c}. \end{aligned} \tag{2.71}$$

The physical meaning of wavefunction c is discussed later. From eq. 2.67, V_{odd} is $\sum A_{tp} {D_p}^{(t)}$ (only odd t is permitted), leading to the ED momentum $\boldsymbol{M} = -e\sum_q {D_q}^{(1)}$. By using this ED momentum, the matrix elements for q are given as follows;

$$\langle \varphi_b | -e {D_q}^{(1)} | \varphi_a \rangle = \sum_c \sum_{tp} e A_{tp} \left\{ \frac{\langle b|{D_q}^{(1)}|c\rangle \langle c|{D_p}^{(t)}|a\rangle}{W_c - W_a} + \frac{\langle b|{D_p}^{(t)}|c\rangle \langle c|{D_q}^{(1)}|a\rangle}{W_c - W_b} \right\}. \tag{2.72}$$

If $|c\rangle$ has an odd-parity like 4f-orbitals, the matrix elements in eq. 2.72 is zero, meaning that the transition is forbidden. Assuming that the electronic configuration of the state c has even-parity, such as $4f^{N-1}5d^1$ and $4f^{N-1}5g^1$, the matrix elements of the ED momentum take a non-zero value, and the ED transition is allowed. Because these electronic configurations with even-parity usually take much higher energy than the $|a\rangle$ and $|b\rangle$ states with the $4f^N$ electronic configuration, $(W_c - W_a)$ and $(W_c - W_b)$ terms can be approximated by the single energy difference ΔW. With the normalization condition $\sum_c |c\rangle \langle c| = 1$, the matrix elements are rewritten as follows;

$$\sum_c \frac{\langle b|{D_q}^{(1)}|c\rangle \langle c|{D_p}^{(t)}|a\rangle}{W_c - W_a} = \frac{1}{\Delta W} \langle b|{D_q}^{(1)} {D_p}^{(t)}|a\rangle, \tag{2.73}$$

which is called *the closure approximation*.

In the case of the $4f^N$ configuration, the states $|a\rangle$, $|b\rangle$, and $|c\rangle$ are $|4f^N\alpha, J, M\rangle$, $|4f^N\alpha', J', M'\rangle$, and $|4f^{N-1}n'l'\alpha'', J'', M''\rangle$, respectively. Here, the k-rank unit tensor operator $U_q^{(k)}$ is introduced, which is defined below;

$$U_q^{(k)} = \frac{\sum_j C_q^{(k)}(\theta_j, \varphi_j)}{\langle l \| C^{(k)} \| l \rangle}, \tag{2.74}$$

with

$$\langle l \| C^{(k)} \| l \rangle = (-1)^l \{(2l+1)(2l'+1)\}^{\frac{1}{2}} \begin{pmatrix} l & k & l' \\ 0 & 0 & 0 \end{pmatrix}. \tag{2.75}$$

The last part in eq. 2.75 of $\begin{pmatrix} l & k & l' \\ 0 & 0 & 0 \end{pmatrix}$ is expressed with *the Wigner 3-j symbols*, which are an alternative to Clebsch-Gordan coefficients for the purpose of adding angular momenta. The 3-*j* symbols are generally represented in $\begin{pmatrix} j_1 & j_2 & j_3 \\ m_1 & m_2 & m_3 \end{pmatrix}$, where the symbols have to satisfy the requirements below; (1) the upper numbers j_1, j_2, and j_3 have to provide a triangle, (2) if the summation of the bottom numbers is not zero (*i.e.*, $m_1 + m_2 + m_3 \neq 0$), the term should be zero, and (3) If all the bottom numbers m are zero, the summation of the upper numbers must be even. By using the unit tensor $U_q^{(k)}$, the matrix elements of $D_q^{(k)}$ between two RS states with the same $4f^N$ configuration is given;

$$\begin{aligned} &\langle nl^N \alpha' S' L' J' M' | D_q^{(k)} | nl^N \alpha S L J M \rangle \\ &\quad = \delta_{ss'} \langle nl | r^k | nl \rangle \times \langle l \| C^{(k)} \| l \rangle \langle nl^N \alpha' S' L' J' M' | U_q^{(k)} | nl^N \alpha S L J M \rangle, \end{aligned} \tag{2.76}$$

where $\delta_{ss'}$ is the Kronecker delta, and the term depending on the radial wavefunction R_{nl} satisfies $\langle nl|r^k|nl\rangle = \int_0^\infty R_{nl}(r) r^k R_{n'l'}(r) r^2 dr$. Besides, the numerator of eq. 2.72, which is a combination of two operators $D_q^{(k)}$ and $D_p^{(t)}$, is transformed to be separated into the geometrical and physical parts as follows;

$$\begin{aligned} &\sum_{\alpha'' J'' M''} \langle nl^N \alpha' J' M' | D_q^{(k)} | n'l'^{N-1} \alpha'' J'' M'' \rangle \langle n'l'^{N-1} \alpha'' J'' M'' | D_p^{(t)} | nl^N \alpha J M \rangle \\ &\quad = \sum_\lambda (-1)^{p+q} (2\lambda+1) \begin{pmatrix} k & \lambda & t \\ q & -p-q & p \end{pmatrix} \begin{Bmatrix} k & \lambda & t \\ l & l' & l \end{Bmatrix} \langle nl|r^k|n'l'\rangle \langle n'l'|r^t|nl\rangle \\ &\qquad \times \langle l \| C^{(k)} \| l' \rangle \langle l' \| C^{(t)} \| l \rangle \langle nl^N \alpha' J' M' | U_{p+q}^{(\lambda)} | nl^N \alpha J M \rangle, \end{aligned} \tag{2.77}$$

where the $\begin{Bmatrix} j_1 & j_2 & j_3 \\ m_1 & m_2 & m_3 \end{Bmatrix}$ term is *the Wigner 6-j symbols*. Unless all the numerical combinations of (j_1, j_2, j_3), (l_1, l_2, j_3), (j_1, l_2, l_3), and (l_1, j_2, l_3) can make a triangle, this term is zero. Under this constraint, λ should be six or less for the $4f^N$ ED transition. Within the closure approximation, in which $[W_c(n'l') - W_a]$ and $[W_c(n'l') - W_b]$ are approximated to be $\Delta W_{n'l'}$, the matrix elements for the ED transition in eq. 2.72 are zero with odd λ. In addition, if λ is zero, $U_0^{(0)}$ is a constant, resulting in $<4f^N\alpha'J'||U_0^{(0)}||4f^N\alpha J>$ with zero value due to the orthogonality of wavefunctions. Here, $<||U||>$ is called *the reduced matrix elements* (RMEs). Therefore, the matrix elements of the ED transition for Ln^{3+} ions take non-zero values only with λ = 2, 4, and 6. By applying Fermi's golden rule in eq. 2.39, the transition strength between two $4f^N$ energy levels is proportional to the squared matrix elements of the ED transition;

$$\sum_{MM'q} \left|\left\langle 4f^N[\alpha' S' L']J' M'\right| -eD_q{}^{(1)} \left|4f^N[\alpha SL]JM\right\rangle\right|^2 = e^2 \sum_{\lambda=2,4,6} \Omega_\lambda \left|\left\langle 4f^N[\alpha' S' L']J'\right\| U^{(\lambda)} \left\|4f^N[\alpha SL]J\right\rangle\right|^2, \tag{2.78}$$

with

$$\Omega_\lambda = \sum_{tp} (2\lambda + 1) \frac{A_{tp}{}^2}{2t+1} \Xi^2(\lambda, t), \tag{2.79}$$

$$\Xi^2(\lambda, t) = 2 \sum_{nl} (2f+1)(2l+1)\,(-1)^{f+l} \begin{Bmatrix} 1 & \lambda & t \\ f & l & f \end{Bmatrix} \times \begin{pmatrix} \mathrm{f} & 1 & l \\ 0 & 0 & 0 \end{pmatrix} \begin{pmatrix} l & t & \mathrm{f} \\ 0 & 0 & 0 \end{pmatrix} \frac{\langle 4f|r|nl\rangle \langle nl|r^t|4f\rangle}{\Delta W_{nl}}, \tag{2.80}$$

where f = 3, and t = 1, 3, 5, and 7. Eqs. 2.78–80 is divided into the geometrical (former) and physical (latter) parts. This treatment follows the *Wigner-Eckert theorem*. Here, Ω_λ is a constant called the Judd-Ofelt intensity parameter. The Ω_λ parameters depend on Ln^{3+} species with a different expansion of 4f electron clouds but not on the combination of initial and terminal levels for ED transition. Focusing on a specific Ln^{3+} ion, one can discuss the compounds (strictly incorporated sites) dependence of the Ω_λ parameters. A great deal of literature has reported that the chemical trends of the Ω_λ parameters. In particular, the Ω_2 parameter depends on the asymmetry of the local structure around a Ln^{3+} ion. In contrast, the Ω_4 and Ω_6 parameters are

possibly correlated with various features of the local structure, such as the overlap of the 4f and 5d orbitals, the 6s electrons density, the ligand-field distortion, the basicity at the Ln^{3+} site, and the degree of covalency in the Ln^{3+}-ligand bond [15]. The Ω_λ parameters for Eu^{3+} in a variety of inorganic crystalline materials are collected and listed in Appendix A.

The RMEs in eq. 2.78 is expanded with the Wigner-Eckert theorem;

$$\begin{aligned}\langle 4f^N[\alpha' S' L']J' \| U^{(\lambda)} \| 4f^N[\alpha SL]J\rangle \\ = (-1)^{S+L+J'+\lambda} \times \{(2J'+1)(2J+1)\}^{\frac{1}{2}} \begin{Bmatrix} L' & \lambda & L \\ J & S & J' \end{Bmatrix} \delta_{SS'} \\ \times \langle 4f^N \alpha' S' L' \| U^{(\lambda)} \| 4f^N \alpha SL\rangle. \end{aligned} \tag{2.81}$$

Because the RMEs for the $|4f^N \alpha SL\rangle$ state have been well-known, the table of the RMEs for the $|4f^N[\alpha SL]J\rangle$ state is accessible (see Appendix B).

The constraint of the 3-*j* and 6-*j* symbols brings about the selection rule for the 4f-4f transition. **Table 2.2** summarizes the nature of the Wigner 3-*j* and 6-*j* symbols and the selection rules in the Judd-Ofelt theory. As mentioned above, under the condition of non-zero 6-*j* symbols, the selection rule for the partially allowed ED transition of Ln^{3+} in odd-parity is $|\Delta J| \leq 6$. Besides, the transition between the level with $J = 0$ and with $J = 0$, 1, 3, and 5 is strictly forbidden. Supposing that *S* and *L* are still good quantum numbers, the allowed transition has to satisfy $\Delta S = 0$ and $|\Delta L| \leq 6$. If the specific state is approximated to be the RS state with the largest contribution, the transition probability is highest in satisfying these selection rules. This is because such a transition is allowed without the spin-orbit interaction. The selection rules for the MD and EQ transition are $\Delta J = 0, \pm 1$ (not $0 \leftrightarrow 0$ transition) and $|\Delta J| \leq 2$ (not $0 \leftrightarrow 0$, 1 transitions), respectively. These transitions are allowed for the 4f-4f transition and are independent of the centrosymmetry of the local structure because they have even-parity. However, taking the crystal field effects into account, the *J* selection rules are strictly invalid because *J* is no longer a good quantum number. The optical 4f-4f transition for Ln^{3+} ions, actually observed through spectroscopy, is assigned to the ED or MD transition due to the mixing of two states with different parities. The actual optical spectra are more complicated than would be expected from the Judd-Ofelt theory. Some forbidden transitions under the Judd-Ofelt theory are observed because of the invalid closure approximation or *J*-mixing (mixing of the adjacent

J-levels due to the crystal field with even-parity).

By using eq. 2.78, the spontaneous emission rate for the ED transition is provided. First, the oscillator strength of the optical absorption process is defined as follows;

$$f = \frac{8\pi^2 m\nu}{3he^2}|\boldsymbol{M}|^2, \tag{2.82}$$

where $\boldsymbol{M}$ is the dipole momentum. The oscillator strength is a dimensionless quantity and is often used to describe the intensity of optical absorption or emission of an atom or molecule. In the case of the ED transition, the oscillator strength of the ED absorption transition is described with the local field correction $\chi_{\mathrm{ED}}{}^{\mathrm{abs}}$ and the number of degeneracy for the excited level;

$$f_{\mathrm{ED}}{}^{\mathrm{abs}} = \frac{8\pi^2 m\nu}{3h}\frac{1}{2J+1}\frac{\chi_{\mathrm{ED}}{}^{\mathrm{abs}}}{n}\sum_{\lambda}\Omega_{\lambda}\left|\langle 4f^N[\alpha' S'L']J'\|U^{(\lambda)}\|4f^N[\alpha SL]J\rangle\right|^2. \tag{2.83}$$

The term $1/n$ is an additional correction other than the local field correction χ because the photon flux does not change upon entering the dielectric medium from the vacuum [15]. There is the following relationship between the *B*-coefficient and oscillator strength $f_{\mathrm{ED}}{}^{\mathrm{abs}}$;

$$B_{\mathrm{ED}} = \frac{e^2}{4hm\varepsilon_0} f_{\mathrm{ED}}{}^{\mathrm{abs}}. \tag{2.84}$$

In addition, by using eq. 2.22, the A_{ED} is given as follows;

$$A_{\mathrm{ED}} = \frac{64\pi^4 e^2\tilde{\nu}^3}{3h(2J+1)}\chi_{\mathrm{ED}}{}^{\mathrm{em}}\sum_{\lambda}\Omega_{\lambda}\left|\langle 4f^N[\alpha' S'L']J'\|U^{(\lambda)}\|4f^N[\alpha SL]J\rangle\right|^2. \tag{2.85}$$

Here, $\tilde{\nu}^3$ is the average energy of the transition in the unit of cm^{-1}. On the other hand, because the MD momentum is given by $L + gS$ (g: g-factor), the A_{MD} is described below;

$$A_{\mathrm{MD}} = \frac{4\pi^2 e^2 h}{3c^2 m^2}\frac{\tilde{\nu}^3}{2J+1}\chi_{\mathrm{MD}}{}^{\mathrm{em}}|\langle 4f^N[\alpha SL]J'\|L+gS\|4f^N[\alpha SL]J\rangle|^2. \tag{2.86}$$

By using the local field correction terms in Table 2.1, the total spontaneous emission rate from a given excited state is summarized as follows;

$$\begin{aligned} &A([S'L']J'M';[SL]JM) \\ &= \frac{64\pi^4 e^2\tilde{\nu}^3}{3h(2J+1)}\left[\begin{array}{c}\dfrac{n(n^2+2)^2}{9}\displaystyle\sum_{\lambda}\Omega_{\lambda}\left|\langle 4f^N[\alpha' S'L']J'\|U^{(\lambda)}\|4f^N[\alpha SL]J\rangle\right|^2 \\ +\dfrac{h^2n^2}{16\pi^2c^2m^2}|\langle 4f^N[\alpha SL]J'\|L+gS\|4f^N[\alpha SL]J\rangle|^2\end{array}\right] \\ &\qquad +A_{\mathrm{forbidden}}. \end{aligned} \tag{2.87}$$

If the forbidden transition caused by the *J*-mixing is not negligible, the spontaneous emission

rate $A_{\text{forbidden}}$ should be considered. The total radiative decay rate of $|4f^N\alpha SLJM\rangle$ is given as the reciprocal of $A([S'L']J'M';[SL]JM)$. Since the decay rate estimated from the Judd-Ofelt theory considers only the radiative process, the non-radiative relaxation processes, such as the multiphonon relaxation, the cross-relaxation, and the energy migration, are not taken into account.

Table 2.2. Summary of the Wigner 3-*j* and 6-*j* symbols and the selection rules in the Judd-Ofelt theory

	3-*j* symbols $\begin{pmatrix} j_1 & j_2 & j_3 \\ m_1 & m_2 & m_3 \end{pmatrix}$	6-*j* symbols $\begin{Bmatrix} j_1 & j_2 & j_3 \\ l_1 & l_2 & l_3 \end{Bmatrix}$
non-zero condition	$j_i \geq 0$ $m_i \leq j_i$ $m_1 + m_2 + m_3 = 0$ j_i, m_i (Integer or half-integer) $\lvert j_1 - j_2 \rvert \leq j_3 \leq j_1 + j_2$	$j_i \geq 0$ $l_i \geq 0$ $\lvert j_1 - j_2 \rvert \leq j_3 \leq j_1 + j_2$ $\lvert l_2 - l_3 \rvert \leq j_1 \leq l_2 + l_3$ $\lvert l_1 - l_3 \rvert \leq j_2 \leq l_1 + l_3$ $\lvert l_1 - l_2 \rvert \leq j_3 \leq l_1 + l_2$
allowed ED transition (f = 3 / t = 1, 3, 5, 7)	$\begin{pmatrix} \mathrm{f} & 1 & l \\ 0 & 0 & 0 \end{pmatrix} \neq 0$ / $\begin{pmatrix} l & t & \mathrm{f} \\ 0 & 0 & 0 \end{pmatrix} \neq 0$	$\begin{Bmatrix} 1 & \lambda & t \\ \mathrm{f} & l & \mathrm{f} \end{Bmatrix} \neq 0$

Selection Rules for 4f-4f Transition in the Judd-Ofelt Theory				
	S	L	J (no 0↔0)	parity
ED transition	$\Delta S = 0$	$\Delta L \leq 6$	$\Delta J \leq 6$ $\Delta J = 2, 4, 6$ (J or $J' = 0$)	odd
MD transition	$\Delta S = 0$	$\Delta L = 0$	$\Delta J = 0, \pm 1$	even
EQ transition	$\Delta S = 0$	$\Delta L = 0, \pm 1, \pm 2$	$\Delta J = 0, \pm 1, \pm 2$	even

2.1.4. Charge Transfer Transition

Optical transition in a variety of functional luminescent materials is not always assigned to a given intrinsic transition in impurity ions, such as transition metals and lanthanoids. The interaction between these activators and ligands or adjacent cations is also an important optical process. In particular, *the charge transfer* (*CT*) *transition* is essential optical absorption and emission process, observed in many inorganic solids, complexes, and organic clusters. The CT transition is considered to be the local physical phenomenon caused by the electron transfer between different atomic/molecular orbitals. Because the CT transition is Laporte allowed, the transition probability is very high. Depending on the transfer process, it is identified as follows; ligand-to-metal CT (LMCT), metal-to-ligand CT (MLCT), metal-to-metal CT (MMCT), and intervalence CT (IVCT). In this section, the LMCT transfer is briefly explained.

The LMCT transition takes place when the metal ion is in the high oxidation state and the ligands have the lone pair. Let us assume that a transition metal M^{n+} ion in an octahedral ligand field forms a $[MO_6]^{(12-n)-}$ ion with six O^{2-} ions. With the excitation energy, an electron in the lone pair of O 2p orbitals transfers to the empty d orbitals (two-fold e_g orbitals) of the M^{n+} ion, accompanied by the valence change ($M^{n+} + e^- \rightarrow M^{(n-1)+}$). This transfer forms the LMCT states for the M^{n+} ion. As the transition metal ion in a high valence state has the d orbital with a low electron density (usually the d^0 state), it can accept an electron at the energy levels with low energy. The electronic transition process related to the LMCT states can be roughly understood by the molecular orbital theory in a diatomic molecule, where a M^{n+} ion and a ligand are extracted from the polyhedra, because the LMCT transition occurs locally. Considering the difference in the electronegativity of M^{n+} and O^{2-} ions, the *M* d and O 2p orbitals form the lowest unoccupied molecular orbital (LUMO) and highest occupied molecular orbital (HOMO), respectively. The electronic transition from the HOMO to the LUMO is considered to be the LMCT transition. Therefore, when the metal ion species are consistent, the smaller electronegativity of ligands tends to the lower CT energy. As specific examples of the LMCT transition, the CT transition in tungstates and Eu^{3+}-doped phosphors is briefly introduced below.

2.1.4.1. Charge Transfer in Tungstates

As mentioned above, the polyhedra with transition metal ions in the high oxidation states (pentavalent cations of V^{5+}, Nb^{5+}, and Ta^{5+}; hexavalent cations of Cr^{6+}, Mo^{6+}, and W^{6+}; heptavalent cations of Mn^{7+}, Tc^{7+}, and Re^{7+}) show the strong absorption band in the UV region through the LMCT transition. Because the LMCT energy is correlated with the ionization tendency, the transition occurs on the ions that are easily reduced with the lowest energy. The visible luminescence assigned to the CT transition is observed in some inorganic compounds, such as vanadates $[VO_4]^{3-}$, tungstates $[WO_4]^{2-}$ or $[WO_6]^{6-}$, and molybdates $[MoO_4]^{2-}$. In this section, the optical transition in tungstates is introduced. The radiative transition is the MLCT transition from W 5d to O 2p orbitals. From now on, the absorption (excitation) and luminescence processes are called the CT transition without identification.

The mineral *scheelite* with the composition of $CaWO_4$ is a famous example for the tungstates showing the CT luminescence, which is transparent and shows bright sky-blue luminescence under UV illumination. Due to the unusual heaviness, it was given the name *tungsten* with the meaning of "heavy stone" in Swedish. As shown in **Figure 2.6a**, the crystal structure of scheelite is tetragonal (space group: $I4_1/a$), in which W^{6+} ions form distorted $[WO_4]^{2-}$ tetrahedra with S_4 symmetry. The $[WO_4]^{2-}$ tetrahedra are isolated in a tetragonal lattice without any corner, edge, and face sharing with other tetrahedra. The bond length between W^{6+} and O^{2-} ions is ~1.8 Å, through which the CT transition takes place, whereas the interatomic distance between a W^{6+} and the second nearest O^{2-} ions is ~3.0 Å. In order to understand the energy level structure of a $[WO_4]^{2-}$ tetrahedron and discuss the radiative electronic transition resulting in CT luminescence, one has to consider many factors, such as the crystal field splitting of W 5d levels, the molecular orbital (MO) composed of O 2p and W 5d orbitals, the large spin-orbit interaction of W caused by the relativistic effect, and the site-symmetry of a tetrahedron. For the sake of brevity, it is assumed that the $[WO_4]^{2-}$ tetrahedra take the cubic T_d symmetry to discuss the radiative CT transition. The character table for T_d symmetry is given in **Table 2.3**. The irreducible representations (irreps) for T_d symmetry are denoted as A_1, A_2, E, T_1, and T_2.

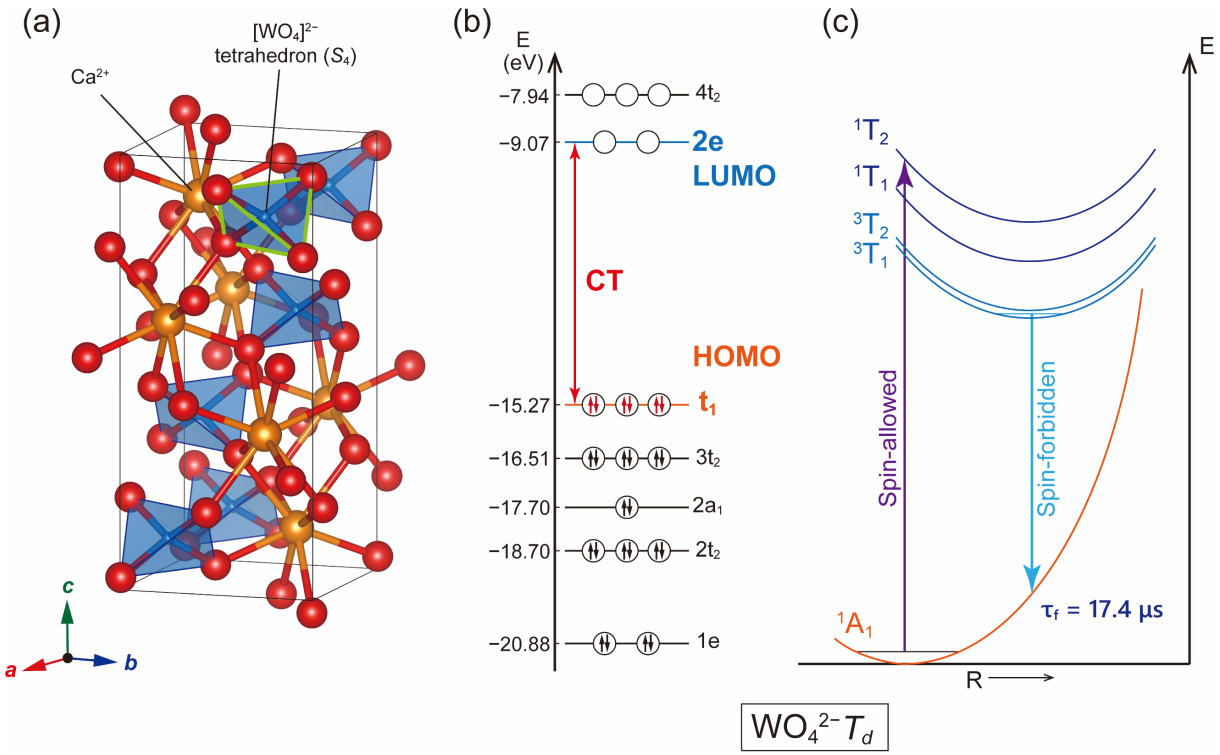

Figure 2.6. (a) Crystal structure of the scheelite-type $CaWO_4$ (tetragonal, space group: $I4_1/a$). (b) MO energy levels for free $[WO_4]^{2-}$ tetrahedral as calculated by the extended Hückel MO calculation. (c) Configurational coordinate diagram for the lowest electron transition of 2e ↔ t_1 in a regular $[WO_4]^{2-}$ tetrahedron with T_d symmetry [17].

The MO calculation with the extended Hückel method performed by Grasser revealed the MO energy levels in $[WO_4]^{2-}$ ions [17], as shown in **Figure 2.6b**. The HOMO and LUMO are labeled by t_1 and 2e, respectively. The CT luminescence is caused by the radiative transition between these two MO levels. The HOMO and LUMO are mainly composed of the O 2p and W 5d orbitals, respectively, indicating the CT transition is caused by the electron transfer accompanied by the reduction of W^{6+} into W^{5+}. The term symbols in the $(t_1)^5(2e)^1$ excited state are estimated by calculating the direct product of $T_1 \otimes E$. The direct products of T_d symmetry are provided in **Table 2.4**. Considering the spin multiplicity, the excited states are denoted with the terms in the order of $^1T_2 > {}^1T_1 > {}^3T_2 \geq {}^3T_1$, as shown in the configurational coordinate diagram in **Figure 2.6c**. On the other hand, the term symbol in the $(t_1)^6$ ground state is $^1A_1$ with total symmetry. By applying the ED approximation, the dominant process for absorption (or excitation) is attributed to the $^1T_2 \leftarrow {}^1A_1$ allowed transition (see section 2.2.1.2 for determination of allowed transition). The initial level for the radiative transition is the $^3T_1$ level that has the

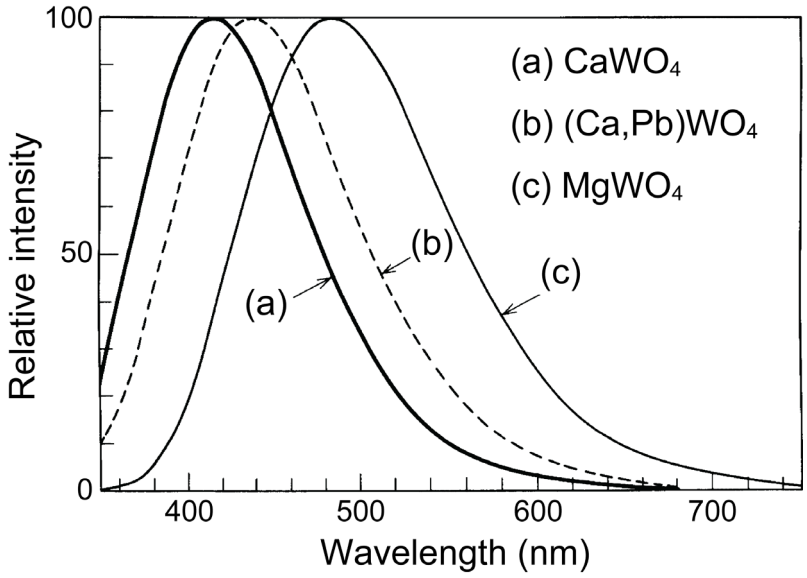

Figure 2.7. Photoluminescence spectra of (a) $CaWO_4$, (b) $(Ca,Pb)WO_4$, and $MgWO_4$ [19].

lowest CT state energy. Although the $^3T_1 \rightarrow {}^1A_1$ transition is spin-forbidden, it is partially allowed because the total spin angular momentum S is not a good quantum number in tungstates. The experimental decay rate on the order of 10^{0-2} μs of the CT luminescence in tungstates [17] corresponds to the feature of forbidden transition. Actually, the lowest $^3T_1$ level splits into two due to the spin-orbit interaction with $\Delta E = \sim 20\ cm^{-1}$, and the crystal field splitting of W 5d levels should be larger because of distortion in the tetrahedron with S_4 symmetry. Nevertheless, this model successfully explains the experimental facts of the CT transition in tungstates.

The compounds with the composition of $M^{2+}WO_4$ (M = Mg, Sr, Ba, Cd, and Pb) take the isostructure scheelite-type structure, resulting in visible and efficient CT luminescence. These scheelite-type materials have been well-known for over 80 years [18], and there is much literature about the systematical studies on structural, electronic, and compositional characteristics. In particular, $CdWO_4$ and $PbWO_4$ have been well developed for scintillator applications due to the high density, the high effective atomic number, and the suitable emission wavelength for detection [19–21]. Although the divalent cations do not interact with the electronic structure of the $[WO_4]^{2-}$ tetrahedra directly, they indirectly affect the crystal field splitting induced by distortion in the tetrahedra or the Madelung potential in the structure. **Figure 2.7** shows the photoluminescence spectra of $CaWO_4$, $(Ca,Pb)WO_4$, and $MgWO_4$. The CT

energy is influenced by many factors including the electronegativity or ionic radius of M^{2+} ions.

In addition, the tungstates are widely studied as the host materials for *Ln* ions [3]. Since the parity-forbidden 4f-4f transition for Ln^{3+} ions leads to the low absorption coefficient and causes the narrow absorption bands because of the small electron-phonon coupling, it is necessary to combine the highly efficient excitation process to obtain the intense luminescence for LED applications. The broad and efficient LMCT absorption band is desirable to sensitize the Ln^{3+} luminescence. For example, the Eu^{3+}-doped tungstates show the intense Eu^{3+} red luminescence under near-UV excitation, which is not obtained in the simple oxide host.

Table 2.3. Character table for T_d group

T_d	E	$8C_3$	$3C_2$	$6S_4$	$6\sigma_d$		
A_1	1	1	1	1	1		$x^2 + y^2 + z^2$
A_2	1	1	1	−1	−1		
E	2	−1	2	0	0		$(2z^2 - x^2 - y^2,\ \sqrt{3}(x^2 - y^2))$
T_1	3	0	−1	1	−1	(R_{xy}, R_{yz}, R_{zx})	
T_2	3	0	−1	−1	1	(x, y, z)	(xy, yz, zx)

Table 2.4. Direct products for T_d group

	A_1	A_2	E	T_1	T_2
A_1	A_1	A_2	E	T_1	T_2
A_2		A_1	E	T_2	T_1
E			$A_1 + A_2 + E$	$T_1 + T_2$	$T_1 + T_2$
T_1				$A_1 + E + T_1 + T_2$	$A_2 + E + T_1 + T_2$
T_2					$A_1 + E + T_1 + T_2$

2.1.4.2. Charge Transfer in Eu^{3+}-Doped Phosphors

In the previous section, the CT transition between the transition metal ions in the high oxidation state and ligands. The CT transition can take place on Ln^{3+} ions as well and is discussed in this section briefly. The Ln^{3+} ions with $4f^N$ electronic configuration take not only the excited states of $4f^N$ or $4f^{N-1}5d^1$ configuration but also the CT excited states with higher energy than 5d excited states. Since the CT transition causes the reduction of Ln^{3+} ions like transition metal ions, the CT excited states take lower energy for the Ln^{3+} ions that have filled or half-filled 4f orbitals and easily be reduced into divalent states, like Sm^{3+}, Eu^{3+}, Tm^{3+}, and Yb^{3+}. In particular, Eu^{3+} has lower CT states than the $4f^55d^1$ states, resulting in the highly efficient excitation process *via* the CT states in various Eu^{3+}-activated phosphors.

The CT energy for Eu^{3+} depends on the electronegativity of anions in inorganic host compounds; accordingly, the CT energy is typically shifted to lower energies in the order of fluorides, oxides, and nitrides. **Figure 2.8** shows the energy levels in the cation-anion bonding with the MO theory and the band structure. In the MO picture, the energy of anion p orbitals lowers, according to the order of the Pauling electronegativity χ_p ($\chi_{p,F} = 3.98 > \chi_{p,O} = 3.44 > \chi_{p,N} = 3.04$) [22]. Here, the anion p orbitals are dominant in the bonding orbitals, while the cation orbitals mainly form the antibonding orbitals. Since an accumulation of these MOs forms the band structure, the bonding orbitals form the valence band (VB). Therefore, the VB top shifts

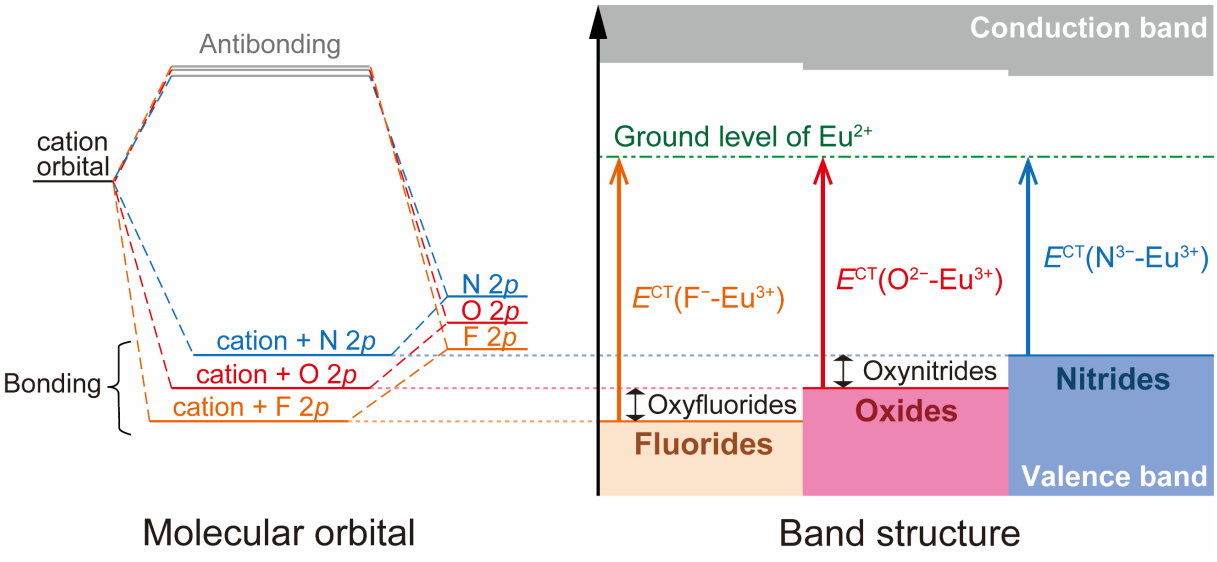

Figure 2.8. Schematic illustrations of the molecular orbital and band structure for fluorides, oxides, and nitrides.

to the high energy side in the order of fluorides < (oxyfluorides <) oxides < (oxynitrides <) nitrides. The CT transition is interpreted as the electronic transition from the VB top (*i.e.*, anion p orbitals) to the 4f ground level of Eu^{2+}, accompanied by the valence state change of $Eu^{3+} + e^{-} \rightarrow Eu^{2+}$. Because the Eu^{2+} ground level is almost unchanged in various compounds due to the shielding effect of inner 4f orbitals, the order of the CT energy roughly follows the order of the anion electronegativity in the host compounds.

2.1.5. Carrier Recombination *via* Exciton States

Until now, the luminescence phenomena related to the impurity ions or isolated polyhedra with transition metals in inorganic compounds are discussed. However, in solids, there are cases where luminescence is derived not from the intrinsic transition in some ions but from a given quantized state. The exciton state is one of the significant states related to photon emission processes. In this section, the exciton in solids and its features are briefly introduced.

2.1.5.1. Exciton in Solids

Let us consider a given semiconductor with a direct bandgap at the Γ point in reciprocal space (*i.e.,* $\boldsymbol{k} = 0$). When an electron is excited to the conduction band (CB) through the band-to-band transition, a hole is generated in the VB. The electron in the CB and hole in the VB are attracted by the Coulomb interaction, indicating that the electron in the CB is excited to the binding state in the electrostatic field formed by the hole. The CB electron and VB hole move together in the crystal and behave as if they were a single neutral particle; this is *the exciton*. The absorption band attributed to (host) exciton creation has lower energy than the bandgap by the binding energy of the exciton $0.008(E^{ex})^2$ (E^{ex}: host exciton creation energy) [4,23]. The loosely binding exciton with a much bigger effective radius than interatomic distances in the lattice is called *the Wannier exciton*. On the other hand, the strongly binding exciton is *the Frenkel exciton*, in which the electron and hole are located on the same atom in the binding state.

In the case of the perfect crystal, the exciton can move freely (*i.e., free exciton*). However, because the actual crystal contains a variety of point defects, including impurity ions and lattice vacancies, the exciton can be trapped in these defects, called *the impurity-trapped exciton* (*ITE*).

Especially at cryogenic temperatures, almost all exciton form the ITE state. In the photon emitting process of the free exciton in the direct bandgap semiconductor, only the free excitons with small momentum contribute to the luminescence, according to the momentum conservation. On the contrary, the transition probability of the ITE state is high because, in the first place, the momentum is small enough. When the exciton is generated in a given alkaline halide *MX*, the hole is trapped by two X^- ions, resulting in a pseudo-molecular state of X_2^-. This state is called V_k-center. In *the self-trapped exciton* (STE) state, the electron is trapped by the V_k-center. The decay rates of luminescence related to the free exciton and STE states are in order of pico-seconds and nano-seconds, respectively. The decay rate of the ITE luminescence is longer than theirs.

2.1.5.2. Anomalous Luminescence Related to Impurity-Trapped Exciton States

Divalent Eu ions show the bright luminescence assigned to the parity-allowed 5d-4f transition. However, in some Eu^{2+}-doped phosphors, anomalous luminescence is observed, which cannot be explained by the typical Eu^{2+}: 5d-4f transition. For example, the BaS:Eu^{2+} phosphor shows the very broad (= 3980 cm^{-1} at T = 293 K) near-infrared luminescence (λ_{em} = 878 nm) with the large Stokes shift of 6925 cm^{-1} [23]. The luminescence properties of the BaS:Eu^{2+} phosphor are unexpected from the chemical tendency of the *AE*S:Eu^{2+} (*AE* = Ca, Sr) materials; that is, the luminescence does not correspond to the tendency that the luminescence peak gets blueshifted with the crystal field strength decreasing. This anomalous luminescence is assigned to the luminescence from the Eu^{2+}-trapped exciton (ETE) states. The anomalous luminescence related to Eu^{2+}- or Yb^{2+}-trapped exciton states is reviewed by Pieter Dorenbos [24]. Here, some features of the ETE luminescence are introduced.

The anomalous luminescence related to the ETE states has the following three characteristics; (1) an abnormally large Stokes shift (5000–10000 cm^{-1}) and width (> 4000 cm^{-1} at ambient temperature) of the emission band, (2) a wavelength of emission that is not consistent with the wavelength anticipated from the properties of the compound, and (3) an anomalous decay time and thermal quenching behavior. These characteristics can be explained by the configuration coordinate diagram (**Figure 2.9**), in which the $5d^1$ and ETE states are considered.

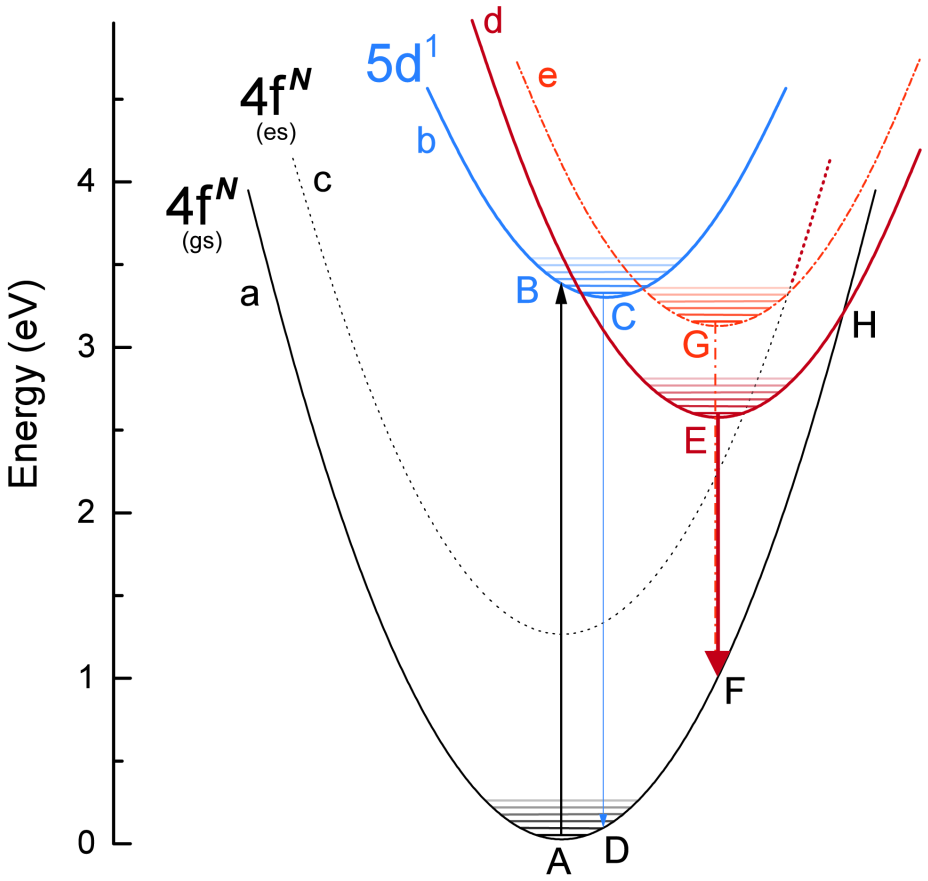

Figure 2.9. Configuration coordinate diagram illustrating normal 5d-4f transition and anomalous luminescence related to Ln^{2+}-trapped exciton states [24].

The parabolas a–e represent the adiabatic potential curves of the following states; a: the $4f^N$ ground state (gs), b: the $4f^{N-1}5d^1$ excited state, c: the $4f^N$ excited state (es), d and e: the ITE states. The typical 5d-4f absorption and emission processes are described by the processes of A → B and C → D, respectively. If the potential curve of the ITE state is located below that of the $5d^1$ excited state, the excited state relaxed down to the minimum point of the ITE parabola accompanied by the lattice relaxation. The ITE state has a larger configuration coordinate offset than the $5d^1$ excited state. In the ITE state, the electron no longer localizes at the Eu^{2+} ion, illustrated by the binding state of $Eu^{2+} \rightarrow Eu^{3+} + e^-$. Because of the strong Coulomb attraction of the small Eu^{3+} ion, the ligand shift in the ITE state should be larger than that of the $5d^1$ excited state. If the binding between the Eu^{3+} and e^- is relatively weak, the electron can exist beyond the lattice, which is called *the Rydberg state* with slightly lower energy than the ETE state. If the ITE state is in the high energy state (parabola e), the ETE state is no longer stable. The parabola e intersects with

the $4f^N$ (es) parabola c nearby the minimum point of the parabola e, leading to the thermal activation crossover quenching with a small activation energy. The stable ETE state is desirable to obtain anomalous luminescence. In this diagram, the observed ETE luminescence is depicted by the process E → F. The large offset provides the large width and Stokes shift of the luminescence band. The ETE state is independent of the $5d^1$ excited state, leading to unexpected features from the chemical tendency of the host composition. The anomalous thermal behavior can be correlated with the non-radiative relaxation process caused by the thermal energy over the binding energy of the exciton state.

2.2. Theory of Host Materials

Inorganic solids are mainly composed of the following two phases; the crystalline phase with the ordered structure over long distances and the amorphous phase with the random structure of locally ordered units. In both phases, the luminescence properties of doped activators depend on the local environment and the electronic structure of the host material. In this section, the point groups in crystals describing structural features of local environments and *the vacuum referred binding energy* (*VRBE*) *diagram* representing the relative positions of the energy levels of impurity ions and host bandgap are introduced. The point groups provide important information about the orbital selection rules of electronic transition. On the other hand, by constructing and applying the VRBE diagram, the thermal quenching mechanism of luminescence and persistent luminescence with the carrier-trapping scheme are explained. Both concepts are essential factors to discuss and evaluate in detail the properties of functional luminescent materials.

2.2.1. Characterization of Local Structure Based on Group Theory

2.2.1.1. Thirty-Two Point Groups of Polyhedra in Solids

The symmetry of molecules, coordination polyhedra, and crystalline lattices can be described by the (mathematical) group theory. The fundamental group theory is referred to in some textbooks [4,26]. Molecules can take countless spatial symmetries. As it must be compatible with

translational symmetry to achieve repetition of the unit cell, however, the number of the symmetrical groups in crystals is only thirty-two. The thirty-two point groups in crystals and their symmetry elements are listed in **Table 2.5**. The point groups in each crystal system are denoted by *the Hermann-Mauguin* (*international*) *notation* and *Schönflies notation*. In this dissertation, the point groups are represented in the Schönflies notation. Considering the order (or dimension) of each group, the same symmetry elements are shown in the coefficients. Here, the identity operation E is omitted except for C_1 symmetry.

The irreducible representation (irrep) Γ_i for each group is denoted by the Mulliken notation. The general symbol in the Mulliken notation is X_{ij}^{s}, where each letter is represented according to the following three rules. (1) The capital letter X means the dimension of irreps. The one-, two-, and three-dimension irreps are denoted as A or B, E, and T, respectively. The character of the main rotation axis determines the symbol of the one-dimension irreps; symmetric A and antisymmetric B. (2) The first subscript i is X_1 if it is symmetric with respect to the two-fold rotation axis C_2 or the vertical mirror plane σ_v, and X_2 if it is antisymmetric. The second subscript j identifies the parity of the group; *i.e.*, gerade (X_g) or ungerade (X_u). (3) The superscript s is X' if it is symmetric with respect to the horizontal mirror plane σ_h, and X" if it is antisymmetric. In the character table for the T_d symmetry, the irreps for the T_d group are denoted as A_1, A_2, E, T_1, and T_2. The summation of the squared dimensions for each irrep corresponds to the number of the symmetry elements (order). All the groups contain the identity representation (or totally symmetric) A.

Table 2.5. Thirty-two point groups in crystal structures

crystal system	order	Hermann-Mauguin notation	Schönflies notation	symmetry elements
Triclinic	1	1	C_1	E
	2	$\bar{1}$	C_i	i
Monoclinic	2	2	C_2	C_2
	2	m	C_s	σ_h
	4	$2/m$	C_{2h}	C_2, σ_h, i
Orthorhombic	4	222	D_2	$C_2(x)$, $C_2(y)$, $C_2(z)$
	4	$mm2$	C_{2v}	C_2, σ_v, $\sigma_{v'}$
	8	mmm	D_{2h}	$C_2(z)$, $C_2(y)$, $C_2(x)$, i, $\sigma(xy)$, $\sigma(yz)$, $\sigma(zx)$
Tetragonal	4	4	C_4	C_4, C_2, C_4^3
	4	$\bar{4}$	S_4	S_4, S_2, S_4^3
	8	$4/m$	C_{4h}	C_4, C_2, C_4^3, i, S_4^3, σ_h, S_4
	8	422	D_4	C_2, $2C_4$, $2C_2$, $2C'_2$
	8	$4mm$	C_{4v}	C_2, $2C_4$, $2\sigma_v$, $2\sigma_{v'}$
	8	$\bar{4}2m$	D_{2d}	C_2, $2S_4$, $2C_2$, $2\sigma_d$
	16	$4/mmm$	D_{4h}	$2C_4$, C_2, $2C_2'$, $2C_2''$, i, $2S_4$, σ_h, $2\sigma_v$, $2\sigma_d$
Trigonal	3	3	C_3	C_3, C_3^2
	6	$\bar{3}$	S_6	C_3, C_3^2, i, S_6^5, S_6
	6	32	D_3	$2C_3$, $3C_2$
	6	$3m$	C_{3v}	$2C_3$, $3\sigma_v$
	12	$\bar{3}m$	D_{3d}	$2S_4$, C_2, $2C_2'$, $2\sigma_d$
Hexagonal	6	6	C_6	C_6, C_3, C_2, C_3^2, C_6^5
	6	$\bar{6}$	C_{3h}	C_3, C_3^2, σ_h, S_3, S_3^5
	12	$6/m$	C_{6h}	C_6, C_3, C_2, C_3^2, C_6^5, i, S_3^5, S_6^5, σ_h, S_6, S_3
	12	622	D_6	C_2, $2C_3$, $2C_6$, $3C_2$, $3C_2'$
	12	$6mm$	C_{6v}	C_2, $2C_3$, $2C_6$, $3\sigma_v$, $3\sigma_{v'}$
	12	$\bar{6}2m$	D_{3h}	$2C_3$, $3C_2$, σ_h, $2S_3$, $3\sigma_v$
	24	$6/mmm$	D_{6h}	$2C_6$, $2C_3$, C_2, $3C_2'$, $3C_2''$, i, $2S_3$, $2S_6$, σ_h, $3\sigma_d$, $3\sigma_v$
Cubic	12	23	T	$4C_3$, $4C_3^2$, $3C_2$
	24	$m3$	T_h	$4C_3$, $4C_3^2$, $3C_2$, i, $4S_6$, $4S_6^2$, $3\sigma_d$
	24	432	O	$6C_4$, $8C_3$, $3C_2$, $6C_2'$
	24	$\bar{4}3m$	T_d	$8C_3$, $3C_2$, $6S_4$, $6\sigma_d$
	48	$m\bar{3}m$	O_h	$8C_3$, $6C_2$, $6C_4$, $3C_2$, i, $6S_4$, $8S_6$, $3\sigma_h$, $6\sigma_d$

2.2.1.2. Orbital Selection Rule — Estimation of Allowed/Forbidden Transition

One of the important discussions with the point groups is the prediction of the orbital selection rules. According to Fermi's golden rule, the transition probability is proportional to the squared matrix elements. If the matrix elements output some non-zero value, the transition is allowed; otherwise, it is forbidden. Although it is necessary to calculate the integrals to obtain the transition probability with computational techniques, one can consider only the symmetry of the wavefunction when it comes to determining whether zero or non-zero. In the case of the transition between states a and b, the wavefunctions Ψ_a and Ψ_b are given, whose symmetries are denoted by the irreps Γ_a and Γ_b. By assuming the transition operator *f*, whose symmetry corresponds to the irreps Γ_f, the matrix elements of the transition are described as follows;

$$\langle \Psi_a | f | \Psi_b \rangle = \int \Psi_a{}^* f \Psi_b dq \,. \tag{2.88}$$

Besides, the whole product in the integral (eq. 2.88) corresponds to the direct product of three irreps $\Gamma_a \otimes \Gamma_f \otimes \Gamma_b$, leading to a reducible representation Γ. If the Γ contains the identity representation A, the matrix elements in eq. 2.88 are not zero, resulting in the allowed transition between the states a and b caused by the operator *f*.

As an example, let us consider the orbital selection rules for the ED transition in the T_d group. The basis of the T_2 irreps is {*x, y, z*}, which exactly corresponds to the components of the radius-vector and, by its definition, ED operator. Thus, the direct product of $\Gamma_a \otimes T_2 \otimes \Gamma_b$ is decomposed to find out whether the ED transition is allowed between two states Γ_a and Γ_b of the T_d group. First, the $A_1 \rightarrow T_2$ ED transition is examined, which is the LMCT transition in the $[WO_4]^{2-}$ tetrahedron. The characters of the direct product $A_1 \otimes T_2 \otimes T_2$ are as follows;

T_d	E	$8C_3$	$3C_2$	$6S_4$	$6\sigma_d$
$A_1 \otimes T_2 \otimes T_2$	9	0	0	1	1

and this 9-dimensional reducible representation can be decomposed into the following irreps of the T_d group: $A_1 + E + T_1 + T_2$. It contains the identity irrep A_1, which makes the $A_1 \rightarrow T_2$ transition allowed in the ED approximation. All other combinations of the irreps in the T_d group can be examined as well. **Table 2.6** shows all allowed (denoted by "+") and forbidden (denoted

by "–") ED transitions in the T_d group.

A similar analysis can be applied to the transition with arbitrary operators between two states in other point groups. Therefore, one can discuss to some extent the assignment of the transition and the selection rules of luminescence phenomena under the ED approximation.

Table 2.6. Allowed and forbidden ED transitions between the states with the symmetry of the irreps of the T_d group

T_d	A_1	A_2	E	T_1	T_2
A_1	–	–	–	–	+
A_2	–	–	–	+	–
E	–	–	–	+	+
T_1	–	+	+	+	+
T_2	+	–	+	+	+

2.2.2. Energy Level Structure of Lanthanoid Ions in Host Band Structure

Lanthanoid ions doped in the inorganic host materials form the local 4f energy level structure in the host bandgap, resulting in unique features. For example, the impurity of Dy^{3+} ions in the $SrAl_2O_4:Eu^{2+}$ phosphor form the electron-trapping level just below the CB bottom, leading to Eu^{2+} persistent luminescence with the long duration > 30 h [26,27]. The 5d excited levels for Ce^{3+} or Eu^{2+} nearby the conduction band bottom can cause thermal quenching even at ambient temperature [28]. Deep insight into the Ln^{2+}/Ln^{3+} energy level structures in the bandgap is inevitable for the study on the *Ln*-activated luminescent materials.

As the difference of 4f energy levels of Ln^{2+}/Ln^{3+} ions is almost independent of the local environment (known as the "zigzag" curves), their relative positions in the host bandgap can be predicted by limited spectroscopic data to some extent. The semi-empirical model depicting the energy level diagram related to the host bandgap and relative positions of 4f levels has been proposed by Pieter Dorenbos [29,30]. *The vacuum referred binding energy* (*VRBE*) *diagram* consists of the following four models; (i) redshift model, (ii) centroid shift model, (iii) charge

transfer model, and (iv) chemical shift model.

(i) Redshift Model. As shown in section 2.1.2.2, the energy difference between the $4f^n$ ground and $5d^1$ excited states for Ln^{Q+} in a compound A $E_{fd}(n, Q, A)$ is smaller than that in the free ion state $E_{fd}(n, Q, \text{free})$. This model suggests that if the Ln^{Q+} ion is incorporated in the same site of compound A, the depression $D(Q, A)$ is independent of the number of the 4f electrons n; *i.e.*, the $D(Q, A)$ value is common for all Ln^{2+}/Ln^{3+} ions. This model is described by the following equation;

$$E_{\mathrm{fd}}(n, Q, A) = E_{\mathrm{fd}}(n, Q, \mathrm{free}) - D(Q, A). \tag{2.89}$$

(ii) Centroid Shift Model. The overlap of the five 5d orbitals for *Ln* ions provides the symmetric spherical distribution function of 5d electrons. Considering such a spherical field, one can discuss the interaction between the 5d orbitals and the chemical features of the ligand field that depends on the covalency or polarizability of coordinating anions. The centroid shift for the Ce^{3+}: 5d levels $\varepsilon_c(1, 3+, A)$ is usually determined because Ce^{3+} has only one 4f electron and it is easy to analyze the crystal field splitting of 5d levels.

(iii) **Charge Transfer Model.** As discussed in section 2.1.4.2, the LMCT transition between the Ln^{3+} ion and ligands takes place. A number of studies on the CT energies of Eu^{3+}-doped compounds $E^{CT}(6, 3+, A)$ are accessible, leading to the following relationship with the VB top $E_V(A)$ and the Eu^{2+} 4f ground level $E_{4f}(n + 1, 2+, A)$;

$$E_{4\mathrm{f}}(n+1, 2+, A) = E_{\mathrm{V}}(A) + E^{\mathrm{CT}}(6, 3+, A) + \Delta E(n+1, 7, 2+), \tag{2.90}$$

where $\Delta E(n + 1, 7, A)$ means the energy difference of Ln^{2+} with respect to the Eu^{2+} 4f ground level; in short, the CT energy of Eu^{3+} enables us to obtain the 4f ground levels for all other Ln^{2+} ions with respect to the VB top. By combining the redshift and CT models, the host referred binding energy (HRBE) diagram is constructed, in which the VB top is set at 0 eV.

(iv) Chemical Shift Model. In order to discuss the luminescent properties of *Ln*-doped compounds as originally intended, it is necessary to compare the Ln^{2+} and Ln^{3+} 4f ground levels in different hosts. By introducing the influence of the Coulomb interaction, the VRBE levels for *Ln* ions are obtained. The Coulomb repulsion energy $U(n, A)$ is defined as follows;

$$U(n, A) \equiv E_{4f}(n, 3+, A) - E_{4f}(n+1, 2+, A). \tag{2.91}$$

Usually, the $U(6, A)$ value for Eu^{3+} is calculated because the Eu^{2+} 4f ground level is accessible from the CT model. By utilizing the centroid shift for the Ce^{3+}: 5d levels, the $U(6, A)$ is experimentally obtained with the following empirical equation;

$$U(6, A) = 5.44 + 2.834 \times \exp\left(-\frac{\varepsilon_c(1, 3+, A)}{2.2}\right). \tag{2.92}$$

By using this $U(6, A)$ value, one can obtain the VRBE for Eu^{2+};

$$E_{4f}(7, 2+, A) = -24.92 + \frac{18.05 - U(6, A)}{0.777 - 0.0353 \times U(6, A)}, \tag{2.93}$$

where −24.92 eV is the vacuum referred Eu^{2+} energy level in the free ion state, 18.05 eV is the Coulomb repulsion energy for the Eu ion in the free ion state, and the coefficients of 0.777 and 0.0353 are obtained from the ionic radii.

Considering these models, one can obtain the VRBE diagram of compound A. **Figure 2.10** shows the VRBE diagram for the $Y_3Al_2Ga_3O_{12}$ host. For example, by using this VRBE diagram, the trap depths of Ln^{2+} ions are estimated, leading to the prediction of the suitable host composition and the selection of the optimal Ln^{2+} ion for the electron-trapping center to obtain the persistent luminescence with a long duration.

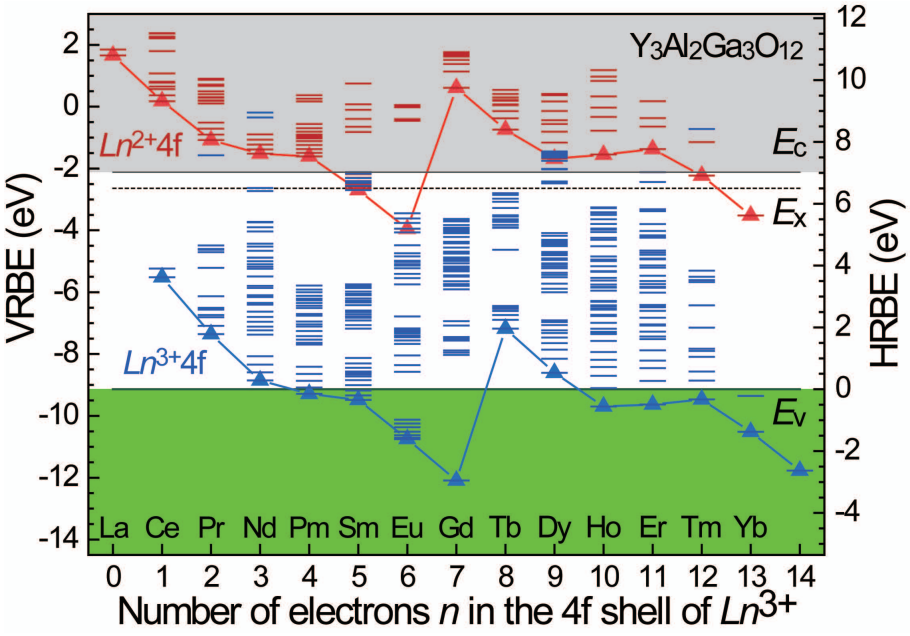

Figure. 2.10. Host and vacuum referred lanthanoid 4f-electron binding energies in the $Y_3Al_2Ga_3O_{12}$ host [31].

References

[1] T. Kushida, "Optical Properties of Condensed Matter". (Asakura Publishing, Tokyo, 1991, *in Japanese)*

[2] P.A. Cox, "The Electronic Structure And Chemistry of Solids". (Oxford Science Publications, Oxford, 1987)

[3] W.M. Yen, S. Shionoya, H. Yamamoto, "PHOSPHOR HANDBOOK". (second ed., CRC Press, Boca Raton, 2007)

[4] M.G. Brik, C.-G. Ma, "Theoretical Spectroscopy of Transition Metal and Rare Earth Ions From Free State to Crystal Field" (Jenny Stanford Publishing, Singapore, 2020)

[5] L.-J. Lyu, D.S. Hamilton, "Radiative and nonradiative relaxation measurements in Ce^{3+} doped crystals". *J. Lumin*. **48–49** (1991) 251–254.

[6] C.K. Duan, M.F. Reid, "Local field effects on the radiative lifetimes of Ce^{3+} in different hosts". *Curr. Appl. Phys*. **6** (2006) 348–350.

[7] T. Kobayasi, S. Mroczkowski, J.F. Owen, L.H. Brixner, "Fluorescence lifetime and quantum efficiency for 5d → 4f transitions in Eu^{2+} doped chloride and fluoride crystals". *J. Lumin.* **21** (1980) 247–257.

[8] S.H.M. Poort, A. Meyerink, G. Blasse, "Lifetime measurements in Eu^{2+}-doped host lattices". *J. Phys. Chem. Solids* **58** (1997) 1451–1456.

[9] S.E. Yoca, P. Palmeri, P. Quinet, G. Jumet, É. Biémont, "Radiative properties and core-polarization effects in the W^{5+} ion". *J. Phys. B At. Mol. Opt. Phys.* **45** (2012) 035002 (6p).

[10] C.K. Jørgensen, "Electron transfer spectra of lanthanide complexes". *Mol. Phys.* **5** (1962) 271–277.

[11] P.A. Tanner, Y. Yuen Yeung, "Nephelauxetic Effects in the Electronic Spectra of Pr^{3+}". *J. Phys. Chem. A* **117** (2013) 10726–10735.

[12] A.L. Allred, "Electronegativity values from thermochemical data". *J. Inorg. Nucl. Chem.* **17** (1961) 215–221.

[13] B.R. Judd, "Optical Absorption Intensities of Rare-Earth Ions". *Phys. Rev.* **127** (1962) 750–761.

[14] G.S. Ofelt, "Intensities of Crystal Spectra of Rare-Earth Ions". *J. Chem. Phys.* **37** (1962) 511–520.

[15] M.P. Hehlen, M.G. Brik, K.W. Krämer, "50th anniversary of the Judd-Ofelt theory: An experimentalist's view of the formalism and its application". *J. Lumin*. **136** (2013) 221–239.

[16] K. Binnemans, "Interpretation of europium(III) spectra". *Coord. Chem. Rev.* **295** (2015) 1–45.

[17] R. Grasser, A. Scharmann, K.-R. Strack, "On the intrinsic nature of the blue luminescence in $CaWO_4$". *J. Lumin.* **27** (1982) 263–272.

[18] F.A. Kröger, F. Urbach,"Some Aspects of the Luminescence of Solids". *Phys. Today.* **1** (1948) 24–25.

[19] E. Sakai, "Recent Measurements on Scintillator-Photodetector Systems". *IEEE Trans. Nucl. Sci.* **34** (1987) 418–422.

[20] V.G. Baryshevsky, M.V. Korzhik, V.I. Moroz, V.B. Pavlenko, A.S. Lobko, A.A. Fyodorov, V.A. Kachanov, V.L. Solovjanov, B.I. Zadneprovsky, V.A. Nefyodov, P.V. Nefyodov, B.A. Dorogovin, L.L. Nagornaja, "Single crystals of tungsten compounds as promising materials for the total absorption detectors of the e.m. calorimeters". *Nucl. Instrum. Methods Phys. Res. A.* **322** (1992) 231–234.

[21] M. Kobayashi, M. Ishii, K. Harada, Y. Usuki, H. Okuno, H. Shimizu, T. Yazawa, "Scintillation and phosphorescence of $PbWO_4$ crystals". *Nucl. Instrum. Methods Phys. Res. A.* **373** (1996) 333–346.

[22] P. Dorenbos, "Charge transfer bands in optical materials and related defect level location". *Opt. Mater.* **69** (2017) 8–22.

[23] P.F. Smet, J.E. Van Haecke, F. Loncke, H. Vrielinck, F. Callens, D. Poelman, "Anomalous photoluminescence in BaS:Eu". *Phys. Rev. B* **74** (2006) 035207 (9p).

[24] P. Dorenbos, Anomalous luminescence of Eu^{2+} and Yb^{2+} in inorganic compounds, *J. Phys. Condens. Matter.* **15** (2003) 2645–2665.

[25] T. Konno, "Symmetry of Matter and Group Theory". (Kyoritsu Shuppan, Tokyo, 2001, *in Japanese*)

[26] T. Matsuzawa, Y. Aoki, N. Takeuchi, Y. Murayama, "A New Long Phosphorescent Phosphor with High Brightness, $SrAl_2O_4$:Eu^{2+},Dy^{3+}". *J. Electrochem. Soc.* **143** (1996) 2670–2673.

[27] H. Takasaki, S. Tanabe, T. Hanada, "Long-lasting afterglow characteristics of Eu, Dy codoped SrO-Al_2O_3 phosphor". *J. Ceram. Soc. Jpn.* **104** (1996) 322–326. (*in Japanese*)

[28] J. Ueda, P. Dorenbos, A.J.J. Bos, A. Meijerink, S. Tanabe, "Insight into the Thermal Quenching Mechanism for $Y_3Al_5O_{12}$:Ce^{3+} through Thermoluminescence Excitation Spectroscopy". *J. Phys. Chem. C.* **119** (2015) 25003–25008.

[29] P. Dorenbos, Modeling the chemical shift of lanthanide 4*f* electron binding energies, *Phys. Rev. B* **85** (2012) 165107 (10p).

[30] P. Dorenbos, A Review on How Lanthanide Impurity Levels Change with Chemistry and Structure of Inorganic Compounds, *ECS J. Solid State Sci. Technol.* **2** (2012) R3001–R3011.

Chapter 3

Intense Hypersensitive Luminescence of Eu^{3+}-Doped Oxynitride with Near-UV Excitation

Abstract

Nowadays, highly efficient red phosphors with blue or near-UV excitation are strongly required to improve the performance of existing white LEDs. With this aim in view, the Eu^{3+}-doped $YSiO_2N$ ceramics with the pseudo-wollastonite structure was fabricated and thoroughly studied spectroscopically. The presence of two anions – O^{2-} and N^{3-} – around Eu^{3+} ions causes a shift of the host valence band (VB) to lower energy and a certain asymmetry of the impurity sites. After illumination by near-UV excitation light (280–360 nm), the $YSiO_2N:Eu^{3+}$ sample exhibited strong red luminescence at around 620 nm assigned to the hypersensitive $^5D_0 \rightarrow {}^7F_2$ transition of the Eu^{3+} ions. Compared with three Eu^{3+}-doped oxides (α-$CaSiO_3:Eu^{3+}$, which has the same pseudowollastonite structure, and α- and *y*-$Y_2Si_2O_7:Eu^{3+}$ which have the same cation composition), the charge transfer (CT) band was redshifted by more than 9500 cm^{-1} because the VB top increases. From the Judd-Ofelt analysis, it was found out that the $YSiO_2N:Eu^{3+}$ sample has the large Judd-Ofelt intensity parameter, Ω_2, which is correlated with the dopant's site asymmetry. As expected, the mixed-anion coordination, which consists of oxide and nitride anions, resulted in the strong hypersensitive transition at 620 nm, which is characteristic Eu^{3+} red luminescence at the lower symmetry site. In addition, the fluorescence lifetime of the Eu^{3+} luminescence at 0 K (τ_0) was estimated experimentally to be 0.664 ms, which was shorter than the radiative lifetime (τ_R), 1.32 ms, based on the Judd-Ofelt analysis. The experimental quantum yield measured with an integrating sphere, 32.3%, was lower than the internal quantum efficiency, 50.3 %, evaluated from the ratio of τ_0/τ_R. The proposed material can be suitable for applications as a red phosphor.

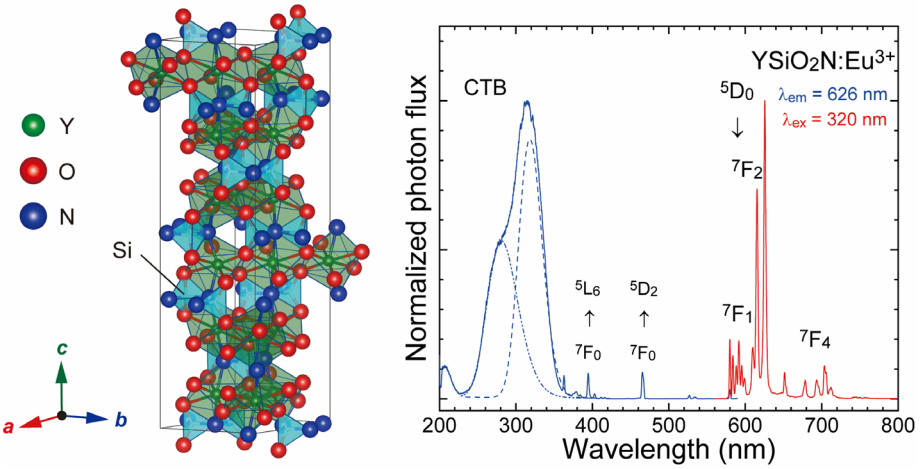

3.1. Introduction

As an eco-friendly light source of the next generation of lighting devices, white light-emitting diodes (w-LEDs) are getting more and more popular because of many factors, such as lower energy consumption, longer lifetime, and higher luminescent efficiency [1,2]. The common commercialized w-LEDs consist of an InGaN blue LED chip and a yellow phosphor, $Y_3Al_5O_{12}:Ce^{3+}$ [2–4]. In this case, the white light is obtained by combining the transmitted blue light and yellow light converted by the phosphor. However, this type of w-LEDs shows a weak emission intensity in the red spectral region, with the result of low color rendering index (CRI) and high correlated color temperature (CCT) [5,6]. To overcome this drawback by increasing CRI and lowering CCT, many phosphors which supply red luminescence with blue or near-UV excitation light have been developed in recent years [7]. For instance, nitrides activated by divalent europium, Eu^{2+}, such as $CaAlSiN_3:Eu^{2+}$ (CASN:Eu^{2+}) [8] and $Sr_2Si_5N_8:Eu^{2+}$ [9], are famous commercialized red phosphors for improving CRI and CCT of w-LEDs. These phosphors have a broad emission band attributed to the Eu^{2+} 5d → 4f parity allowed transition from yellow to deep-red light because the 5d energy level is shifted to lower energy due to the nephelauxetic effect of nitrogen with higher covalency. Since CASN:Eu^{2+} exhibits broad emission from 600 nm to 750 nm peaking at 660 nm (which can be excited by blue light), it can be a suitable phosphor for w-LEDs with high CRI. However, because of the big mismatch between the sensitivity curve of photopic vision and the luminescence spectrum of CASN:Eu^{2+}, the luminous efficacy in the w-LED system using the CASN:Eu^{2+} phosphor is not so high (**Figure 3.1**). In this respect, the phosphors with a narrow emission band at around 620 nm are more suitable, because in this case, overlap with the human eye sensitivity curve is enhanced, thus leading to the increased efficacy.

In this work, trivalent europium Eu^{3+} is used as the luminescent impurity. Usually, Eu^{3+} ions show the characteristic luminescence with narrow bands in the red spectral region (590–640 nm), attributed to the 4f-4f parity forbidden transitions. However, conventional Eu^{3+}-doped oxide phosphors have an intense excitation band only in the deep-UV (~250 nm) region [10,11],

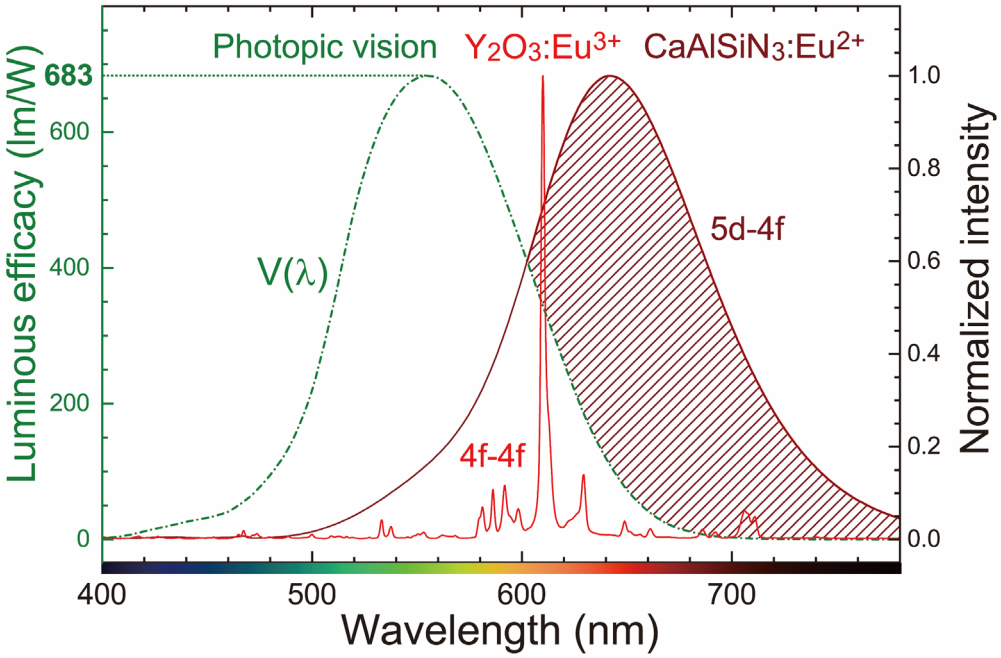

Figure 3.1 Photoluminescence spectra of conventional Eu-activated red phosphors (CASN:Eu^{2+} and Y_2O_3:Eu^{3+}) and sensitivity curve of photopic vision.

where very few commercialized LEDs with high power and efficiency are yet available. As this excitation band depends on the energy of the VB top [12], red phosphors activated by Eu^{3+} for w-LED applications require the upward energy shift of the VB. In oxides, the VB is mainly formed by the O 2p orbitals, and many oxide compounds have a similar VB top energy. On the other hand, in (oxy)nitrides, the VB consists of both O 2p and N 2p orbitals, and the VB top is dominated by the N 2p states because the electronegativity of nitrogen is smaller than that of oxygen. As a result, the VB top of (oxy)nitrides is located higher than that of oxides [13]. Hence, it is expected that, in (oxy)nitrides, the Eu^{3+} red luminescence can be obtained with lower excitation energy. Moreover, in some cases of the Eu^{3+}-doped oxynitrides, enhancement of red luminescence intensity can be anticipated. Red phosphors activated by Eu^{3+} ions show several characteristic narrow bands assigned to the $^5D_0 \rightarrow {}^7F_{2,4,6}$ electric dipole (ED) transitions, whose transition probability largely depends on the local environment around Eu^{3+} [14,15]. In some oxynitrides, Eu^{3+} is coordinated not only by oxide anions but also nitride anions, and the local environment with such mixed-anion coordination affects the Eu^{3+} luminescence.

In this paper, we report the photoluminescent properties of the Eu^{3+}-doped yttrium

silicon oxynitride, $YSiO_2N$, with the pseudowollastonite structure [16]. This compound was chosen because of the anticipated upward energy shift of the VB top on the one hand and the low symmetry local structure around Eu^{3+} ions due to the mixed-anion coordination on the other hand. To evaluate the mixed-anion effect, three Eu^{3+}-doped oxides, α-$CaSiO_3$:Eu^{3+}, α-$Y_2Si_2O_7$:Eu^{3+}, and *y*-$Y_2Si_2O_7$:Eu^{3+}, were also prepared with the aim of comparing their luminescent properties with the selected oxynitride. These oxides were chosen because of their structural and compositional features strongly related to those of $YSiO_2N$: α-$CaSiO_3$ is isostructural with $YSiO_2N$ [15]; α-$Y_2Si_2O_7$:Eu^{3+} has the same cation composition and coordination number of Y^{3+} sites (eight-fold) [17–19]; *y*-$Y_2Si_2O_7$:Eu^{3+} has the same cation composition but different coordination number of Y^{3+} sites (six-fold) [17,18]. The photoluminescence spectra were analyzed based on the Judd-Ofelt theory [20–22], which allows for quantitative estimations of the radiative transition probabilities of the lanthanide ions emission transitions. Since the Judd-Ofelt intensity parameter Ω_2 is strongly correlated with the site asymmetry around lanthanides [23,24], a comparative analysis of these Ω_2 parameters in all prepared samples was performed to discuss the mixed-anion effect on the Eu^{3+} 4f-4f red luminescence.

3.2. Experimental Procedure

3.2.1. Synthesis

Eu^{3+}-doped and non-doped yttrium silicon oxynitride samples with the compositions of $Y_{0.99}SiO_2N$:$Eu^{3+}_{0.01}$ and $YSiO_2N$ were fabricated by the solid-state reaction method. The starting materials, Y_2O_3 (99.99%, Mitsuwa Chemicals), SiO_2 (99.9%, Kojundo Chemical Laboratory), Si_3N_4 (99.9%, Kojundo Chemical Laboratory), and Eu_2O_3 (99.99%, Furuuchi Chemical), were weighed in the glove box filled with high-purity argon gas and mixed homogeneously by ball milling with ethanol for an hour. The mixed powder was dried at 100 °C for 24 h. After the mixture was pressed into a pellet, the pellet was covered with BN pellets and laid in an alumina crucible. This crucible was put into another larger alumina crucible with carbon powder, and

then the sample pellet was sintered at 1600 °C for 24 h under nitrogen gas flow. Upon cooling to room temperature, the as-made Eu^{3+}-doped sample was annealed at 700 °C for 24 h under nitrogen gas flow. In addition, to compare the photoluminescence properties, three Eu^{3+}-doped oxide phosphors, α-$CaSiO_3$:Eu^{3+}, α-$Y_2Si_2O_7$:Eu^{3+}, and *y*-$Y_2Si_2O_7$:Eu^{3+}, were prepared by the solid-state reaction method with rapid cooling (1250 °C, 6 h, in the air), the sol-gel method (1100 °C, 6 h, in the air) [16], and annealing the $YSiO_2N$:Eu^{3+} sample in the air atmosphere (1000 °C, 24 h), respectively.

3.2.2. Characterization

X-ray diffraction (XRD) measurements were carried out with a diffractometer (XRD-6000, Shimadzu) with CuKα radiation. Thermogravimetry (TG) and differential thermal analysis (DTA) of the non-doped $YSiO_2N$ sample were performed with a TG-DTA analyzer (TG8120, Rigaku). The sample and the reference compound, α-Al_2O_3, were weighed in the platinum pan and heated up to 1000 °C at a rate of 10 K min^{-1}. Diffuse reflectance spectra of samples were measured by a spectrophotometer (UV-3600, Shimadzu) equipped with an integrating sphere. Photoluminescence (PL) and photoluminescence excitation (PLE) spectra of all Eu^{3+}-doped samples were measured by using two monochromators (SP-2300i and SP-300i, Acton), a PMT detector (R11041, Hamamatsu Photonics), and a xenon lamp (R300-3J, Eagle Engineering Aerospace). To observe the PL and PLE at low temperatures (~ 90 K), the spectra were measured with a temperature-controlled stage (10035L, Linkam). For the fluorescence lifetime measurement, a fluorescence lifetime spectrometer (Quantaurus-Tau-C11367, Hamamatsu Photonics) was used. To estimate the PL quantum yield (QY), a Si CCD spectrometer (USB-2000+, Ocean Optics), a 10 inches integrating sphere (LMS-100, Labsphere), and a 325 nm He-Cd laser (IK3452R-F, Kimmon Koha) were used. All the spectra were calibrated with a standard halogen lamp (CSFS-600, Labsphere).

3.2.3. Judd-Ofelt Analysis

In the framework of the Judd-Ofelt theory, the spontaneous emission rate of lanthanide ions for the ED transition (A_R^{ED}) and the magnetic dipole (MD) transition (A_R^{MD}) from an initial state

$|(S', L')J'>$ to a terminal state $|(S, L)J>$ is described by eqs. 3.1 and 3.2, respectively [25]:

$$A_{\mathrm{R}}{}^{\mathrm{ED}}[(S'L')J';(SL)J] = \frac{64\pi^4 e^2 \nu^3}{3h(2J'+1)} \left(\frac{n(n^2+2)^2}{9}\right) \sum_{t=2,4,6} \Omega_t |\langle (S', L')J \| \mathrm{U}^t \| (S, L)J \rangle|^2, \quad (3.1)$$

$$A_{\mathrm{R}}{}^{\mathrm{MD}}[(S'L')J';(SL)J] = \frac{64\pi^4 n^3 \nu^3}{3h(2J'+1)} S_{\mathrm{MD}}, \quad (3.2)$$

where e is the charge of electron (= 4.803×10^{10} esu), ν is the centroid frequency of the transition, h is the Planck constant (= 6.626×10^{-27} erg s^{-1}), n is the refractive index of the host material, Ω_t (t = 2, 4, and 6) are the Judd-Ofelt intensity parameters, which are sensitive to the local environment of lanthanide ions, and $|\langle (S', L')J \| U^t \| (S, L)J \rangle|^2$ terms are the doubly reduced matrix elements (RMEs) of the unit tensor operators, U^t, which are almost constant in all compounds. The value of S_{MD}, the line strength of the MD transition, is constant because the MD transition probability is not changed largely in any host material. In the case of the Eu^{3+} 4f-4f luminescence, S_{MD} was calculated at 9.6×10^{-46} esu^2 cm^2 [26]. If Eu^{3+} ions are the luminescence center, the Judd-Ofelt intensity parameters, Ω_2 and Ω_4, can be calculated easily from the PL spectrum by using these two equations and the following equation, eq. 3.3 [23]:

$$\frac{A_R(\ {}^5\mathrm{D}_0 \rightarrow\ {}^7\mathrm{F}_{2,4})}{A_R(\ {}^5\mathrm{D}_0 \rightarrow\ {}^7\mathrm{F}_1)} = \frac{I_{\mathrm{area}}(\ {}^5\mathrm{D}_0 \rightarrow\ {}^7\mathrm{F}_{2,4})}{I_{\mathrm{area}}(\ {}^5\mathrm{D}_0 \rightarrow\ {}^7\mathrm{F}_1)}, \quad (3.3)$$

where I_{area} is the area under the corresponding peak in the PL spectrum, whose vertical axis is proportional to the photon flux. By using eqs. 3.1–3.3, not only the Judd-Ofelt intensity parameters, Ω_2 and Ω_4, but also the spontaneous emission rates, $A_{\mathrm{R}}({}^7\mathrm{F}_J)$ (J = 1, 2, 4), were calculated. The Judd-Ofelt parameter Ω_6 is usually calculated for the 4f-4f transitions of lanthanides except for trivalent europium. The ${}^5\mathrm{D}_0 \rightarrow {}^7\mathrm{F}_6$ emission transition of Eu^{3+} is too weak to be detected and the $|\langle (S', L')J \| U^6 \| (S, L)J \rangle|^2$ RME is much smaller than other RMEs, $|\langle (S', L')J \| U^t \| (S, L)J \rangle|^2$ (t = 2, 4) [13,23,24]. This is why Ω_6 and $A_{\mathrm{R}}({}^7\mathrm{F}_6)$ were not calculated, and the total spontaneous emission rate A_{R} (= $A_{\mathrm{R}}{}^{\mathrm{ED}} + A_{\mathrm{R}}{}^{\mathrm{MD}}$) did not contain the contribution of the ${}^5\mathrm{D}_0 \rightarrow {}^7\mathrm{F}_6$ transition. For these calculations, the following values of refractive index were used: $n(\mathrm{YSiO_2N})$ = 1.94 [27], $n(\mathrm{Y_2Si_2O_7})$ = 1.76 [28], and $n(\mathrm{CaSiO_3})$ = 1.62 [29]. Although they were obtained by the first-principle calculation, these values are reasonable enough, considering the refractive index of SiO_2 (n = 1.46) [30] and Si_3N_4 (n = 2.05) [31]. Furthermore, the radiative lifetime, τ_{R}, was estimated from eq. 3.4:

$$\tau_R = \frac{1}{A_R}. \tag{3.4}$$

3.3. Results

3.3.1. Crystal Structure of Prepared $YSiO_2N:Eu^{3+}$ Sample and Other Oxide Samples

Figure 3.2a shows the XRD patterns of the fabricated oxynitride samples and the reference data for $YSiO_2N$ (JCPDS#01-074-7384). Compared with this reference data, the prepared oxynitride samples were identified as a single-phase of $YSiO_2N$. From the XRD patterns of as-made and annealed Eu^{3+}-doped $YSiO_2N$, no difference was observed, *i.e.*, the crystal structure of $YSiO_2N:Eu^{3+}$ did not change after annealing at 700 °C under nitrogen gas flow. **Figure 3.2b**

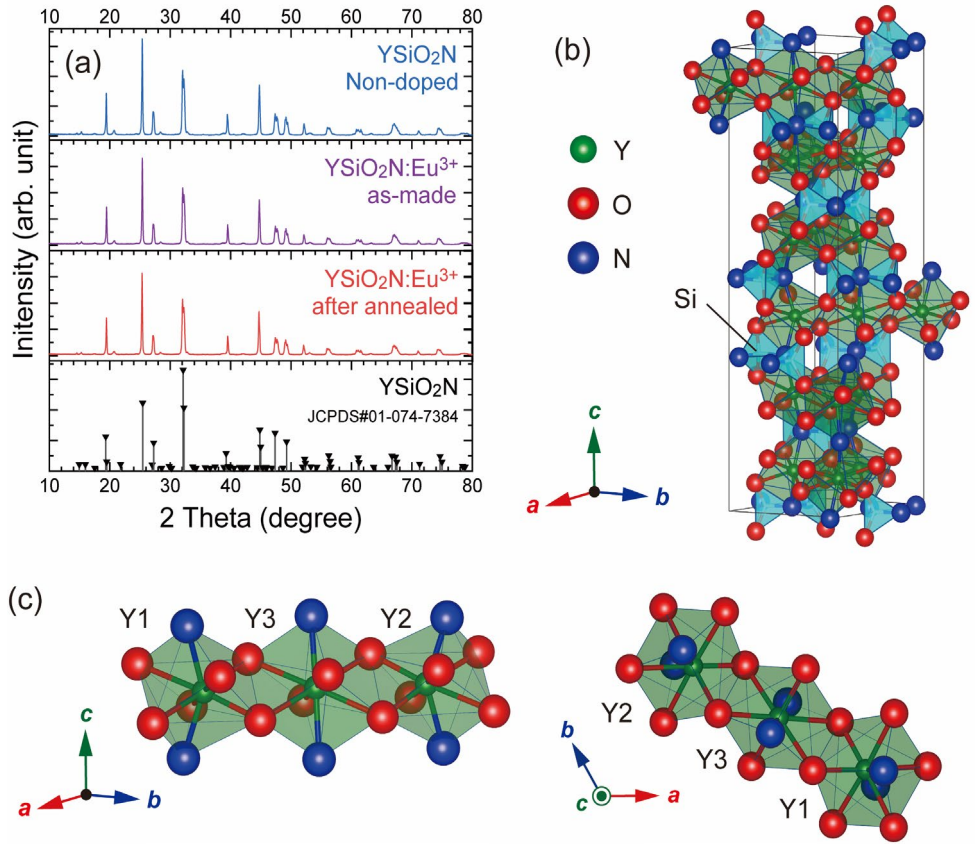

Figure 3.2. (a) XRD patterns of fabricated oxynitride samples, non-doped $YSiO_2N$, and as-made and annealed Eu^{3+}-doped $YSiO_2N$, with the reference data for $YSiO_2N$ (JCPDS #01-074-7384). (b) Crystal structure of $YSiO_2N$ with pseudowollastonite structure. (c) Enlarged local structures of three different Y^{3+} sites from different points of view.

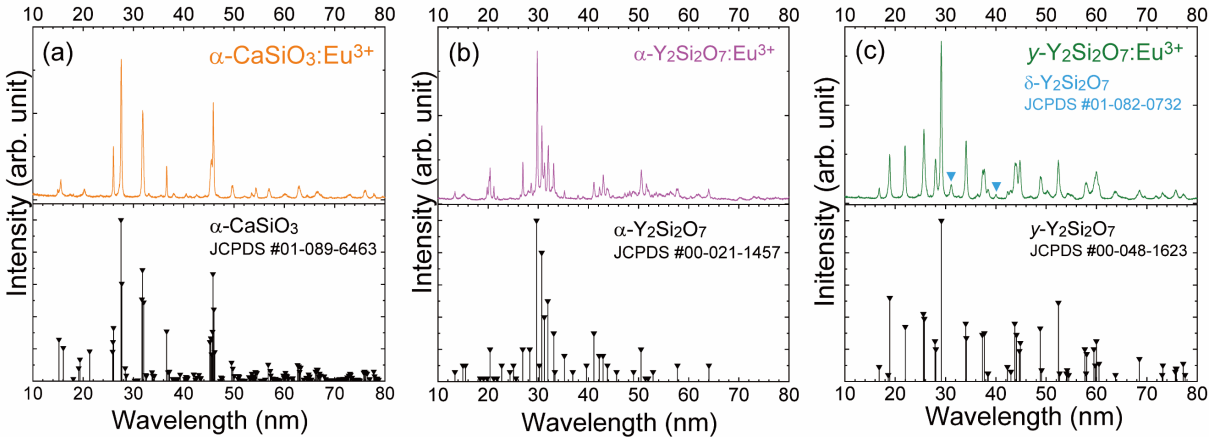

Figure 3.3. XRD patterns of oxide samples, (a) α-$CaSiO_3$:Eu^{3+}, (b) α-$Y2Si_2O_7$:Eu^{3+}, and (c) *y*-$Y_2Si_2O_7$:Eu^{3+}. Each pattern is shown with the reference data (JCPDS #01-089-6463, #00-021-1457, and #00-048-1623, respectively). In Figure 3.3c, an impurity phase, δ-$Y_2Si_2O_7$, is observed and shown with its reference data, JCPDS #01-082-0732.

shows the unit cell of $YSiO_2N$ with the pseudowollastonite structure, and **Figure 3.2c** shows the enlarged local structures of Y^{3+} sites, which are edge-shared by each other. These crystal structures were drawn by using the VESTA program [32]. According to the previous report [25], the structure of $YSiO_2N$ is described by the $P6_122$ space group and has three different Y^{3+} sites with eight-fold coordination, Y1, Y2, and Y3 sites. Y1 and Y2 sites have similar bond angles N-Y-N, 148.8° and 147.6°, respectively. On the other hand, Y3 sites have a different bond angle N-Y-N, 179.2°. Therefore, $YSiO_2N$ has two distinct kinds of Y^{3+} sites; one is the high symmetric site, Y1 and Y2, and the other is the high symmetric site, Y3. All Y^{3+} sites are coordinated by six oxide anions and two nitride anions. The XRD patterns of prepared oxides are shown in **Figures 3.3a–3c**. The prepared α-$CaSiO_3$:Eu^{3+} and α-$Y_2Si_2O_7$:Eu^{3+} samples were a single phase of the target compound. Only in the *y*-$Y_2Si_2O_7$:Eu^{3+} XRD patterns, there are small peaks at around 31° and 40° due to the impurity phases. These peaks correspond to the reference data for δ-$Y_2Si_2O_7$ (JCPDS#01-082-0732).

In general, in the case of oxynitride compounds, it is difficult to identify O^{2-} and N^{3-} positions from the XRD analysis due to their smaller difference in atomic scattering factors for X-ray. In this work, the net nitrogen ratio toward oxygen in the sample was estimated by the TG-DTA. **Figure 3.4** shows the TG and DTA curves of non-doped $YSiO_2N$. For the DTA curve, an exothermic peak was observed around 900–1000 °C. Similarly, for the TG curve, the weight

of the sample started to increase at about 900 °C. The ratio of the increased mass of the sample from room temperature to 1000 °C (ΔM) to the initial mass (M_0) was 5.86%. These facts and Figure 3.3c indicate that the following oxidation of oxynitride (reaction **(5)**) occurred over 900 °C.

$$2YSiO_2N + 3/2O_2 \rightarrow y\text{-}Y_2Si_2O_7 + N_2 \uparrow \quad (5)$$

In this reaction (5), the theoretical weight increases were calculated to be 6.13%. Therefore, it is assumed that the sample almost has the stoichiometric nitrogen ratio.

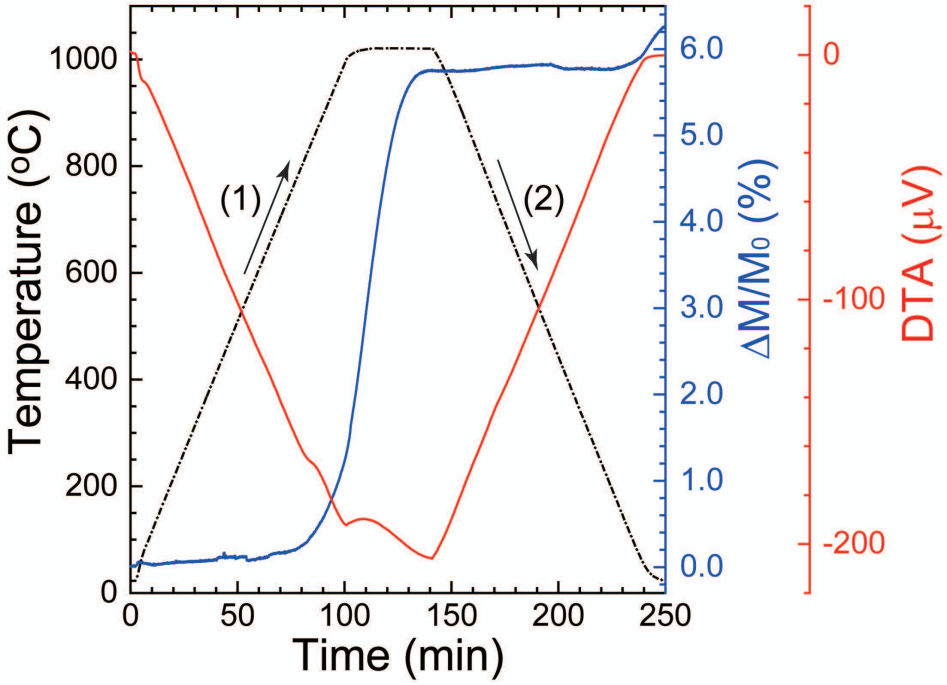

Figure 3.4. TG (blue) and DTA (red) curves of non-doped $YSiO_2N$ sample. The broken line shows the temperature profile of (1) heating and (2) cooling process.

3.3.2. Luminescence Properties of Eu^{3+}-Doped $YSiO_2N$

The images of the fabricated oxynitride samples, as-made and annealed $YSiO_2N:Eu^{3+}$, are shown in **Figure 3.5a.** Under w-LEDs lighting, the annealed sample looks white, while the color of the as-made sample is yellow. Under a Hg lamp excitation (365 nm), only the annealed sample shows the strong Eu^{3+} red emission, and the luminescence of the as-made sample is very weak.

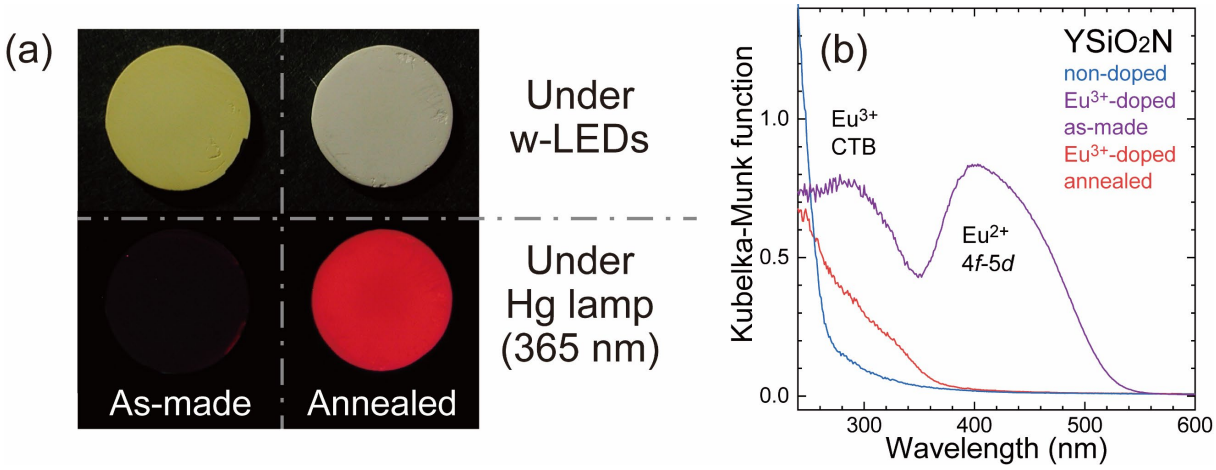

Figure 3.5. (a) Images of as-made (left) and annealed (right) $YSiO_2N:Eu^{3+}$ sample, taken under w-LEDs lightning (top) and UV excitation (365 nm) (bottom). (b) Diffuse reflectance spectra of the non-doped, and as-made and annealed Eu^{3+}-doped samples. The vertical axis is converted to the Kubelka-Munk function.

To investigate the origin of this difference between the as-made and annealed samples, diffuse reflectance spectra of all oxynitride samples were measured and shown in **Figure 3.5b**. The vertical axis is converted to the Kubelka-Munk function [32]. In the spectrum of non-doped $YSiO_2N$, no absorption band was observed above 280 nm except for the influence of the Rayleigh scattering in the UV region. In both spectra of the as-made and annealed samples, one absorption band in the near-UV region (280–340 nm) was observed. However, the absorption band in the visible region (360–520 nm) was seen only in the as-made sample. The origin of this broadband is discussed in section 3.4.1.

Figure 3.6a shows the PLE spectra of all the Eu^{3+}-doped samples at 90 K by detecting the peak of Eu^{3+} red luminescence ($YSiO_2N$: 626 nm, α-$CaSiO_3$: 613 nm, α-$Y_2Si_2O_7$: 611 nm, and *y*-$Y_2Si_2O_7$: 589 nm). All the spectra are normalized by the peak intensity of the $^5D_1 \leftarrow {}^7F_0$ MD transition ($\Delta J = 1$), which is not sensitive towards the Eu^{3+} local environment and is similar in any host material. For the annealed $YSiO_2N:Eu^{3+}$ sample, three broad bands and several narrow bands were observed. These several narrow bands were assigned to the following parity forbidden 4f-4f transitions of the Eu^{3+} ions: $^5D_4 \leftarrow {}^7F_1$ (363 nm), $^5L_6 \leftarrow {}^7F_0$ (394 nm), $^5L_6 \leftarrow {}^7F_1$ (403 nm), $^5D_2 \leftarrow {}^7F_0$ (466 nm), $^5D_1 \leftarrow {}^7F_0$ (527 nm), and $^5D_0 \leftarrow {}^7F_0$ (580 nm). Similarly, other Eu^{3+}-doped oxide samples show one broadband and several narrow bands, also assigned to the Eu^{3+} 4f-4f transitions. The PLE spectra in the range between 350 nm and 550 nm are enlarged in **Figure**

3.6b. In general, for many Eu^{3+}-doped compounds, the $^5L_6 \leftarrow {}^7F_0$ transition shows the strongest PLE intensity among all Eu^{3+} 4f-4f transitions [13]. For all the Eu^{3+}-doped oxide samples, the intensity of this transition was the strongest among all 4f-4f transitions. On the other hand, for the $YSiO_2N:Eu^{3+}$ sample, the PLE intensity of the $^5D_2 \leftarrow {}^7F_0$ transition was as strong as that of the $^5L_6 \leftarrow {}^7F_0$ transition.

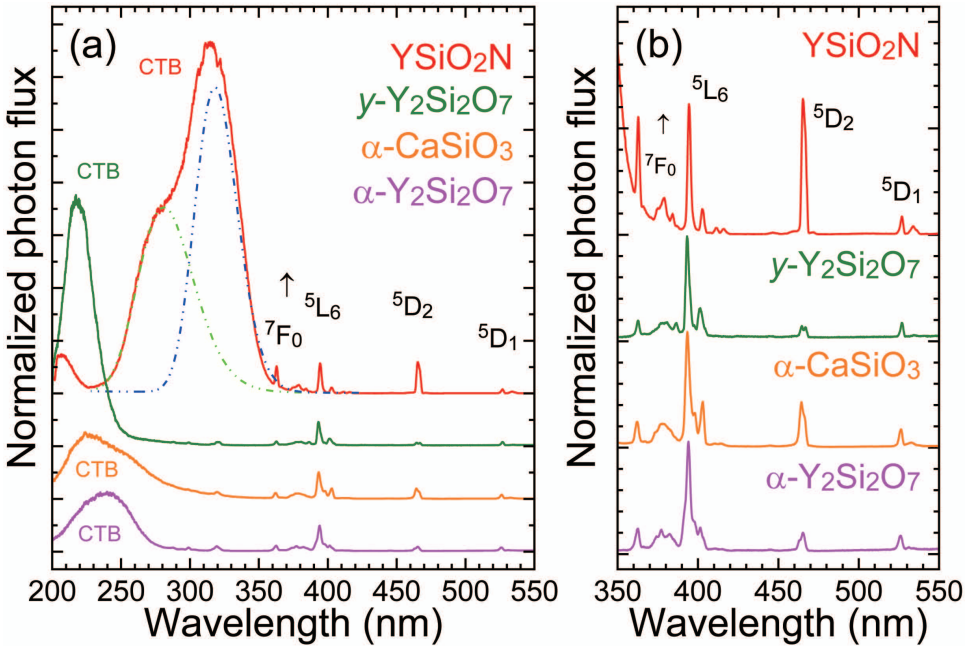

Figure 3.6. (a) Comparison of PLE spectra of all oxide and oxynitride samples at 90 K, normalized by the peak intensity of the $^5D_1 \leftarrow {}^7F_0$ MD transition, which is not sensitive towards the Eu^{3+} local environment and similar in any host material ($YSiO_2N:Eu^{3+}$; λ_{em} = 626 nm, α-$CaSiO_3:Eu^{3+}$; λ_{em} = 613 nm, y-$Y_2Si_2O_7:Eu^{3+}$; λ_{em} = 589 nm, α-$Y_2Si_2O_7:Eu^{3+}$; λ_{em} = 611 nm). (b) Figure 3.6a in the range between 350 and 550 nm is enlarged.

In **Figure 3.7,** the PL spectra of all Eu^{3+}-doped samples at 90 K are compared. All the PL spectra were normalized by the peak intensity of the $^5D_0 \rightarrow {}^7F_1$ MD transition (ΔJ = 1). All the samples were excited to the charge transfer state. Many sharp 4f-4f transition bands of Eu^{3+}, assigned to the $^5D_0 \rightarrow {}^7F_0$ (580 nm), $^5D_0 \rightarrow {}^7F_1$ (585–600 nm), $^5D_0 \rightarrow {}^7F_2$ (610–630 nm), $^5D_0 \rightarrow {}^7F_3$ (~650 nm), and $^5D_0 \rightarrow {}^7F_4$ (680–720 nm) transitions, were observed. The intensity of the $^5D_0 \rightarrow {}^7F_5$ and $^5D_0 \rightarrow {}^7F_6$ transitions was too weak to be detected. Each sample showed totally different spectral shapes and branching ratios of the $^5D_0 \rightarrow {}^7F_J$ (J = 0–4) emission. The $YSiO_2N:Eu^{3+}$ sample exhibited quite strong $^5D_0 \rightarrow {}^7F_2$ emission bands compared with the $^5D_0 \rightarrow {}^7F_1$ bands. As a result,

the $YSiO_2N:Eu^{3+}$ sample showed a much larger $^5D_0 \rightarrow {}^7F_2$ transition probability than other oxide samples. These luminescence features of the $YSiO_2N:Eu^{3+}$ sample are discussed in section 4.2.

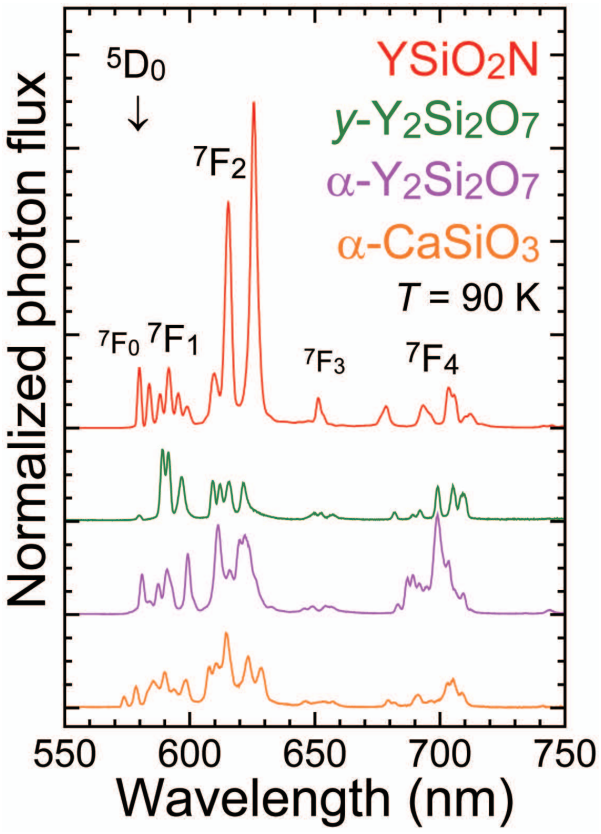

Figure 3.7. Comparison of PL spectra of all oxide and oxynitride samples at 90 K, normalized by the intensity of the $^5D_0 \rightarrow {}^7F_1$ MD transition ($YSiO_2N:Eu^{3+}$; λ_{ex} = 320 nm, *y*-$Y_2Si_2O_7:Eu^{3+}$; λ_{ex} = 220 nm, α-$Y_2Si_2O_7:Eu^{3+}$; λ_{ex} = 250 nm, α-$CaSiO_3:Eu^{3+}$; λ_{ex} = 250 nm).

To estimate the intrinsic lifetime and the quenching temperature of the Eu^{3+} luminescence in the $YSiO_2N$ host, the temperature dependence of fluorescence decay curves of the Eu^{3+} $^5D_0$ excited state was measured, and the results are shown in **Figure 3.8a**. The decay curves below 400 K were quite similar, and above 425 K, the slope of decay curves was getting steeper with increasing temperature. In order to estimate the lifetime at each temperature, each decay curve was fitted by using the following function:

$$I = I_0 \exp(-t/\tau_f), \tag{3.6}$$

where I_0 is the initial intensity, and τ_f is the fluorescence lifetime at each temperature. The

estimated fluorescence lifetime vs. temperature was plotted in **Figure 3.8b** and fitted by the following function:

$$\tau_f = \frac{1}{\Gamma_\nu + \Gamma_0 \exp(-E_a / kT)}, \tag{3.7}$$

where Γ_ν is the radiative rate, Γ_0 is the attempt rate of the nonradiative process, E_a is the activation energy, k is the Boltzmann constant, and T is temperature. The results of fitting are listed in **Table 3.1**. According to this result, the fluorescence lifetime at 0 K (τ_0) and the quenching temperature of the Eu^{3+} emission in the $YSiO_2N$ host were estimated to be 0.664 ms and 523 K, respectively.

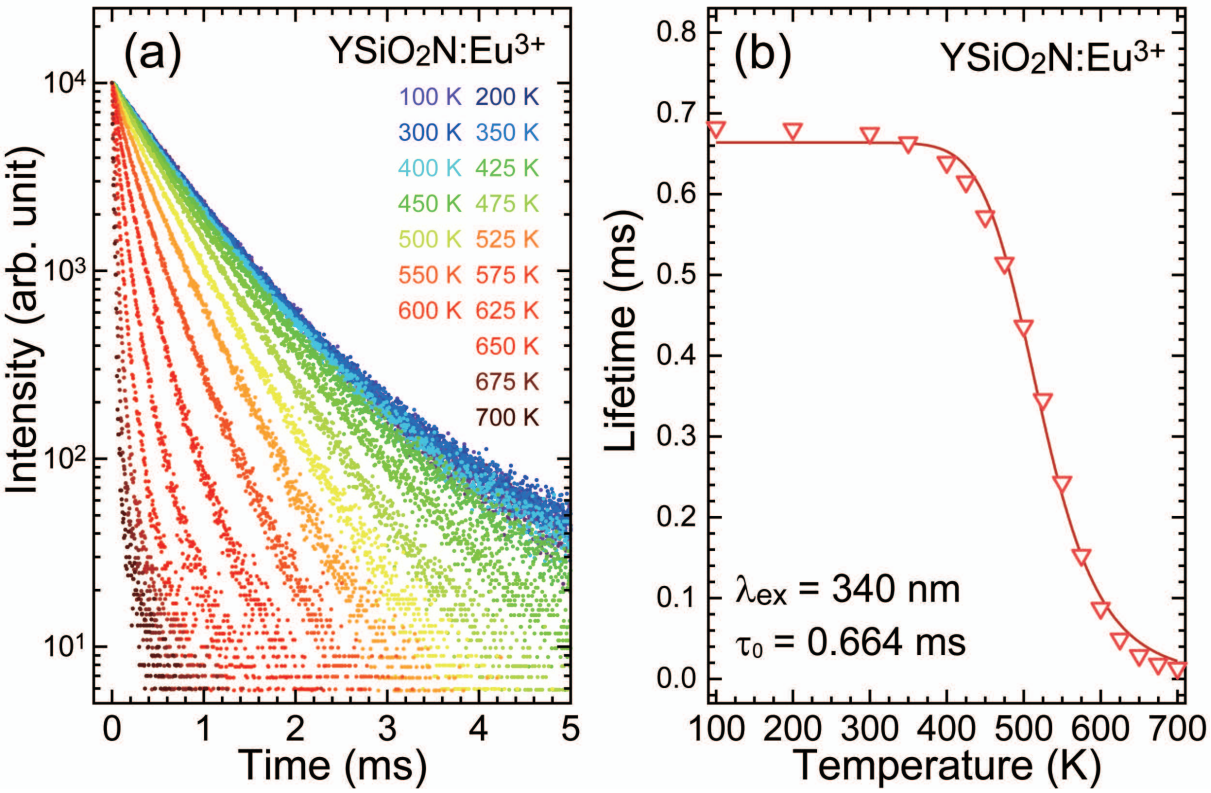

Figure 3.8. (a) Temperature dependence of fluorescence decay curves of $YSiO_2N:Eu^{3+}$ sample excited at 340 nm. (b) Temperature dependence of fluorescence lifetime of $YSiO_2N:Eu^{3+}$ and fitting curve (eq. 3.7).

Table 3.1. Calculated values from the temperature dependence of fluorescence lifetime measurement; the fluorescence lifetime (τ_0), the radiative rate (Γ_v), the attempt rate of the nonradiative process (Γ_0), and the quenching temperature of Eu^{3+} ($T_{50\%}$)

τ_0 (ms)	E_a (eV)	Γ_v (s^{-1})	Γ_0 (s^{-1})	$T_{50\%}$ (K)
0.664	0.600	1.51×10^3	9.11×10^8	523

Figure 3.9 shows the spectral distribution of the photon emission rate of the $YSiO_2N:Eu^{3+}$ sample excited by the He-Cd laser (λ = 325 nm) and the photograph of the integrating sphere with a phosphor sample during the measurement. As the standard halogen lamp for calibration has no emission below 350 nm, the photon number of the He-Cd laser was corrected by the PL spectra of sodium salicylate, whose quantum yield (QY) in the UV region is known [33]. From these emission spectra, the QY of the $YSiO_2N:Eu^{3+}$ sample was calculated to be 32.3%.

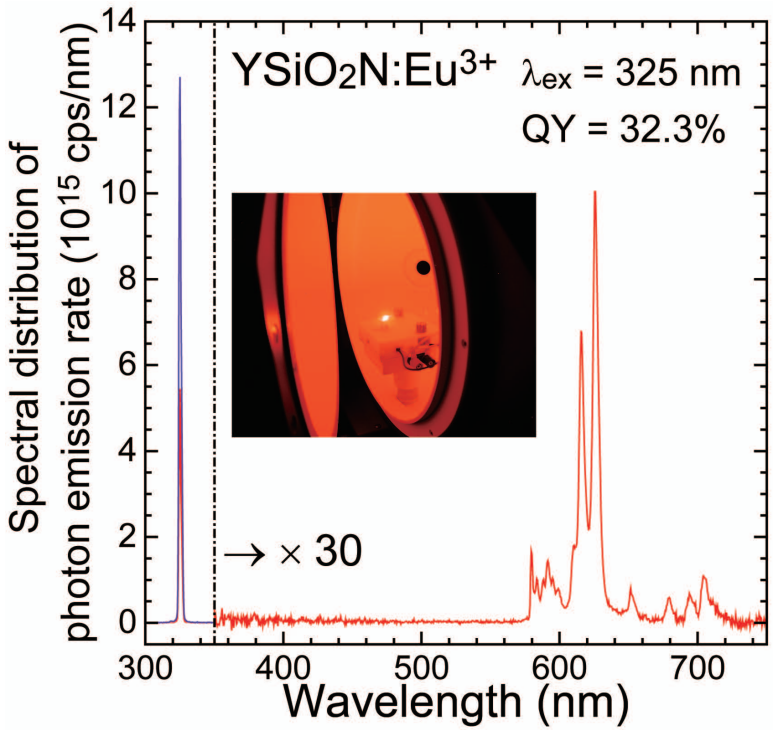

Figure 3.9. Photon distribution spectra of $YSiO_2N:Eu^{3+}$ sample (red line) and He-Cd laser (blue line). After 350 nm, the spectrum of $YSiO_2N:Eu^{3+}$ is enlarged to 30 times. (inset) Photograph of integrating sphere with a phosphor sample excited by He-Cd laser (325 nm).

3.4. Discussion

3.4.1. Oxidation Effect on Europium by Annealing at a Lower Temperature under N_2 Gas Flow

From diffuse reflectance spectra (Figure 3.5b), it was found out that the as-made $YSiO_2N:Eu^{3+}$ sample has a broad absorption band in the visible region (250–520 nm). Due to this absorption, the color of the as-made sample is yellow. As on the Ellingham diagram Eu^{3+} tends to be reduced to Eu^{2+} during the sintering process at very high temperatures (in this case at 1600 °C) [34], this band can be assigned to the 5d ← 4f transition of Eu^{2+}. The Eu^{2+} ions can occupy the Y^{3+} sites of $YSiO_2N$ because the crystalline phase does not change before and after annealing from the XRD patterns (Figure 3.2a). On the other hand, the annealed sample does not have any absorption bands in the visible range assigned to the CT band from anions to Eu^{3+}; thus, its color is white. This result shows that Eu^{2+} can be oxidized into Eu^{3+} by annealing at 700 °C under nitrogen gas flow. For the as-made sample, $Eu_Y^{'}$ can be charge-compensated by positively charged defects, such as $V_N^{\cdot\cdot\cdot}$ or $O_N^{\cdot}$, so that the oxidation of europium to Eu^{3+} is caused by the occupation of these defects by nitride anions.

In addition, no luminescence was observed in the as-made $YSiO_2N:Eu^{3+}$ sample at room temperature when the sample was excited by any excitation light from the UV to the visible region. In the PLE spectrum of the $YSiO_2N:Eu^{3+}$ sample (Figure 3.6), a small broad band around 210 nm was assigned to the absorption from the VB top to the conduction band bottom, and the bandgap of the $YSiO_2N:Eu^{3+}$ sample was calculated to be 6.48 eV [35]. Based on the bandgap energy (6.48 eV), the charge transfer energy (320 nm = 3.88 eV), and the $5d_1$ ← 4f energy of Eu^{2+} (400 nm = 3.1 eV), the lowest $5d_1$ state of Eu^{2+} is located within the conduction band. Thus, the luminescence quenching can be caused by the strong autoionization process. The weak red emission due to the Eu^{3+} 4f-4f transitions in the as-made $YSiO_2N:Eu^{3+}$ sample by 365 nm excitation can be caused by the strong parity allowed 5d ← 4f absorption of the Eu^{2+} ions at the excitation wavelength and the decrease of Eu^{3+} concentration.

3.4.2. Mixed-Anion Effect on Eu^{3+} Red Luminescence and Eu^{3+} Local Environment

From the results of PLE and PL spectra (Figures 3.6 and 3.7), it was found out that only the $YSiO_2N:Eu^{3+}$ sample exhibits some special features; the specific broad excitation band in the near-UV region (280–360 nm), the strong intensities deriving from the $^5D_2 \leftarrow {}^7F_0$ transition (in the PLE spectrum, at 466 nm), and the $^5D_0 \rightarrow {}^7F_2$ transition (in the PL spectrum, at 626 nm). Any oxide samples prepared in this study did not show these features. Thus, these specific luminescent properties of phosphors activated by Eu^{3+} can be caused by "the Mixed-anion effects."

In the PLE spectrum of the samples, each sample showed one or two broad excitation bands. These bands are assigned to the CT band from coordinating anions. The PLE intensity of the CT band was much higher than other 4f-4f bands; that is, the transition probability of CT from anions to Eu^{3+} is much greater than other transitions. Compared with the CT bands of the oxide samples, the peak wavelength of the CT bands of the $YSiO_2N:Eu^{3+}$ sample was redshifted by more than 80 nm (= 9500 cm^{-1}). In the case of the $YSiO_2N:Eu^{3+}$ sample, the CT bands can be deconvoluted into two Gaussian functions. This deconvolution was conducted to the PLE spectrum in the wavenumber scale, and the broken lines in Figure 3.6a show the result of the CT bands deconvolution. The CT energy for Eu^{3+} is defined as the energy gap between the VB top and the 4f ground level of Eu^{2+} [11]. Since the N 2p orbitals have higher energy than the O 2p orbitals due to the smaller N electronegativity, the N 2p orbitals dominate around the upper part of the VB. Therefore, these two bands, at the higher and lower energies, were assigned to the following Eu^{3+} CT bands: $O^{2-} \rightarrow Eu^{3+}$ and $N^{3-} \rightarrow Eu^{3+}$, respectively. It is suggested that mixed-anion compounds like oxynitrides have the potential to control the energy level of the VB top and the location of the CT band. In Figure 3.6b, only the $YSiO_2N:Eu^{3+}$ sample had the quite strong PLE intensity assigned to the $^5D_2 \leftarrow {}^7F_0$ transition for the $^5L_6 \leftarrow {}^7F_0$ transition; that is, the $^5D_2 \leftarrow {}^7F_0$ transition probability was very large. This large transition probability derives from the local environment of Eu^{3+}. In general, for many Eu^{3+}-doped compounds, the $^5L_6 \leftarrow {}^7F_0$ transition shows the strongest intensity among all Eu^{3+} 4f-4f transitions because the $^5L_6 \leftarrow {}^7F_0$ transition

have the $|\langle\|U^{2,4,6}\|\rangle|^2$ values of 0, 0.0011, and 0.0150, respectively, and these values are on average greater than those for other 4f-4f transitions [13]. On the other hand, the $^5D_2 \leftarrow {}^7F_0$ transition has only one non-zero RME, $|\langle\|U^2\|\rangle|^2$ of 0.0008, which is called the hypersensitive transition [13]. The line strength of this transition is very sensitive to the local environment of Eu^{3+} sites, which is related to the Ω_2 parameter. In particular, if the symmetry of Eu^{3+} sites is quite low, the hypersensitive transition probability gets drastically increasing, because the Ω_2 parameter increases and Ω_2 $|\langle(S', L')J'\|U^2\|(S, L)J\rangle|^2$ becomes larger. The $^5D_2 \leftarrow {}^7F_0$ transition intensity of the $YSiO_2N:Eu^{3+}$ sample was very high for the $^5L_6 \leftarrow {}^7F_0$ transition, and this trend was not observed in the prepared Eu^{3+}-doped oxides. Hence, in the $YSiO_2N$ host, Eu^{3+} occupy the Y^{3+} sites whose site symmetry is lower due to the existence of the N^{3-} ions in the local environment around the Eu^{3+} ions.

In the PL spectra, it is also possible to discuss the asymmetry of the Eu^{3+} ligand fields. The $YSiO_2N:Eu^{3+}$ sample and the α-$CaSiO_3:Eu^{3+}$ sample had a similar pattern of PL spectrum: the intensity of the $^5D_0 \rightarrow {}^7F_2$ ED transition is much stronger than that of the $^5D_0 \rightarrow {}^7F_1$ MD transition, which is not sensitive towards the Eu^{3+} local environment and similar in any host material. The $^5D_0 \rightarrow {}^7F_2$ transition is also assigned to the hypersensitive transition due to the non-zero RME, $|\langle\|U^2\|\rangle|^2$ of 0.0032 [36]. The ratio $(^5D_0 \rightarrow {}^7F_2)/(^5D_0 \rightarrow {}^7F_1)$ of the $YSiO_2N$ sample is the largest among samples of α-$CaSiO_3:Eu^{3+}$, α-, *y*-$Y_2Si_2O_7:Eu^{3+}$ and $YSiO_2N:Eu^{3+}$. The luminescent properties of $YSiO_2N:Eu^{3+}$ also support that the asymmetry by the mixed-anion coordination around the Eu^{3+} ions increases the hypersensitive transition probability.

In the $YSiO_2N:Eu^{3+}$ PL spectrum, five components of $^5D_0 \rightarrow {}^7F_1$ bands were observed. The maximum number of luminescence bands for $^5D_0 \rightarrow {}^7F_1$ transition should be three (= $2J + 1$) because of the Stark splitting for the $^7F_1$ level. A great number of emission peaks is probably because the Eu^{3+} ions substitute three different Y^{3+} sites (Figure 3.2c), the local environments of which are slightly different.

3.4.3. Judd-Ofelt Analysis of Eu^{3+} Luminescence in $YSiO_2N$

For quantitative discussion on the Eu^{3+} 4f-4f transition probability, the PL spectra of samples were analyzed based on the Judd-Ofelt theory. The results of calculation, the Judd-Ofelt intensity parameters (Ω_2 and Ω_4), the spontaneous emission rates of the $^5D_0 \rightarrow {}^7F_J$ transition ($A_R(^7F_J)$), and the radiative lifetimes (τ_R), are shown in **Table 3.2**, and for comparison, the calculated Ω_2 and Ω_4 parameters of each sample are also shown in **Figure 3.10a**. It is well known the Ω_2 parameter has a correlation with the asymmetry of the crystal sites occupied by lanthanides [21,22]. The Ω_2 value of the $YSiO_2N:Eu^{3+}$ sample is about twice as large as that of other oxide samples. The $YSiO_2N:Eu^{3+}$ sample and α-$CaSiO_3:Eu^{3+}$ sample, which are isostructural (pseudowollastonite structure), have the larger Ω_2 and the smaller Ω_4. Thus, the cation sites themselves for the Eu^{3+} ions in the pseudowollastonite structure have low symmetry. In addition to this original structural asymmetry, the $YSiO_2N:Eu^{3+}$ sample should have much lower symmetry of the Eu^{3+} ions because of partial substitution of ligand anions from O^{2-} to N^{3-}. Compared with other

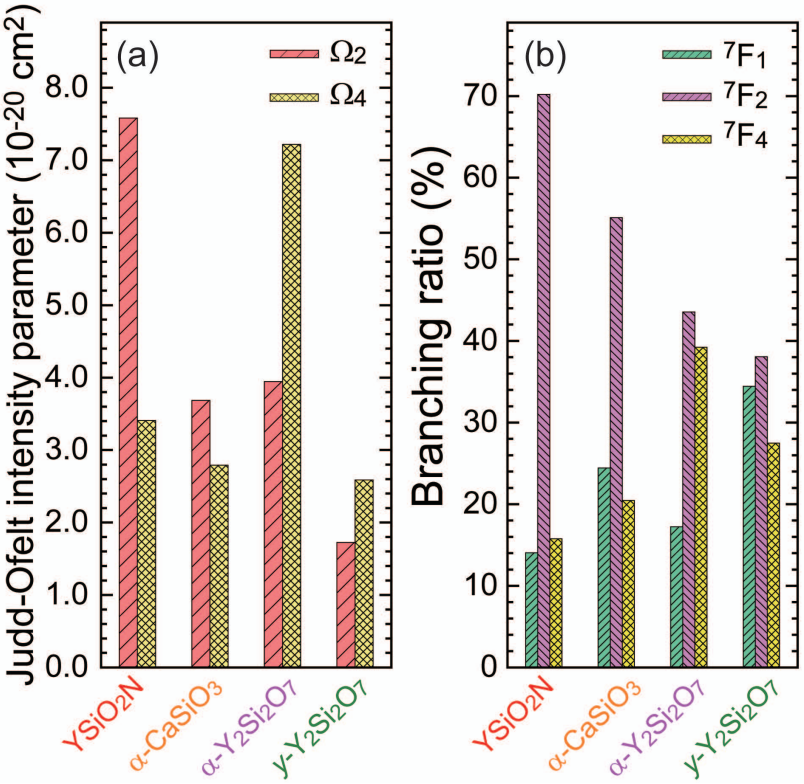

Figure 3.10. (a) Judd-Ofelt intensity parameters, Ω_2 and Ω_4, of Eu^{3+} ions, and (b) branching ratio of $^5D_0 \rightarrow {}^7F_J$ transition (J=1, 2, 4) for Eu^{3+} ions in oxynitride and oxide samples.

oxides, the Ω_2 parameter of the $YSiO_2N:Eu^{3+}$ sample is much larger due to the mixed-anion coordination. As the hypersensitive transition probability depends on Ω_2, in $YSiO_2N:Eu^{3+}$ spectral intensity of the $^5D_2 \leftarrow {}^7F_0$ transition in PLE spectrum and the $^5D_0 \rightarrow {}^7F_2$ transition in PL spectrum are quite strong because of the large Ω_2. At the same time, the calculated spontaneous emission rate of the $^5D_0 \rightarrow {}^7F_2$ transition in $YSiO_2N:Eu^{3+}$, 5.31×10^2 s^{-1}, is considerably larger than that in other oxide samples. That is, this parity forbidden 4f-4f transition gets more allowed by the mixed-anion coordination. On the other hand, the Ω_4 parameter is said to have less sensitivity to the ligand field and some correlation with the bond ionicity [21,22]. However, there is no apparent evidence of the relationship between the Ω_4 parameter and the crystal structure or chemical composition. In this case, α-$Y_2Si_2O_7:Eu^{3+}$ has a quite large Ω_4 parameter while the Ω_4 for *y*-$Y_2Si_2O_7:Eu^{3+}$ is small. From these data only, it is difficult to find out some chemical trend for the Ω_4 intensity parameter. Therefore, it is necessary to closely investigate the Ω_4 parameter variation in a number of materials, including mixed-anion compounds.

In the Judd-Ofelt analysis, the radiative lifetime (τ_R) is calculated from the total value of the spontaneous emission rates of the $^5D_0 \rightarrow {}^7F_J$ transition, $A_R(^7F_J)$, by using eq. 3.4. For the $YSiO_2N:Eu^{3+}$ sample, the calculated τ_R was 1.32 ms, which was much shorter than the other three oxide samples because this sample has the large Ω_2 parameter and the large $^5D_0 \rightarrow {}^7F_2$ transition probability owing to the specific Eu^{3+} sites originating from the mixed-anion coordination of O^{2-} and N^{3-}. However, from the temperature dependence of the fluorescence lifetime, the estimated τ_0 was 0.664 ms, and this value is shorter than the calculated τ_R. The reason for this is that, in the Judd-Ofelt theory, all nonradiative processes are not considered. In general, the ratio of τ_0 to τ_R (*i.e.*, τ_0/τ_R) should correspond to the internal quantum efficiency (IQE). In the $YSiO_2N:Eu^{3+}$ sample, this calculated IQE based on the Judd-Ofelt analysis was 50.3%. The experimentally obtained QY by CT excitation was 32.3%. In the Judd-Ofelt analysis, the ratio between the radiative and nonradiative rate from the $^5D_0$ level can be considered, while in the QY measurement by CT excitation, all the radiative and nonradiative processes from the CT excitation to the ground state are also taken into account. In addition, the concentration quenching can occur because of a slightly high concentration, 1% Eu^{3+}.

In **Table 3.3** and **Figure 3.10b**, the calculated branching ratios of the $^5D_0 \rightarrow {}^7F_J$ (J = 1, 2, 4) emission transition in oxynitride and oxide samples are shown. Both pseudowollastonite samples, $YSiO_2N:Eu^{3+}$ and α-$CaSiO_3:Eu^{3+}$, have a high branching ratio of $^7F_2$ because of the low symmetry of the impurity sites. This tendency is almost the same as Ω_2.

In conclusion of this analysis, the Eu^{3+}-doped oxynitride sample, $YSiO_2N:Eu^{3+}$, shows intense red luminescence assigned to the $^5D_0 \rightarrow {}^7F_2$ hypersensitive transition due to the characteristic Eu^{3+} sites with lower symmetry derived from the mixed-anion coordination as we expected. It is suggested that partial substitution from O^{2-} to N^{3-} in ligands around the Eu^{3+} ions is a good strategy to enhance the Eu^{3+} red luminescence.

Table 3.2. Calculated Judd-Ofelt intensity parameters, Ω_2 and Ω_4, spontaneous emission rates of the $^5D_0 \rightarrow {}^7F_J$ transition, A_R (^7F_J), and radiative lifetime, τ_R, for Eu^{3+} ions in oxynitride and oxide hosts[a]

	$YSiO_2N$	α-$CaSiO_3$	α-$Y_2Si_2O_7$	y-$Y_2Si_2O_7$
Ω_2 (10^{-20} cm^2)	7.58	3.95	3.95	1.72
Ω_4 (10^{-20} cm^2)	3.41	2.79	7.22	2.58
$A_R(^7F_1)$ (10^2 s^{-1})	1.06	0.623	0.784	0.788
$A_R(^7F_2)$ (10^2 s^{-1})	5.31	1.40	1.98	0.871
$A_R(^7F_4)$ (10^2 s^{-1})	1.19	0.521	1.78	0.629
τ_R (ms)	1.32	3.92	2.20	4.37

[a] Reported values of refractive indices (n ($YSiO_2N$)=1.94 [27], n ($Y_2Si_2O_7$)=1.76 [28], and n ($CaSiO_3$)=1.62 [29]) were used for calculation.

Table 3.3. Calculated branching ratios (%) of the $^5D_0 \rightarrow {}^7F_J$ (J = 1, 2, 4) emission transition in oxynitride and oxide hosts

		$YSiO_2N$	α-$CaSiO_3$	α-$Y_2Si_2O_7$	y-$Y_2Si_2O_7$
	$^7F_1$	14.0	24.4	17.3	34.4
$^5D_0 \rightarrow$	$^7F_2$	70.2	55.1	43.5	38.1
	$^7F_4$	15.8	20.5	39.2	27.5

3.5. Conclusions

The Eu^{3+}-doped $YSiO_2N$ oxynitride was fabricated by the solid-state reaction method, and its luminescent properties were investigated. It was shown that the Eu^{3+} luminescence could be obtained by using lower excitation energy. The XRD patterns showed the prepared sample had the single-phase of $YSiO_2N$ belonging to the $P6_122$ space group, which has three Y^{3+} sites with eight-fold coordination. Whether the sample contained nitrogen in its composition was confirmed by TG-DTA. The $YSiO_2N:Eu^{3+}$ sample was excited efficiently by near-UV light (280–360 nm) and showed very intense red luminescence assigned to the Eu^{3+} 4f-4f transitions. Compared with prepared Eu^{3+}-doped oxide samples (α-$CaSiO_3:Eu^{3+}$, α-$Y_2Si_2O_7:Eu^{3+}$, and *y*-$Y_2Si_2O_7:Eu^{3+}$), in $YSiO_2N:Eu^{3+}$, there were two major different luminescent features: the CT excitation band got redshifted by more than 9500 cm^{-1} because the energy of the VB top got increased due to the N 2p orbitals; the spectral intensity of the $^5D_0 \rightarrow {}^7F_2$ transition (the hypersensitive transition, at 626 nm) got stronger because the Eu^{3+} occupied asymmetric Y^{3+} sites due to partial substitution of O^{2-} by N^{3-}. From the Judd-Ofelt analysis, the $YSiO_2N:Eu^{3+}$ sample had the much larger Judd-Ofelt intensity parameter, Ω_2, which depends on the site asymmetry, than other oxide samples. As expected, the transition probability of the hypersensitive transition was enhanced by constructing the mixed-anion ligand fields. The fluorescence lifetime at 0 K (τ_0) was estimated experimentally to be 0.664 ms, which was shorter than the radiative lifetime (τ_R) based on the Judd-Ofelt analysis, 1.32 ms. Although the ratio between these two values should be the same as the IQE, the experimental QY (32.3 %) was lower than the calculated IQE (50.3%). For the development of red phosphors activated by Eu^{3+} for w-LEDs applications, Eu^{3+}-doped mixed-anion compounds have a significant potential to improve the main parameters of white LEDs (CRI and CCT).

Acknowledgements

This work was supported by JSPS Grant-in-Aid for Scientific Research on Innovative Areas "Mixed-Anion" (Grant Number JP16H06441). M.G. Brik appreciates Guest Professorship at Kyoto University (Prof. S. Tanabe laboratory.)

References

[1] S. Nakamura, G. Fasol, "The Blue Laser Diode: GaN Based Light Emitters and Lasers". (Springer, Berlin, 1997)

[2] S. Nishiura, S. Tanabe, K. Fujioka, Y. Fujimoto, "Properties of transparent Ce:YAG ceramic phosphors for white LED". *Opt. Mater.* **33** (2011) 688–691.

[3] K. Bando, K. Sakano, Y. Noguchi, Y. Shimizu, "Development of High-bright and Pure-white LED Lamps". *J. Light Visual Environ.* **22** (1998) 2–5.

[4] M. Shang, C. Li, J. Lin, "How to produce white light in a single-phase host?". *Chem. Soc. Rev.* **43** (2014) 1372–1386.

[5] B. Wang, H. Lin, J. Xu, H. Chen, Y. Wang, "$CaMg_2Al_{16}O_{27}:Mn^{4+}$-based Red Phosphor: A Potential Color Converter for High-Powered Warm W-LED". *ACS Appl. Mater. Interfaces.* **6** (2014) 22905–22913.

[6] M. Peng, X. Yin, P.A. Tanner, M.G. Brik, P. Li, "Site Occupancy Preference, Enhancement Mechanism, and Thermal Resistance of Mn^{4+} Red Luminescence in $Sr_4Al_{14}O_{25}:Mn^{4+}$ for Warm WLEDs". *Chem. Mater.* **27** (2015) 2938–2945.

[7] I. Ahemen, D.K. De, F.B. Dejene, B. Viana, "White light tunable emissions from $ZnS:Eu^{3+}$ nanophosphors over 330–465 nm excitation range for white LED applications". *Mater. Res. Express.* **3** (2016) 045016 (13p).

[8] K. Uheda, N. Hirosaki, Y. Yamamoto, A. Naito, T. Nakajima, H. Yamamoto, "Luminescence Properties of a Red Phosphor, $CaAlSiN_3:Eu^{2+}$, for White Light-Emitting Diodes". *Electrochem. Solid-State Lett.* **9** (2006) H22–H25.

[9] R.-J. Xie, N. Hirosaki, T. Suehiro, F.-F. Xu, M. Mitomo, "A Simple, Efficient Synthetic Route to $Sr_2Si_5N_8:Eu^{2+}$-Based Red Phosphors for White Light-Emitting Diodes". *Chem. Mater.* **18** (2006) 5578–5583.

[10] J.M.P.J. Verstegen, D. Radielović, L.E. Vrenken, "A New Generation Deluxe Fluorescent Lamp—Combining an Efficacy Greater than 80 lm/W with a Color Rendering Index of about 85". *J. Illum. Eng. Soc.* **4** (1975) 90–98.

[11] A.K. Levine, F.C. Palilla, "A new, highly efficient red-emitting cathodoluminescent phosphor (YVO_4:Eu) for color television". *Appl. Phys. Lett.* **5** (1964) 118–120.

[12] P. Dorenbos, "Charge transfer bands in optical materials and related defect level location". *Opt. Mater.* **69** (2017) 8–22.

[13] H. Kageyama, K. Hayashi, K. Maeda, J.P. Attfield, Z. Hiroi, J.M. Rondinelli, K.R. Poeppelmeier,

"Expanding frontiers in materials chemistry and physics with multiple anions". *Nat. Commun.* **9** (2018) 772 (15p).

[14] K. Binnemans, "Interpretation of europium(III) spectra". *Coord. Chem. Rev.* **295** (2015) 1–45.

[15] P.A. Tanner, "Some misconceptions concerning the electronic spectra of tri-positive europium and cerium". *Chem. Soc. Rev.* **42** (2013) 5090–5101.

[16] P.E.D. Morgan, P.J. Carroll, F.F. Lange, "Crystal structure of $YSiO_2N$ and a reappraisal of the vaterite type, YBO_3". *Mater. Res. Bull.* **12** (1977) 251–259.

[17] V. Kahlenberg, W. Wertl, D.M. Többens, R. Kaindl, P. Schuster, H. Schottenberger, "Rietveld Analysis and Raman Spectroscopic Investigations on α-$Y_2Si_2O_7$". *Z. Anorg. Allg. Chem.* **634** (2008) 1166–1172.

[18] A.I. Becerro, A. Escudero, P. Florian, D. Massiot, M.D. Alba, "Revisiting $Y_2Si_2O_7$ and Y_2SiO_5 polymorphic structures by ^{89}Y MAS-NMR spectroscopy". *J. Solid State Chem.* **177** (2004) 2783–2789.

[19] Z. Sun, M. Li, Y. Zhou, "Recent progress on synthesis, multi-scale structure, and properties of Y–Si–O oxides". *Int. Mater. Rev*. **59** (2014) 357–383.

[20] B.R. Judd, "Optical Absorption Intensities of Rare-Earth Ions". *Phys. Rev.* 127 (1962) 750–761.

[21] G.S. Ofelt, "Intensities of Crystal Spectra of Rare-Earth Ions". *J. Chem. Phys.* **37** (1962) 511–520.

[22] M.P. Hehlen, M.G. Brik, K.W. Krämer, "50th anniversary of the Judd-Ofelt theory: An experimentalist's view of the formalism and its application". *J. Lumin.* **136** (2013) 221–239.

[23] S. Tanabe, T. Ohyagi, N. Soga, T. Hanada, "Compositional dependence of Judd-Ofelt parameters of Er^{3+} ions in alkali-metal borate glasses". *Phys. Rev. B* **46** (1992) 3305–3310.

[24] J.C. Boyer, F. Vetrone, J.A. Capobianco, A. Speghini, M. Bettinelli, "Variation of Fluorescence Lifetimes and Judd-Ofelt Parameters between Eu^{3+} Doped Bulk and Nanocrystalline Cubic Lu_2O_3". *J. Phys. Chem. B.* **108** (2004) 20137–20143.

[25] M.A.K. Elfayoumi, M. Farouk, M.G. Brik, M.M. Elokr, "Spectroscopic studies of Sm^{3+} and Eu^{3+} co-doped lithium borate glass". *J. Alloys Compd.* **492** (2010) 712–716.

[26] M.H.V. Werts, R.T.F. Jukes, J.W. Verhoeven, "The emission spectrum and the radiative lifetime of Eu^{3+} in luminescent lanthanide complexes". *Phys. Chem. Chem. Phys.* **4** (2002) 1542–1548.

[27] L. Ouyang, H. Yao, S. Richey, Y.-N. Xu, W.Y. Ching, "Crystal structure and properties of $YSiO_2N$". *Phys. Rev. B* **69** (2004) 094112 (6p).

[28] W.Y. Ching, L. Ouyang, Y.-N. Xu, "Electronic and optical properties of Y_2SiO_5 and $Y_2Si_2O_7$ with comparisons to α-SiO_2 and Y_2O_3". *Phys. Rev. B* **67** (2003) 245108 (8p).

[29] W.-L. Huang, P.J. Wyllie, "Melting and Subsolidus Phase Relationships for $CaSiO_3$ to 35 Kilobars Pressure". *Am. Mineral.* **60** (1975) 213–217.

[30] I.H. Malitson, "Interspecimen comparison of the refractive index of fused silica". *J. Opt. Soc. Am.* **55** (1965) 1205–1209.

[31] K. Luke, Y. Okawachi, M.R.E. Lamont, A.L. Gaeta, M. Lipson, "Broadband mid-infrared frequency comb generation in a Si_3N_4 microresonator". *Opt. Lett.* **40** (2015) 4823–4826.

[32] Y. Katayama, T. Kayumi, J. Ueda, P. Dorenbos, B. Viana, S. Tanabe, "The role of Ln^{3+} (Ln = Eu, Yb) in persistent red luminescence in $MgGeO_3$:Mn^{2+}". *J. Mater. Chem. C.* **5** (2017) 8893–8900.

[33] W. Slavin, R.W. Mooney, D.T. Palumbo, "Energy-Recording Spectrofluorimeter". *J. Opt. Soc. Am.* **51** (1961) 93–97.

[34] V. Viallet, J.-F. Marucco, J. Saint, M. Herbst-Ghysel, N. Dragoe, "Structural, magnetic and electrical properties of a perovskite containing divalent europium $EuZrO_3$". *J. Alloys Compd.* **461** (2008) 346–350.

[35] P. Dorenbos, "Electronic structure and optical properties of the lanthanide activated $RE_3(Al_{1-x}Ga_x)5O_{12}$ (RE = Gd, Y, Lu) garnet compounds". *J. Lumin.* **134** (2013) 310–318.

[36] Ä. Andresen, A.-N. Bahar, D. Conradi, I.-I. Oprea, R. Pankrath, U. Voelker, K. Betzler, M. Wöhlecke, U. Caldiño, E. Martín, D. Jaque, J.G. Solé, "Spectroscopy of Eu^{3+} ions in congruent strontium barium niobate crystals". *Phys. Rev. B* **77** (2008) 214102 (10p).

Chapter 4

Site-Selective Eu^{3+} Luminescence in the Monoclinic Phase of $YSiO_2N$

Abstract

Eu^{3+}-doped $YSiO_2N$ phosphor was synthesized, and its crystal structure was analyzed by the single-crystal X-ray and neutron powder diffraction techniques. The new crystal structure of $YSiO_2N$ with the monoclinic lattice (space group $C2/c$) composed of nonequivalent $[YO_6N_2]$ dodecahedra was identified, and, in this structure, five different Y^{3+} sites take C_i or C_n symmetry. Based on the experimentally determined crystal structure, we characterized the luminescence properties of the Eu^{3+} ions with the site-selective and time-resolved spectroscopy. The Eu^{3+} ions at the Y: C_n sites show intense $^5D_0 \rightarrow {}^7F_2$ electric dipole luminescence peaking at 626 nm with a short lifetime (0.61 ms) due to the lack of inversion center. In the centrosymmetric C_i sites, the lifetime of the $^5D_0$ level was quite long (5.51 ms), and the strongest three peaks are assigned to the $^5D_0 \rightarrow {}^7F1$ magnetic dipole transition instead of $^5D_0 \rightarrow {}^7F_2$. The anomalous temperature dependence of the long lifetime for the Eu^{3+}: $^5D_0$ at this C_i site at low temperatures suggests that the slow radiative rate can be influenced by the thermal distortion of centrosymmetry. The thermal quenching mechanism of the Eu^{3+}: $^5D_0$ luminescence at both sites is considered to be due to the charge transfer states related to the N^{3-} ions in the $[Eu^{3+}O_6N_2]$ dodecahedra rather than the multiphonon relaxation mechanism. This study shows the potentials of Eu^{3+} luminescence in oxynitride coordination and provides new insights into the material design guidelines for near-UV excitable red phosphor activated with Eu^{3+} ions.

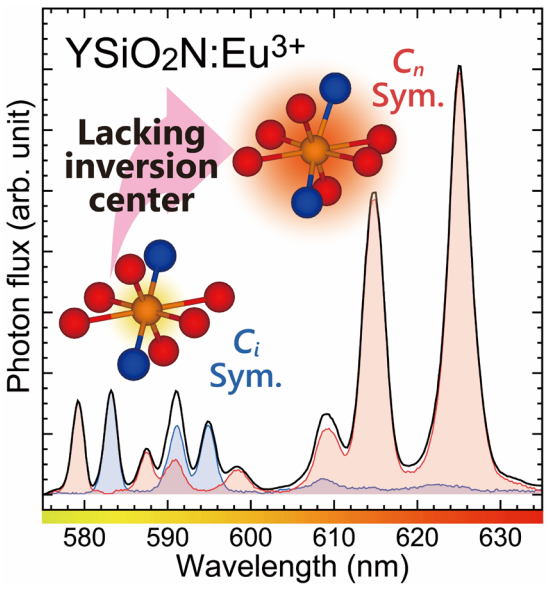

4.1. Introduction

Light-emitting diodes (LEDs) are ubiquitous in daily life, being seen as ceiling lights, displays for smartphones and laptops, traffic lights, and even UV emitters to inactivate coronavirus [1]. For solid-state lighting, LEDs are used in combination with phosphors, named "phosphor-converted LEDs (pc-LEDs)." Although the most popular pc-LED achieves bright cool-white emission owing to the combination of an InGaN blue LED chip and a yellow phosphor $Y_3Al_5O_{12}:Ce^{3+}$ (YAG:Ce) [2], it lacks red-emitting components, which is undesirable for lighting application. In order to compensate for the lack of red light components, a variety of red phosphors have been developed with divalent europium (Eu^{2+}) ions. In (oxy)nitride hosts, Eu^{2+} ions show intense orange-red luminescence due to 5d-4f parity allowed transition, leading to some commercialized red phosphors such as $CaAlSiN_3:Eu^{2+}$ (CASN) [3], $(Sr,Ca)AlSiN_3:Eu^{2+}$ (SCASN) [4], and $Sr_2Si_5N_8:Eu^{2+}$ [5]. However, their luminescence bands extend over 650 nm, where the sensitivity of human eyes is low [6]. In terms of luminous efficacy (unit: lm W^{-1}), red luminescence with broad bands is not optimal. Recently, some Eu^{2+}-doped narrow-band red emission phosphors with a ~1200 cm^{-1} bandwidth have been developed, such as $Sr[LiAl_3N_4]:Eu^{2+}$ (SLA) [7] or $Sr[Mg_3SiN_4]:Eu^{2+}$ (SMS) [8], to overcome this drawback. Although they are highly efficient red-emitting phosphors for pc-LED application, the possible candidates in Eu^{2+}-doped narrow-band phosphors are restricted from the structural and compositional points of view [9]. In contrast, trivalent europium (Eu^{3+}) ions can be more efficient than those Eu^{2+}-doped phosphors because of the narrow luminescence bands due to $^5D_0 \rightarrow {}^7F_2$ transition, located in highly sensitive regions for human eyes (610–630 nm). Despite the desired spectrum in the red region, many oxide phosphors activated with Eu^{3+} ions cannot show strong luminescence without deep-UV excitation (usually λ_{ex} = 250–280 nm). The efficient excitation band for Eu^{3+}-doped oxides is attributed to the charge transfer (CT) transition from O^{2-} to Eu^{3+} ions. The energy of CT states depends on the electronegativity of ligands [10,11]; accordingly, the CT energy is typically shifted to lower energies in order of fluorides, oxides, and nitrides.

For the purpose of extending the CT excitation toward longer wavelengths, we fabricated the Eu^{3+}-doped oxynitride sample, $YSiO_2N:Eu^{3+}$, and reported its luminescence properties [12].

Compared with other Eu^{3+}-doped oxides (α-$CaSiO_3$:Eu^{3+}, α-$Y_2Si_2O_7$:Eu^{3+}, and *y*-$Y_2Si_2O_7$:Eu^{3+}), the $YSiO_2N$:Eu^{3+} showed the CT excitation bands redshifted over 9500 cm^{-1} and the 2.7–6.0 times stronger $^5D_0 \rightarrow {}^7F_2$ luminescence (at 626 nm) due to partial N^{3-} coordination. Nevertheless, there are still two unclear points in the luminescence properties of the $YSiO_2N$:Eu^{3+}. One is the presence of five luminescence peaks assigned to the $^5D_0 \rightarrow {}^7F_1$ transition. The number of $^5D_0 \rightarrow {}^7F_1$ luminescence bands for Eu^{3+} ions in a single site is three or less because the maximum number of the Stark sublevels of the terminal state ($^7F_1$) is three. Although the five peaks indicate that Eu^{3+} ions are incorporated in more than one kind of Y^{3+} site with different coordination environments, and it is not obvious which luminescence bands correspond to which local environments. The other ambiguous point is the assignment of the split CT excitation bands. Previously, we concluded the assignment of the broad excitation bands to be the CT transition from N^{3-} and O^{2-} to Eu^{3+} [12]. Considering that the Eu^{3+} luminescence depends on the occupying sites, we have to take another possibility into account; the CT transition from only N^{3-} in crystallographically different sites. By clarifying the Eu^{3+} luminescent properties in the different local environments with the [$Eu^{3+}O_6N_2$] oxynitride polyhedron, we can obtain new insight into the material design guidelines for Eu^{3+}-activated luminescent materials.

In this study, we first investigate the crystal structure of $YSiO_2N$. Since the composition and possible crystal structure of $YSiO_2N$ were first reported more than 40 years ago [13,14], the precise crystal structure was not completely clear. One can find four candidates for the crystal structure of $YSiO_2N$ on the Inorganic Crystal Structure Database (ICSD) [15]: the monoclinic *Pm* [14], orthorhombic *Cmcm* [16], hexagonal $P6_122$ [17], and tetragonal *P*4/*mmm* [18]. The monoclinic *Pm* structure is the first identified phase by Morgan *et al.*, which has a hexagonal subcell in a lattice. All the Y^{3+} sites take C_1 symmetry. The orthorhombic *Cmcm* structure is isostructure to YBO_3, but there is no detailed description of $YSiO_2N$ in the literature. By using a computational technique, Ouyang *et al.* found that the possible structure with the highest symmetry of $YSiO_2N$ was the hexagonal phase with the space group of $P6_122$, where all the Y^{3+} sites take C_2 symmetry. The tetragonal *P*4/*mmm* lattice is the theoretically predicted perovskite-type structure by machine learning. However, the identification of these crystal structures is not

well-founded because all the literature sources were not based on fully accurate data from experimental diffraction results of a pure $YSiO_2N$ sample. In addition, the X-ray diffraction patterns of $YSiO_2N$ samples in the previous reports [12,19] show the mismatch with the reference patterns based on assumed structures, as shown in **Figure 4.1**. Thus, the precise structural analysis of $YSiO_2N$ is inevitable to discuss the characteristic Eu^{3+} luminescence in oxynitride coordination. Here, we finally identify the precise crystal structure of $YSiO_2N$ with the single-crystal X-ray and neutron diffraction techniques, which is the monoclinic *C*2/*c*. Based on this monoclinic structure, we investigate the luminescence properties of the $YSiO_2N:Eu^{3+}$ sample with the perspective of the site-selective and time-resolved spectroscopy. The detailed characterization of Eu^{3+} 4f-4f luminescence reveals how the site symmetry plays a crucial role in enhancing Eu^{3+} red luminescence.

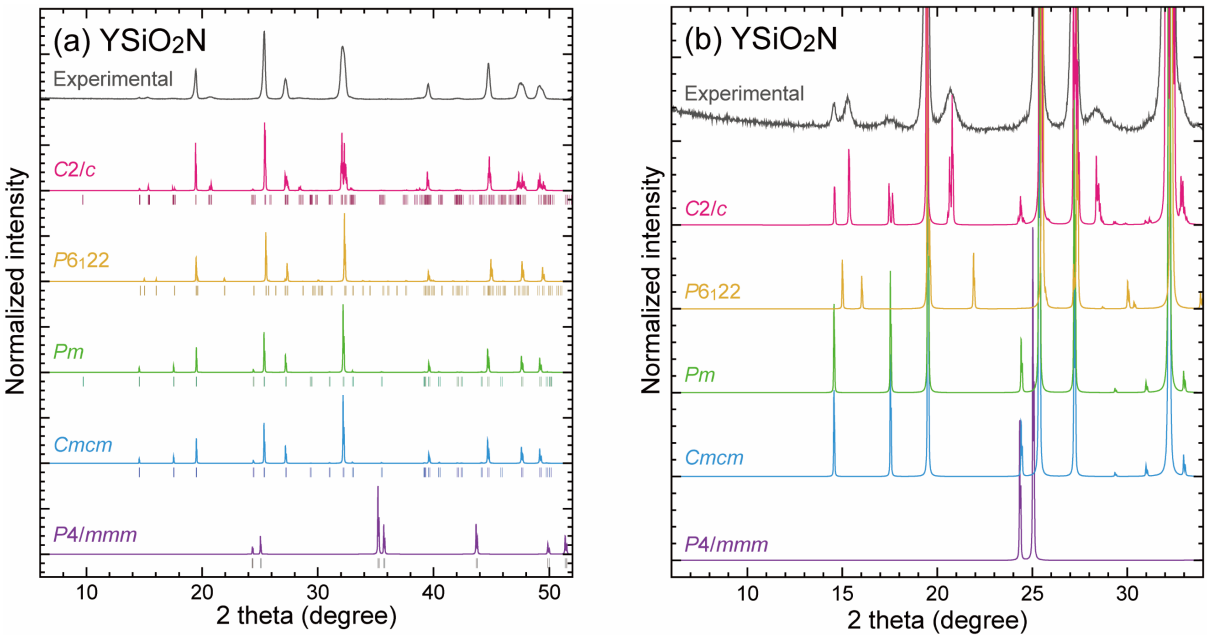

Figure 4.1. (a) Experimental and simulated XRD patterns of $YSiO_2N$. The simulation was performed by the VESTA program, based on the CIF in the ICSD. The tick marks represent the Bragg peak positions for each structure. (b) Enlarged patterns of Figure 4.1a in the 2θ range of 6–34°.

4.2. Experimental Section

4.2.1. Synthesis

A series of oxynitride ceramic samples, whose compositions are $YSiO_2N$, $Y_{0.999}Eu^{3+}_{0.001}SiO_2N$, $Y_{0.995}Eu^{3+}_{0.005}SiO_2N$, and $Y_{0.99}Eu^{3+}_{0.01}SiO_2N$, was prepared by the solid-state reaction method. Starting chemicals, Y_2O_3 (99.99%, Kojundo Chemical Laboratory), SiO_2 (99.9%, Kojundo Chemical Laboratory), Si_3N_4 (99.9%, Kojundo Chemical Laboratory), and Eu_2O_3 (99.99%, Furuuchi Chemical), were weighed in the glove box filled with high-purity Ar gas. Powders of starting chemicals were mixed with a ball milling system (Premium Line P-7, Fritsch) with ethanol (> 99.5%). The obtained slurry was dried at 120 °C for 24 h. The mixture was pelletized with dry pressing and sintered at 1600 °C under N_2 gas flow for 24 h. Because Eu^{3+} ions in the as-made samples were partially reduced into Eu^{2+} states, the Eu^{3+}-doped as-made samples were annealed at 700 °C under N_2 gas flow for 24 h to oxidize reduced europium ions, according to the Ellingham diagram [12,20].

4.2.2. Materials Characterization.

The prepared $YSiO_2N:Eu^{3+}$ samples were pulverized into powder form for crystal structure analysis. Some small particles were picked up under microscope observation and mounted at the top of a glass capillary with glue. The single-crystal X-ray diffraction (SC-XRD) data of a single particle were collected using a diffractometer (SMART APEX II Ultra, Bruker-AXS) with Mo Kα radiation (λ = 0.71073 Å) and multilayer focusing mirrors as a monochromator operated at 50 kV and 50 mA. The absorption corrections were applied using the multiscan procedure SADABS [21]. The crystal structure was solved and refined by SHELX-97 [22].

The time-of-flight neutron powder diffraction (TOF-NPD) data of the non-doped $YSiO_2N$ sample at 24 °C were obtained at beamline BL20 (iMATERIA) in Japan Proton Accelerator Research Complex (J-PARC). Cylindrical absorption corrections were applied to the TOF-NPD data using the inner density (2.021 g cm^{-3}). The Rietveld refinement was simultaneously carried out with the software Z-Rietveld [23] using the TOF-NPD data taken by the backscattering bank (BS; time focusing point at $2\theta = 172°$) and 90° bank (time focusing point

at $2\theta = 90°$).

The X-ray powder diffraction (XRPD) pattern of the sample was measured with an X-ray diffractometer using Cu Kα radiation (Ultima IV, Rigaku). The measured sample was mixed with 50 wt% Standard Reference Material of silicon powder (640d, NIST). The Rietveld refinement of the obtained XRPD pattern was performed using the RIETAN-FP program [24].

Photoluminescence (PL) and photoluminescence excitation (PLE) spectra were obtained by monochromatic excitation light with a 500 W Xe short arc lamp (OPM2-502XQ, Ushio Inc.) equipped with a double monochromator system by two monochromators (SP-300i, Acton Research Corp.), detected by using a photomultiplier tube (PMT) detector (R10699, Hamamatsu Photonics) coupled with a monochromator (SP-2300i, Princeton Instruments). The obtained PL and PLE spectra were calibrated by the spectrum of a deuterium-tungsten halogen light source (DH-2000, Ocean Optics) and the spectrum of the Xe lamp (light source) detected by a calibrated Si photodiode (S1337-1010BQ, Bunkoukeiki Co., Ltd.), respectively. The sample temperature was controlled by a cryostat with a closed-cycle He gas cryogenic refrigerator (CRT-A020-SE00, Ulvac Cryogenics) or a liquid nitrogen cryostat (VPF-800, Janis) in different temperature ranges of 4–300 K and 300–450 K.

Luminescence decay measurements at various temperatures (T = 20–700 K) were performed with a setup consisting of a nitrogen laser (KEC-200, USHO Optical Systems), a silicon photodiode (DET10, Thorlabs Inc.), an oscilloscope (HDO4104, Teledyne-LeCroy), a monochromator (G-250, Nikon), and a PMT detector (R1104, Hamamatsu Photonics). The sample temperature was controlled by a closed-cycle He cryostat (Mini Stat CRT-006-2600, Iwatani) at 20 K or a liquid nitrogen cryostat (Helitran LT3, Advanced Research Systems) at 100–700 K.

4.2.3. *Ab initio* Calculations.

The *ab initio* calculations with the density functional theory (DFT) were performed by the CASTEP module [25] of the Materials Studio 2020 package. The exchange-correlation functional was represented by the generalized gradient approximation (GGA) of Perdew-Burke-Ernzerhof functional for solids (PBEsol) [26]. The ionic core electrons were replaced by on-the-

fly ultrasoft pseudopotentials implemented in the CASTEP: [Ar] $4s^2 4p^6 5s^2 4d^1$ for Y, [Ne] $3s^2 3p^2$ for Si, [He] $2s^2 2p^4$ for O, and [He] $2s^2 2p^3$ for N [27]. Relativistic effects were taken into account at the level of the Koelling-Harmon approximation of the Dirac equation [28]. The plane-wave basis cut-off energy and k-point grids were 630 eV and 2 × 1 × 1, respectively. The convergence criteria were set as follows: total energy tolerance 5.0×10^{-6} eV $atom^{-1}$, maximum force tolerance 0.01 eV $Å^{-1}$, maximum stress component 0.02 GPa, and maximum displacement 5.0×10^{-4} Å. The *ab initio* electronic structure analysis to monoclinic $YSiO_2N$ was applied, where the site occupancies for all elements were fixed at unity, supposing that the nitride and oxide ions are bridging and non-bridging in the $[Si_3O_6N_3]$ units, respectively.

4.3. Results and Discussion

4.3.1. Crystal Structure Analysis of Monoclinic $YSiO_2N$

For the oxynitride $YSiO_2N$ sample, it was challenging to prepare a single-crystal particle for two reasons; the desorption of nitrogen through long-time sintering and the limitation of the appropriate flux for growth [29]. In this work, we successfully obtained a tiny single-crystal particle (9 μm × 11 μm × 12 μm) only in the $Y_{0.99}SiO_2N:Eu^{3+}_{0.01}$ sample (**Figure. 4.2**). The SC-XRD of the $Y_{0.99}SiO_2N:Eu^{3+}_{0.01}$ sample was investigated to determine lattice constants experimentally. The results of the SC-XRD analysis show that the $YSiO_2N$ crystal has a

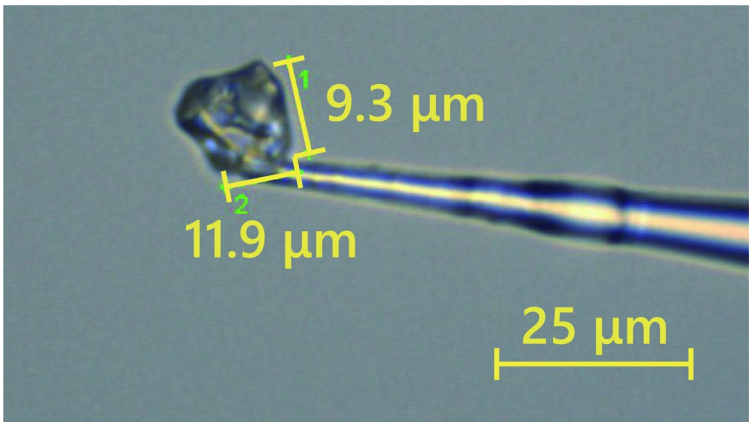

Figure 4.2. Photograph of a selected single-crystal particle of the $Y_{0.99}SiO_2N:Eu^{3+}_{0.01}$ sample.

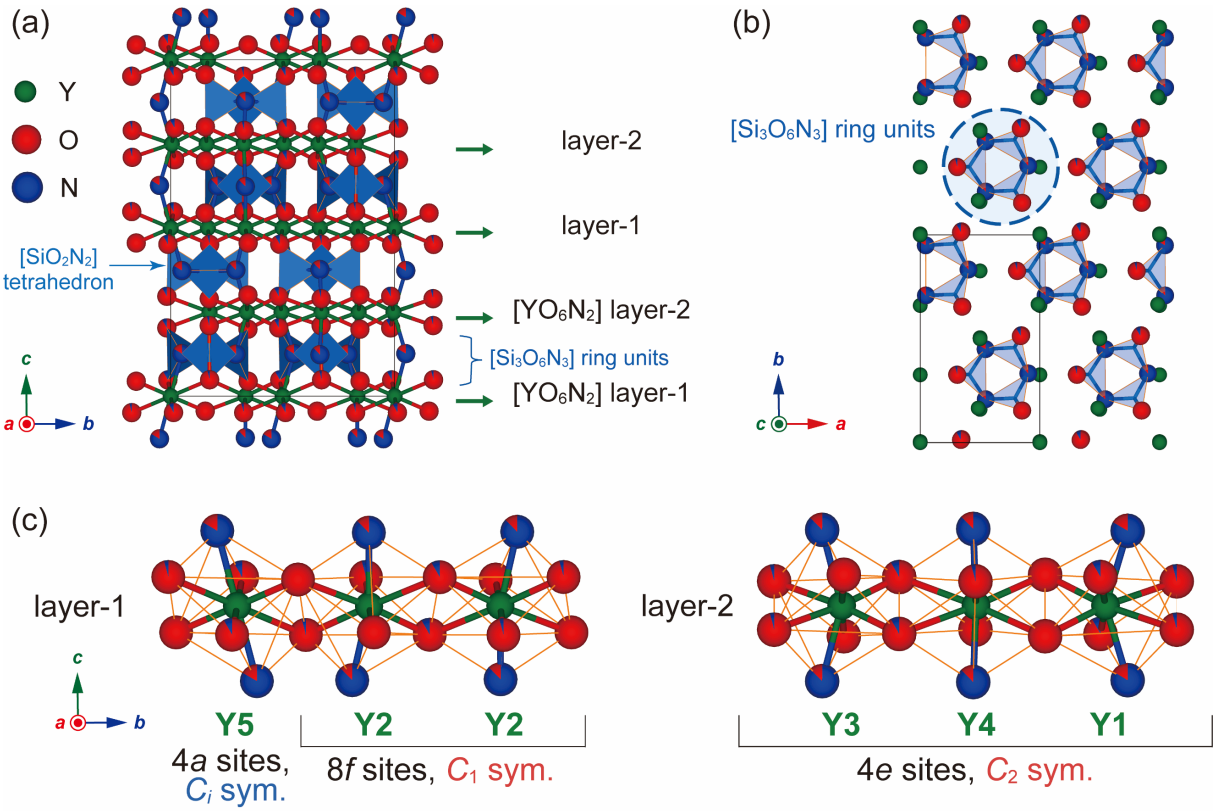

Figure 4.3. (a) Crystal structure of monoclinic $YSiO_2N$ viewed along the *a*-axis depicted with $[YO_6N_2]$ dodecahedra and $[SiO_2N_2]$ tetrahedra. The occupancy of anions sites, represented with mixed-colored spheres, reflects the results of the Rietveld refinement for the TOF-NPD data. The black line represents a unit cell. (b) A single layer composed of $[Si_3O_6N_3]$ ring units, viewed along the *c*-axis. (c) Local structures around Eu^{3+} ions in different kinds of layers. Layer-1 composes Y^{3+} sites with C_i and C_1 symmetry, and layer-2 composes Y^{3+} sites with only C_2 symmetry. These Y^{3+} sites are characterized by the *b*-axis. The crystal structures are drawn with the VESTA program [31].

monoclinic unit cell of a = 6.9973(10) Å, b = 12.1470(17) Å, c = 18.255(3) Å, and β = 90.735(3)° with the space group $C2/c$. The crystallographical data and structural parameters of the single crystal sample are given in **Tables 4.1** and **4.2**, respectively. The anisotropic displacement parameters U_{ij} are listed in the Supporting Information (**Table 4.3**). The obtained crystal structure is depicted in **Figure 4.3a**. The reason why it has been misunderstood as an orthorhombic or hexagonal lattice is due to the fact that β in the monoclinic lattice is close to 90°. As mentioned by Morgan [14], monoclinic $YSiO_2N$ is isostructural to the mineral pseudowollastonite (α-$CaSiO_3$), which is a high-temperature phase of $CaSiO_3$ (a = 6.8394 Å, b = 11.8704 Å, c = 19.63129 Å, and β = 90.667°, space group $C2/c$) [30]. Ca^{2+} of α-$CaSiO_3$ is replaced by Y^{3+} with one-third O^{2-} replaced by N^{3-} to satisfy charge neutrality. In the structure

of monoclinic $YSiO_2N$, a $[SiO_2N_2]$ tetrahedron shares two N atoms with two other tetrahedra, forming a ring unit $[Si_3O_6N_3]$ with three members (**Figure 4.3b**). Only N is the bridging atom, whereas all O atoms are non-bridging.

Y^{3+} ions, for which lanthanoid ions can substitute, are located in the interlayer composed of $[Si_3O_6N_3]$ units, leading to the two different Y^{3+}-layers (layer-1 and layer-2, shown in Figure 4.3a). The SC-XRD analysis reveals five crystallographically nonequivalent coordination environments for Y^{3+} ions. As depicted in **Figure 4.3c**, all the five Y^{3+} sites form an eight-fold dodecahedron $[YO_6N_2]$, whose symmetry differs depending on the N–Y–N bond angle. The Y^{3+} ions located at the Wyckoff 4*e* sites have one two-fold rotation axis (C_2 symmetry), and those at the 8*f* sites have only identity operation (C_1 symmetry). Unlike these C_n (n = 1, 2) symmetry, the Y^{3+} ions at the Wyckoff 4*a* sites have an inversion center (C_i symmetry). All Y^{3+} sites in monoclinic $YSiO_2N$ can be divided into two groups in terms of centrosymmetry, C_n and C_i sites.

Table 4.1. Crystallographic data and refinement detail of $YSiO_2N$ with SC-XRD

formula mass (g mol^{-1})	163.01
crystal system	Monoclinic
space group	*C* 2/*c* (No. 15)
cell parameters (Å)	a = 6.9973(10), b = 12.1470(17), c = 18.255(3), β = 90.735(3)°
volume (Å^3)	1551.5(6)
Z	24
crystal size (mm^3)	0.009 × 0.011 × 0.012
temperature (K)	296
crystal form	block
diffractometer	Bruker APEXII CCD area detector
radiation type	Mo Kα (λ = 0.71073 Å)
scan mode	ω scan
absorption correction	multiscan (SADABS)
μ (mm^{-1})	22.731
$2\theta_{max}$ (°)	45.28
measured reflection	13829
independent reflections	2358
observed reflections [$I > 2\sigma(I)$]	1303
$R[F^2 > 2\sigma(F^2)]$	0.031
$wR(F^2)$	0.068
S	0.86
$\Delta\rho_{max}$, $\Delta\rho_{min}$ (e Å^{-3})	1.01, −0.79

Table 4.2. Atomic coordinates and isotropic atomic displacement parameters for $YSiO_2N$, refined with SC-XRD data

site	Wyckoff	*x*	*y*	*z*	U_{eq} (Å)
Y1	4*e*	1	0.99246(5)	0.25	0.00730(16)
Y2	8*f*	0.98401(6)	0.33505(5)	0.49930(2)	0.00750(11)
Y3	4*e*	1	0.34365(6)	0.25	0.00804(15)
Y4	4*e*	0	0.67498(7)	0.25	0.01002(15)
Y5	4*a*	1	1	0.5	0.01076(17)
Si1	8*f*	0.7937(2)	0.79073(10)	0.37835(8)	0.0075(3)
Si2	8*f*	0.41849(17)	0.67110(12)	0.37145(7)	0.0078(2)
Si3	8*f*	0.78628(19)	0.54394(10)	0.37512(8)	0.0082(3)
O1	8*f*	0.3065(4)	0.6747(3)	0.29203(17)	0.0109(7)
O2	8*f*	0.8578(5)	0.8480(3)	0.30125(18)	0.0130(8)
O3	8*f*	0.8398(5)	0.4861(3)	0.29688(19)	0.0113(8)
O4	8*f*	0.8370(5)	0.4838(3)	0.45341(19)	0.0127(8)
O5	8*f*	0.8521(5)	0.8453(3)	0.45793(17)	0.0115(7)
O6	8*f*	0.3026(4)	0.6732(3)	0.44873(17)	0.0135(7)
N7	8*f*	0.5529(5)	0.7885(3)	0.3744(2)	0.0071(9)
N8	8*f*	0.9037(5)	0.6651(3)	0.37689(19)	0.0074(7)
N9	8*f*	0.5429(5)	0.5512(3)	0.3733(2)	0.0059(9)

Table 4.3. Anisotropic atomic displacement parameters U_{ij} (Å^2) of the non-doped $YSiO_2N$ sample obtained with the SC-XRD analysis

	U_{11}	U_{22}	U_{33}	U_{12}	U_{13}	U_{23}
Y1	0.0088(4)	0.0066(4)	0.0065(4)	0	−0.0004(3)	0
Y2	0.0072(2)	0.0088(2)	0.0064(2)	0.0018(2)	−0.00028(17)	0.0004(2)
Y3	0.0114(3)	0.0062(3)	0.0065(3)	0	0.0006(2)	0
Y4	0.0051(3)	0.0180(4)	0.0070(3)	0	−0.0010(2)	0
Y5	0.0157(4)	0.0101(4)	0.0065(4)	−0.0074(3)	0.0009(3)	−0.0012(2)
Si1	0.0085(7)	0.0069(6)	0.0070(7)	−0.0012(5)	−0.0006(6)	−0.0003(5)
Si2	0.0070(6)	0.0083(6)	0.0081(6)	0.0003(6)	0.0004(5)	−0.0008(6)
Si3	0.0094(7)	0.0073(7)	0.0078(7)	0.0007(5)	−0.0002(6)	−0.0002(5)
O/N1	0.0083(15)	0.0173(18)	0.0071(17)	0.0009(16)	−0.0002(12)	−0.0003(16)
O/N2	0.0188(19)	0.0102(19)	0.0100(18)	−0.0036(14)	0.0028(14)	0.0033(14)
O/N3	0.0155(19)	0.0095(18)	0.0090(19)	0.0046(14)	0.0025(15)	−0.0002(14)
O/N4	0.019(2)	0.0130(18)	0.006(2)	0.0043(15)	0.0022(15)	0.0034(14)
O/N5	0.0185(18)	0.0098(18)	0.0062(17)	−0.0031(14)	−0.0008(13)	−0.0005(14)
O/N6	0.0088(15)	0.0228(19)	0.0089(18)	0.0002(16)	0.0042(13)	−0.0019(17)
O/N7	0.010(2)	0.0060(19)	0.005(2)	0.0015(15)	0.0000(17)	0.0016(15)
O/N8	0.0081(17)	0.0064(17)	0.0076(19)	−0.0013(17)	−0.0007(14)	−0.0012(18)
O/N9	0.007(2)	0.006(2)	0.005(2)	0.0008(14)	−0.0020(17)	0.0003(15)

The XRD measurements are insufficient for the structural analysis of some mixed-anion compounds [32]. It is difficult for oxynitrides to distinguish N from O with XRD because the atomic scattering factors are similar. NPD is a powerful tool when it comes to the determination of the atomic positions of neighboring elements in the periodic table [33,34]. Neutron coherent scattering lengths of O (5.803(4) fm) and N (9.36(2) fm) [32] are different enough to distinguish their atomic positions.

The Rietveld refinement of the TOF-NPD data for the non-doped sample with the monoclinic structure of $YSiO_2N$ was performed to determine the O/N occupancies of anion sites. Here, the crystal parameters of the $Y_{0.99}SiO_2N:Eu^{3+}_{0.01}$ sample obtained by the SC-XRD analysis, including the atomic displacement parameters, were applied as a set of initial parameters. Through the entire analysis, we fixed the site occupancies for Y^{3+}, Si^{4+}, and anions at unity and simultaneously refined the anisotropic atomic displacement parameters. In order to improve the overall fitting of diffraction patterns, we applied the partial profile relaxation to some diffraction peaks. The diffraction patterns and the final results of refinement with the different detector banks (BS and 90° banks) are shown in **Figure 4.4**. The observed and refined patterns show an excellent overall fit with small reliability factors (BS bank: R_{wp} = 7.65%, 90° bank: R_{wp} = 5.96%). The refined lattice constants with the TOF-NPD data (a = 7.007984(12) Å, b = 12.15329(2) Å, c = 18.24736(3) Å, and β = 90.70583(17)°) are slightly larger than those obtained with the SC-XRD analysis. For comparison, the refined PXRD pattern and the obtained parameters with different diffraction techniques are listed in **Figure 4.5** and **Table 4.4**, respectively. This difference is caused by the averaged parameters in the polycrystalline phase. The refined occupancy of each site and bond valence sums (BVS) are listed in **Table 4.5**. Other refined parameters, including atomic coordinates in a unit cell, isotropic atomic displacement parameters U_{eq}, and anisotropic displacement parameters U_{ij} are listed in the Supporting Information (**Tables 4.6** and **4.7**). The refined occupancies of anion sites indicate that while the anion defects ($O_N^{\cdot}$, $N_O^{\prime}$) are generated through the sintering process, oxygen and nitrogen atoms are mainly ordered in the lattice of monoclinic $YSiO_2N$. The total amounts of the anion occupancies for O and N are found to be 2.062 and 0.938, respectively, almost corresponding to

the anion stoichiometry for $YSiO_2N$. The BVS of each atom was calculated with the refined bond lengths and site occupancies. The BVSs of Y, Si, O, and N are in good agreement with their formal charges. Thus, the occupancies of anion sites in the refined monoclinic $YSiO_2N$ structure are valid.

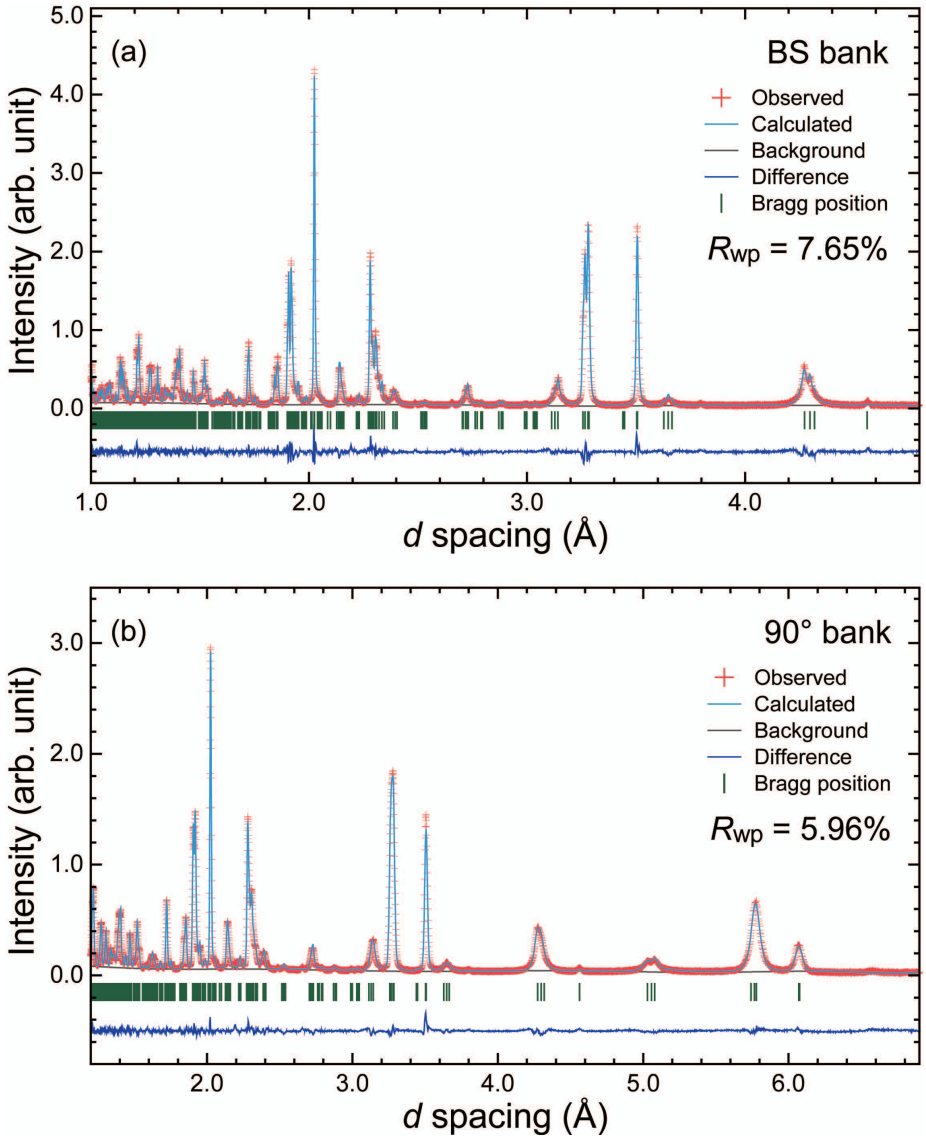

Figure 4.4. TOF-NPD patterns taken by (a) the backscattering (BS) and (b) the 90° bank of the monoclinic $YSiO_2N$ sample at 24 °C. The observed and calculated intensities and difference plot are shown by red + marks, cyan solid line, and blue solid line, respectively. Green tick marks indicate calculated Bragg peak positions. Reliability factors: R_{wp} = 7.65%, R_p = 6.18%, R_e = 1.70%, R_B = 4.02%, and R_F = 3.18% for the data taken by the BS bank; R_{wp} = 5.96%, R_p = 4.96%, R_e = 1.11%, R_B = 3.29%, and R_F = 2.64% for the data taken by the 90° bank.

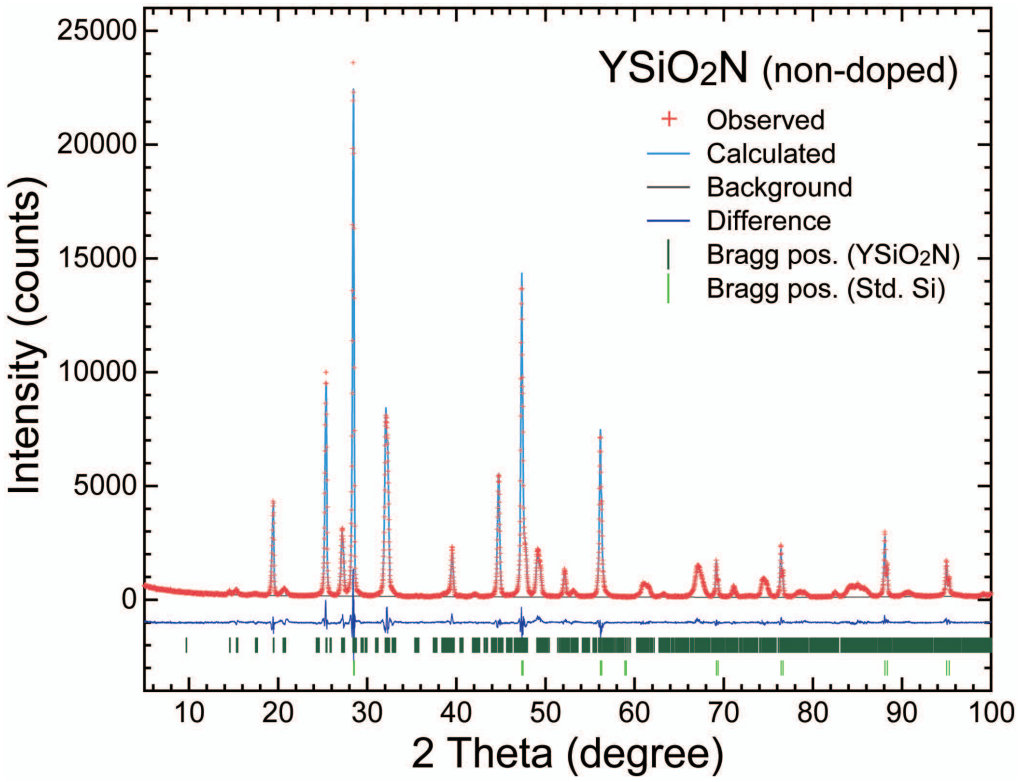

Figure 4.5. XRPD pattern of the $YSiO_2N$ sample with 50 wt% Si reference (640d, NIST) and the refined plot through the Rietveld method. Reliability factors: R_{wp} = 8.23%, R_p = 6.48%, and R_e = 4.33%.

Table 4.4. Comparison of the lattice constants obtained with the SC-XRD analysis, the TOF-NPD analysis, the XRPD analysis, and the DFT calculation[a]

	a (Å)	*b* (Å)	*c* (Å)	*β* (°)
TOF-NPD	7.007984(12)	12.15329(2)	18.24736(3)	90.70583(17)
SC-XRD	6.9973(10)	12.1470(17)	18.255(3)	90.735(3)
	[−0.152%]	[−0.052%]	[−0.044%]	[+0.032%]
XRPD	7.0144(5)	12.1634(8)	18.243(1)	90.673(3)
	[+0.092%]	[+0.083%]	[−0.024%]	[−0.036%]
DFT	6.9974	12.1435	18.1664	90.8721
	[−0.151%]	[−0.081%]	[−0.444%]	[+0.183%]

[a] The values in brackets are the difference from the parameter in the TOF-NPD analysis.

Table 4.5. Site occupancies and bond valence sums of $YSiO_2N$, as refined with TOF-NPD data

site	Wyckoff	occupancy	BVS
Y1	4*e*	1.000	2.89
Y2	8*f*	1.000	2.71
Y3	4*e*	1.000	3.13
Y4	4*e*	1.000	2.85
Y5	4*a*	1.000	2.78
Si1	8*f*	1.000	4.36
Si2	8*f*	1.000	4.00
Si3	8*f*	1.000	4.36
O1	8*f*	0.9548(17)	1.98
N1		0.0452(17)	
O2	8*f*	1.000	1.91
N2		0	
O3	8*f*	0.922(2)	2.00
N3		0.078(2)	
O4	8*f*	0.921(2)	1.70
N4		0.079(2)	
O5	8*f*	1.000	1.79
N5		0	
O6	8*f*	0.9703(17)	1.76
N6		0.0297(17)	
O7	8*f*	0.124(2)	3.26
N7		0.876(2)	
O8	8*f*	0.135(2)	3.46
N8		0.865(2)	
O9	8*f*	0.159(3)	3.16
N9		0.841(3)	

Table 4.6. Atomic coordinations and isotropic displacement parameters for $YSiO_2N$, refined with TOF-NPD data

site	Wyckoff	*x*	*y*	*z*	U_{eq} (Å)
Y1	4*e*	1	0.99509(11)	0.25	0.0073(2)
Y2	8*f*	0.98455(9)	0.33390(5)	0.49957(2)	0.00747(13)
Y3	4*e*	1	0.33970(11)	0.25	0.00811(16)
Y4	4*e*	0	0.67341(12)	0.25	0.0100(2)
Y5	4*a*	1	1	0.5	0.0108(3)
Si1	8*f*	0.79066(16)	0.78585(8)	0.37693(6)	0.0075(2)
Si2	8*f*	0.40941(14)	0.67177(11)	0.37007(5)	0.00785(16)
Si3	8*f*	0.78777(18)	0.54231(8)	0.37372(6)	0.0082(2)
O1 N1	8*f*	0.30793(11)	0.67206(13)	0.28996(4)	0.0109(2)
O2 N2	8*f*	0.30793(11)	0.67206(13)	0.28996(4)	0.0130(3)
O3 N3	8*f*	0.85261(12)	0.84507(9)	0.30079(4)	0.0114(2)
O4 N4	8*f*	0.85261(12)	0.84507(9)	0.30079(4)	0.0127(3)
O5 N5	8*f*	0.84511(14)	0.48262(9)	0.29703(4)	0.0115(2)
O6 N6	8*f*	0.84511(14)	0.48262(9)	0.29703(4)	0.0135(2)
O7 N7	8*f*	0.83961(14)	0.48730(9)	0.45159(4)	0.00702(8)
O8 N8	8*f*	0.83961(14)	0.48730(9)	0.45159(4)	0.00737(7)
O9 N9	8*f*	0.85003(12)	0.84595(9)	0.45552(4)	0.00600(8)

Table 4.7. Anisotropic atomic displacement parameters U_{ij} (Å^2) of the non-doped $YSiO_2N$ sample obtained with the TOF-NPD analysis

	U_{11}	U_{22}	U_{33}	U_{12}	U_{13}	U_{23}
Y1	0.0089(6)	0.0066(6)	0.0065(5)	0	−0.00038(2)	0
Y2	0.0072(3)	0.0089(4)	0.0063(3)	0.00177(11)	−0.00025(1)	0.00038(2)
Y3	0.0114(7)	0.0062(4)	0.0065(3)	0	0.00063(3)	0
Y4	0.0051(3)	0.0180(13)	0.0070(3)	0	−0.00101(4)	0
Y5	0.0157(11)	0.0101(10)	0.0065(5)	−0.0074(5)	0.00089(4)	−0.00114(6)
Si1	0.0085(8)	0.0070(6)	0.0070(6)	−0.00114(8)	−0.00063(4)	−0.00025(1)
Si2	0.0070(6)	0.0084(5)	0.0081(5)	0.00025(2)	0.00038(2)	−0.00076(5)
Si3	0.0094(8)	0.0073(6)	0.0079(5)	0.00076(5)	−0.00025(1)	−0.00025(2)
O/N1	0.0084(5)	0.0174(9)	0.0071(4)	0.00089(5)	−0.00025(1)	−0.00025(2)
O/N2	0.0189(11)	0.0103(5)	0.0100(5)	−0.00355(18)	0.00279(11)	0.00326(16)
O/N3	0.0156(9)	0.0095(6)	0.0090(5)	0.00456(27)	0.00253(10)	−0.00025(1)
O/N4	0.0191(11)	0.0130(8)	0.0060(3)	0.00431(22)	0.00215(9)	0.00342(17)
O/N5	0.0186(9)	0.0098(6)	0.0062(3)	−0.00317(16)	−0.00076(2)	−0.00051(3)
O/N6	0.0089(4)	0.0228(11)	0.0089(4)	0.00025(2)	0.00418(17)	−0.00190(11)
O/N7	0.0100(4)	0.0060(2)	0.0049(1)	0.00152(5)	0.00000(0)	0.00165(3)
O/N8	0.0081(3)	0.0065(2)	0.0076(2)	−0.00127(5)	−0.00076(2)	−0.00114(3)
O/N9	0.0070(3)	0.0060(2)	0.0049(2)	0.00076(2)	−0.00203(6)	0.00025(1)

4.3.2. *Ab initio* Geometry Optimization and Electronic Structure Calculations

For almost two decades, the hexagonal $P6_122$ has been considered to be the stable structure for $YSiO_2N$ with the *ab initio* calculation by Ouyang [17]. First, we discuss the stability of the monoclinic and hexagonal $YSiO_2N$ with the *ab initio* geometry optimizations. The obtained total energy of the monoclinic lattice is −480.8335 eV $atom^{-1}$, which is 1.0 meV lower than that of the hexagonal lattice (= −480.8325 eV $atom^{-1}$). The lattice constants of the optimized monoclinic structure show a good agreement with the experimental values (Table 4.4). As a result, the *ab initio* calculation supports that the reasonable crystal structure of $YSiO_2N$ is the monoclinic lattice, as well as the crystal structure analysis. In order to understand the electronic properties, we performed the electronic state analysis of monoclinic $YSiO_2N$. **Figure 4.6a** depicts the band structure, showing the direct bandgap at the Γ point, E_g = 4.265 eV. **Figure 4.6b** shows the calculated total and partial density of electronic states (DOS and PDOS) for monoclinic $YSiO_2N$. The PDOS indicates that N 2p orbitals have a significant contribution around the valence band (VB) top. We also calculated the bandgap and PDOS for the isostructural α-$CaSiO_3$ with the same conditions (**Figure 4.7**). The bandgap, which is mainly composed of O 2p and Ca 3p orbitals, takes a larger value (4.708 eV), supporting that the existence of nitrogen contributes to the elevation of VB top in monoclinic $YSiO_2N$.

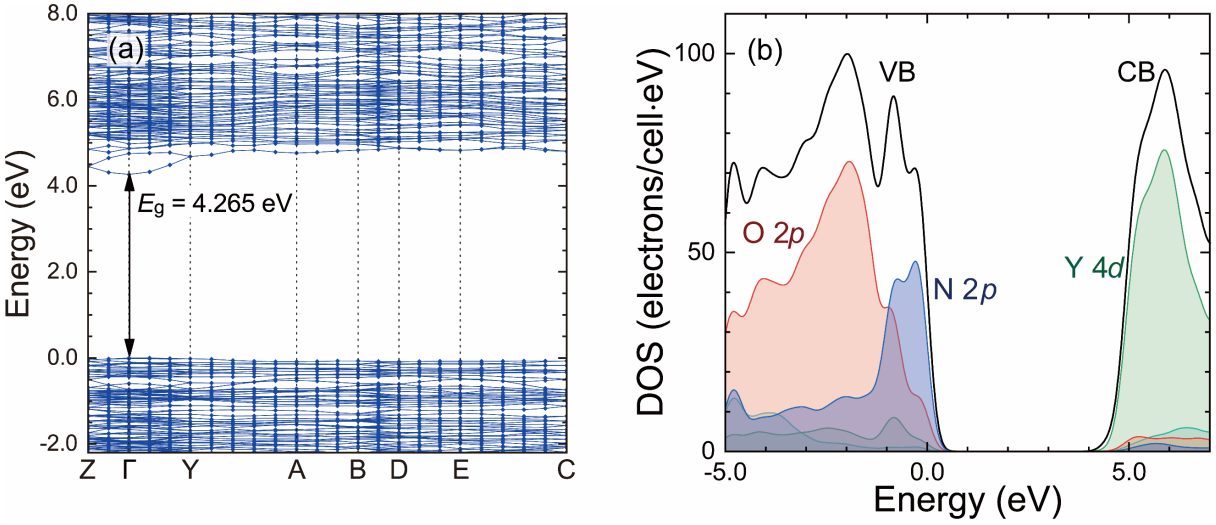

Figure 4.6. (a) Electronic band structure of monoclinic $YSiO_2N$ (space group $C2/c$). (b) Calculated total and partial density of electronic states for monoclinic $YSiO_2N$, enlarged in the range from −5.0 to 7.0 eV around the Fermi level. The PDOS curves for O 2p, N 2p, and Y 4d orbitals are overshadowed.

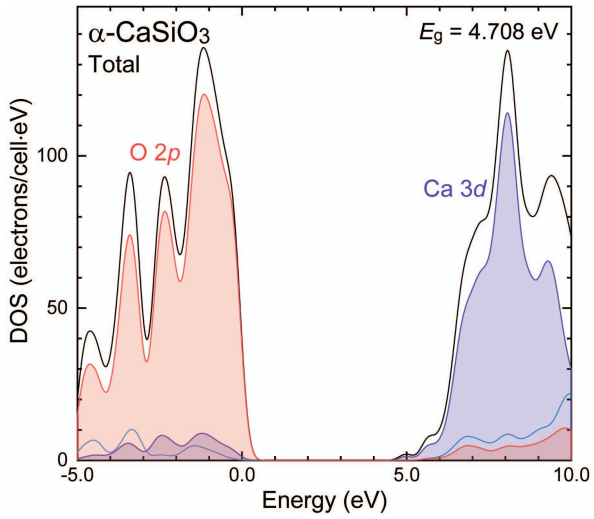

Figure 4.7. Calculated total and partial density of states for α-$CaSiO_3$ (space group *C*2/*c*), enlarged in the range from −5.0 to 10.0 eV around the Fermi level. The PDOS curves for O 2p and Ca 3p orbitals are overshadowed.

4.3.3. Detection of Different Eu^{3+} Luminescence Components by Site-Selective and Time-Resolved Spectroscopy

We investigate the PL and PLE spectra of the $YSiO_2N:Eu^{3+}$ sample with multiple Y sites. **Figure 4.8a** shows the PL spectra of the $YSiO_2N:Eu^{3+}$ sample at 4 K *via* the different excitation processes; the CT transition (λ_{ex} = 320 nm) and the $^5D_2 \leftarrow {}^7F_0$ electric dipole (ED) transition (λ_{ex} = 466 nm). The schematic energy diagram of radiative and non-radiative electronic transition is depicted in **Figure 4.8b**. In both spectra, the luminescence bands are observed only below 17400 cm^{-1}; *i.e.*, no distinct luminescence attributed to the radiative transition from the $^5D_1$ and $^5D_2$ states is observed. These depopulated $^5D_1$ and $^5D_2$ states can be explained by a high multiphonon relaxation (MPR) rate. The Raman spectrum of the $YSiO_2N$ sample provided in **Figure 4.9** indicates that the maximum phonon energy $\hbar\omega_{max}$ for the monoclinic $YSiO_2N$ is 918 cm^{-1}. This large phonon energy is due to the vibrational mode of the Si-N bonding, resulting in the relaxation from the $^5D_2$ to the $^5D_1$ levels (~2500 cm^{-1}) or the $^5D_1$ to the $^5D_0$ levels (~1700 cm^{-1}) with only two or three phonon emissions [35]. Thus, all the sharp luminescence bands are assigned to the $^5D_0 \rightarrow {}^7F_J$ (J = 0–6) transition. For the assignment of Eu^{3+}: 4f-4f PL and PLE bands at different sites, the general relationship between spectroscopic features and crystallographical

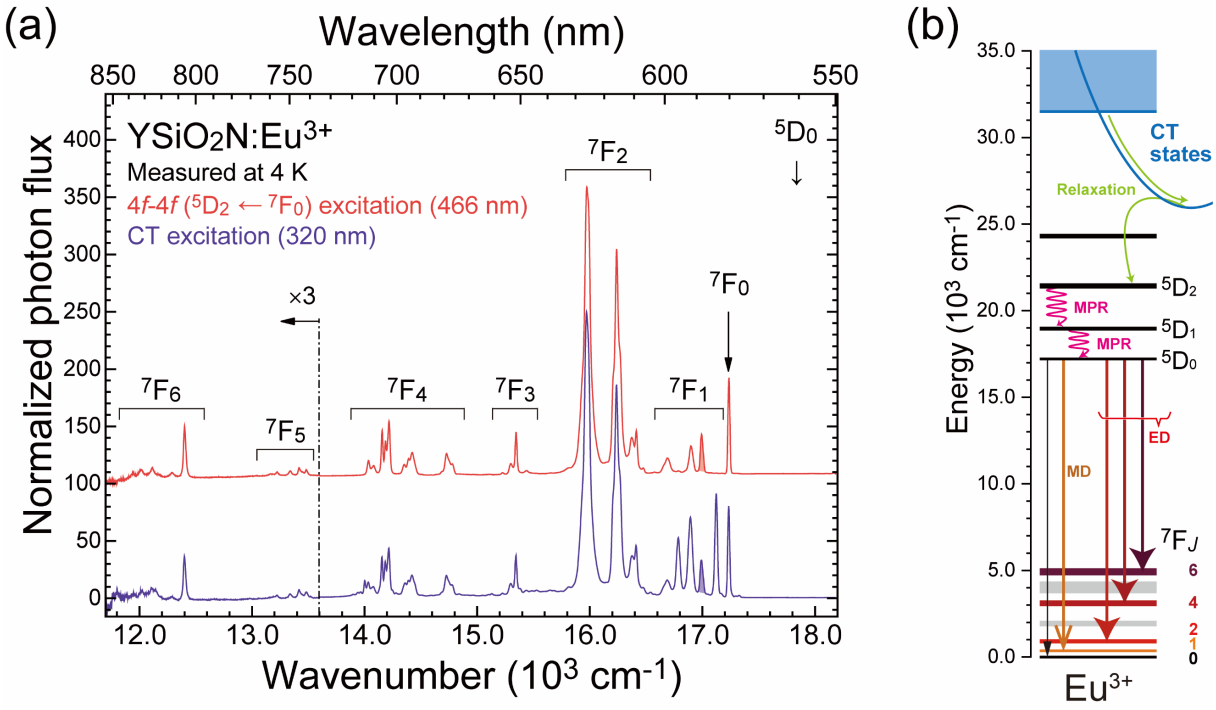

Figure 4.8. (a) Normalized PL spectra at 4 K excited by CT transition (λ_{ex} = 320 nm) and $^5D_2 \leftarrow {}^7F_0$ transition (λ_{ex} = 466 nm). The PL intensities are normalized by the integrated PL intensities for one of the $^5D_0 \rightarrow {}^7F_1$ MD luminescence bands peaking at 16992 cm^{-1} (overshadowed). Below 13600 cm^{-1} (= ~735 nm), the spectra are enlarged three times. (b) Energy level diagram of Eu^{3+} ions in monoclinic $YSiO_2N$.

structure for Eu^{3+} ions is summarized in **Table 4.8**. Under the CT excitation, the spectral shape is almost the same as the reported one [12]. The five luminescence peaks in the range of 16600–17200 cm^{-1} are assigned to the $^5D_0 \rightarrow {}^7F_1$ magnetic dipole (MD) transition. Considering the PL spectra with different Eu^{3+} concentrations (0.1, 0.5, 3.0%, shown in **Figure 4.10**), five nonequivalent Y^{3+} sites can equally accommodate Eu^{3+} ions without any priority. As the CT excitation bands broadly spread over the UV region, all Eu^{3+} ions at Y^{3+} sites can be efficiently excited and show 4f-4f luminescence. On the other hand, only the three $^5D_0 \rightarrow {}^7F_1$ luminescence peaks are observed under the $^5D_2 \leftarrow {}^7F_0$ ED transition, indicating that only Eu^{3+} ions that occupy a particular site emit red luminescence with the 466 nm excitation. Since the line strength of the $^5D_2 \leftarrow {}^7F_0$ excitation takes a large value only for hypersensitive distorted sites [36], the PL spectrum with the 466 nm excitation is attributed to the luminescence of the Eu^{3+} ions at non-centrosymmetric C_n sites ($Eu^{3+}(C_n)$). Only one sharp luminescence band at 17236 cm^{-1} (λ = 580.2 nm) is assigned to the $^5D_0 \rightarrow {}^7F_0$ transition, which is used to determine the number of sites

due to no Stark splitting for the terminal $^7F_0$ level [37], indicating that the ^7F_J levels for $Eu^{3+}(C_1)$ and $Eu^{3+}(C_2)$ are hardly distinguished in the monoclinic $YSiO_2N:Eu^{3+}$.

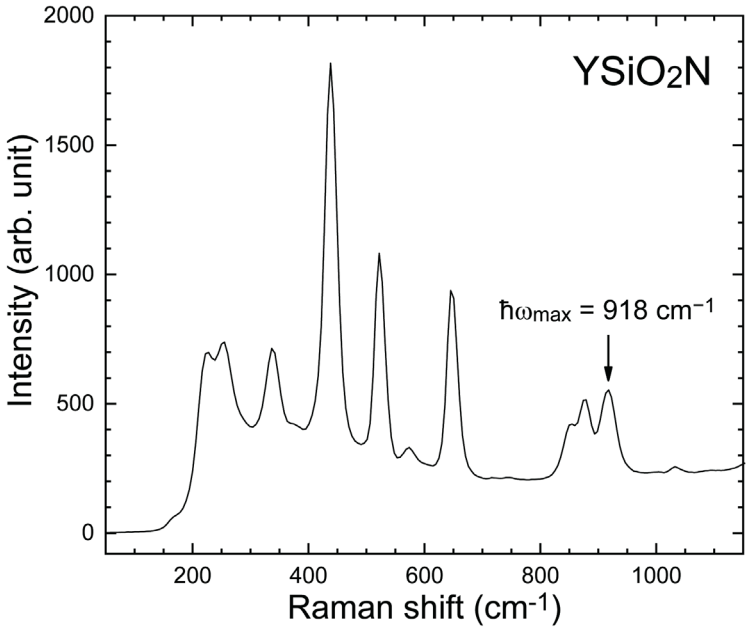

Figure 4.9. Raman spectrum of the $YSiO_2N$ sample at room temperature with 785 nm laser irradiation.

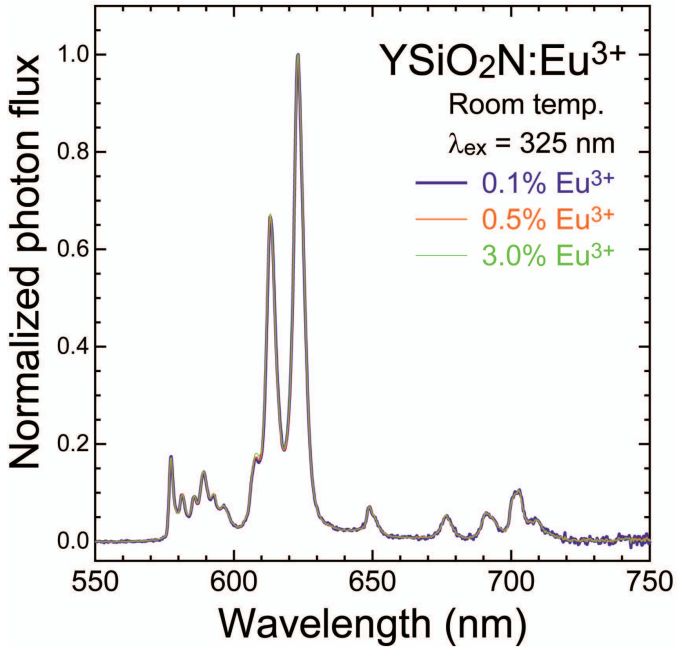

Figure 4.10. Normalized PL spectra for the Eu^{3+}-doped $YSiO_2N$ samples with different concentrations (0.1, 0.5, and 3.0%) at room temperature. The samples were excited by a He-Cd laser (λ_{ex} = 325 nm).

Table 4.8. Overview of relative intensities in PL and PLE spectra for Eu^{3+}-doped phosphors[a]

	PL		PLE		
character of transition [b]	ED	MD	ED	MD	CT
initial level	$[^5D_0]$	$[^5D_0]$	$[^7F_0]$	$[^7F_0]$	—
non-centrosymmetric (C_n sites)	++	+	++	+	+++
centrosymmetric (C_i sites)	−	+	−	+	+++

[a]Relative intensity of each transition is represented with the following notations; +++ = very strong, ++ = strong, + = medium, − = (very) weak

[b]ED = Electric dipole transition, MD = magnetic dipole transition, CT = charge transfer transition

Figure 4.11 shows the PL-PLE contour plot of the $Y_{0.995}SiO_2N:Eu^{3+}_{0.005}$ sample at 20 K to identify luminescence for Eu^{3+} ions incorporated in a variety of coordination environments. Here, the sample doped with 0.5% Eu^{3+} was used only for this measurement to obtain the spectra with a sufficiently high signal-to-noise ratio. It had been confirmed that the $YSiO_2N$ samples doped with 0.1 and 0.5% Eu^{3+} show the same shapes of PL spectra, as displayed in Figure 4.10. The Eu^{3+} ions in the $YSiO_2N$ host were excited by the $^5D_1 \leftarrow {}^7F_0$ MD transition, whose transition probability is insensitive to site-symmetry of the local environment [37,38] and spectral shape is relatively simple due to the small number of Stark sublevels (three or less). The contour plot successfully separates two Eu^{3+} luminescence spectra plotted in the right panel of Figure 4.11.

Under the 527.0 nm excitation light illumination, the intense luminescence with hypersensitive $^5D_0 \rightarrow {}^7F_2$ ED transition is observed. This luminescence is attributed to $Eu^{3+}(C_n)$ ions because of the similar PL spectrum with the $^5D_2 \leftarrow {}^7F_0$ ED excitation shown in Figure 4.8a. On the other hand, only three sharp luminescence bands attributed to the Eu^{3+} $^5D_0 \rightarrow {}^7F_1$ MD transition are distinctly observed under the 524.5 nm excitation light irradiation. Compared with the $Eu^{3+}(C_n)$ luminescence, the $^5D_0 \rightarrow {}^7F_2$ luminescence in the range of 605–630 nm is much weaker. Considering relatively strong MD luminescence with three peaks, we assign this PL

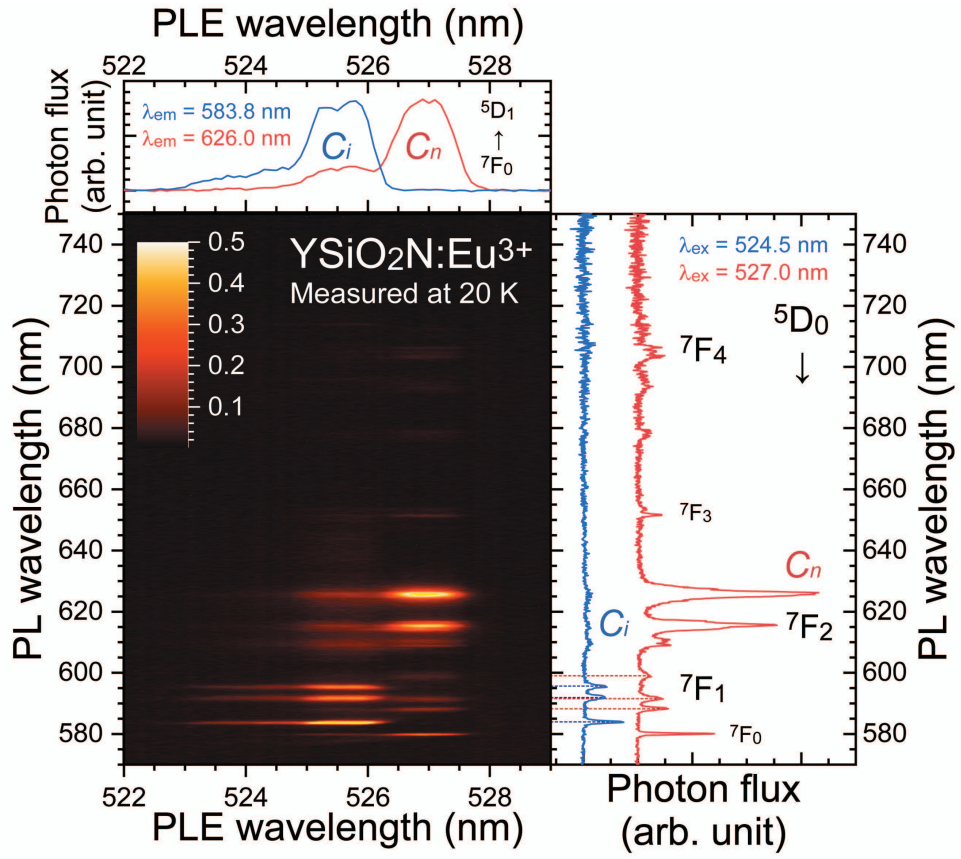

Figure 4.11. PL-PLE contour plot (λ_{ex} vs. λ_{em}) of the $Y_{0.995}SiO_2N:Eu^{3+}{}_{0.005}$ sample at 20 K, constructed by PL spectra with different excitation wavelengths (λ_{ex} = 522–529 nm). The right and top panels show PL and PLE spectra at particular excitation and emission wavelengths.

spectrum to the Eu^{3+} luminescence at the centrosymmetric C_i sites ($Eu^{3+}(C_i)$). By combining these two PL spectra for $Eu^{3+}(C_n)$ and $Eu^{3+}(C_i)$ ions, we can reproduce the PL spectra excited by the CT transition (**Figure 4.12**). In this contour plot, the relative intensity of the $^5D_0 \rightarrow {}^7F_1$ luminescence does not reflect the ratio between the number of the C_n and C_i sites because the PL intensity is determined by the quantum efficiency of each transition and branching ratio of the MD transition.

The site-selective spectroscopy suggests that the $[Eu^{3+}O_6N_2]$ dodecahedron with C_n symmetry generates very effective red luminescence because of the lack of an inversion center. The degree of enhancement of luminescence due to site distortion can be evaluated with the Judd-Ofelt theory [38–41]. According to the Judd-Ofelt theory, the spontaneous emission rate of 4f-4f transition from the initial excited states $|\Psi'J'\rangle$ to the terminal ground states $|\Psi J\rangle$ $A_R(\Psi J, \Psi'J')$ is proportional to the summation of the matrix elements, described below,

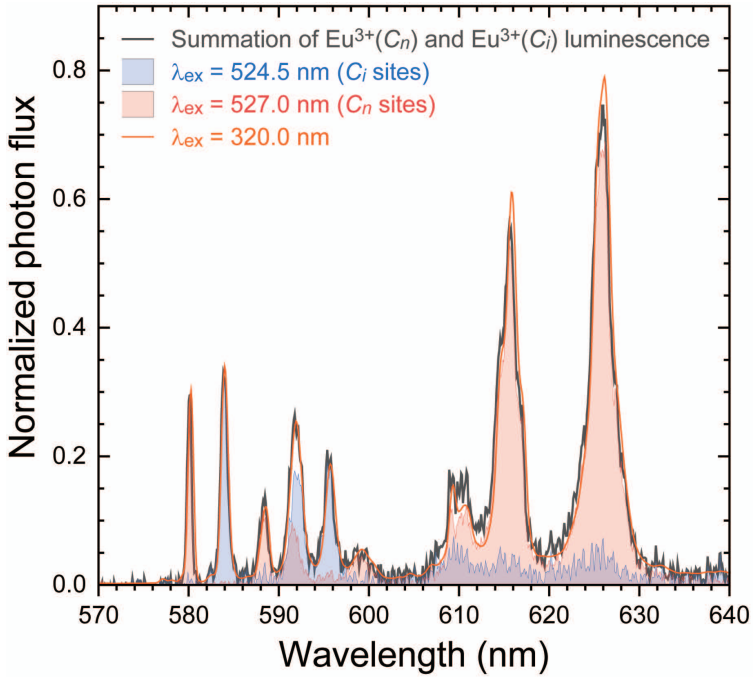

Figure 4.12. Normalized PL spectra excited with 320.0, 524.5, and 527.0 nm. The spectrum with a solid gray line represents the summation of the spectra for the $Eu^{3+}(C_n)$ and $Eu^{3+}(C_i)$ luminescence depicted with the red- and blue-overshadowed spectra. The summation spectrum well reproduces the PL spectrum with the CT excitation.

$$A_{\mathrm{R}}(\Psi J, \Psi' J') = \frac{64\pi^4 \tilde{\nu}^3 e^2}{3h(2J'+1)} \left[\frac{n(n^2+2)^2}{9} S_{\mathrm{ED}} + n^3 S_{\mathrm{MD}} \right], \tag{4.1}$$

$$S_{\mathrm{ED}} = \sum_{t=2,4,6} \Omega_t |\langle \Psi' J' \| U^t \| \Psi J \rangle|^2 . \tag{4.2}$$

In eq. 4.1, $\tilde{\nu}$ is the centroid energy of a radiative transition, e is the elementary charge (= 4.803 × 10^{-10} esu), h is the Planck constant (= 6.626 × 10^{-27} erg s^{-1}), n is the refractive index of a host material (1.94 for $YSiO_2N$ [17]), and S_{ED} and S_{MD} are the line strengths of ED and MD transition, respectively. Here, the S_{ED} parameter is sensitive to the local environment around lanthanoid ions, while the MD transition is insensitive to the local environment [38,42]. In eq. 4.2, the S_{ED} is described by the summation of the product of two parameters; the Judd-Ofelt intensity parameter Ω_t (t = 2, 4, 6) and the squared reduced matrix elements (RMEs) $|\langle||U^t||\rangle|^2$, which have unique values for each transition. Only the Ω_t parameter is a powerful tool to characterize the luminescence properties of the 4f-4f transition depending on the local environment.

We performed the Judd-Ofelt analysis with the integrated photon flux estimated from the PL spectra (Figure 4.8a), proportional to the spontaneous emission rates of the $^5D_0 \rightarrow {}^7F_J$

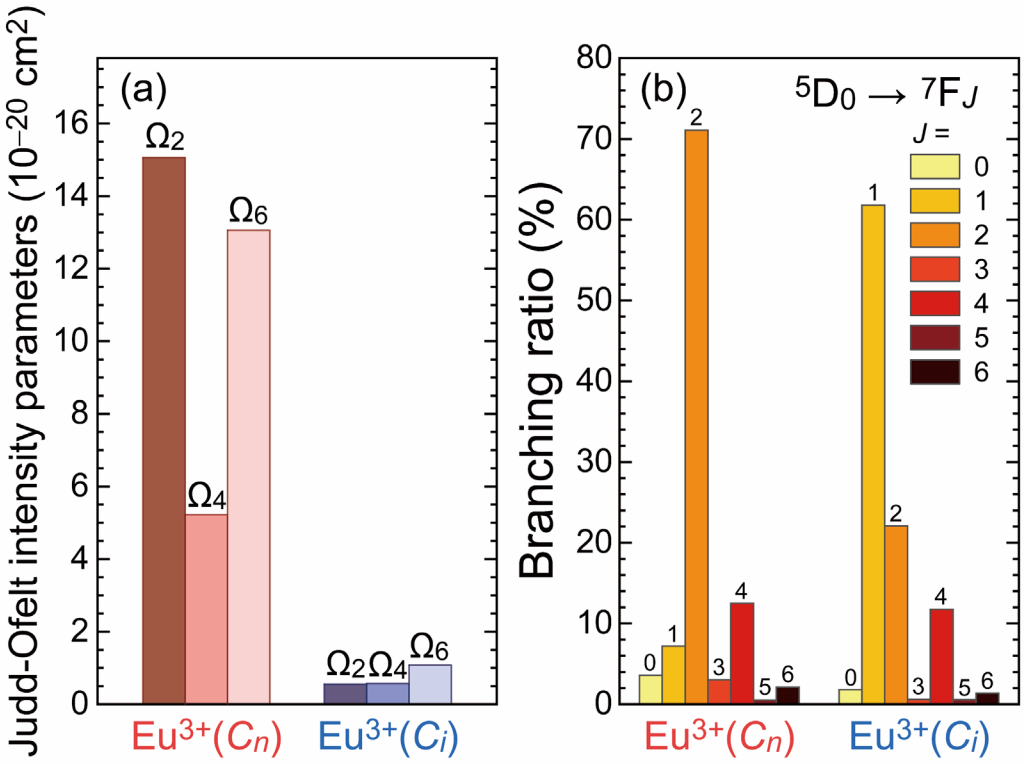

Figure 4.13. (a) Histogram of calculated Judd-Ofelt intensity parameters Ω_t ($t = 2, 4, 6$) for the $Eu^{3+}(C_n)$ and $Eu^{3+}(C_i)$ in monoclinic $YSiO_2N$, based on the PL spectra shown in Figure 4a. (b) Histogram of the branching ratio of the $^5D_0 \rightarrow {}^7F_J$ ($J = 0$–6) transition for the $Eu^{3+}(C_n)$ and $Eu^{3+}(C_i)$ ions.

transition ($J = 0$–6). The spontaneous emission rates for $Eu^{3+}(C_i)$ were estimated by the difference between the PL spectra excited by the CT and $^5D_2 \leftarrow {}^7F_0$ transitions. The calculated Ω_t parameters, the spontaneous emission rates A_R, and the radiative lifetimes τ_R are listed in **Table 4.9**. The A_R values and the branching ratios for all $^5D_0 \rightarrow {}^7F_J$ transitions are given and visualized in the Supporting Information (**Tables 4.10** and **4.11**, and **Figure 4.13**).

Many previous studies concluded that the Ω_2 parameter strongly correlates with the asymmetry of a coordination polyhedron [36,38,41]. The C_n sites show the very large Ω_2 parameter, 15.1×10^{-20} cm^2, which is comparable to the value for the $Y_2O_2S:Eu^{3+}$ (13.0×10^{-20} cm^2) [43]. On the other hand, the C_i sites have quite a small Ω_2 value (0.554×10^{-20} cm^2) due to centrosymmetry. In the case of the $[Eu^{3+}O_6N_2]$ dodecahedron, lacking an inversion center enhances the PL intensity of the $^5D_0 \rightarrow {}^7F_2$ ED transition about 27 times. The chemical trend of the Ω_4 and Ω_6 parameters is still under discussion. For inorganic crystals, the covalent bonding character between Eu^{3+} ions and ligands seems to correlate with the $\Omega_{4,6}$ values [44]. For the

$Eu^{3+}(C_n)$, only the Ω_6 parameter is considerably large, resulting in strong $^5D_0 \rightarrow {}^7F_6$ luminescence, while the Ω_4 parameter takes a typical value for Eu^{3+}-doped aluminates and silicates [12,45]. The Ω_4 and Ω_6 parameters possibly relate to other variables such as the 6s electron density [46], ligand-field distortion [47], and basicity around lanthanoid ions [48], thereby making it difficult to conclude the origin of the large Ω_6 parameter. The $Eu^{3+}(C_i)$ takes the small Ω_4 and Ω_6 values as well as the Ω_2 because of the strong parity-forbidden character stemming from the centrosymmetric field.

Table 4.9. Calculated parameters for Eu^{3+} ions in the C_n and C_i sites of the monoclinic $YSiO_2N$ host by the Judd-Ofelt analysis; the Judd-Ofelt intensity parameters Ω_t (t = 2, 4, 6), the spontaneous emission rates of the $^5D_0 \rightarrow {}^7F_J$ transition $A_R(^7F_J)$ (J = 1, 2, 4, 6), the radiative rates Γ_R, and the radiative lifetimes τ_R

	Ω_2 (10^{-20} cm^2)	Ω_4 (10^{-20} cm^2)	Ω_6 (10^{-20} cm^2)	$A_R(^7F_1)$ (10^2 s^{-1})	$A_R(^7F_2)$ (10^2 s^{-1})	$A_R(^7F_4)$ (10^2 s^{-1})	$A_R(^7F_6)$ (10^2 s^{-1})	Γ_R (10^2 s^{-1})	τ_R (ms)
C_n	15.1	5.22	13.1	1.06	10.4	1.84	0.310	14.7	0.681
C_i	0.554	0.570	1.07	1.07	0.382	0.204	0.024	1.74	5.75

Table 4.10. Calculated spontaneous emission rates (unit: 10^2 s^{-1}) of the Eu^{3+}: $^5D_0 \rightarrow {}^7F_J$ (J = 0–6) transition for the C_n and C_i sites in monoclinic $YSiO_2N$

	$A_R(^5D_0 \rightarrow {}^7F_J)$						
	J = 0	J = 1	J = 2	J = 3	J = 4	J = 5	J = 6
C_n	0.526	1.06	10.4	0.443	1.84	0.0762	0.310
C_i	0.0314	1.07	0.384	0.0105	0.204	0.00980	0.0236

Table 4.11. Branching ratios (%) of the Eu^{3+}: $^5D_0 \rightarrow {}^7F_J$ (J = 0–6) transition for the C_n and C_i sites in monoclinic $YSiO_2N$

	$^5D_0 \rightarrow {}^7F_J$						
	J = 0	J = 1	J = 2	J = 3	J = 4	J = 5	J = 6
C_n	3.58	7.20	71.1	3.01	12.5	0.519	2.11
C_i	1.81	61.8	22.1	0.601	11.8	0.564	1.36

The Judd-Ofelt analysis also reveals that the radiative lifetime of the Eu^{3+}: $^5D_0$ states at the C_n sites (= 0.681 ms) and the C_i sites (= 5.75 ms) are totally different due to the difference of spontaneous emission rates of ED transition related to centrosymmetry around Eu^{3+} ions, suggesting that it is possible to separate the luminescence of $Eu^{3+}(C_n)$ and $Eu^{3+}(C_i)$ in terms of time-resolved spectroscopy. The contour plot in **Figure 4.14** shows the time-resolved PL spectra of the $YSiO_2N:Eu^{3+}$ samples in milliseconds and the different luminescence decay curves of each PL peak. The intense luminescence with fast decay below a few milliseconds is attributed to the $Eu^{3+}(C_n)$ ions. In contrast, the luminescence with a slow decay in a few tens of milliseconds is attributed to the $Eu^{3+}(C_i)$ ions. The top panel shows the integrated PL spectra with different integration time ranges. In the time range of 0–10 ms, both Eu^{3+} luminescence at the C_n and C_i sites are observed, whose spectral shape is similar to the PL spectra with the CT excitation

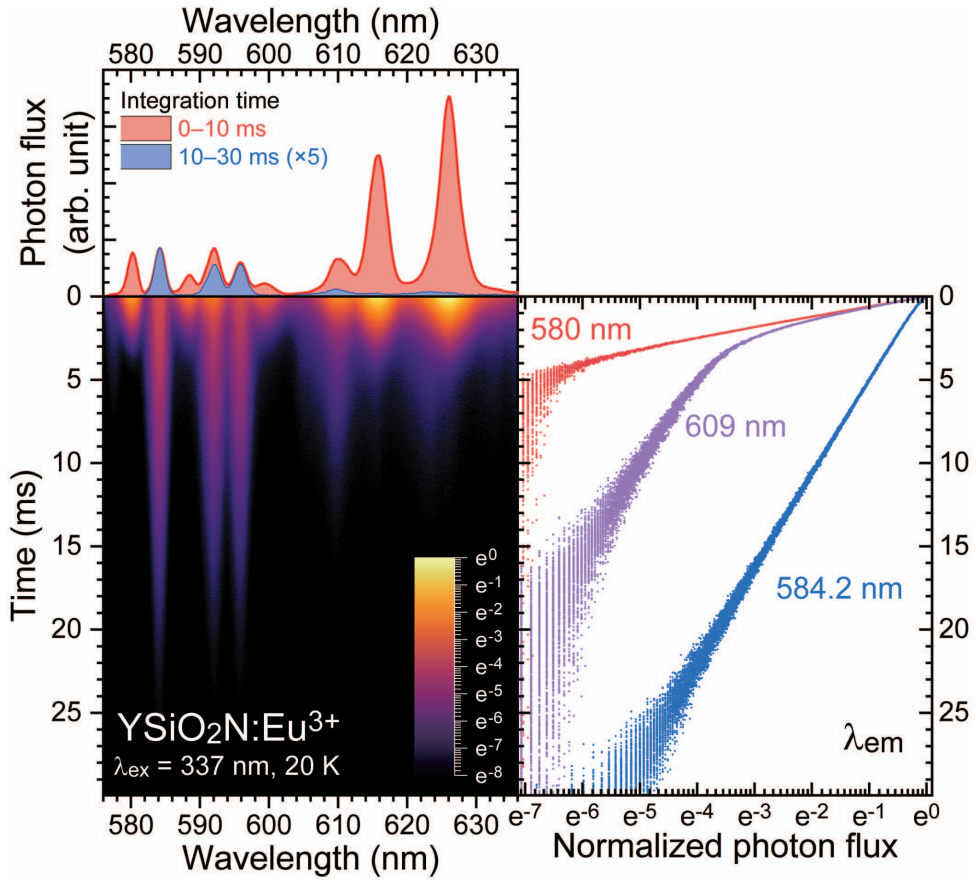

Figure 4.14. Contour plot for time-resolved PL spectra of the $YSiO_2N:Eu^{3+}$ sample at 20 K in the region of 575–635 nm. (Right panel) Luminescence decay curves monitored by 580, 584.2, and 609 nm. (Top panel) Integrated PL spectra with different integration time ranges: (red) 0–10 ms, (blue) 10–30 ms.

(Figure 4.8a). In the time range of 10–30 ms, in which the $Eu^{3+}(C_n)$ luminescence is completely quenched, it is possible to extract the $Eu^{3+}(C_i)$ luminescence with a high signal-to-noise ratio. This spectrum shows a weak Eu^{3+} luminescence in the range of 600–630 nm assigned to the $^5D_0 \rightarrow {}^7F_2$ ED transition.

The right panel shows the luminescence decay curves with different monitored wavelengths, 580, 584.2, and 609 nm. As seen in the contour plot, the luminescence bands peaking at 580 and 584.2 nm are assigned to the pure $Eu^{3+}(C_n)$ and $Eu^{3+}(C_i)$ luminescence, respectively. We estimated the luminescence lifetimes of the $^5D_0$ excited states for the $Eu^{3+}(C_n)$ and $Eu^{3+}(C_i)$ ions with a single-exponential function to be 0.610 and 5.51 ms. The estimated luminescence lifetimes show a good agreement with the radiative lifetimes obtained by the Judd-Ofelt analysis, which supports that the assignment of PL spectra is valid. Under the 609 nm detection, the luminescence for Eu^{3+} ions at both C_n and C_i sites is observed. The decay curve is characterized by the $Eu^{3+}(C_n)$ ions in the short range below a few milliseconds because the slope is similar to the curve monitored at 580 nm. Over 5.0 ms, the slope is parallel to that for the $Eu^{3+}(C_i)$ ions. Thus, the decay profile is interpreted as the convolution of two characteristic single-exponential for the $Eu^{3+}(C_n)$ and $Eu^{3+}(C_i)$.

By detecting the distinguished Eu^{3+} $^5D_0 \rightarrow {}^7F_1$ luminescence bands located at 588.4 nm for $Eu^{3+}(C_n)$ and 583.9 nm for $Eu^{3+}(C_i)$, the site-selective PLE spectra of the $YSiO_2N:Eu^{3+}$ sample were obtained at 4 K, as shown in **Figure 4.15**. In both spectra, weak sharp lines assigned to the 4f-4f forbidden transition, a weak band below 28000 cm^{-1} related to intrinsic defects of the host oxynitride, and strong CT excitation bands over 28000 cm^{-1} are observed.

The CT bands for both $Eu^{3+}(C_n)$ and $Eu^{3+}(C_i)$ have two distinct peaks in the near-UV region, deconvoluted with two Gaussian functions in the energetic scale. The Gaussian-shaped fitted lines are shown with overshadowed broken lines, labeled with $CT_I(C_n)$, $CT_{II}(C_n)$, $CT_I(C_i)$, and $CT_{II}(C_i)$. The peak position and full width at half maximum (FWHM) of each Gaussian profile are listed in **Table 4.12**. The energy differences between two Gaussian peaks of CT_I and CT_{II} ($\Delta E(CT_I\text{-}CT_{II})$) for $Eu^{3+}(C_i)$ and $Eu^{3+}(C_n)$ are 4834 cm^{-1} (= 0.599 eV) and 4508 cm^{-1} (= 0.559 eV), respectively. The CT-band energy depends on the electronegativity of coordinating anions

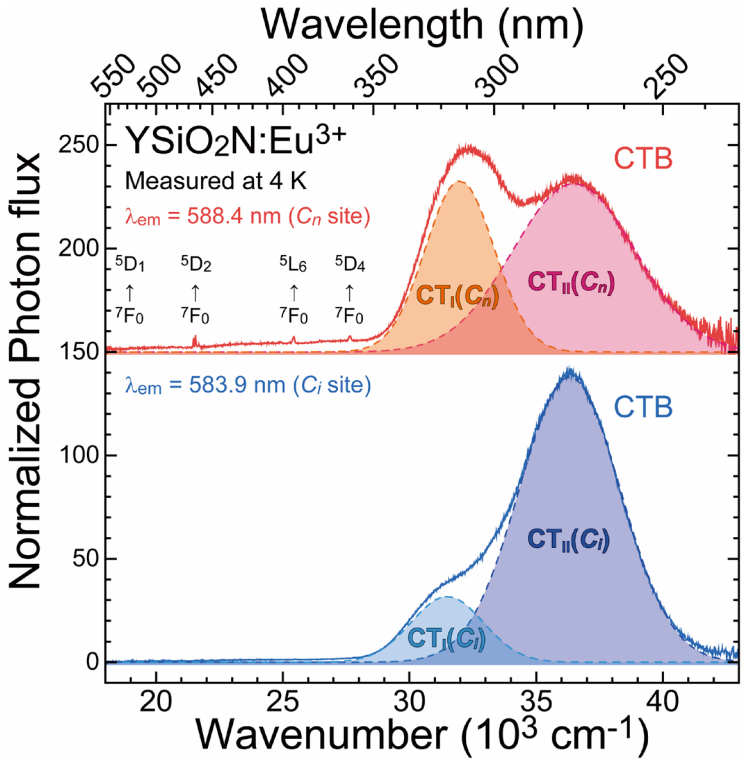

Figure 4.15. Normalized site-selective PLE spectra of the $YSiO_2N:Eu^{3+}$ sample at 4 K monitored at 583.9 nm for $Eu^{3+}(C_i)$ and 588.4 nm for $Eu^{3+}(C_n)$. The PLE intensities are normalized by the $^5D_1 \leftarrow {}^7F_0$ MD transition. The overshadowed broken lines show the fitted curves for the CT excitation bands with Gaussian functions.

because the CT transition is considered to be the transition from the VB top to the Eu^{2+} 4f ground state in a band structure [49]. Therefore, the well-separated CT_I and CT_{II} bands are attributed to electron transfer from different anions, $N^{3-}(CT_I)$ and $O^{2-}(CT_{II})$ ions. As shown in the PDOS curves (Figure 4.6b), the N 2p orbitals with higher energy than the O 2p orbitals cause the smaller CT-band energy. Note that the energy difference of N and O 2p orbitals in PDOS (= ~2.0 eV) does not correspond to that between CT_I and CT_{II} (0.599 eV for $Eu^{3+}(C_i)$ and 0.559 eV for $Eu^{3+}(C_n)$) because the energy for anion p orbitals is over/under-estimated due to the self-interaction of electrons within the DFT framework. Besides, since the CT transition is a local phenomenon associated with the coordination environment around Eu^{3+} ions, it is difficult to characterize the absolute CT energy with the band structure. Nevertheless, as the chemical trend is reliable, the PDOS results support the assignment of the CT excitation bands related to the different anion species. This result suggests that the CT band energy depends hardly on the site symmetry around Eu^{3+} in the monoclinic $YSiO_2N$ host but severely on the ligand species.

Table 4.12. Peak positions and FWHMs for the deconvoluted CT excitation bands with two Gaussian functions

	CT_I		CT_{II}		
site symmetry	peak position (cm^{-1})	FWHM (cm^{-1})	peak position (cm^{-1})	FWHM (cm^{-1})	$\Delta E(CT_I\text{-}CT_{II})$
C_n	31984	2719	36492	4800	4834
C_i	31488	2853	36322	3991	4508

4.3.4. Thermal Quenching Behavior Correlated with Temperature-Variation of Local Environment

We characterize the thermal quenching behavior of the $YSiO_2N:Eu^{3+}$ through luminescence decay measurements, detecting the different luminescence bands peaking at 583.4 and 625.4 nm. **Figure 4.16a** shows the luminescence decay curves at various temperatures (T = 100–700 K) monitored with the $^5D_0 \rightarrow {}^7F_2$ luminescence peaking at 625.4 nm. According to the time-resolved PL spectra (Figure 4.11), $Eu^{3+}(C_n)$ ions dominate in the $^5D_0 \rightarrow {}^7F_2$ luminescence, indicating that these decay curves have the characteristics mainly of the $^5D_0$ states for the $Eu^{3+}(C_n)$ ions. In addition to the decay profile for the $Eu^{3+}(C_n)$ ions, the luminescence component with a long

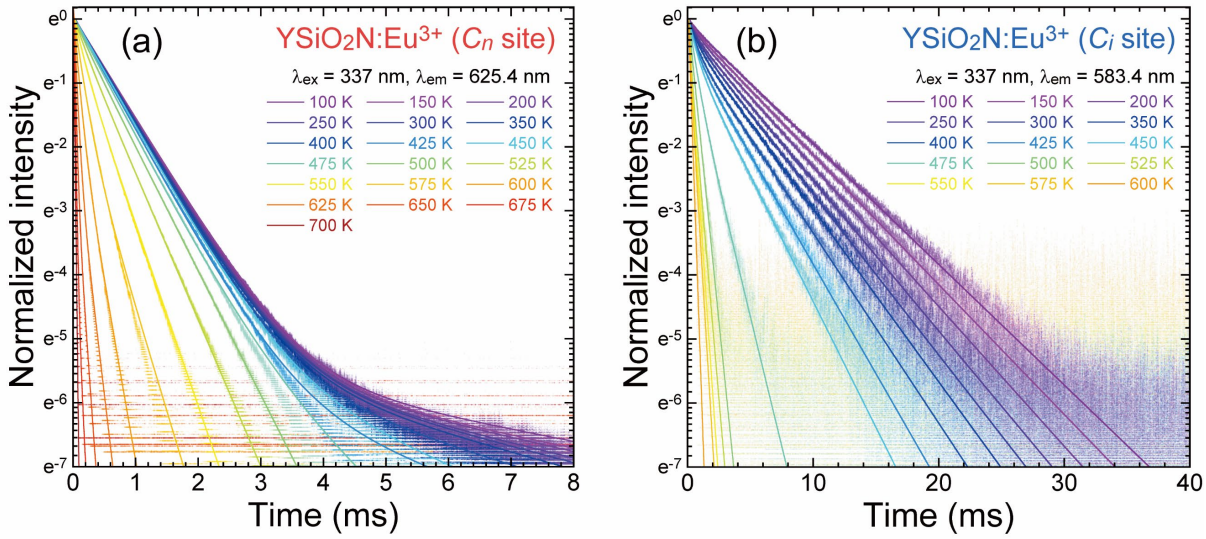

Figure 4.16. Luminescence decay curves of Eu^{3+}: $^5D_0$ luminescence at various temperatures (T = 100–700 K) excited by the CT transition (λ_{ex} = 337 nm) in (a) C_n and (b) C_i sites of monoclinic $YSiO_2N$. The solid lines represent the fitting curves with a second-ordered exponential function (eq. 4.3).

lifetime for the $Eu^{3+}(C_i)$ ions is observed, particularly at low temperatures. **Figure 4.16b** shows the decay curves up to 600 K monitored with the $^5D_0 \rightarrow {}^7F_1$ luminescence peaking at 583.4 nm, which is precisely attributed to the $Eu^{3+}(C_i)$ luminescence. Although these decay curves seem to have a single-exponential profile as well, they largely deviate from the single-exponential in the range of a few milliseconds. This is because the $Eu^{3+}(C_n)$ luminescence with a short lifetime is detectable even at 583.4 nm due to the thermal broadening of PL bands.

For both luminescence decay curves monitored at 583.4 and 625.4 nm, we should take the contribution of both $Eu^{3+}(C_i)$ and $Eu^{3+}(C_n)$ ions into account. The luminescence decay curves at each temperature were fitted with a second-ordered exponential function described below,

$$I(t) = A_{C_n} \exp\left(-t/\tau_{C_n}\right) + A_{C_i} \exp\left(-t/\tau_{C_i}\right), \tag{4.3}$$

where A_{Cn} and A_{Ci} are amplitudes, and τ_{Cn} and τ_{Ci} are luminescence lifetimes for $Eu^{3+}(C_n)$ and $Eu^{3+}(C_i)$ ions, respectively. Two decay curves at the same temperature were fitted simultaneously with the common lifetimes τ_{Cn} and τ_{Ci}. The fitted lines are shown in Figures 4.16a and 4.16b with solid lines. The RMS errors for the fitting are relatively small. The temperature dependence of output amplitudes is provided in **Figure 4.17**, indicating that the fitting results are reliable because it shows a similar trend to the lifetimes.

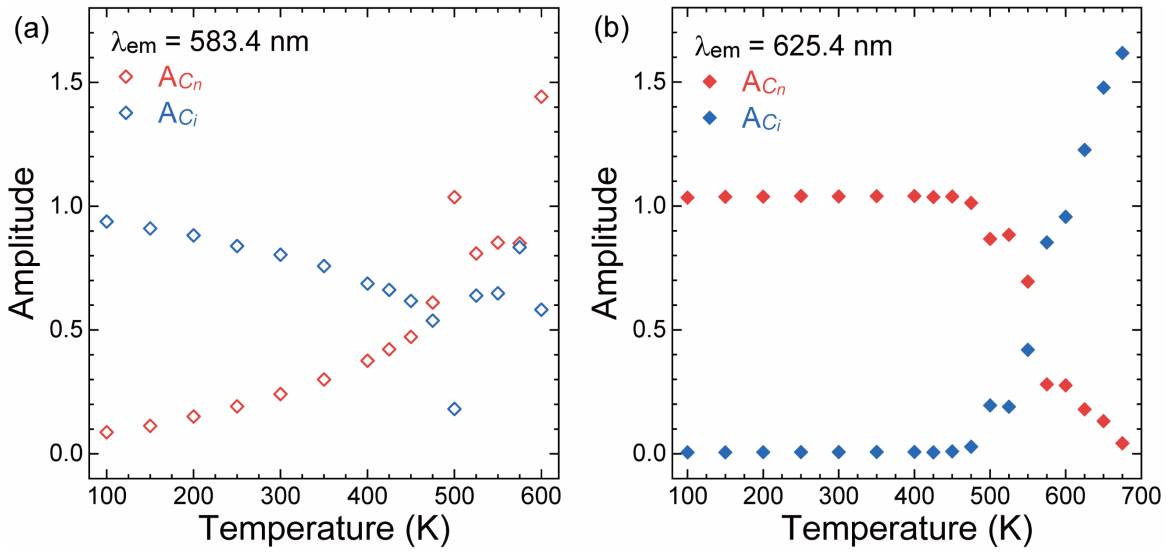

Figure 4.17. Temperature dependence of the amplitudes obtained by the fitting of luminescence decay curves with eq. 4.3.

The estimated luminescence lifetimes of the $^5D_0$ states for $Eu^{3+}(C_n)$ and $Eu^{3+}(C_i)$ ions are plotted against temperature in **Figure 4.18**. The $Eu^{3+}(C_n)$ ions show the typical quenching behavior described by the single potential barrier model.

$$\tau = \frac{1}{\Gamma_\nu + \Gamma_0 \exp\left(-E_a/kT\right)}, \tag{4.4}$$

where Γ_ν is the radiative transition rate, Γ_0 is the attempt rate of the non-radiative process, E_a is the activation energy of thermal quenching, k is the Boltzmann constant (= 8.617 ×10^{-5} eV K^{-1}) and T is temperature. The lifetime of $Eu^{3+}(C_n)$ luminescence does not change drastically up to ~460 K, which is approximately 0.60 ms.

On the other hand, the lifetime of $Eu^{3+}(C_i)$: $^5D_0$ luminescence monotonously decreases with temperature even at low temperatures below 400 K, indicating that other temperature-driven quenching processes can exist. The MPR from the $^5D_0$ to the $^7F_6$ levels is one possible

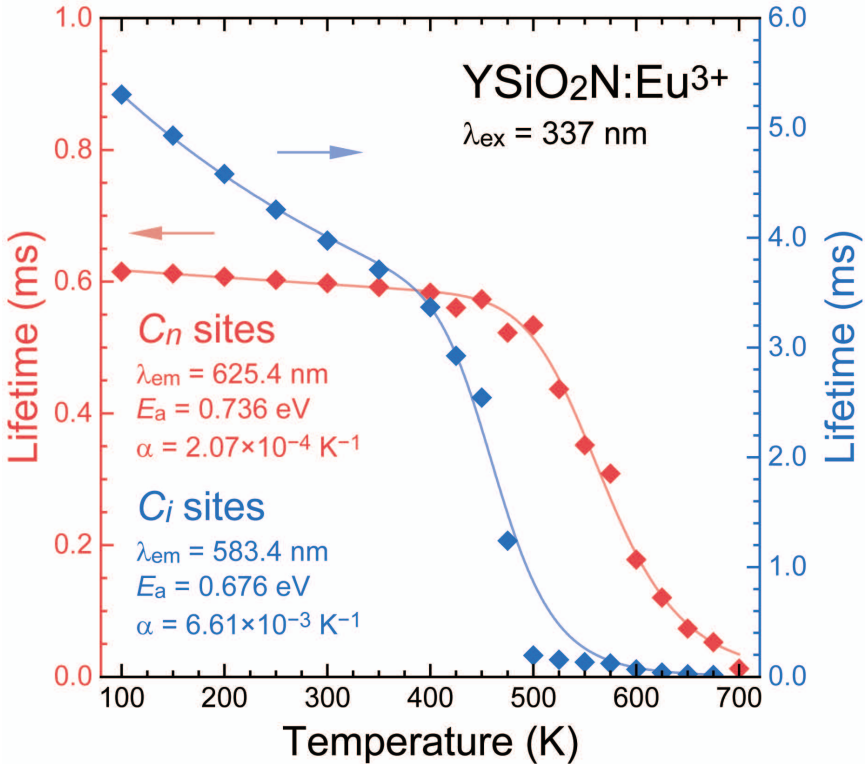

Figure 4.18. Temperature profile of luminescence lifetimes. The left and right axes show the lifetimes for $Eu^{3+}(C_n)$ ions (τ = 0–1.0 ms) and $Eu^{3+}(C_i)$ ions (τ = 0–6.0 ms). The plots are fitted by the modified single barrier quenching curves described by eqs. 4.6 and 4.7.

relaxation pathway. However, as shown in Figure 4.8b, the energy difference between the $^5D_0$ and $^7F_6$ levels is approximately 12000 cm^{-1}, which is too large to make the $^5D_0$ state relax down with a high MPR rate. This is because more than ten phonons are necessary with the maximum phonon energy for $YSiO_2N$, $\hbar\omega_{max}$ = 918 cm^{-1}. Therefore, the MPR process to the $^7F_6$ level cannot be a quenching route for the $^5D_0$ state. Although another possible relaxation pathway is the cross-relaxation between neighboring Eu^{3+} ions, the Eu^{3+} ions in the $YSiO_2N$ matrix are well isolated because of the sufficiently low Eu^{3+} concentration (0.1%), leading to a very small probability of interaction between adjacent Eu^{3+} ions.

In the framework of the single barrier quenching model, we assume that the radiative transition rate Γ_v is independent of temperature. According to the Judd-Ofelt theory, the spontaneous emission rate for the 4f-4f transition A_R is described by eqs. 4.1 and 4.2, where there is no temperature-dependent term. However, the Judd-Ofelt intensity parameters can be variable with temperature. If some character of local environments around Eu^{3+} ions varies with temperature, only the Judd-Ofelt intensity parameter Ω_t can be influenced, resulting in the temperature-variation of the radiative transition rate Γ_v.

The temperature dependence of the PL spectrum recorded with 523.5 nm excitation (T = 4–300 K) is provided in the Supporting Information (**Figure 4.19**) to confirm that the Ω_2 parameter changes with temperature for the C_i sites in monoclinic $YSiO_2N$. The relative PL intensity of the $^5D_0 \rightarrow {}^7F_2$ ED transition to the $^5D_0 \rightarrow {}^7F_1$ MD transition seems to be enhanced at high temperatures. However, the spectral shape at 300 K is similar to the PL spectrum shown in Figure 4.8a due to the $Eu^{3+}(C_n)$ luminescence induced by the thermal broadening of the $^5D_1 \leftarrow {}^7F_0$ excitation band peaking at 527 nm. Therefore, it is difficult to discuss the temperature dependence of the Ω_2 parameter from the PL spectra.

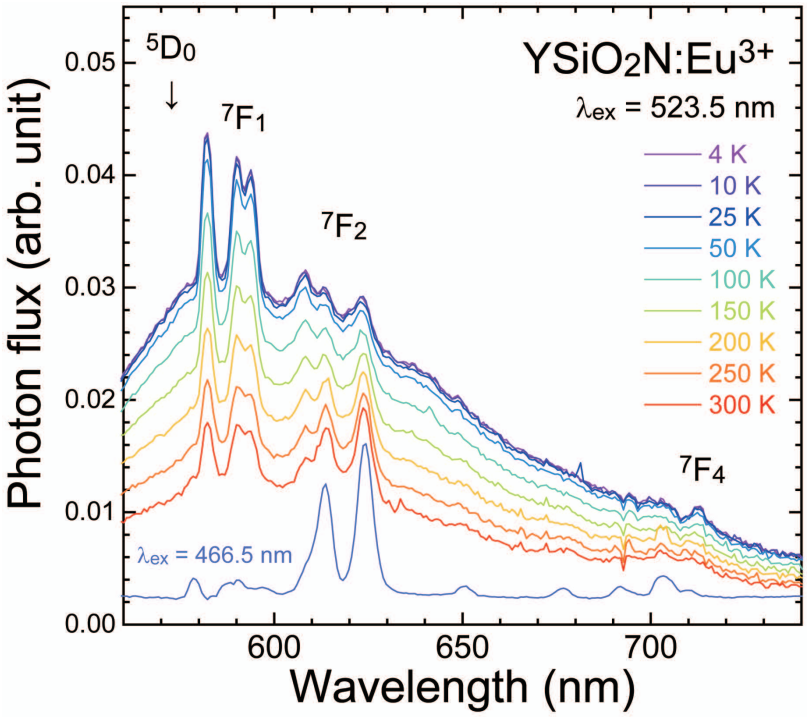

Figure 4.19. PL spectra of the $YSiO_2N:Eu^{3+}$ sample at various temperatures (T = 4–300 K) excited with the $^5D_1 \leftarrow {}^7F_0$ MD transition for $Eu^{3+}(C_i)$ ions (λ_{ex} = 523.5 nm).

In the PLE spectra for $Eu^{3+}(C_i)$ luminescence peaking at 583.9 nm, the site selectivity is still valid at high temperatures because no PL peak related to $Eu^{3+}(C_n)$ ions overlaps in the range of 582–584 nm. For the $^5D_2 \leftarrow {}^7F_0$ ED transition, S_{ED} depends only on the Ω_2 parameter because this ED transition has only one non-zero value of $|\langle||U^2||\rangle|^2 = 0.0009$ [35]. Thus, the temperature variation of the relative PLE intensity of the $^5D_2 \leftarrow {}^7F_0$ ED transition to the $^5D_1 \leftarrow {}^7F_0$ MD transition is a good indicator to discuss the temperature dependence of the Ω_2 parameter with site-selective spectroscopy. The PLE spectra measured at different temperatures (T = 4–450 K) in the region of 455–530 nm are shown in **Figure 4.20a**. The excitation peak assigned to the $^5D_1 \leftarrow {}^7F_0$ MD transition is consistent, and no other excitation peak appears over 526 nm, indicating that the site-selective detection of $Eu^{3+}(C_i)$: $^5D_0 \rightarrow {}^7F_1$ luminescence is successful below 450 K. At low temperatures (< ~300 K), weak excitation bands originating from intrinsic defects are observed as a background of the $^5D_2 \leftarrow {}^7F_0$ peak. The PLE intensity of the $^5D_2 \leftarrow {}^7F_0$ ED transition peaking at 463–464 nm increased with temperature. The integrated areas of the $^5D_2$ peak are plotted against temperature in **Figure 4.20b**, which is enhanced by approximately 5.6 times compared to that at 4K.

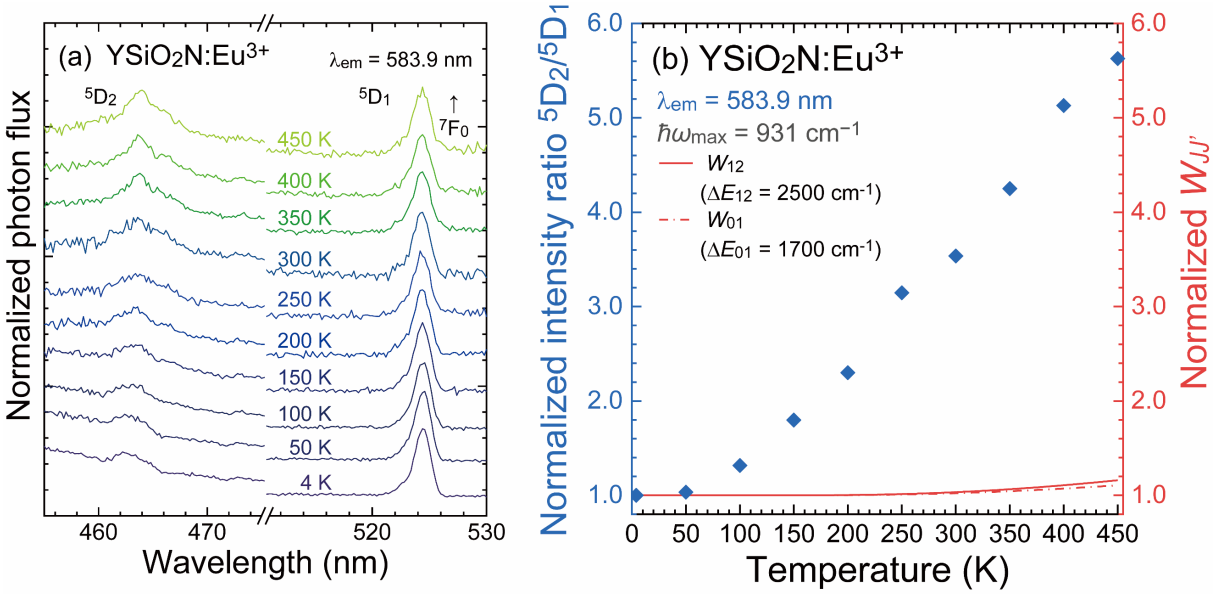

Figure 4.20. (a) PLE spectra of $Eu^{3+}(C_i)$ ions at various temperatures (T = 4–450 K). The PLE intensities are normalized by the integrated area of the $^5D_1 \leftarrow {}^7F_0$ MD transition peaking at 524.5 nm. (b) Temperature variation of relative PLE intensities of the $^5D_2 \leftarrow {}^7F_0$ ED transition to the $^5D_1 \leftarrow {}^7F_0$ MD transition. The red solid and broken lines show the calculated temperature-dependent non-radiative MPR rate $W_{JJ'}$ described by the Reisfeld-model (eq. 5). The intensity ratio of $^5D_2/^5D_1 \leftarrow {}^7F_0$ and $W_{JJ'}$ are normalized by each value at 4 K.

There may be another possibility that MPR from the $^5D_2$ to $^5D_1$ levels or from the $^5D_1$ to $^5D_0$ levels facilitated by temperature enhances the Eu^{3+}: $^5D_0$ luminescence because the temperature profile in Figure 4.20b shows a similar trend to the temperature-dependent MPR rate for lanthanoid ions [50]. However, the enhancement by MPR can be kicked out by the following discussion. The non-radiative MPR rate between the neighboring J-sublevels ($W_{JJ'}$, $J' \rightarrow J$) is described by the following Reisfeld-model [35,50–53];

$$W_{JJ'} = B\exp(-\beta\Delta E_{JJ'})\left[1-\exp\left(-\frac{\hbar\omega_{\max}}{kT}\right)\right]^{-\Delta E_{JJ'}/\hbar\omega_{\max}}, \qquad (4.5)$$

where the relative non-radiative term like B and β are constants for each compound, $\Delta E_{JJ'}$ is the energy gap to the next lower level, $\hbar\omega_{\max}$ is the maximum phonon energy for the host compounds (918 cm^{-1} for monoclinic $YSiO_2N$), k is the Boltzmann constant, and T is temperature. The ΔE_{12} ($^5D_2$-$^5D_1$) and ΔE_{01} ($^5D_1$-$^5D_0$) are approximately 2500 and 1700 cm^{-1}, respectively [35]. Employing B (1.204×10^8 s^{-1}) and β (3.53×10^{-3} cm) of the Y_2O_3 host [35,50], the temperature-dependent MPR rate is calculated and shown in Figure 4.20b with the solid and broken red lines. The increases of the non-radiative rate $W_{JJ'}$ are only about 1.16 (W_{12}) and 1.11

(W_{01}) times, even at 450 K. This is because the MPR rates are significant even at low temperatures (W_{12} = 1.77 × 10^4 s^{-1} and W_{01} = 2.98 × 10^5 s^{-1} at 4 K) enough to cause the depopulation of the $^5D_2$ and $^5D_1$ sublevels due to the large phonon energy. This discussion is consistent with no luminescence peaks assigned to the $^5D_1$ and $^5D_2$ luminescence in the PL spectrum (Figure 4.8a). Therefore, the Ω_2 parameter for the C_i sites in monoclinic $YSiO_2N$ depends on the temperature due to the thermally induced site distortion with anion displacement. The time-resolved PL spectra at room temperature also support the enhancement of the Ω_2 parameter leading to the large spontaneous emission rate of the $^5D_0 \rightarrow {}^7F_2$ transition, as provided in **Figure 4.21**.

According to the curves shown in Figure 4.20b, the intensity ratio $^5D_2/^5D_1$, depending only on the Ω_2 parameter, linearly increases over 100 K. Thus, we assume that the spontaneous emission rate of the ED transition in the Γ_v value is proportional to the temperature variation in the temperature range of 100–700 K. The modified single barrier quenching model is described below;

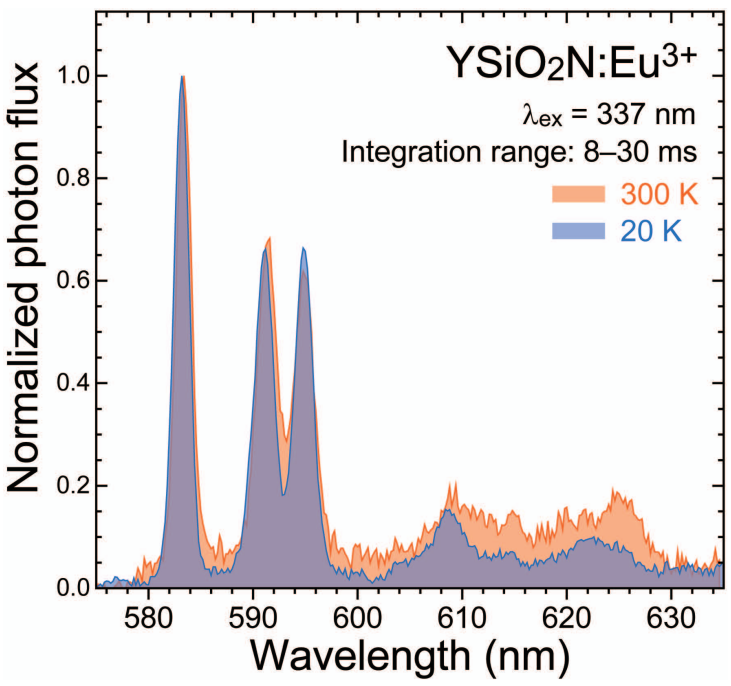

Figure 4.21. Integrated time-resolved spectra for the $YSiO_2N$ sample at different temperatures (T = 20 and 300 K) with the time range of 8–30 ms, at which the Eu^{3+}(C_n) luminescence with the ~0.6 ms lifetime is quenched.

$$\tau = \frac{1}{\Gamma_\nu[T] + \Gamma_0 \exp\left(-E_a/kT\right)}, \tag{4.6}$$

$$\Gamma_\nu[T] = (1 + \alpha T)A_{\mathrm{R,ED}} + A_{\mathrm{R,MD}} + A_{\mathrm{R,forbidden}}, \tag{4.7}$$

where we introduce α, correlated with a sensitivity of radiative rates for ED transition to thermal distortion of a local structure. The α parameter should be specific to a local structure. The temperature-dependent radiative rate $\Gamma_\nu[T]$ is described by the summation of the spontaneous emission rates A_R for the ED ($^5D_0 \rightarrow {}^7F_{2,4,6}$), MD ($^5D_0 \rightarrow {}^7F_1$), and forbidden ($^5D_0 \rightarrow {}^7F_{0,3,5}$) transitions. The A_R parameters obtained by the Judd-Ofelt analysis are used as the initial parameters for the fitting. The temperature profile of the luminescence lifetimes for the $Eu^{3+}(C_n)$ and $Eu^{3+}(C_i)$ ions are fitted with this modified model. For the $Eu^{3+}(C_i)$ curve, the plots largely deviate from the fitting line over 500 K because the $Eu^{3+}(C_i)$ luminescence is hardly detectable due to the severe quenching and overlapping with the profile for the strong $Eu^{3+}(C_n)$ luminescence. The obtained parameters are listed in **Table 4.13**. The A_R values for both $Eu^{3+}(C_n)$ and $Eu^{3+}(C_i)$ ions take similar values to the radiative rates estimated by the Judd-Ofelt analysis. The small deviation is caused by the error in the refractive index (n = 1.94 [17]) for the Judd-Ofelt analysis or the temperature difference between 0 and 4 K. The attempt rates Γ_0, which correlate with the maximum phonon energy of a host compound [49], take similar values for both C_n and C_i sites. The α value is very large only for the $Eu^{3+}(C_i)$ because the slight distortion from the centrosymmetry is critical to induce the ED transition for the 4f-4f parity forbidden transition. Therefore, the anomalous temperature profile for the $Eu^{3+}(C_i)$ luminescence lifetime is due to enhancing the radiative ED transition with temperatures. The luminescence decay analysis outputs the activation energy for the thermal quenching of Eu^{3+} ions. The energy difference between the E_a values for the $Eu^{3+}(C_n)$ and $Eu^{3+}(C_i)$ is 0.060 eV, corresponding to the energy difference between the lower CT_I bands relating to the electron transfer from N^{3-} to Eu^{3+} ions, 0.061 eV. This result indicates that the principal thermal quenching route for the Eu^{3+}: $^5D_0$ states in monoclinic $YSiO_2N$ takes place *via* the N^{3-}-Eu^{3+} CT states.

Table 4.13. Fitting results with the modified single barrier quenching model

	$A_{R,ED}$[a] ($10^2\ s^{-1}$)	$A_{R,MD}$[a] ($10^2\ s^{-1}$)	$A_{R,forbidden}$[a] ($10^2\ s^{-1}$)	$\Gamma_v[0]$ ($10^2\ s^{-1}$)	Γ_0 ($10^9\ s^{-1}$)	E_a (eV)	α ($10^{-3}\ K^{-1}$)
C_n sites	13.8 (12.6)	1.06 (1.06)	1.04 (1.04)	15.9	5.48	0.736	0.207
C_i sites	0.463 (0.612)	0.106 (0.107)	0.0541 (0.0517)	1.58	5.52	0.676	6.61

[a]The A_R values in parentheses are the initial value for the fitting, estimated by the Judd-Ofelt analysis with the PL spectra at 4 K.

4.4. Conclusions

In this study, we investigated the Eu^{3+} luminescence properties thoroughly in oxynitride coordination environments for $YSiO_2N$ in terms of the site-selective and time-resolved spectroscopy with the precise crystallographical data. The single-crystal X-ray diffraction and the time-of-flight neutron diffraction successfully identified the crystal structure of $YSiO_2N$ as the monoclinic lattice with the space group $C2/c$. In this lattice, all Eu^{3+} ions are incorporated in the $[YO_6N_2]$ dodecahedra, classified into two groups with centrosymmetry; C_n and C_i sites. Eu^{3+} ions at the C_n and C_i sites showed a completely different radiative rate for the electric dipole transition, resulting in the 27 times enhanced $^5D_0 \rightarrow {}^7F_2$ luminescence and the 8.4 times shorter luminescence lifetime by lacking an inversion center. The temperature dependence of the luminescence lifetime for the Eu^{3+} ions in C_i sites revealed that the thermally induced deviation from centrosymmetry increases the radiative rate with the Judd-Ofelt intensity parameter Ω_t increasing. Despite the significant difference in the radiative rate, the ligands-Eu^{3+} charge transfer states were affected scarcely by site symmetry but severely by anion species. The *ab initio* calculation results and the photoluminescence excitation spectra suggested that the thermal quenching of the Eu^{3+}: $^5D_0$ luminescence occurs *via* the charge transfer states between N^{3-} and Eu^{3+} ions. The results indicate that not only the mixed-anion coordination but also the local structure that induces some distortion is necessary for the improvement of Eu^{3+} luminescence. The $YSiO_2N$:Eu^{3+} provides a new possibility for developing the near-UV excitable narrow-band red phosphors with partial N^{3-} coordination.

Acknowledgements

Work by Y.K. was financially supported by the Grant-In-Aid for JSPS Fellows (JP19J23280). This work was supported by JSPS Grant-in-Aid for Scientific Research on Innovative Areas "Mixed-Anion" (JP16H06438, JP16H06439, JP16H06440, and JP16H06441). The neutron experiments at the Materials and Life Science Experimental Facility of J-PARC were performed under the user program (Proposal No. 2017A0023 and 2017A0064). The computations in this work have been performed using the facilities of the Research Center for Advanced Computing Infrastructure at JAIST. This work was supported by NIMS Joint Research Hub Program.

References

[1] T. Minamikawa, T. Koma, A. Suzuki, T. Mizuno, K. Nagamatsu, H. Arimochi, K. Tsuchiya, K. Matsuoka, T. Yasui, K. Yasutomo, M. Nomaguchi, "Quantitative evaluation of SARS-CoV-2 inactivation using a deep ultraviolet light-emitting diode". *Sci. Rep.* **11** (2021) 5070 (9p).

[2] K. Bando, K. Sakano, Y. Noguchi, Y. Shimizu, "Development of High-bright and Pure-white LED Lamps". *J. Light Visual Environ.* **22** (1998) 2–5.

[3] K. Uheda, N. Hirosaki, Y. Yamamoto, A. Naito, T. Nakajima, H. Yamamoto, "Luminescence Properties of a Red Phosphor, $CaAlSiN_3:Eu^{2+}$, for White Light-Emitting Diodes". *Electrochem. Solid State Lett.* **9** (2006) H22–H25.

[4] H. Watanabe, H. Wada, K. Seki, M. Itou, N. Kijima, "Synthetic Method and Luminescence Properties of $Sr_xCa_{1-x}AlSiN_3:Eu^{2+}$ Mixed Nitride Phosphors". *J. Electrochem. Soc.* **155** (2008) F31–F36.

[5] R.-J. Xie, N. Hirosaki, T. Suehiro, F.-F. Xu, M. Mitomo, "A Simple, Efficient Synthetic Route to $Sr_2Si_5N_8:Eu^{2+}$-Based Red Phosphors for White Light-Emitting Diodes". *Chem. Mater.* **18** (2006) 5578–5583.

[6] A.A. Setlur, V.R. Emil, S.H. Claire, J.-H. Her, M.S. Alok, N. Karkada, M. Satya Kishore, N. Prasanth Kumar, D. Aesram, A. Deshpande, B. Kolodin, S.G. Ljudmil, U. Happek, "Energy-efficient, high-color-rendering LED lamps using oxyfluoride and fluoride phosphors". *Chem. Mater.* **22** (2010) 4076–4082.

[7] P. Pust, V. Weiler, C. Hecht, A. Tücks, A.S. Wochnik, A.K. Henß, D. Wiechert, C. Scheu, P.J. Schmidt, W. Schnick, "Narrow-band red-emitting $Sr[LiAl_3N_4]:Eu^{2+}$ as a next-generation LED-

phosphor material". *Nat. Mater.* **13** (2014) 891–896.

[8] S. Schmiechen, H. Schneider, P. Wagatha, C. Hecht, P.J. Schmidt, W. Schnick, "Toward new phosphors for application in illumination-grade white pc-LEDs: The nitridomagnesosilicates $Ca[Mg_3SiN_4]:Ce^{3+}$, $Sr[Mg_3SiN_4]:Eu^{2+}$, and $Eu[Mg_3SiN_4]$". *Chem. Mater.* **26** (2014) 2712–2719.

[9] M.H. Fang, J.L. Leano, R.S. Liu, "Control of Narrow-Band Emission in Phosphor Materials for Application in Light-Emitting Diodes". *ACS Energy Letters*. **3** (2018) 2573–2586.

[10] P. Dorenbos, "The Eu^{3+} charge transfer energy and the relation with the band gap of compounds". *J. Lumin.* **111** (2005) 89–104.

[11] N. Li, S. Zhang, "Dependence of charge transfer energy on crystal structure and composition in Eu^{3+}-doped compounds". *J. Phys. Chem. B.* **110** (2006) 21438–21443.

[12] Y. Kitagawa, J. Ueda, M.G. Brik, S. Tanabe, "Intense hypersensitive luminescence of Eu^{3+}-doped $YSiO_2N$ oxynitride with near-UV excitation". *Opt. Mater*. **83** (2018) 111–117.

[13] F.F. Lange, S.C. Singhal, R.C. Kuznicki, "Phase relations and stability studies in the Si_3N_4-SiO_2-Y_2O_3 pseudoternary system". *J. Am. Ceram. Soc.* **60** (1977) 249–252.

[14] P.E.D. Morgan, P.J. Carroll, F.F. Lange, "Crystal structure of $YSiO_2N$ and a reappraisal of the vaterite type, YBO_3". *Mater. Res. Bull.* **12** (1977) 251–259.

[15] A. Belkly, M. Helderman, V.L. Karen, P. Ulkch, "New developments in the Inorganic Crystal Structure Database (ICSD): Accessibility in support of materials research and design". *Acta Crystallogr. B.* **58** (2002) 364–369.

[16] K.C. Mishra, B.G. Deboer, P.C. Schmidt, I. Osterloh, M. Stephan, V. Eyert, K.H. Johnson, "Electronic structures and nature of host excitation in borates". *Ber. Bunsenges. Phys. Chem.* **102** (1998) 1772–1782.

[17] L. Ouyang, H. Yao, S. Richey, Y.-N. Xu, W.Y. Ching, "Crystal structure and properties of $YSiO_2N$". *Phys. Rev. B* **69** (2004) 094112 (6p).

[18] C. Kim, G. Pilania, R. Ramprasad, "Machine Learning Assisted Predictions of Intrinsic Dielectric Breakdown Strength of ABX_3 Perovskites". *J. Phys. Chem. C.* **120** (2016) 14575–14580.

[19] F. Lu, L. Bai, Z. Yang, Q. Liu, "Photoluminescence properties of Ce^{3+} doped $YSiO_2N$ blue-emitting phosphors". *J. Rare Earths.* **30** (2012) 851–855.

[20] V. Viallet, J.-F. Marucco, J. Saint, M. Herbst-Ghysel, N. Dragoe, "Structural, magnetic and electrical properties of a perovskite containing divalent europium $EuZrO_3$". *J. Alloys Compd*. **461** (2008) 346–350.

[21] G.M. Sheldrick, "SADABS, v. 2: Multi-Scan Absorption Correction". (Bruker-AXS, Kennewick, WA, 2012)

[22] G.M. Sheldrick, "A short history of SHELX". *Acta Crystallogr. A*. **64** (2008) 112–122.

[23] R. Oishi-Tomiyasu, M. Yonemura, T. Morishima, "Application of matrix decomposition algorithms for singular matrices to the Pawley method in Z-Rietveld". *J. Appl. Crystallogr.* **45** (2012) 299–308.

[24] F. Izumi, K. Momma, "Three-dimensional visualization in powder diffraction". *Solid State Phenom.* **130** (2007) 15–20.

[25] S.J. Clark, M.D. Segall, C.J. Pickard, P.J. Hasnip, M.I.J. Probert, K. Refson, M.C. Payne, "First principles methods using CASTEP". *Z. Kristallogr. Cryst. Mater.* **220** (2005) 567–570.

[26] J.P. Perdew, A. Ruzsinszky, G.I. Csonka, O.A. Vydrov, G.E. Scuseria, L.A. Constantin, X. Zhou, K. Burke, "Restoring the density-gradient expansion for exchange in solids and surfaces". *Phys. Rev. Lett.* **100** (2008) 136406 (4p).

[27] D. Vanderbilt, "Soft self-consistent pseudopotentials in a generalized eigenvalue formalism". *Phys. Rev. B*. **41** (1990) 7892–7895.

[28] D.D. Koelling, B.N. Harmon, "A technique for relativistic spin-polarised calculations". *J. Phys. C: Solid State Phys*. **10** (1977) 3107–3114.

[29] A. Hosono, Y. Masubuchi, S. Yasui, M. Takesada, T. Endo, M. Higuchi, M. Itoh, S. Kikkawa, "Ferroelectric $BaTaO_2N$ Crystals Grown in a $BaCN_2$ Flux". *Inorg. Chem.* **58** (2019) 16752–16760.

[30] H. Yang, C.T. Prewitt, "On the crystal structure of pseudowollastonite ($CaSiO_3$)". *Am. Mineral.* **84** (1999) 929–932.

[31] K. Momma, F. Izumi, "VESTA 3 for three-dimensional visualization of crystal, volumetric and morphology data". *J. Appl. Crystallogr*. **44** (2011) 1272–1276.

[32] H. Kageyama, K. Hayashi, K. Maeda, J.P. Attfield, Z. Hiroi, J.M. Rondinelli, K.R. Poeppelmeier, "Expanding frontiers in materials chemistry and physics with multiple anions". *Nat. Commun.* **9** (2018) 772 (15p).

[33] K. Hibino, M. Yashima, T. Oshima, K. Fujii, K. Maeda, "Structures, electron density and characterization of novel photocatalysts, $(BaTaO_2N)_{1-x}(SrWO_2N)_x$ solid solutions". *Dalton Trans.* **46** (2017) 14947–14956.

[34] C. Tassel, Y. Kuno, Y. Goto, T. Yamamoto, C.M. Brown, J. Hester, K. Fujita, M. Higashi, R. Abe, K. Tanaka, Y. Kobayashi, H. Kageyama, "$MnTaO_2N$: polar $LiNbO_3$-type oxynitride with a helical spin order". *Angew. Chem. Int. Ed Engl.* **54** (2015) 516–521.

[35] A.A. Kaminskii, "Crystalline Lasers: Physical Processes and Operating Schemes". (CRC Press, Boca Raton, 1996)

[36] B.R. Judd, "Hypersensitive transitions in rare-earth ions". *J. Chem. Phys*. **44** (1966) 839–840.

[37] P.A. Tanner, "Some misconceptions concerning the electronic spectra of tri-positive europium and cerium". *Chem. Soc. Rev.* **42** (2013) 5090–5101.

[38] K. Binnemans, "Interpretation of europium(III) spectra". *Coord. Chem. Rev.* **295** (2015) 1–45.

[39] B.R. Judd, "Optical Absorption Intensities of Rare-Earth Ions". *Phys. Rev.* **127** (1962) 750–761.

[40] G.S. Ofelt, "Intensities of Crystal Spectra of Rare-Earth Ions". *J. Chem. Phys.* **37** (1962) 511–520.

[41] M.P. Hehlen, M.G. Brik, K.W. Krämer, "50th anniversary of the Judd-Ofelt theory: An experimentalist's view of the formalism and its application". *J. Lumin*. **136** (2013) 221–239.

[42] M.H.V. Werts, R.T.F. Jukes, J.W. Verhoeven, "The emission spectrum and the radiative lifetime of Eu^{3+} in luminescent lanthanide complexes". *Phys. Chem. Chem. Phys.* **4** (2002) 1542–1548.

[43] O.J. Sovers, M. Ogawa, T. Yoshioka, "Detailed branching ratios for M_2O_2S:Eu^{3+}, Tb^{3+} and Pr^{3+} fluorescence from Judd-Ofelt intensity theory". *J. Lumin*. **18–19** (1979) 336–340.

[44] Y. Kitagawa, J. Ueda, K. Arai, H. Kageyama, S. Tanabe, "Difference of Eu^{3+} luminescent properties in YOCl and YOBr oxyhalide hosts". *J. Appl. Phys.* **129** (2021) 183104 (11p).

[45] M.J. Weber, T.E. Varitimos, B.H. Matsinger, "Optical intensities of rare-earth ions in yttrium orthoaluminate". *Phys. Rev. B* **8** (1973) 47–53.

[46] S. Tanabe, T. Hanada, T. Ohyagi, N. Soga, "Correlation between ^{151}Eu Mössbauer isomer shift and Judd-Ofelt Ω_6 parameters of Nd^{3+} ions in phosphate and silicate laser glasses". *Phys. Rev. B* **48** (1993) 10591–10594.

[47] T. Izumitani, H. Toratani, H. Kuroda, "Radiative and nonradiative properties of neodymium doped silicate and phosphate glasses". *J. Non-Cryst. Solids*. **47** (1982) 87–99.

[48] S. Tanabe, T. Ohyagi, N. Soga, T. Hanada, "Compositional dependence of Judd-Ofelt parameters of Er^{3+} ions in alkali-metal borate glasses". *Phys. Rev. B* **46** (1992) 3305–3310.

[49] P. Dorenbos, "The hole picture as alternative for the common electron picture to describe hole trapping and luminescence quenching". *J. Lumin.* **197** (2018) 62–65.

[50] D. Yu, J. Ballato, R.E. Riman, "Temperature-dependence of multiphonon relaxation of rare-earth ions in solid-state hosts". *J. Phys. Chem. C.* **120** (2016) 9958–9964.

[51] L.A. Riseberg, H.W. Moos, "Multiphonon Orbit-Lattice Relaxation of Excited States of Rare-Earth Ions in Crystals". *Phys. Rev.* **174** (1968) 429–438.

[52] M.J. Weber, "Radiative and multiphonon relaxation of rare-earth ions in Y_2O_3". *Phys. Rev.* **171** (1968) 283–291.

[53] J. Ueda, S. Matsuishi, T. Tokunaga, S. Tanabe, "Preparation, electronic structure of gadolinium oxyhydride and low-energy 5d excitation band for green luminescence of doped Tb^{3+} ions". *J. Mater. Chem.* **6** (2018) 7541–7548.

Chapter 5

Deep-Red to Near-Infrared Luminescence from Eu^{2+}-Trapped Exciton States in $YSiO_2N$

Abstract

The valence state of Eu ions doped in inorganic compounds is easily influenced by the synthesizing condition. In this study, the X-ray absorption spectroscopy revealed that almost half of Eu ions incorporated in the $YSiO_2N$ host were reduced into the divalent state through the sintering process at 1600 °C under the N_2 gas atmosphere without any annealing processes. The prepared $Eu^{2+/3+}$-doped $YSiO_2N$ sample showed the anomalous deep-red to near-infrared luminescence below 300 K under violet light illumination, whose luminescent properties are discussed with the detailed spectroscopic analyses. In the photoluminescence spectra at 4 K, the broad luminescence band ranging from 550 to 1100 nm with a large Stokes shift of 5677 cm^{-1} was observed, assigned to the recombination emission related to the Eu^{2+}-trapped exciton state. The temperature dependence of luminescence lifetime suggests that the thermal quenching of Eu^{2+}-trapped exciton luminescence takes place through complicated processes in addition to thermal ionization. The energy diagrams based on the spectroscopic results indicate that Eu^{2+}-trapped exciton luminescence in the $YSiO_2N:Eu^{2+/3+}$ sample was observed because all the Eu^{2+}: 5d excited levels are degenerated with the host conduction band, and the relatively stable Eu^{2+}-trapped exciton state in the Y^{3+} sites is formed just below the conduction band bottom. The comprehensive discussion on the deep-red to near-infrared luminescence in the $YSiO_2N$ host could give new insights into the mechanism of Eu^{2+}-trapped exciton luminescence in Y^{3+} sites, which has the potential to the near-infrared emitting devices.

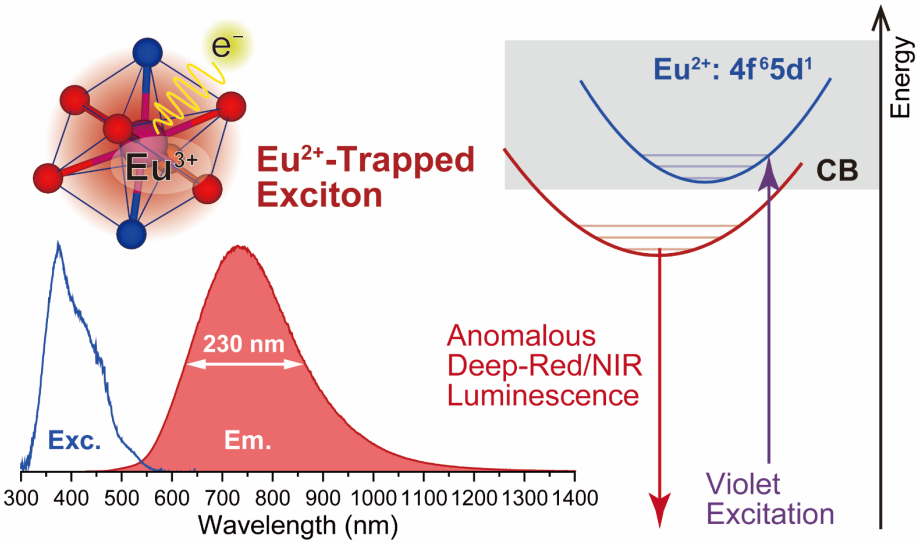

5.1. Introduction

Divalent europium ion (Eu^{2+}) is one of the most studied luminescence centers for functional luminescent materials activated with lanthanoid ions. Its applications are various; *e.g.,* solid-state lighting [1–3], high-resolution LED displays [4,5], and persistent phosphors [6,7]. Eu^{2+} ions in inorganic compounds show highly efficient luminescence due to the parity allowed 5d → 4f transition. Unlike the Ce^{3+}: 5d → 4f luminescence, the typical luminescence lifetime of Eu^{2+} is relatively long, 0.4–3.3 μs [8,9], due to the partially spin-forbidden transition from the mixing state of sextet and octet $4f^6 5d^1$ to $4f^7$ $^8S_{7/2}$ levels. The luminescence wavelengths are correlated with the anion species coordinating around Eu^{2+} ions and crystal field [10,11]. In terms of tailoring the luminescence color, the 5d energy shift in a specific ligand field has been studied in a variety of compounds. Recently, more and more researchers have been focusing on the exploration of materials showing the broadband deep-red and near-infrared (NIR) luminescence for applications, such as lighting, sensing, and bio-imaging devices [12–14]. The deep-red to NIR phosphors in many reports utilize the Cr^{3+}: 3d-3d luminescence in the octahedral coordination [15]. On the other hand, there are not so many examples of deep-red to NIR luminescence of Eu^{2+}-doped oxides despite the broadband luminescence through highly efficient 5d-4f parity allowed transition [16–21]. For materials exploration, (oxy)nitrides can be a desirable host compound for the deep-red to NIR phosphors because of the redshifted Eu^{2+} luminescence caused by the large nephelauxetic effect of nitrogen [22]. In literature, there are only a few reports about the deep-red to NIR emitting Eu^{2+}-doped nitrides with a luminescence peak λ_{em} over 700 nm, such as $Mg_3(BN_2)N:Eu^{2+}$ (λ_{em} = 710 nm) [23] and $Ca_3Mg[Li_2Si_2N_6]:Eu^{2+}$ (λ_{em} = 734 nm) [24].

However, luminescence in the Eu^{2+}-doped compounds is not always attributed to the Eu^{2+}: 5d → 4f transition. For example, the $BaS:Eu^{2+}$ shows NIR luminescence peaking at 878 nm at ambient temperature with quite broad widths of 3980 cm^{-1} [25]. This luminescence is not anticipated from the chemical trend of Eu^{2+}: 5d → 4f transition in *AE*S materials (*AE* = Ca, Sr, and Ba). Such anomalous luminescence is attributed to the recombination emission from the impurity-trapped exciton state [26,27]. The features and problems of anomalous luminescence

related to Eu^{2+}- or Yb^{2+}-trapped exciton states have been reviewed in Dorenbos's report [26]. The impurity-trapped exciton state takes large lattice relaxation, resulting in the anomalously broad and redshifted luminescence band with a large Stokes shift. Recently, some studies have claimed that the mechanism of anomalous luminescence is due to the intervalence charge transfer (IVCT) transition [28,29].

In this study, the Eu^{2+}-related luminescence in the $YSiO_2N$ host is characterized and discussed. Previously, we have reported the intense red luminescence of the Eu^{3+}-doped $YSiO_2N$ phosphor under near-UV excitation [30]. While the as-made $YSiO_2N:Eu^{3+}$ sample, which was prepared by the solid-state reaction at 1600 ºC under N_2 gas flow, showed the strong absorption band in the range of 380–500 nm and weak Eu^{3+} luminescence, the annealing process of the sample at 700 ºC under N_2 gas flow successfully enhanced Eu^{3+} luminescence intensity. According to the Ellingham diagram, this enhancement was possibly due to the oxidization of Eu ions that were reduced into the divalent state during the high-temperature synthesis under the inert atmosphere. However, there was no direct evidence showing the existence of Eu^{2+} ions. First, we reveal the valence state of Eu ions in the as-made and annealed $YSiO_2N$:Eu sample with the X-ray absorption spectroscopy, and discuss the suitable sintering condition for Eu^{2+}- or Eu^{3+}-doped oxynitride phosphors. Besides, we find that the $Eu^{2+/3+}$-doped $YSiO_2N$ sample shows the deep-red to NIR luminescence ranging from 550 to 1100 nm at low temperatures below 300 K and investigate the properties of this anomalous luminescence for the assignment; whether the Eu^{2+}: 5d → 4f transition or the recombination emission related to the impurity-trapped exciton states.

5.2. Experimental Section

5.2.1. Sample Preparation

Polycrystalline ceramic $YSiO_2N$ samples doped with 1.0% Eu ions, $Y_{0.99}Eu_{0.01}SiO_2N$, were prepared by the solid-state reaction method. The starting chemicals Y_2O_3 (99.99%, Kojundo Chemical Laboratory), SiO_2 (99.9%, Kojundo Chemical Laboratory), Si_3N_4 (99.9%, Kojundo

Chemical Laboratory), and Eu_2O_3 (99.99%, Furuuchi Chemical) were weighed in the glove box filled with high-purity Ar gas. Powders of chemicals were mixed with a ball milling system (Premium Line P-7, Fritsch) with ethanol (>99.5%). The obtained slurry was dried at 120 °C for 24 h. The mixture was pelletized with dry pressing and put in an inner alumina crucible. This crucible was set in another large alumina crucible with carbon powder, and then sintered at 1600 °C under N_2 gas flow for 24 h. One of the as-made samples was annealed at 700 °C under N_2 gas flow for 24 h. The crystalline phase of the prepared samples was confirmed by X-ray diffraction (XRD) measurements with a diffractometer (Rigaku, Ultima IV). As a reference, the simulated diffraction pattern of the monoclinic $YSiO_2N$ was simulated with the VESTA program [31,32].

5.2.2. Characterization

The X-ray absorption spectroscopy (XAS) was performed at the beamline BL-9A of Photon Factory (KEK, Japan). The Eu L_{III} X-ray absorption near edge structure (XANES) spectra were recorded in the transmission mode. As references, $EuCl_2$ and EuN chemicals were also measured. Obtained data were analyzed with the Athena software package [33].

Photoluminescence excitation (PLE) spectra at 4 K were measured by monochromatic excitation light with a 500 W Xe short arc lamp (OPM2-502XQ, Ushio Inc.) equipped with a double monochromator system by two monochromators (SP-300i, Acton Research Corp.), detected by using a photomultiplier tube (PMT) detector (R10699, Hamamatsu Photonics) coupled with a monochromator (SP-2300i, Princeton Instruments). The obtained PLE spectra were calibrated by the spectrum of the Xe lamp (light source) detected by a calibrated Si photodiode (S1337-1010BQ, Bunkoukeiki Co., Ltd.). For photoluminescence (PL) measurements, the sample was excited by the monochromatic excitation light of the Xe lamp or a 405 nm laser diode (LD) (SDL-405-LM-100T, Shanghai Dream Lasers Technology), and luminescence was detected with a Si CCD spectrometer ($\lambda < 1050$ nm, QE65Pro, Ocean Optics) and an InGaAs spectrometer ($950 < \lambda < 1650$ nm, NIRQuest-512-1.7, Ocean Optics) connected with UV-vis or NIR optical fibers. The obtained PL spectra were calibrated by the spectrum of a deuterium-tungsten halogen light source (DH-2000, Ocean Optics). The sample temperatures

were controlled by a cryostat with a closed-cycle He gas cryogenic refrigerator (CRT-A020-SE00, Ulvac Cryogenics). The diffuse reflectance spectra at the ambient temperature were collected by a UV-VIS-NIR spectrophotometer (UV-3600, Shimadzu) equipped with an integrating sphere.

Time-resolved luminescence spectroscopy of the bulk sample was performed on an optical setup mainly consisting of Ti:Sapphire solid-state laser with optical parametric generator (OPG), 3D Raman confocal microscope system, high-resolution monochromator, and streak camera. The sample was excited with OPG (Chameleon Vision-S, Coherent, inc.) pumped by a pulsed Ti:Sapphire laser with emission wavelength at 800 nm, which was able to generate the SHG laser beam at 400 nm with 75 fs pulse width and 50 MHz repetition rate. The 3D Raman confocal microscope system (Nanofinder 30, Tokyo Instruments, Inc.) acts as a real-time imaging spectrometer to monitor the emission from the phosphor under the OPO laser excitation. The reflected optical signal through a fluorescence microscope (BX51M, Olympus Co., Ltd.) was collected by a high-resolution monochromator (SpectraPro HRS-300, Princeton Instruments) and a streak camera (C14831-110, Hamamatsu Photonics). The emission spectral range was monitored between 430 nm and 800 nm with a 40 g/mm grating groove. Timescales for measurement were set to be 500 ns/20 ns, and temperature dependence experiments were performed in a microscopy cryostat (Janis ST-500, Lake Shore Cryotronics) with temperature control at 4, 150, and 300 K.

The luminescence decay measurements at low temperatures (T = 20–300 K) were measured by a luminescence lifetime spectrometer (Quantaurus-Tau, Hamamatsu Photonics), using a time-correlated single-photon counting (TCSPC) method under excitation with a 405 nm pico-second LED. The sample temperature was controlled by a closed-cycle He cryostat (Mini Stat CRT-006-2600, Iwatani).

5.3. Results and Discussion

5.3.1. Determination of Valence States of Europium Ions in $YSiO_2N$ Host

We investigated the valence state of Eu ions in the as-made (body color: yellow) and annealed

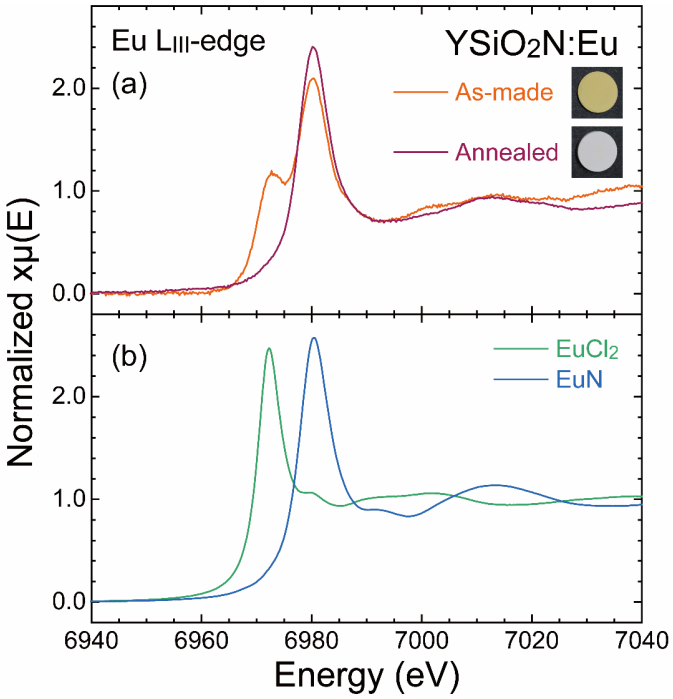

Figure 5.1. Normalized Eu L_{III}-edge XANES spectra of (a) as-made and annealed Eu-doped $YSiO_2N$ samples, and (b) $EuCl_2$ and EuN chemicals as references for divalent and trivalent states. The photographs of the as-made and annealed samples are given in the inset.

(body color: white) samples to discuss the effect of the annealing process for the Eu-doped $YSiO_2N$. **Figure 5.1a** shows the normalized Eu L_{III}-edge XANES spectra for the as-made and annealed $YSiO_2N$:Eu samples. The XANES spectra of the reference chemicals for divalent and trivalent Eu ions, Eu(II)Cl_2 and Eu(III)N, are displayed in **Figure 5.1b**. The annealed sample shows a white line at 6980 eV, corresponding to the X-ray absorption peak of Eu^{3+}. In the annealed $YSiO_2N$:Eu sample, all the Eu ions take the trivalent state. Therefore, the annealing process at 700 ºC under the N_2 atmosphere is very effective in obtaining intense Eu^{3+} luminescence in oxynitride hosts. On the other hand, the as-made sample shows another peak at 6974 eV, which is in accordance with the X-ray absorption peak of Eu^{2+}, in addition to the Eu^{3+} peak at 6980 eV. The existence of Eu^{2+} indicates that some Eu^{3+} ions doped as Eu_2O_3 were reduced into divalent states in the $YSiO_2N$ host with high-temperature synthesis at 1600 °C under an inert atmosphere. By performing the linear combination fitting of the Eu^{2+} and Eu^{3+} peaks [34], the amount of Eu^{2+} ions is estimated to be 46.5%. Almost half of Eu ions were reduced into divalent states, leading to the as-made sample composition of $Y_{0.99}Eu^{2+}_{\sim 0.005}Eu^{3+}_{\sim 0.005}SiO_2N$,

after this called $YSiO_2N:Eu^{2+/3+}$.

5.3.2. Characterization of Anomalous Deep-Red to NIR Luminescence in $YSiO_2N:Eu^{2+/3+}$

Because the yellow as-made $YSiO_2N:Eu^{2+/3+}$ sample shows very weak luminescence at room temperature under UV excitation, the sample was cooled down to 4 K, resulting in the strong deep-red to NIR luminescence with a violet LD excitation (λ_{ex} = 405 nm). **Figure 5.2a** shows the PL spectra of the $YSiO_2N:Eu^{2+/3+}$ sample at various temperatures (T = 4–300 K). At 4 K, the $YSiO_2N:Eu^{2+/3+}$ sample shows a strong and broad luminescence band peaking at 13229 cm^{-1} (= 756 nm) by the 405 nm excitation. The full width at half maximum (FWHM) of this band is 4061 cm^{-1}, which is broader even at 4 K than the typical bandwidth for Eu^{2+}-doped compounds, 800–3500 cm^{-1} [10,26]. Compared with many Eu^{2+}-activated (oxy)nitride phosphors [22], such as α-Ca-SiAlON:Eu^{2+} (λ_{em} = 585 nm) [35–39], $CaAlSiN_3:Eu^{2+}$ (λ_{em} = 650 nm) [1], and $Sr[LiAl_3N_4]:Eu^{2+}$ (λ_{em} = 650 nm) [4], the $YSiO_2N:Eu^{2+/3+}$ sample shows the significant redshifted luminescence, unexpected from the host chemical composition of $YSiO_2N$. These spectroscopic features suggest that anomalous deep-red to NIR luminescence is not attributed to Eu^{2+}: 5d → 4f transition.

The PL intensity of the $YSiO_2N:Eu^{2+/3+}$ sample decreases monotonously over 4 K. At 200 K, the PL intensity is less than only 10% of the initial PL intensity at 4 K. Over 200 K, the additional luminescence components appear as the anomalous deep-red to NIR luminescence band is quenched with temperature. **Figure. 5.2b** shows the PL spectra enlarged by a factor of 50 (T = 200–300 K). Here, sharp luminescence bands assigned to the Eu^{3+} 4f-4f transition are observed in the range of 15500–17500 cm^{-1}. In addition, the bandwidth of the broad luminescence gets larger, probably due to the additional band in the range of 15000–20000 cm^{-1} with a different thermal quenching behavior. In short, the PL spectra of the $YSiO_2N:Eu^{2+/3+}$ sample below ambient temperature (T = 4–300 K) indicate that there are at least three luminescence components with violet light excitation; (i) strong anomalous deep-red to NIR luminescence, (ii) considerably weak visible luminescence, and (iii) Eu^{3+} luminescence at the Y

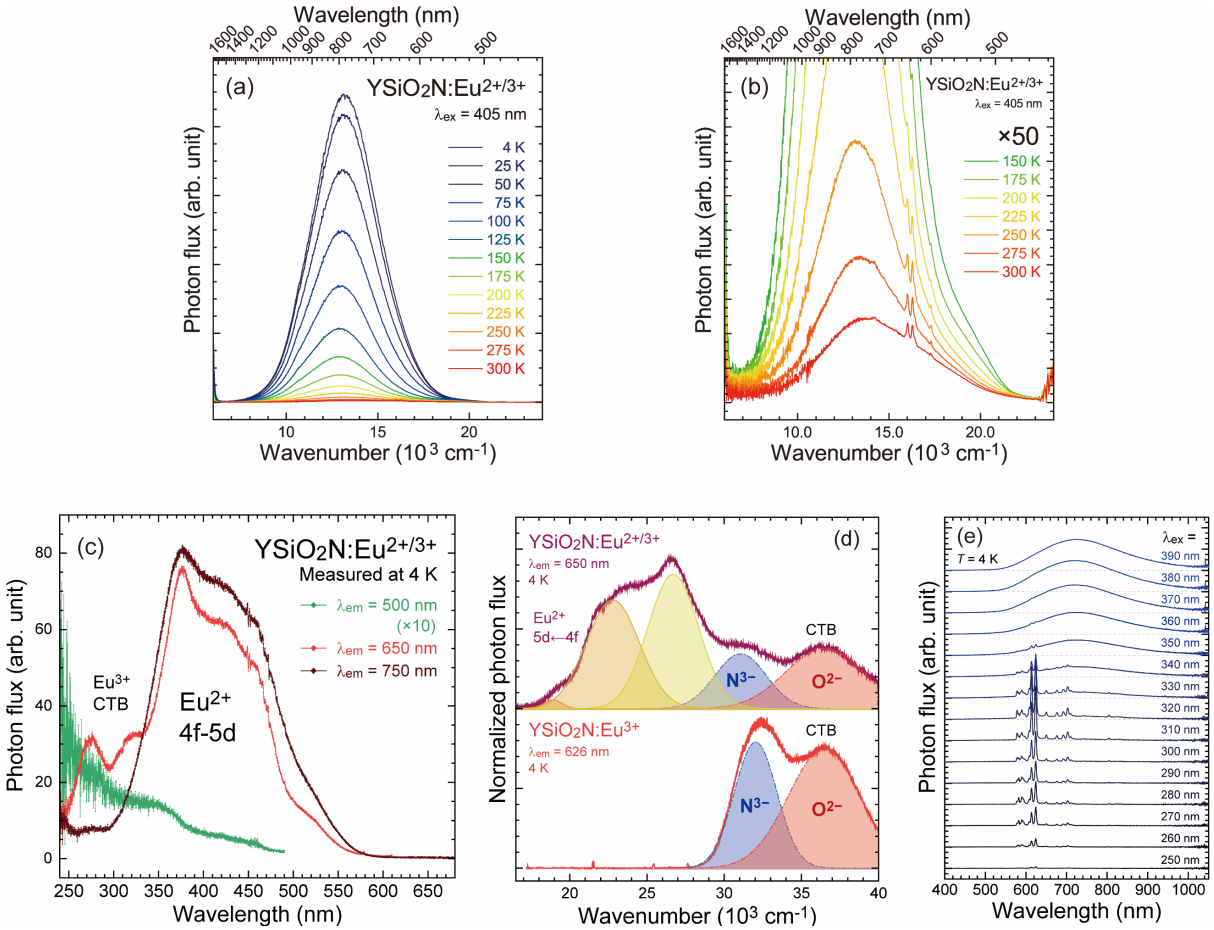

Figure 5.2. (a) PL spectra of the $YSiO_2N:Eu^{2+/3+}$ sample at low temperatures (T = 4–300 K), excited with a violet LD (λ_{ex} = 405 nm). (b) Enlarged PL spectra shown in Figure 5.2a (×50). (c) PLE spectra at 4 K with different monitored wavelengths (λ_{em} = 470–750 nm). (d) Normalized PLE spectra for the as-made $YSiO_2N:Eu^{2+/3+}$ and annealed $YSiO_2N:Eu^{3+}$ samples at 4 K. The Gaussian profiles after deconvolution are shown in overshadowed. (e) PL spectra at 4 K with different excitation wavelengths (λ_{ex} = 250–390 nm).

sites. The thermal quenching behavior is discussed in detail in the following section.

Figure 5.2c shows the PLE spectra at 4 K with different monitored wavelengths (λ_{em} = 500, 650, and 750 nm) to understand the excitation process for each luminescence component. In the PLE spectra (λ_{em} = 500 nm) of weak visible luminescence, an excitation plateau is observed in the range between 300 and 450 nm. In the PLE spectra of the deep-red to NIR luminescence (λ_{em} = 650, 750 nm), several excitation bands are observed below 600 nm. The strong excitation band in the range of 300–600 nm, especially in the PLE spectrum with λ_{em} = 750 nm, is assigned to the Eu^{2+}: 5d ← 4f transition because the spectral shape and range are similar to those of the Eu^{2+}: 5d ← 4f transition in oxynitrides, such as Ca-α-SiAlON and β-SiAlON [22,36,38,40]. This

excitation band corresponds to the absorption band observed in the diffuse reflectance spectra (Figure 3.5b). Here, no other absorption was observed over 650 nm, suggesting that the Eu^{2+}: 5d ← 4f transition is the dominant excitation pathway for the anomalous deep-red to NIR luminescence. In the diffuse reflectance spectra for the annealed $YSiO_2N:Eu^{3+}$ sample, any absorption band was not detected in the visible range over 400 nm because the absorption coefficient of Eu^{3+}: 4f-4f forbidden transition is quite low. In the PLE spectra with λ_{em} = 650 nm, two additional excitation bands peaking at 276 and 315 nm are assigned to the charge transfer (CT) transition from coordinating anions (O^{2-} and N^{3-}) to Eu^{3+} because the Eu^{3+}: $^5D_0 \rightarrow {}^7F_3$ luminescence is detectable simultaneously [32]. Considering these CT excitation bands, the PLE spectra with λ_{em} = 650 nm can be deconvoluted into five Gaussian profiles, two CT and three Eu^{2+}: 5d ← 4f bands. **Figure 5.2d** shows the PLE spectra of the $YSiO_2N:Eu^{2+/3+}$ (as-made) and $YSiO_2N:Eu^{3+}$ (annealed) sample with the results of Gaussian fitting. In the monoclinic $YSiO_2N$ host, there are five crystallographically nonequivalent [YO_6N_2] dodecahedral sites; one C_i site (Wyckoff 4*a*), one C_1 site (Wyckoff 8*f*), and three C_2 sites (Wyckoff 4*e*) [31]. The 5d excited levels of Eu^{2+} ions incorporated in these sites can be split into five due to the lower site symmetry. Besides, the Eu^{2+} $4f^6 5d^1$ electronic configuration brings about a more complicated energy level structure than the Ce^{3+} $4f^0 5d^1$ electronic configuration because of the spin polarization. Therefore, the Eu^{2+}: 5d ← 4f excitation band shows the complicated spectral shape with multiple Gaussian-shaped components, and it is difficult to reveal the precise number of the Gaussian functions to use. However, the purpose of the Gaussian deconvolution is not to calculate the precise 5d energies and energy level distributions but to estimate the energy of the lowest 5d excited level. In order to reproduce the PLE spectra band with the minimum numbers of the Gaussian functions, the Eu^{2+}: 5d ← 4f excitation band was fitted with just three Gaussian functions for simplicity. For the $YSiO_2N:Eu^{3+}$ sample, the excitation bands were deconvoluted into only two profiles of the CT transition from N^{3-} and O^{2-} to Eu^{3+} ions. Similarly, the Eu^{3+} CT bands for the $YSiO_2N:Eu^{2+/3+}$ sample were represented by two Gaussian functions with slightly broad widths because of the overlap with Eu^{2+} 5d bands. According to the Gaussian fitting, the lowest 5d band for Eu^{2+} is located at 18906 cm^{-1} (= 2.34 eV), which provides a large Stokes shift

of 5677 cm^{-1} between the peaks of the luminescence band and the lowest 5d excitation band. Considering the typical Stokes shift for Eu^{2+}-activated phosphors of 800–4000 cm^{-1} [26,41,42], the Stokes shift of deep-red to NIR luminescence band for the $YSiO_2N:Eu^{2+/3+}$ sample is anomalous. According to Dorenbos, the anomalous luminescence of impurity-trapped exciton states in Eu^{2+}-doped materials has the following three features; (1) an abnormally large Stokes shift (5000–10000 cm^{-1}) and width (> 4000 cm^{-1} at ambient temperature) of the emission band, (2) an emission wavelength that is not consistent with the wavelength anticipated from the compositional and structural properties of compounds, and (3) an anomalous decay and thermal quenching behavior [10,26]. Therefore, The large FWHM (4061 cm^{-1}) and the large Stokes shift (5677 cm^{-1}) for the $YSiO_2N:Eu^{2+/3+}$ sample suggest that the deep-red to NIR luminescence observed only in the as-made $YSiO_2N:Eu^{2+/3+}$ sample is related to the Eu^{2+}-trapped exciton (ETE) state [26].

Figure 5.2e shows the PL spectra at 4 K with various excitation wavelengths (λ_{ex} = 250–390 nm). Under the excitation light below 360 nm, sharp luminescence bands assigned to the Eu^{3+}: 4f-4f transition are observed. On the other hand, the deep-red to NIR ETE luminescence is observed with the excitation over 310 nm. These results are consistent with the deconvolution results of the PLE spectra shown in Figure 5.2d, implying that ETE states and Eu^{3+} ions are excited only through the Eu^{2+}: 5d ← 4f and CT transitions, respectively.

In order to characterize the two broad luminescence bands in terms of the radiative decay rate, the time-resolved PL spectra of the $YSiO_2N:Eu^{2+/3+}$ sample were obtained at different temperatures (T = 4, 150, and 300 K). **Figures 5.3a–3c** and **Figures 5.3d–3f** show the contour plots of the time-resolved PL spectra taken with the streak camera in the different time ranges of 0–450 and 0–20 ns, respectively. The projections of each time-resolved PL spectrum are plotted as the integrated PL spectrum with different time ranges Δt (0–450 and 0–20 ns) in **Figure 5.4.** In the range of 0–450 ns, the deep-red luminescence related to the ETE states is observed with lifetimes of a few hundreds of nanoseconds. The PL intensity of the ETE band severely decreases with temperatures, as shown in the integrated PL spectra with Δt = 0–450 ns. At 300 K, the ETE luminescence is almost quenched, and only a luminescence band with a fast

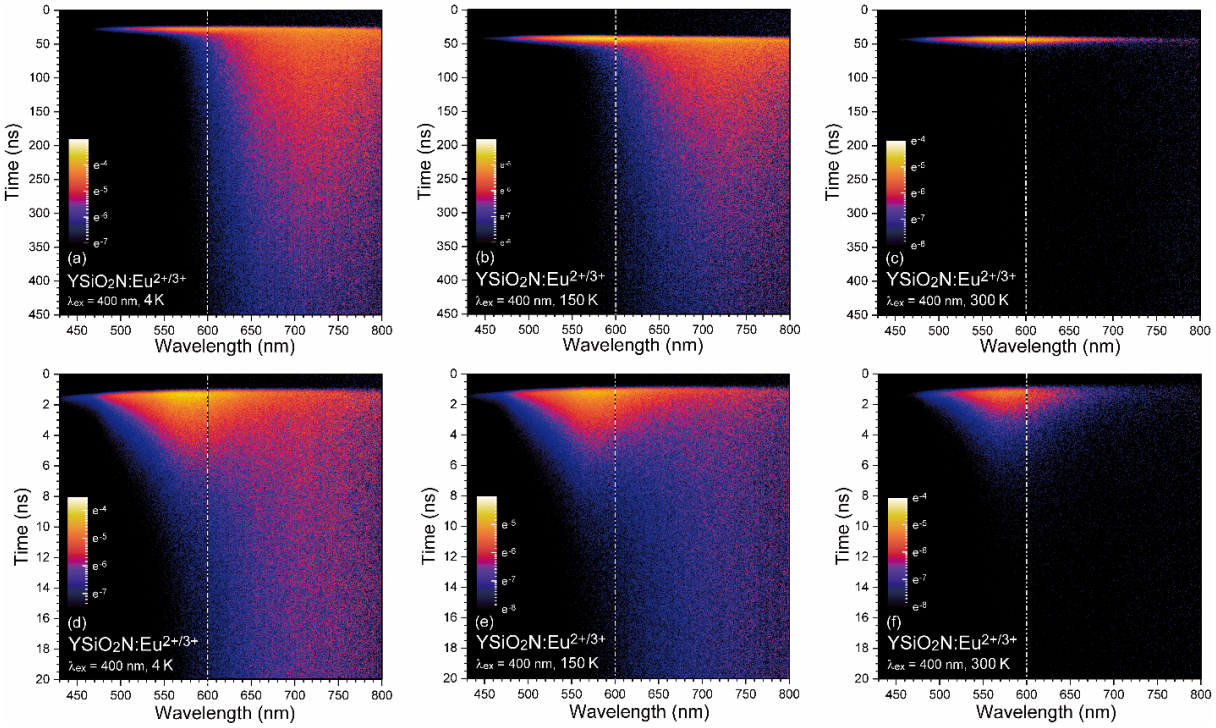

Figure 5.3. Time-resolved PL spectra of the $YSiO_2N:Eu^{2+/3+}$ sample with different time ranges (0–450 and 0–20 ns) at different temperatures (T = 4, 150, 300 K). The PL intensities depending on monitored wavelengths were calibrated by the spectra with the continuous wave (cw) light source. Two spectra with the same condition were combined at 600 nm (shown with broken white lines).

decay is observed. Figures. 5.3d–3f and 5.4 show that this luminescence band has a very short lifetime on the order of a few nanoseconds. The band shape and lifetime of this luminescence seem not to be affected by temperature. The time-resolved PL spectrum of the non-doped $YSiO_2N$ sample with the same measurement condition at 4 and 300 K is provided in **Figure 5.5**, showing the PL band with the same decay time, spectral shape, and thermal stability. Therefore, it is suggested that the luminescence band independent of doped lanthanoid ions in the range of 480–800 nm with a ns-order lifetime is due to intrinsic defects in the $YSiO_2N$ host.

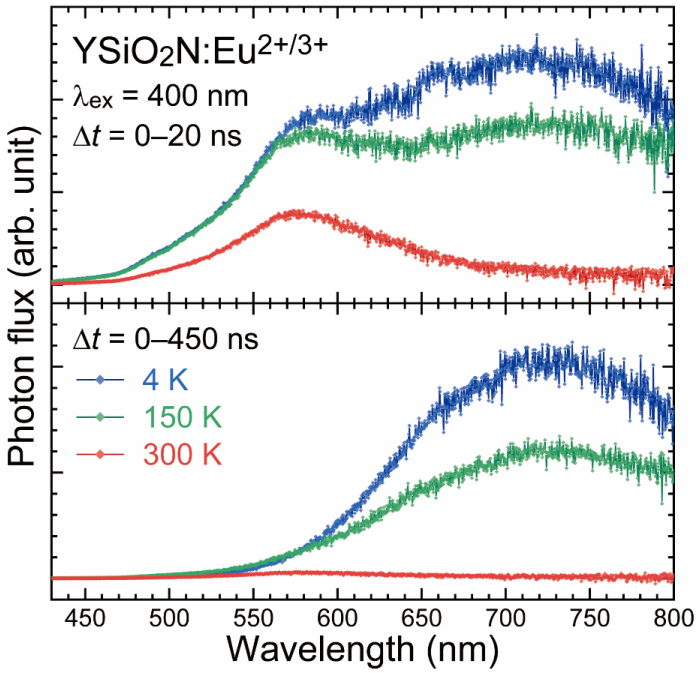

Figure 5.4. Integrated time-resolved PL spectra at 4, 150, and 300 K with different integration time ranges Δt (0–20 and 0–450 ns).

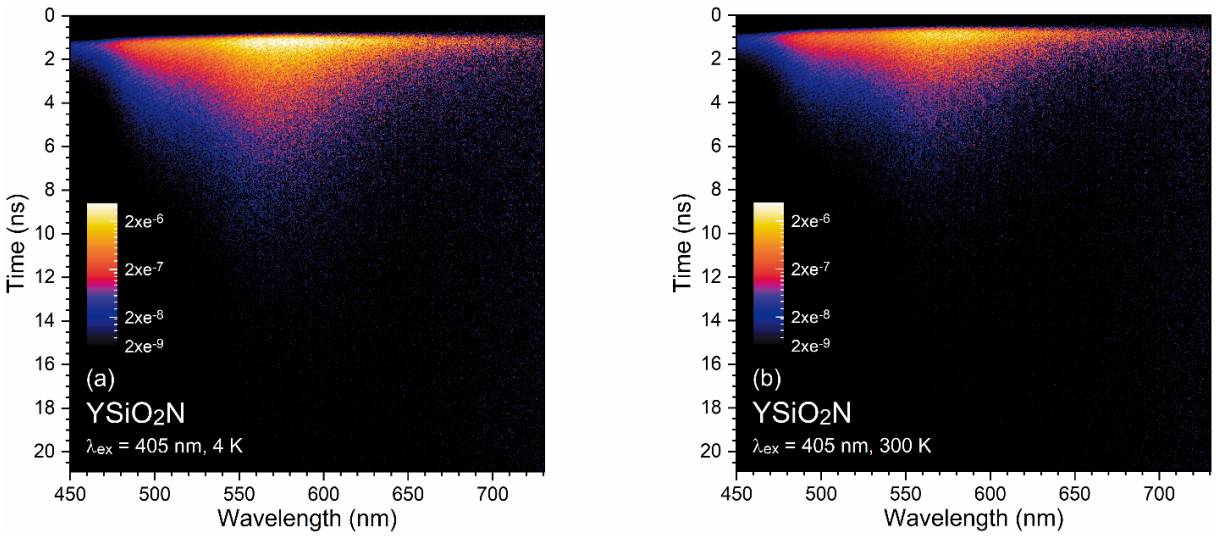

Figure 5.5. Time-resolved PL spectra of the non-doped $YSiO_2N$ sample at 4 and 300 K.

5.3.3. Thermal Quenching Behavior of Eu^{2+}-Trapped Exciton and Defects Related Luminescence

The broad luminescence bands observed in the $YSiO_2N:Eu^{2+/3+}$ sample are mainly composed of two luminescence centers; Eu^{2+}-trapped exciton (ETE) state and intrinsic defects. The thermal quenching behaviors of two luminescence centers were characterized by the analyses of the temperature dependence of the PL spectra and luminescence lifetimes. Because two luminescence bands severely overlap in the PL spectra at low temperatures (T = 4–300 K), we first deconvoluted the PL band at each temperature into two Gaussian profiles to discuss each temperature dependence separately. As shown in **Figure 5.6a**, the spectra were well fitted by two Gaussian profiles. All the obtained Gaussian profiles at the temperatures of 4–300 K and the FWHM and peak center of each Gaussian profile are plotted in **Figure 5.7**. The spectral shape of the ETE band below 200 K is mostly unchanged with the width of ~3550 cm^{-1} and the peak at ~13100 cm^{-1}. Over 200 K, the FWHM is broadened up to ~4300 cm^{-1} due to the thermal broadening. On the other hand, the luminescence band related to intrinsic defects shows different behavior of the large thermal broadening (2050 cm^{-1} → 3100 cm^{-1}) and the large redshift (16600 cm^{-1} → 18000 cm^{-1}) even below 200 K. This behavior suggests that a variety of intrinsic defects, such as $O_N^{\cdot}$, $N_O^{'}$, and $V_N^{\cdot\cdot\cdot}$, contributes to the weak luminescence in the visible

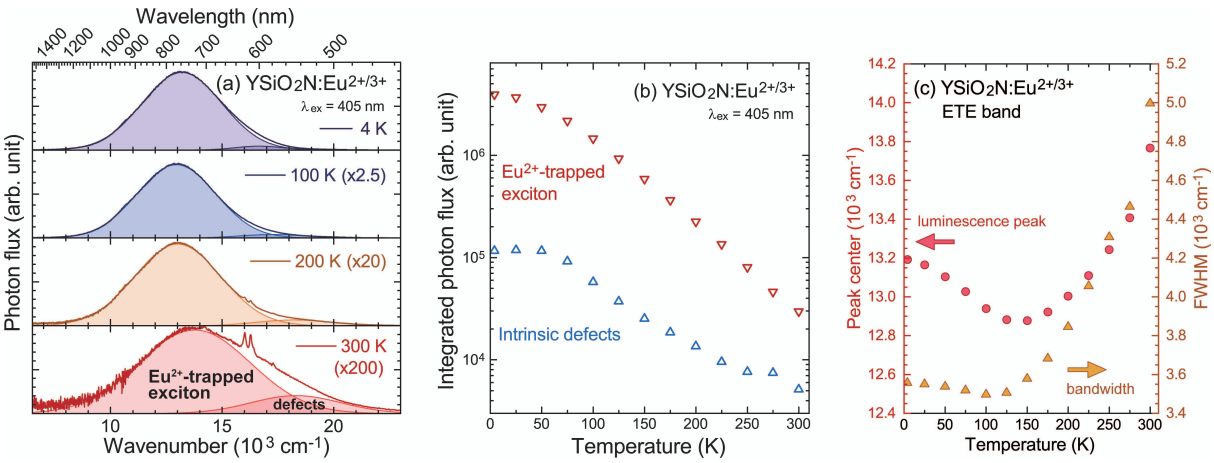

Figure 5.6. (a) PL spectra (T = 4, 100, 150, and 300 K) with two Gaussian profiles related to the Eu^{2+}-trapped exciton state and intrinsic defects. (b) Temperature dependence of the integrated PL intensities for the Eu^{2+}-related exciton and intrinsic defects. (c) Temperature dependence of the peak center and FWHM for the Gaussian profiles of the ETE band.

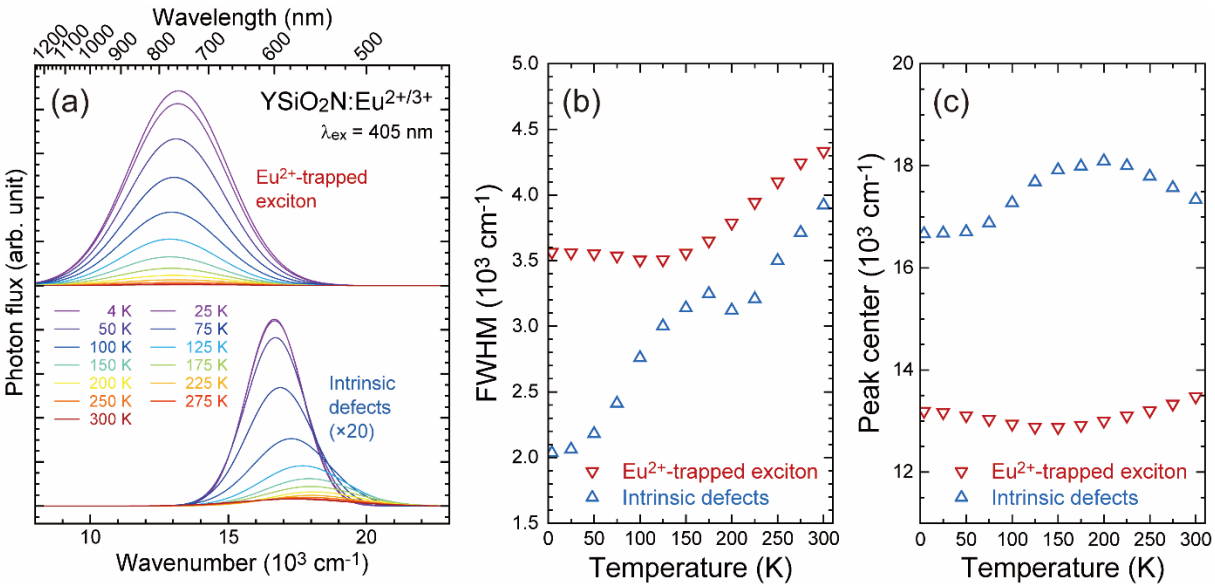

Figure 5.7. (a) Gaussian profiles obtained by fitting of the PL spectra at low temperatures (T = 4–300 K). (b–c) Fitting outputs of FWHM and peak center for the Gaussian profiles of Eu^{2+}-trapped exciton and intrinsic defects emission.

region. **Figure 5.6b** displays the temperature dependence of the integrated PL intensity for two kinds of luminescence. Despite the very short lifetime, the PL intensity of intrinsic defects is much weaker than that of ETE luminescence, indicating that the number of luminescence centers related to intrinsic defects is much smaller than that of the ETE centers. The quenching profile of the ETE luminescence cannot be described by the typical quenching curve, possibly due to the temperature dependence of the absorption coefficient.

The temperature-dependent peak center and FWHM of the ETE luminescence band are plotted in **Figure 5.6c**, which shows two different behavior against temperature increase; from 4 to 150 K, the luminescence wavelength gets redshifted with temperature increasing while the bandwidth is almost unchanged; over 150 K, as the temperature increases, the luminescence wavelength gets blueshifted by about 1000 cm^{-1}, and the bandwidth gets broader up to ~4300 cm^{-1}. The blueshift of the ETE luminescence band has been reported in the literature. For the ETE luminescence of the $CsCaF_3:Eu^{2+}$, $Ba_{0.3}Sr_{0.7}F_2:Eu^{2+}$, and $Sr_4Al_{14}O_{25}:Eu^{2+}$ phosphors, the blueshift of the luminescence band was caused by the emergence of a different luminescence band at shorter wavelength side, which is explained by the thermally enhanced change of electron population through the crossover of the ETE and Eu^{2+} $4f^65d^1$ parabolas [44–46].

However, the Gaussian-shaped single ETE luminescence band of the $YSiO_2N:Eu^{2+/3+}$ sample shifted without any other luminescence band emerging. Although a similar blueshift and thermal broadening of the ETE luminescence band was observed in the $BaS:Eu^{2+}$ phosphor, which was reported by Smet *et al.* (λ_{em} = 938 nm at 70 K → λ_{em} = 878 nm at 300 K, the energy shift was ~730 cm^{-1}), the reason of the spectral shape changing was not discussed in detail [25]. The spectral shape of the ETE luminescence band for the $YSiO_2N:Eu^{2+/3+}$ sample can depend on the following two factors;

1. The ETE state is influenced by the temperature dependence of the bandgap. As the temperature increases, the bandgap becomes narrower because of an increase in the amplitudes of atomic vibrations. While the electron population on the vibrational levels of the potential parabolas is unchanged at quite low temperatures, the conduction band (CB) bottom and ETE state are lowered, resulting in the redshift of the ETE luminescence band with almost no change in bandwidth. A similar shift accompanied by the bandgap shift was observed in the pressure dependence of the ETE luminescence for the $LiBaF_3:Eu^{2+}$ phosphor [47]. By inducing the pressure, the bandgap became wider, and the CB bottom and ETE state shifted higher, leading to the blueshifted ETE luminescence.
2. The spectral shapes of the broad luminescence band can be affected by the electron population on the excited states that obeys the Boltzmann distribution. With the temperature increasing, the excited electrons are distributed along the potential curve to the higher vibrational levels coupled with several phonons, resulting in the blueshifted luminescence band with a broader bandwidth. This temperature dependence is also observed in the normal Eu^{2+}: 5d → 4f luminescence [48].

At low temperatures, these two factors compete and lead to the abnormal temperature behavior of the peak wavelength and bandwidth of the ETE luminescence band for the $YSiO_2N:Eu^{2+/3+}$ sample; *i.e.*, at low temperatures below 150 K, the influence of the temperature dependence of the bandgap is dominant; on the other hand, over 150 K, the electronic transition from the higher vibrational levels causes the thermal broadening and blueshift of the ETE luminescence band.

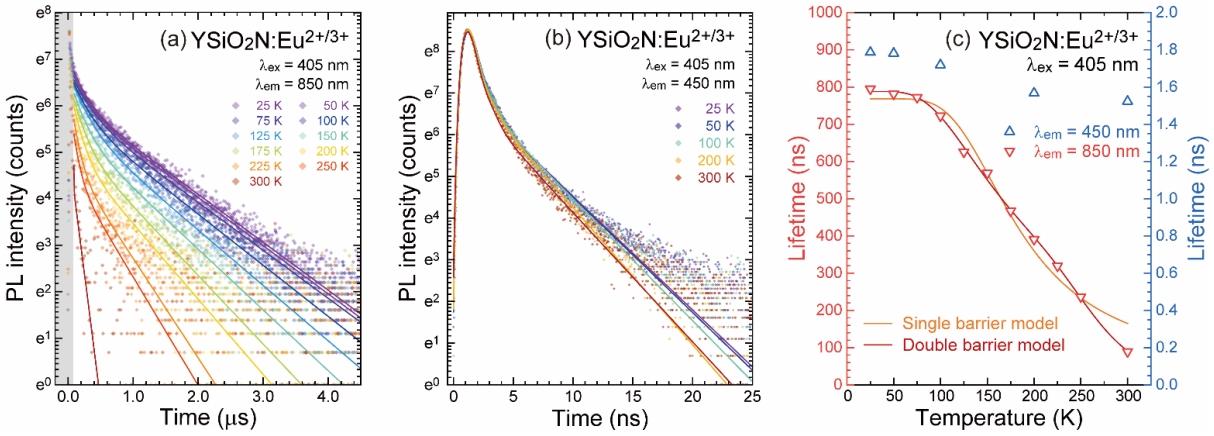

Figure 5.8. (a) Luminescence decay curves at various temperatures (T = 20–300 K) with the monitored wavelengths of (a) λ_{em} = 850 nm and (b) λ_{em} = 450 nm. (c) Temperature dependence of the luminescence lifetimes estimated by second-order exponential functions. The solid curves represent the fitting function with the single (orange) and double (red) quenching barrier models.

From the results of the time-resolved PL spectra and the deconvolution of PL bands, the monitoring wavelengths for the decay measurements of the luminescence related to the ETE states and intrinsic defects are determined to be 850 and 450 nm, respectively, to avoid the overlap of these bands. **Figure 5.8a** shows the decay curves of the ETE luminescence. Each decay curve shows a deviation from the single exponential profile. Thus, all the luminescence decay curves were fitted with a second-order exponential function, described below;

$$I(t) = A_1 \exp(-t/\tau_1) + A_2 \exp(-t/\tau_2), \tag{5.1}$$

where A_1 and A_2 are amplitudes for each decay component and τ_1 and τ_2 are the luminescence lifetime at each temperature. The initial part of the ETE luminescence decay curves below 100 ns was eliminated for the better overall fitting because the influence of excitation pulse or the defect-related luminescence is not negligible over 100 K. The fitted profiles are shown in solid lines in Figure 5.8a. The average luminescence lifetime at each temperature τ_{ave} was calculated by the following equation;

$$\tau_{ave} = \frac{A_1{\tau_1}^2 + A_2{\tau_2}^2}{A_1\tau_1 + A_2\tau_2}. \tag{5.2}$$

Figure 5.8b shows the luminescence decay curves related to intrinsic defects. They were also fitted with a second-order exponential function, and their average lifetimes were estimated. For the luminescence decay curves related to intrinsic defects, the instrumental response

function (IRF) was taken into account in the overall fitting.

Figure 5.8c shows the temperature dependence of the lifetimes of the ETE and intrinsic defects luminescence. The decay rate of the luminescence related to intrinsic defects is mostly unchanged even at 300 K despite the significant decrease in the PL intensity, which is the same as the trend suggested from the time-resolved PL spectra (Figures 5.3d–3f).

On the other hand, the ETE luminescence lifetime (770 ns at 4 K) shows a monotonous decrease over 50 K and reaches a lifetime of 89 ns at 300 K. In order to estimate the activation energy for thermal quenching, we performed the profile fitting with the typical single barrier quenching model described below;

$$\tau = \frac{1}{\Gamma_\nu + \Gamma_0 \exp\left(-{E_a}/{kT}\right)}. \tag{5.3}$$

Here, Γ_ν is the radiative transition rate, Γ_0 is the attempt rate of the non-radiative process, E_a is the activation energy of thermal quenching, k is the Boltzmann constant (= 8.617×10^{-5} eV K^{-1}), and T is temperature. The fitting function with the parameters ($\Gamma_\nu = 1.30 \times 10^6$ s^{-1}, $\Gamma_0 = 4.95 \times 10^7$ s^{-1}, and $E_a = 0.0605$ eV) is depicted in the solid orange curve in Figure 5.8c, which largely deviates from the ETE lifetime plot. The Γ_0 for the quenching process, such as thermal ionization and thermal activation crossover, usually takes the value with the order of 10^{10}–10^{12} s^{-1} [43]. However, the estimated Γ_0 for the ETE luminescence was quite small, indicating that a simple quenching process with a single potential barrier no longer describes the thermal quenching behavior of the ETE state in the $YSiO_2N$ host. In literature, the thermal quenching of the ETE luminescence is discussed by assuming the competition of two quenching processes; from the Arrhenius plot, Smet *et al.* obtained the thermal activation energies of 14 and 190 meV for the ETE luminescence of the BaS:Eu^{2+} phosphor, which correspond to the exciton dissociation and thermal ionization, respectively [25]; Mahlik *et al.* obtained the activation energies of 33 and 273 meV for the $Ba_{0.5}Sr_{0.5}F_2$:Eu^{2+} phosphor, related to the tunnelling from the higher vibronic levels and thermal activation crossover, respectively [44]. In order to improve the fitting results, we applied the double barrier quenching model to the profile fitting, described below;

$$\tau = \frac{1}{\Gamma_\nu + \Gamma_{0\mathrm{I}} \exp\left(-E_{\mathrm{aI}}/kT\right) + \Gamma_{0\mathrm{II}} \exp\left(-E_{\mathrm{aII}}/kT\right)}, \tag{5.4}$$

where the Γ_0 and E_a for the quenching processes I and II are labeled with the subscripts. The profile was well fitted with the parameters of $\Gamma_\nu = 1.27 \times 10^6$ s^{-1}, $\Gamma_{0\mathrm{I}} = 1.16 \times 10^7$ s^{-1}, $\Gamma_{0\mathrm{II}} = 6.34 \times 10^{10}$ s^{-1}, $E_{\mathrm{aI}} = 0.0394$ eV, and $E_{\mathrm{aII}} = 0.235$ eV. Although the $\Gamma_{0\mathrm{I}}$ value is still low, the fitting result seems to be good. The low $\Gamma_{0\mathrm{I}}$ value can be derived from the complicated thermal quenching pathways for the ETE luminescence, such as the energy transfer to Eu^{3+} ions or intrinsic defects and a slight difference in decay rates of ETE states with the variation of incorporated sites. Nevertheless, the fitting results indicate that as least two quenching processes with the activation energies of 39.4 and 235 meV can be involved.

5.3.4. Mechanism of Eu^{2+}-Trapped Exciton Luminescence in $YSiO_2N$ Host

In this section, we discuss the mechanism of the anomalous deep-red to NIR luminescence in the $YSiO_2N:Eu^{2+/3+}$ sample with the energy diagrams. The ETE luminescence is strongly correlated with the relative energy of the Eu^{2+}: 5d excited levels with respect to the host conduction band (CB) [26,45]. **Figure 5.9a** shows the energy level diagram of the $YSiO_2N:Eu^{2+/3+}$ sample, whose *y*-axis is represented in host referred binding energy (HRBE) [51–55]. The bandgap energy E_g at a low temperature was obtained from the host-exciton creation energy E^{ex} by adding the exciton binding energy estimated as $0.008(E^{ex})^2$ [56,57]. From the PLE spectrum of the annealed $YSiO_2N:Eu^{3+}$ sample shown in Figure 6.3, the E^{ex} value for $YSiO_2N$ was estimated to be 5.87 eV, resulting in the E_g of 6.14 eV. The energy difference between the VB top and Eu^{2+} 4f ground level, which corresponds to the CT energy E_{CT} for Eu^{3+} ions, was determined to be 3.96 eV from the PLE spectrum of the annealed $YSiO_2N:Eu^{3+}$ sample in Figure 5.2d. These values lead to the ionization energy of 2.18 eV, which is the energy gap between the ground level of $Eu^{2+}(^8S_{7/2})$ and the CB bottom. Because the lowest 5d excited level is 2.34 eV higher than the 4f ground level, all the 5d excited levels are located within the CB. Thus, the 5d excited states are easily deactivated because of the strong autoionization through the CB [25], and no 5d → 4f luminescence is observed. After the autoionization, the ETE states of $Eu^{3+} + e^-$ can be formed.

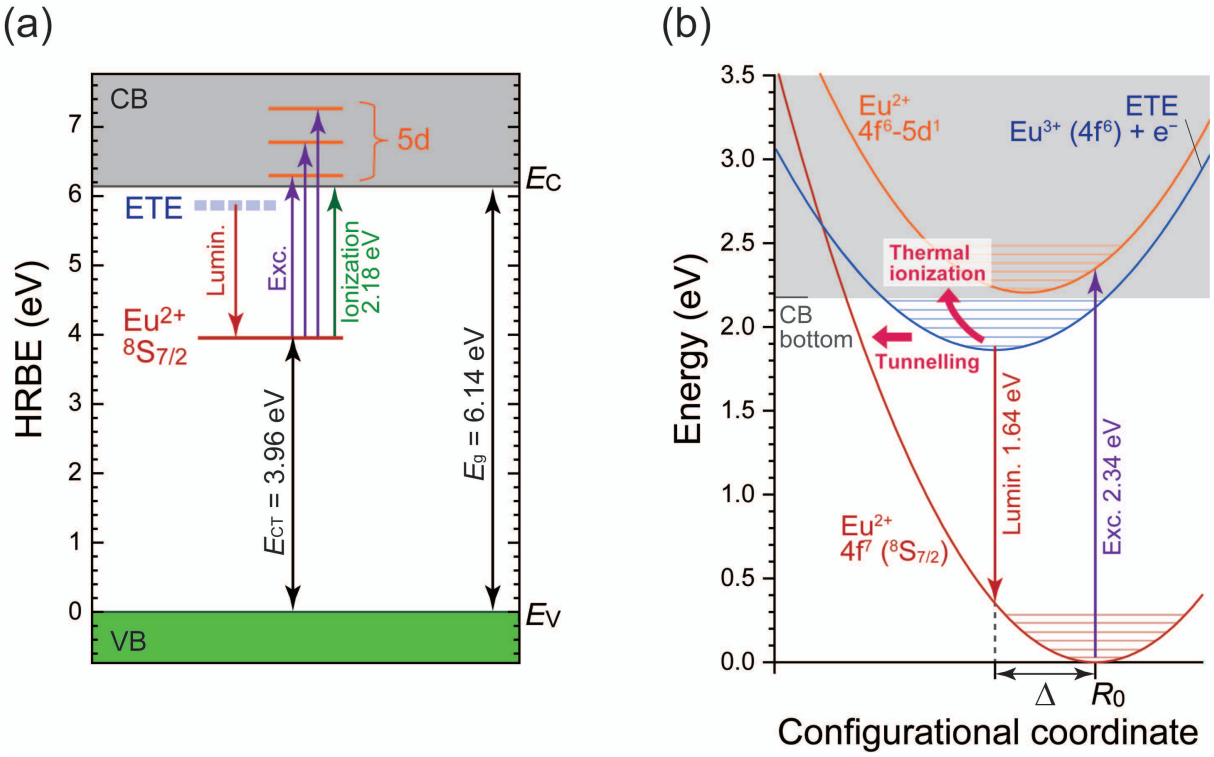

Figure 5.9. (a) Constructed energy level diagram for Eu^{2+} ions in the $YSiO_2N$ host. The *y*-axis is converted to the host referred binding energy (HRBE). (b) Configurational coordinate diagram representing the energy level structure of the Eu^{2+} ion and Eu^{2+}-trapped exciton states.

Although the direct excitation band related to the transition from the 4f to the ETE states in the PLE spectra was not observed, the ETE states can be formed below the CB bottom [44].

In order to consider the luminescence behavior after structural relaxation in the ground and excited states, the configurational coordinate diagram for the $YSiO_2N:Eu^{2+/3+}$ is constructed and provided in **Figure 5.9b**. Here, the R_0 and Δ represent the equilibrium position of a Eu^{2+} ion to ligands and the shift of ligands in the ETE state (*i.e.*, the offset of the ETE parabola). As observed in the PLE spectra in Figure 5.2c, the Eu^{2+} ground state ($4f^7$) is excited to the 5d excited states ($4f^6$-$5d^1$), according to the Franc-Condon principle. The absence of the Eu^{2+}: 5d → 4f luminescence implies that the Eu^{2+} $4f^6$-$5d^1$ parabola buries in the CB. The recent *ab initio* study has revealed that the bond length between a Eu^{2+} ion and ligands in the Eu^{2+}($4f^6$-$5d^1$) excited states is shorter than that in the Eu^{2+}($4f^7$) ground states [58,59]. In the 5d excited states, the hole generated in the inner 4f shell attracts the ligands stronger, resulting in a short bond length of excited states and the negative offset in the configurational coordinate diagram [60]. The

parabola for the ETE state is located below the CB bottom with the luminescence energy of 1.64 eV. For the ETE state, the electronic configuration is described to be $Eu^{3+}(4f^6) + e^-$, indicating that an electron is weakly bound by a Eu^{3+} ion. The energy of the ETE parabola at R_0 is slightly smaller than the CB bottom by the binding energy of the exciton. This parabola has a larger offset Δ than the parabola for the $Eu^{2+}(4f^6\text{-}5d^1)$ configuration because the trivalent state brings about a stronger Coulomb attraction and a smaller ionic radius than the divalent states [26]. Despite the absence of any ETE absorption bands, the excited states relax down along the ETE parabola, resulting in the deep-red to NIR luminescence from the ETE states in the $YSiO_2N:Eu^{2+/3+}$ sample. The necessary condition for the ETE luminescence is that the Eu^{2+}: 5d levels are degenerated with the CB or located just below the CB bottom. As mentioned by Dorenbos, the divalent lanthanoid ion incorporated in a trivalent cation site show no 5d → 4f luminescence because the Coulomb attraction is small and the 5d level is located above the CB bottom [26]. Besides, the trivalent site can stabilize the ETE state with $Eu^{3+}(4f^6)\text{-}e^-$ configuration because of the valence state matching. Therefore, the Y^{3+} sites, which can accommodate Eu^{2+} ions, play an important role in the anomalous deep-red to NIR luminescence in the $YSiO_2N:Eu^{2+/3+}$ sample.

The thermal quenching behavior of the ETE luminescence is discussed by the configurational coordinate diagram in Figure 5.9b. According to Smet [25], the thermal quenching process of the ETE luminescence is explained by the thermal ionization of the ETE state to the CB, which is supported by the blueshifted and broadened ETE band (Figure 5.6c) caused by the Boltzmann distribution on the vibrational levels. In the diagram, the energy gap between the lowest energy of the ETE state and the CB bottom, which is the ionization energy of the ETE state, is relatively small to cause the thermal quenching of the anomalous luminescence even below 300 K. The observed activation energy of 235 meV for the $YSiO_2N:Eu^{2+/3+}$ sample corresponds to the constructed energy level diagram. Also, it is a typical value, such as the activation energy for ETE luminescence of 190 meV in $BaS:Eu^{2+}$ and of 273 meV in $Ba_{0.5}Sr_{0.5}F_2:Eu^{2+}$. The double-barrier quenching fitting reveals a quenching pathway with a small activation energy of 39.4 meV, which can be related to the exciton binding energy or the

thermally activated tunnelling process [25,44]. As mentioned in the previous section, the actual energy level diagram should be more complicated due to various defects in the $YSiO_2N:Eu^{2+/3+}$ sample, including intrinsic defects, Eu^{3+} ions, and Eu^{2+} ions in different sites. These defects can act as some quenching center, resulting in the complicated quenching behavior shown in Figures 5.8c. For the identification of the thermal quenching pathways for the ETE state in the $YSiO_2N$ host, it is necessary to investigate the luminescence properties of the $YSiO_2N$ doped with only Eu^{2+} ions with low concentration.

5.4. Conclusions

Photoluminescence properties of the Eu-doped $YSiO_2N$ sample at low temperatures were investigated in detail. The X-ray absorption spectroscopy revealed that almost half Eu ions in the sample were reduced into a divalent state through the high-temperature synthesis under the inert atmosphere. The as-made sample, including Eu^{2+} ions, showed the deep-red to near-infrared luminescence at low temperatures below 300 K. This luminescence was anomalous in terms of the following points;

- The photoluminescence band took an abnormally large bandwidth (4061 cm^{-1}) and Stokes shift (5677 cm^{-1}) even at 4 K, not assigned to the typical Eu^{2+}: 5d-4f transition.
- Deep-red to near-infrared luminescence only at low temperatures was observed, which is not anticipated from the 5d → 4f luminescence of other Eu^{2+}-doped (oxy)nitrides, despite not such a large N/O ratio.
- The temperature dependence of luminescence lifetime was complicated, which could not be explained by a simple quenching model.

These features indicated that the anomalous luminescence in the $YSiO_2N:Eu$ sample is related to the Eu^{2+}-trapped exciton state. The vacuum referred binding energy diagram suggests that the typical Eu^{2+}: 5d → 4f luminescence is not observed because all the Eu^{2+}: 5d excited levels degenerated with the host conduction band. The configurational coordinate diagram explained the anomalous luminescence from the Eu^{2+}-trapped exciton states ($Eu^{3+} + e^-$) which were located

just below the conduction band bottom, by taking the lattice relaxation into account. This study provides new insight into the Eu^{2+}-trapped exciton luminescence in Y sites to obtain the deep-red to near-infrared luminescence, leading to new candidates for near-infrared applications, such as lighting, sensing, and bio-imaging devices.

Acknowledgements

We acknowledge Prof. Hiroyo Segawa in NIMS for XAS measurements. Work by Y.K. was financially supported by the Grant-In-Aid for JSPS Fellows (JP19J23280). This work was financially supported by JSPS Grant-in-Aid for Scientific Research on Innovative Areas "Mixed-Anion" (JP16H06441), NIMS NIMS Joint Research Hub Program, the Core Research for Evolutional Science and Technology (CREST, No. JPMJCR19J2) of JST, and JSPS Grant-in-Aid for Young Scientists (No. 21K14409). The XAS measurements have been performed under the approval of the Photon Factory Program Advisory Committee (No. 2020G105).

References

[1] K. Uheda, N. Hirosaki, Y. Yamamoto, A. Naito, T. Nakajima, H. Yamamoto, "Luminescence Properties of a Red Phosphor, $CaAlSiN_3:Eu^{2+}$, for White Light-Emitting Diodes". *Electrochem. Solid State Lett*. **9** (2006) H22–H25.

[2] R.-J. Xie, N. Hirosaki, T. Suehiro, F.-F. Xu, M. Mitomo, "A Simple, Efficient Synthetic Route to $Sr_2Si_5N_8:Eu^{2+}$-Based Red Phosphors for White Light-Emitting Diodes". *Chem. Mater.* **18** (2006) 5578–5583.

[3] H. Watanabe, H. Wada, K. Seki, M. Itou, N. Kijima, "Synthetic Method and Luminescence Properties of $Sr_xCa_{1-x}AlSiN_3:Eu^{2+}$ Mixed Nitride Phosphors". *J. Electrochem. Soc.* **155** (2008) F31–F36.

[4] P. Pust, V. Weiler, C. Hecht, A. Tücks, A.S. Wochnik, A.K. Henß, D. Wiechert, C. Scheu, P.J. Schmidt, W. Schnick, "Narrow-band red-emitting $Sr[LiAl_3N_4]:Eu^{2+}$ as a next-generation LED-phosphor material". *Nat. Mater.* **13** (2014) 891–896.

[5] S. Schmiechen, H. Schneider, P. Wagatha, C. Hecht, P.J. Schmidt, W. Schnick, "Toward new phosphors for application in illumination-grade white pc-LEDs: The nitridomagnesosilicates $Ca[Mg_3SiN_4]:Ce^{3+}$, $Sr[Mg_3SiN_4]:Eu^{2+}$, and $Eu[Mg_3SiN_4]$". *Chem. Mater.* **26** (2014) 2712–2719.

[6] T. Matsuzawa, Y. Aoki, N. Takeuchi, Y. Murayama, "A New Long Phosphorescent Phosphor with High Brightness, $SrAl_2O_4:Eu^{2+},Dy^{3+}$". *J. Electrochem. Soc.* **143** (1996) 2670–2673.

[7] J. Ueda, T. Shinoda, S. Tanabe, "Photochromism and near-infrared persistent luminescence in Eu^{2+}-Nd^{3+}-co-doped $CaAl_2O_4$ ceramics". *Opt. Mater. Express.* **3** (2013) 787–793.

[8] T. Kobayasi, S. Mroczkowski, J.F. Owen, L.H. Brixner, "Fluorescence lifetime and quantum efficiency for 5d → 4f transitions in Eu^{2+} doped chloride and fluoride crystals". *J. Lumin.* **21** (1980) 247–257.

[9] S.H.M. Poort, A. Meyerink, G. Blasse, "Lifetime measurements in Eu^{2+}-doped host lattices". *J. Phys. Chem. Solids.* **58** (1997) 1451–1456.

[10] P. Dorenbos, "Energy of the first $4f^7 \rightarrow 4f^6 5d$ transition of Eu^{2+} in inorganic compounds". *J. Lumin.* **104** (2003) 239–260.

[11] J. McKittrick, L.E. Shea-Rohwer, "Review: Down conversion materials for solid-state lighting". *J. Am. Ceram. Soc.* **97** (2014) 1327–1352.

[12] V. Rajendran, H. Chang, R.S. Liu, "(INVITED) Recent progress on broadband near-infrared phosphors-converted light emitting diodes for future miniature spectrometers". *Opt. Mater. X.* **1** (2019) 100011 (11p).

[13] J.J. Joos, D. Van der Heggen, L.I.D.J. Martin, L. Amidani, P.F. Smet, Z. Barandiarán, L. Seijo, "Broadband infrared LEDs based on europium-to-terbium charge transfer luminescence". *Nat. Commun.* **11** (2020) 3647 (11p).

[14] Y. Wei, P. Dang, Z. Dai, G. Li, J. Lin, "Advances in Near-Infrared Luminescent Materials without Cr^{3+}: Crystal Structure Design, Luminescence Properties, and Applications". *Chem. Mater.* **33** (2021) 5496–5526.

[15] W. Xie, W. Jiang, R. Zhou, J. Li, J. Ding, H. Ni, Q. Zhang, Q. Tang, J.-X. Meng, L. Lin, "Disorder-Induced Broadband Near-Infrared Persistent and Photostimulated Luminescence in $Mg_2SnO_4:Cr^{3+}$". *Inorg. Chem.* **60** (2021) 2219–2227.

[16] Q. Zhang, X. Wang, Z. Tang, Y. Wang, "A $K_3ScSi_2O_7:Eu^{2+}$ based phosphor with broad-band NIR emission and robust thermal stability for NIR pc-LEDs". *Chem. Commun.* **56** (2020) 4644–4647.

[17] J. Qiao, G. Zhou, Y. Zhou, Q. Zhang, Z. Xia, "Divalent europium-doped near-infrared-emitting phosphor for light-emitting diodes". *Nat. Commun.* **10** (2019) 5267 (7p).

[18] I.V. Berezovskaya, V.P. Dotsenko, A.S. Voloshinovskii, S.S. Smola, "Near infrared emission of Eu^{2+} ions in $Ca_3Sc_2Si_3O_{12}$". *Chem. Phys. Lett.* **585** (2013) 11–14.

[19] L. Zhou, P.A. Tanner, W. Zhou, Y. Ai, L. Ning, M.M. Wu, H. Liang, "Unique Spectral Overlap and

Resonant Energy Transfer between Europium(II) and Ytterbium(III) Cations: No Quantum Cutting". *Angew. Chem. Int. Ed.* **56** (2017) 10357–10361.

[20] Z. Tang, Q. Zhang, Y. Cao, Y. Li, Y. Wang, "Eu^{2+}-doped ultra-broadband VIS-NIR emitting phosphor". *Chem. Eng. J.* **388** (2020) 124231 (8p).

[21] N. Yamashita, "Coexistence of the Eu^{2+} and Eu^{3+} Centers in the CaO:Eu Powder Phosphor". *J. Electrochem. Soc.* **140** (1993) 840–843.

[22] L. Wang, R.-J. Xie, T. Suehiro, T. Takeda, N. Hirosaki, "Down-Conversion Nitride Materials for Solid State Lighting: Recent Advances and Perspectives". *Chem. Rev.* **118** (2018) 1951–2009.

[23] J. Schölch, T. Dierkes, D. Enseling, M. Ströbele, T. Jüstel, H.-J. Meyer, "Synthesis and Photoluminescence Properties of the Red-Emitting Phosphor $Mg_3(BN_2)N$ doped with Eu^{2+}". *Z. Anorg. Allg. Chem.* **641** (2015) 803–808.

[24] C. Poesl, W. Schnick, "Crystal Structure and Nontypical Deep-Red Luminescence of $Ca_3Mg[Li_2Si_2N_6]:Eu^{2+}$". *Chem. Mater.* **29** (2017) 3778–3784.

[25] P.F. Smet, J.E. Van Haecke, F. Loncke, H. Vrielinck, F. Callens, D. Poelman, "Anomalous photoluminescence in BaS:Eu". *Phys. Rev. B* **74** (2006) 035207 (9p).

[26] P. Dorenbos, Anomalous luminescence of Eu^{2+} and Yb^{2+} in inorganic compounds, *J. Phys. Condens. Matter.* **15** (2003) 2645 (22p).

[27] M. Grinberg, S. Mahlik, "Impurity trapped exciton states related to rare earth ions in crystals under high hydrostatic pressure". *Crystallogr. Rep.* **58** (2013) 139–143.

[28] Z. Barandiarán, L. Seijo, "Intervalence charge transfer luminescence: Interplay between anomalous and 5d-4f emissions in Yb-doped fluorite-type crystals". *J. Chem. Phys.* **141** (2014) 234704 (21p).

[29] C. MacKeen, F. Bridges, M. Kozina, A. Mehta, M.F. Reid, J.-P.R. Wells, Z. Barandiarán, "Evidence That the Anomalous Emission from $CaF_2:Yb^{2+}$ Is Not Described by the Impurity Trapped Exciton Model". *J. Phys. Chem. Lett.* **8** (2017) 3313–3316.

[30] Y. Kitagawa, J. Ueda, M.G. Brik, S. Tanabe, "Intense hypersensitive luminescence of Eu^{3+}-doped $YSiO_2N$ oxynitride with near-UV excitation". *Opt. Mater.* **83** (2018) 111–117.

[31] Y. Kitagawa, J. Ueda, K. Fujii, M. Yashima, S. Funahashi, T. Nakanishi, T. Takeda, N. Hirosaki, K. Hongo, R. Maezono, S. Tanabe, "Site-Selective Eu^{3+} Luminescence in the Monoclinic Phase of $YSiO_2N$". *Chem. Mater.* **33** (2021) 8873–8885.

[32] V. Viallet, J.-F. Marucco, J. Saint, M. Herbst-Ghysel, N. Dragoe, "Structural, magnetic and electrical properties of a perovskite containing divalent europium $EuZrO_3$". *J. Alloys Compd.* **461** (2008)

346–350.

[33] K. Momma, F. Izumi, "VESTA 3 for three-dimensional visualization of crystal, volumetric and morphology data". *J. Appl. Crystallogr.* **44** (2011) 1272–1276.

[34] B. Ravel, M. Newville, "*ATHENA*, *ARTEMIS*, *HEPHAESTUS*: data analysis for X-ray absorption spectroscopy using *IFEFFIT*". *J. Synchrotron Radiat.* **12** (2005) 537–541.

[35] J.A. Sampaio, M.C. Filadelpho, A.A. Andrade, J.H. Rohling, A.N. Medina, A.C. Bento, L.M. da Silva, F.C.G. Gandra, L.A.O. Nunes, M.L. Baesso, "Study on the observation of Eu^{2+} and Eu^{3+} valence states in low silica calcium aluminosilicate glasses". *J. Phys. Condens. Matter.* **22** (2010) 055601 (5p).

[36] G.Z. Cao, R. Metselaar, "α'-Sialon Ceramics: A Review". *Chem. Mater.* **3** (1991) 242–252.

[37] J.W.H. Van Krevel, J.W.T. Van Rutten, H. Mandal, H.T. Hintzen, R. Metselaar, "Luminescence Properties of Terbium-, Cerium-, or Europium-Doped α-Sialon Materials". *J. Solid State Chem.* **165** (2002) 19–24.

[38] R.-J. Xie, M. Mitomo, K. Uheda, F.-F. Xu, Y. Akimune, "Preparation and luminescence spectra of calcium- and rare-earth (R = Eu, Tb, and Pr)-codoped α-SiAlON ceramics". *J. Am. Ceram. Soc.* **85** (2004) 1229–1234.

[39] R.-J. Xie, N. Hirosaki, K. Sakuma, Y. Yamamoto, M. Mitomo, "Eu^{2+}-doped Ca-α-SiAlON: A yellow phosphor for white light-emitting diodes". *Appl. Phys. Lett.* **84** (2004) 5404–5406.

[40] R.-J. Xie, N. Hirosaki, M. Mitomo, Y. Yamamoto, T. Suehiro, K. Sakuma, "Optical Properties of Eu^{2+} in α-SiAlON". *J. Phys. Chem. B.* **108** (2004) 12027–12031.

[41] R.-J. Xie, N. Hirosaki, H.-L. Li, Y.Q. Li, M. Mitomo, "Synthesis and Photoluminescence Properties of β-sialon:Eu^{2+} ($Si_{6-z}Al_zO_zN_{8-z}$:Eu^{2+}): A Promising Green Oxynitride Phosphor for White Light-Emitting Diodes". *J. Electrochem. Soc.* **154** (2007) J314–J319.

[42] P. Dorenbos, "The $4f^n \leftrightarrow 4f^{n-1}5d$ transitions of the trivalent lanthanides in halogenides and chalcogenides". *J. Lumin.* **91** (2000) 91–106.

[43] P. Dorenbos, "f → d transition energies of divalent lanthanides in inorganic compounds". *J. Phys. Condens. Matter.* **15** (2003) 575–594.

[44] S. Mahlik, K. Wiśniewski, M. Grinberg, R.S. Meltzer, "Temperature and pressure dependence of the luminescence of Eu^{2+}-doped fluoride crystals $Ba_xSr_{1-x}F_2$ (x = 0, 0.3, 0.5 and 1): Experiment and model". *J. Phys. Condens. Matter.* **21** (2009) 245601 (12p).

[45] U. Happek, M. Aycibin, A.M. Srivastava, H. Comanzol, S. Camardello, "On the Luminescence of Octahedrally Coordinated Eu^{2+} in $CsCaF_3$". *ECS Trans.* **25** (2009) 39–43.

[46] D. Dutczak, C. Ronda, T. Jüstel, A. Meijerink, "Anomalous trapped exciton and d-f emission in $Sr_4Al_{14}O_{25}:Eu^{2+}$". *J. Phys. Chem. A* **118** (2014) 1617–1621.

[47] S. Mahlik, K. Wisniewski, M. Grinberg, H.J. Seo, "Luminescence of $LiBaF_3$ and $KMgF_3$ doped with Eu^{2+}". *J. Non-Cryst. Solids* **356** (2010) 1888–1892.

[48] J. Ueda, S. Tanabe, K. Takahashi, T. Takeda, N. Hirosaki, "Thermal Quenching Mechanism of $CaAlSiN_3:Eu^{2+}$ Red Phosphor". *Bull. Chem. Soc. Jpn.* **91** (2018) 173–177.

[49] P. Dorenbos, "The hole picture as alternative for the common electron picture to describe hole trapping and luminescence quenching". *J. Lumin.* **197** (2018) 62–65.

[50] M. Grinberg, "Impurity trapped excitons under high hydrostatic pressure". *Opt. Mater.* **35** (2013) 2006–2012.

[51] P. Dorenbos, "Modeling the chemical shift of lanthanide 4*f* electron binding energies". *Phys. Rev. B* **85** (2012) 165107 (10p).

[52] P. Dorenbos, "A Review on How Lanthanide Impurity Levels Change with Chemistry and Structure of Inorganic Compounds". *ECS J. Solid State Sci. Technol.* **2** (2012) R3001–R3011.

[53] P. Dorenbos, "Ce^{3+} 5d-centroid shift and vacuum referred 4f-electron binding energies of all lanthanide impurities in 150 different compounds". *J. Lumin.* **135** (2013) 93–104.

[54] P. Dorenbos, "Lanthanide 4f-electron binding energies and the nephelauxetic effect in wide band gap compounds". *J. Lumin.* **136** (2013) 122–129.

[55] Y. Kitagawa, J. Ueda, S. Tanabe, "Blue persistent phosphor of $YSiO_2N:Ce^{3+}$ developed by co-doping Sm^{3+} or Tm^{3+} ions and thermoluminescence analysis of their trap distributions". *Phys. Status Solidi A.* (2021) *in press.*

[56] P. Dorenbos, "Charge transfer bands in optical materials and related defect level location". *Opt. Mater.* **69** (2017) 8–22.

[57] T. Lyu, P. Dorenbos, "Charge carrier trapping processes in lanthanide doped $LaPO_4$, $GdPO_4$, YPO_4, and $LuPO_4$". *J. Mater. Chem. C* **6** (2018) 369–379.

[58] Z. Barandiarán, L. Seijo, "Quantum chemical analysis of the bond lengths in fn and $f^{n-1}d^1$ states of Ce^{3+}, Pr^{3+}, Pa^{4+}, and U^{4+} defects in chloride hosts". *J. Chem. Phys.* **119** (2003) 3785–3790.

[59] J.J. Joos, P.F. Smet, L. Seijo, Z. Barandiarán, "Insights into the complexity of the excited states of Eu-doped luminescent materials". *Inorg. Chem. Front.* **7** (2020) 871–888.

[60] W. Gryk, D. Dyl, W. Ryba-Romanowski, M. Grinberg, "Spectral properties of $LiTaO_3:Pr^{3+}$ under high hydrostatic pressure". *J. Phys. Condens. Matter.* **17** (2005) 5381–5395.

Chapter 6
Time-Resolved and Temperature-Dependent Spectroscopy for Blue Luminescence of Monoclinic $YSiO_2N:Ce^{3+}$ Phosphor

Abstract

The monoclinic $YSiO_2N$ activated with Ce^{3+} ions was synthesized, and its luminescence spectra were investigated to reveal the energy level structure of the Ce^{3+}: 5d excited states. Depending on excitation wavelengths, two types of photoluminescence bands in violet and blue regions are observed, which differ in spectral shapes and thermal quenching behaviors. While one of them can easily be assigned to the Ce^{3+}: $5d_1 \rightarrow {}^2F_{5/2}$, ${}^2F_{7/2}$ transitions from the major sites, the other shows an anomalously broad weak luminescence band for the latter band. The time-resolved spectroscopy shows a luminescence lifetime distribution of 33–58 ns in the range of 440–540 nm that is also typical for the Ce^{3+}: $5d_1$ levels. It is suggested that the broad luminescence bands and the distribution of Ce^{3+} luminescence lifetimes are due to various minor Ce^{3+} centers with slightly different coordination environments probably caused by intrinsic or anti-site anion defects. By analyzing the temperature dependence of decay curves for Ce^{3+}: 5d luminescence, the activation energy for thermal quenching and the quenching temperature are estimated to be 0.272 eV and 422 K, respectively. The vacuum-UV spectroscopy found out the five separated 5d excitation levels, leading to the estimated centroid energy of 5d levels, 33112 cm^{-1}.

6.1. Introduction

Ce^{3+} luminescence with the order of nanoseconds lifetime due to the 5d-4f parity allowed transition is very attractive, leading to multiple types of applications, such as LED phosphors [1,2], persistent phosphors [3,4], scintillators [5–7], and dosimeters [8]. The systematical investigation of luminescence properties in the various host compounds has revealed the relationship between the transition energies for Ce^{3+} ions and local environments. Ce^{3+}-doped phosphors based on the compounds with only one type of anions, such as oxides, halides, nitrides, and sulfides, have been widely investigated. As the field of materials exploration is rapidly expanding with improvements in the technologies for synthesis, compositional and structural analysis, and computational calculation, more and more researchers are focusing on mixed-anion compounds containing multiple kinds of anions in their composition [9]. In particular, oxynitrides have been widely studied for phosphor hosts because of their good chemical stability due to the covalency of nitrides and their relatively mild synthesis conditions [10]. Since Krevel *et al.* firstly reported the luminescent properties of Ce^{3+}-doped Y-Si-O-N materials in 1998 [11], many Ce^{3+}-doped oxynitrides, such as Ca-α-SiAlON:Ce^{3+} [12], La-Si-O-N:Ce^{3+} [13], β-SiAlON:Ce^{3+} [14], and $LaAl(Si_{6-z}Al_z)(N_{10-z}O_z)$:$Ce^{3+}$ [15], have been developed.

In this study, we have focused on an oxynitride host, $YSiO_2N$. The photoluminescence (PL) and photoluminescence excitation (PLE) spectra of the Ce^{3+}-doped $YSiO_2N$ were already reported [11,16]. In the literature, under near-UV excitation (λ_{ex} = ~360 nm), $YSiO_2N:Ce^{3+}$ shows blue luminescence in the range of 400–500 nm. In Krevels's report [11], it was suggested that relatively high N^{3-} content among the Y-Si-O-N materials brings about the large crystal field splitting and the bridging N^{3-} ions between $[SiO_2N_2]$ tetrahedra reduces the nephelauxetic effect to decrease the centroid shift of Ce^{3+}: 5d levels. Lu *et al.* characterized the PL and PLE spectra at 77, 150, 250, and 350 K and discussed the possible thermal quenching route of Ce^{3+} luminescence.

Recently, we reported the new monoclinic crystal structure of $YSiO_2N$ with the space group of *C*2/*c* through the single-crystal and neutron diffraction techniques [17]. In the monoclinic lattice, there are five crystallographically nonequivalent Y^{3+} sites with oxynitride

coordination of $[YO_6N_2]$. Although it has been thought that all Y^{3+} sites have C_1 symmetry in the previously known structure with the space group of *Pm* [18], in fact, they have either C_i, C_2, or C_1 symmetry. We discuss the luminescence properties of Ce^{3+}-doped $YSiO_2N$ affected by the local environments based on the new monoclinic crystal structure. In addition, we characterize the crystal field splitting of the Ce^{3+} 5d levels in $YSiO_2N$ by revealing all the 5d excitation bands.

6.2. Experimental Details

6.2.1. Preparation of Sample

A Ce^{3+}-doped yttrium silicon oxynitride sample with the composition of $Y_{0.995}SiO_2N:Ce^{3+}_{0.005}$ was prepared with the solid-state reaction method. The starting chemicals of Y_2O_3 (99.9%, Mitsuwa Chemical), SiO_2 (99.9%, Kojundo Chemical Laboratory), Si_3N_4 (99.9%, Kojundo Chemical Laboratory), and CeO_2 (99.99%, Furuuchi Chemical) were weighed in the glovebox filled with high-purity argon gas and mixed homogeneously in ethanol for an hour with the ball milling technique (Premium Line P-7, Fritsch). The obtained sully was dried at 120 °C for 24 h, formed into a pellet with a 20 mm diameter by pressing. The sample pellet was put between the BN pellets and laid in an alumina crucible. This crucible was put into another larger alumina crucible with carbon powder, and then the samples were sintered at 1600 °C for 24 h under nitrogen gas flow. The crystalline phase of the prepared sample was identified by the X-ray diffraction (XRD) with a diffractometer (Rigaku, Ultima IV). As a reference, the simulated diffraction pattern of the monoclinic $YSiO_2N$ was described with the VESTA program [17,19].

6.2.2. Characterization

Photoluminescence excitation (PLE) spectra at 4 and 300 K were measured by monochromatic excitation light with a 500 W Xe short arc lamp (OPM2-502XQ, Ushio Inc.) equipped with a double monochromator system by two monochromators (SP-300i, Acton Research Corp.), detected by using a photomultiplier tube (PMT) detector (R10699, Hamamatsu Photonics) coupled with a monochromator (SP-2300i, Princeton Instruments). The obtained PLE spectra were calibrated by the spectrum of the Xe lamp (light source) detected by a calibrated Si

photodiode (S1337-1010BQ, Bunkoukeiki Co., Ltd.). For photoluminescence (PL) measurements at various temperatures (T = 4, 80–600 K), the sample was excited by the monochromatic excitation light of the Xe lamp, and luminescence was detected with a CCD spectrometer (QE65Pro, Ocean Optics) connected with an optical fiber. The obtained PL spectra were calibrated by the spectrum of a deuterium-tungsten halogen light source (DH-2000, Ocean Optics). The sample temperatures were controlled by a cryostat with a closed-cycle He gas cryogenic refrigerator (CRT-A020-SE00, Ulvac Cryogenics) or a liquid nitrogen cryostat (VPF-800, Janis) at 4 K and 80–600 K.

The UV-VUV PLE spectra of the sample were collected under liquid helium cooling (10 K) at beamline BL3B of the UVSOR facility in the Institute for Molecular Science [20], with a PMT detector (R928, Hamamatsu Photonics) coupled with a monochromator (SP-2300i, Princeton Instruments).

The time-resolved PL spectrum and luminescence decay curves at various temperatures (T = 20–600 K) were measured by a luminescence lifetime spectrometer (Quantaurus-Tau, Hamamatsu Photonics), using a time-correlated single-photon counting (TCSPC) method under excitation with 340 and 280 nm pico-seconds LEDs. The sample temperature was controlled by a closed-cycle He cryostat (T = 20 K, Mini Stat CRT-006-2600, Iwatani) or a liquid nitrogen cryostat (T = 100–600 K, Helitran LT3, Advanced Research Systems).

6.3. Results

6.3.1. PL and PLE Spectra

The prepared $YSiO_2N:Ce^{3+}$ sample shows intense blue luminescence with near-UV excitation at room temperature and low temperatures. **Figure 6.1a** shows the normalized PL spectra of the $YSiO_2N:Ce^{3+}$ sample at 4 K with different excitation wavelengths (λ_{ex} = 250–350 nm). The whole spectral shape of PL bands for the $YSiO_2N:Ce^{3+}$ sample gradually changes with excitation wavelengths. The spectra seem to be composed of two luminescence centers; one is the split PL bands peaking at 400 and 427 nm in the range of 390–500 nm (PL-I), and the other is the

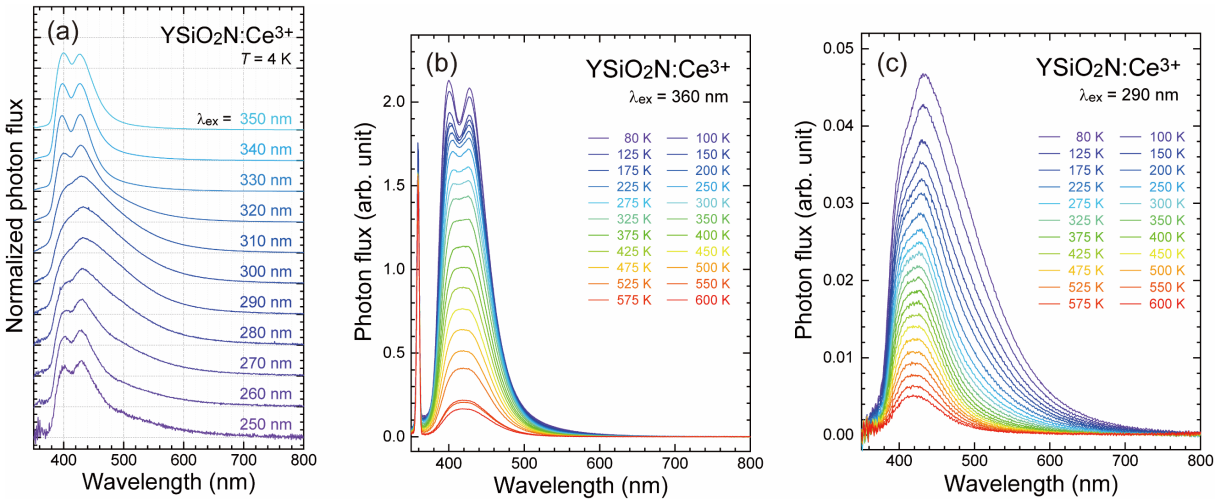

Figure 6.1. (a) Normalized PL spectra of the $YSiO_2N:Ce^{3+}$ sample at 4 K with different excitation wavelengths (λ_{ex} = 250–350 nm). (b),(c) PL spectra of the $YSiO_2N:Ce^{3+}$ sample at various temperatures (T = 80–600 K) with 360 and 290 nm excitation.

anomalously broad PL band peaking at 434 nm and extends to ~700 nm (PL-II).

Under 350 nm excitation light illumination, the split PL-I bands are mainly observed, showing a similar PL spectrum of Ce^{3+}-doped $YSiO_2N$ in literature [11,16]. As mentioned by Krevel *et al.* [11], these two luminescence bands are assigned to the Ce^{3+}: 5d → $^2F_{5/2}$ (400 nm, 25000 cm^{-1}) and $^2F_{7/2}$ (427 nm, 23419 cm^{-1}) transitions in the $YSiO_2N$ host.

As the excitation wavelength is changed from 350 to 250 nm, an additional PL-II band appears on the long-wavelength side of the PL-I bands. The PL-II band is dominant remarkably in the PL spectrum with 300 nm excitation, which has no splitting even at 4 K and whose tail reaches ~700 nm. The full width at half maximum (FWHM) of the PL-II band with λ_{ex} = 300 nm is ~6200 cm^{-1}. The maximum intensity of the PL-II band with 300 nm excitation is smaller than that of the PL-I bands, suggesting that the PL-II band can be originated from a given minor luminescence center.

Figures 6.1b and **6.1c** show the temperature dependence of PL spectra of the $YSiO_2N:Ce^{3+}$ sample with different excitation (λ_{ex} = 360 and 290 nm). Two luminescence centers bringing about PL-I and PL-II exhibit different behavior with respect to temperature. For the PL-I band shown in Figure 6.1b, the relative intensity ratio of the two luminescence bands attributed to the Ce^{3+}: $5d_1$ → 4f ($^2F_{5/2}$ and $^2F_{7/2}$) transition is mostly unchanged up to ~300 K, while the bands unite

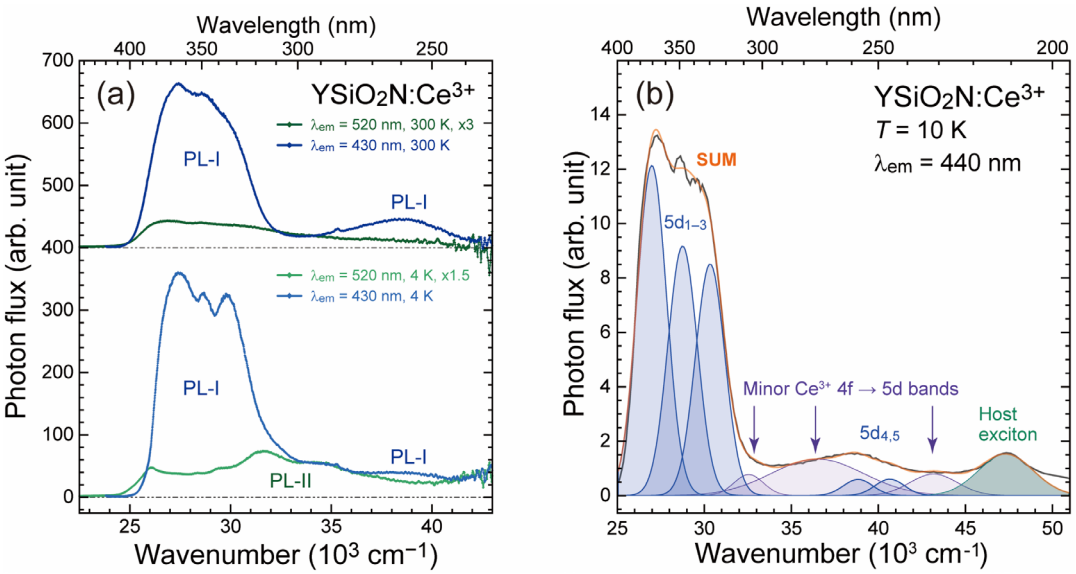

Figure 6.2. (a) PLE spectra of the $YSiO_2N:Ce^{3+}$ sample at 4 and 300 K, monitored with Ce^{3+} luminescence at 430 and 520 nm. (b) UV-VUV PLE spectrum of the $YSiO_2N:Ce^{3+}$ sample at 10 K, which is deconvoluted with multiple Gaussian functions (overshadowed).

into one because of the thermally induced broadening over ~300 K. The centroid of the PL-I bands is almost constant at 430–434 nm. On the other hand, the centroid of the PL band by 290 nm excitation gets largely blue-shifted from 473 to 444 nm.

Figure 6.2a shows the PLE spectra at 4 and 300 K, monitored with different luminescence bands (430 nm for PL-I and 520 nm for PL-II). The PLE spectra of the PL-I and PL-II are largely different. In the PLE spectrum of PL-I at 4 K, the PLE bands are observed at around 27500, 28500, 30000, 32000, 34000, and 39000 cm^{-1}. The PLE spectrum of PL-II shows main bands at 32000 and 34000 cm^{-1}. The PLE bands at around 27500, 28500, 30000, and 39000 cm^{-1}, which are observed only in the PLE spectrum monitored with 430 nm, can be assigned to the transition of the luminescence center showing PL-I. The difference between the PLE spectra with λ_{em} = 430 and 520 nm indicates that the excitation bands for the PL-II are located at around 32000 and 34000 cm^{-1}. In the PLE spectrum at 300 K monitored with 430 nm luminescence, the PLE bands correlated with the PL-II at around 32000 and 34000 cm^{-1} become weaker, supporting the assignment of the 5d excitation bands related to the PL-I.

With the PLE measurement setup with a Xe lamp, one cannot obtain reliable excitation spectra below ~250 nm because of the poor emission of the Xe arc lamp. In order to discuss the

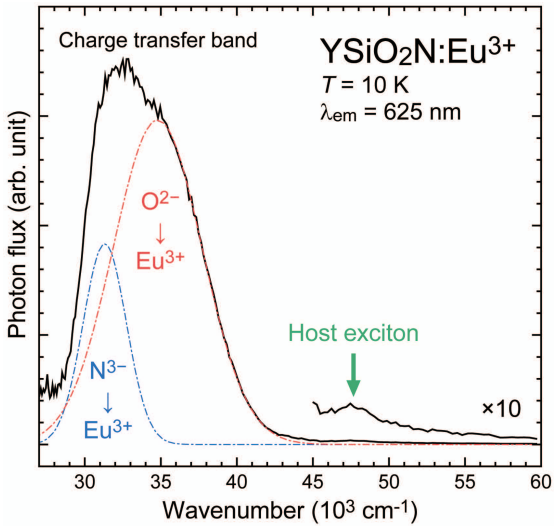

Figure 6.3. UV-VUV PLE spectrum of the $YSiO_2N:Eu^{3+}$ sample at 10 K. The broad excitation band was deconvoluted into two Gaussian profiles, assigned to the charge transfer transition from N^{3-} and O^{2-} to Eu^{3+} ions.

PLE spectra in the deep-UV to VUV region below 250 nm in detail, the UV-VUV PLE spectrum at 10 K was obtained and shown in **Figure 6.2b**. Compared with the PLE spectra shown in Figure 6.2a, an additional excitation band is observed at 47328 cm^{-1} (= 211 nm). This band is also observed in the PLE spectra of the Eu^{3+}-doped $YSiO_2N$ sample (**Figure 6.3**), suggesting that it is assigned to the absorption for the host exciton creation. The Gaussian fitting of the UV-VUV PLE spectra is discussed in section 6.4.2.

6.3.2. Time-Resolved PL Spectra and Luminescence Decay Curves

The luminescence decay curves and lifetimes of the $YSiO_2N:Ce^{3+}$ sample were investigated to characterize the PL-I and PL-II centers. **Figure 6.4a** shows the time-resolved PL spectrum of the sample at 20 K. The dominant broad luminescence band with a few tens of nanoseconds lifetime is observed in the contour plot. In the top panel of Figure 6.4a, the normalized integrated PL spectra with different integration time ranges Δt are shown. The PL spectrum with fast decay (Δt = 5–50 ns) exhibits a similar spectral shape with the PL spectrum with 360 nm excitation. Two peaks related to the terminal ^2F_J (J = 2/5 and 7/2) levels are distinctly observed. On the other hand, the luminescence bands with slow decay time are getting dominant in the spectra with the long delay-time (Δt = 150–200 and 250–300 ns), resulting in the same spectral shape as the PL-II bands with 300 nm excitation.

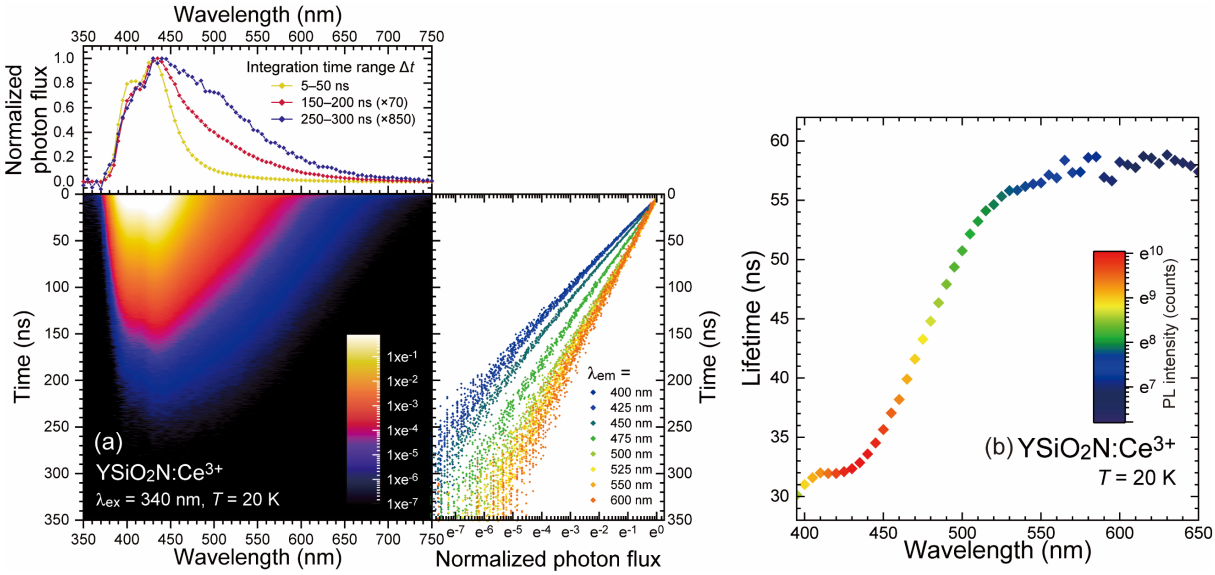

Figure 6.4. (a) Contour plot for time-resolved PL spectrum of the $YSiO_2N:Ce^{3+}$ sample at 20 K in the region of 350–750 nm. (Right panel) Luminescence decay curves monitored by different wavelengths (λ_{em} = 400–600 nm). (Top panel) Normalized integrated PL spectra with different integration time ranges. (b) Luminescence lifetimes at 20 K as a function of monitored wavelengths (λ_{em} = 400–650 nm). The maximum PL intensity of each decay curve is represented with a color map.

In the right panel of Figure 6.4a, the luminescence decay curves at 20 K with different monitored wavelengths (λ_{em} = 400–600 nm) are shown. Although all the decay curves show a single-exponential profile, their slope decreases gradually as the monitoring wavelength moves to the longer side. In order to estimate the luminescence lifetimes, all the decay curves are fitted with a single-exponential function. The obtained lifetimes are plotted in **Figure 6.4b** as a function of the monitoring wavelengths (λ_{em} = 400–650 nm). The luminescence lifetimes in the range of 350–400 and 650–750 nm could not be estimated with a relatively small error because the maximum PL intensities of the decay curves were below 500 counts. The decay curves in wavelength ranges of 400–650 nm are well fitted with small RMS errors. This lifetime plot can be divided into three parts in terms of luminescence lifetimes; (i) the first flat part with lifetimes of ~32 ns in 400–440 nm, (ii) the luminescence lifetime increasing from 33 to 56 ns in 440–540 nm, and (iii) the second flat part with lifetimes of 56–58 ns over 540 nm. The luminescence lifetimes in the range (i) of 32–33 ns are typical values for Ce^{3+} $5d_1 \rightarrow 4f$ luminescence. In the range (ii), the luminescence lifetimes increase linearly up to ~56 ns, even though they still show a first-order exponential profile. The lifetime distribution in the range (ii) suggests that the PL-

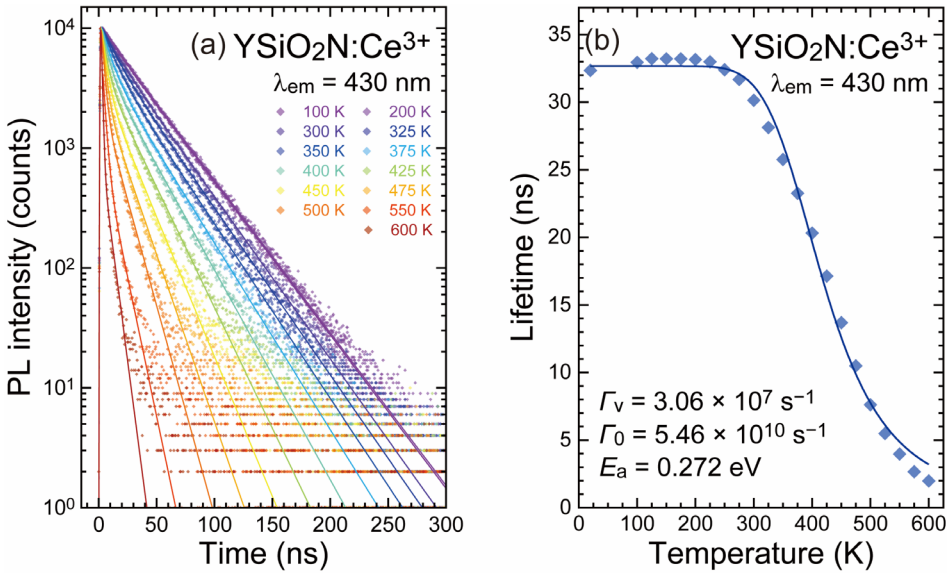

Figure 6.5. (a) Luminescence decay curves of the Ce^{3+} luminescence at various temperatures (T = 100–600 K), monitored with 430 nm. (b) Temperature dependence of luminescence lifetimes estimated by a second-order exponential function. The plots are fitted by the single barrier quenching model, described by eq. (3).

II band is composed of multiple luminescence centers with various decay rates. The luminescence lifetime finally reaches 56–58 ns and becomes unchanged in the range (iii), indicating that the luminescence band with the lowest energy is located at ~540 nm.

Figure 6.5a shows the decay curves of PL-I at various temperatures (T = 100–600 K, λ_{em} = 430 nm). The slope of the decay curve is almost unchanged below 300 K, and the decay rate increases with a temperature above 300 K. The decay profiles are not represented by the first-order exponential function, particularly for those above 400 K. All the luminescence decay curves are fitted with a second-order exponential function, described below;

$$I(t) = A_1 \exp\left(-t/\tau_1\right) + A_2 \exp\left(-t/\tau_2\right), \tag{6.1}$$

where A_1 and A_2 are amplitudes for each decay component and τ_1 and τ_2 are the luminescence lifetime at each temperature. The instrumental response function (IRF) was taken into account for each fitting. The average luminescence lifetime of the $5d_1$ excited state at each temperature τ_{ave} was calculated by the following equation;

$$\tau_{ave} = \frac{A_1{\tau_1}^2 + A_2{\tau_2}^2}{A_1\tau_1 + A_2\tau_2}. \tag{6.2}$$

The average lifetime at each temperature (T = 100–600 K) is plotted against temperature

and shown in **Figure 6.5b**. The lifetime of the PL-I shows the typical temperature dependence, fitted with the single barrier quenching model described in the following equation;

$$\tau_{ave} = \frac{1}{\Gamma_\nu + \Gamma_0 \exp\left(-E_a / kT\right)}, \tag{6.3}$$

where Γ_ν is the radiative transition rate, Γ_0 is the attempt rate of the nonradiative process, E_a is the activation energy of thermal quenching, k is the Boltzmann constant (= 0.695 $cm^{-1}\cdot K^{-1}$), and T is temperature. The quenching curve was well fitted with $\Gamma_\nu = 3.06 \times 10^7$ s^{-1} and $\Gamma_0 = 5.46 \times 10^{10}$ s^{-1}. The activation energy E_a and the quenching temperature $T_{50\%}$, at which the lifetime is half of the initial one, were estimated to be 0.272 eV and 422 K, respectively.

The temperature dependence of the decay curves for the PL-II is displayed in **Figure 6.6**. The PL-II center shows a decrease in the decay rate even at 100 K. The slope of the decay curves over 300 K is no longer described by a second-order exponential function, suggesting that multiple luminescence centers with various luminescence energies and thermal activation energies are related to the PL-II band. Because of the complicated decay profiles, the lifetimes of the PL-II were not estimated.

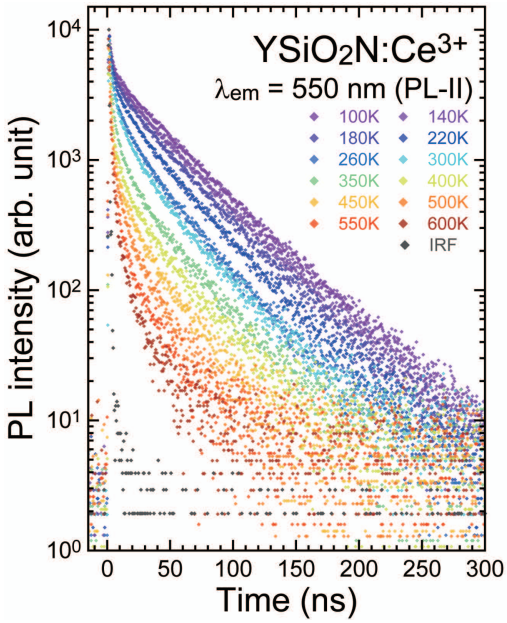

Figure 6.6. Luminescence decay curves of the Ce^{3+} luminescence at various temperatures (T = 100–600 K), monitored with 550 nm.

6.4. Discussion

6.4.1. Identification of PL-I and PL-II Centers

As we mentioned in the results section, the luminescence bands peaking at 400 and 427 nm are assigned to the Ce^{3+}: 5d → 4f ($^2F_{5/2}$ and $^2F_{7/2}$) luminescence in the $YSiO_2N$ host. However, in the PL spectra of the $YSiO_2N:Ce^{3+}$ sample, there are two unclear points; (1) the origin of the broad PL-II band and (2) the difference in Ce^{3+} luminescence at the nonequivalent Y^{3+} sites. In this section, we discuss and identify the PL-I and PL-II centers in the $YSiO_2N:Ce^{3+}$ sample.

First, we consider the origin of the PL-II from the PL spectra (Figure 6.1) and time-resolved PL spectrum (Figure 6.4). One possible assignment of the PL-II band is the Ce^{3+} luminescence at Y^{3+} sites with different site symmetry. In the monoclinic lattice of $YSiO_2N$, there are five nonequivalent Y^{3+} sites with C_1 (Wyckoff 8*f*), C_2 (Wyckoff 4*e*), and C_i (Wyckoff 4*a*) symmetry stemming from the difference in N–Y–N bond angles [17]. Ce^{3+} ions at different Y^{3+} sites can show various PL spectra depending on the crystal field strength. However, because all the Y^{3+} sites have a similar local environment consisting of a $[Y^{3+}O_6N_2]$ dodecahedron, it is less likely to result in the weak, broad, and redshifted PL-II band without the ^2F_J (J = 5/2 and 7/2) splitting. Thus, a different luminescence center can be generated in the $YSiO_2N$ matrix other than Ce^{3+} ions showing typical 5d → 4f luminescence in $[Y^{3+}O_6N_2]$ dodecahedra.

Luminescence lifetime can provide an important clue for the identification of luminescence centers. The time-resolved PL spectrum of the non-doped $YSiO_2N$ sample at 300 K is shown in chapter 5. A broad luminescence band peaking at around 560 nm is observed, whose lifetime is estimated to be 3.61 ns. The time-resolved PL spectrum of the $YSiO_2N:Ce^{3+}$ sample at 20 K reveals that the PL-II lifetime takes various values of 33–58 ns for different monitored wavelengths, which is quite long for the luminescence related to some intrinsic defects as observed in the non-doped sample. These observed lifetimes are in the typical values of the Ce^{3+}: 5d → 4f luminescence (17–65 ns) in a variety of inorganic host compounds, depending on the local structure, wavelength, or refractive index [21,22]. Considering the luminescence lifetimes below 60 ns in the range of 440–650 nm, the PL-II band can be assigned to the Ce^{3+}: 5d → 4f transition as well as the PL-I. As mentioned above, the PL-II band cannot be

assigned to the Ce^{3+} luminescence in $[Y^{3+}O_6N_2]$ dodecahedra because of the weak PL intensity and anomalous spectral shape without splitting even at 4 K. Thus, it is suggested that Ce^{3+} ions related to the PL-II are incorporated in some minor sites that are not the major $[Y^{3+}O_6N_2]$ dodecahedra. The XRD pattern of the sample shows no peak of an impurity phase or no halo of an amorphous phase. One possible minor site is a dodecahedron with defects. The crystal structure analysis with neutron diffraction for the non-doped $YSiO_2N$ indicated that the anion anti-site defects $O_N^{\cdot}$ and $N_O^{\prime}$ are generated through the sintering process under the reduction atmosphere [17]. In the monoclinic lattice of $YSiO_2N$, O^{2-} and N^{3-} ions are arranged at six and three different sites, respectively; that is, disordered intrinsic defects or anion anti-site defects forming a $[Ce^{3+}O_6N\square]$, $[Ce^{3+}O_5\square N_2]$, $[Ce^{3+}O_7N]$, or $[Ce^{3+}O_5N_3]$ dodecahedron can provide a variety of ligand fields, resulting in the very broad luminescence band and lifetime distribution of PL-II.

Considering that the PL-II is caused not by $[Ce^{3+}O_6N_2]$ dodecahedron with different site-symmetry but by minor Ce dodecahedra with some defects, the Ce^{3+} ions at any $[Y^{3+}O_6N_2]$ dodecahedra show similar luminescence properties, including the spectral shapes and the luminescence lifetimes, despite different site-symmetry, resulting in the PL-I bands. The luminescence bands of the Ce^{3+} ions incorporated in the various Y^{3+} sites with C_1, C_2, and C_i symmetry severely overlap in the PL spectra shown in Figure 6.1a. In the monoclinic $YSiO_2N$, the C_1, C_2, and C_i sites have similar bond lengths and the same anion composition (six O^{2-} and two N^{3-} ions), possibly leading to the similar crystal field splitting of Ce^{3+}: 5d levels. Therefore, the Ce^{3+} ions in the different Y^{3+} sites are unidentified, and the PL-I properties can be regarded as the average of the $[Ce^{3+}O_6N_2]$ centers, regardless of the site-symmetry of dodecahedra.

6.4.2. Characterization of 5d → 4f Luminescence of $[Ce^{3+}O_6N_2]$ Dodecahedra

Based on the assignment of the excitation bands mentioned above, the UV-VUV PLE spectrum (Figure 6.2b) was deconvoluted into nine Gaussian profiled, including five 5d bands for the major $[Ce^{3+}O_6N_2]$ center, three bands for Ce^{3+} ions in minor sites with anion defects, and a host exciton band. While the major Ce^{3+} ions related to the PL-I show the distinct structure of the 5d levels, the structure of the excited states for the minor Ce^{3+} ions is ambiguous due to the complex

site variation caused by nonstoichiometric defects. The Ce^{3+}: 5d excitation bands were successfully resolved into five PLE bands with the same width of 1691 cm^{-1}, peaking at 26985, 28754, 30335, 38835, and 40651 cm^{-1} (= 3.346, 3.565, 3.761, 4.815, and 5.040 eV). The crystal field splitting of the $YSiO_2N:Ce^{3+}$ was calculated to be 13666 cm^{-1} (= 1.694 eV) from these 5d energy levels, which is a typical value for the eight-fold coordination [23,24]. From the mean value of these 5d excited levels, the centroid energy was calculated to be 33112 cm^{-1} (= 4.11 eV). In the previous study, Krevel *et al.* estimated the Ce^{3+} centroid energy in $YSiO_2N$ of 38000–40000 cm^{-1} with a non-experimental assumption based on the site symmetry [11]. However, all the Y^{3+} had been considered to take C_1 symmetry because they assumed a different crystal structure of $YSiO_2N$ (space group: *Pm*), leading to a large Ce^{3+}: 5d centroid energy. On the other hand, Dorenbos calculated the Ce^{3+}: 5d centroid energy in the $LaSiO_2N$ host of 32900 cm^{-1} (= 4.08 eV) from the experimentally obtained PLE spectrum [25,26]. Considering these experimental facts, the estimated Ce^{3+} centroid energy of 33112 cm^{-1} is reasonable. The Ce^{3+}: 5d centroid shift is affected by the nephelauxetic effect depending on ligand species [27]. One can expect small centroid energy in a covalent host, such as nitrides, sulfides, and selenides [26]. Considering the centroid energy of 6.35 eV in free ion state, the centroid shift ε_c of the $YSiO_2N:Ce^{3+}$ sample is estimated to be 2.24 eV, which is roughly in the middle between the ε_c values of oxides (0.876–2.589 eV) and nitrides (2.26–3.42 eV) [26,28,29]. Despite N^{3-} coordination, the ε_c of the $YSiO_2N:Ce^{3+}$ is smaller than that of Ce^{3+}-doped nitrides because of the partial coordination of O^{2-} ions and the covalent bonding between N^{3-} and Si^{4+} ions. In particular, N^{3-} ions are bridging between the $[SiO_2N_2]$ tetrahedra, forming the $[Si_3O_6N_3]$ ring units. The electrons of N^{3-} ions are mainly localized on the six-membered ring of the $[Si_3O_6N_3]$ unit. As a result, the contribution of covalent N^{3-} ions to a Ce^{3+} ion can weaken, leading to the ε_c value of 2.24 eV that is the middle of oxides and nitrides.

6.5. Conclusions

Luminescence properties of Ce^{3+} ions in the monoclinic $YSiO_2N$ host were investigated at the wide temperature range of 4–600 K. The photoluminescence spectra showed the minor luminescence component besides the typical Ce^{3+} luminescence, depending on excitation wavelengths. The time-resolved spectroscopy revealed that the minor luminescence center took the distribution of luminescence lifetime of 34–58 ns, which is typical for Ce^{3+}: 5d → 4f transition. The results suggested that the minor luminescence was assigned to the Ce^{3+} luminescence in some Y^{3+} sites with intrinsic anion defects. By taking the contribution of this minor Ce^{3+} luminescence into account, Ce^{3+} luminescence in the $[YO_6N_2]$ dodecahedra was characterized. Despite the site-symmetry, Ce^{3+} ions in the five nonequivalent Y sites showed almost the same properties and were not identified due to the structural similarity of the $[YO_6N_2]$ dodecahedra. The temperature dependence of luminescence lifetimes provided the activation energy for thermal quenching of 0.272 eV. All the 5d ← 4f excitation bands of Ce^{3+} ions in the $[YO_6N_2]$ dodecahedra were observed with the vacuum-UV spectroscopy, leading to the crystal field splitting of 13666 cm^{-1} and centroid energy of 33112 cm^{-1}.

Acknowledgements

Work by Y.K. was financially supported by the Grant-In-Aid for JSPS Fellows (JP19J23280). This work was supported by JSPS Grant-in-Aid for Scientific Research on Innovative Areas "Mixed-Anion" (JP16H06441). The UV-VUV spectroscopy was performed at the UVSOR facility under the Joint Science Program (Project number: 30-822, BL-3B) of the Institute for Molecular Science.

References

[1] G. Blasse, A. Bril, "A new phosphor for flying-spot cathode-ray tubes for color television: Yellow-emitting $Y_3Al_5O_{12}$-Ce^{3+}". *Appl. Phys. Lett.* **11** (1967) 53–55.

[2] K. Bando, K. Sakano, Y. Noguchi, Y. Shimizu, "Development of High-bright and Pure-white LED Lamps". *J. Light Visual Environ*. **22** (1998) 2–5.

[3] J. Ueda, K. Kuroishi, S. Tanabe, "Bright persistent ceramic phosphors of Ce^{3+}-Cr^{3+}-codoped garnet able to store by blue light". *Appl. Phys. Lett.* **104** (2014) 101904 (4p).

[4] K. Van den Eeckhout, D. Poelman, P.F. Smet, "Persistent Luminescence in Non-Eu^{2+}-Doped Compounds: A Review". *Materials* . **6** (2013) 2789–2818.

[5] C.L. Melcher, J.S. Schweitzer, "A promising new scintillator: cerium-doped lutetium oxyorthosilicate". *Nucl. Instrum. Methods Phys. Res. A*. **314** (1992) 212–214.

[6] A. Lempicki, M.H. Randles, D. Wisniewski, M. Balcerzyk, C. Brecher, A.J. Wojtowicz, "$LuAlO_3$:Ce and other aluminate scintillators". *IEEE Trans. Nucl. Sci.* **42** (1995) 280–284.

[7] M. Nikl, E. Mihoková, J.A. Mareš, A. Vedda, M. Martini, K. Nejezchleb, K. Blažek, "Traps and timing characteristics of LuAG:Ce^{3+} scintillator". *Phys. Status Solidi A* **181** (2000) R10–R12.

[8] E.G. Yukihara, E.D. Milliken, B.A. Doull, "Thermally stimulated and recombination processes in MgB_4O_7 investigated by systematic lanthanide doping". *J. Lumin.* **154** (2014) 251–259.

[9] H. Kageyama, K. Hayashi, K. Maeda, J.P. Attfield, Z. Hiroi, J.M. Rondinelli, K.R. Poeppelmeier, "Expanding frontiers in materials chemistry and physics with multiple anions". *Nat. Commun.* **9** (2018) 772 (15p).

[10] R.-J. Xie, N. Hirosaki, "Silicon-based oxynitride and nitride phosphors for white LEDs—A review". *Sci. Technol. Adv. Mater.* **8** (2007) 588–600.

[11] J.W.H. van Krevel, H.T. Hintzen, R. Metselaar, A. Meijerink, "Long wavelength Ce^{3+} emission in Y–Si–O–N materials". *J. Alloys Compd.* **268** (1998) 272–277.

[12] J.W.H. van Krevel, J.W.T. van Rutten, H. Mandal, H.T. Hintzen, R. Metselaar, "Luminescence properties of terbium-, cerium-, or europium-doped α-sialon materials". *J. Solid State Chem.* **165** (2002) 19–24.

[13] B. Dierre, R.-J. Xie, N. Hirosaki, T. Sekiguchi, "Blue emission of Ce^{3+} in lanthanide silicon oxynitride phosphors". *J. Mater. Res.* **22** (2007) 1933–1941.

[14] L. Liu, R.-J. Xie, N. Hirosaki, T. Takeda, C.-N. Zhang, J. Li, X. Sun, "Optical properties of blue-emitting $Ce_xSi_{6-z}Al_{z-x}O_{z+1.5x}N_{8-z-x}$ for white light-emitting diodes". *J. Electrochem. Soc.* **157** (2010) H50–H54.

[15] K. Takahashi, M. Harada, K.-I. Yoshimura, H. Fukunaga, Y. Tomomura, N. Hirosaki, R.-J. Xie, "Improved Photoluminescence of Ce^{3+} Activated $LaAl(Si_{6-z}Al_z)(N_{10-z}O_z)$ (z~1) Blue Oxynitride Phosphors by Calcium Co-Doping". *ECS J. Solid State Sci. Technol.* **1** (2012) R109–R112.

[16] F. Lu, L. Bai, Z. Yang, Q. Liu, "Photoluminescence properties of Ce^{3+} doped $YSiO_2N$ blue-emitting phosphors". *J. Rare Earths.* **30** (2012) 851–855.

[17] Y. Kitagawa, J. Ueda, K. Fujii, M. Yashima, S. Funahashi, T. Nakanishi, T. Takeda, N. Hirosaki, K. Hongo, R. Maezono, S. Tanabe, "Site-Selective Eu^{3+} Luminescence in the Monoclinic Phase of $YSiO_2N$". *Chem. Mater.* **33** (2021) 8873–8885.

[18] P.E.D. Morgan, P.J. Carroll, F.F. Lange, "Crystal structure of $YSiO_2N$ and a reappraisal of the "vaterite" type, YBO_3". *Mater. Res. Bull.* **12** (1977) 251–259.

[19] K. Momma, F. Izumi, "VESTA 3 for three-dimensional visualization of crystal, volumetric and morphology data". *J. Appl. Crystallogr.* **44** (2011) 1272–1276.

[20] K. Fukui, R.I. Ikematsu, Y. Imoto, M. Kitaura, K. Nakagawa, T. Ejima, E. Nakamura, M. Sakai, M. Hasumoto, S.I. Kimura, "Design and performance of a new VIS-VUV photoluminescence beamline at UVSOR-III". *J. Synchrotron Radiat.* **21** (2014) 452–455.

[21] L.-J. Lyu, D.S. Hamilton, "Radiative and nonradiative relaxation measurements in Ce^{3+} doped crystals". *J. Lumin.* **48–49** (1991) 251–254.

[22] C.K. Duan, M.F. Reid, "Local field effects on the radiative lifetimes of Ce^{3+} in different hosts". *Curr. Appl. Phys*. **6** (2006) 348–350.

[23] P. Dorenbos, "Crystal field splitting of lanthanide $4f^{n-1}5d$-levels in inorganic compounds". *J. Alloys Compd*. **341** (2002) 156–159.

[24] S. Wang, Z. Song, Y. Kong, Z. Xia, Q. Liu, "Crystal field splitting of $4f^{n-1}5d$-levels of Ce^{3+} and Eu^{2+} in nitride compounds". *J. Lumin.* **194** (2018) 461–466.

[25] H. Long, X. Xue-Wen, L. Zun-Ming, F. Ying, L. Yang-Xian, T. Cheng-Chun, "Luminescence of Ce^{3+} in lanthanum silicon oxynitride". *Chin. Physics B.* **19** (2010) 127807 (5p).

[26] P. Dorenbos, "Ce^{3+} 5d-centroid shift and vacuum referred 4f-electron binding energies of all lanthanide impurities in 150 different compounds". *J. Lumin.* **135** (2013) 93–104.

[27] P. Dorenbos, "Energy of the first $4f^7 \rightarrow 4f^6 5d$ transition of Eu^{2+} in inorganic compounds". J. Lumin. 104 (2003) 239–260.

[28] S. Wang, Z. Song, Y. Kong, Z. Xia, Q. Liu, "5d-level centroid shift and coordination number of Ce^{3+} in nitride compounds". J. Lumin. 200 (2018) 35–42.

[29] Y. Zhuo, S. Hariyani, S. You, P. Dorenbos, J. Brgoch, "Machine learning 5d-level centroid shift of Ce^{3+} inorganic phosphors". J. Appl. Phys. 128 (2020) 013104 (7p).

Chapter 7

Blue Persistent Phosphor of $YSiO_2N:Ce^{3+}$ Developed by Co-doping Sm^{3+} or Tm^{3+} Ions and Thermoluminescence Analysis of Their Trap Distributions

Abstract

By estimating the trap depth from the relative position of the zigzag curve of divalent lanthanoid ions and conduction band bottom, the $YSiO_2N:Ce^{3+}$-based blue persistent phosphors are developed, and their persistent luminescence and thermoluminescence properties are characterized to identify the electron trap distributions. Taking the nephelauxetic effect caused by covalent nitrogen into account for the vacuum referred binding energy diagram, it is predicted that Tm^{3+} and Sm^{3+} ions with the trap depth of 0.726 and 1.04 eV are an optimal co-dopant to obtain Ce^{3+} persistent luminescence. The prepared $YSiO_2N:Ce^{3+}$-Ln^{3+} (Ln = Sm or Tm) samples enhance the Ce^{3+}: 5d → 4f blue persistent luminescence intensity. In the thermoluminescence glow curves, the Ce^{3+} singly-doped sample shows two glow peaks related to intrinsic defects; on the other hand, the Ln^{3+} co-doped samples show an additional glow peak related to the Ln^{3+}-traps. The thermoluminescence glow curve analyses through the initial rise method combined with the thermal cleaning and trap density methods reveal that the electron traps of Ln^{3+}-related defects have a distribution with ~0.25 eV width and depths of 0.802 eV (Tm^{3+}) and 1.10 eV (Sm^{3+}).

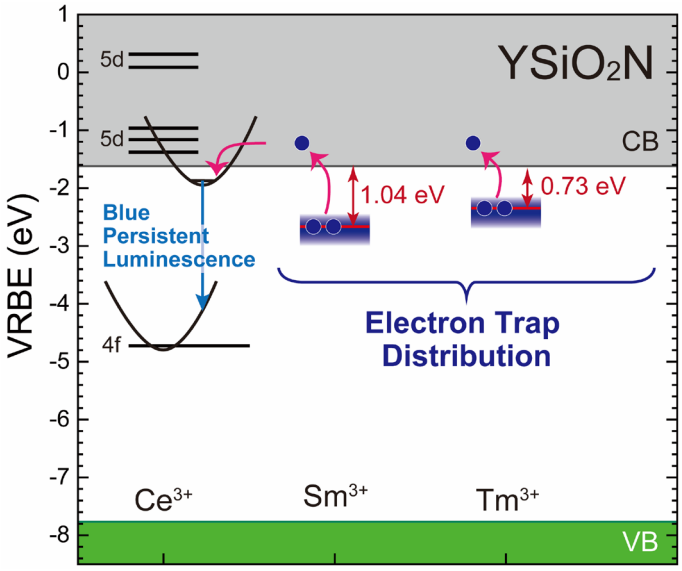

7.1. Introduction

Persistent phosphors are unique luminescent materials, which show long-lasting luminescence after ceasing excitation light illumination. They have been applied to luminous paints for the face of watches and safety signs from several decades ago [1]. Recently, researchers have recognized potentials for various applications, such as bio-imaging [2–5], and reducing flickering in AC-driven LEDs [6–8], leading to the expanded research field of persistent phosphors [8]. A representative example of persistent phosphors is $SrAl_2O_4:Eu^{2+}$-Dy^{3+} [9] or $Y_3Al_2Ga_3O_{12}:Ce^{3+}$-$Cr^{3+}$ [10,11], which show persistent luminescence (PersL) with more than ten hours duration. These persistent phosphors are characterized by very high luminance (unit: mcd m^{-2}) because of their luminescence at the green region, which is very sensitive to the cone cell of human eyes [1]. On the other hand, the blue persistent phosphor, such as $CaAl_2O_4:Eu^{2+}$-Nd^{3+} [9], is suitable for the rod cell of human eyes, which mainly works after adoption to a dark environment. In terms of the luminescence efficiency, Ce^{3+} ions are very attractive because of their parity allowed 5d → 4f transition with a high radiative rate. However, many Ce^{3+}-activated oxide (persistent) phosphors show near-UV to blue luminescence unless the Ce^{3+} ions are incorporated in a strong crystal field, namely in the garnet-type structure, resulting in luminescence with low luminance. In order to obtain the practical Ce^{3+}-activated persistent phosphors, the redshift of Ce^{3+} luminescence bands is required through ligand field engineering related to ligand species and the shape of coordination polyhedra. The oxynitride coordination can form a promising ligand field to bring the redshift of Ce^{3+}: 5d → 4f luminescence because of two features below; (1) a large centroid shift caused by the large nephelauxetic effect due to covalent nitrogen, and (2) a large crystal field splitting derived from a distortion induced by mixed-anion coordination with O^{2-} and N^{3-} ions. Although the Ce^{3+} luminescence in oxynitride hosts has been reported in the literature [12–15], there is no report about Ce^{3+}-activated persistent phosphor with oxynitride composition as far as we know. In contrast, one can find a variety of Eu^{2+}-activated persistent phosphors in literature [16].

The PersL in the Ce^{3+}-activated phosphors takes place through the electron trapping-detrapping scheme [1]. For Ce^{3+}-activated phosphors, upon being excited through the 5d ← 4f

transition, the holes are localized on the Ce^{3+} 4f level with the formal valence change, $Ce^{3+} \rightarrow Ce^{4+} + e^-$, because the hole-capturing state Ce^{4+} is relatively stable. The excited electrons are captured simultaneously with proper trapping levels related to impurities. The trapped electrons are released by thermal energy *via* the host conduction band (CB) to the hole-trapped Ce^{3+} (*i.e.,* Ce^{4+}) at a rate on the order of minutes to hours. This electron detrapping process is the rate-determining step, leading to Ce^{3+}: 5d → 4f PersL. The duration of PersL depends on the electron trap depth, an energy gap between the CB bottom and the trapping levels. Therefore, in order to develop a persistent phosphor with a long duration, it is necessary to schematically investigate the relationship between the CB bottom and energy levels for impurity lanthanoid ions. One can predict the proper co-dopant lanthanoid species by applying the semi-empirical model proposed by Dorenbos [17–20]. The vacuum referred binding energy (VRBE) diagram, constructed by the spectroscopic parameters, reveals the relative positions of the CB bottom, valence band (VB) top, and 4f ground levels of divalent and trivalent lanthanoid ions. By applying this VRBE diagram, some persistent phosphors, such as $Ca_3Si_2O_7:Eu^{2+}$-Ln^{3+} (*Ln* = Sm or Tm) [21], Li*RE*(Si,Ge)O_4:Ln^{3+}-Tm^{3+} (*RE* = Y, Lu / *Ln* = Ce, Pr, Tb) [22], and $Gd_3Ga_5O_{12}:Pr^{3+}$-Tb^{3+}-Eu^{3+} [23], have been successfully developed, and their PersL properties have been characterized.

In this study, we have focused on an oxynitride $YSiO_2N$ with a monoclinic lattice for the host compound of a Ce^{3+} persistent phosphor. In fact, Ce^{3+}-doped $YSiO_2N$ shows blue luminescence peaking at 400 and 427 nm, whose redshift is not so large and is not the best material in terms of luminance, but it is suitable for the dark-adapted eyes [12,24]. However, there are only a few examples of persistent phosphor designs based on the VRBE diagram for oxynitrides [25–28]. In addition, recently, Dorenbos reported a composition dependence on the Ln^{2+} and Ln^{3+} ground levels and argued that the nephelauxetic effect, depending on the polarizability of the coordinating anion species, has to be taken into account in the Ln^{2+}/Ln^{3+} zigzag curves [29,30]. Therefore, the VRBE diagram for covalent materials, including oxynitrides, should be investigated in terms of the correlation between the trap depths estimated from the VRBE diagram and the experimental results. We predict the optimal electron trap

centers Ln^{3+} for Ce^{3+} PersL in $YSiO_2N$ from the VRBE diagram constructed by the spectroscopic data and investigate the electron trap distributions in the host bandgap through the characterization of Ce^{3+} PersL and thermoluminescence (TL). The electron trap depths and trap densities are estimated experimentally by the TL glow curve analyses with the combination of the thermal cleaning (TC) and initial rise methods (IRM) [31].

7.2. Experimental Section

7.2.1. Materials and Synthesis Procedures

A series of yttrium silicon oxynitride samples with the composition of $Y_{0.995}SiO_2N:Ce^{3+}_{0.005}$, and $Y_{0.994}SiO_2N:Ce^{3+}_{0.005}$-$Ln^{3+}_{0.001}$ (Ln = Sm or Tm), were prepared by the solid-state reaction method. Hereinafter, each sample is denoted as $YSiO_2N:Ce^{3+}$, and $YSiO_2N:Ce^{3+}$-Ln^{3+}, respectively. The starting chemicals of Y_2O_3 (99.9%, Kojundo Chemical Laboratory), SiO_2 (99.9%, Kojundo Chemical Laboratory), Si_3N_4 (99.9%, Kojundo Chemical Laboratory), CeO_2 (99.99%, Furuuchi Chemicals), Sm_2O_3 (99.9%, Mitsuwa Chemicals), and Tm_2O_3 (99.9%, Mitsuwa Chemicals) were weighed in the glove box filled with high-purity argon gas and mixed homogeneously in ethanol for one hour with the ball milling technique (Premium Line P-7, Fritsch). The mixture was dried at 120 °C for 24 h, formed into a pellet with a 20 mm diameter by pressing. The sample pellets were put between the BN pellets and laid in an alumina crucible. This crucible was put into another larger alumina crucible with carbon powder, and then the samples were sintered at 1600 °C for 24 h under nitrogen gas flow. The crystalline phase of the prepared samples was identified by the X-ray diffraction (XRD) with a diffractometer (Rigaku, Ultima IV). The XRD patterns are shown in **Figure 7.1**. As a reference, the simulated diffraction pattern of the monoclinic $YSiO_2N$ was described with the VESTA program [32,33].

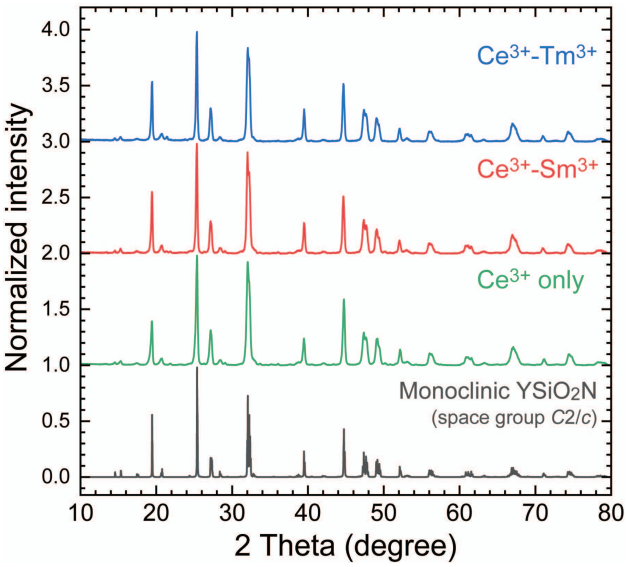

Figure 7.1. XRD patterns of the prepared samples with the reference data of monoclinic $YSiO_2N$.

7.2.2. Characterization

For the photoluminescence (PL) and PersL measurements at room temperature, the samples were excited by a 325 nm He-Cd laser (IK3452R-F, Kinmon Koha), and the luminescence of the samples was detected with a CCD spectrometer (QE65Pro, Ocean Optics) connected with an optical fiber. In the case of PersL measurements, the signal was obtained 10 s after the excitation illumination ceased for 10 s. The obtained spectra were calibrated by the spectrum of a calibrated deuterium-tungsten halogen light source (DH-2000, Ocean Optics). The PersL decay curves of the samples were obtained at room temperature with a photomultiplier tube (PMT) detector (R11041, Hamamatsu Photonics), after being excited for 10 min by the 300 W Xe lamp (MAX-302, Asahi Spectra) with a UV mirror module (λ = 250–380 nm). To convert PersL intensity to luminance (unit; mcd m^{-2}), the PersL spectra of the samples 30 seconds after the excitation illumination ceased were detected a calibrated CCD spectrometer (GlacierX BTC112E, B&W Tek). The TL glow curves of the samples were measured, following the procedure below. The sample was set in a liquid nitrogen cryostat (Helitran LT3, Advanced

Research Systems) to control its temperatures (T = 100–600 K) and first illuminated with UV light from the Xe lamp (MAX-302) at 100 K for 10 min, then heated 10 min after the UV illumination ceased up to 600 K with a rate of 10 K min^{-1}. The sample signal was simultaneously detected with the PMT detector (R11041) and the CCD spectrometer (QE65Pro). For TL glow curve analyses with the initial rise method (IRM), the TL measurement was combined with the thermal cleaning (TC) method [31]. First, the sample was exposed to UV excitation light for 10 min at 100 K. 10 min after the excitation light illumination, the sample was heated up to arbitrary temperature (TC temperature) with a rate of 10 K min^{-1}. Keeping the sample temperature at the TC temperature for 10 min, the sample was cooled down to 100 K again and then immediately heated up to 600 K with a rate of 100 K while detecting the TL signal with the PMT detector. The TC temperature range for the $YSiO_2N:Ce^{3+}$, $YSiO_2N:Ce^{3+}$-Sm^{3+}, and $YSiO_2N:Ce^{3+}$-Tm^{3+} samples were 100–380 K, 200–410 K, and 150–400 K in 10 K increments, respectively.

7.3. Results and Discussion

7.3.1. Prediction of the Optimal Electron-Trap Centers for Ce^{3+} Luminescence in $YSiO_2N$

In order to design the persistence for Ce^{3+} by choosing a suitable electron trap, we constructed the VRBE diagram for $YSiO_2N$ with the spectroscopic data (**Figure 7.2**) [19,29,30,34]. Here, the vertical axis is the binding energy based on the vacuum level for each divalent and trivalent lanthanoid ion, Ln^{2+} and Ln^{3+}. The red and blue zigzag curves connect the Ln^{2+} and Ln^{3+} ground levels, respectively, where the nephelauxetic effect derived from the covalency of the oxynitride composition is taken into account [29,30].

Table 7.1. Input data for constructing the VRBE diagram obtained from the spectroscopic parameters in literature and parameters calculated therefrom.

Experimental input	(eV)
E^{ex}	5. 87
$E^{C}(1, 3+, YSiO_2N)$	4.11
$E^{CT}(6, 3+, YSiO_2N)$	3.96
$\varepsilon_c(1, 3+, YSiO_2N)$	2.24
$U(6, YSiO_2N)$	6.46
E_g	6.14
Model output	**(eV)**
$E_{4f}(7, 2+, YSiO_2N)$	−3.81
$E_{4f}(1, 3+, YSiO_2N)$	−4.73
E_V	−7.77
E_C	−1.62

The VRBE diagram for the $YSiO_2N$ host was constructed with the spectroscopic data in our other report, following the procedure below. The experimental input and model output parameters for the construction of the VRBE diagram are listed in **Table 7.1**. First, the bandgap E_g at a low temperature was calculated from the host exciton energy (E^{ex} = 5.87 eV) with vacuum ultraviolet (VUV) spectroscopy by adding the exciton binding energy estimated as $0.008(E^{ex})^2$ [35,36]. The E_g value for the $YSiO_2N$ host was estimated to be 6.14 eV. The charge transfer (CT) energy $E^{CT}(6, 3+, YSiO_2N)$, which is the energy gap between the VB top and the ground level of Eu^{2+}, was determined to be 3.96 eV [32]. In the Eu^{3+}-doped $YSiO_2N$, the CT transition is considered to be the electron transfer from N^{3-} to Eu^{3+}. We did not take into account the contribution of the CT from O^{2-} to Eu^{3+} ions because the VB top of the monoclinic $YSiO_2N$ is composed of mainly N 2p orbitals. Because the CT energy differs slightly in the symmetry for the occupied site, we determined the CT energy by taking the number of the nonequivalent Y^{3+}

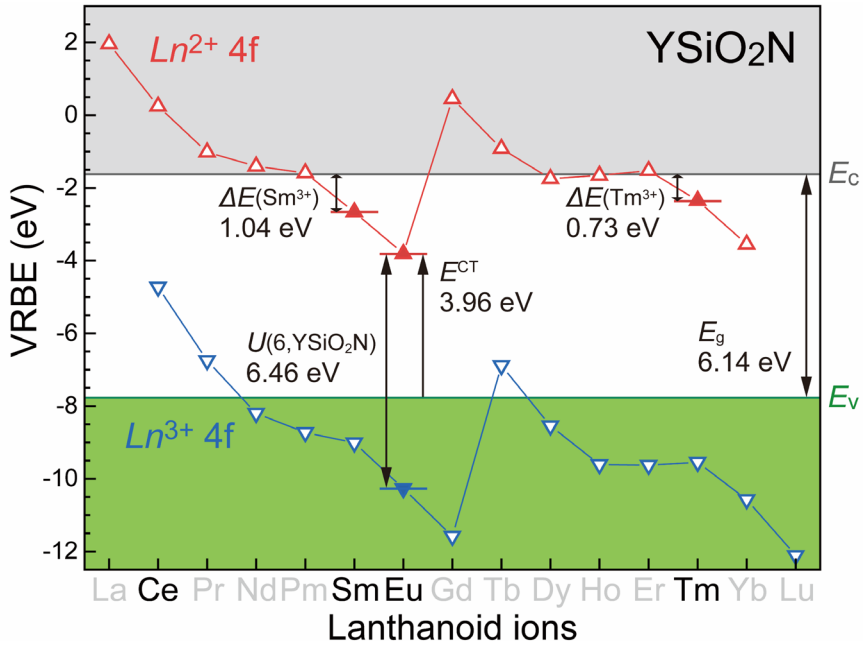

Figure 7.2. Vacuum referred binding energy (VRBE) diagram for the $YSiO_2N$ host, constructed with spectroscopic data.

sites into account. The electron repulsion energy $U(6, A)$, which corresponds to the energy difference between the ground levels of divalent and trivalent Eu ions in a host compound A, was estimated from the centroid shift of Ce^{3+}: 5d level in $YSiO_2N$ using

$$U(6, A) = 5.44 + 2.834 \exp\left(-\epsilon_c / 2.2\right). \quad (7.1)$$

The centroid energy of the Ce^{3+} 5d state in the $YSiO_2N$ host was determined to be 4.11 eV from the UV-VUV photoluminescence excitation (PLE) spectrum. Considering the Ce^{3+}: 5d energy in free ion (= 6.35 eV), the centroid shift ε_c was 2.24 eV, leading to $U(6, YSiO_2N)$ = 6.46 eV. The $\varepsilon_c(1, 3+, A)$ and $U(6, A)$ values depend on the polarizability of the anion ligands around Ce^{3+} ions [19]. (Oxy)nitrides tend to show a smaller $U(6, A)$ than oxides or chlorides, according to the nephelauxetic sequence [19,37]. Because the obtained $U(6, YSiO_2N)$ value is smaller than $U(6, A)$ values for many reported oxides (*e.g.*, $U(6, Y_3Al_5O_{12})$ = 6.79 eV, $U(6, YBO_3)$ = 6.85 eV, $U(6, LaAlO_3)$ = 6.67 eV, and $U(6, SrSiO_3)$ = 6.63 eV) [19] and almost the same as the $U(6, LaSiO_2N)$ value (= 6.45 eV) reported by Dorenbos [19,38], this estimated value is valid. The VRBE of Eu^{2+} ground level $E_{4f}(7, 2+, A)$ can be calculated with the following equation;

$$E_{4f}(7, 2+, A) = -24.92 + \frac{18.05 - U(6, A)}{0.777 - 0.0353U(6, A)}. \quad (7.2)$$

The VRBE of Eu^{2+} ground level is calculated to be −3.81 eV, leading to the outputs, including all VRBE of VB top (E_V), CB bottom (E_C), and the ground levels for Ln^{2+} and Ln^{3+}. For the correction related to the nephelauxetic effect on ground levels for Ln^{2+} and Ln^{3+} ions with $q > 7$ (q: number of 4f electrons), the nephelauxetic parameter β is introduced and estimated to be 0.914 from $U(6, A)$. The β parameter takes a small value in a covalent host, such as nitrides, sulfides, and selenides [29,30]. According to literature, the β for fluorides, chlorides, oxides, and sulfides take ~0.96, ~0.95, ~0.95–0.92, and ~0.90, respectively [29]. Based on this chemical trend, the β value of 0.914 for the $YSiO_2N$ host is regarded as reasonable.

The lower position of Ln^{2+} ground levels below E_C is the necessary condition for Ln^{3+} co-dopants to act as electron traps. Based on the constructed VRBE diagram for $YSiO_2N$, only Sm^{2+}, Eu^{2+}, Dy^{2+}, Tm^{2+}, and Yb^{2+} satisfy the condition. However, these lanthanoid ions cannot necessarily act as proper electron traps for PersL. Zhuang *et al.* studied the suitable trap depth in an oxynitride host $SrSi_2AlO_2N_3$, concluding that the proper electron trap takes the depth in the range of 0.5–0.7 eV [25]. Other studies have also referred to the suitable depth, < ~0.7 eV [36,39–41]. Therefore, Tm^{3+}, which has the best electron trap depth of 0.726 eV in the obtained VRBE diagram of $YSiO_2N$, was selected as an optimum co-dopant lanthanoid ion at ambient temperature. Besides, Sm^{3+} was also expected as an electron trap center for the Ce^{3+} PersL at ambient temperature because it has a large but still possible electron trap depth of 1.04 eV to obtain Ce^{3+} PersL. Following these assumptions, we prepared the Ce^{3+}-Ln^{3+} (Ln = Sm or Tm) co-doped $YSiO_2N$ samples and investigated their PersL and TL properties.

7.3.2. Characterization of Ce^{3+} Persistent Luminescence in $YSiO_2N$ Host

Figure 7.3a shows the appearance of the prepared samples under UV illumination (λ_{ex} = 254 nm) and 10 s after excitation ceased. Although all the samples show the blue PersL, the co-

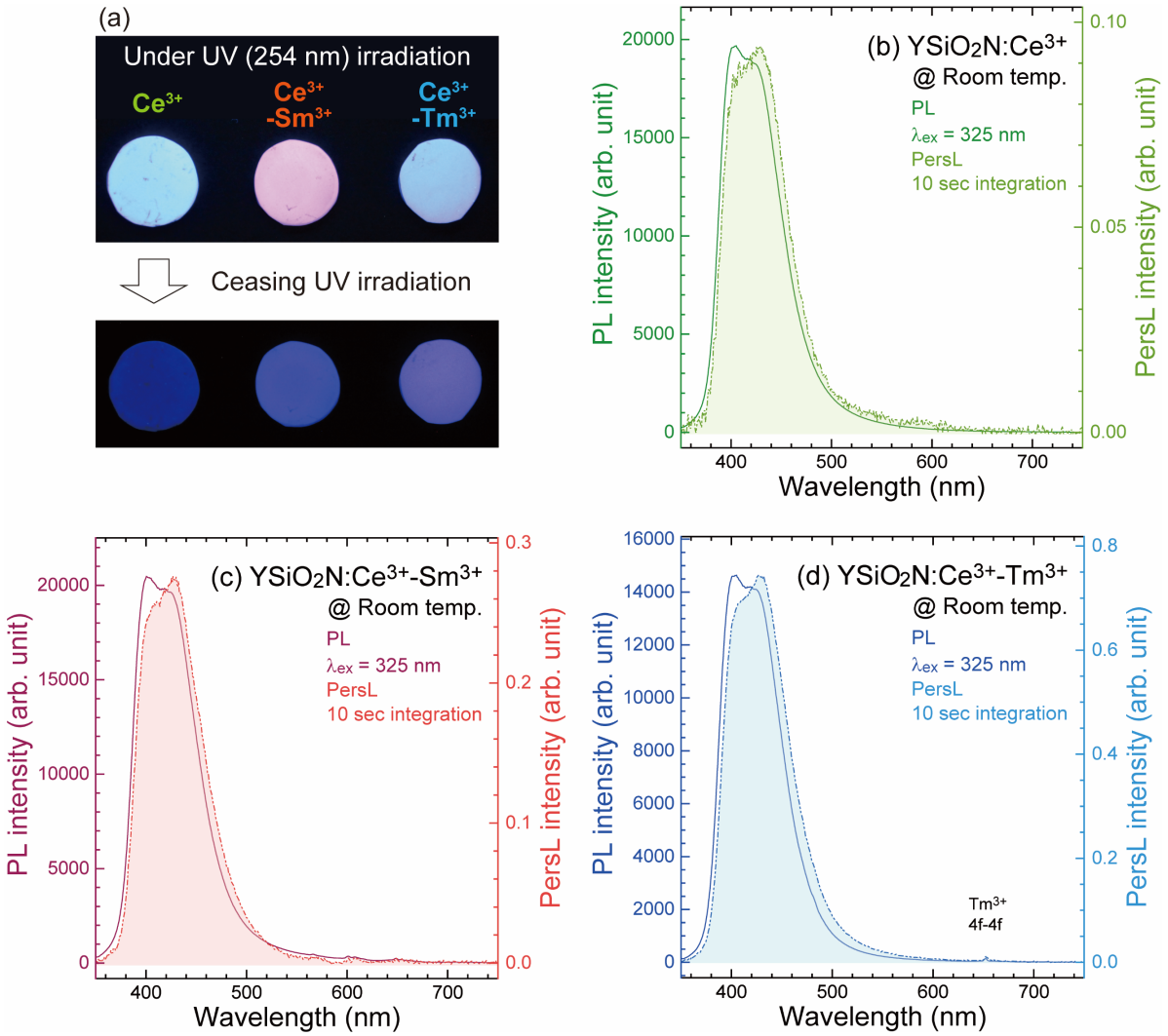

Figure 7.3. (a) Photographs of the $YSiO_2N:Ce^{3+}$ and $YSiO_2N:Ce^{3+}$-Ln^{3+} (Ln = Sm, Tm) samples (top) under UV light illumination and (bottom) 10 s after excitation ceased. (b–d) Comparison of PL and PersL spectra for (b) $YSiO_2N:Ce^{3+}$, (c) $YSiO_2N:Ce^{3+}$-Sm^{3+}, and (d) $YSiO_2N:Ce^{3+}$-Tm^{3+} samples. The y-axes of the PL and PersL spectra for each sample are comparable.

dopants of Sm^{3+} and Tm^{3+} ions enhance the PersL intensity. Only for the $YSiO_2N:Ce^{3+}$-Sm^{3+} sample, the PL color under UV illumination is different, which can be explained by the PLE spectra of the samples in **Figure 7.4**. For the Ce^{3+}-Ln^{3+} co-doped sample, the Ln^{3+} 4f-4f luminescence (Sm^{3+}: $^4G_{5/2} \rightarrow {}^6H_{7/2}$, Tm^{3+}: $^1G_4 \rightarrow {}^3F_4$) was detected. The $YSiO_2N:Ce^{3+}$-Sm^{3+} sample shows the strong excitation band peaking at 245 nm, which is assigned to the CT transition from N^{3-} to Sm^{3+} ions, as expected by the VRBE diagram (E^{CT}(5, 3+, $YSiO_2N$) = 5.21 eV). Therefore, Sm3+: 4f-4f orange to red luminescence is observed under UV illumination.

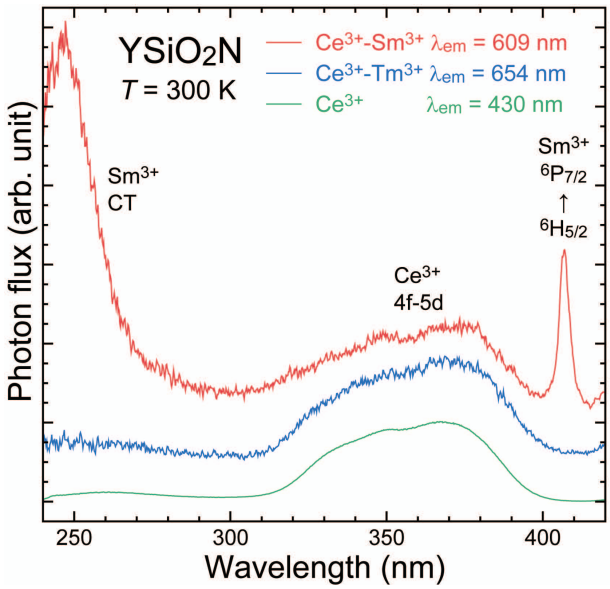

Figure 7.4. PLE spectra of the samples at room temperature.

In **Figures 7.3b–3d**, the comparisons of the PL and PersL spectra of each sample are shown. The left and right axes indicate the PL and PersL intensities, respectively. In the PL spectra, the samples show the typical Ce^{3+}: $5d_1 \rightarrow 4f$ ($^2F_{5/2}$ and $^2F_{7/2}$) blue luminescence. The Ce^{3+}-Ln^{3+} co-doped sample shows weak 4f-4f luminescence bands (Sm^{3+}; $^4G_{5/2} \rightarrow {}^6H_{7/2}$, $^6H_{9/2}$, Tm^{3+}; $^1G_4 \rightarrow {}^3F_4$) due to the energy transfer from Ce^{3+}: 5d levels to Sm^{3+}: $^4G_{5/2}$ or Tm^{3+}: $^1G_4$ levels. In the PersL spectra, all the samples show blue PersL assigned to the Ce^{3+}: $5d_1 \rightarrow 4f$ transition, and the luminescence components at the longer-wavelength side are strong. In our other study on the Ce^{3+}-doped $YSiO_2N$, we observed multiple kinds of Ce^{3+} luminescence in the $YSiO_2N$ host. The major Ce^{3+} center showed a typical spectral shape composed of two luminescence bands peaking at 400 and 427 nm, assigned to the Ce^{3+}: $5d \rightarrow {}^2F_{5/2}$ and $^2F_{7/2}$ transitions. The minor Ce^{3+} center showed a broad luminescence band in the range of 380–700 nm, whose luminescence lifetimes at 20 K were 32–58 ns depending on the monitored wavelengths. Considering the typical lifetime for the Ce^{3+}: $5d \rightarrow 4f$ luminescence and relatively weak PL intensity compared with the major Ce^{3+} luminescence, it was suggested that the minor Ce^{3+} luminescence was derived from the Y^{3+} sites with some anion defects, forming the $[Ce^{3+}O_{6\pm\delta}N_{2\mp\delta}]$ dodecahedra. The

difference between the PL and PersL spectra can be caused by the relative intensity of the major and minor Ce^{3+} luminescence. The Tm^{3+} ions more enhance the Ce^{3+} PersL intensity at 10 s after the excitation illumination ceased than the Sm^{3+} ions.

Figure 7.5 shows the PersL decay curves of all the samples, whose *y*-axis was converted into luminance (unit: mcd m^{-2}), which takes the sensitivity of human eyes into account. For comparison of PersL intensity, the decay curve of the commercial blue persistent phosphor $CaAl_2O_4:Eu^{2+}$-Nd^{3+} (λ_{em} = 440 nm, *Luminova*® V-300M, Nemoto & Co., Ltd.) is also plotted as a reference. As a benchmark of PersL intensity, the luminance value of 0.32 mcd m^{-2} is shown in a broken line, which is the minimum value commonly used by the safety signage industry (about 100 times the sensitivity of the dark-adapted eye) [42]. The Ce^{3+} singly doped sample shows Ce^{3+} PersL lasting over an hour to reach 0.32 mcd m^{-2} after excitation illumination ceased. By co-doping of proper lanthanoid ions, Sm^{3+} or Tm^{3+}, the initial PersL intensity is enhanced

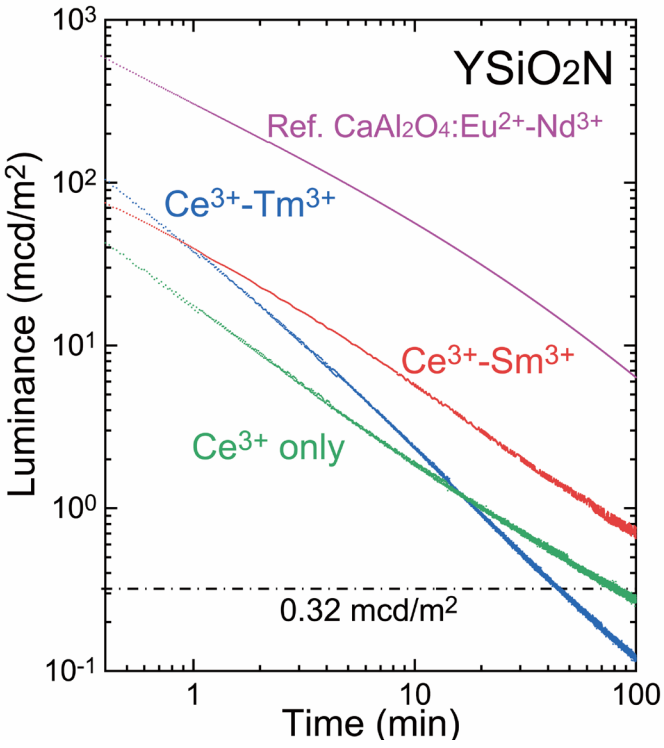

Figure 7.5. PersL decay curves of all the samples. As a reference, the decay curve of the commercial blue persistent phosphor, $CaAl_2O_4:Eu^{2+}$-Nd^{3+} (*Luminova*® V-300M, Nemoto & Co., Ltd.), is shown.

by 2–3 times at 30 s, indicating that they successfully act as the electron trap centers. The $YSiO_2N:Ce^{3+}$-Sm^{3+} samples show the decay curves with a similar slope to that of the $YSiO_2N:Ce^{3+}$ sample. On the other hand, the decay curves of the $YSiO_2N:Ce^{3+}$-Tm^{3+} samples have a steep slope, resulting in a strong initial PersL intensity and a short duration time. The steeper slope of the decay curve for the $YSiO_2N:Ce^{3+}$-Tm^{3+} than that for the $YSiO_2N:Ce^{3+}$-Sm^{3+} suggests that the Tm^{3+}-related electron traps have a smaller trap depth than the Sm^{3+}-related one as expected from the VRBE diagram.

The PersL-related electron detrapping process can be characterized by the TL glow curves. **Figure 7.6a** shows the TL glow curves of all the samples. The temperature in the *x*-axis and the TL intensity in the *y*-axis are correlated with the carrier trap depth and the number of captured electrons, respectively. **Figure 7.6b** illustrates the behavior of captured electrons after excitation illumination ceased. (i) The excited electrons localized at the trap levels are stimulated by thermal energy and move to the $5d_1$ excited level *via* the host CB. (ii) The Ce^{3+} luminescence intensity is proportional to the number of released electrons. However, (iii) the thermally

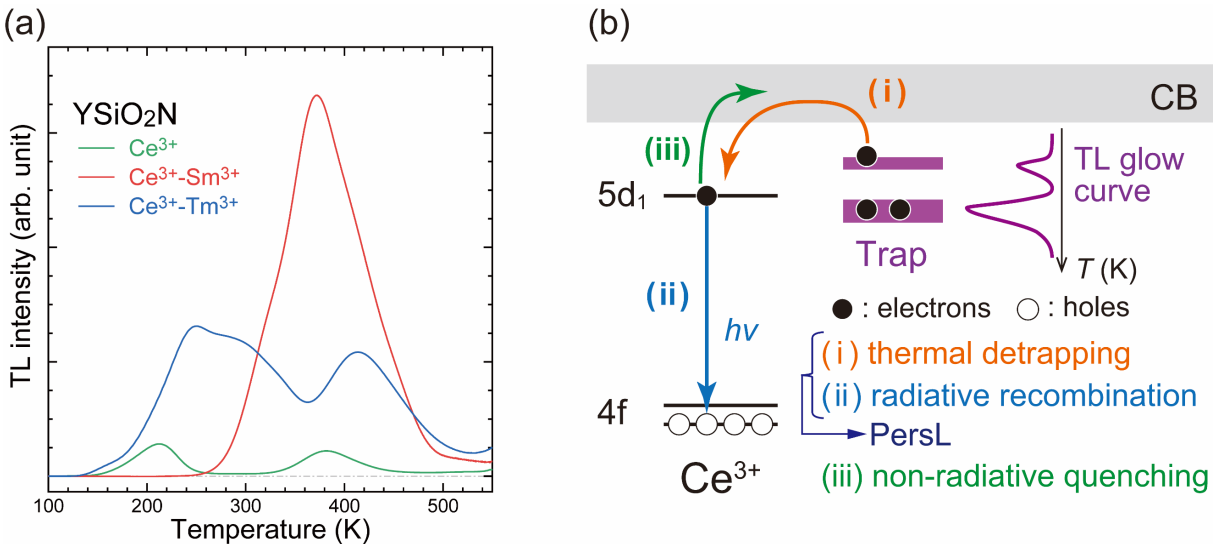

Figure 7.6. (a) TL glow curves of the samples, monitored with Ce^{3+} blue luminescence. (b) Schematic illustration of TL process. Arrows in the figure show the behavior of excited electrons; (i) thermal detrapping, (ii) radiative transition, and (iii) non-radiative thermal quenching processes.

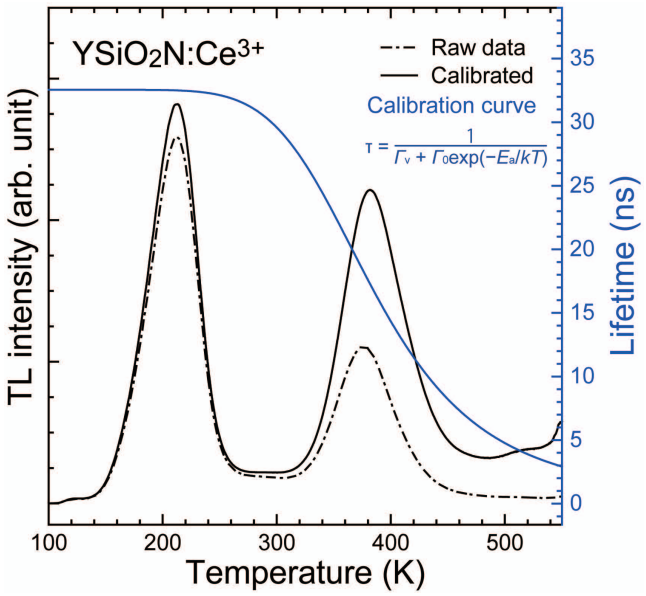

Figure 7.7. TL glow curves of the $YSiO_2N:Ce^{3+}$ sample before and after calibration (before; broken line, after; solid line) with the thermal quenching curve (blue line).

activated ionization process gets dominant with temperature. Therefore, in order to qualitatively estimate the electron trap distribution, all the glow curves were calibrated with the thermal quenching curve described by the single barrier quenching model in which the radiative rate Γ_v, the attempt rate for the non-radiative process Γ_0, and thermal activation energy E_a are 3.06×10^7 s^{-1}, 5.46×10^{10} s^{-1}, and 0.272 eV, respectively. The TL glow curves before and after calibration and the thermal quenching curve are given in the Supporting Information (**Figure 7.7**).

The $YSiO_2N:Ce^{3+}$ sample shows two glow peaks at 212 and 382 K. These peaks can be related to the intrinsic defects in the $YSiO_2N$ host. Possible positive defects acting as the electron traps are $V_N^{\cdots}$ and $O_N^{\cdot}$, generated during the high-temperature synthesis under a reduction atmosphere. Between two glow peaks (T = 250–310 K), the TL intensity takes a continuously non-zero value. Because this non-zero region is composed of a very weak and broad glow curve, the continuous TL can be due to the thermally assisted tunnelling process [43].

The Ln^{3+} co-doped samples show different shapes of the glow curves. The $YSiO_2N:Ce^{3+}$-

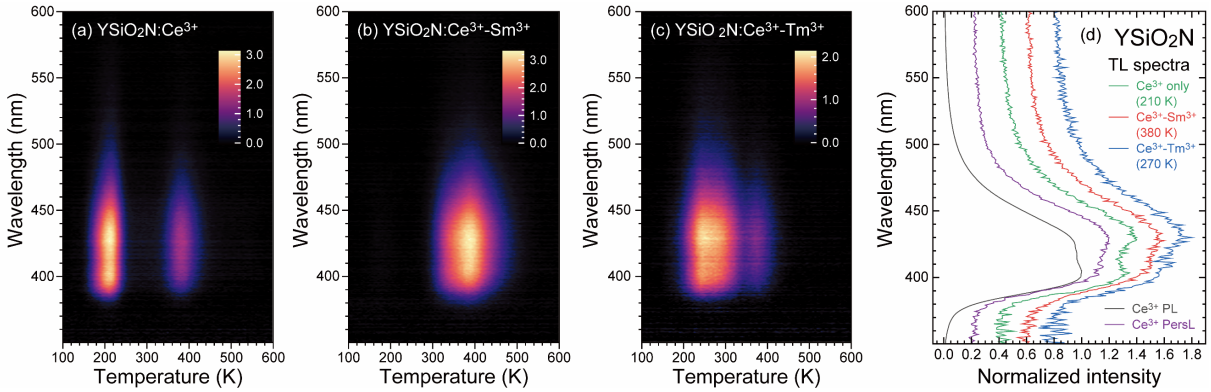

Figure 7.8. Temperature-TL wavelength contour plot of (a) $YSiO_2N:Ce^{3+}$, (b) $YSiO_2N:Ce^{3+}$-Sm^{3+}, and $YSiO_2N:Ce^{3+}$-Tm^{3+} samples. (d) Normalized TL spectra of the samples at the temperature where each sample shows the strongest Ce^{3+} luminescence. For comparison, the PL and PersL spectra of the $YSiO_2N:Ce^{3+}$ sample, shown in Figure 7.3b, are also plotted.

Sm^{3+} sample shows an intense TL glow curve over ~250 K. This glow curve seems to consist of two components with quite similar peak temperatures. Considering the shape of the glow curve for the Ce^{3+} singly-doped sample, one TL glow curve can be assigned to the electron traps related to the intrinsic defects. Because the TL intensity is largely enhanced by Sm^{3+} co-doping, the TL glow curve due to the traps related to the doped Sm^{3+} ions overlap with the TL glow band related to intrinsic defects. The $YSiO_2N:Ce^{3+}$-Tm^{3+} sample shows a very broad and complicated shape of the glow curve. It consists of at least three independent curves, two of which at ~240 and 420 K are related to the intrinsic defects like the $YSiO_2N:Ce^{3+}$ sample. The TL glow peak at ~260–320 K is related to the Tm^{3+} related defects. Considering the enhancement of TL intensities of glow peaks related to intrinsic defects, Ln^{3+} co-doping increases the number of intrinsic defects caused by not only Ce_Y^x but also Sm_Y^x and Tm_Y^x.

In order to investigate the luminescence center in the PersL and TL process, the TL spectra of the samples were investigated in the wide temperature range (T = 100–600 K). The temperature-TL wavelengths contour plots of the samples are shown in **Figures 7.8a–8c**. All the contour plots suggest that only the Ce^{3+}: $5d_1 \rightarrow 4f$ luminescence is observed during the TL process. **Figure 7.8d** shows the normalized TL spectra of the samples at the temperature with

the strongest TL intensity. The spectral shapes of all the samples are similar to the PersL spectra. The relative intensity of the Ce^{3+}: $5d_1 \rightarrow {}^2F_{7/2}$ band to the ${}^2F_{5/2}$ band is high, as seen in the PersL spectra, indicating that weak minor Ce^{3+} luminescence related to some anion defects overlaps with the major Ce^{3+} luminescence.

7.3.3. Analysis of Electron-Trap Distribution with Initial Rise Method

The levels of electron traps caused by the impurities are not always represented by a single energy level, but possibly show some distribution [44,45]. In this study, the trap depth distribution in the $YSiO_2N$ host was characterized by the TL glow curve analyses with the initial rise method (IRM) combined with the thermal cleaning (TC) method. In the framework of the IRM, the number of trapped electrons is regarded as nearly constant in the initial rising part of the glow peak on the low-temperature side. Thus one obtains the approximation that the TL intensity is proportional to $\exp(-\varepsilon/kT)$ (ε; trap depth and k; Boltzmann constant) without supposing frequency factors and trapping kinetics [31]. In this study, an initial part of TL glow curves with 1–15% of the peak TL intensity is defined as the initial rising part.

Figures 7.9a–9c show the TL glow curves of the samples with different TC temperatures. With the TC temperatures changing, the TL glow peaks shift toward the high-temperature side. According to McKeever, the shifted TL glow peaks depending on the TC temperature indicate that the multiple TL glow curves severely overlap because of the electron trap distribution [45]. Therefore, the electron traps with a similar depth are continuously distributed in a series of Ce^{3+} singly- or Ce^{3+}-Ln^{3+} co-doped samples.

The $YSiO_2N:Ce^{3+}$ sample has two glow peaks, named as ID1 and ID2 (ID; intrinsic defects). Both ID1 and ID2 show the monotonous peak temperature shift with increasing TC temperature. Between ID1 and ID2, the range with non-zero TL intensity, possibly related to the thermally assisted tunnelling process, is named as C (continuous). Although the

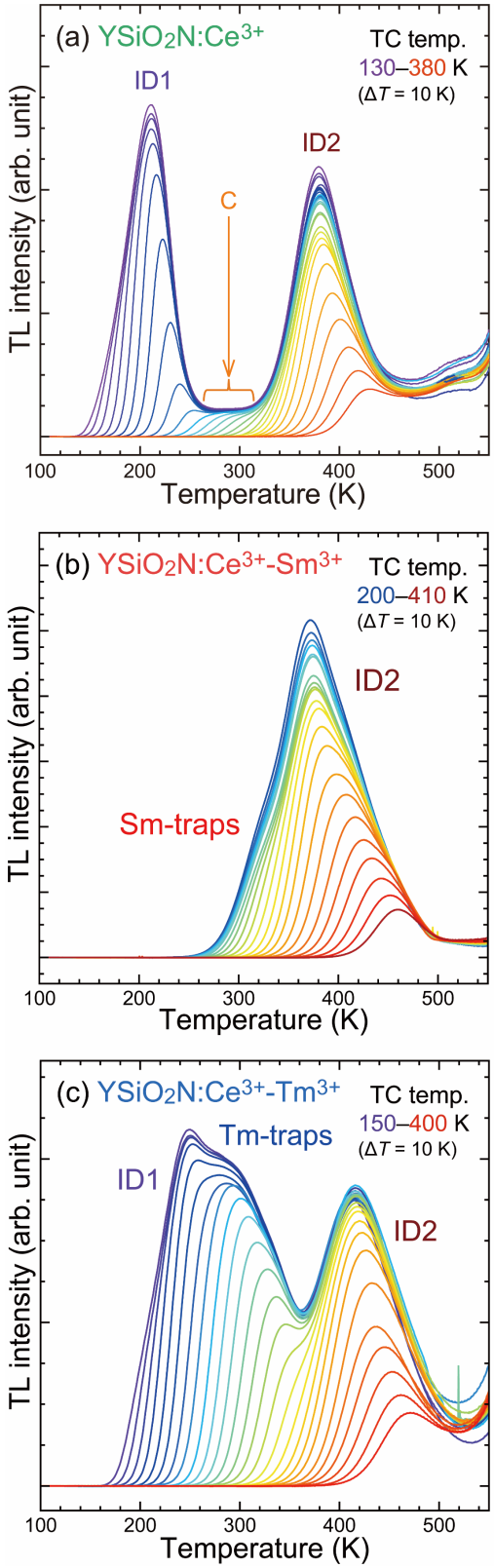

Figure 7.9. TL glow curves after thermal cleaning (TC) at various temperatures of (a) $YSiO_2N:Ce^{3+}$, (b) $YSiO_2N:Ce^{3+}$-Sm^{3+}, and (c) $YSiO_2N:Ce^{3+}$-Tm^{3+} samples. All the glow curves are labeled with notations as follows; ID (intrinsic defects), Sm-traps, and Tm-traps.

$YSiO_2N:Ce^{3+}$-Sm^{3+} sample shows only one glow peak, the first derivative of the slope on the low-temperature side was not constant. Besides, with TC temperatures of 200–260 K, the TL glow peak temperature did not shift despite the inflection point shifting. Taking the glow curves of the $YSiO_2N:Ce^{3+}$ sample into account, the glow peaks at the low- and high-temperature sides can be denoted by Sm-traps and ID2, respectively. The $YSiO_2N:Ce^{3+}$-Tm^{3+} sample has three glow peaks at 250, 290, and 410 K. They are labeled as ID1, Tm-traps, and ID2.

For these TL glow curves with various TC temperatures, we estimated the trap depth with the IRM. The difference of area between two TC temperatures, T_1 and T_2 ($T_1 < T_2$), is proportional to the number of released electrons between T_1 and T_2. We assumed that by combining it with the output trap depth by the IRM, we could estimate the trap density as a function of trap depth [31]. The Ahrrenis plots of the TL glow curves with the initial rise fitting, the estimated electron trap depths as a function of TC temperatures, and the differential curves for the TL glow curves at T_1 and T_2 ($T_2 = T_1 + 10$ K) are provided in the Supporting Information (**Figures 7.10–12**).

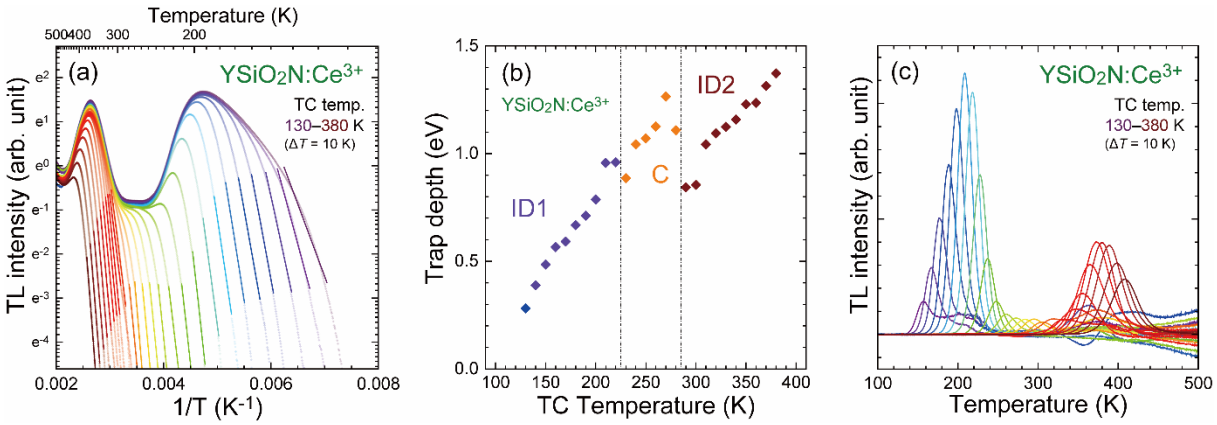

Figure 7.10. (a) Arrhenius plot of the TL glow curves in the $YSiO_2N:Ce^{3+}$ sample as a function of TC temperatures. Colored solid lines represent the fitting function, whose slope is described as $-\varepsilon/k$ (ε: trap depth (eV) and k: Boltzmann constant). (b) Estimated trap depths in the $YSiO_2N:Ce^{3+}$ sample as a function of TC temperature. (c) Differential curves between the TL glow curves at two adjacent temperatures, T and $T + 10$ K.

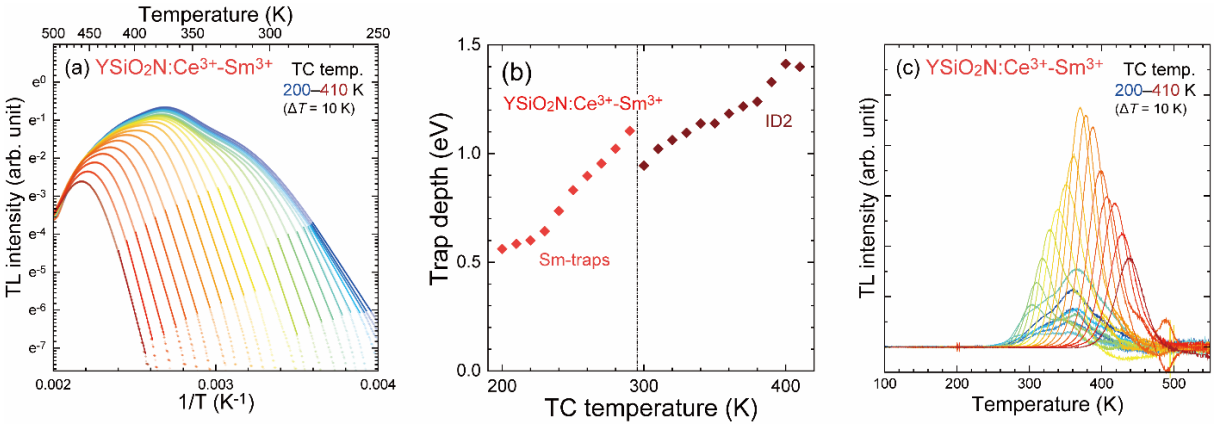

Figure 7.11. (a) Arrhenius plot of the TL glow curves in the $YSiO_2N:Ce^{3+}$-Sm^{3+} sample as a function of TC temperatures. (b) Estimated trap depths in the $YSiO_2N:Ce^{3+}$-Sm^{3+} sample as a function of TC temperature. (c) Differential curves between the TL glow curves at two adjacent temperatures.

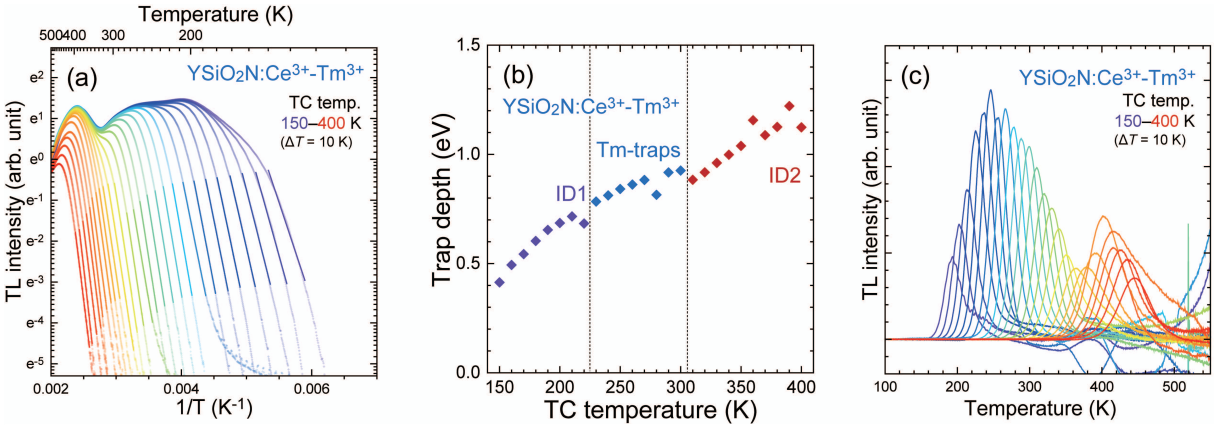

Figure 7.12. (a) Arrhenius plot of the TL glow curves in the $YSiO_2N:Ce^{3+}$-Tm^{3+} sample as a function of TC temperatures. (b) Estimated trap depths in the $YSiO_2N:Ce^{3+}$-Tm^{3+} sample as a function of TC temperature. (c) Differential curves between the TL glow curves at two adjacent temperatures.

Figure 7.13 shows the histogram describing the electron trap distributions for the $YSiO_2N:Ce^{3+}$ and $YSiO_2N:Ce^{3+}$-Ln^{3+} samples. Assuming the Gaussian-shaped distribution [46,47], the centroid trap depths were estimated with the Gaussian fitting and listed with the bandwidths in **Table 7.2**. The $YSiO_2N:Ce^{3+}$ sample has two trap distributions centered at 0.657 and 1.18 eV, which are related to the intrinsic defects. These distributions are also observed in the $YSiO_2N:Ce^{3+}$-Tm^{3+} sample with slightly different depths (0.663 and 1.03 eV) and similar

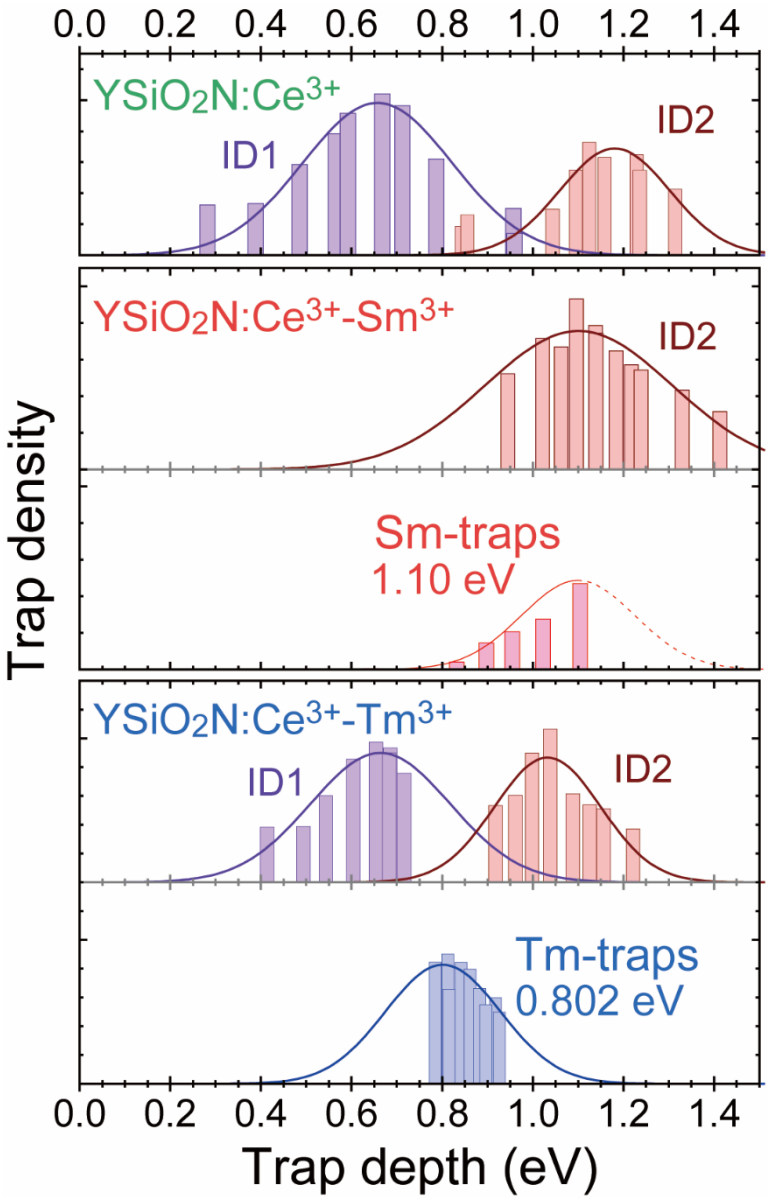

Figure 7.13. Histogram describing electron trap distribution in energetic scale (unit: eV) for the $YSiO_2N:Ce^{3+}$ and $YSiO_2N:Ce^{3+}$-Ln^{3+} (Ln = Sm or Tm) samples. Each histogram is fitted with a Gaussian function.

widths. The ID1 and ID2 traps become shallower and deeper by Tm^{3+} co-doping, respectively. In the TL glow curve for the $YSiO_2N:Ce^{3+}$-Sm^{3+} sample, the ID1 curve was not detectable, resulting in trap depths estimation only for the ID2- and Sm-traps, 1.10 eV. Because these curves severely overlap, the ID2- and Sm-traps take the same depth but different widths. The trap density of the deep ID-trap is largely enhanced. For the $YSiO_2N:Ce^{3+}$-Tm^{3+} sample, the density of both ID1 and ID2 traps is also enhanced. These results suggest that introducing the *Ln*-traps affects not only the trap distribution but also trap density of intrinsic defects.

The estimated trap depths based on the TL analyses for Tm^{3+} and Sm^{3+} are 0.802 and 1.10 eV, respectively. The severe overlap can cause some errors in the estimated values. Nevertheless, considering the depths estimated from the VRBE diagram (Tm^{3+}; 0.726 eV, Sm^{3+}; 1.04 eV), the differences between the predicted and experimental trap depths are just 0.076 eV (Tm^{3+}) and 0.056 eV (Sm^{3+}), indicating that the prediction of co-dopants based on the VRBE diagram calibrated with the nephelauxetic effect worked well in the covalent host $YSiO_2N$.

Table 7.2. Estimated trap depths and bandwidths for trap distributions with a Gaussian profile for intrinsic (ID), Sm-traps, and Tm-traps (unit: eV)

		ID1	ID2	Sm-traps	Tm-traps
$YSiO_2N:Ce^{3+}$	center	0.657	1.18	—	—
	width	0.329	0.242	—	—
$YSiO_2N:Ce^{3+}$-Sm^{3+}	center	—	1.10	1.10	—
	width	—	0.413	0.250	—
$YSiO_2N:Ce^{3+}$-Tm^{3+}	center	0.663	1.03	—	0.802
	width	0.308	0.234	—	0.254

7.4. Conclusions

The Ce^{3+} persistent luminescence in the $YSiO_2N$ host was successfully enhanced by co-doping Sm^{3+} and Tm^{3+} ions, as predicted by the semi-empirical vacuum referred binding energy (VRBE) diagram. The VRBE diagram of the YSiO2N host was constructed with the experimentally obtained parameters, including the host exciton creation energy, the charge transfer energy for Eu^{3+}, and the centroid shift of Ce^{3+} 5d levels, leading to the optimal co-dopant lanthanoid ions, Sm^{3+} and Tm^{3+}, to obtain Ce^{3+} persistent luminescence at ambient temperature. The electron trap depths for Tm^{3+} and Sm^{3+} ions were estimated to be 0.726 and 1.04 eV, respectively. The prepared $YSiO_2N:Ce^{3+}$-Ln^{3+} (Ln = Sm or Tm) samples enhanced the Ce^{3+} blue persistent luminescence at 30 s after the excitation ceased by 2–3 times. The thermoluminescence (TL) glow curves of the Ln^{3+} co-doped samples showed additional glow peaks related to Ln-traps and enhanced the TL intensity related to intrinsic defects. The TL glow curve analyses with the initial rise method combined with the thermal cleaning and trap density methods revealed that the Ln-traps located below the conduction band have a distribution with ~0.25 eV width, whose centers were similar to the predicted trap depth by the constructed VRBE diagram.

Acknowledgements

We acknowledge Prof. Pieter Dorenbos in Delft University of Technology for the construction of the VRBE diagram. This work was financially supported by the Grant-In-Aid for JSPS Fellows (JP19J23280) and JSPS Grant-In-Aid for Scientific Research on Innovative Areas “Mixed-Anion” (JP16H06441).

References

[1] J. Xu, S. Tanabe, "Persistent luminescence instead of phosphorescence: History, mechanism, and perspective". *J. Lumin*. **205** (2019) 581–620.

[2] Q. le Masne de Chermont, C. Chanéac, J. Seguin, F. Pellé, S. Maîtrejean, J.-P. Jolivet, D. Gourier, M. Bessodes, D. Scherman, "Nanoprobes with near-infrared persistent luminescence for in vivo imaging". *Proc. Natl. Acad. Sci. U. S. A.* **104** (2007) 9266–9271.

[3] T. Lécuyer, E. Teston, G. Ramirez-Garcia, T. Maldiney, B. Viana, J. Seguin, N. Mignet, D. Scherman, C. Richard, "Chemically engineered persistent luminescence nanoprobes for bioimaging". *Theranostics.* **6** (2016) 2488–2524.

[4] B. Viana, S.K. Sharma, D. Gourier, T. Maldiney, E. Teston, D. Scherman, C. Richard, "Long term in vivo imaging with Cr^{3+} doped spinel nanoparticles exhibiting persistent luminescence". *J. Lumin.* **170** (2016) 879–887.

[5] J. Xu, D. Murata, Y. Katayama, J. Ueda, S. Tanabe, "Cr^{3+}/Er^{3+} co-doped $LaAlO_3$ perovskite phosphor: a near-infrared persistent luminescence probe covering the first and third biological windows". *J. Mater. Chem. B.* **5** (2017) 6385–6393.

[6] D. Van der Heggen, J.J. Joos, P.F. Smet, "Importance of Evaluating the Intensity Dependency of the Quantum Efficiency: Impact on LEDs and Persistent Phosphors". *ACS Photonics.* **5** (2018) 4529–4537.

[7] K. Asami, J. Ueda, S. Tanabe, "Flicker Suppression of AC Driven White LED by Yellow Persistent Phosphor of Ce^{3+}–Cr^{3+} Co-doped Garnet". *J. Sci. Technol. Light.* **41** (2018) 89–92.

[8] D. Poelman, D. Van der Heggen, J. Du, E. Cosaert, P.F. Smet, "Persistent phosphors for the future: Fit for the right application". *J. Appl. Phys.* **128** (2020) 240903 (13p).

[9] T. Matsuzawa, Y. Aoki, N. Takeuchi, Y. Murayama, "A New Long Phosphorescent Phosphor with High Brightness, $SrAl_2O_4:Eu^{2+},Dy^{3+}$". *J. Electrochem. Soc.* **143** (1996) 2670–2673.

[10] J. Ueda, K. Kuroishi, S. Tanabe, "Bright persistent ceramic phosphors of Ce^{3+}-Cr^{3+}-codoped garnet able to store by blue light". *Appl. Phys. Lett.* **104** (2014) 101904 (4p).

[11] J. Ueda, K. Kuroishi, S. Tanabe, "Yellow persistent luminescence in Ce^{3+}–Cr^{3+}-codoped gadolinium aluminum gallium garnet transparent ceramics after blue-light excitation". *Appl. Phys. Express.* **7** (2014) 062201 (3p).

[12] J.W.H. van Krevel, H.T. Hintzen, R. Metselaar, A. Meijerink, "Long wavelength Ce^{3+} emission in Y–Si–O–N materials". *J. Alloys Compd.* **268** (1998) 272–277.

[13] B. Dierre, R.-J. Xie, N. Hirosaki, T. Sekiguchi, "Blue emission of Ce^{3+} in lanthanide silicon

oxynitride phosphors", *J. Mater. Res.* **22** (2007) 1933–1941.

[14] L. Liu, R.-J. Xie, N. Hirosaki, T. Takeda, C.-N. Zhang, J. Li, X. Sun, "Optical properties of blue-emitting $Ce_xSi_{6-z}Al_{z-x}O_{z+1.5x}N_{8-z-x}$ for white light-emitting diodes". *J. Electrochem. Soc.* **157** (2010) H50–H54.

[15] K. Takahashi, M. Harada, K.-I. Yoshimura, H. Fukunaga, Y. Tomomura, N. Hirosaki, R.-J. Xie, "Improved Photoluminescence of Ce^{3+} Activated $LaAl(Si_{6-z}Al_z)(N_{10-z}O_z)$ (z~1) Blue Oxynitride Phosphors by Calcium Co-Doping". *ECS J. Solid State Sci. Technol.* **1** (2012) R109–R112.

[16] P.F. Smet, J. Botterman, K. Van den Eeckhout, K. Korthout, D. Poelman, "Persistent luminescence in nitride and oxynitride phosphors: A review". *Opt. Mater.* **36** (2014) 1913–1919.

[17] P. Dorenbos, "Modeling the chemical shift of lanthanide 4*f* electron binding energies". *Phys. Rev. B* **85** (2012) 165107 (10p).

[18] P. Dorenbos, "A Review on How Lanthanide Impurity Levels Change with Chemistry and Structure of Inorganic Compounds". *ECS J. Solid State Sci. Technol.* **2** (2012) R3001–R3011.

[19] P. Dorenbos, "Ce^{3+} 5d-centroid shift and vacuum referred 4f-electron binding energies of all lanthanide impurities in 150 different compounds". *J. Lumin.* **135** (2013) 93–104.

[20] P. Dorenbos, "Lanthanide 4f-electron binding energies and the nephelauxetic effect in wide band gap compounds". *J. Lumin.* **136** (2013) 122–129.

[21] J. Ueda, R. Maki, S. Tanabe, "Vacuum Referred Binding Energy (VRBE)-Guided Design of Orange Persistent $Ca_3Si_2O_7:Eu^{2+}$ Phosphors". *Inorg. Chem.* **56** (2017) 10353–10360.

[22] T. Lyu, P. Dorenbos, "Towards information storage by designing both electron and hole detrapping processes in bismuth and lanthanide-doped $LiRE(Si,Ge)O_4$ (RE = Y, Lu) with high charge carrier storage capacity". *Chem. Eng. J.* **400** (2020) 124776 (17p).

[23] J. Ueda, S. Miyano, J. Xu, P. Dorenbos, S. Tanabe, "Development of white persistent phosphors by manipulating lanthanide ions in gadolinium gallium garnets". *Adv. Photo. Res.* **2** (2021) 2000102 (11p).

[24] F. Lu, L. Bai, Z. Yang, Q. Liu, "Photoluminescence properties of Ce^{3+} doped $YSiO_2N$ blue-emitting phosphors". *J. Rare Earths.* **30** (2012) 851–855.

[25] Y. Zhuang, Y. Lv, Y. Li, T. Zhou, J. Xu, J. Ueda, S. Tanabe, R.-J. Xie, "Study on Trap Levels in $SrSi_2AlO_2N_3:Eu^{2+},Ln^{3+}$ Persistent Phosphors Based on Host-Referred Binding Energy Scheme and Thermoluminescence Analysis". *Inorg. Chem.* **55** (2016) 11890–11897.

[26] Y. Zhuang, Y. Lv, L. Wang, W. Chen, T.-L. Zhou, T. Takeda, N. Hirosaki, R.-J. Xie, "Trap Depth Engineering of $SrSi_2O_2N_2:Ln^{2+},Ln^{3+}$ (Ln^{2+} = Yb, Eu; Ln^{3+} = Dy, Ho, Er) Persistent Luminescence

Materials for Information Storage Applications". *ACS Appl. Mater. Interfaces.* **10** (2018) 1854–1864.

[27] W. Ji, S. Wang, Z. Song, Q. Liu, "Luminescent thermal stability and electronic structure of narrow-band green-emitting Sr-Sialon:Eu^{2+} phosphors for LED/LCD backlights". *J. Alloys Compd.* **805** (2019) 1246–1253.

[28] S. Wang, X. Liu, B. Qu, Z. Song, Z. Wang, S. Zhang, F. Wang, W.-T. Geng, Q. Liu, "Green persistent luminescence and the electronic structure of β-Sialon:Eu^{2+}". *J. Mater. Chem.* **7** (2019) 12544–12551.

[29] P. Dorenbos, "The nephelauxetic effect on the electron binding energy in the $4f^q$ ground state of lanthanides in compounds". *J. Lumin.* **214** (2019) 116536 (9p).

[30] P. Dorenbos, "[INVITED] Improved parameters for the lanthanide $4f^q$ and $4f^{q-1}5d$ curves in HRBE and VRBE schemes that takes the nephelauxetic effect into account". *J. Lumin.* **222** (2020) 117164 (11p).

[31] K. Van den Eeckhout, A.J.J. Bos, D. Poelman, P.F. Smet, "Revealing trap depth distributions in persistent phosphors". *Phys. Rev. B* **87** (2013) 045126 (11p).

[32] Y. Kitagawa, J. Ueda, K. Fujii, M. Yashima, S. Funahashi, T. Nakanishi, T. Takeda, N. Hirosaki, K. Hongo, R. Maezono, S. Tanabe, "Site-Selective Eu^{3+} Luminescence in the Monoclinic Phase of $YSiO_2N$". *Chem. Mater.* **33** (2021) 8873–8885.

[33] K. Momma, F. Izumi, "VESTA 3 for three-dimensional visualization of crystal, volumetric and morphology data". *J. Appl. Crystallogr.* **44** (2011) 1272–1276.

[34] P. Dorenbos, "Determining binding energies of valence-band electrons in insulators and semiconductors via lanthanide spectroscopy". *Phys. Rev. B* **87** (2013) 035118 (8p).

[35] P. Dorenbos, "Charge transfer bands in optical materials and related defect level location". *Opt. Mater.* **69** (2017) 8–22.

[36] T. Lyu, P. Dorenbos, "Charge carrier trapping processes in lanthanide doped $LaPO_4$, $GdPO_4$, YPO_4, and $LuPO_4$". *J. Mater. Chem.* **6** (2018) 369–379.

[37] C.K. Jørgensen, "Electron transfer spectra of lanthanide complexes". *Mol. Phys.* **5** (1962) 271–277.

[38] H. Long, X. Xue-Wen, L. Zun-Ming, F. Ying, L. Yang-Xian, T. Cheng-Chun, "Luminescence of Ce^{3+} in lanthanum silicon oxynitride". *Chin. Physics B.* **19** (2010) 127807 (5p).

[39] H. Luo, A.J.J. Bos, P. Dorenbos, "Controlled Electron–Hole Trapping and Detrapping Process in $GdAlO_3$ by Valence Band Engineering". *J. Phys. Chem. C.* **120** (2016) 5916–5925.

[40] J. Ueda, A. Hashimoto, S. Takemura, K. Ogasawara, P. Dorenbos, S. Tanabe, "Vacuum referred binding energy of 3*d* transition metal ions for persistent and photostimulated luminescence

phosphors of cerium-doped garnets". *J. Lumin.* **192** (2017) 371–375.

[41] K. Asami, J. Ueda, S. Tanabe, "Trap depth and color variation of Ce^{3+}-Cr^{3+} co-doped $Gd_3(Al,Ga)_5O_{12}$ garnet persistent phosphors". *Opt. Mater.* **62** (2016) 171–175.

[42] K. Van den Eeckhout, D. Poelman, P.F. Smet, "Persistent Luminescence in Non-Eu^{2+}-Doped Compounds: A Review". *Materials* . **6** (2013) 2789–2818.

[43] A. Dobrowolska, A.J.J. Bos, P. Dorenbos, "Electron tunnelling phenomena in YPO_4:Ce,Ln (Ln = Er, Ho, Nd, Dy)". *J. Phys. D Appl. Phys.* **47** (2014) 335301 (10p).

[44] J.T. Randall, M.H.F. Wilkins, M.L.E. Oliphant, "Phosphorescence and electron traps - I. The study of trap distributions". *Proc. R. Soc. Lond.* A. **184** (1945) 365–389.

[45] S.W.S. McKeever, "On the analysis of complex thermoluminescence. Glow-curves: Resolution into individual peaks". *Phys. Status Solidi A.* 62 (1980) 331–340.

[46] A.C. Coleman, E.G. Yukihara, "On the validity and accuracy of the initial rise method investigated using realistically simulated thermoluminescence curves". *Radiat. Meas.* 117 (2018) 70–79.

[47] J. Ueda, P. Dorenbos, A.J.J. Bos, K. Kuroishi, S. Tanabe, "Control of electron transfer between Ce^{3+} and Cr^{3+} in the $Y_3Al_{5-x}Ga_xO_{12}$ host via conduction band engineering". *J. Mater. Chem. C.* 3 (2015) 5642–5651.

Chapter 8

Difference of Eu^{3+} Luminescent Properties in YOCl and YOBr Oxyhalide Hosts

Abstract

The photoluminescence spectra, luminescence lifetimes, and their temperature dependence of the Eu^{3+}-doped oxyhalides, YO*X*:Eu^{3+} (*X* = Cl or Br) with different halide species of mixed-anion coordinations were investigated and analyzed. In terms of the ionic and covalent nature of a bonding, Eu^{3+} ions form the different coordination polyhedra in the isostructural YOCl and YOBr hosts; a nine-fold [$Eu^{3+}O_4Cl_5$] and an eight-fold [$Eu^{3+}O_4Br_4$] polyhedron. The Judd-Ofelt Ω_2 parameter for the YOCl:Eu^{3+} takes a very large value (= 8.81 × 10^{-20} cm^2) due to the nine-fold polyhedron with the C_{4v} symmetry. On the other hand, despite the same C_{4v} symmetry, the YOBr:Eu^{3+} shows the very small Ω_2 parameter (= 2.72 × 10^{-20} cm^2) because of the structural similarity to the square antiprism polyhedron with the D_4 symmetry. The Ω_4 parameters for the YO*X*:Eu^{3+} are much larger than those of other Eu^{3+}-doped oxides, possibly related to the covalency of halide anions, Cl^- and Br^-, showing an intense luminescence band ($^5D_0 \rightarrow {}^7F_4$) at around 700 nm. The Eu^{3+} ions in these YO*X* hosts were excitable by charge transfer bands in 270–280 nm regions. The relaxation pathways from the charge transfer states to the initial states for luminescence are discussed, using the configuration coordinate diagrams with the spectroscopic characterizations.

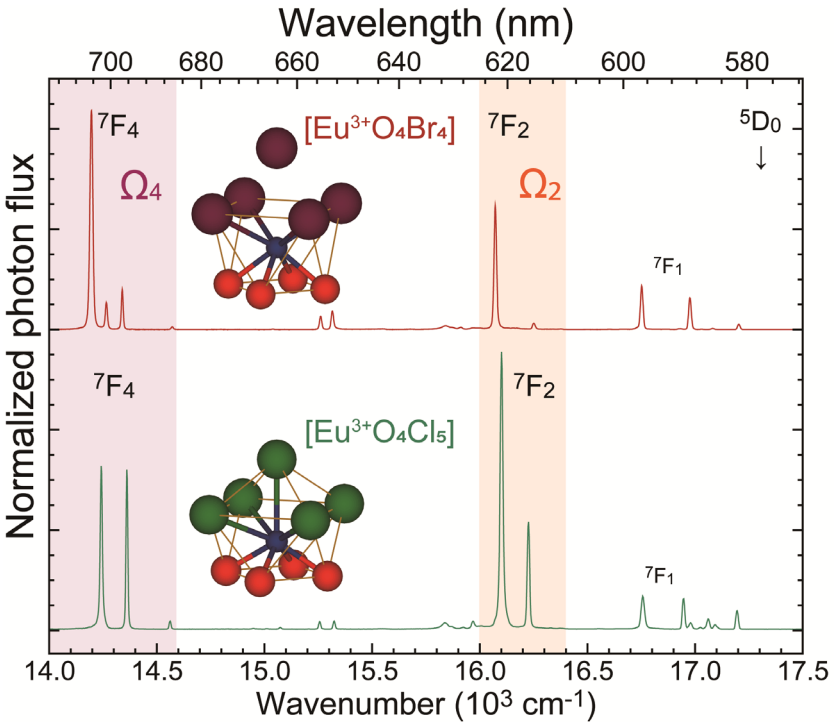

8.1. Introduction

Red luminescent materials activated with trivalent europium ions, Eu^{3+}, have been investigated for various applications [1,2], such as cathode ray tubes [3–5], fluorescent tubes [6–8], white light-emitting diodes (w-LEDs) [9–11], displays [12,13], and anti-counterfeiting paints for banknotes [14]. The Eu^{3+} luminescence is attractive due to the three reasons; the sharp luminescence lines attributed to the 4f-4f transition with a small effect of the electron-phonon coupling, the hypersensitivity of the $^5D_0 \rightarrow {}^7F_2$ transition depending crucially on a local environment around Eu^{3+}, and the efficient charge transfer (CT) excitation from ligands. The enormous amount of inorganic compounds has been considered to obtain the intense Eu^{3+} orange-red luminescence with high luminous efficacy for radiation ($lm \cdot W^{-1}$). Mono-anion materials, including oxides, nitrides, halides, and sulfides, have been regarded as the widely used host compounds of inorganic phosphors because it is relatively easy to prepare and analyze their crystalline phases and compositions. Nowadays, the mixed-anion compounds attract materials scientists' attention because of the possibility of developing a new functional material [15]. When a Eu^{3+} ion is surrounded by multiple types of anions with different characters (*e.g.*, electronegativity, polarizability, ionic radius, and valence state), its luminescent properties can be significantly affected by increasing the local asymmetry and enhancing the crystal field splitting [15]. According to the Judd-Ofelt theory, which quantitatively evaluates the transition probabilities of lanthanoid ions [16–18], the Eu^{3+} $^5D_0 \rightarrow {}^7F_2$ luminescence around 620 nm is sensitive to the asymmetry of the local environment, and then the Eu^{3+} red luminescence enhancement in the mixed-anion coordination is expected.

In this study, we focus on the compounds with the oxyhalide coordination, represented by the chemical composition of YO*X* (*X* = Cl or Br), to investigate the influence on Eu^{3+} luminescence. The YO*X* is one of the matlokites containing rare-earth elements. Matlockites is the name of the mineral with the composition PbClF, whose layered structure has a tetragonal unit cell with the space group *P*4/*nmm* (No. 129) [19]. In both YOCl and YOBr, the Y^{3+} sites have the monocapped square antiprism with the C_{4v} symmetry accommodating trivalent lanthanoid ions Ln^{3+} without any charge compensation. This local structure has only two

symmetrical operations, a four-fold rotation axis C_4 and a mirror plane σ_v; no inversion center in the C_{4v} sites. In addition, Ln^{3+} ions are surrounded by both X^- and O^{2-}, possibly leading to further distortion in the local field and enhancement of the transition probabilities.

In a few previous studies [20–22], strong Eu^{3+} luminescence in the YO*X* hosts was observed and discussed. First, Blasse reported some essential characteristics of the Eu^{3+} luminescence in a series of *RE*O*X* hosts (*RE* = Y, Gd, La, and *X* = Cl, Br), such as the relative PL intensity and quantum yields with a cation and anion variation [20]. He concluded that the choice of X^- significantly affected the crystal field around a Eu^{3+} ion and the spectral energy distribution of Eu^{3+} 4f-4f luminescence. Subsequently, Hölsä calculated the crystal field parameters for YOCl:Eu^{3+} and YOBr:Eu^{3+} based on spectroscopy and simulated the energy diagrams for Eu^{3+} with the Stark splitting [21,22]. While the Judd-Ofelt intensity parameters Ω_t are the powerful tool to predict the radiative decay rates and relative intensities of the electric dipole transition, there have been no reports on detailed analyses of lanthanoid ions in these oxyhalide compounds based on the Judd-Ofelt theory.

In this work, the effect of an oxyhalide ligand field on the Eu^{3+} luminescence was characterized based on the Judd-Ofelt theory [16–18]. Here, the Eu^{3+} concentration is fixed to be 0.5%, which is lower than that in Blasse's (5%) and Hölsä's (1%) studies [20–22], to investigate intrinsic properties of isolated Eu^{3+} ions. The estimated Judd-Ofelt intensity parameters Ω_t (t = 2, 4, 6) of the Eu^{3+}: $^5D_0 \rightarrow {}^7F_{2,4,6}$ luminescence reveals that the existence of chloride Cl^- and bromide Br^- ions cause the different spectral shapes and the variation of relative PL intensity. In addition, the spectroscopic characterization at various temperatures gives essential information about the relaxation process to the Eu^{3+}: $^5D_0$ state and its quenching process. The insight into the relaxation mechanism of the Eu^{3+} 4f and Eu^{3+}-X^- CT excited states helps us develop a novel red-emitting phosphor activated with Eu^{3+}.

8.2. Experimental Procedure

The Eu^{3+}-doped oxyhalide samples, YO*X*:Eu^{3+} (*X* = Cl or Br), were fabricated through the synthesis procedures described below. The oxychloride powder sample doped with 0.5 mol%

Eu^{3+}, $Y_{0.995}Eu_{0.005}OCl$, was prepared by oxidation of a chloride compound. The starting chemicals of $YCl_3{\cdot}6H_2O$ (99.9%, Mitsuwa Chemicals) and Eu_2O_3 (99.99%, Kojundo Chemical Laboratory) were weighed and mixed homogenously with an alumina mortar. The mixture was calcinated at 500 °C for six hours in the air atmosphere. The oxybromide powder sample doped with 0.5 mol% Eu^{3+}, $Y_{0.995}Eu_{0.005}OBr$, was synthesized through bromination of an oxide compound. The starting chemicals of Y_2O_3 (99.99%, Kojundo Chemical Laboratory) and Eu_2O_3 (99.99%, Kojundo Chemical Laboratory) were weighed and mixed. 150 wt% NH_4Br (99%, FUJIFILM Wako Chemicals), a bromination agent, was added to the mixture and sintered at 500 °C for two hours under N_2 gas flow. Since the prepared oxyhalide samples easily reacted with moisture, they were kept in a glovebox filled with high purity Ar gas. For luminescence properties measurements, the powder form samples were sealed in a quartz tube with an inner diameter of 6 mm under a vacuum.

Synchrotron X-ray diffraction (SXRD) data of the YO*X*:Eu^{3+} samples were obtained at 300 K on a monochromated incident beam at the BL02B2 JASRI beamline (λ = 0.413269 Å) of Spring-8. The sample in powder form was put in a Lindeman capillary tube with an inner diameter of 0.1 mm. The sealed capillary was rotated during measurements to suppress the effect of preferential orientation. The obtained SXRD patterns were analyzed with the Rietveld method using the RIETAN program [23]. For the Rietveld refinement, the atomic positions and the isotropic displacement parameter U_{iso} for Eu incorporated in Y sites are restricted to be the same as those of Y.

Photoluminescence excitation (PLE) spectra were measured with a setup consisting of a Xe short arc lamp (OPM2-502XQ, Ushio Inc.), double monochromators (SP-300i, Acton Research Corp.), and a photomultiplier tube (R3896, Hamamatsu Photonics). The sample was cooled down to 4 K by a closed-cycle He gas cryogenic refrigerator (CRT-A020-SE00, Ulvac Cryogenics). The PLE spectra were calibrated by the spectrum of the Xe lamp (excitation light source) detected by a Si standard photodiode (S1337-1010BQ, Bunkoukeiki & Co. Ltd.).

For photoluminescence (PL) measurements, luminescence was detected by a photomultiplier tube (R10699, Hamamatsu Photonics) equipped with a monochromator (SP-2300i, Princeton

Instruments). The monochromatic excitation light was obtained by the double monochromator system with the Xe lamp, which is the same as the PLE measurements.

The temperature-dependent PL spectra excited with a near-UV LED (UV17-0399-B, DOWA Electronics Materials Co., Ltd., λ = 280 nm) were detected by a CCD spectrometer (USB-2000+, Ocean Optics) connected with an optical fiber. The sample was attached in a liquid nitrogen cryostat (Helitran LT3, Advanced Research Systems) to control its temperatures from 100 to 800 K. The obtained PL spectra were calibrated by the spectrum of a deuterium-tungsten halogen light source (DH-2000, Ocean Optics).

The luminescence decay curves were investigated at various temperatures (100–800 K) with a luminescence lifetime spectrometer equipped with a Xe flash lamp (Quantaurus-Tau-C11367, Hamamatsu Photonics). The sample temperature was controlled by the liquid nitrogen cryostat.

8.3. Results

8.3.1. Structural Analysis of Matlockite-Type YO*X* (*X* = Cl or Br)

The SXRD data of the YO*X*:Eu^{3+} samples were collected to identify the crystalline phase and refine the lattice parameters. The diffraction patterns shown in **Figure 8.1** indicate that the single phases of matlockite-type YOCl and YOBr crystals were successfully prepared. The Rietveld refinement of these SXRD patterns was performed based on the tetragonal structure (space group: *P*4/*nmm*, No. 129). The refined lattice parameters of a tetragonal unit cell are $a = b =$ 3.90018(5) Å and c = 6.5919(2) Å for the YOCl:Eu^{3+}, and $a = b$ = 3.83931(8) Å and c = 8.2622(5) Å for the YOBr:Eu^{3+}. Other crystallographic parameters obtained by the Rietveld refinement are provided in **Tables 8.1** and **8.2**. The output reliability factors R_{wp}(YOCl) and R_{wp}(YOBr) were 6.201% and 6.106%, respectively, indicating a good agreement between the observed and fitted patterns. The layered crystal structures of YOCl and YOBr along the a-axis are depicted in **Figure 8.2a**. Comparing the lattice parameters between YOCl and YOBr, the unit cell varies anisotropically by substituting small Cl^- (1.81 Å) with large Br^- (1.96 Å) [24], in the matlockite

structure. Along the in-plane direction [100] and [010], the lattice constant *a* and *b* of the YOBr:Eu^{3+} were slightly smaller by 0.06087(9) Å (only −1.56%) than that of the YOCl:Eu^{3+}. In contrast, the lattice constant *c* of the YOBr:Eu^{3+} is considerably larger than that of the YOCl:Eu^{3+}, which was unexpected from the ionic radius difference.

The distances between two [*X*-Y-O-Y-*X*] sheets were refined to be 1.669(3) Å for the YOCl:Eu^{3+} and 2.774(2) Å for the YOBr:Eu^{3+}, respectively. In terms of the local structure around Y^{3+} ions in the YO*X* hosts, the critical difference is the bond length between Y^{3+} and X^- ions across the two sheets. Local environments around Y^{3+} in YO*X* hosts are picked up and shown in **Figure 8.2b**. Here, X^- ions in the same and adjacent [*X*-Y-O-Y-*X*] sheets are labeled as X_I^- and X_{II}^-, respectively. Based on the refined structure of the YOCl:Eu^{3+}, the distance from Y^{3+} to Cl_I^- and Cl_{II}^- are 3.0735(10) and 3.026(3) Å, resulting in the nine-fold monocapped square antiprism [YO_4Cl_5]. In contrast, the bond lengths between Y^{3+} and Br^- in the refined YOBr:Eu^{3+} structure are 3.1658(13) Å for Y^{3+}-Br_I^- and 4.403(3) Å for Y^{3+}-Br_{II}^-. The length of Y^{3+}-Br_I^- bonding is longer by 0.0923(16) Å than that of Y^{3+}-Cl_I^- bonding, as expected due to the larger ionic radius of Br^-. The Y^{3+}-Br_{II}^- bonding is relatively long because the two [Br-Y-O-Y-Br] sheets are well separated. The significant difference in the bond length between Y^{3+}-Br_I^- and Y^{3+}-Br_{II}^- leads to the eight-fold distorted square antiprism [YO_4Br_4]. This eight-fold coordination polyhedron is also considered in other lanthanoid oxybromide compounds with the matlockite structure [20]. The different coordination number of the Y^{3+} sites in the YO*X* hosts possibly contributes to the luminescent properties of accommodated lanthanoid ions, whereas both local structures belong to the same point group C_{4v}.

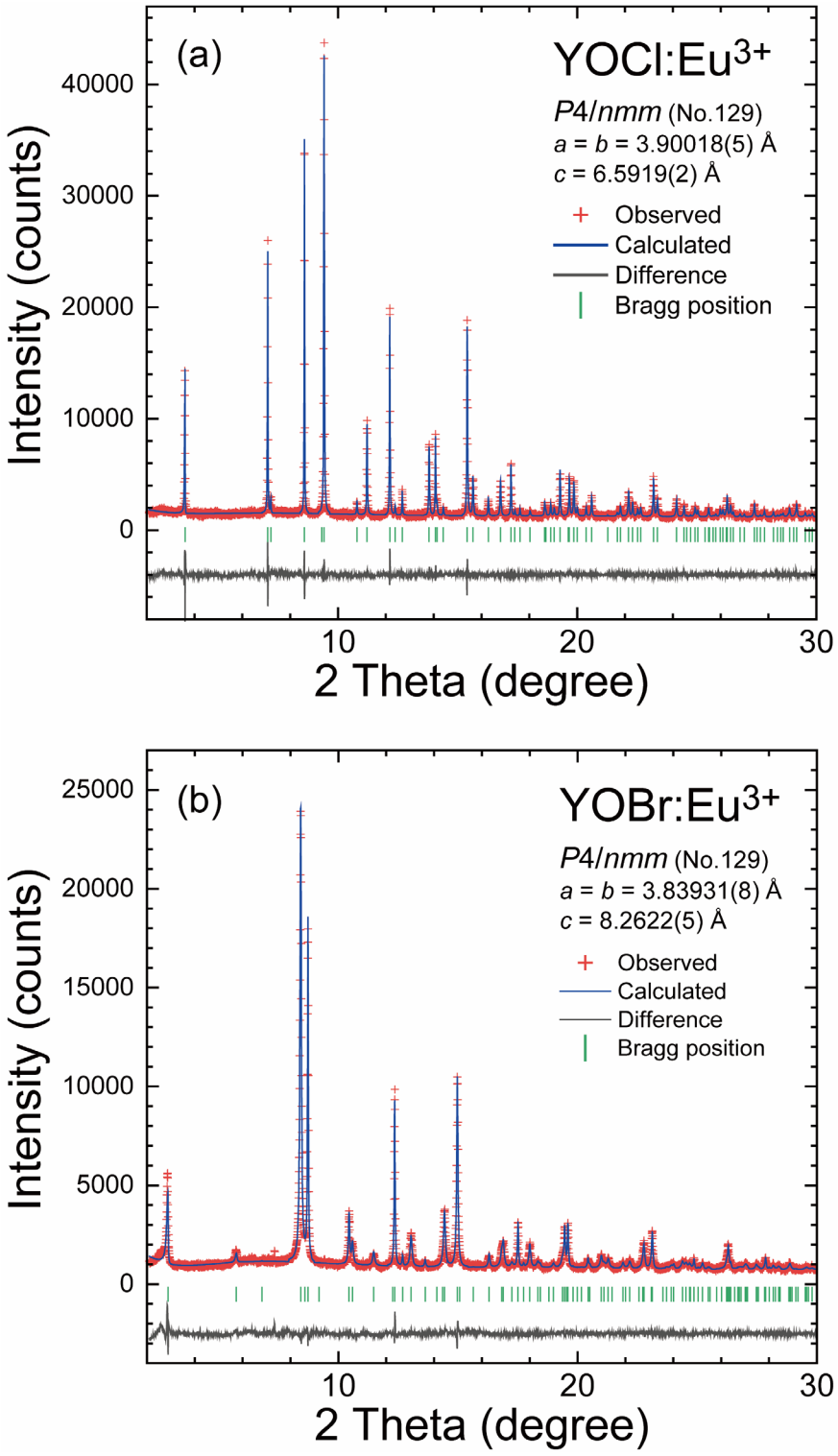

Figure 8.1. SXRD patterns of the (a) YOCl:Eu^{3+} and (b) YOBr:Eu^{3+} samples at room temperature (λ = 0.413269 Å). The observed and calculated intensities and difference plots are shown by red + marks, solid blue lines, and solid grey lines, respectively. Green tick marks indicate calculated Bragg peak positions based on matlockite-type tetragonal structure belonging to the space group *P4/nmm*. Reliability factors: R_{wp} = 6.201 %, R_p = 4.788%, and R_e = 2.383% for the YOCl:Eu^{3+}; R_{wp} = 6.106%, R_p = 4.550%, and R_e = 2.844% for the YOBr:Eu^{3+}.

Table 8.1. Crystallographic parameters of the YOCl:Eu^{3+} sample obtained by the Rietveld refinement of SXRD data at room temperature

YOCl:Eu^{3+}	$a = b = 3.90018(5)$ Å, $c = 6.5919(2)$ Å, $R_{wp} = 6.201\%$, $R_p = 4.788\%$, $R_e = 2.383\%$					
atom	occupancy	site	x	y	z	U_{iso} (Å^2)
Y	0.995	2*c*	0.00000	0.50000	0.1676(1)	0.0064(4)
Eu	0.005	2*c*	0.00000	0.50000	0.1676(1)	0.0064(4)
O	1.000	2*a*	0.00000	0.00000	0.00000	0.005(2)
Cl	1.000	2*c*	0.00000	0.50000	0.6266(3)	0.0145(6)

Table 8.2. Crystallographic parameters of the YOBr:Eu^{3+} sample obtained by the Rietveld refinement of SXRD data at room temperature

YOBr:Eu^{3+}	$a = b = 3.83931(8)$ Å, $c = 8.2622(5)$ Å, $R_{wp} = 6.106\%$, $R_p = 4.549\%$, $R_e = 2.839\%$					
atom	occupancy	site	x	y	z	U_{iso} (Å^2)
Y	0.995	2*c*	0.00000	0.50000	0.1350(2)	0.0089(6)
Eu	0.005	2*c*	0.00000	0.50000	0.1350(2)	0.0089(6)
O	1.000	2*a*	0.00000	0.00000	0.00000	0.003(2)
Br	1.000	2*c*	0.00000	0.50000	0.6679(2)	0.0174(7)

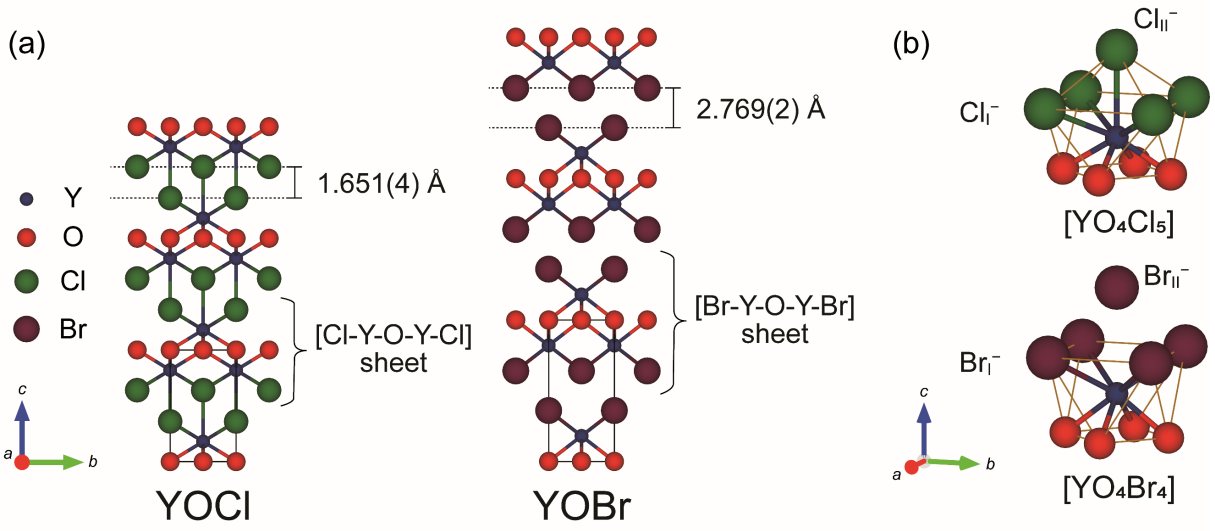

Figure 8.2. (a) Crystal structure of YO*X* (*X* = Cl or Br) along the *a*-axis. The solid black line indicates a tetragonal unit cell. The distance between the two [*X*-Y-O-Y-*X*] sheets is shown. (b) Local structures of a nine-fold $[YO_4Cl_5]$ and an eight-fold $[YO_4Br_4]$ polyhedron. The crystal structures were depicted with the VESTA program [25].

8.3.2. Charge Transfer Excited States of Eu^{3+} in Oxyhalide YO*X*

The prepared YO*X*:Eu^{3+} samples showed red luminescence under UV light illumination (**Figure 8.3**). **Figure 8.4** shows the PLE spectra of the YO*X*:Eu^{3+} samples at 4 K monitored with Eu^{3+} luminescence over 600 nm. In both spectra of the YO*X*:Eu^{3+}, the excitation lines and bands are classified into three categories; the Eu^{3+} 4f-4f transition, the CT transition from ligands, and the defects-related absorption.

The sharp lines are assigned to the 4f-4f transition of Eu^{3+}: from $^7F_0$ to $^5D_1$ (~19000 cm^{-1} = ~526 nm), $^5D_2$ (~21500 cm^{-1} = ~465 nm), $^5L_6$ (~25300 cm^{-1} = ~395 nm), $^5D_4$ (~27600 cm^{-1} = ~362 nm), and $^5H_6$ (31300 cm^{-1} = ~319 nm) states. Many sharp lines in the range of 26000–27400 cm^{-1} are due to the convolution of the ^5L_J, $^5G_J \leftarrow {}^7F_0$ transitions [21,22].

The broad and asymmetric excitation bands located over 31000 cm^{-1} are attributed to the CT transition from coordinating anions (X^- or O^{2-}) to Eu^{3+} ions. Since the CT transition is Laporte-allowed [2], PLE intensities of the CT bands are much more intense than that of Eu^{3+} 4f-4f excitation lines. The YOCl:Eu^{3+} exhibited stronger CT bands than the YOBr:Eu^{3+}. The centroid energies of asymmetric CT-bands (E^{CT}) are estimated to be 38163 cm^{-1} for the

YOCl:Eu^{3+} and 36686 cm^{-1} for the YOBr:Eu^{3+} by Gaussian fitting (**Figure 8.5**).

A very weak excitation band was observed below the CT excitation bands attributed to the defects-related absorption of intrinsic vacancies of the host oxyhalides.

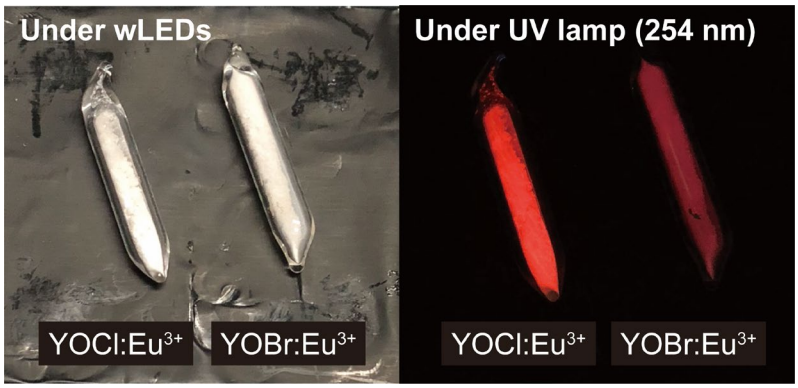

Figure 8.3. Pictures of the obtained YO*X*:Eu^{3+} (*X* = Cl or Br) samples under a white-LED lamp (left) and a UV lamp (λ = 254 nm). The samples in powder form were filled into a quartz tube.

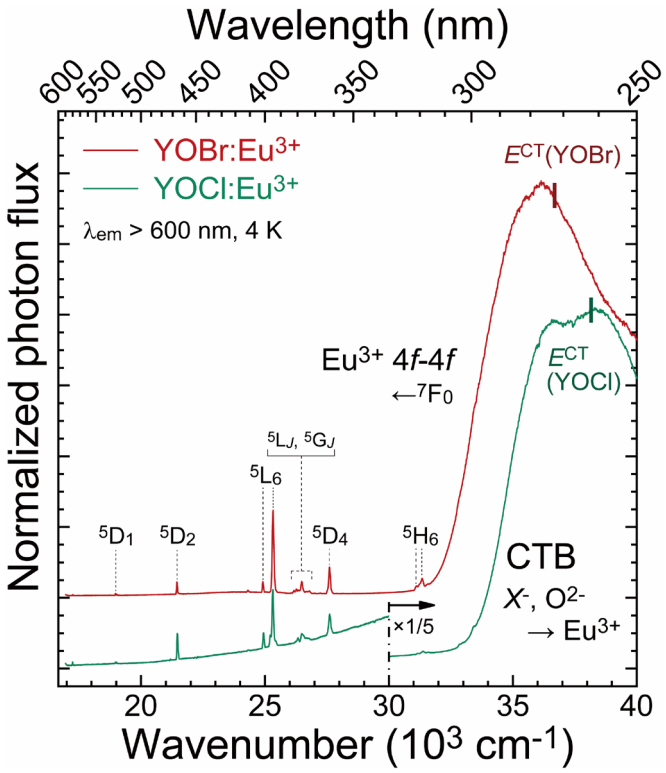

Figure 8.4. PLE spectra of the YO*X*:Eu^{3+} samples at 4 K, monitored with Eu^{3+} 4f-4f luminescence over 600 nm. The PLE intensities are normalized by the integrated area of the $^5D_1 \leftarrow {}^7F_0$ magnetic dipole transition, whose line strength is insensitive to the local environment around Eu^{3+} ions. PLE intensity of the YOCl:Eu^{3+} over 30000 cm^{-1} is divided by five.

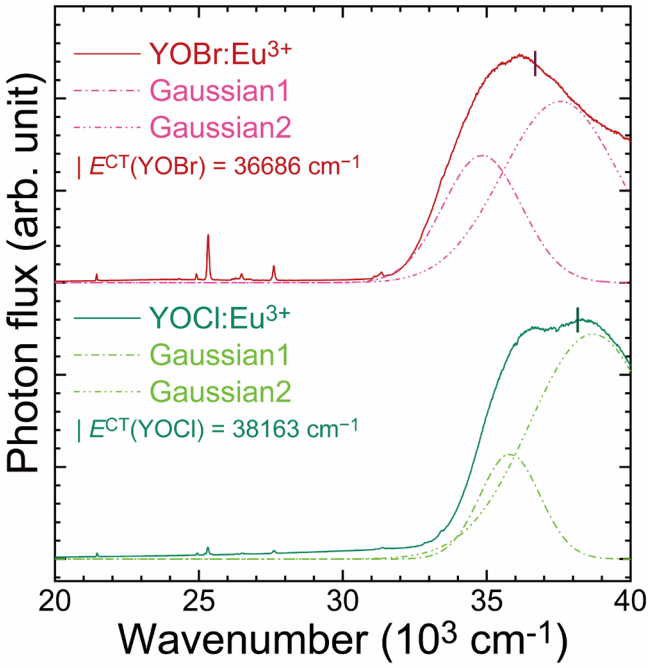

Figure 8.5. PLE spectra of the YO*X*:Eu^{3+} samples. The CT excitation bands up to 40000 cm^{-1} were deconvoluted with two Gaussian functions, and then the centroid energy of the reproduced CT bands with those two Gaussian functions was calculated; E^{CT}(YOCl) and E^{CT}(YOBr) are 38163 cm^{-1} and 36686 cm^{-1}, respectively.

8.3.3. Assignment of Eu^{3+} 4f-4f Luminescence

Figure 8.6a shows the PL spectra of the YO*X*:Eu^{3+} samples at 4 K under CT excitation (λ_{ex} = 280 nm). Characteristic Eu^{3+}: $^5D_0$ luminescence lines were observed in the range from 580 to 850 nm. The number of the $^5D_0$ luminescence lines in the C_{4v} symmetry and the energy diagram of Eu^{3+} *4f levels* for the YO*X* hosts were calculated by Forsberg [26] and Hölsä [21,22], respectively. Thus, the $^5D_0$ luminescence lines were assigned, listed in **Tables 8.3** and **8.4**. In the range of 16900–17100 cm^{-1}, the luminescence lines of the $^5D_0 \rightarrow {}^7F_1$ magnetic dipole (MD) transition are overlapped with those of the $^5D_1 \rightarrow {}^7F_3$ electric dipole (ED) transition from the higher excited state. The complicated structure due to the severe overlap makes the correct assignment difficult. In order to distinguish the $^5D_0$ luminescence from a small contribution of the $^5D_1$ luminescence, the PL spectra of the YO*X*:Eu^{3+} samples were measured at 4 K, excited by the different excitation pathways; the CT transition (λ_{ex} = 280 nm) and the $^5L_6 \leftarrow {}^7F_0$ transition (λ_{ex} = 395 nm). The

enlarged PL spectra in the range of 16650–17300 cm^{-1} for the YO*X*:Eu^{3+} samples are shown in **Figure 8.6b**, where the PL intensities are normalized with the integrated area of the $^5D_0 \rightarrow {}^7F_0$ transition peaking at 17195 cm^{-1} for the YOCl:Eu^{3+} and 17203 cm^{-1} for the YOBr:Eu^{3+}. The population of the $^5D_0$ and $^5D_1$ levels was changed by two different excitation routes, the CT and 4f-4f transition, because of the different relaxation processes. As the branching ratio and the relevant spectral shape of the $^5D_0$ and $^5D_1$ luminescence are not affected by excitation processes, the PL lines with the consistent relative intensity indicate the precise assignment of the $^5D_0 \rightarrow {}^7F_1$ luminescence in the normalized PL spectra. The two luminescence lines peaking at 16757 and 16946 cm^{-1} for the YOCl:Eu^{3+} and 16752 and 16976 cm^{-1} for the YOBr:Eu^{3+} are assigned to the $^5D_0 \rightarrow {}^7F_1$ MD transition.

Figure 8.6c displays the enlarged spectra at 4 K in the range from 17300 cm^{-1} (= ~578 nm) to 19800 cm^{-1} (= ~505 nm). As reported by Hölsä [21,22], many luminescence lines attributed to the Eu^{3+} 4f-4f transition from the higher excited states $^5D_1$ and $^5D_2$ were observed. The $^5D_2$ luminescence is drastically enhanced under the 4f-4f excitation at 395 nm, compared with the CT excitation. These different intensity ratios between the $^5D_1 \rightarrow {}^7F_J$ and $^5D_2 \rightarrow {}^7F_J$ transitions enable us to assign the complicated luminescence structures. The enhancement of the $^5D_2$ luminescence intensity was significant in the YOBr:Eu^{3+}. The assignment of each luminescence line is listed in **Table 8.5** and represented in Figure 8.6c. All the assigned luminescence lines corresponded with the assignment in the previous reports by Hölsä [21,22].

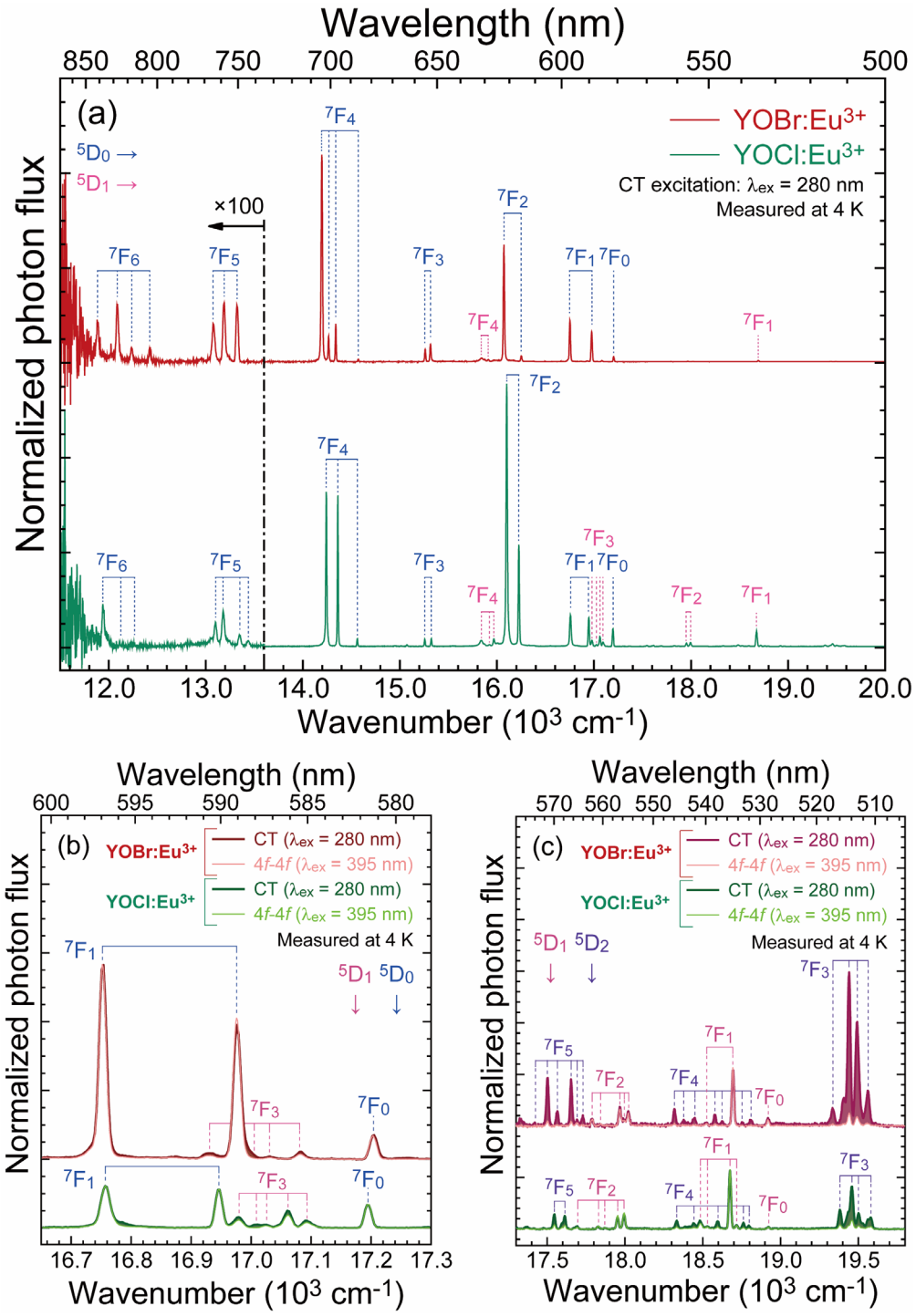

Figure 8.6. (a) PL spectra of the YOX:Eu^{3+} samples at 4 K, excited by the CT transition (λ_{ex} = 280 nm). The PL intensities are normalized by the integrated area of the $^5D_0 \rightarrow {}^7F_1$ magnetic dipole transition, whose line strength does not depend on the local environment around Eu^{3+} ions. Below 13600 cm^{-1} (λ > ~735 nm), the spectra were obtained with a low spectral resolution and displayed with the PL intensity enlarged 100 times. (b), (c) Enlarged PL spectra at 4 K with different excitation wavelengths, 280 nm (shown in solid lines, CT transition) and 395 nm (shown in broken lines, $^5L_6 \leftarrow {}^7F_0$ transition). The PL intensities are normalized by the integrated area of the (b) $^5D_0 \rightarrow {}^7F_0$ and (c) $^5D_1 \rightarrow {}^7F_1$ transition.

Table 8.3. Peak positions and relative intensities of Eu^{3+}: $^5D_0$ emission in YOCl:Eu^{3+}

	^7F_J	wavenumber (cm^{-1})	wavelength (nm)	relative intensity (this work)	relative intensity (reported by Blasse [20])
$^5D_0$ →	$J = 0$	17195	581.56	2.27	3
	$J = 1$	16946	590.11	10.0	10
		16757	596.77		
	$J = 2$	16226	616.29	59.2	70
		16101	621.08		
	$J = 3$	15323	652.61	1.68	3
		15257	655.44		
	$J = 4$	14562	686.72	37.2	48
		14361	696.33		
		14242	702.15		
	$J = 5$	13436	744.27	0.358	—
		13349	749.12		
		13179	758.78		
		13098	763.48		
	$J = 6$	12239	817.06	0.203	—
		12127	824.61		
		11944	837.24		

Table 8.4. Peak positions and relative intensities of Eu^{3+}: $^5D_0$ emission in YOBr:Eu^{3+}

	^7F_J	wavenumber (cm^{-1})	wavelength (nm)	relative intensity (this work)	relative intensity (reported by Blasse [20])
$^5D_0$ →	$J = 0$	17203	581.29	0.654	1
	$J = 1$	16976	589.07	10.0	10
		16752	596.94		
	$J = 2$	16251	615.35	18.1	20
		16072	622.20		
	$J = 3$	15315	652.95	4.15	4
		15261	655.27		
	$J = 4$	14571	686.29	42.0	35
		14339	697.40		
		14265	701.02		
		14196	704.42		
	$J = 5$	13323	750.58	0.569	—
		13188	758.27		
		13078	764.64		
	$J = 6$	12423	804.96	0.561	—
		12236	817.26		
		12088	827.27		
		11886	841.33		

Table 8.5. Assignment of emission peaks from ^5D_J states

initial state	terminal state	YOCl:Eu^{3+}		YOBr:Eu^{3+}	
		wavenumber (cm^{-1})	wavelength (nm)	wavenumber (cm^{-1})	wavelength (nm)
$^5D_1$	$^7F_0$	18922	528.49	18920	528.54
	$^7F_1$	18717	534.27		
		18675	535.48	18694	534.93
		18527	539.75	18522	539.90
		18485	540.98		
	$^7F_2$	17994	555.74	18021	554.91
		17952	557.04	17994	555.74
		17869	559.63	17967	556.58
		17829	560.88	17844	560.41
		17691	565.26	17790	562.11
				17690	565.29
	$^7F_3$			17082	585.41
		17092	585.07	17030	578.20
		17061	586.13	16930	590.67
		17025	587.37	16865	592.94
		17008	587.96	16828	594.25
		16979	588.96	16660	600.24
				16597	602.52

Table 8.5. Assignment of emission peaks from ^5D_J states (*continued*)

initial state	terminal state	YOCl:Eu^{3+}		YOBr:Eu^{3+}	
		wavenumber (cm^{-1})	wavelength (nm)	wavenumber (cm^{-1})	wavelength (nm)
$^5D_2$	$^7F_3$	19579	510.75	19562	511.20
		19562	511.20	19491	523.06
		19527	512.11	19440	514.40
		19502	512.77	19406	515.30
		19458	513.93	19335	517.20
		19433	514.59	19316	517.71
		19382	515.94		
	$^7F_4$			18808	531.69
		18798	531.97	18786	532.31
		18761	533.02	18753	533.25
		18596	537.75	18625	536.91
		18560	538.79	18577	538.30
		18443	542.21	18447	542.09
		18399	543.51	18404	543.36
		18332	545.49	18378	544.13
				18318	545.91
	$^7F_5$	17691	565.26		
		17614	567.73	17728	564.08
		17596	568.31	17690	565.29
		17546	569.93	17654	566.44
		17476	572.21	17589	568.54
		17414	574.25	17564	569.35
		17368	575.77	17501	571.40
		17298	578.10		

8.3.4. Temperature Dependence of Eu^{3+}: $^5D_0$ Luminescence in YO*X*

The PL spectra of the YO*X*:Eu^{3+} samples were measured at various temperatures (T = 100–800 K), with the excitation by the CT transition (λ_{ex} = 280 nm). **Figures 8.7a** and **8.7b** show the measured spectra in the region of the principal radiative transitions of Eu^{3+} ($^5D_0 \rightarrow {}^7F_{0-4}$). In **Figure 8.7c**, the integrated PL intensities in the range of 14000–15000 cm^{-1} ($^5D_0 \rightarrow {}^7F_4$) are plotted against temperature to eliminate the influence of the $^5D_1$ luminescence. For both oxyhalide samples, the Eu^{3+} luminescence intensity was decreased monotonously from 100 K. The temperature profile of the Eu^{3+}: $^5D_0$ luminescence does not correspond to the typical single barrier quenching curve described in the Boltzmann distribution.

Temperature dependence of luminescence lifetime is a good indicator to discuss the thermal quenching behavior of the Eu^{3+}: $^5D_0$ luminescence without the effect of the possibly temperature-dependent absorption coefficient. **Figures 8.8a** and **8.8b** show the luminescence decay curves of the YO*X*:Eu^{3+} samples at various temperatures (T = 100–800 K) excited by the CT transition (λ_{ex} = 280 nm). In contrast to the temperature-dependent PL intensity, the slope of the decay curves was almost unchanged up to ~600 K, and then increased. All the decay curves slightly deviated from the single exponential profile, fitted by a second-order exponential function, described below:

$$I(t) = A_1 \exp(-t/\tau_1) + A_2 \exp(-t/\tau_2)\,, \tag{8.1}$$

where A_1 and A_2 are the amplitudes of each decay component, and τ_1 and τ_2 are the luminescence

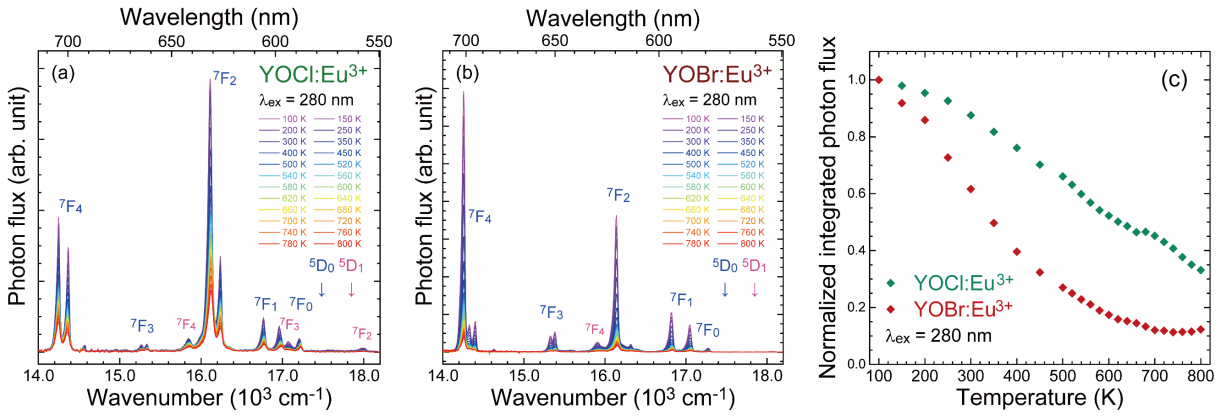

Figure 8.7. PL spectra of the YO*X*:Eu^{3+} samples at various temperatures (T = 100–800 K) excited with a near-UV LED (λ_{ex} = 280 nm). (c) Temperature-dependent integrated PL intensity of $^5D_0 \rightarrow {}^7F_4$ transition.

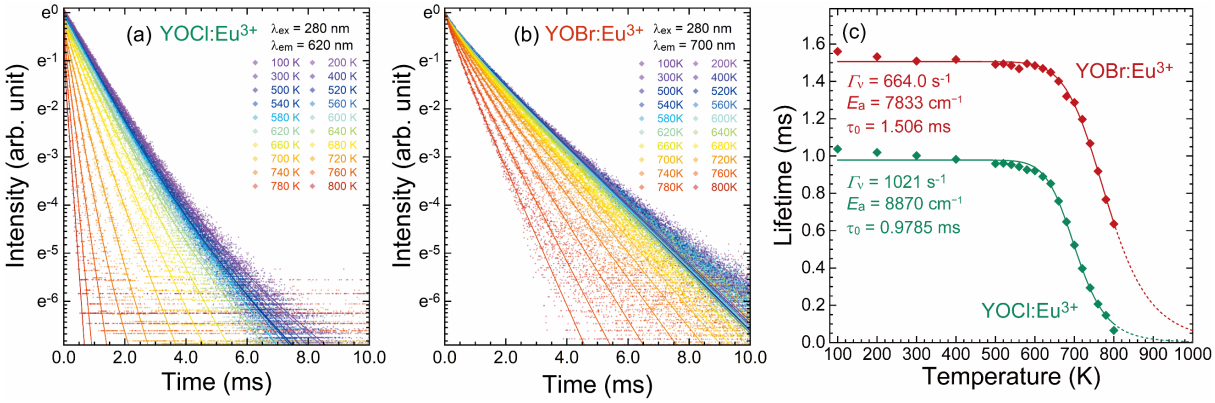

Figure 8.8. (a), (b) Luminescence decay curves of the YO*X*:Eu^{3+} samples at various temperatures (T = 100–800 K) excited by the CT transition (λ_{ex} = 280 nm). (c) Temperature dependence of luminescence lifetimes estimated by a second-ordered exponential function (Eq. (1)). The plots were fitted by the single barrier quenching curves, shown in Eq. (3). The fitted curves over 800 K are represented in broken lines.

lifetime at each temperature. In general, the Eu^{3+}: $^5D_0$ luminescence shows the single-exponential decay profile. However, in the YO*X*:Eu^{3+} samples, the decay curves could not be fitted with a single-exponential function, indicating the existence of a slight energy transfer (ET) process. As the purpose is to discuss the possible quenching process, the average luminescence lifetime of the $^5D_0$ state at each temperature $\tau_f(T)$ was estimated by the following eq. 8.2:

$$\tau_f(T) = \frac{A_1\tau_1{}^2 + A_2\tau_2{}^2}{A_1\tau_1 + A_2\tau_2}. \tag{8.2}$$

The average lifetimes at each temperature from 100 to 800 K are plotted against temperature and shown in **Figure 8.8c**. These profiles were fitted with the typical quenching curves following the single barrier quenching model described below [27]:

$$\tau_f(T) = \frac{1}{\Gamma_\nu + \Gamma_0 \exp(-E_a/kT)}, \tag{8.3}$$

where Γ_ν is the radiative transition rate for Eu^{3+}: $^5D_0$ luminescence, Γ_0 is the attempt rate of the nonradiative process, E_a is the activation energy of thermal quenching, k is the Boltzmann constant (= 0.695 $cm^{-1}\cdot K^{-1}$), and T is temperature. Since the nonradiative term $\Gamma_0 \exp(-E_a/kT)$ is negligible at low temperatures, the Γ_ν value is described by the reciprocal number of the luminescence lifetime at low temperature, τ_0. The RMS errors for the fitting are relatively small. The obtained parameters, Γ_ν, τ_0, Γ_0, E_a, and the quenching temperature $T_{50\%}$, are listed in **Table 8.6**. At $T_{50\%}$, the lifetime is half of the τ_0, where the Γ_ν and the nonradiative term become equal.

Table 8.6. Obtained values by the single barrier quenching curve fitting; the output is the radiative transition rate for Eu^{3+}: $^5D_0$ luminescence Γ_v, the luminescence lifetime at low temperatures τ_0, the attempt rate of the nonradiative process Γ_0, the thermal activation energy E_a, and the quenching temperature $T_{50\%}$

	Γ_v (10^3 s^{-1})	τ_0 (ms)	Γ_0 (10^9 s^{-1})	E_a (cm^{-1})	$T_{50\%}$ (K)
YOCl:Eu^{3+}	1.021	0.979	75.4	8870	704
YOBr:Eu^{3+}	0.664	1.51	1.17	7833	783

8.4. Discussion

8.4.1. Difference in Local Environment with Multiple Anions

In order to characterize a luminescence center ion, deep insight into the local environment is inevitable. First, we discuss the geometrical and chemical environments of the Y^{3+} sites where impurity lanthanoid ions are incorporated. As mentioned in section 8.3.1, the YOCl and YOBr are isostructural, yet with different coordination environments; the nine-fold monocapped square antiprism polyhedron [YO_4Cl_5] and the eight-fold distorted square antiprism polyhedron [YO_4Br_4]. Both polyhedra have the C_{4v} symmetry despite the different coordination numbers. Considering only the geometry of anion polyhedra around Y^{3+}, the eight-fold [YO_4Br_4] polyhedron is similar to the regular square antiprism with the D_4 symmetry. In fact, the [YO_4Br_4] polyhedron loses the two-fold rotation axis and belongs to the C_{4v} symmetry.

The critical difference in shapes of the coordination polyhedron is derived from the distance between two [*X*-Y-O-Y-*X*] sheets; 1.669(3) Å for the YOCl:Eu^{3+} and 2.774(2) Å for the YOBr:Eu^{3+}. In analogy to the isostructural BiO*X* (*X* = F, Cl, Br, I), the two sheets are held together by Coulomb interaction between Y^{3+} and X^- and nonbonding van der Waals interaction along the [001] direction [28–30]. These bonding and nonbonding interactions are cooperative. For the YOCl host, the ionicity of the interaction between Y^{3+} and Cl_{II}^- in the neighboring two sheets is strong because of the high electronegativity of Cl. On the contrary, the ionicity of the bonding between Y^{3+} and Br^- is weak due to the long bond length stemming from a large ionic radius of Br^- and the low electronegativity of Br. The nonbonding van der Waals interaction, which is

comparatively weak, is dominant between the two [Br-Y-O-Y-Br] sheets, consequently as the considerable distance as 2.774(2) Å.

8.4.2. Judd-Ofelt Analysis Based on PL Spectra

We perform the Judd-Ofelt analysis of the PL spectra shown in Figure 8.6a with the static model [11,18,31]. The detailed procedure is provided below. In this work, we quantitatively characterized the Eu^{3+}: $^5D_0 \rightarrow {}^7F_J$ (J = 0–6) luminescence in the YO*X* hosts based on the Judd-Ofelt analysis. Notably, it is possible to perform the Judd-Ofelt analysis for Eu^{3+}-doped compounds based not only on an absorption spectrum but also on a PL spectrum. There are two reasons; Eu^{3+}: $^5D_0$ emission lines are well-separated, and each ED transition has only one non-zero squared reduced matrix elements. The spontaneous emission rate of each transition $A_R(^5D_0 \rightarrow {}^7F_J)$ is used as the input data, which is proportional to the integrated PL intensity in the scale of photon flux. However, in the PL spectra of the YO*X*:Eu^{3+} samples, the $^5D_1$ emission were overlapped with the $^5D_0$ emission, leading to overestimation of spontaneous emission rates. The PL spectra were fitted by Voigt functions to eliminate the weak $^5D_{1,2}$ emission during the integrating process. While the original profile of 4f-4f emission lines is the Lorentzian shape, the inhomogeneous broadening is taken into account with the Gaussian component in a Voigt function. The observed (dot-lines) and reproduced (solid lines) PL spectra were shown in **Figures 8.9a** and **8.9b**. The number of emission lines of Eu^{3+} in C_{4v} symmetry had been calculated by Forsberg [26,32]: a $^7F_0$ line, two $^7F_1$ lines, two $^7F_2$ lines, two $^7F_3$ lines, and four $^7F_4$ lines. However, in the YOCl:Eu^{3+} sample, only the three $^7F_4$ emission lines were observed because the first two lines ($A_1 \rightarrow E$, A_1) at around 14500 cm^{-1} were exactly overlapped [21]. The ten and eleven Voigt functions for the YOCl:Eu^{3+} and YOBr:Eu^{3+} well reproduced the $^5D_0$ emission spectra.

The calculated values are listed in **Table 8.7**. The histogram representing the comparison of the calculated Judd-Ofelt intensity parameters Ω_t (t = 2, 4, 6) is depicted in **Figure 8.10a**. For the comparison, the reported Ω_t parameters in some inorganic compounds are listed in **Table 8.8**. The branching ratios of the $^5D_0$ luminescence for the YO*X* hosts are shown in **Figure 8.10b** and **Table 8.9**.

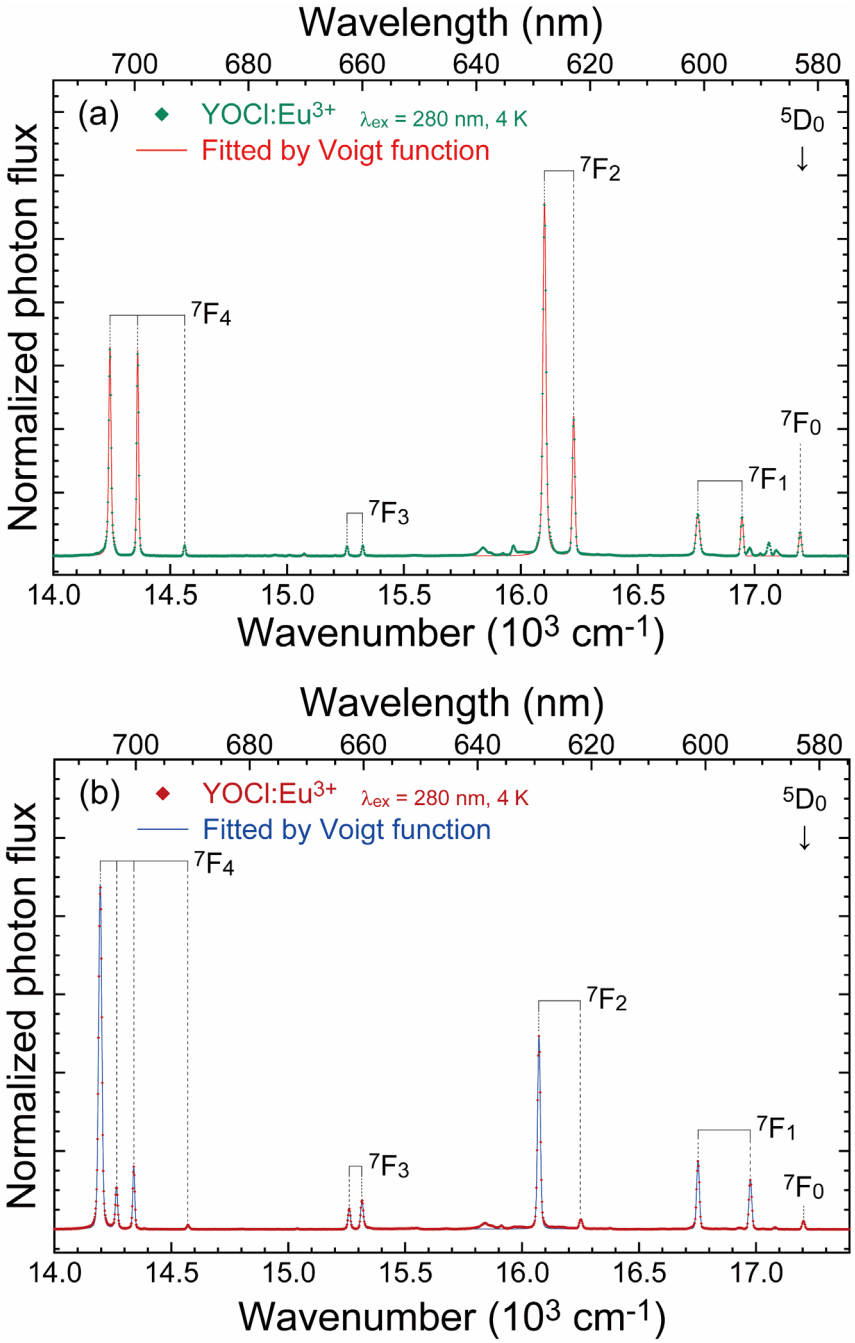

Figure 8.9. Observed PL spectra of the (a) YOCl:Eu^{3+} and (b) YOBr:Eu^{3+} samples (shown in dot-lines) and reproduced emission lines of the $^5D_0 \rightarrow {}^7F_{0-4}$ transition with Voight functions.

The validity of the Judd-Ofelt analysis is evaluated by comparing the results of the luminescence decay measurements. The calculated spontaneous emission rates A_R show a similar trend to the Γ_v values determined by the luminescence decay curves. For the YOCl:Eu^{3+}, the Γ_v (= 1.02×10^3 s^{-1}) is greater than for the YOBr:Eu^{3+} (= 6.64×10^2 s^{-1}), which corresponds to the larger A_R for the ED transition in the YOCl:Eu^{3+}. However, both Eu^{3+}-doped oxyhalides

YO*X* have some differences between the experimental lifetime τ_0 and the calculated lifetime τ_R values. The A_R also depends on the refractive index of the host material. Thus, the difference can be caused by the error of the refractive index used for the calculation.

It is considered that the Ω_2 parameter correlates with the site asymmetry around Eu^{3+} [33]. The Ω_2 parameter of the YOCl:Eu^{3+} takes 8.81×10^{-20} cm^2, comparable to that of Y_2O_3:Eu^{3+} (9.86×10^{-20} cm^2) [34] or YVO_4:Eu^{3+} (7.49×10^{-20} cm^2) [35] which are known to be phosphors with a high Ω_2 parameter (Table 8.8). It is due to the noncentrosymmetric nine-fold [$Eu^{3+}O_4Cl_5$] structure with the C_{4v} symmetry. For the YOBr:Eu^{3+}, despite the same site symmetry C_{4v}, the Ω_2 parameter is 2.72×10^{-20} cm^2, which is less than one-third of the YOCl:Eu^{3+}. As mentioned in section 8.4.1, the main difference in the local environment around Eu^{3+} ions between the YOCl and YOBr is the coordination number of halide ions. In the YOBr host, Eu^{3+} ions occupy the

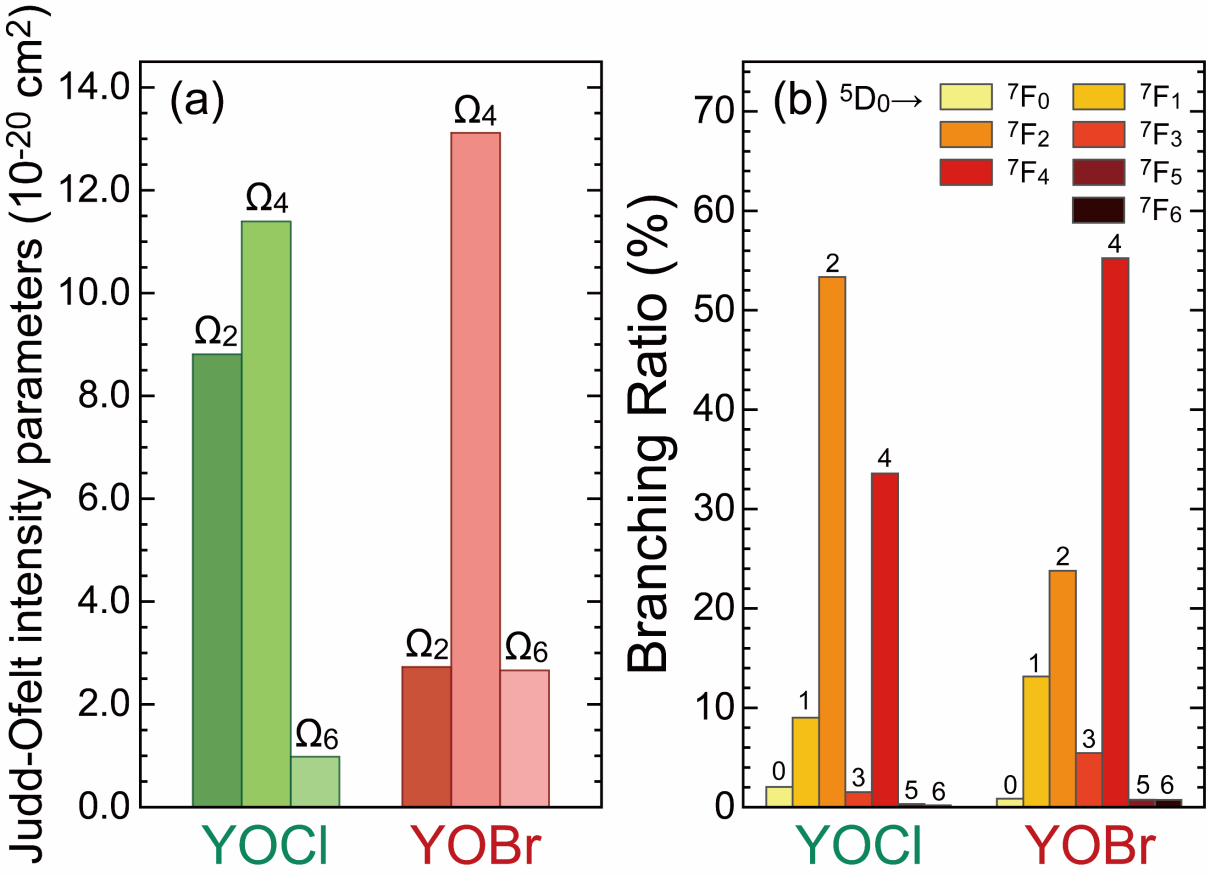

Figure 8.10. (a) Histogram of calculated Judd-Ofelt intensity parameters Ω_t (t = 2, 4, 6) for the YO*X*:Eu^{3+} samples, based on the PL spectra shown in Figure 8.6a. (b) Histogram of the branching ratios of $^5D_0 \rightarrow {}^7F_J$ (J = 0–6) transition for Eu^{3+} ions in the YO*X* hosts.

eight-fold distorted square antiprism structure [$Eu^{3+}O_4Br_4$], whose geometry is similar to a regular square antiprism with the D_4 symmetry. According to Judd, the hypersensitive $^5D_0 \rightarrow {}^7F_2$ ED transition described by the Ω_2 parameter is observed remarkably not in the D_4 but in the C_{4v} symmetry [36]. For the eight-fold [$Eu^{3+}O_4Br_4$] polyhedron, the pseudo-D_4 character may cause a significant Ω_2 difference between the YOCl and YOBr hosts with coordination number decreasing although the actual symmetry is C_{4v}. It is found that the Ω_2 parameter correlated with the asymmetry cannot be determined only by the site symmetry. The shape of a coordination polyhedron around Eu^{3+} should be considered to control the Ω_2 parameter which determines the spontaneous emission rate of the hypersensitive $^5D_0 \rightarrow {}^7F_2$ ED transition at 620–630 nm.

The Ω_4 and Ω_6 parameters are considered to show a similar trend to the variation of the local environment [36]. A few previous studies reported that the $\Omega_{4,6}$ parameters correlate with the covalency of a Ln^{3+}-O^{2-} bonding [37,38]. Table 8.8 shows the tendency for the inorganic crystalline materials in the magnitude of the Ω_4 parameters. The Ω_4 parameters for the YO*X*:Eu^{3+} samples are considerably large (11.4×10^{-20} cm^2 for the YOCl:Eu^{3+} and 13.1×10^{-20} cm^2 for the YOBr:Eu^{3+}). Both the Ω_4 and Ω_6 parameters for the YOBr:Eu^{3+} are larger than those for the isostructural YOCl:Eu^{3+}. Considering the electronegativity of anions, chlorine and bromine have the smaller Pauling electronegativities χ_P (χ_P(Cl) = 3.16 and χ_P(Br) = 2.96) than oxygen (χ_P(O) = 3.44) [39]. Thus, the YO*X* can be regarded as more covalent host material compared with many oxides. In the case of a comparison between the isostructural YOCl:Eu^{3+} and YOBr:Eu^{3+}, the Y^{3+}-Br^- bonding is more covalent than the Y^{3+}-Cl^- bonding. In fact, the results of the Ω_4 and Ω_6 parameters for the YO*X*:Eu^{3+} followed this tendency of covalency. Especially, the coordination of covalent Br contributes to the significant $\Omega_{4,6}$ parameters in the YOBr:Eu^{3+}. The large Ω_4 is also confirmed in the covalent host Y_2O_2S (= 10.2×10^{-20} cm^2). Although Eu^{3+}-doped oxides show various Ω_4 values with the compositional and structural differences, all the values are smaller than those of the covalent YO*X* and Y_2O_2S hosts. Fluorides show the small Ω_4 values due to the large electronegativity of fluorine (χ_P(F) = 3.98) [39]. The vanadates and phosphates, which form the oxide tetrahedron unit with strong bonding and give less covalency to Eu^{3+}, have very small values. These results support that the $\Omega_{4,6}$ parameters are correlated with the bonding

character between Eu^{3+} and coordinating anions.

Compared with other Eu^{3+}-doped phosphors, the YO*X*:Eu^{3+} takes a considerably large Ω_4 value by the covalent properties of halide anions. Moreover, the Ω_2 parameter is controlled by the shape of the anion polyhedron, which cannot be described only by the site symmetry in the YO*X*:Eu^{3+}. Those results will give us information to design the luminescence spectral distribution. Remarkably, the YOBr:Eu^{3+} exhibits a high branching ratio of the $^5D_0 \rightarrow {}^7F_4$ transition over 50% due to both small Ω_2 and large Ω_4 parameters in a unique Y^{3+} site. The $^5D_0 \rightarrow {}^7F_4$ luminescence is located at 680–710 nm, where the transmittance of bio-tissues is high, and the sensitivity of a Si detecter is high (the so-called first biological window) [40,41]. The Eu^{3+}-doped covalent oxybromide with the intense $^5D_0 \rightarrow {}^7F_4$ luminescence is expected as a candidate for bio-imaging phosphor with the first biological window.

Table 8.7. Calculated values based on the Judd-Ofelt analysis; the output is the Judd-Ofelt intensity parameters Ω_t (t = 2, 4, 6), the spontaneous emission rates of the $^5D_0 \rightarrow {}^7F_J$ MD and ED transition $A_R(^7F_J)$ (J = 1, 2, 4, 6), and the radiative lifetime τ_R, for Eu^{3+} ions in the YOCl and YOBr hosts

	Ω_2 (10^{-20} cm^2)	Ω_4 (10^{-20} cm^2)	Ω_6 (10^{-20} cm^2)	$A_R(^7F_1)$ (10^2 s^{-1})	$A_R(^7F_2)$ (10^2 s^{-1})	$A_R(^7F_4)$ (10^2 s^{-1})	$A_R(^7F_6)$ (10^2 s^{-1})	τ_R (ms)
YOCl	8.81	11.4	0.982	1.10	6.49	4.09	0.0223	0.821
YOBr	2.72	13.1	2.66	1.11	2.00	4.64	0.0620	1.19

Table 8.8. Calculated Judd-Ofelt intensity parameters Ω_t (t = 2, 4, 6) for a variety of Eu^{3+}-doped crystalline materials in order of the Ω_4 parameters

host compounds	Ω_2 (10^{-20} cm^2)	Ω_4 (10^{-20} cm^2)	Ω_6 (10^{-20} cm^2)
YOBr (this work)	2.72	13.1	2.66
YOCl (this work)	8.81	11.4	0.982
Y_2O_2S [42]	13.0	10.2	—
α-$Y_2Si_2O_7$ [41]	3.95	7.22	—
$YAlO_3$ [43]	2.66	6.33	0.8
$YSiO_2N$ [40]	7.58	3.41	—
α-$CaSiO_3$ [42]	3.69	2.79	—
CaF_2 [44]	0.73	2.53	—
Y_2O_3 [45]	9.86	2.23	< 0.32
Gd_2O_3 [46]	15.6	1.42	—
Lu_2O_3 [46]	12.2	1.2	—
LaF_3 [48]	1.19	1.16	0.39
YVO_4 [35]	7.49	0.47	—
YPO_4 [35]	0.78	0.38	—

Table 8.9. Branching ratios (%) of the Eu^{3+}: $^5D_0 \rightarrow {}^7F_J$ (J = 0–6) transition in the YOCl and YOBr hosts

	$^5D_0 \rightarrow {}^7F_J$						
	J = 0	J = 1	J = 2	J = 3	J = 4	J = 5	J = 6
YOCl	2.05	9.02	53.3	1.51	33.6	0.322	0.183
YOBr	0.860	13.2	23.8	5.46	55.2	0.748	0.738

8.4.3. Relaxation Dynamics of Excited States in YO*X*:Eu^{3+}

In this section, we discuss the dynamics of the excited states for Eu^{3+} ions in the YO*X* hosts. As shown in section 8.3.4, Eu^{3+} luminescence in the YO*X* hosts quenches at high temperatures (> 600 K). First, we consider the validity of the single barrier quenching model used for the fitting in Figure 8.8c. There are two possible quenching processes for Eu^{3+}: $^5D_0$ luminescence; the multiphonon relaxation (MPR) and the thermal activation *via* the CT states. The MPR rate to the lower $^7F_6$ level can be low because the energy difference is as large as ~12300 cm^{-1} and the maximum phonon energy of the YO*X* hosts is only ~600 cm^{-1} due to the vibrational mode of the Y-O bonding [48]. Therefore, the possible thermal quenching process is the thermal activation *via* the CT states with a single potential barrier. The relaxation process from the $^5D_0$ to the ^7F_J ground states through the CT states is a typical quenching process [49]. Dorenbos reported that there is a clear trend between the quenching temperature and the CT energy position. From this trend, the lower CT energy leads to a lower quenching temperature. In the PLE spectra (Figures 8.4 and 8.5), the CT energy related to the Eu^{3+}-X^- CT states are determined to be 38163 cm^{-1} for the YOCl:Eu^{3+} and 36686 cm^{-1} for the YOBr:Eu^{3+}. The results that the larger thermal activation energy of the YOCl:Eu^{3+} (E_a = 8870 cm^{-1}), compared with the YOBr:Eu^{3+} (E_a = 7833 cm^{-1}), corresponds to the prediction from the quenching model through the CT states.

In Figure 8.6c, the $^5D_1$ and $^5D_2$ luminescence intensity ratio considerably depends on excitation pathways. The principal relaxation process after the 4f-4f excitation is the MPR from one excited 4f level to the next lower level. Once Eu^{3+} ions are excited through the $^5L_6 \leftarrow {}^7F_0$ transition, they relax down into ^5D_J levels with several phonons emission because of the small energy difference between two adjacent 4f levels ($^5L_6$–$^5D_3$: 1500 cm^{-1}, $^5D_3$–$^5D_2$: 2400 cm^{-1}, $^5D_2$–$^5D_1$: 2500 cm^{-1}, and $^5D_1$–$^5D_0$: 1700 cm^{-1}) [50]. On the other hand, the weak $^5D_1$ and $^5D_2$ luminescence with respect to the $^5D_0$ luminescence under the CT excitation (Figure 8.6a) can be explained by the weak feeding process from the CT to the $^5D_{1,2}$ states and the strong feeding process to the $^5D_0$ state. Based on these results, the activation energy to the $^5D_0$ state is smaller than that to the $^5D_1$ and $^5D_2$ states. Nevertheless, the very weak $^5D_1$ and $^5D_2$ luminescence even at low temperatures are due to a small contribution of the tunneling effect.

Although the $^5D_0$ luminescence is not quenched up to ~600 K from the lifetime analysis, the PL intensity of the Eu^{3+}: $^5D_0$ luminescence in the YO*X* hosts monotonously decreases from 100 K with temperature (Figure 8.7c). As mentioned above, the excited Eu^{3+} ions with the CT transition relax to the minimum of the potential curve and then relax to the $^5D_0$ initial state of the radiative transition. If all of the population of CT states relax to the $^5D_0$ state, the temperature dependence of PL intensity follows that of PL lifetime. The observed difference between the temperature dependence of PL and lifetime can be caused by the temperature dependence of the feeding process. It is assumed that the CT states have another relaxation route *via* an intersection with the $^7F_6$ state. Therefore, the monotonous decreasing PL intensity is observed even in the temperature range where the $^5D_0$ lifetime is unchanged.

In order to explain the obtained results, the conventional coordinate diagrams (CCD) of the YO*X*:Eu^{3+} are constructed and shown in **Figure 8.11**. R_0 represents the equilibrium position of a Eu^{3+} ion to a ligand. The offset of the 4f states does not change because the Eu^{3+}-ligands distances are almost the same between the ground and excited states. In contrast, the offset of the CT parabolas is very large [49,51]. We assumed that the parabolas for the CT states have the same curvature as that for the 4f states. The bottom energy of the CT and the offset value are not determined quantitatively by the obtained results. On the other hand, based on the results of the tunneling process from the CT to the $^5D_{1,2}$ states, the relaxation process from the CT to the $^5D_0$ and ^7F_J states, and the activation energy from the $^5D_0$ to the CT states, the bottom of the CT parabolas should be located above the $^5D_2$ level (~21500 cm^{-1}) and between two parabolas of the $^5D_0$ and $^7F_6$ states, as shown in Figure 8.11. It is clear that the CT states play a crucial role in the dynamics of the excitation process. The large offset of the CT states in the YO*X*:Eu^{3+} is disadvantageous to the relaxation from the CT to $^5D_0$ states for the efficient and thermally stable $^5D_0$ luminescence. Tailoring the small lattice relaxation following the CT excitation is also essential to develop the novel Eu^{3+}-activated phosphors with high efficiency and thermal stability. In this CCD, the values of $S\hbar\omega$ (S, $\hbar$, and ω are the Huang-Rhys factor, the Dirack constant, and the phonon energy, respectively,) are 12271 cm^{-1} for the YOCl:Eu^{3+} and 11995 cm^{-1} for the YOBr:Eu^{3+}. Since Eu^{3+} do not show CT luminescence, the Sħω cannot be determined directly

from the Stokes shift ($2S\hbar\omega$). In contrast, the Yb^{3+}-doped materials can show CT luminescence, and the $S\hbar\omega$ values are reported between 3000–8750 cm^{-1} [46]. Considering the phonon energy of the Y-*X* and the comparison with the values for Yb^{3+} CT luminescence, the $S\hbar\omega$ values for the YO*X*:Eu^{3+} are large. It is not clear at the present that the obtained large Sħω in YOX:Eu^{3+} is reasonable or not. To determine the precise position of the CT parabolas, further investigation for the dynamics of the excited states related to the CT states in Eu^{3+}-doped materials is necessary.

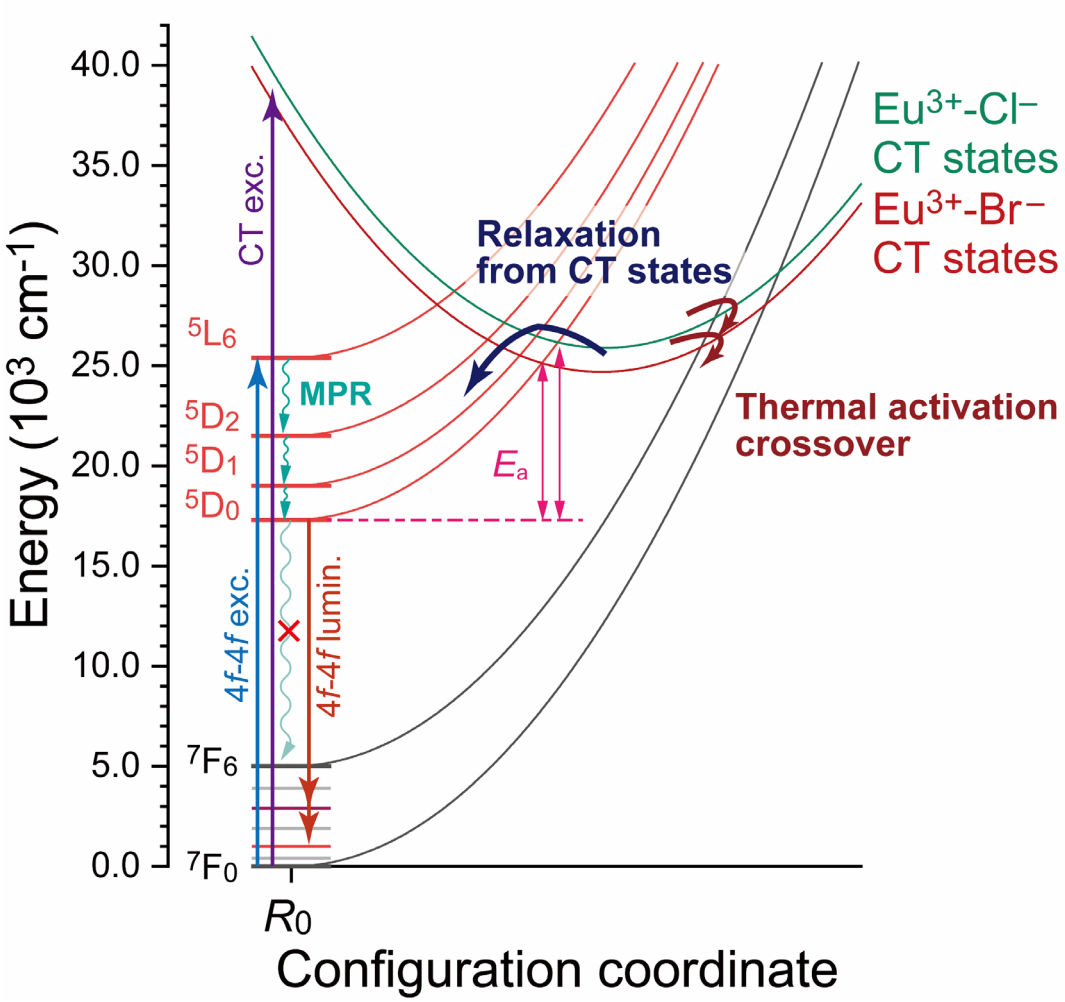

Figure 8.11. Configuration coordinate diagram of Eu^{3+} $4f^6$ levels and Eu^{3+}-X^- charge transfer states for the YO*X*:Eu^{3+}. Arrows depicted in the diagram represent the pathways of excitation, luminescence, and relaxation processes.

8.5. Conclusions

The influence of the anion variation on Eu^{3+}: ^5D_J luminescence in the isostructural YO*X* (*X* = Cl or Br) hosts, yet with the different coordination environment, was investigated from the spectroscopic perspective. For Eu^{3+} ions in the YOCl host incorporated in the nine-fold monocapped square antiprism polyhedra [YO_4Cl_5] with the noncentrosymmetric C_{4v} symmetry, the Judd-Ofelt Ω_2 parameter of the YOCl:Eu^{3+} was 8.81 × 10^{-20} cm^2, comparable to the Eu^{3+}-doped oxides Y_2O_3 or YVO_4. The Ω_4 parameter also took a large value, 11.4 × 10^{-20} cm^2. On the other hand, the YOBr host consisted of the eight-fold distorted square antiprism [YO_4Br_4] with the C_{4v} symmetry due to the large separation of two [Br-Y-O-Y-Br] sheets attributed to the covalency of Br. The Ω_2 parameter of the YOBr:Eu^{3+} was relatively small, 2.72 × 10^{-20} cm^2, because of the structural similarity to the eight-fold regular square antiprism with the D_4 symmetry. The Ω_4 parameter was also significantly large, 13.1 × 10^{-20} cm^2, due to the strongly covalent environment [$Eu^{3+}O_4Br_4$]. The charge transfer band energies E^{CT} for the YOCl:Eu^{3+} and YOBr:Eu^{3+} were estimated to be 38163 cm^{-1} and 36686 cm^{-1}, respectively. The smaller E^{CT} for the YOBr:Eu^{3+} resulted in the low thermal activation energy of the $^5D_0$ luminescence quenching. The difference in the relaxation processes of excited electrons between the charge transfer and 4f-4f transitions made the precise assignment of complicated spectral structures possible. The large offset of the charge transfer states in the configuration coordinate diagram for the YO*X*:Eu^{3+} caused thermally unstable and inefficient Eu^{3+} luminescence with the charge transfer transition. This work reveals that the Judd-Ofelt intensity parameters Ω_t are significantly affected by the geometry of coordination polyhedra and the bonding character between Eu^{3+} ions and coordinating anions. The mixed-anion host materials with the regular square antiprism-like local geometry have the great potential to show the intense $^5D_0 \rightarrow {}^7F_4$ luminescence located at ~700 nm, which is desirable as a fluorescence probe in biological applications.

Acknowledgements

This work was supported by JSPS Grant-in-Aid for Scientific Research on Innovative Areas "Mixed-Anion" (Grant Number JP16H06439 and JP16H06441) and JSPS fellow (Grant Number JP19J23280). The SXRD experiments were performed at the BL02B2 of SPring-8 with the approval of JASRI (2019B1764).

References

[1] W.M. Yen, S. Shionoya, H. Yamamoto, "PHOSPHOR HANDBOOK". (second ed., CRC Press, Boca Raton, 2007)

[2] K. Binnemans, "Interpretation of europium(III) spectra". *Coord. Chem. Rev*. **295** (2015) 1–45.

[3] A. Abdel-Kader, M.M. Elkholy, "Cathodoluminescence emission spectra of trivalent europium-doped yttrium oxysulphide". *J. Mater. Sci.* **27** (1992) 2887–2895.

[4] L. Ozawa, M. Itoh, "Cathode Ray Tube Phosphors". *Chem. Rev.* **103** (2003) 3835–3855.

[5] O.J. Sovers, T. Yoshioka, "Fluorescence of Trivalent-Europium-Doped Yttrium Oxysulfide". *J. Chem. Phys*. **49** (1968) 4945–4954.

[6] N.C. Chang, "Fluorescence and stimulated emission from trivalent europium in yttrium oxide". *J. Appl. Phys.* **34** (1963) 3500–3504.

[7] T. Jüstel, H. Nikol, C. Ronda, "New developments in the field of luminescent materials for lighting and displays". *Angew. Chem. Int. Ed. Engl.* **37** (1998) 3084–3103.

[8] C.R. Ronda, T. Jüstel, H. Nikol, "Rare earth phosphors: Fundamentals and applications". *J. Alloys Compd.* **275–277** (1998) 669–676.

[9] Y. Hu, W. Zhuang, H. Ye, D. Wang, S. Zhang, X. Huang, "A novel red phosphor for white light emitting diodes". *J. Alloys Compd.* **390** (2005) 226–229.

[10] P. Du, X. Huang, J.S. Yu, "Facile synthesis of bifunctional Eu^{3+}-activated $NaBiF_4$ red-emitting nanoparticles for simultaneous white light-emitting diodes and field emission displays". *Chem. Eng. J.* **337** (2018) 91–100.

[11] Y. Kitagawa, J. Ueda, M.G. Brik, S. Tanabe, "Intense hypersensitive luminescence of Eu^{3+}-doped $YSiO_2N$ oxynitride with near-UV excitation". *Opt. Mater.* **83** (2018) 111–117.

[12] Q. Zhang, X. Wang, X. Ding, Y. Wang, "A Potential Red-Emitting Phosphor $BaZrGe_3O_9:Eu^{3+}$ for WLED and FED Applications: Synthesis, Structure, and Luminescence Properties". *Inorg. Chem.* **56** (2017) 6990–6998.

[13] B. Mitchell, V. Dierolf, T. Gregorkiewicz, Y. Fujiwara, "Perspective: Toward efficient GaN-based red light emitting diodes using europium doping". *J. Appl. Phys.* **123** (2018) 160901 (12p).

[14] J.F. Suyver, A. Meijerink, "Europium beveiligt de euro". *Chem. Weekbl.* **98** (2002) 12–13.

[15] H. Kageyama, K. Hayashi, K. Maeda, J.P. Attfield, Z. Hiroi, J.M. Rondinelli, K.R. Poeppelmeier, "Expanding frontiers in materials chemistry and physics with multiple anions". *Nat. Commun.* **9** (2018) 772 (15p).

[16] B.R. Judd, "Optical absorption intensities of rare-earth ions". *Phys. Rev.* **127** (1962) 750–761.

[17] G.S. Ofelt, "Intensities of Crystal Spectra of Rare-Earth Ions". *J. Chem. Phys.* **37** (1962) 511–520.

[18] M.P. Hehlen, M.G. Brik, K.W. Krämer, "50th anniversary of the Judd-Ofelt theory: An experimentalist's view of the formalism and its application". *J. Lumin.* **136** (2013) 221–239.

[19] F.A. Bannister, "The crystal-structure and optical properties of matlockite (PbFC1)". *Mineral. Mag.* **23** (1934) 587–597.

[20] G. Blasse, A. Bril, "Fluorescence of Eu^{3+}-activated lanthanide oxyhalides LnOX". *J. Chem. Phys.* **46** (1967) 2579–2582.

[21] J. Hölsä, P. Porcher, "Free ion and crystal field parameters for $REOCl:Eu^{3+}$". *J. Chem. Phys.* **75** (1981) 2108–2117.

[22] J. Hölsä, P. Porcher, "Crystal field effects in $REOBr:Eu^{3+}$". *J. Chem. Phys*. **76** (1982) 2790–2797.

[23] F. Izumi, K. Momma, "Three-dimensional visualization in powder diffraction". *Solid State Phenom.* **130** (2007) 15–20.

[24] R.D. Shannon, "Revised effective ionic radii and systematic studies of interatomic distances in halides and chalcogenides". *Acta Crystallogr. A.* **32** (1976) 751–767.

[25] K. Momma, F. Izumi, "VESTA 3 for three-dimensional visualization of crystal, volumetric and morphology data". *J. Appl. Crystallogr.* **44** (2011) 1272–1276.

[26] J.H. Forsberg, "Complexes of lanthanide (III) ions with nitrogen donor ligands". *Coord. Chem. Rev.* **10** (1973) 195–226.

[27] J. Ueda, P. Dorenbos, A.J.J. Bos, A. Meijerink, S. Tanabe, "Insight into the Thermal Quenching Mechanism for $Y_3Al_5O_{12}:Ce^{3+}$ through Thermoluminescence Excitation Spectroscopy". *J. Phys.*

Chem. C. **119** (2015) 25003–25008.

[28] K.L. Zhang, C.M. Liu, F.Q. Huang, C. Zheng, W.D. Wang, "Study of the electronic structure and photocatalytic activity of the BiOCl photocatalyst". *Appl. Catal. B.* **68** (2006) 125–129.

[29] J. Li, Y. Yu, L. Zhang, "Bismuth oxyhalide nanomaterials: Layered structures meet photocatalysis". *Nanoscale*. **6** (2014) 8473–8488.

[30] A.M. Ganose, M. Cuff, K.T. Butler, A. Walsh, D.O. Scanlon, "Interplay of Orbital and Relativistic Effects in Bismuth Oxyhalides: BiOF, BiOCl, BiOBr, and BiOI". *Chem. Mater.* **28** (2016) 1980–1984.

[31] O.L. Malta, L.D. Carlos, "Intensities of 4f-4f transitions in glass materials". *Quim. Nova.* **26** (2003) 889–895.

[32] P.A. Tanner, "Some misconceptions concerning the electronic spectra of tri-positive europium and cerium". *Chem. Soc. Rev.* **42** (2013) 5090–5101.

[33] S. Tanabe, T. Ohyagi, N. Soga, T. Hanada, "Compositional dependence of Judd-Ofelt parameters of Er^{3+} ions in alkali-metal borate glasses". *Phys. Rev. B* **46** (1992) 3305–3310.

[34] Ž. Antić, R. Krsmanović, V. Đorđević, T. Dramićanin, M.D. Dramićanin, "Optical properties of Y_2O_3:Eu^{3+} red emitting phosphor obtained via spray pyrolysis". *Acta Phys. Pol. A.* **116** (2009) 622–624.

[35] G. Pan, H. Song, Q. Dai, R. Qin, X. Bai, B. Dong, L. Fan, F. Wang, "Microstructure and optical properties of Eu^{3+} activated $YV_{1-x}P_xO_4$ phosphors". *J. Appl. Phys.* **104** (2008) 084910 (9p).

[36] B.R. Judd, "Hypersensitive transitions in rare-earth ions". *J. Chem. Phys.* **44** (1966) 839–840.

[37] Y. Nageno, H. Takebe, K. Morinaga, "Correlation between Radiative Transition Probabilities of Nd^{3+} and Composition in Silicate, Borate, and Phosphate Glasses". *J. Am. Ceram. Soc.* **76** (1993) 3081–3086.

[38] Y. Nageno, H. Takebe, K. Morinaga, T. Izumitani, "Effect of modifier ions on fluorescence and absorption of Eu^{3+} in alkali and alkaline earth silicate glasses". *J. Non-Cryst. Solids.* **169** (1994) 288–294.

[39] A.L. Allred, "Electronegativity values from thermochemical data". *J. Inorg. Nucl. Chem.* **17** (1961) 215–221.

[40] A.M. Smith, M.C. Mancini, S. Nie, "Bioimaging: second window for *in vivo* imaging". *Nat. Nanotechnol.* **4** (2009) 710–711.

[41] E. Hemmer, A. Benayas, F. Légaré, F. Vetrone, "Exploiting the biological windows: current perspectives on fluorescent bioprobes emitting above 1000 nm". *Nanoscale Horiz.* **1** (2016) 168–

184.

[42] O.J. Sovers, M. Ogawa, T. Yoshioka, "Detailed branching ratios for M_2O_2S: Eu^{3+}, Tb^{3+} and Pr^{3+} fluorescence from Judd-Ofelt intensity theory". *J. Lumin.* **18–19** (1979) 336–340.

[43] M.J. Weber, T.E. Varitimos, B.H. Matsinger, "Optical intensities of rare-earth ions in yttrium orthoaluminate". *Phys. Rev. B* **8** (1973) 47–53.

[44] E. Cantelar, J.A. Sanz-García, A. Sanz-Martín, J.E. Muñoz Santiuste, F. Cussó, "Structural, photoluminescent properties and Judd-Ofelt analysis of Eu^{3+}-activated CaF_2 nanocubes". *J. Alloys Compd.* **813** (2020) 152194 (9p).

[45] M.J. Weber, "Radiative and multiphonon relaxation of rare-earth ions in Y_2O_3". *Phys. Rev.* **171** (1968) 283–291.

[46] R.M. Krsmanović Whiffen, Ž. Antić, A. Speghini, M.G. Brik, B. Bártová, M. Bettinelli, M.D. Dramićanin, "Structural and spectroscopic studies of Eu^{3+} doped Lu_2O_3–Gd_2O_3 solid solutions". *Opt. Mater.* **36** (2014) 1083–1091.

[47] H.M. Crosswhite, H.W. Moos, "Optical Properties of Ions in Crystals". (John Wiley & Sons, New York, 1967)

[48] G. Shwetha, V. Kanchana, M.C. Valsakumar, "Excitonic effects in oxyhalide scintillating host compounds". *J. Appl. Phys.* **116** (2014) 133510 (9p).

[49] P. Dorenbos, "The hole picture as alternative for the common electron picture to describe hole trapping and luminescence quenching". *J. Lumin.* **197** (2018) 62–65.

[50] A.A. Kaminskii, "Crystalline Lasers: Physical Processes and Operating Schemes". (CRC Press, Boca Raton, 1996).

[51] C.W. Struck, W.H. Fonger, "Role of the charge-transfer states in feeding and thermally emptying the ^5D states of Eu^{+3} in yttrium and lanthanum oxysulfides". *J. Lumin.* **1–2** (1970) 456–469.

Chapter 9

Characterization of Charge Transfer Luminescence of $[WO_6]^{6-}$ Octahedron and $[WO_5]^{4-}$ Square Pyramid with *Ab initio* Energy Level Calculation

Abstract

Charge transfer (CT) luminescence of different polyhedra of $[WO_5]^{4-}$ in $Ca_3WO_5Cl_2$ and $[WO_6]^{6-}$ in Ca_3WO_6 are characterized by spectroscopy and the *ab initio* molecular orbital calculation. W^{6+} ions form five-fold $[WO_5]^{4-}$ square pyramids in $Ca_3WO_5Cl_2$ because of a long interatomic distance between W^{6+} and Cl^- of 3.29 Å. A broad luminescence band peaking at 488 nm of the single-crystal $Ca_3WO_5Cl_2$ is observed, assigned to the CT transition from W 5d to O 2p orbitals in the $[WO_5]^{4-}$ square pyramid. Compared with the $[WO_6]^{6-}$ octahedron in Ca_3WO_6, the $[WO_5]^{4-}$ square pyramid shows the higher CT absorption and lower luminescence energies, which cannot be explained by the simple molecular orbital energy levels in the typical tungstates. The *ab initio* configuration interaction calculation with the relativistic discrete-variational multi-electron (DVME) method indicates that the Madelung potential related to Cl^- ions in the structure of $Ca_3WO_5Cl_2$ causes the upward energy shift of the CT states of the $[WO_5]^{4-}$ square pyramid. The redshift of the CT luminescence and small activation energy for thermal quenching of the $Ca_3WO_5Cl_2$ are explained, assuming that the CT state of the $[WO_5]^{4-}$ square pyramid takes a larger offset in the configurational coordinate diagram than that of the $[WO_6]^{6-}$ octahedron.

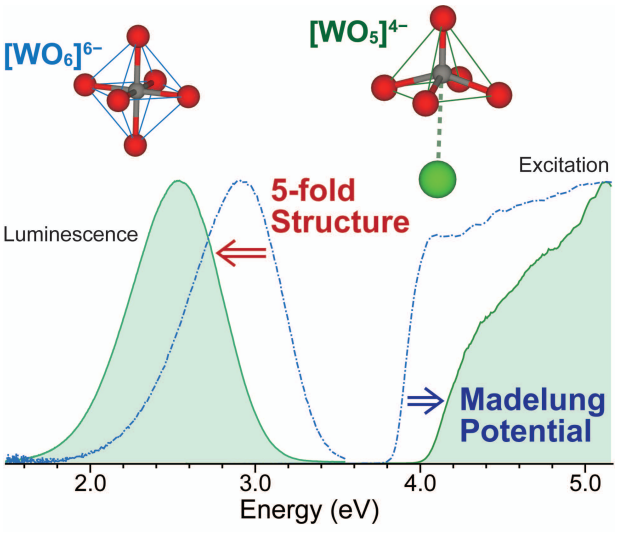

9.1. Introduction

With the remarkable development and innovation of optoelectronics, researchers have reported many new functional luminescent materials. Many highly efficient phosphors and scintillators are activated by a small amount of impurity, including lanthanoid ions and transition metal ions, in a ceramic host. The luminescence center is not always caused by the intrinsic transition of such an impurity ion. The tungstate ion is one example of the luminescence center in an inorganic ceramic compound. The mineral scheelite, which has a chemical composition of $CaWO_4$, shows blue luminescence under UV light illumination [1,2]. Other scheelite-type materials $M^{2+}WO_4$ (M = Mg, Sr, Ba, Cd, and Pb) also show the visible luminescence due to the charge transfer (CT) transition between W^{6+} and O^{2-} ions, whose luminescence properties depend on the characteristics of M^{2+} ions [3–7]. These scheelite-type materials have been well-known for over 80 years, and there is much literature about the systematical studies on structural, electronical, and compositional features [8]. In particular, $CdWO_4$ and $PbWO_4$ have been well developed for scintillator applications due to the high density, the high effective atomic number, and the suitable emission wavelength for detection [9–11]. In the scheelite-type structure, the $[WO_4]^{2-}$ tetrahedra are isolated in a tetragonal lattice without any corner, edge, and face sharing with other tetrahedra. The slightly distorted $[WO_4]^{2-}$ tetrahedron with S_4 symmetry acts as the luminescence center, leading to the efficient luminescence with a decay rate on the order of 10^{0-2} μs [1,8,12]. The observed luminescence in the scheelite-type materials is attributed to the CT transition between O 2p and W 5d orbitals in a $[WO_4]^{2-}$ tetrahedron. In order to understand the energy level structure of a $[WO_4]^{2-}$ tetrahedron and discuss the radiative electronic transition resulting in CT luminescence, one has to consider many factors, such as the crystal field splitting of W 5d levels, the molecular orbitals (MO) composed of O 2p and W 5d orbitals, the large spin-orbit interaction of W caused by the relativistic effect, and the site-symmetry of a tetrahedron. The CT luminescence in the scheelite-type MWO_4 is well understood with a three-level energy scheme [8,13]. The MO calculation of a $[WO_4]^{2-}$ tetrahedron with T_d symmetry reveals the highest occupied MO (HOMO) of t_1 and the lowest unoccupied MO (LUMO) of 2e, leading to the ground state ($^1A_1$) and excited states ($^3T_1 \leq {}^3T_2 < {}^1T_1 < {}^1T_2$). Although the absorption and

luminescence energies vary slightly depending on the crystal field strength and the site-symmetry of a tetrahedron, the relevant processes are considered to be the $^1T_1 \leftarrow {}^1A_1$ spin-allowed transition (absorption) and the $^3T_1 \rightarrow {}^1A_1$ spin-forbidden transition (luminescence), respectively. The initial level of luminescence $^3T_1$ is split into two because of the spin-orbit interaction [13]. The simple model explains the mechanism of CT luminescence in tungstates as long as the coordination polyhedra are approximated to be the regular tetrahedron with T_d symmetry or the regular octahedron with O_h symmetry.

In terms of the exploration of various CT luminescence in tungstates, much previous work has focused on the oxide compounds [14–16]. However, considering the ratio of ionic radii for O^{2-} (1.35–1.42 Å) and W^{6+} (0.42–0.60 Å) [17], the possible coordination polyhedra are generally restricted to be a $[WO_4]^{2-}$ tetrahedron and a $[WO_6]^{6-}$ octahedron. As these polyhedra are usually rigid, we cannot expect further distortion from T_d or O_h symmetry, leading to the poor variation of the crystal field splitting for W 5d levels. Although the luminescent properties of tungstates depend on the M^{2+} ions in the structure, it is difficult to achieve the desirable properties because M^{2+} ions are not directly involved in the electronic structure of the $[WO_4]^{2-}$ or $[WO_6]^{6-}$ polyhedra. For improvement in the variation of the local environments, mixed-anion coordination by replacing an O^{2-} ion with a different anion can be a good strategy to introduce further distortion in a coordination polyhedron. We can expect the mixed-anion coordination to cause a tunable crystal field splitting and local asymmetry [18]. There are only a few reports about the CT luminescence in mixed-anion tungstates [19,20]. Blasse reported that the oxychloride $La_3WO_6Cl_3$, which has the remarkable $[WO_6]^{6-}$ trigonal prism with C_{3h} symmetry, showed the CT luminescence with a smaller Stokes shift (~10500 cm^{-1}) than other tungstates with a $[WO_6]^{6-}$ octahedron (~12000 cm^{-1}) and a $[WO_4]^{2-}$ tetrahedron (~15000 cm^{-1}) [20]. Recently, Ayer et al. reported the scintillation properties of the oxyfluoride $BaWO_2F_4$, in which the W^{6+} ion form the *cis*-$[WO_2F_4]^{2-}$ distorted octahedron with C_{2v} symmetry [21]. $BaWO_2F_4$ showed the green luminescence peaking at ~520 nm with a high quantum yield under UV light illumination. Because of the limitation of the material variation and the MO calculation technique, the CT luminescence of tungstates with various coordination has not been explored

widely.

In this study, we have focused on the oxychloride $Ca_3WO_5Cl_2$, which has unique coordination around a W^{6+} ion with a square pyramid structure, $[WO_5]^{4-}$ [22]. This compound is isostructural to $Ca_3ReO_5Cl_2$. The single-crystal $Ca_3ReO_5Cl_2$ shows pleochroism because of the unique $[ReO_5]^{4-}$ square pyramid with C_s symmetry, which causes the polarization-dependence of the selection rule for the d-d transition of Re^{6+} [23]. The square-pyramidal $[WO_5]^{4-}$ structure is derived from the large Cl^- ion substitution in a typical $[WO_6]^{6-}$ octahedron, possibly leading to the unique CT luminescence. We characterize the luminescence properties of the single-crystal $Ca_3WO_5Cl_2$ and double perovskite Ca_3WO_6, which has the same cation ratio as $Ca_3WO_5Cl_2$ and the $[WO_6]^{6-}$ octahedra with C_i symmetry in a lattice. In addition, we investigate the MO and multiplet energy levels of the $[WO_5]^{4-}$ and $[WO_6]^{6-}$ polyhedra with the *ab initio* non-relativistic and relativistic MO calculation using the discrete-variational Xα (DV-Xα) method and configuration interaction (CI) calculation using the DV multi-electron (DVME) method and discuss the mechanism of CT luminescence in the single-crystal $Ca_3WO_5Cl_2$ and Ca_3WO_6. Compared with the density functional theory (DFT) calculation, the DV methods have the following advantages; (1) the four-components wavefunction enables to perform the full-relativistic calculation with a small calculation cost, (2) the DV calculation of the electronic transition between the multiplet states can consider both multi-electron effect and spin-orbit interaction, and (3) in the DVME method, the linear combination of Slater determinants represent the specific wavefunctions of the multiplet excited states, which enable to calculate the excited states with the minimum basis functions like the ground state [24,25].

9.2. Experimental Section

9.2.1. Preparation of Single-Crystal Sample

The single-crystal oxychloride $Ca_3WO_5Cl_2$ and oxide Ca_3WO_6 samples were grown by a flux method. The starting chemicals CaO, WO_3, and $CaCl_2$ in a molar ratio of 17:4.1:1 were mixed in an agate mortar in an argon-filled glove box, and the mixture was put in a gold tube and sealed

in an evacuated quartz ampoule. The ampoule was heated at 1030 °C and then slowly cooled with two steps; (1) to 1020 °C for 60 h, and (2) to 800 °C for 240 h. After cooling to room temperature for 4 h, the crystals were obtained after excess $CaCl_2$ flux was washed away by distilled water. The crystalline phase of the obtained crystals was identified by X-ray diffraction. For spectroscopic characterization at low temperatures, the single-crystal samples were attached to a copper specimen holder with carbon tape.

9.2.2. Spectroscopic Characterization

Diffuse transmittance spectra of the single-crystal samples at room temperature were measured with a UV-VIS-NIR spectrometer (UV-3600, Shimadzu) equipped with an integrating sphere. The photoluminescence excitation (PLE) spectra at 4 K were measured by monochromatic excitation light with a 500 W Xe short arc lamp (OPM2-502XQ, Ushio Inc.) equipped with a double monochromator system by two monochromators (SP-300i, Acton Research Corp.), detected by using a photomultiplier tube (PMT) detector (R10699, Hamamatsu Photonics) coupled with a monochromator (SP-2300i, Princeton Instruments). The obtained PLE spectra were calibrated by the spectrum of the Xe lamp (light source) detected by a calibrated Si photodiode (S1337-1010BQ, Bunkoukeiki Co., Ltd.). For the photoluminescence measurements at low temperatures (T = 4–300 K), the sample was excited by the monochromatic light of the Xe lamp, and luminescence was detected with a CCD spectrometer (QE65Pro, Ocean Optics) connected with an optical fiber. The obtained PL spectra were calibrated by the spectrum of a calibrated deuterium-tungsten halogen light source (DH-2000, Ocean Optics). The sample temperatures were controlled by a cryostat with a closed-cycle He gas cryogenic refrigerator (CRT-A020-SE00, Ulvac Cryogenics).

9.2.3. *Ab initio* Molecular Orbital Calculation

In order to prepare the model clusters for MO calculations, the geometrical optimizations with the density functional theory (DFT) for the crystal structures of $Ca_3WO_5Cl_2$ and Ca_3WO_6 were performed by the CASTEP module [26] of the Materials Studio 2021 package. The exchange-correlation functional was represented by the generalized gradient approximation (GGA) of

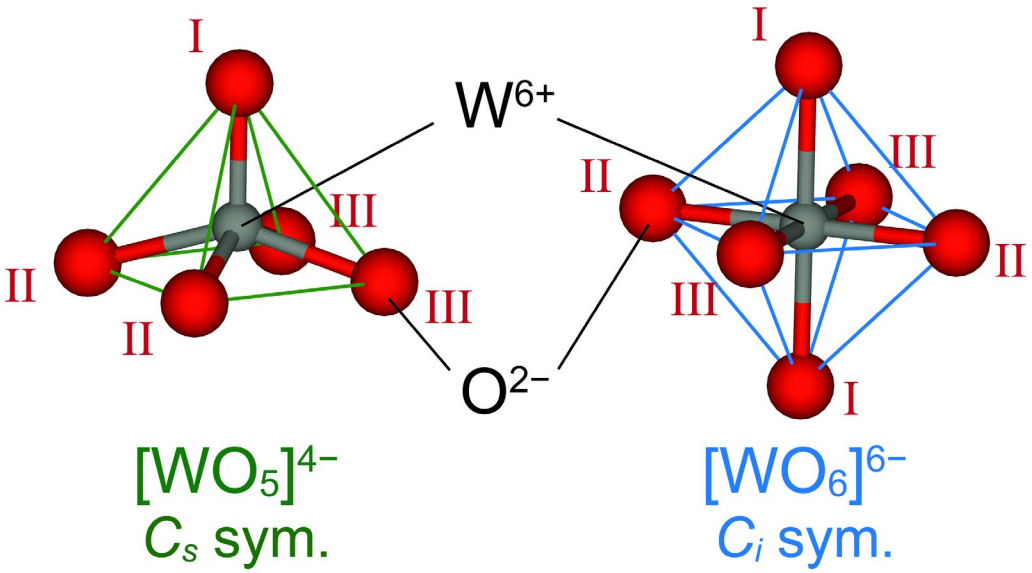

Figure 9.1. Model clusters of a $[WO_5]^{4-}$ square pyramid with C_s symmetry and a $[WO_6]^{6-}$ octahedron with C_i symmetry for the MO calculations.

Perdew-Burke-Ernzerhof functional for solids (PBEsol) [27]. The ionic core electrons were replaced by on-the-fly ultrasoft pseudopotentials implemented in the CASTEP [28]. Relativistic effects were taken into account at the level of the Koelling-Harmon approximation of the Dirac equation [29]. The plane-wave basis cut-off energy and k-point grids were 571.4 eV and 1 × 1 × 3, respectively.

The molecular orbital (MO) energy level and multiplet energy level diagrams were estimated by the non-relativistic and relativistic discrete-variational Xα (DV-Xα) method [24,30] and the DV multi-electron (DVME) method [25,31]. The detailed analyses of CT states using the DVME method were reported for transition metal ions in alumina [32], rare-earth ions in fluorite [33], and Eu^{3+} in Y_2O_3 and Y_2O_2S [34]. The $[WO_5]^{4-}$ and $[WO_6]^{6-}$ clusters were taken from the optimized structure with DFT calculation. The model clusters are depicted in **Figure 9.1**, and the interatomic distances between W^{6+} ion and ligands are listed in **Table 9.1**. The effective Madelung potential was produced by surrounding the cluster with point charges at external atomic sites. In the DVME calculations, the considered electronic configurations for the calculations were $(W\ 5d)^0(O\ 2p)^{6n}$ and $(W\ 5d)^1(O\ 2p)^{6n-1}$, where n is the number of coordination oxygen, and the configuration-dependent correction (CDC) [34] for these configurations was taken into account. The considered basis functions for the non-relativistic

calculations were 1s, 2s, 2p, 3s, 3p, 3d, 4s, 4p, 4d, 4f, 5s, 5p, 5d, 6s, 6p for W ion, and 1s, 2s, 2p for O ion, respectively. For the relativistic calculations, the considered basis functions were $1s_{1/2}$, $2s_{1/2}$, $2p_{1/2}$, $2p_{3/2}$, $3s_{1/2}$, $3p_{1/2}$, $3p_{3/2}$, $3d_{3/2}$, $3d_{5/2}$, $4s_{1/2}$, $4p_{1/2}$, $4p_{3/2}$, $4d_{3/2}$, $4d_{5/2}$, $4f_{5/2}$, $4f_{7/2}$, $5s_{1/2}$, $5p_{1/2}$, $5p_{3/2}$, $5d_{3/2}$, $5d_{5/2}$, $6s_{1/2}$, $6p_{1/2}$, $6p_{3/2}$ for W ion, and $1s_{1/2}$, $2s_{1/2}$, $2p_{1/2}$, $2p_{3/2}$ for O ion, respectively. For comparison, the regular (undistorted) cluster of the $[WO_5]^{4-}$ square pyramid with C_{4v} symmetry and the $[WO_6]^{6-}$ octahedron with O_h symmetry were prepared, and their MO energy levels were also calculated. The bond lengths for the regular structures are also given in Table 9.1, which are the mean value of the relevant distorted structure. In addition, with the data obtained by the one-electron DV-Xα method, the CT energies were calculated by Slater's transition state method [35].

Table 9.1. Inter atomic distances between W^{6+} and ligands (unit: Å)

bonding[a]	$Ca_3WO_5Cl_2$		Ca_3WO_6	
	distorted (C_s sym.)	regular (C_{4v} sym.)	distorted (C_i sym.)	regular (O_h sym.)
W^{6+}-O^{2-}_{I}	1.745	1.745	1.945	1.931
W^{6+}-O^{2-}_{II}	1.898	1.906	1.920	1.931
W^{6+}-O^{2-}_{III}	1.914	1.906	1.935	1.931
W^{6+}-Cl^-	3.289	—	—	—

[a]The different O^{2-} ions are labeled with Roman numerals, I–III, shown in Figure 9.1.

9.3. Results and Discussion

9.3.1. Spectroscopic Characterization of Single-Crystal $Ca_3WO_5Cl_2$ and Ca_3WO_6 Samples

The optical properties of the prepared single-crystal $Ca_3WO_5Cl_2$ and Ca_3WO_6 samples were characterized by spectroscopy at room temperature and low temperatures. **Figure 9.2** shows the diffuse transmittance spectra at room temperature and the photographs of the prepared samples.

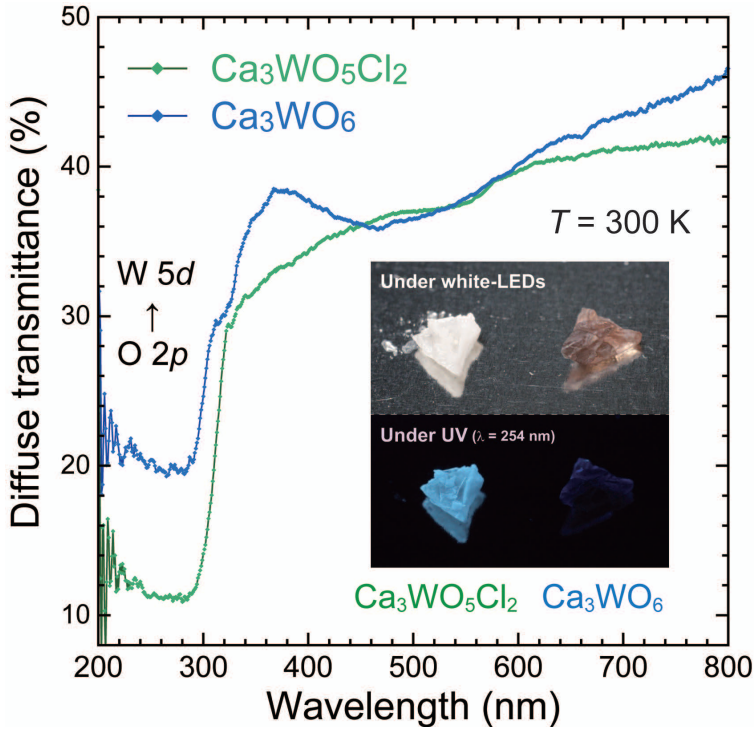

Figure 9.2. Diffuse transmittance spectra of the single-crystal $Ca_3WO_5Cl_2$ and Ca_3WO_6 samples at room temperature and (inset) photographs of the prepared single-crystal samples under white-LEDs and UV light illumination.

While the $Ca_3WO_5Cl_2$ sample is colorless, the Ca_3WO_6 sample is brown. In the transmittance spectrum of the Ca_3WO_6 sample, a broad absorption band is observed in the range of 380–600 nm. This absorption band was not observed in the previous studies on the CT transfer of Ca_3WO_6 [36,37], suggesting that it can be due to some color center associated with defects or impurities generated in the crystalline growth procedure of this study. The fundamental absorption edge is located at ~345 nm. This absorption is assigned to the CT from O 2p to W 5d orbitals. For the $Ca_3WO_5Cl_2$ sample, there is no absorption band in the visible range. The fundamental absorption edge related to the CT transition is located at ~325 nm. In general, the compounds with covalent anions take a small CT absorption energy because of the higher energy levels of p orbitals. Despite the covalency of Cl, whose electronegativity of 3.16 is smaller than O (electronegativity: 3.44) [38], the absorption edge is blue-shifted compared with the Ca_3WO_6 sample. The interatomic distance of 3.289 Å between W and Cl atoms is too far to form a W-Cl bonding, based on the ionic radii of W^{6+} (0.6 Å) and Cl^- (1.81 Å) [17], suggesting that the W-Cl CT transition is negligible in $Ca_3WO_5Cl_2$. The first neighbor for a W^{6+} ion is five O^{2-}

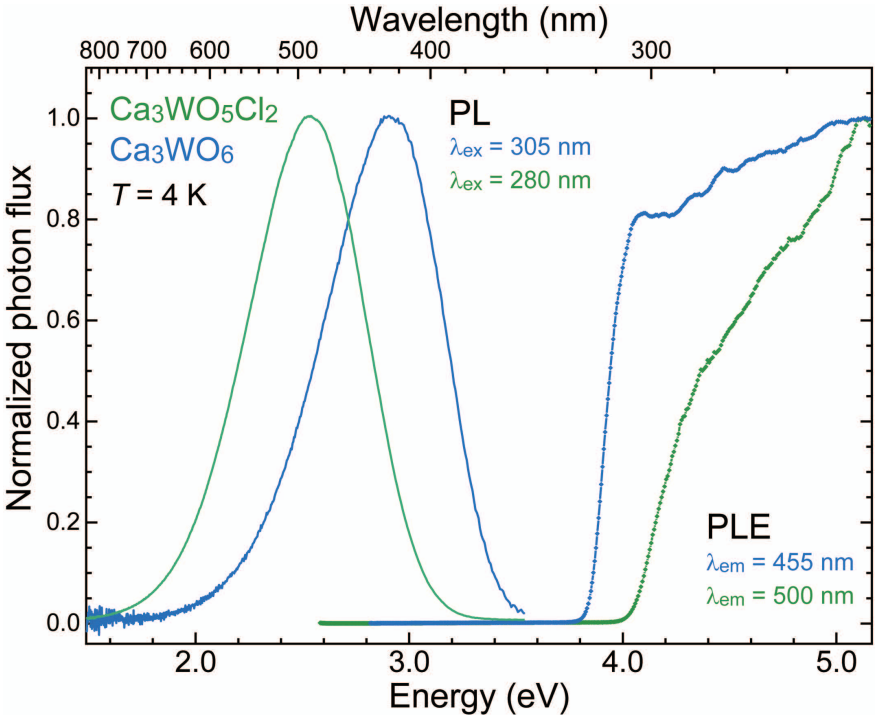

Figure 9.3. Normalized PL and PLE spectra of the samples at 4 K.

ions which form a square pyramid $[WO_5]^{4-}$, leading to the effective CT transition from O 2p to W 5d orbitals. Thus, the absorption edge of the $Ca_3WO_5Cl_2$ sample is assigned to the W 5d ← O 2p CT transition, as well.

At low temperatures, both samples show the CT luminescence under UV light illumination. **Figure 9.3** shows the normalized PL and PLE spectra of the samples at 4 K. In the PLE spectra, both samples show a similar fundamental absorption edge due to the W 5d ← O 2p CT transition. Through the linear fitting for the slope of the absorption edge, the CT energies for the $Ca_3WO_5Cl_2$ and Ca_3WO_6 samples are estimated to be 4.037 eV (= 307 nm) and 3.841 eV (= 323 nm), respectively. The CT energy at room temperature, as shown in Figure 9.2, is smaller than that at 4 K because of the small bandgap at high temperatures caused by an increase in the amplitudes of atomic vibrations. In the PL spectra, broad luminescence bands assigned to the CT transition are observed at 2.54 eV (= 488 nm) for the $Ca_3WO_5Cl_2$ and 2.91 eV (= 426 nm) for the Ca_3WO_6 samples. While both samples show a similar spectral shape, the luminescence band for the $Ca_3WO_5Cl_2$ is redshifted by 0.36 eV. These luminescence bands are typical for the W 5d → O 2p CT luminescence in various tungstates [8].

The difference in the absorption and luminescence energies for the W-O CT transition between Ca_3WO_6 and $Ca_3WO_5Cl_2$ can be derived from the crystal field strength of the coordination polyhedra. In the Ca_3WO_6 double perovskite, a W^{6+} ion form an octahedron $[WO_6]^{6-}$ with six O^{2-} ions within the first coordination. The octahedron takes C_i symmetry due to a slight distortion from the regular octahedron with O_h symmetry. On the other hand, a W^{6+} ion in the oxychloride $Ca_3WO_5Cl_2$ forms a square pyramid $[WO_5]^{4-}$ because an O^{2-} ion is replaced by a large Cl^- ion. The square pyramid takes C_s symmetry, caused by a small trapezoidal distortion of the basal plane with a loss of one mirror plane [22,23]. In addition, the introduction of Cl^- brings about a shift of the W^{6+} ion in the opposite direction to that of Cl^-, resulting in the shorter bond lengths between W^{6+} and O^{2-} ions in the $[WO_5]^{4-}$ square pyramid than in the $[WO_6]^{6-}$ octahedron [22]. Thus, the square-pyramidal $[WO_5]^{4-}$ structure can cause a different crystal field splitting for W 5d levels, resulting in a shift of the absorption edge and the luminescence peak. However, the results of the energy shift in the PLE and PL spectra are not consistent; *i.e.,* compared with the Ca_3WO_6, the $Ca_3WO_5Cl_2$ takes high absorption and low luminescence energies. This opposite tendency in the $Ca_3WO_5Cl_2$ sample cannot be understood with the simple MO model in O_h symmetry.

Figures 9.4 show the PL spectra of the single-crystal $Ca_3WO_5Cl_2$ and Ca_3WO_6 samples at low temperatures (T = 4–300 K). The spectral shape of the CT luminescence for the $Ca_3WO_5Cl_2$ sample is mostly unchanged up to room temperature despite the severe thermal quenching. In the Ca_3WO_6 sample, the peak of the CT band is slightly redshifted at 4–100 K. The temperature dependence of the integrated PL intensities of the $Ca_3WO_5Cl_2$ and Ca_3WO_6 samples are plotted in **Figure 9.5**. The plots were fitted by a function described by a single barrier quenching model;

$$I(T) = \frac{I_0}{1 + {\Gamma_0}/{\Gamma_\nu} \exp\left(-{E_a}/{kT}\right)}, \tag{9.1}$$

where I is the luminescence intensity at each temperature, Γ_ν is the radiative rate of the CT transition, Γ_0 is the attempt rate of the nonradiative process, E_a is the activation energy for the thermal quenching process, k is the Boltzmann constant (= 8.617×10^{-5} eV K^{-1}), and T is temperature. The quenching curve for the Ca_3WO_6 sample shows a good agreement with the

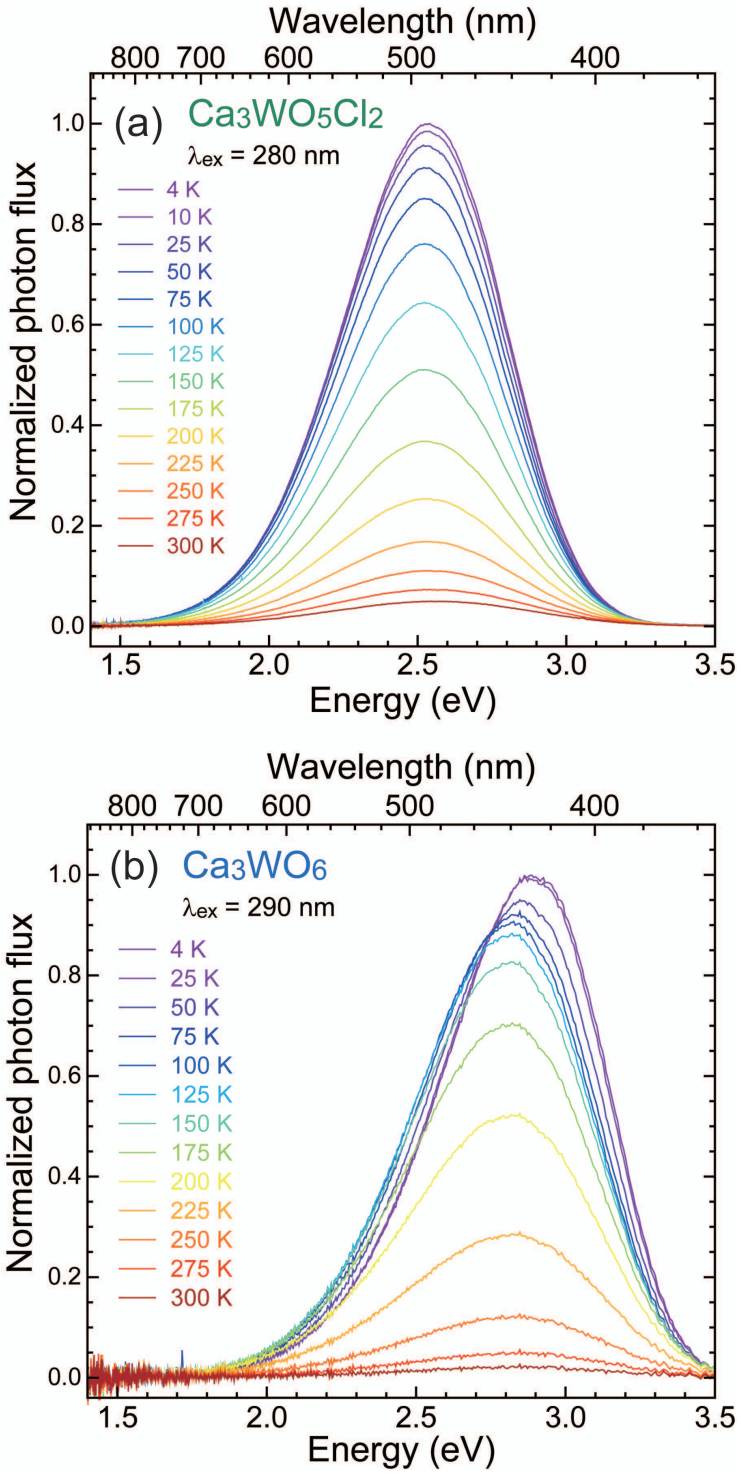

Figure 9.4. PL spectra at various temperatures (T = 4–300 K) for (a) $Ca_3WO_5Cl_2$ and (b) Ca_3WO_6 samples.

experimental plots with the Γ_0/Γ_v value of 6.80 $\times 10^3$, leading to the E_a of 156 meV. In contrast, although the estimated E_a value was 48.6 meV, we could not obtain good fitting parameters for the $Ca_3WO_5Cl_2$ sample, the Γ_0/Γ_v value of 46.9, which is too small and possibly not valid. The

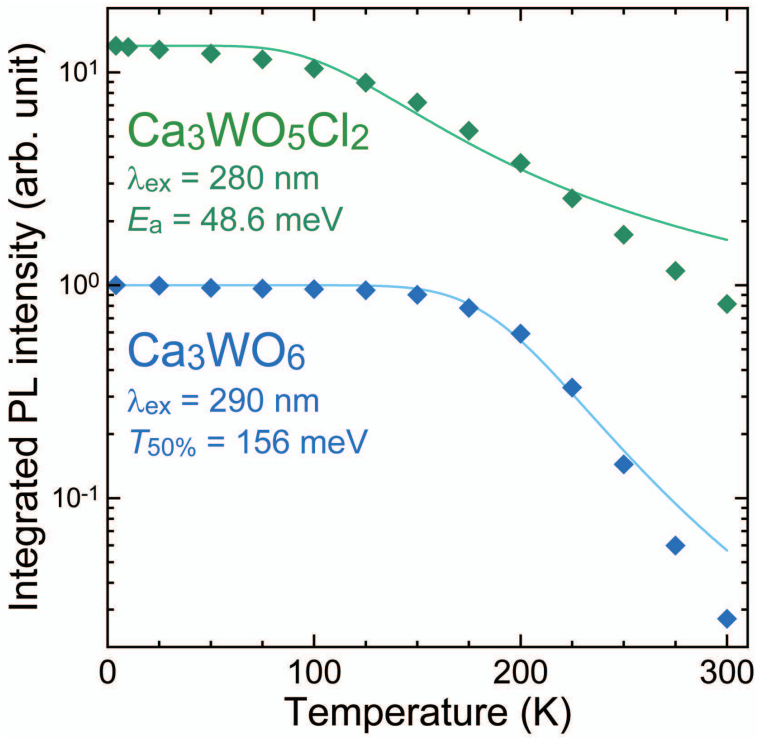

Figure 9.5. Temperature dependence of integrated PL intensity of the $Ca_3WO_5Cl_2$ and Ca_3WO_6 samples. The PL intensities at each temperature are normalized by the PL intensity at 4 K. The plots are fitted with the single barrier quenching model described by eq. 9.1.

quenching behavior of the CT luminescence in $Ca_3WO_5Cl_2$ cannot be described by the single quenching barrier model, and the actual process is more complicated. Since the temperature dependence of the absorption coefficient is not taken into account, it is difficult to estimate the E_a value only from the temperature dependence of PL spectra. Nevertheless, the CT luminescence of the $Ca_3WO_5Cl_2$ is easily quenched with temperature, compared with that of the Ca_3WO_6. From the temperature dependence plots, the quenching temperatures $T_{50\%}$, at which the PL intensity is half of the initial one, are estimated to be ~150 K for the $Ca_3WO_5Cl_2$ and ~205 K for the Ca_3WO_6 samples. These $T_{50\%}$ values indicate that the $Ca_3WO_5Cl_2$ takes small activation energy for thermal quenching. Note that the PL intensity of the $Ca_3WO_5Cl_2$ sample at room temperature was comparable to that of the Ca_3WO_6 sample at 4 K, suggesting that the $Ca_3WO_5Cl_2$ can have high absorption efficiency.

9.3.2. Influence of Cl^- Ion on Coordination Polyhedra in $Ca_3WO_5Cl_2$

In terms of the bond lengths between the W^{6+} ion and ligands, the reasonable coordination around W^{6+} ions in $Ca_3WO_5Cl_2$ is the $[WO_5]^{4-}$ square pyramid. Here, the validity of this five-fold coordination is examined by the theoretical electronic calculation. The relativistic DV-Xα calculations for the $[WO_5]^{4-}$ square pyramid and $[WO_5Cl]^{5-}$ distorted octahedron were performed, and their total and partial density of states (DOS and PDOS) curves are depicted in **Figures 9.6a** and **9.6b**. For the PDOS curves of the $[WO_5Cl]^{5-}$ distorted octahedron, the Cl 3p orbitals are observed around the HOMO level, which mainly form the valence band in the $Ca_3WO_5Cl_2$ lattice. However, near the LUMO level, only the W 5d and O 2p orbitals are observed, suggesting that the Cl 3p orbitals are not related to the antibonding character and have the nonbonding character. In the comparison for these two clusters, the curves of W 5d and O 2p orbitals are hardly influenced by the existence of a Cl^- ion. The DV-Xα calculation can perform the compositional analysis of the energy levels. The results of the compositional

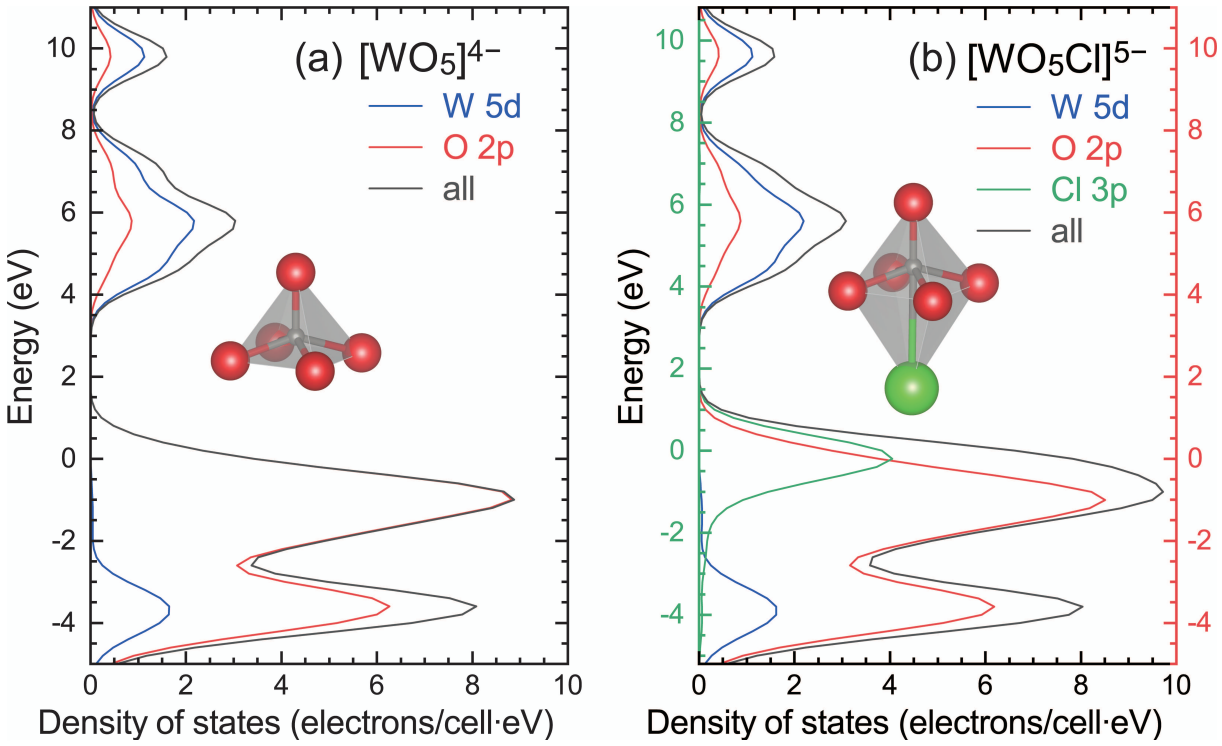

Figure 9.6. Total and partial density of electronic states for (a) the $[WO_5]^{4-}$ and (b) $[WO_5Cl]^{5-}$ clusters in $Ca_3WO_5Cl_2$, which were calculated by the relativistic DV-Xα method. The HOMO levels mainly composed of Cl 3p and O 2p orbitals are set at 0 eV in the left and right *y*-axes of Figure 4b, respectively.

analysis for the $[WO_5Cl]^{5-}$ distorted octahedron are summarized in **Table 9.2**. The first, second, and fourth levels of the HOMO level are labeled top1, top2, and top4, respectively, in order of decreasing energy. These levels are mainly composed of the Cl $3p_x$, $3p_y$, and $3p_z$ orbitals. A small contribution of O 2p orbitals is confirmed, possibly due to the close proximity of the MO energy levels. On the other hand, the contribution of Cl 3p orbitals in the $5d_1$ LUMO level is almost zero. Therefore, it is suggested that the Cl^- ion has no orbital hybridization with lower W 5d orbitals.

This inference is supported by the calculation results for other (oxy)chloride coordination. **Figure 9.7** shows the DOS and PDOS curves of the relevant (oxy)chloride octahedron; a $[WO_4Cl_2]^{4-}$ octahedron in WO_2Cl_2 [39], a $[WO_2Cl_4]^{2-}$ octahedron in $WOCl_4$ [40], and a $[WCl_6]$ octahedron in WCl_6 [41]. They were also calculated by the relativistic DV-Xα method. In these octahedra, the interatomic distances between W^{6+} and Cl^- are 2.268–2.285 Å, which is shorter than that in $Ca_3WO_5Cl_2$ (3.289 Å). For the oxychloride octahedra with the composition of $[WO_{6-x}Cl_x]^{(6-x)-}$ (x = 0, 2, 4, and 6), the contributions of Cl 3p orbitals are observed in the antibonding LUMO level, and the energy differences between the HOMO and LUMO levels for the $[WO_6]^{6-}$, $[WO_4Cl_2]^{4-}$, $[WO_2Cl_4]^{2-}$, and $[WCl_6]$ octahedra are 4.51, 3.05, 2.24, and 2.33 eV, respectively. The results indicate that Cl 3p orbitals interact with W 5d orbitals to cause the

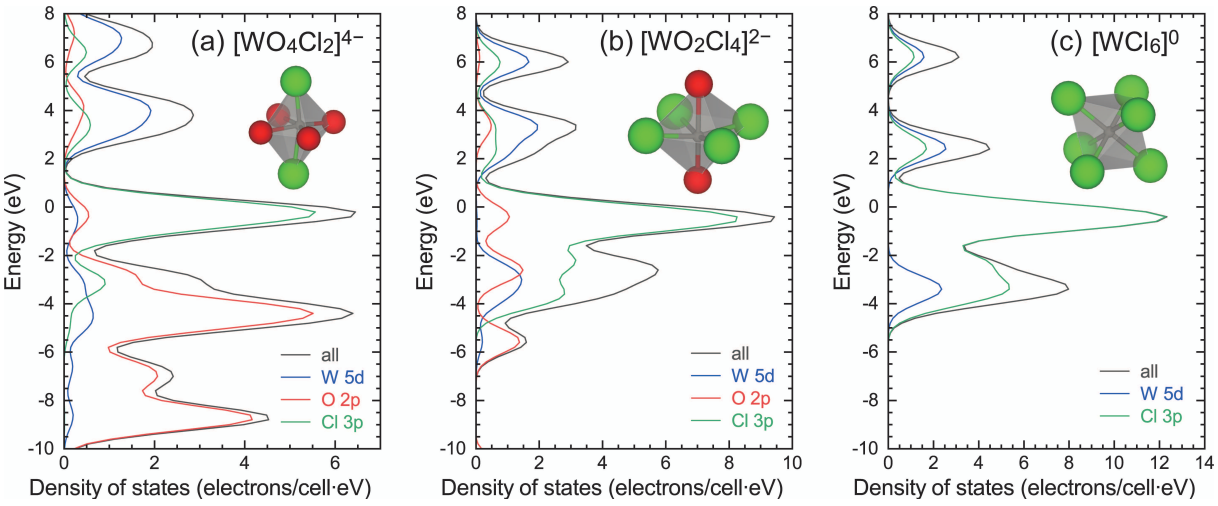

Figure 9.7. Total and partial density of electronic states for (a) a $[WO_4Cl_2]^{4-}$ cluster in WO_2Cl_2 (ICSD 28510), (b) a $[WO_2Cl_4]^{2-}$ cluster in $WOCl_4$ (ICSD 25519), and (c) a $[WCl_6]$ cluster in WCl_6 (ICSD 425147), which were calculated by the relativistic DV-Xα method. The HOMO mainly composed of Cl 3p orbitals is set at 0 eV.

downward shift of the LUMO level and the CT energy. Note that the downshift of the LUMO level for the $[WO_2Cl_4]^{2-}$ octahedron is larger than that for the $[WCl_6]$ octahedron, possibly because of the larger crystal field splitting induced by the mixed-anion coordination.

Consequently, in the crystal lattice of $Ca_3WO_5Cl_2$, the Cl 3p orbitals no longer affect the W 5d orbitals, and the Cl– ions behave just as negative point charges, affecting the MO of the five-fold $[WO_5]^{4-}$ polyhedra.

Table 9.2. Results of compositional analysis of MO levels calculated by the relativistic DV-Xα calculation (unit: %)[a]

	top1[b]	top2[b]	top4[b]	$5d_1$	$5d_2$	$5d_3$	$5d_4$	$5d_5$
W 5d	0.04	0.03	0.01	80.03	68.51	70.98	51.21	70.67
O 2p	11.59	16.57	13.47	19.85	29.13	26.94	23.85	26.06
Cl 3p	88.15	83.56	85.91	0.00	0.04	0.03	1.13	0.00

[a]Note that the total percentages are less than 100% because of small contributions of other orbitals, such as O 2s, W 6s, and W 6p orbitals.

[b]The first, second, and fourth levels of the HOMO level are labeled top1, top2, and top4, respectively, in order of decreasing energy, mainly composed of the Cl $3p_x$, $3p_y$, and $3p_z$ orbitals.

9.3.3. Luminescence Mechanism of $[WO_6]^{6-}$ and $[WO_5]^{4-}$ Polyhedra with *Ab initio* MO and CI Calculations

The MO energy diagram of $[WO_6]^{6-}$ and $[WO_5]^{4-}$ polyhedra were estimated by the non-relativistic (non-rel) and relativistic (rel) DV-Xα methods, which is based on the one-electron calculation, and shown in **Figures 9.8a** and **8b**. In the diagrams, the HOMO mainly composed of O 2p orbitals is set at 0 eV. For the $[WO_6]^{6-}$ octahedron with C_i symmetry, the non-relativistic DV-Xα calculation output the W 5d levels split into almost two, which consist of three a_g levels (low energy) and two a_g levels (high energy). The degenerated t_{2g} and e_g levels in O_h symmetry are hardly resolved because the distortion in the $[WO_6]^{6-}$ octahedron to lose the symmetry elements but the inversion center is very small. The spin-orbit interaction provides the upward

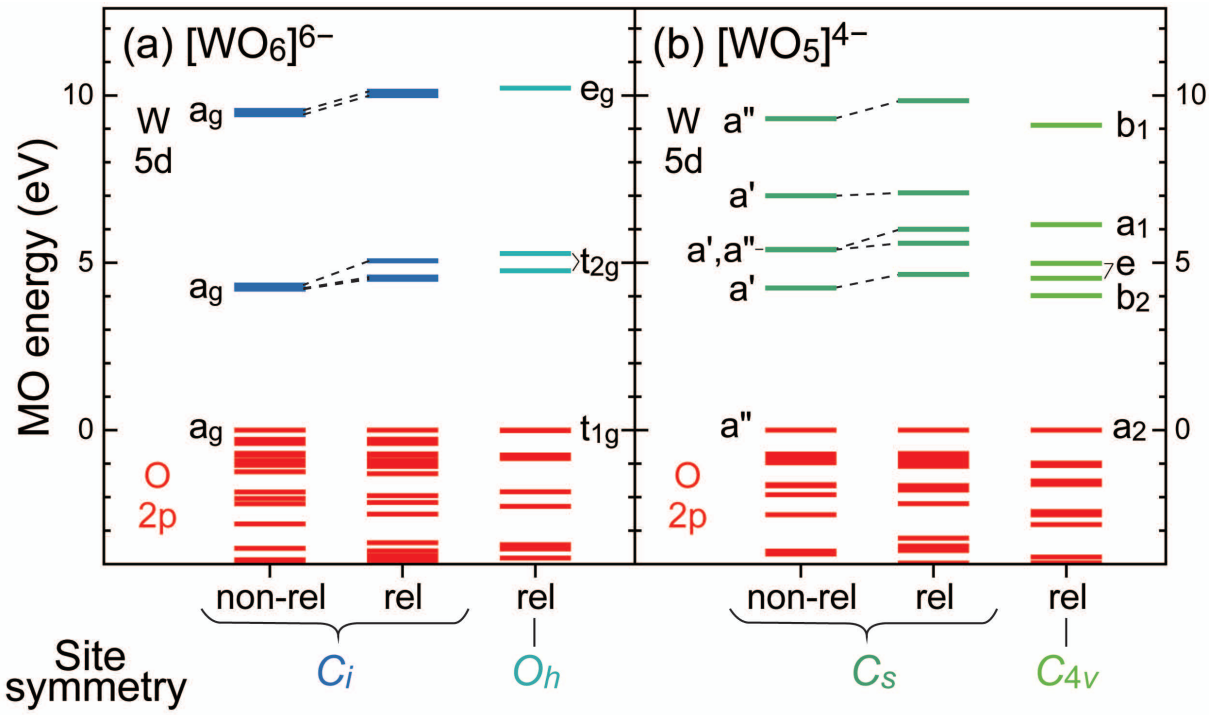

Figure 9.8. MO energy diagrams of (a) $[WO_6]^{6-}$ and (b) $[WO_5]^{4-}$ clusters calculated with the non-relativistic (non-rel) and relativistic (rel) DV-Xα methods.

energy level shift of 0.3–0.7 eV due to the large atomic number of $_{74}$W.

The $[WO_5]^{4-}$ square pyramid has a more complicated energy level structure than the $[WO_6]^{6-}$ octahedron because of the five-fold coordination with C_s symmetry. The W 5d levels are resolved into five levels (three a' and two a" levels), and the spin-orbit interaction causes the upward energy level shift of 0.2–0.6 eV. The population analysis reveals that 99.96% of HOMO consists of O 2p orbitals in the basal plane of the square pyramid (labeled with O_{II} and O_{III} in Figure 9.1). Although the apical O^{2-} ion (O_I) is the closest to the W^{6+} ion, the CT transition in the $[WO_5]^{4-}$ square pyramid occurs from the O_{II} and O_{III} in the basal plane.

For both $[WO_6]^{6-}$ and $[WO_5]^{4-}$ polyhedra, the calculations for the undistorted structures with O_h and C_{4v} symmetry were also performed. Here, the Madelung potential around clusters was not taken into account. The MO energy levels are depicted in the third column of Figures 9.8a and 8b. Note that the degenerated t_{2g} levels for O_h and e levels for C_{4v} are resolved because of the spin-orbit interaction. The energy level structures of the W 5d orbital in O_h and C_{4v} symmetry are quite similar to those in C_i and C_s, respectively. Therefore, small distortion in the $[WO_6]^{6-}$ octahedron with C_i symmetry and the $[WO_5]^{4-}$ square pyramid with C_s symmetry

hardly affect the crystal field splitting of W 5d levels.

Although the DV-Xα method based on the one-electron calculation is a good approximation to discuss the characteristics of CT luminescence, the non-relativistic and relativistic DVME method based on the multiple-electron calculation, taking CDC into account, was applied to obtain the multiplet energy diagram of $[WO_6]^{6-}$ and $[WO_5]^{4-}$ polyhedra. The results are shown in **Figures 9.9a** and **9b**. Here, the energy of the ground state (^1A_g for C_i and $^1A'$ for C_s) of the $(W\ 5d)^0(O\ 2p)^{6n}$ configuration is set at 0 eV.

All the multiplet energy diagrams show the closed CT states, forming the band structure. For the $[WO_6]^{6-}$ octahedron with C_i symmetry, the ground level is described with the term of ^1A_g. The non-relativistic DVME calculation reveals that the lowest energy level of the CT state is ^3A_g. Thus, the radiative CT transition from W 5d to O 2p orbitals for the $[WO_6]^{6-}$ octahedron is assigned to the $^3A_g \rightarrow {}^1A_g$ spin-forbidden transition. The large difference in the experimental absorption and luminescence energies of 0.933 eV suggests that the terminal level for the excitation process is located at higher energy than the ^3A_g level. Applying the selection rule for the electric dipole transition based on the group theory [42], we obtained the allowed transition of $^1A_u \leftarrow {}^1A_g$, which is the possible excitation transition for the $[WO_6]^{6-}$ with C_i symmetry with the highest transition probability. The energy gap between the lowest ^1A_u and ^3A_g levels is 0.563 eV, leading to the absorption energy of 5.01 eV. The spin-orbit interaction increases the CT energy with 0.3–0.7 eV and the lowest ^3A_g level with 0.468 eV, resulting in the energy difference between ^1A_g and ^3A_g levels of 4.91 eV. For the Ca_3WO_6 host, the Madelung potential increases the lowest CT energy by only 0.029 eV, indicating that the CT states of the $[WO_6]^{6-}$ octahedron are hardly influenced by other ions outside the octahedron, such as Ca^{2+} or outer O^{2-} ions.

The non-relativistic DVME calculation also revealed the term symbol for the ground state ($^1A'$) and the lowest CT excited state ($^3A'$) for the $[WO_5]^{4-}$ square pyramid with C_i symmetry. Thus, the radiative CT transition is the $^3A' \rightarrow {}^1A'$ spin-forbidden transition with an energy of 4.82 eV. Based on the group theory, the terminal levels for the allowed electric dipole transition from the ground $^1A'$ level are the $^1A'$ level for the σ-polarization and the $^1A''$ level for the π-polarization. The lowest $^1A'$ and $^1A''$ excited levels are located at 5.45 and 5.46 eV, which are 0.63–0.64 eV

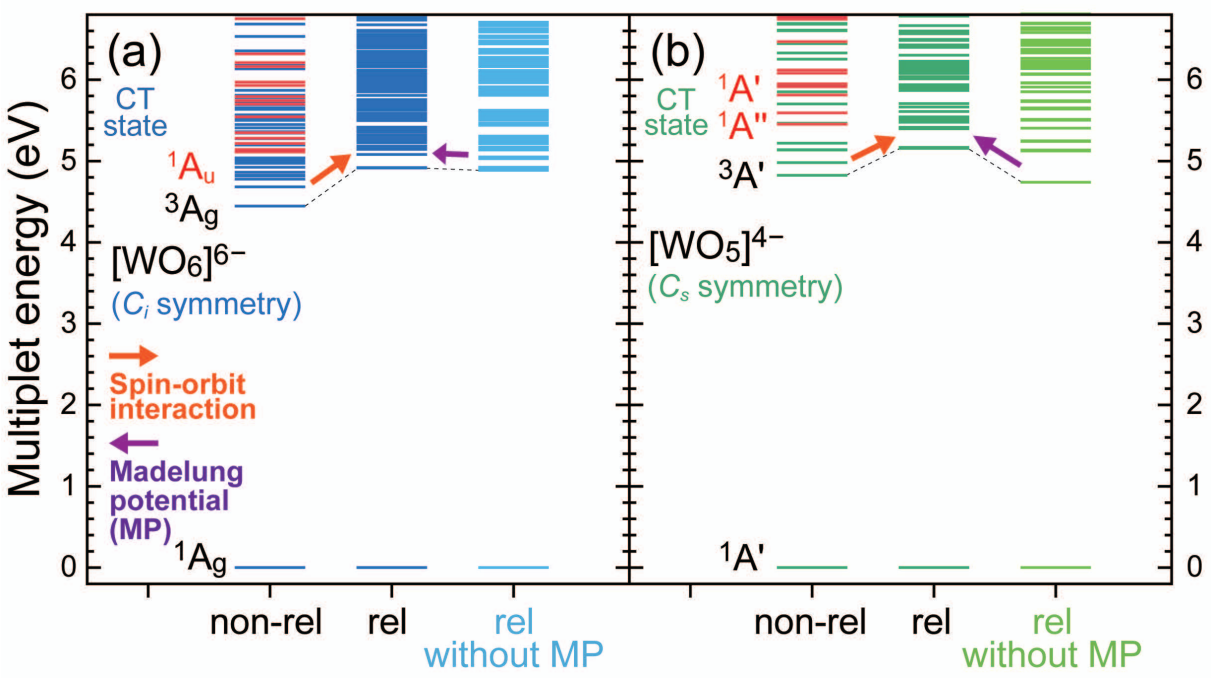

Figure 9.9. Multiplet energy diagrams of (a) $[WO_6]^{6-}$ (C_i symmetry) and (b) $[WO_5]^{4-}$ (C_s symmetry) clusters calculated with the non-relativistic (non-rel) and relativistic (rel) DVME methods.

higher than the ^{3}A' level. The energy of CT states increases due to the spin-orbit interaction, and the lowest ^{3}A' level is shifted upward with 0.332 eV. As shown in the results of the DV-Xα calculations, the influence of the spin-orbit interaction in the $[WO_5]^{4-}$ square pyramid is smaller than that in the $[WO_6]^{6-}$ octahedron. The CT energy of the $[WO_5]^{4-}$ square pyramid without the Madelung potential was also calculated with the relativistic DVME method, leading to 0.415 eV lower CT energy, which is not anticipated from the tendency shown in the $[WO_6]^{6-}$ octahedron with C_i symmetry. This lower CT energy suggests that the structural features of the $[WO_5]^{4-}$ square pyramid with short W-O bond lengths, do not bring about the upward energy shift of the CT states. The lowest CT energy of a single $[WO_5]^{4-}$ square pyramid is located at 4.74 eV, whereas that of a single $[WO_6]^{6-}$ octahedron is at 4.89 eV. Although the square pyramidal structure causes the redshift of the CT states due to the strong crystal field, the significant contribution of the Madelung potential cancels out the redshift and brings about the large absorption edge of the CT transition for the $[WO_5]^{4-}$ cluster. The significant difference in the Madelung potentials of $Ca_3WO_5Cl_2$ and Ca_3WO_6 is the existence of Cl^- ions in a lattice. Whereas the first neighboring anions from the $[WO_6]^{6-}$ octahedron is O^{2-} ions at 3.98–4.08 Å distance

away, that from the $[WO_5]^{4-}$ square pyramid is a Cl^- ion 3.29 Å away in the opposite direction of the apical $O^{2-}{}_I$ ion. The nonbonding $[WO_5]^{4-}$–Cl^- electrostatic interaction can cause the high-energy shift of the whole energy levels of the CT states.

The calculated CT energies and measured spectroscopic data are listed in **Table 9.2**. The one-electron CT energies were evaluated by Slater's transition state methods with the electronic configuration of $(W\ 5d_1)^{0.5}(O\ 2p\ top)^{1.5}$. Note that since the relativistic MO calculation considering the spin-orbit interaction identifies the energy levels through the irreducible representations with the Bethe notation, we cannot obtain information about the spin multiplicity and the degree of spin-orbital splitting. Nevertheless, the lowest CT energy, which is the energy gap between the ground state of the $(W\ 5d)^0(O\ 2p)^{6n}$ configuration and the lowest CT level, is available for discussion. Both the one-electron and multiple-electron MO calculations show the same tendency; the CT states shift upward by 0.2–0.4 eV due to the spin-orbit interaction of W, and the $[WO_5]^{4-}$ square pyramid takes higher CT energy than the $[WO_6]^{6-}$ octahedron. The terminal level of CT excitation can be located at 0.3–0.6 eV higher energy than the lowest CT state. Here, the energy difference between the $^1A'$ and $^1A''$ levels in the $[WO_5]^{4-}$ square pyramid obtained by the non-relativistic DVME calculation is at most 0.01 eV, suggesting that the polarization of excitation light can have a negligible effect on the PLE spectra. Despite an overestimation of as much as ~1–2 eV, the calculated CT energy reproduces the higher absorption energy in $Ca_3WO_5Cl_2$ than that in Ca_3WO_6. The *ab initio* MO calculation reveals that the five-fold $[WO_5]^{4-}$ square pyramid, even with a strong crystal field, takes a high CT absorption energy due to the Madelung Potential related to Cl^- ions in the lattice.

The observed CT luminescence is assigned to the spin-forbidden transition from the lowest CT level to the ground level of the $(W\ 5d)^0(O\ 2p)^{6n}$ configuration. As discussed above, the energy of CT states for the $[WO_5]^{4-}$ square pyramid is higher than that for the $[WO_6]^{6-}$ octahedron, indicating that the CT luminescence of the $Ca_3WO_5Cl_2$ is predicted to be located at the shorter wavelength side of that of the Ca_3WO_6. However, the results of the *ab initio* calculations cannot provide a reasonable explanation for the redshift of CT luminescence in the $Ca_3WO_5Cl_2$ sample. As the energy diagram obtained by the MO and CI calculation cannot

consider the structural relaxation at the excited states, the disagreement in the luminescence energy between the experimental and computed values can be related to the oscillation potential of the CT state.

Table 9.3. CT energies of $[WO_6]^{6-}$ and $[WO_5]^{4-}$ clusters by the non-relativistic (non-rel) and relativistic (rel) MO and CI calculation (one-electron DV-Xα method and multi-electron DVME method) and the spectroscopic experiments (unit: eV)

methods	$[WO_6]^{6-}$ non-rel[b]	rel	$[WO_5]^{4-}$ non-rel[b]	rel
DV-Xα	4.21 $[a_g(W\ 5d_1)\text{-}a_g(O\ 2p)]$	4.51	4.25 $[a'(W\ 5d_1)\text{-}a''(O\ 2p)]$	4.65
Slater's transition state method	4.86 $[a_g(W\ 5d)^{0.5}\text{-}a_g(O\ 2p)^{1.5}]$	5.19	4.92 $[a'(W\ 5d)^{0.5}\text{-}a''(O\ 2p)^{1.5}]$	5.36
DVME	4.74 $[^3A_g\text{-}^1A_g]$	4.91	4.82 $[^3A'\text{-}^1A']$	5.16
	5.01 $[^1A_u\text{-}^1A_g]$	—	5.45 $[^1A'\text{-}^1A']$ (σ) 5.46 $[^1A''\text{-}^1A']$ (π)	—
experimental absorption	3.84		4.04	
experimental luminescence	2.91		2.54	

[b]The computed parameters by the non-rel MO calculation are listed with the irreducible representations for the initial and terminal levels of applicable transition in brackets.

Figures 9.10a and **10b** show the supposed configurational coordinate diagram for the $[WO_6]^{6-}$ octahedron with C_i symmetry and the $[WO_5]^{4-}$ square pyramid with C_s symmetry. R_0 is

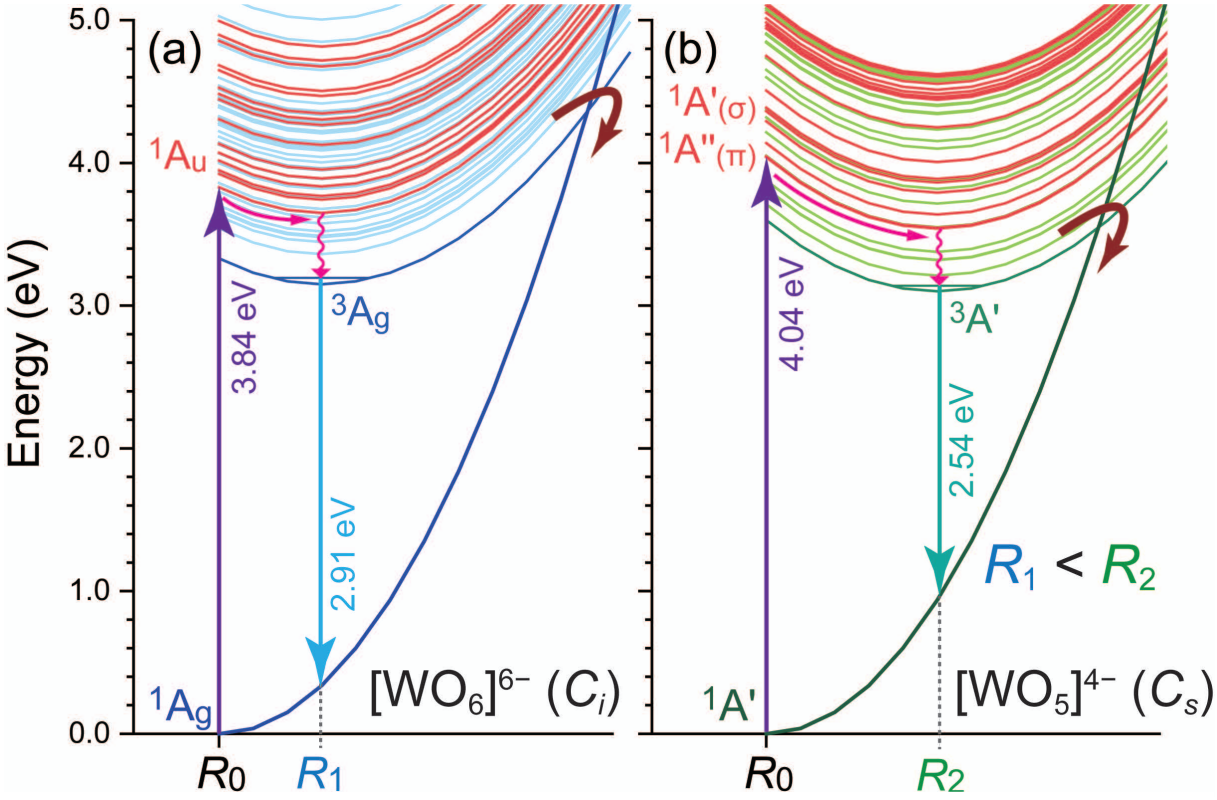

Figure 9.10. Possible configurational coordinate diagram for (a) the $[WO_6]^{6-}$ octahedron (C_i symmetry) and (b) $[WO_5]^{4-}$ (C_s symmetry) square pyramid. The terminal states of the allowed electric dipole transition for absorption are drawn in red.

the equilibrium position of W^{6+} and O^{2-} ions. R_1 and R_2 are the offset from the equilibrium position R_0, indicating the shift of O^{2-} ions in the CT excited states. For the sake of brevity, the same curvatures are applied in the parabolas for the ground level and CT states. Upon excitation through the spin-allowed electric dipole transitions ($^1A_u \leftarrow {}^1A_g$ for $[WO_6]^{6-}$ and $^1A'$ or $^1A'' \leftarrow {}^1A'$ for $[WO_5]^{4-}$), excited electrons relax down into the initial level of CT luminescence (^3A_g for $[WO_6]^{6-}$ and $^3A'$ for $[WO_5]^{4-}$). For the $[WO_5]^{4-}$ square pyramid, we can put the parabolas of the CT states with large offset (*i.e.*, $R_1 < R_2$) to obtain the small luminescence energy of 2.54 eV. The large offset leads to a small activation energy for the thermal activation crossover quenching (shown in red arrows), which is consistent with the experimental fact that the CT luminescence of the $Ca_3WO_5Cl_2$ sample is easily quenched with temperature. Mainly four O^{2-} ions in the basal plane of the $[WO_5]^{4-}$ square pyramid contribute to the CT states, suggesting that the anisotropic structural relaxation of the coordination polyhedron can cause the large configurational offset in the oscillator potentials, unlike the $[WO_6]^{6-}$ octahedron with an inversion center.

9.4. Conclusions

The square pyramidal $[WO_5]^{4-}$ cluster in the oxychloride $Ca_3WO_5Cl_2$ showed the cyan charge transfer (CT) luminescence between W 5d and O 2p orbitals. Compared with the blue CT luminescence of the $[WO_6]^{6-}$ octahedron in the oxide Ca_3WO_6, this cyan CT luminescence was characteristics in the following respects;

• The CT absorption energy of the $[WO_5]^{4-}$ square pyramid was estimated to be 4.04 eV from the fundamental absorption edge in the photoluminescence excitation spectrum at 4 K, which was 0.2 eV larger than that of the $[WO_6]^{6-}$ octahedron.

• The peak of the CT luminescence band of the $[WO_5]^{4-}$ square pyramid was located at 2.54 eV, which was 0.37 eV redshifted from the CT luminescence peak of the $[WO_6]^{6-}$ octahedron.

Because these characteristics of the $[WO_5]^{4-}$ square pyramid were not explained by the simple molecular orbital diagram for O_h symmetry, the *ab initio* calculations with the discrete-variational Xα (DV-Xα) and DV multi-electron (DVME) methods were performed to discuss the luminescence properties of the $Ca_3WO_5Cl_2$. Both the one- and multi-electron calculations revealed that the $[WO_5]^{4-}$ square pyramid takes the larger CT energy due to not the crystal field splitting but the Madelung potential related to the existence of Cl^- ions in a lattice. However, since the *ab initio* molecular orbital and configuration interaction calculation cannot take the structural relaxation of the excited states into account, the redshift of the CT luminescence for the $[WO_5]^{4-}$ cluster could not be understood by these *ab initio* calculation results. Supposing that the CT excited states of the $[WO_5]^{4-}$ cluster takes the larger offset in the qualitative configurational coordinate diagram, the redshift and the lower quenching temperature of the CT luminescence for the $[WO_5]^{4-}$ square pyramid were accounted for. There are only a few reports about the CT luminescence of the tungstates with a unique coordination polyhedron. The results in this study are expected to promote research on the CT luminescence of tungstates in a variety of material groups including mixed-anion compounds.

Acknowledgements

Work by Y.K. was financially supported by the Grant-In-Aid for JSPS Fellows (JP19J23280). This work was financially supported by JSPS Grant-in-Aid for Scientific Research on Innovative Areas "Mixed-Anion" (JP16H06441). Computation time for DFT calculations was provided by the SuperComputer System, Institute for Chemical Research, Kyoto University. This work was supported by NIMS Joint Research Hub Program.

References

[1] M.J. Treadaway, R.C. Powell, "Luminescence of calcium tungstate crystals". *J. Chem. Phys.* **61** (1974) 4003–4011.

[2] R. Grasser, A. Scharmann, "Luminescent sites in $CaWO_4$ and $CaWO_4$:Pb crystals". *J. Lumin.* **12–13** (1976) 473–478.

[3] F.A. Kröger, F. Urbach, "Some Aspects of the Luminescence of Solids". *Phys. Today.* **1** (1948) 24–25.

[4] G. Blasse, G.J. Dirksen, M. Hazenkamp, J.R. Günter, "The luminescence of magnesium tungstate dihydrate, $MgWO_4 \cdot 2H_2O$". *Mater. Res. Bull.* **22** (1987) 813–817.

[5] W. Van Loo, "Luminescence of lead molybdate and lead tungstate. I. experimental". *Phys. Status Solidi A.* **27** (1975) 565–574.

[6] W. Van Loo, "Luminescence of lead molybdate and lead tungstate. II. discussion". *Phys. Status Solidi A.* **28** (1975) 227–235.

[7] J.A. Groenink, G. Blasse, "Some new observations on the luminescence of $PbMoO_4$ and $PbWO_4$". *J. Solid State Chem.* **32** (1980) 9–20.

[8] W.M. Yen, S. Shionoya, H. Yamamoto, "PHOSPHOR HANDBOOK" (second ed., CRC Press, Boca Raton, 2007)

[9] E. Sakai, "Recent Measurements on Scintillator-Photodetector Systems". *IEEE Trans. Nucl. Sci.* **34** (1987) 418–422.

[10] V.G. Baryshevsky, M.V. Korzhik, V.I. Moroz, V.B. Pavlenko, A.S. Lobko, A.A. Fyodorov, V.A. Kachanov, V.L. Solovjanov, B.I. Zadneprovsky, V.A. Nefyodov, P.V. Nefyodov, B.A. Dorogovin, L.L. Nagornaja, "Single crystals of tungsten compounds as promising materials for the total absorption

detectors of the e.m. calorimeters". *Nucl. Instrum. Methods Phys. Res. A.* **322** (1992) 231–234.

[11] M. Kobayashi, M. Ishii, K. Harada, Y. Usuki, H. Okuno, H. Shimizu, T. Yazawa, "Scintillation and phosphorescence of $PbWO_4$ crystals". *Nucl. Instrum. Methods Phys. Res. A.* **373** (1996) 333–346.

[12] M.J.J. Lammers, G. Blasse, D.S. Robertson, "The luminescence of cadmium tungstate ($CdWO_4$)". *Phys. Status Solidi A.* **63** (1981) 569–572.

[13] G. Blasse, "Structure and Bonding". (Springer, Heidelberg, 1980)

[14] G. Blasse, A.F. Corsmit, "Electronic and vibrational spectra of ordered perovskites". *J. Solid State Chem.* **6** (1973) 513–518.

[15] A.B. van Oosterhout, "An *ab initio* calculation on the WO_6^{6-} octahedron with an application to its luminescence". *J. Chem. Phys.* **67** (1977) 2412–2418.

[16] T. Yamase, M. Sugeta, "Charge-transfer photoluminescence of polyoxo-tungstates and -molybdates". *J. Chem. Soc. Dalton Trans.* **0** (1993) 759–765.

[17] R.D. Shannon, "Revised effective ionic radii and systematic studies of interatomic distances in halides and chalcogenides". *Acta Crystallogr. A.* **32** (1976) 751–767.

[18] H. Kageyama, K. Hayashi, K. Maeda, J.P. Attfield, Z. Hiroi, J.M. Rondinelli, K.R. Poeppelmeier, "Expanding frontiers in materials chemistry and physics with multiple anions". *Nat. Commun.* **9** (2018) 772 (15p).

[19] G. Blasse, L.H. Brixner, "Luminescence in gadoliniumchlorotungstate ($GdWO_4Cl$)". *J. Solid State Chem.* **47** (1983) 368–372.

[20] G. Blasse, G.J. Dirksen, L.H. Brixner, "Luminescence in trilanthanumtrichlorotungstate ($La_3WO_6Cl_3$)". *J. Solid State Chem.* **46** (1983) 294–305.

[21] G.B. Ayer, V.V. Klepov, M.D. Smith, M. Hu, Z. Yang, C.R. Martin, G. Morrison, H.-C. Zur Loye, "$BaWO_2F_4$: A Mixed Anion X-Ray Scintillator with Excellent Photoluminescence Quantum Efficiency". *Dalton Trans.* **49** (2020) 10734–10739.

[22] Z. Zikmund, "The crystal structure of $Ca_3WO_6Cl_2$ and the configuration of the WO_5^{4-} ion". *Acta Crystallogr. B.* **30** (1974) 2587–2593.

[23] D. Hirai, T. Yajima, D. Nishio-Hamane, C. Kim, H. Akiyama, M. Kawamura, T. Misawa, N. Abe, T.-H. Arima, Z. Hiroi, ""Visible" 5d Orbital States in a Pleochroic Oxychloride". *J. Am. Chem. Soc.* **139** (2017) 10784–10789.

[24] H. Adachi, M. Tsukada, C. Satoko, "Discrete variational Xα cluster calculations. I. application to metal clusters". *J. Phys. Soc. Jpn.* **45** (1978) 875–883.

[25] K. Ogasawara, T. Ishii, I. Tanaka, H. Adachi, "Calculation of multiplet structures of Cr^{3+} and V^{3+} in α-Al_2O_3 based on a hybrid method of density-functional theory and the configuration interaction". *Phys. Rev. B* **61** (2000) 143–161.

[26] S.J. Clark, M.D. Segall, C.J. Pickard, P.J. Hasnip, M.I.J. Probert, K. Refson, M.C. Payne, "First principles methods using CASTEP". *Z. Kristallogr. Cryst. Mater.* **220** (2005) 567–570.

[27] J.P. Perdew, A. Ruzsinszky, G.I. Csonka, O.A. Vydrov, G.E. Scuseria, L.A. Constantin, X. Zhou, K. Burke, "Restoring the density-gradient expansion for exchange in solids and surfaces". *Phys. Rev. Lett.* **100** (2008) 136406 (4p).

[28] D. Vanderbilt, "Soft self-consistent pseudopotentials in a generalized eigenvalue formalism". *Phys. Rev. B* **41** (1990) 7892–7895.

[29] D.D. Koelling, B.N. Harmon, "A technique for relativistic spin-polarised calculations". *J. Phys. C: Solid State Phys.* **10** (1977) 3107–3114.

[30] A. Rosén, D.E. Ellis, H. Adachi, F.W. Averill, "Calculations of molecular ionization energies using a self-consistent-charge Hartree–Fock–Slater method". *J. Chem. Phys.* **65** (1976) 3629–3634.

[31] K. Ogasawara, T. Iwata, Y. Koyama, T. Ishii, I. Tanaka, H. Adachi, "Relativistic cluster calculation of ligand-field multiplet effects on cation $L_{2,3}$ x-ray-absorption edges of $SrTiO_3$ NiO, and CaF_2". *Phys. Rev. B* **64** (2001) 115413 (5p).

[32] S. Takemura, K. Ogasawara, "Systematic first-principles calculations of charge transfer transitions of transition metal ions (Sc^{3+}, Ti^{3+}, V^{3+}, Cr^{3+}, Mn^{3+}, Fe^{3+}) in α-Al_2O_3" *Opt. Mater. X.* **1** (2019) 100005 (6p).

[33] S. Takemura, K. Ogasawara, "Systematic first-principles calculations of charge transfer transitions of trivalent rare earth ions in CaF_2". *J. Lumin.* **214** (2019) 116542 (6p).

[34] S. Takemura, K.C. Mishra, J. Collins, K. Ogasawara, "First-Principles Calculations of Charge Transfer Transitions of Eu^{3+} in Y_2O_3 and Y_2O_2S". *ECS J. Solid State Sci. Technol.* **9** (2020) 066005 (7p).

[35] J.C. Slater, "Quantum Theory of Molecules and Solids". **4**, (1974). (McGraw-Hill, New York)

[36] J.H.G. Bode, A.B. Van Oosterhout, "Defect Luminescence of Ordered Perovskites A_2BWO_6". *J. Lumin.* **10** (1975) 237–242.

[37] A.B. Van Oosterhout, "Tungstate Luminescence in Ordered Perovskites". *Phys. Status Solidi A* **41** (1977) 607–617.

[38] A.L. Allred, "Electronegativity values from thermochemical data". *J. Inorg. Nucl. Chem.* **17** (1961) 215–221.

[39] O. Jarchow, F. Schröder, H. Schulz, "Kristallstruktur und Polytypie von WO_2Cl_2". *Z. Anorg. Allg. Chem.* **363** (1968) 58–72.

[40] H. Hess, H. Hartung, "Die Kristallstruktur von Wolframoxidchlorid $WOCl_4$ und Wolframoxidbromid $WOBr_4$". *Z. Anorg. Allg. Chem.* **344** (1966) 157–166.

[41] F. Tamadon, K. Seppelt, "The Elusive Halides VCl_5, $MoCl_6$, and $ReCl_6$". *Angew. Chem. Int. Ed Engl.* **52** (2013) 767–769.

[42] M.G. Brik, C.-G. Ma, "Theoretical Spectroscopy of Transition Metal and Rare Earth Ions From Free State to Crystal Field" (Jenny Stanford Publishing, Singapore, 2020)

Chapter 10

Development of Ce^{3+} and Li^{+} Co-doped Magnesium Borate Glass Ceramics for Optically Stimulated Luminescence Dosimetry

Abstract

Magnesium tetraborate, MgB_4O_7, is an attractive host material for dosimetry due to the two characteristics: its low effective atomic number (Z_{eff} = 8.4) and high neutron capture cross-section of the ^{10}B isotope. Particularly, Ce^{3+} and Li^{+} ions co-doped MgB_4O_7 has shown optically stimulated luminescence (OSL) signal comparable to that of Al_2O_3:C, which is a well-known OSL dosimetry material. In this work, for further improvement of the dosimetric properties, a new synthesis route for MgB_4O_7:Ce^{3+}-Li^{+} is described: glass-ceramic (GC) MgB_4O_7:Ce^{3+}-Li^{+} samples were prepared by heat treatment of the magnesium borate glass with the composition, $25MgO\text{-}72B_2O_3\text{-}3Li_2O\text{-}0.3Ce^{3+}$. The prepared GC samples show UV-blue radioluminescence assigned to the Ce^{3+} 5d → 4f transition under X-ray irradiation and two thermoluminescence (TL) glow peaks related to the shallow and deep electron traps. Although fading of the TL and OSL signal was observed due to electron release from the shallow traps, the electrons captured by deep traps were stable at room temperature. Particularly, GC samples annealed at 750 °C and 800 °C, named GC750 and GC800, showed stable OSL up to ten hours following β-ray irradiation, after an initial fading mainly due to the presence of shallow traps in the material. From the viewpoint of this fading ratio, GC750 and GC800 showed potential as a practical OSL dosimeter.

10.1. Introduction

The fast-paced technological advances in a variety of fields which either uses ionizing radiation (X-rays, β-rays, γ-rays, neutrons, as well as accelerated particles such as protons, and other heavy ions) directly for its therapeutical or analytical properties, or which produces radiation as a by-product, or both, imposes increasing challenges for the dosimetry of such fields. Some of the most challenging aspects nowadays are the dosimetry of small fields such as those found in modern radiation therapy and radiosurgery due to the large dose gradients involved [1], the dosimetry of pulsed fields created in modern accelerators (including laser-based accelerators) due to the high instantaneous dose-rates during the pulses [2,3], and the dosimetry in the presence of magnetic fields such as in those fields found in Magnetic Resonance Imaging-Guided Radiation Therapy (MRIgRT) [4].

Dosimetry refers to the quantification of the energy deposited by ionizing radiation for purposes of radiation protection, quality assurance, and overall characterization of the radiation fields. A wide variety of active and passive dosimeters are available, but all have advantages and disadvantages for each specific application [5]. Passive detectors, while not offering real-time information, are very popular in radiation protection because of their small size, low cost, high sensitivity, precision, and convenience. From those, luminescence detectors, such as those based on radiophotoluminescence (RPL) [6,7], thermoluminescence (TL) [8], and optically stimulated luminescence (OSL) [9,10] are among the most popular for radiation measurements. The readout of RPL and OSL detectors, in particular, is completely optical, therefore practical and suitable for the development of 2D dosimetry techniques for measurements in high dose-gradient fields [11–13]. Since the luminescence processes in these detectors are based on the electron-hole trapping/detrapping processes taking place in solid-state insulating crystalline materials in a time-scale of 10^{-15}–10^{-13} s [14], the techniques may also offer advantages such as independence on dose-rate [15] and magnetic field [16].

Figure 10.1 illustrates the electron trapping-detrapping processes occurring within the luminescence detectors exposed to ionizing radiation. First, electrons in the host valence band (VB) are excited by ionizing radiation (arrow 1). Since the energy of ionizing radiation is much

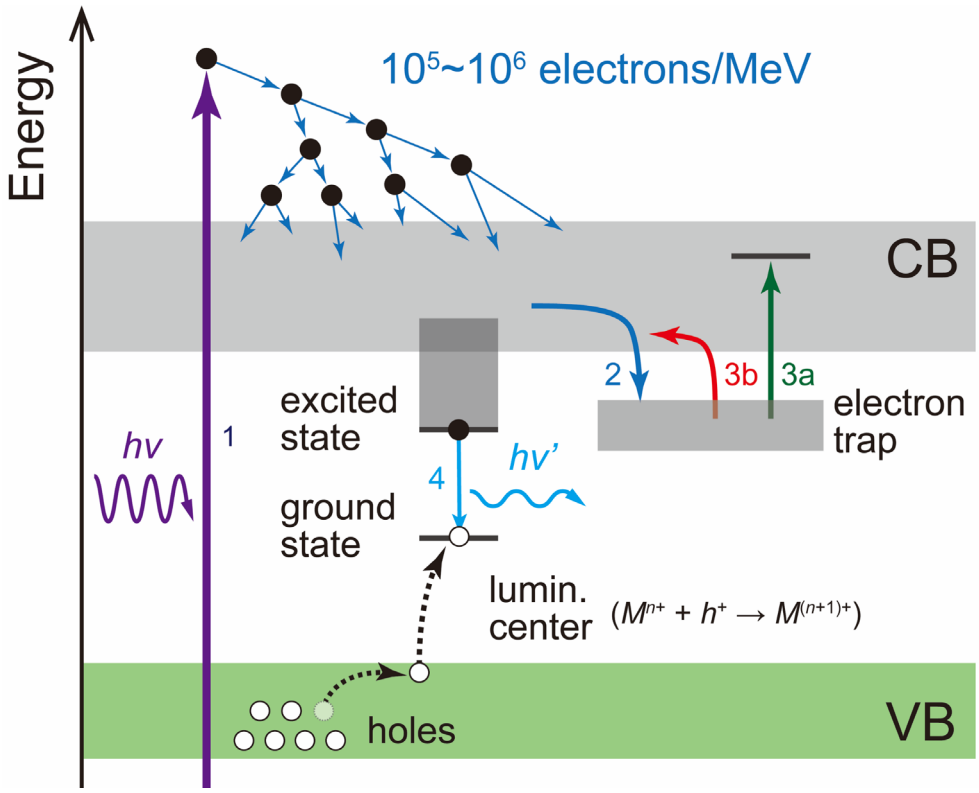

Figure 10.1. Schematic illustration of the TL and OSL process, related to the electron trapping and detrapping process: 1. Excitation of electrons with ionizing radiation; 2. Electron trapping; 3a. Optically stimulated electron detrapping; 3b. Thermally stimulated electron detrapping; 4. Radiative electron-hole recombination. During this process, holes generated at the host VB by the ionizing radiation move to the ground state of the luminescence center ion, resulting in the change of the valence state ($M^{n+} + h^{+} \rightarrow M^{(n+1)+}$).

higher than the bandgap of host compounds, electrons in the order of 10^5–10^6 per MeV are generated. In the case of scintillators, electron-hole recombination takes place immediately. However, if energy levels related to impurities or defects are introduced just below the host conduction band (CB), they can act as electron traps, temporarily capturing the excited electrons (arrow 2). The trapped electrons can be released to the CB by optical (arrow 3a) or thermal (arrow 3b) stimulation, and then luminescence is observed upon the carrier recombination (arrow 4). At this moment, the luminescence related to the optically and thermally stimulating process is called OSL and TL, respectively.

Although they are based on a similar scheme, the OSL technique has some advantages in comparison to the TL technique [17,18]. First, it requires no heating, only optical stimulation. As a result, during the readout processing, OSL is not affected by the thermal quenching of the

luminescence [17]. Second, by adjusting the stimulating light intensity, fast readouts can be realized, resulting in rapid analysis of a large number of dosimeters (high throughput) [18].

Despite the properties and potential advantages discussed above, the availability of materials with features suitable for some applications is still restricted. For example, the only OSL materials used in commercial dosimetry systems nowadays are Al_2O_3:C and BeO, both of which have relatively slow luminescence lifetimes for laser-scanning 2D dosimetry (35 ms [19] and ~27 μs [20,21], respectively). Al_2O_3:C,Mg has been introduced with a higher concentration of fast luminescence centers (F^+-centers, < 7 ns), but the dominant emission is still from slow luminescence centers (F-centers, 35 ms) [22]. Considering for example a 30.0 cm by 30.0 cm film and ~0.1 mm pixel size, or 9 megapixels, the lifetime has to be lower than ~10 μs for the image to be read within 5 min, assuming that the laser stays three lifetimes over each pixel to avoid pixel bleeding. OSL materials used in image plates (*e.g.*, BaFBr:Eu^{2+}) typically have a high effective atomic number and the OSL signal fades with time after irradiation, which makes them unsuitable for precise dosimetry applications [23–25].

Several new OSL materials have been investigated thus far [26–28]. Magnesium tetraborate, MgB_4O_7, has been attracting attention as a host material for dosimetry based on the OSL or TL technique for several reasons [29–33]. First, it has a low effective atomic number, Z_{eff} = 8.4. In radiation dosimetry, materials with an effective atomic number similar to the human body are required to avoid large photon energy dependence; the materials with an effective atomic number similar to water (Z_{eff} = 7.51) or tissues (Z_{eff} = 7.35–7.65) are suitable. The second reason is the possibility to control the neutron sensitivity by controlling the host content of ^{10}B isotope, which has a high neutron capture cross-section. Ce^{3+}-doped MgB_4O_7 has also been proposed as a potential OSL material for 2D dosimetry, because of the fast luminescence associated with its Ce^{3+} emission due to 5d → 4f parity allowed transition [34] and also identified by other groups as a potential OSL material for dosimetry [35].

In a previous report, Yukihara *et al.* evaluated the luminescent properties of Ce^{3+}-doped MgB_4O_7 [33]. Both radioluminescence (RL) and TL were observed in the near-UV region at around 340–360 nm. The fluorescence lifetime of Ce^{3+} 5d → 4f luminescence in MgB_4O_7, 31.5 ns,

was short enough for the use of this material for imaging applications by laser scanning [34], opening the possibility of 2D dosimetry [36]. According to the TL glow curves of MgB_4O_7 doped with a variety of lanthanoid ions, the glow peak of $MgB_4O_7:Ce^{3+}$ was located at around 240 °C, which means that $MgB_4O_7:Ce^{3+}$ has a suitable trap depth for OSL dosimetry. In a separate report [37], it was shown that Ce^{3+} and Li^{+} co-doped MgB_4O_7 has some attractive dosimetric properties compared to the well-known commercial OSL material Al_2O_3:C. The OSL dose-response of Al_2O_3:C saturates at around 100 Gy, whereas that of $MgB_4O_7:Ce^{3+}$-Li^{+} is proportional to the irradiation dose up to 800 Gy with no saturation, which is desirable for proton and heavily charged particle beams. Besides, it is possible to increase its neutron sensitivity by enriching it with ^{10}B or decrease it by enriching it with ^{11}B. Therefore, the Ce^{3+}-Li^{+} co-doped MgB_4O_7 is a promising material for OSL dosimetry. Nevertheless, the $MgB_4O_7:Ce^{3+}$-Li^{+} reported previously [34] suffers from sensitivity changes and anomalous fading of the main dosimetric peak at 240 °C, which motivates the search for new synthesis routes that could improve its dosimetric properties.

To try to improve the dosimetric properties of $MgB_4O_7:Ce^{3+}$-Li^{+}, we propose precipitation of the MgB_4O_7 crystals in a borate glass matrix, which is the glass-ceramic (GC) MgB_4O_7. GC materials have many advantages, such as good formability, low cost, mass production, and denser materials than conventional powder-packed materials [38,39], which are favorable properties for practical application and commercialization. In this work, the MgB_4O_7 GC samples were prepared by ceramming the as-made magnesium borate glass, and their luminescent properties (photoluminescence (PL), RL, TL, and OSL) of the GC $MgB_4O_7:Ce^{3+}$-Li^{+} were investigated. Besides, the potential of the GC $MgB_4O_7:Ce^{3+}$-Li^{+} for practical OSL application is discussed.

The objective of this work is to demonstrate that $MgB_4O_7:Ce^{3+}$-Li^{+} can be obtained using the glass-ceramic route with intensity and basic properties at least equivalent to those of $MgB_4O_7:Ce^{3+}$-Li^{+} prepared by solution combustion. A complete dosimetric characterization of the samples is beyond the scope of this work, since it requires a more in-depth characterization of the TL and OSL properties than what can be presented here.

10.2. Experimental Details

10.2.1. Fabrication of Samples

Magnesium borate glass samples were prepared with the composition of 25MgO-72B_2O_3-3Li_2O-0.3Ce^{3+} (mol%). To obtain the precipitated MgB_4O_7 crystals in the glass matrix, the molar ratio between B_2O_3 and MgO should be close to 1:2. However, during the melting process at a high temperature (~1200 °C), evaporation of B_2O_3 needs to be taken into account. The optimized concentration of Li^{+} and Ce^{3+} ions was determined in the previous report [37]. Therefore, the composition 25MgO-72B_2O_3-3Li_2O-0.3Ce^{3+} was adopted in this work. The starting chemicals of MgO (99.99%, Furuuchi Chemical), B_2O_3 (99.9% up, Kojundo Chemical Laboratory), Li_2CO_3 (99.99%, Kojundo Chemical Laboratory), and CeO_2 (99.99%, Furuuchi Chemical) were weighed and mixed homogeneously in an alumina mortar. The mixture was put into a platinum crucible and calcinated at 600 °C for four hours with the aim of decarbonating Li_2CO_3. After calcination, this mixture was melted at 1200 °C for an hour. The melt was poured on a stainless-steel plate and pressed by another plate. Through this procedure, the as-made magnesium borate glass sample was fabricated. The glass transition temperature (T_g) and the crystallization temperature (T_x) of the as-made glass sample were evaluated with the differential thermogravimetric analyzer (TG-DTA TG8120, Rigaku). For the purpose of obtaining the precipitated crystalline phase of MgB_4O_7 in the glass matrix, the as-made glass was heat-treated at 600 °C, 650 °C, 700 °C, 750 °C, 800 °C, and 850 °C for three hours. Here, some samples were heat-treated over T_x to increase the crystallinity of the MgB_4O_7 phase. The obtained glass-ceramic samples are called GCxxx (xxx means the ceramming temperature in °C), *e.g.,* GC600 or GC750.

10.2.2. Characterization

The crystalline phases of all samples were identified with an X-ray diffractometer using Cu Kα radiation (Ultima IV, Rigaku).

The scanning transmission electron microscope (STEM) images and the elemental mappings with energy dispersive X-ray (EDX) spectroscopy of the microstructure were obtained with a monochromated atomic resolution analytical electron microscope (JEM-

ARM200F, JEOL Ltd.).

The photoluminescence excitation (PLE) spectra were measured with a setup consisting of a Xe lamp (CERMAX® PE300BUV, Excelitas Technologies Corp.), two monochromators (SP-2300i, Princeton Instruments, and SP-300i, Acton Research Corp.), and a photomultiplier tube (R928, Hamamatsu Photonics). The PLE spectra were calibrated by the spectrum of the Xe lamp (light source) detected by a standard Si photodiode (S1337-1010BQ, Bunkoukeiki & Co., Ltd.). For PL measurements, the samples were excited by dispersed UV light of the Xe lamp (λ = 280 nm), and the luminescence of the samples was detected with a CCD spectrometer (QE65Pro, Ocean Optics) connected with an optical fiber. In the case of RL measurements, the samples were excited by Cu Kα characteristic X-ray (40 kV and 30 mA), and the luminescence was detected with the same setup as for PL measurements. The obtained PL and RL spectra were calibrated by the spectrum of a deuterium-tungsten halogen light source (DH-2000, Ocean Optics).

TL and OSL measurements were carried out using two equipment: a *lexsyg* smart extended reader (Freiberg Instruments GmbH) and a Risø TL/OSL-DA-20 (DTU Nutech). The *lexsyg* smart extended is equipped with a UV-VIS photomultiplier tube (model 9235QB, Electron Tubes Inc.) for luminescence detection, a six-position filter wheel, and a $^{90}Sr/^{90}Y$ source for irradiation (1.53 GBq activity on 6 February 2018, Eckert & Ziegler, Germany, ~50 mGy/s dose rate at the sample position). OSL measurements in the *lexsyg* smart reader were performed using blue light-emitting diodes (centered at 460 nm, 72 mW/cm^2 irradiance). As reported by Gustafson *et al.,* the shorter the stimulation wavelength, the higher the OSL intensity [34]. The optical filters used for detection were Hoya U-340 (5.0 mm total thickness, Hoya Corporation) + Delta BP365/50 EX (Delta Optical Thin Films A/S). The Risø reader is equipped with an Electron Tubes PMD 9107-CP-TTL photomultiplier tube (ET Enterprises, Ltd.) for light detection, an Automated Detection and Stimulation Head (DASH) and a beta irradiation unit (1.48 GBq, Sr-90 source, Eckert & Ziegler Nuclitec GmbH). The OSL measurements in the Risø reader were performed with blue LEDs (centered at 470 nm, 80 mW/cm^2 irradiance). The optical filters used for detection were Hoya U-340 filters (7.5 mm total thickness, Hoya Corporation).

TL measurements were performed at 5 °C/s in the presence of N_2 in both instruments. Samples measured in ceramic form had ~20.2–45.2 mg. Samples measured in powder form had typically ~2.0–4.0 mg. When relevant, the signal was normalized by the sample mass for comparison.

10.3. Results and Discussions

10.3.1. Thermal Behavior of As-made Glass

Figure 10.2 shows the differential thermal analysis (DTA) curve of the as-made magnesium borate glass sample. From the position of a sharp exothermic peak, T_x was 716 °C. The baseline below and over ~625 °C was different, which means the glass transition took place at around 625 °C. According to the analysis of this DTA curve, T_g of the as-made glass sample was estimated to be 624 °C. One endothermic peak was observed at around 820 °C, which is related to the partial melting of the glass phase. Because of this melting, the GC samples cerammed over 900 °C could not be prepared in a proper shape.

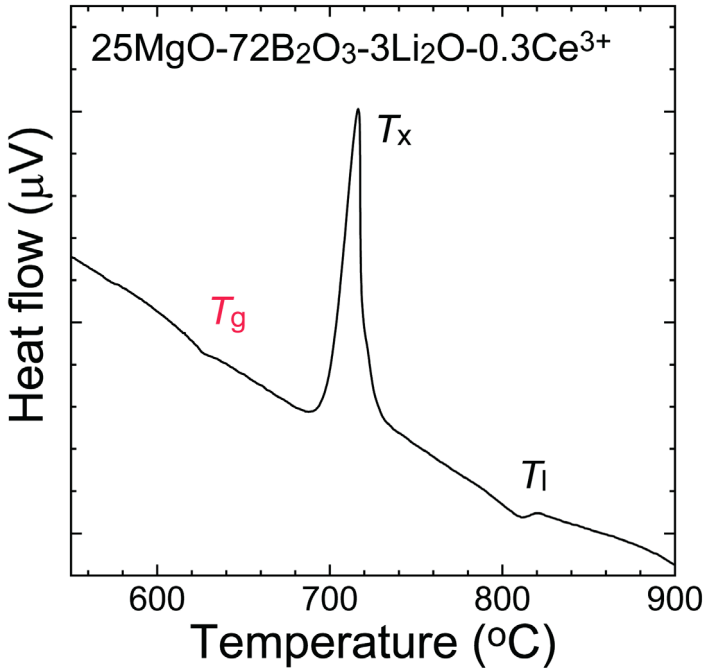

Figure 10.2. DTA curve of the as-made glass sample. T_g, T_x, and T_l mean the glass transition, crystallization, and partial melting temperature, respectively.

10.3.2. Structural Analysis

Figure 10.3 shows the X-ray diffraction (XRD) patterns of the as-made glass and all the prepared GC samples with the reference pattern for orthorhombic MgB_4O_7 (PDF #01-076-0666), which belongs to the space group *Pbca* (No. 61). The as-made glass sample shows two halo peaks due to the amorphous phase of the magnesium borate glass. For the GC samples, the MgB_4O_7 crystals were precipitated after heat treatment at and above 600 °C. Only in the XRD pattern of GC600, the weak halo peaks of the amorphous phase were still observed. Therefore, the ceramization process of MgB_4O_7 was almost completed by heat treatment above 650 °C. Although almost all diffraction peaks were assigned to orthorhombic MgB_4O_7, one weak peak of an impurity phase, assigned to triclinic $Mg_2B_2O_5$ (PDF #01-083-0625), was observed at 2θ = ~35°. With increasing heat treatment temperature, the peak intensity of impurity $Mg_2B_2O_5$ increases. To prevent this B_2O_3-poor phase from being precipitated, heat treatment at lower temperatures (650–750 °C) is a suitable condition for the preparation of the GC MgB_4O_7 samples.

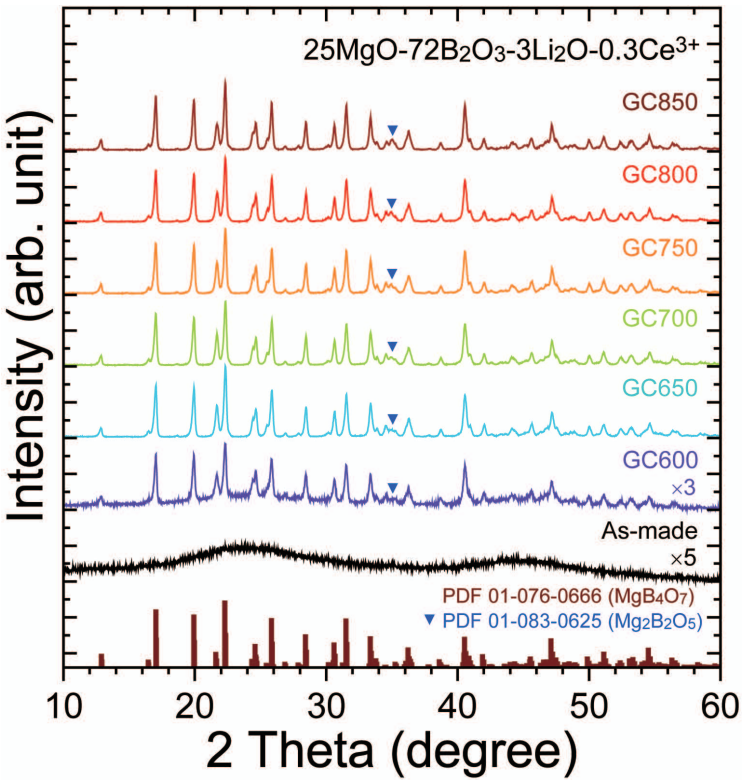

Figure 10.3. XRD patterns of the prepared samples with the reference data of crystalline MgB_4O_7 (PDF #01-076-0666).

In the unit cell of orthorhombic MgB_4O_7 shown in **Figure 10.4**, there are eight interstitial sites coordinated by some BO_3 and BO_4 units. From this point of view, Ce^{3+} ions, which are the luminescence center and have the larger ionic radius (r = 1.01 Å, CN = 6) than Mg^{2+} ions (r = 0.72 Å, CN = 6) [40], can prefer these large interstitial sites to the Mg^{2+} sites. At the same time, Li^{+} ions (r = 0.76 Å, CN = 6) [40] are able to occupy the Mg^{2+} site, which results in the charge compensation for the trivalent Ce^{3+} ions. With the Kröger-Vink notation, the Li^{+} ions at this site can be denoted as Li'_{Mg}.

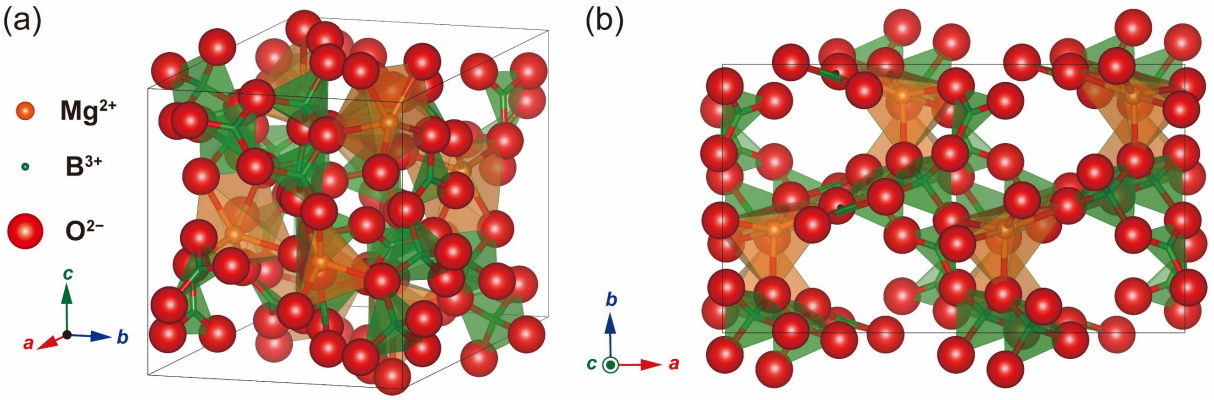

Figure 10.4. Crystal structure of the orthorhombic MgB_4O_7, (a) in the standard orientation of the crystal shape, and (b) in the view along the *c*-axis.

Figure 10.5 shows the STEM images and elemental mappings with EDX for different elements (Mg, B, O, and Ce) for GC700. Before the STEM measurements, the GC samples were crushed into powder form and then put on a microgrid. When the images are taken in low-magnification, the observed particles are not the precipitated MgB_4O_7 crystals but the pulverized GCs. Some rod-shaped particles in the order of hundreds of nm were observed around the edge of the pulverized GCs. While B and O were spread out homogeneously and characteristic X-ray intensity of B and O was proportional to the thickness of the sample, Mg was concentrated on these particles, resulting in the high contrast mapping. By taking into account this localization of Mg and the XRD patterns in Figure 10.3, these particles were microcrystals of orthorhombic MgB_4O_7, and the glass matrix had boron-rich composition compared with the composition of MgB_4O_7. Ce^{3+} ions were also located homogeneously in both the crystalline and glass phases.

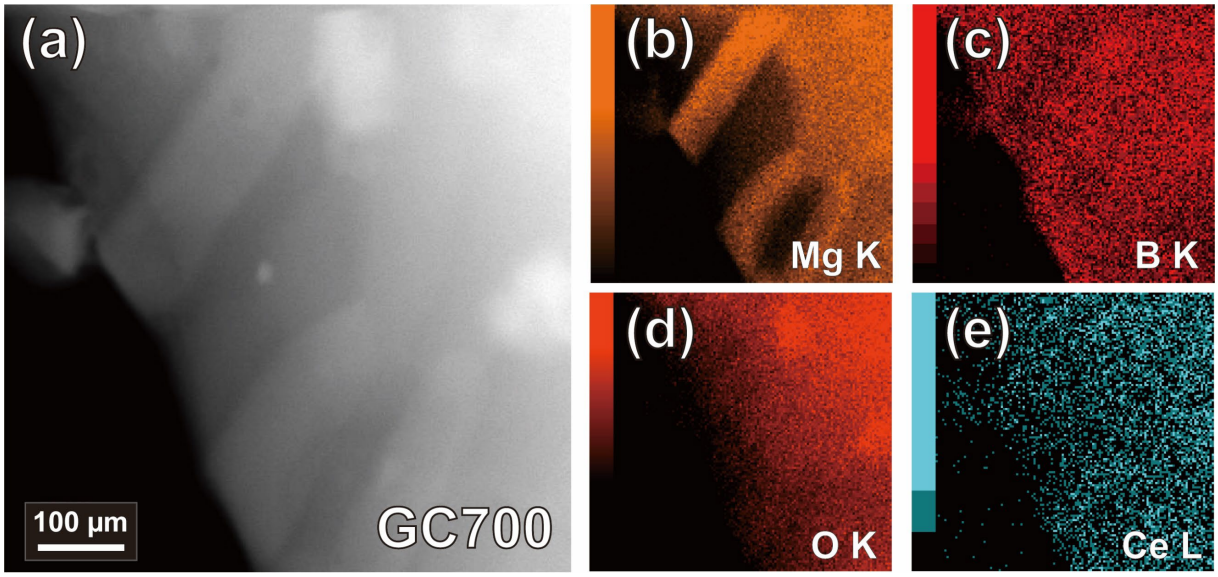

Figure 10.5. (a) STEM image of GC700, and (b–e) EDX mappings for different elements (Mg, B, O, and Ce).

Figure 10.6 shows the EDX spectra of GC600, GC700, and GC850. For GC600 and GC700, two peaks assigned to Ce Lα and Ce Lβ were observed at around 4.85 and 5.28 keV, respectively. These signals were feeble because of the low Ce^{3+} concentration. However, there was no signal attributed to Ce in GC850 because the microcrystals of Ce^{3+}-doped MgB_4O_7 had aggregated due to the high-temperature heat treatment, and no longer existed on the surface of particles.

Ce^{3+} and Li^{+} concentrations were determined by following the previous report [37] to obtain the sample with the best dosimetric performance of the GC MgB_4O_7:Ce^{3+}-Li^{+}. Due to the co-existence of the glass and crystalline phase, the actual Ce^{3+} and Li^{+} concentrations in the MgB_4O_7 crystals can differ from the assumed one. Considering the very small volume fraction of the glassy phase, the deviation of the concentration could be small. Moreover, the Ce^{3+} concentration is also affected by the oxidation state. The Ce^{4+} state is stable in the glass phase of very high basicity through the melt-quenching method in the strong oxidizing atmosphere. Since the magnesium borate glass has low basicity, only a very small amount of Ce can be oxidized into the tetravalence state. A significant amount of Ce^{4+} ions would interact with Ce^{3+} ions through the intervalence charge transfer, resulting in the brownish color of the sample. The color of the GC samples is white, and no strong absorption is observed in the visible range (the diffuse reflectance spectra are shown in **Figure 10.7**), indicating the absence of Ce^{4+}.

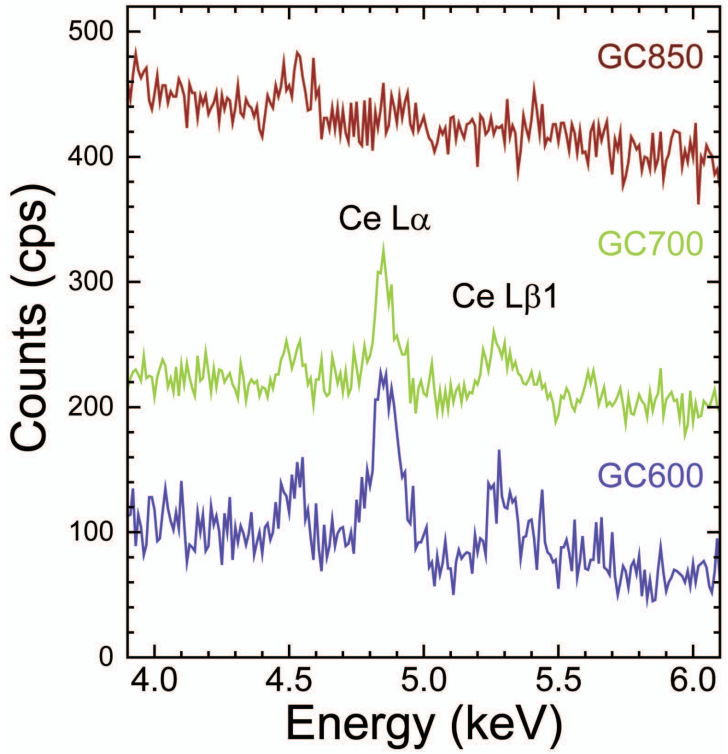

Figure 10.6. EDX spectra of GC600, GC700, and GC850.

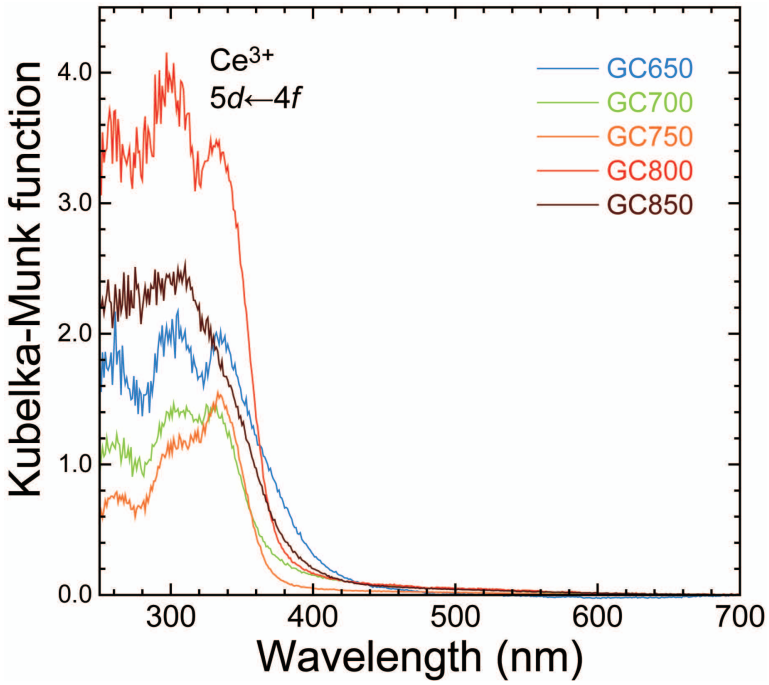

Figure 10.7. Diffuse reflectance spectra of the GC samples. The *y*-axis is converted to the Kubelka-Munk function, which is proportional to the absorption coefficient.

10.3.3. PL Properties of Magnesium Borate Glass and Glass-Ceramic Samples

Based on spectroscopy, the luminescent properties of the prepared samples were investigated. **Figure 10.8a** shows the PLE spectra monitoring at 380 nm. The as-made glass sample showed the weak excitation bands peaking at 315 nm. These bands are assigned to the 5d ← 4f transition of Ce^{3+} ions in the glass phase. For the GC samples (GC650–850), the broad excitation bands were observed in the UV region below 350 nm, having three major components peaking at 320, 290, and 270 nm, respectively. In the previous research reported by Gustafson *et al.* [34], the ceramic MgB_4O_7:Ce^{3+} sample showed the typical Ce^{3+} 5d ← 4f excitation bands peaking at ~320 nm, ~293 nm, and ~270 nm. Therefore, these excitation bands are assigned to the 5d ← 4f transition of Ce^{3+} ions in the crystalline phase of MgB_4O_7. Despite precipitation of the crystalline MgB_4O_7, the GC600 showed a similar spectral shape to the as-made glass. Judging from the weak XRD peak intensity described in Figure 10.3, this similarity is because Ce^{3+} luminescence in the glass phase was dominant due to the low crystallinity of MgB_4O_7. For the GC850 sample, the PLE intensity was much weaker than other samples. The cause of this phenomenon will be discussed in the following paragraph.

Figure 10.8b shows the PL spectra under UV excitation (λ_{ex} = 280 nm). The samples

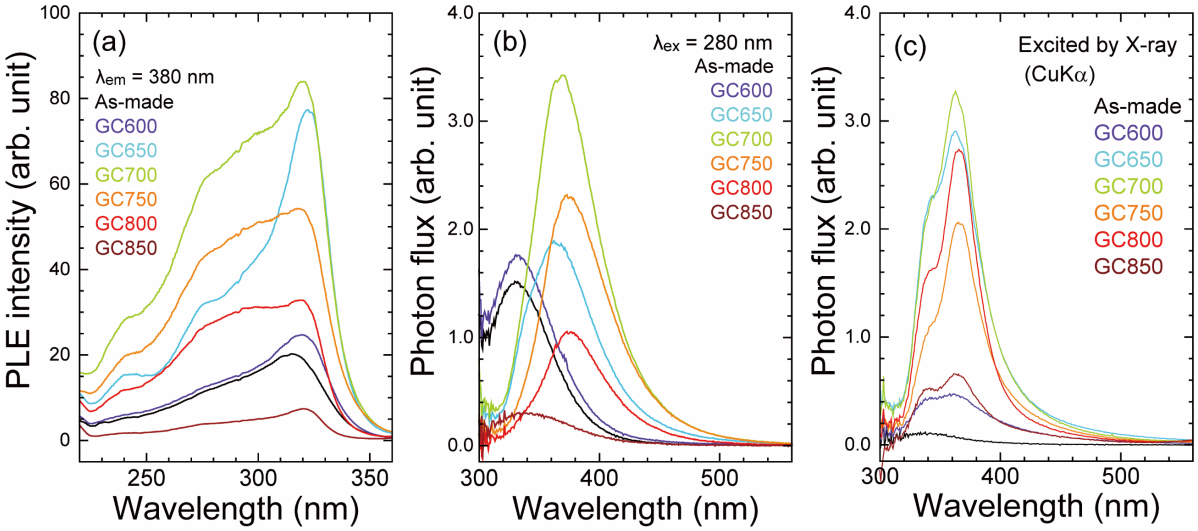

Figure 10.8. (a) PLE spectra of all the samples, monitoring Ce^{3+} emission at 380 nm. (b) PL spectra of all the samples under UV (λ_{ex} = 280 nm) illumination. (c) RL spectra of all the samples under Cu Kα characteristic X-ray illumination.

showed UV-to-blue luminescence ranging under 300 to 500 nm, which is assigned to the 5d → 4f transition of Ce^{3+} ions. For the as-made glass and GC600 samples, where most of the Ce^{3+} ions are accommodated in the glass matrix, the broad emission bands were located at the UV region, peaking at ~330 nm (= 30300 cm^{-1}). On the other hand, for other GC samples, the PL bands attributed to the Ce^{3+} 5d → 4f transition in the MgB_4O_7 host are peaked at ~370 nm (= 27000 cm^{-1}), and the spectral shape of these bands was similar to the previous report [34]. When Ce^{3+} ions are in the coordinated environment, 5d excited levels get depressed by the nephelauxetic effect by surrounding anions and split by the crystal field [41,42]. In both the glass and crystalline phases, Ce^{3+} ions are surrounded by the same anion species, oxide anions of borate groups. Accordingly, the degree of the centroid shift for the as-made glass and GC samples should be similar, and the energy difference of luminescence between them (= 33000 cm^{-1}) can mainly be due to the ligand field effect. In other words, Ce^{3+} ions in the crystalline MgB_4O_7 phase show redshifted luminescence because of the crystal field splitting derived from the ordered interstitial sites. The Ce^{3+} luminescence intensity in the glass phase was weaker than that in the MgB_4O_7 crystalline phase. This is because of the high concentration of intrinsic disordered defects in the amorphous phase, which can cause luminescence quenching through nonradiative relaxation paths. For GC850, the PL intensity was also quite weak, and the peak wavelength was blueshifted, compared with other GC samples. As this spectral shape was similar to the PL bands in the glass matrix discussed above, Ce^{3+} luminescence in the glass phase, which was slightly present between the MgB_4O_7 particles, was mainly observed. In the MgB_4O_7 crystalline phase in GC850, the concentration quenching of Ce^{3+} 5d → 4f luminescence occurred, because the distance between adjacent Ce^{3+} ions got shorter owing to the aggregation of MgB_4O_7:Ce^{3+} crystals.

10.3.4. RL Properties of Magnesium Borate Glass and Glass-Ceramic Samples

In **Figure 10.8c**, the RL spectra excited by Cu Kα characteristic X-ray at room temperature are shown. The as-made glass sample showed very weak emission under X-ray irradiation; it can be difficult to excite 4f electrons of Ce^{3+} ions in the glass matrix with ionizing radiation. In contrast, the GC samples showed stronger RL intensity than the as-made glass sample; that is, X-ray could

excite the Ce^{3+} ions efficiently in the crystalline phase. This is the reason the GC600 and GC850, in which the Ce^{3+} luminescence in the glass phase was dominant (see Section 10.3.3), showed weak RL.

As with the PL spectra, the characteristic Ce^{3+} 5d → 4f emission bands were observed, peaking at ~340 and ~360 nm. However, compared with the PL spectra shown in Figure 10.8b, the two emission peaks in the RL spectra were clearly observed, and the width of the bands was narrower. The possible explanation for these narrow bands is that luminescence *via* electron-hole recombination takes place only on interstitial Ce^{3+} ions, not on Ce^{3+} in the disordering environment, due to the efficient energy transfer from the host material. In the energetic scale, the energy difference between these two peaks is ~2000 cm^{-1}, which is a similar value to the energy difference between $^2F_{5/2}$ and $^2F_{7/2}$ levels for Ce^{3+} due to the spin-orbital interaction of the 4f ground state. These two bands can be assigned to the transitions from the lowest excited level $5d_1$ to the $^2F_{5/2}$ and $^2F_{7/2}$ levels.

Despite excitation with the high-power ionizing radiation (~8.0 keV, 1200 W), the RL intensity was similar in the order of magnitude as the PL intensity, which means that the efficiency of RL was not so high. As previously stated in the introduction, the excitation with ionizing radiation creates a lot of electron-hole pairs, which will only produce Ce^{3+} emission if the excitons become localized on the Ce^{3+}, or if Ce^{3+} captures a hole followed by an electron with the valence state change ($Ce^{3+} + h^{+} \rightarrow Ce^{4+}$). Nevertheless, since there are other recombination routes, the RL intensity is normally much less efficient than direct excitation of the Ce^{3+} ions.

10.3.5. TL Properties of the Glass-Ceramic Samples

Figure 10.9a shows the TL glow curves of the GC samples after $^{90}Sr/^{90}Y$ β-ray irradiation. During the synthesis process, the GC samples were heat-treated over the maximum temperature of TL measurements (400 °C) for three hours. The as-made and GC samples did not show any endo- and exothermic peaks in the DTA curves below 500 °C, indicating the nucleation and crystal growth process did not take place during TL measurements.

While only GC600, which still has a large amount of glass matrix, showed weak TL, all GC samples show two TL glow peaks at ~100 and ~220 °C (labeled peak 1 and peak 2,

respectively), whose intensity variations show similar trends to those of PL and RL intensities. These two glow peak temperatures are related to their electron trap depth, which is the activation energy from some trap levels (donor level) to the host CB; peak 1 and peak 2 are related to shallow and deep electron traps, respectively. According to the previous work [29,33,43–51], it is well-known that lanthanoid and lithium ions in the crystal lattice of MgB_4O_7 can help form electron trapping centers related to impurity-related defects. Notably, the shape of the TL glow peak 2 for GC samples was similar to that of the powder MgB_4O_7:Ce^{3+}-Li^{+} prepared through the combustion synthesis method, except for GC600 [34]. For GC600, the TL intensity of peak 2 was quite weak because the ceramization process was not completed. Therefore, these TL glow curves indicate that the precipitation of MgB_4O_7:Ce^{3+}-Li^{+} worked well for the electron trap formation. With increasing heat treatment temperature, peak 2 was shifted toward the high-temperature side, and GC850 showed an additional TL glow peak at ~300 °C. Considering the impurity phase confirmed by XRD, it suggests that this additional peak at the higher temperature region can be assigned to the electron traps related to the impurity $Mg_2B_2O_5$ phase.

For further investigation into the behavior of electron traps, the TL glow curves of GC750 with different delays between $^{90}Sr/^{90}Y$ β-ray irradiation and TL readout (0–60 min) are shown in **Figure 10.9b**. Those of the other samples are shown in **Figure 10.10**. The TL intensity of peak 1 declined gradually with the delay time. This decline is called fading, which is interpreted as electron release from the trap levels *via* the thermally activating process at room temperature [52,53]. This fading is undesirable in dosimetry because the time-dependent of the resultant TL signal makes the precise estimation of the radiation dose difficult. In contrast, the TL intensity of peak 2 associated with the deep trap was almost unchanged, which indicates that the electrons in the associated trapping centers are stable.

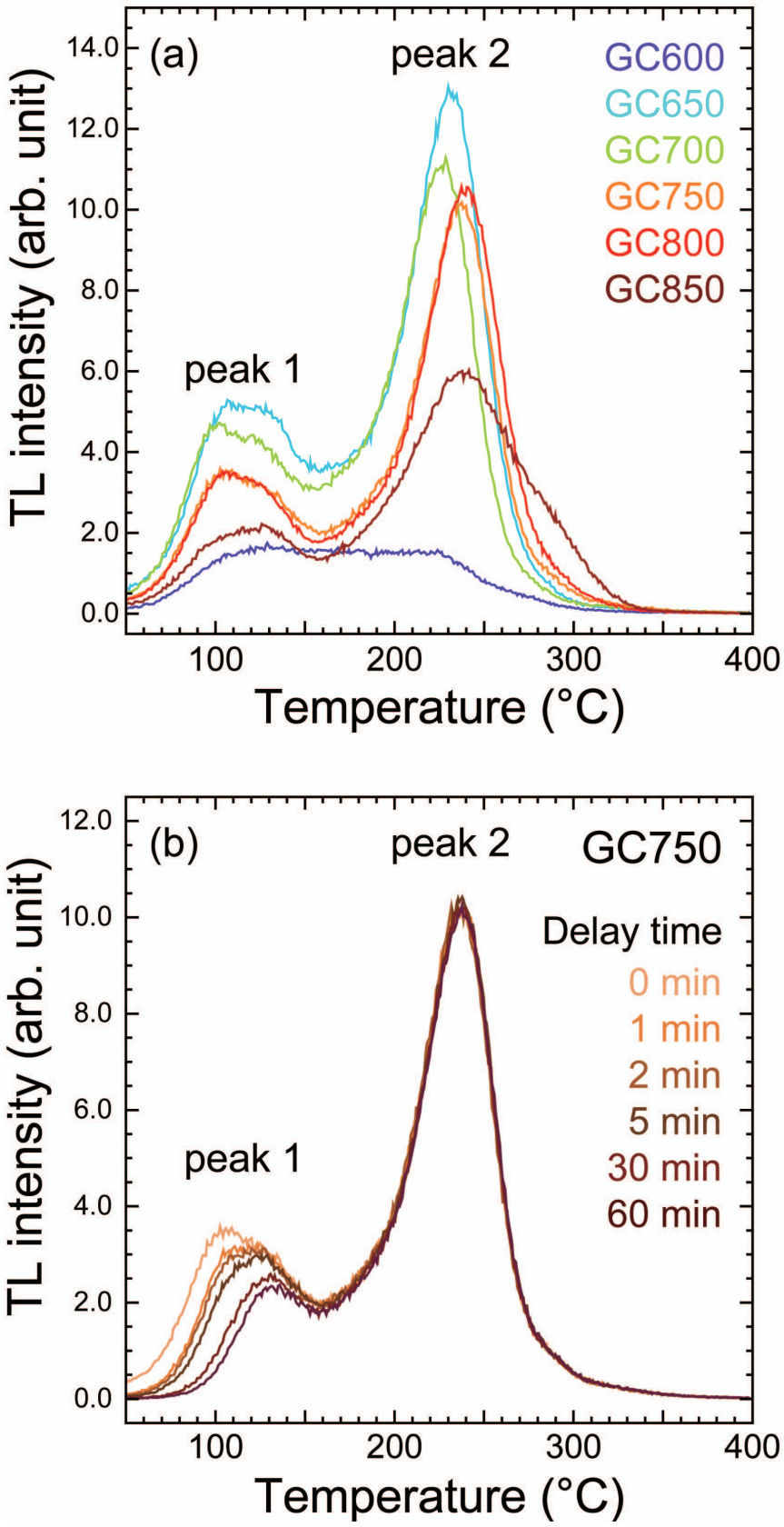

Figure 10.9. TL glow curves of (a) all the GC samples, and (b) GC700 with different delay time (0–60 min).

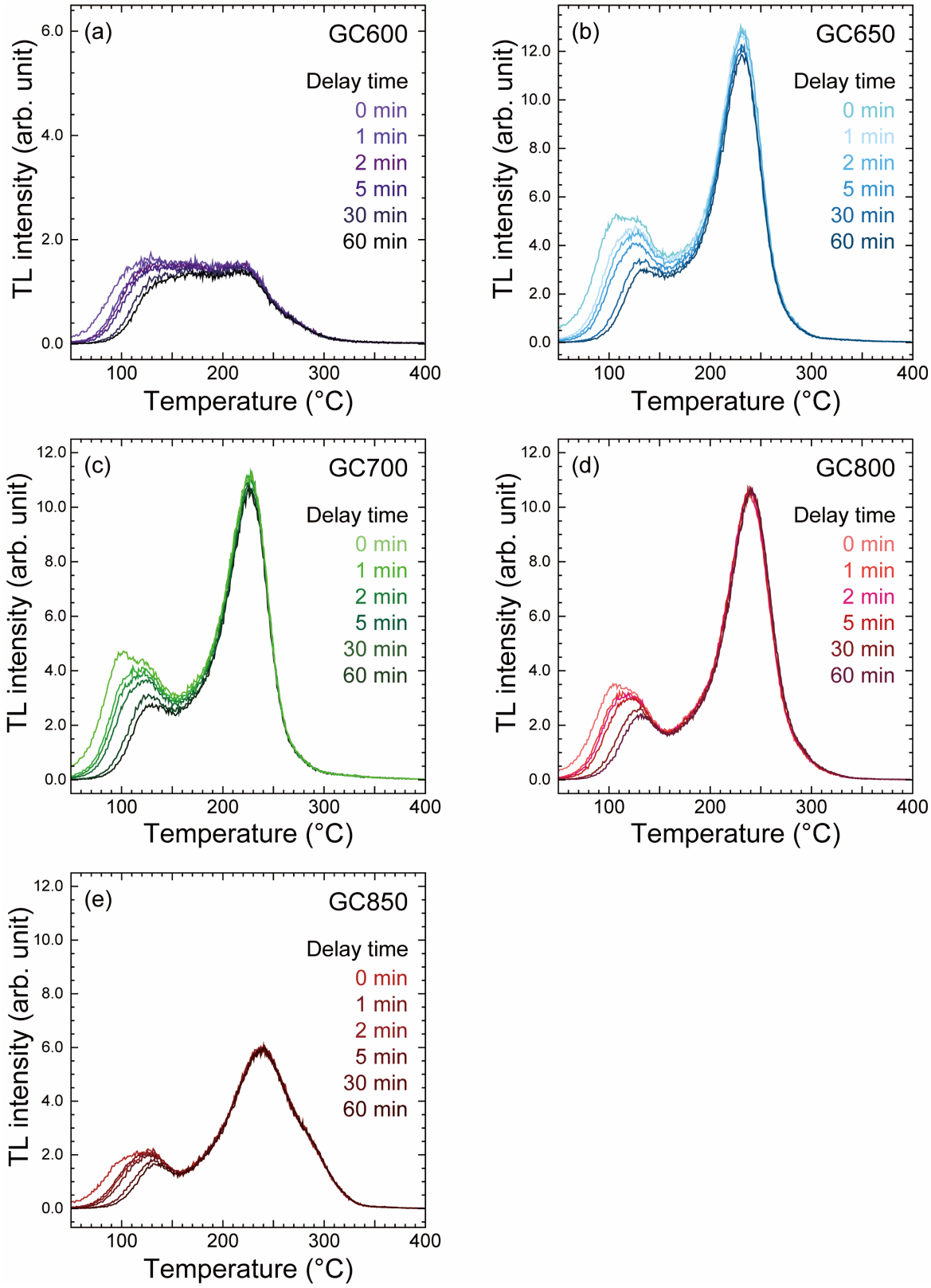

Figure 10.10. TL glow curves with different delay time (0–60 min) for (a) GC600, (b) GC650, (c) GC700, (d) GC800, and (e) GC850 samples.

10.3.6. OSL Properties of the Glass-Ceramic Samples

The GC samples show OSL under visible light stimulation due to the electron traps confirmed by the TL glow curves. The typical OSL emission and stimulation spectra of the GC700 are shown in **Figure 10.11**. The OSL emission bands had the same spectral shapes as the RL spectra of the GC samples (Figure 10.8c). The results indicate the origin of the OSL emission was the Ce^{3+} 5d → 4f transition in the MgB_4O_7 crystal. The OSL emission intensity decreased monotonously with the stimulating duration, which is characteristic of OSL emission due to releasing the trapped electrons. The OSL stimulation spectra showed a similar shape to the spectra reported by Gustafson [34].

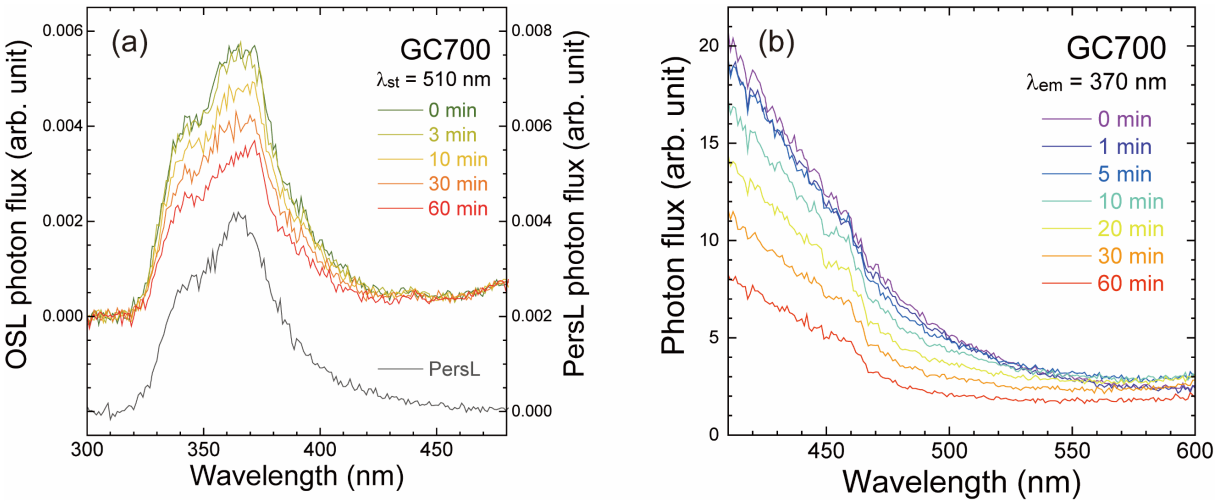

Figure 10.11. (a) Persistent luminescence (PersL) and OSL emission spectra of the GC700 sample at room temperature. The right and left axis indicate OSL and PersL intensity, respectively. First, the sample was irradiated by X-ray (40 kV, 30 mA) for 10 min. Under no irradiation of light, PersL related to the shallow traps was observed. After the PersL spectrum was measured, the OSL emission was obtained. The stimulation light was the monochromatic green light with a wavelength of 510 nm obtained by a Xe lamp. (b) OSL stimulation spectra of the GC700 sample monitored at 370 nm. After the irradiation of X-ray, the sample was heat-treated at 80 °C for 30 min to release electrons trapped by the shallow traps and eliminate the effect of PersL. The time in the legend means the stimulating duration by blue light with a wavelength of 410 nm.

For a test and comparison of the performance of each GC sample as an OSL dosimeter, the OSL signal was measured with various delays (1–600 min) after β-ray irradiation. **Figure 10.12** shows the total OSL fading curves of each sample, where the OSL signal was plotted as a

function of delay time. All GC samples show the monotonic decline of the OSL intensity owing to fading. As expected from the RL spectra (Figure 10.8c) and the TL glow curves (Figure 10.9a), the total OSL intensity of GC650 and GC700 were strong. However, they were still declining between 300 and 600 min, indicating that further fading may take place. On the other hand, for GC750 and GC800, the total OSL intensity stays essentially unchanged after 300 min delay, which indicates possibly low fading of the OSL intensity above 600 min, allowing a more precise estimation of the radiation dose.

To examine the stability of the electrons captured by traps, the fading ratio, defined as the ratio of the OSL signal with 600 min delay to the initial OSL signal, can be a good indicator. The fading ratio of each sample is listed in **Table 10.1**. Although GC650 and GC 700 showed very strong OSL, their fading ratio is high, which implies that around one-fourth of trapped electrons is lost after 600 min delay; they are less suitable for dosimetry applications. By contrast, GC750 and GC800 show low fading ratios, 12.7 and 17.5%, respectively, due to the deep traps which show little fading. These characteristics are very suitable for the OSL dosimetry of high

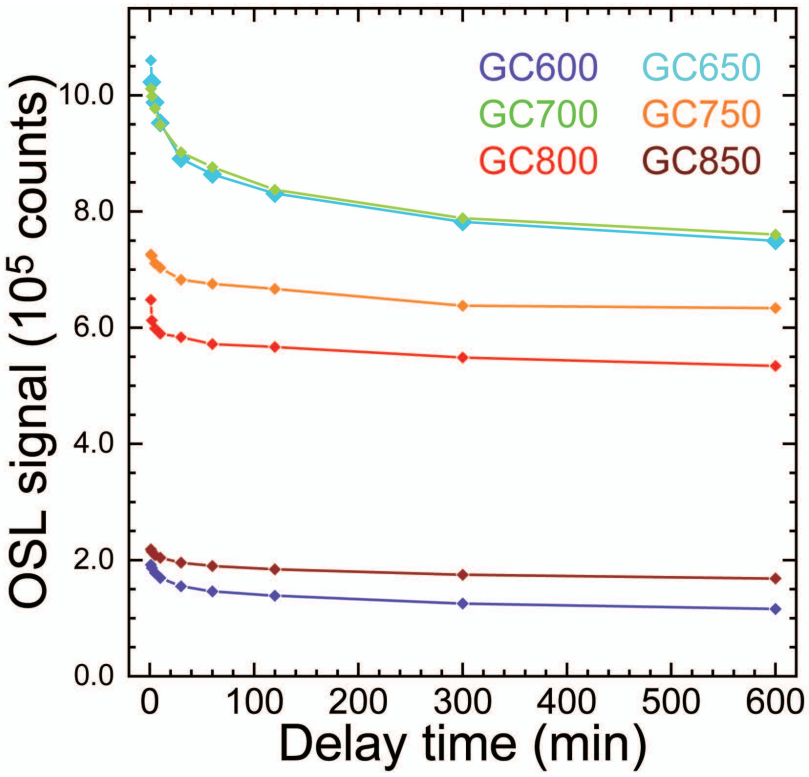

Figure 10.12. Fading curves of total OSL signal for all the GC samples.

performance.

Finally, the OSL intensity of the GC700 sample was compared with two OSL materials, the $MgB_4O_7:Ce^{3+}$-Li^{+} sample prepared by solution combustion (SC) described by Gustafson et al. [34] and commercial Al_2O_3:C. For improvement of the comparison, all samples were used in powder form, and the results were normalized by the powder mass. The GC700 sample was crushed using an agate mortar and pestle. Approximate 2.0 mg $MgB_4O_7:Ce^{3+}$-Li^{+} SC, 4.1 mg of GC700 sample, and 6.4 mg of Al_2O_3:C were used in each cup. Nevertheless, one must keep in mind that this is only an order of magnitude comparison because other factors such as grain size and the different optimum stimulation/detection wavelength for $MgB_4O_7:Ce^{3+}$-Li^{+} and Al_2O_3:C were not taken into account at this stage. The Hoya U-340 filters used in the Risø readers are not optimum for Al_2O_3:C because they block a large part of the main F-center emission band of this material.

Table 10.1. Fading ratio of OSL signal for all the GC samples. Charged GC samples were stimulated by the blue LED after each delay time (0–600 min).

Sample	GC600	GC650	GC700	GC750	GC800	GC850
Fading ratio (%)	39.8	29.3	24.8	12.7	17.5	22.9

The OSL curves of the samples are shown in **Figure 10.13**. Here, the *y*-axis is a logarithmic scale for better visualization of the OSL curve. The results demonstrate that the OSL intensity of GC700 is comparable to that of commercial Al_2O_3:C and to that of $MgB_4O_7:Ce^{3+}$-Li^{+} powder reported in previous studies [34]. The advantage of the GC samples in comparison with the $MgB_4O_7:Ce^{3+}$-Li^{+} SC sample is the potential lower fading of the signal because of the higher crystallinity of MgB_4O_7 in the ceramics, since the TL curves show that the main dosimetric peak at ~220 °C is reproducible and does not fade within the experimental conditions used here.
This work demonstrates that $MgB_4O_7:Ce^{3+}$-Li^{+} as bright as the one obtained by solution combustion can also be obtained by the glass-ceramic route, but a more detailed dosimetric comparison between the different materials is planned.

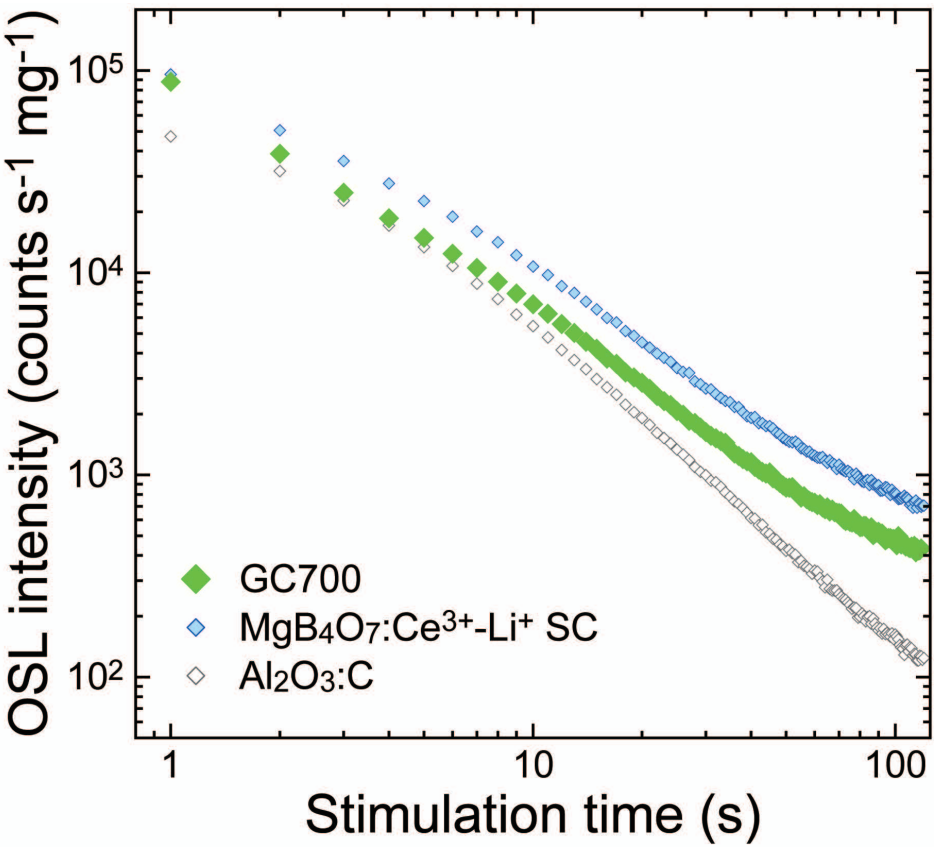

Figure 10.13. Comparison between the OSL intensity of $MgB_4O_7:Ce^{3+}$-Li^{+} sample (~2.0 mg) prepared by combustion synthesis, $MgB_4O_7:Ce^{3+}$-Li^{+} GC700 sample (4.1 mg), and commercial Al_2O_3:C (6.4 mg). All samples were measured in powder form and the OSL intensity was normalized by the sample mass.

10.4. Conclusions

For the expansion of the possibility of the prospective dosimetric material, Ce^{3+} and Li^{+} co-doped MgB_4O_7, the GC samples of MgB_4O_7:Ce^{3+}-Li^{+} were successfully synthesized by ceramming a magnesium borate glass with the composition of $25MgO\text{-}72B_2O_3\text{-}3Li_2O\text{-}0.3Ce^{3+}$ at 600, 650, 700, 750, 800, and 850 °C. It was confirmed by XRD that the obtained GC samples had the MgB_4O_7 crystals as the main phase with a small amount of impurity $Mg_2B_2O_5$ phase. The GC samples showed a typical blue PL band due to the Ce^{3+} 5d → 4f transition under UV illumination, whose peak was redshifted from the peak in the as-made glass. For the GC samples, the RL bands of Ce^{3+} luminescence under X-ray irradiation were narrower than the PL bands because the Ce^{3+} ions in the MgB_4O_7 phase were selectively excited. In the TL glow curves after β-ray irradiation, the GC samples showed two TL glow peaks at ~100 °C and ~220 °C. Due to the presence of the shallow electron traps, the fading of TL and OSL took place. Considering the fading ratio of the OSL intensity stimulated by a blue LED, GC750 and GC800 showed good stability for the radiation dose storage. These results show that GC750 and GC800 have the potential to be an excellent material for dosimetry if the influence of shallow traps can be reduced either during the synthesis process or by application of a pre-heating before the OSL readout.

Acknowledgements

This work was supported by Kyoto University Microstructural Characterization Platform as a program of "Nanotechnology Platform" of the Ministry of Education, Culture, Sports, Science, and Technology (MEXT), Japan, and KAKENHI for the Grant-in-Aid for Scientific Research B (Grant Numbers JP19H02798 and JP16H06441) and JSPS Fellow (Grant Number JP19J23280) from JSPS. The Risø TL/OSL-DA-20 reader (DTU Nutech, Denmark) was acquired with partial support from the Swiss National Science Foundation (R'Equip project 206021_177028).

References

[1] I.J. Das, G.X. Ding, "A. Ahnesjö, Small fields: Nonequilibrium radiation dosimetry". *Med. Phys.* **35** (2008) 206–215.

[2] F. Borne, D. Delacroix, J. M. Gelé, D. Massé, F. Amiranoff, "Radiation Protection for an Ultra-high Intensity Laser". *Radiat. Prot. Dosimetry.* **102** (2002) 61–70.

[3] R.J. Clarke, D. Neely, R.D. Edwards, P.N.M. Wright, K.W.D. Ledingham, R. Heathcote, P. McKenna, C.N. Danson, P.A. Brummitt, J.L. Collier, P.E. Hatton, S.J. Hawkes, C. Hernandez-Gomez, P. Holligan, M.H.R. Hutchinson, A.K. Kidd, W.J. Lester, D.R. Neville, P.A. Norreys, D.A. Pepler, T.B. Winstone, R.W.W. Wyatt, B.E. Wyborn, "Radiological characterisation of photon radiation from ultra-high-intensity laser–plasma and nuclear interactions". *J. Radiol. Prot.* **26** (2006) 277–286.

[4] D.J. O'Brien, N. Schupp, S. Pencea, J. Dolan, G.O. Sawakuchi, "Dosimetry in the presence of strong magnetic fields". *J. Phys. Conf. Ser.* **847** (2017) 012055 (7p).

[5] G.F. Knoll, "Radiation detection and measurement". (3rd ed., John Wiley & Sons, New York, 2000)

[6] T. Yamamoto, D. Maki, F. Sato, Y. Miyamoto, H. Nanto, T. Iida, "The recent investigations of radiophotoluminescence and its application". *Radiat. Meas*. **46** (2011) 1554–1559.

[7] Y. Miyamoto, Y. Takei, H. Nanto, T. Kurobori, A. Konnai, T. Yanagida, A. Yoshikawa, Y. Shimotsuma, M. Sakakura, K. Miura, K. Hirao, Y. Nagashima, T. Yamamoto, "Radiophotoluminescence from silver-doped phosphate glass". *Radiat. Meas.* **46** (2011) 1480–1483.

[8] Y.S. Horowitz, "Thermoluminescence and Thermoluminescent Dosimetry". (CRC Press, Boca Raton, 1983)

[9] L. Bøtter-Jensen, S.W.S. McKeever, A.G. Wintle, "Optically Stimulated Luminescence Dosimetry". (Elsevier B.V., Amsterdam, 2003)

[10] S. McKeever, E.G. Yukihara, "Optically Stimulated Luminescence: Fundamentals and Applications". (John Wiley & Sons, Chichester, 2011)

[11] M.F. Ahmed, N. Shrestha, S. Ahmad, E. Schnell, M.S. Akselrod, E.G. Yukihara, "Demonstration of 2D dosimetry using Al_2O_3 optically stimulated luminescence films for therapeutic megavoltage x-ray and ion beams". *Radiat. Meas.* **106** (2017) 315–320.

[12] K. Idri, L. Santoro, E. Charpiot, J. Herault, A. Costa, N. Aillères, R. Delard, J.R. Vaillé, J. Fesquet, L. Dusseau, "Quality control of intensity modulated radiation therapy with optically stimulated luminescent films". *IEEE Trans. Nucl. Sci*. **51** (2004) 3638–3641.

[13] L.F. Nascimento, W. Crijns, G. Goveia, Z. Mirotta, L.F. Souza, F. Vanhavere, C. Saldarriaga Vargas, M. De Saint-Hubert, "2D reader for dose mapping in radiotherapy using radiophotoluminescent

films". *Radiat. Meas.* **129** (2019) 106202 (9p).

[14] P.A. Rodnyi, "Physical Processes in Inorganic Scintillators". (CRC Press, Boca Raton, 1997)

[15] Y. Horowitz, L. Oster, I. Eliyahu, "Review of Dose-rate Effects in the Thermoluminescence of LiF:Mg,Ti". *Radiat. Prot. Dosimetry.* **179** (2018) 184–188.

[16] C.K. Spindeldreier, O. Schrenk, M.F. Ahmed, N. Shrestha, C.P. Karger, S. Greilich, A. Pfaffenberger, E.G. Yukihara, "Feasibility of dosimetry with optically stimulated luminescence detectors in magnetic fields". *Radiat. Meas.* **106** (2017) 346–351.

[17] S.W.S. McKeever, "Optically stimulated luminescence dosimetry". *Nucl. Instrum. Methods Phys. Res. B*. **184** (2001) 29–54.

[18] S.W.S. McKeever, "New millennium frontiers of luminescence dosimetry". *Radiat. Prot. Dosimetry.* **100** (2002) 27–32.

[19] M.S. Akselrod, N. Agersnap Larsen, V. Whitley, S.W.S. McKeever, "Thermal quenching of F-center luminescence in Al_2O_3:C". *J. Appl. Phys.* **84** (1998) 3364–3373.

[20] E.G. Yukihara, "Luminescence properties of BeO optically stimulated luminescence (OSL) detectors". *Radiat. Meas.* **46** (2011) 580–587.

[21] E. Bulur, B.E. Saraç, "Time-resolved OSL studies on BeO ceramics". *Radiat. Meas.* **59** (2013) 129–138.

[22] G. Denis, M.G. Rodriguez, M.S. Akselrod, T.H. Underwood, E.G. Yukihara, "Time-resolved measurements of optically stimulated luminescence of Al_2O_3:C and Al_2O_3:C,Mg". *Radiat. Meas.* **46** (2011) 1457–1461.

[23] C. Wouter, V. Dirk, L. Paul, D. Tom, "A reusable OSL-film for 2D radiotherapy dosimetry". *Phys. Med. Biol.* **62** (2017) 8441–8454.

[24] H.H. Li, A.L. Gonzalez, H. Ji, D.M. Duggan, "Dose response of BaFBrI:Eu^{2+} storage phosphor plates exposed to megavoltage photon beams". *Med. Phys.* **34** (2006) 103–111.

[25] E. Ariga, S. Ito, S. Deji, T. Saze, K. Nishizawa, "Development of dosimetry using detectors of diagnostic digital radiography systems". *Med. Phys.* **34** (2006) 166–174.

[26] E.G. Yukihara, S.W.S. McKeever, "Optically stimulated luminescence (OSL) dosimetry in medicine". *Phys. Med. Biol.* **53** (2008) R351–R379.

[27] A.S. Pradhan, J.I. Lee, J. Kim, "Recent developments of optically stimulated luminescence materials and techniques for radiation dosimetry and clinical applications". *J. Med. Phys*. **33** (2008) 85–99.

[28] B.A. Doull, L.C. Oliveira, D.Y. Wang, E.D. Milliken, E.G. Yukihara, "Thermoluminescent properties of lithium borate, magnesium borate and calcium sulfate developed for temperature sensing". *J. Lumin.* **146** (2014) 408–417.

[29] M. Prokić, "Development of highly sensitive $CaSO_4$:Dy/Tm and MgB_4O_7:Dy/Tm sintered thermoluminescent dosimeters". *Nucl. Instrum. Methods.* **175** (1980) 83–86.

[30] C.M.H. Driscoll, S.J. Mundy, J.M. Elliot, "Sensitivity and Fading Characteristics of Thermoluminescent Borate". *Radiat. Prot. Dosimetry.* **1** (1981) 135–137.

[31] M. Prokić, L. Bøtter-Jensen, "Comparison of Main Thermoluminescent Properties of Some TL Dosemeters". *Radiat. Prot. Dosimetry.* **47** (1993) 195–199.

[32] M. Prokić, "Individual monitoring based on magnesium borate". *Radiat. Prot. Dosimetry.* **125** (2007) 247–250.

[33] E.G. Yukihara, E.D. Milliken, B.A. Doull, "Thermally stimulated and recombination processes in MgB_4O_7 investigated by systematic lanthanide doping". *J. Lumin.* **154** (2014) 251–259.

[34] T.D. Gustafson, E.D. Milliken, L.G. Jacobsohn, E.G. Yukihara, "Progress and challenges towards the development of a new optically stimulated luminescence (OSL) material based on MgB_4O_7:Ce,Li". *J. Lumin*. **212** (2019) 242–249.

[35] L.F. Souza, A.M.B. Silva, P.L. Antonio, L.V.E. Caldas, S.O. Souza, F. d'Errico, D.N. Souza, "Dosimetric properties of MgB_4O_7:Dy,Li and MgB_4O_7:Ce,Li for optically stimulated luminescence applications". *Radiat. Meas.* **106** (2017) 196–199.

[36] N. Shrestha, D. Vandenbroucke, P. Leblans, E.G. Yukihara, "Feasibility studies on the use of MgB_4O_7:Ce,Li-based films in 2D optically stimulated luminescence dosimetry". *Physics Open.* **5** (2020) 100037 (10p).

[37] E.G. Yukihara, B.A. Doull, T. Gustafson, L.C. Oliveira, K. Kurt, E.D. Milliken, "Optically stimulated luminescence of MgB_4O_7:Ce,Li for gamma and neutron dosimetry". *J. Lumin.* **183** (2017) 525–532.

[38] S. Tanabe, S. Fujita, A. Sakamoto, S. Yamamoto, "Glass Ceramics for Solid State Lighting". *Ceram. Trans.* **173** (2006) 19–25.

[39] T. Nakanishi, S. Tanabe, "Novel Eu^{2+}-Activated Glass Ceramics Precipitated With Green and Red Phosphors for High-Power". *IEEE J. Sel. Top. Quantum Electron.* **15** (2009) 1171–1176.

[40] R.D. Shannon, "Revised effective ionic radii and systematic studies of interatomic distances in halides and chalcogenides". *Acta Crystallogr. A*. **32** (1976) 751–767.

[41] Z. Xia, A. Meijerink, "Ce^{3+}-Doped garnet phosphors: Composition modification, luminescence

properties and applications". *Chem. Soc. Rev.* **46** (2017) 275–299.

[42] P. Dorenbos, "Lanthanide 4f-electron binding energies and the nephelauxetic effect in wide band gap compounds". *J. Lumin.* **136** (2013) 122–129.

[43] T. Karali, P.D. Townsend, M. Prokić, A.P. Rowlands, "Comparison of TL spectra of co-doped dosimetric materials". *Radiat. Prot. Dosimetry.* **84** (1999) 281–284.

[44] T. Karali, A.P. Rowlands, M. Prokic, P.D. Townsend, E. Halmagean, "Thermoluminescent spectra of rare earth doped MgB_4O_7 dosemeters". *Radiat. Prot. Dosimetry.* **100** (2002) 333–336.

[45] N.K. Porwal, R.M. Kadam, T.K. Seshagiri, V. Natarajan, A.R. Dhobale, A.G. Page, "EPR and TSL studies on MgB_4O_7 doped with Tm: role of BO_3^{2-} in TSL glow peak at 470K". *Radiat. Meas.* **40** (2005) 69–75.

[46] N. Salah, S. Habib, S.S. Babkair, S.P. Lochab, V. Chopra, "TL response of nanocrystalline MgB_4O_7:Dy irradiated by 3 MeV proton beam, 50 MeV Li^{3+} and 120 MeV Ag^{9+} ion beams". *Radiat. Phys. Chem.* **86** (2013) 52–58.

[47] C. Furetta, M. Prokic, R. Salamon, G. Kitis, "Dosimetric characterisation of a new production of MgB_4O_7:Dy,Na thermoluminescent material". *Appl. Radiat. Isot.* **52** (2000) 243–250.

[48] E.C. Karsu, M. Gökçe, A. Ege, T. Karali, N. Can, M. Prokic, "Kinetic characterization of MgB_4O_7:Dy,Na thermoluminescent phosphor". *J. Phys. D Appl. Phys.* **39** (2006) 1485–1488.

[49] A. Cano, P.R. González, C. Furetta, "Further Studies of Some TL Characteristics of MgB_4O_7:Dy, Na Phosphor". *Mod. Phys. Lett. B*. **22** (2008) 1997–2006.

[50] O. Annalakshmi, M.T. Jose, U. Madhusoodanan, B. Venkatraman, G. Amarendra, "Synthesis and thermoluminescence characterization of MgB_4O_7:Gd,Li'. *Radiat. Meas.* **59** (2013) 15–22.

[51] E.G. Yukihara, E.D. Milliken, L.C. Oliveira, V.R. Orante-Barrón, L.G. Jacobsohn, M.W. Blair, "Systematic development of new thermoluminescence and optically stimulated luminescence materials". *J. Lumin.* **133** (2013) 203–210.

[52] A. Vedda, M. Fasoli, "Tunneling recombinations in scintillators, phosphors, and dosimeters". *Radiat. Meas.* **118** (2018) 86–97.

[53] E.G. Yukihara, A.C. Coleman, R.H. Biswas, R. Lambert, F. Herman, G.E. King, "Thermoluminescence analysis for particle temperature sensing and thermochronometry: Principles and fundamental challenges". *Radiat. Meas.* **120** (2018) 274–280.

Summary

In this dissertation, it was investigated how the unique electronic structure and local environment of various mixed-anion compounds affect the properties of the luminescence centers through spectroscopic methods, and the luminescent properties of some oxynitrides and oxyhalides were characterized in a complex manner by combining spectroscopy with other techniques such as crystal structure analysis and *ab initio* calculations.

In Chapter 1, as the general introduction, the mixed-anion phosphors focused on as the novel functional materials are overviewed. Although the type of luminescence is determined by the cation species acting as the activator, the luminescence properties depend on the electronic structure and coordination environment, which can be controlled by the coordinating anion species. In the research on luminescent materials, anion-based material design is a useful strategy. Some studies about the mixed-anion phosphors following these concepts are introduced. The purposes and contents of the studies in this dissertation are briefly explained.

In Chapter 2, the fundamentals of luminescence phenomena discussed in this dissertation, related to the 5d-4f, 4f-4f transitions, charge transfer (CT) transition, and exciton states, are overviewed briefly. As the character of the host materials providing unique luminescence properties, the point groups in crystals and the band structure are introduced. Especially, the band structure for the luminescence materials activated by lanthanoid ions is described by the vacuum referred binding energy (VRBE) diagram, which is very useful to predict the luminescence properties and discuss the luminescence mechanisms.

In Chapter3, the Eu^{3+}-doped $YSiO_2N$ oxynitride was fabricated, and its luminescent properties were investigated. The $YSiO_2N:Eu^{3+}$ sample was excited efficiently by near-UV light (280–360 nm) and showed very intense red luminescence assigned to the Eu^{3+} 4f-4f transitions. Compared with prepared Eu^{3+}-doped oxide samples (α-$CaSiO_3:Eu^{3+}$, α-$Y_2Si_2O_7:Eu^{3+}$, and *y*-$Y_2Si_2O_7:Eu^{3+}$), in $YSiO_2N:Eu^{3+}$, there were two major different luminescent features: the CT excitation band got redshifted by more than 9500 cm^{-1} because the energy of the valence band (VB) top got increased due to the N 2p orbitals; the spectral intensity of the $^5D_0 \rightarrow {}^7F_2$ transition peaking at 626 nm got stronger because the Eu^{3+} occupied asymmetric Y^{3+} sites due to partial

substitution of O^{2-} by N^{3-}. From the Judd-Ofelt analysis, the $YSiO_2N:Eu^{3+}$ sample had the much larger Judd-Ofelt intensity parameter, Ω_2, which depends on site-asymmetry, than other oxide samples. The fluorescence lifetime was estimated experimentally to be 0.664 ms, which was shorter than the radiative lifetime based on the Judd-Ofelt analysis of 1.32 ms. The experimental quantum yield of 32.3 % was lower than the calculated internal quantum efficiency of 50.3%. For development of red phosphors activated by Eu^{3+} for LEDs applications, Eu^{3+}-doped mixed-anion compounds have a significant potential to improve the main parameters of white LEDs.

In Chapter 4, the Eu^{3+} luminescence properties in oxynitride coordination environments for $YSiO_2N$ were thoroughly investigated in terms of the site-selective and time-resolved spectroscopy with the precise crystallographical data. The single-crystal X-ray and the time-of-flight neutron diffraction successfully identified the crystal structure of $YSiO_2N$ as the monoclinic lattice with the space group $C2/c$. In this lattice, all Eu^{3+} ions are incorporated in the $[YO_6N_2]$ dodecahedra, classified into two groups with centrosymmetry; C_n and C_i sites. Eu^{3+} ions at the C_n and C_i sites showed a completely different radiative rate for the electric dipole transition, resulting in the 27 times enhanced $^5D_0 \rightarrow {}^7F_2$ luminescence and the 8.4 times shorter luminescence lifetime by lacking an inversion center. The temperature dependence of the luminescence lifetime for the Eu^{3+} ions in C_i sites revealed that the thermally induced deviation from centrosymmetry increases the radiative rate with the Judd-Ofelt intensity parameter Ω_t increasing. Despite the significant difference in the radiative rate, the ligands-Eu^{3+} CT states were affected scarcely by site symmetry but severely by anion species. The *ab initio* calculation results and the photoluminescence excitation (PLE) spectra suggested that the thermal quenching of the Eu^{3+}: $^5D_0$ luminescence occurs *via* the CT states between N^{3-} and Eu^{3+} ions. The results indicate that not only the mixed-anion coordination but also the local structure that induces some distortion is necessary for the improvement of Eu^{3+} luminescence. The $YSiO_2N:Eu^{3+}$ provides a new possibility for developing the near-UV excitable narrow-band red phosphors with partial N^{3-} coordination.

In Chapter 5, the photoluminescence (PL) properties of the Eu^{2+}-doped $YSiO_2N$ sample at low temperatures were investigated in detail. The X-ray absorption spectroscopy revealed that

almost half Eu ions in the sample were reduced into a divalent state through the high-temperature synthesis under the inert atmosphere. The as-made sample, including Eu^{2+} ions, showed the deep-red to near-infrared (NIR) luminescence at low temperatures below 300 K. Compared with typical Eu^{2+}: 5d-4f luminescence, this luminescence was anomalous in terms of the following points; an abnormally large bandwidth (4061 cm^{-1}) and Stokes shift (5677 cm^{-1}) even at 4 K, deep-red to NIR luminescence peaking at 756 nm, and a complicated thermal quenching behavior. These features indicated that the anomalous luminescence in the $YSiO_2N:Eu^{2+/3+}$ sample is related to the Eu^{2+}-trapped exciton states. The VRBE diagram suggested that the typical Eu^{2+}: 5d → 4f luminescence was not observed because all the Eu^{2+}: 5d excited levels degenerated with the host conduction band (CB). The configurational coordinate diagram explained the anomalous luminescence from the Eu^{2+}-trapped exciton states ($Eu^{3+} + e^-$) which were located just below the CB bottom, by taking the lattice relaxation into account. This study provides new insight into the Eu^{2+}-trapped exciton luminescence in Y sites to obtain the deep-red to NIR luminescence, leading to new candidates for NIR applications, such as lighting, sensing, and bio-imaging devices.

In Chapter 6, luminescence properties of Ce^{3+} ions in the monoclinic $YSiO_2N$ host were investigated at the wide temperature range of 4–600 K. The PL spectra showed the minor luminescence component besides the typical Ce^{3+} luminescence, depending on excitation wavelengths. The time-resolved spectroscopy revealed that the minor luminescence center took the distribution of luminescence lifetime of 34–58 ns, which is typical for Ce^{3+}: 5d → 4f transition. The results suggested that the minor luminescence was assigned to the Ce^{3+} luminescence in some Y^{3+} sites with intrinsic anion defects. By taking the contribution of this minor Ce^{3+} luminescence into account, Ce^{3+} luminescence in the $[YO_6N_2]$ dodecahedra was characterized. Despite the site-symmetry, Ce^{3+} ions in the five nonequivalent Y sites showed almost the same properties and were not identified due to the structural similarity of the $[YO_6N_2]$ dodecahedra. The temperature dependence of luminescence lifetimes provided the activation energy for thermal quenching of 0.272 eV. All the 5d ← 4f excitation bands of Ce^{3+} ions in the $[YO_6N_2]$ dodecahedra were observed with the vacuum-UV spectroscopy, leading to the crystal field

splitting of 1.69 eV and centroid energy of 4.11 eV.

In Chapter 7, the Ce^{3+} persistent luminescence (PersL) in the $YSiO_2N$ host was successfully enhanced by co-doping Sm^{3+} and Tm^{3+} ions, as predicted by the semi-empirical VRBE diagram. The VRBE diagram of the YSiO2N host was constructed with the experimentally obtained parameters, including the host exciton creation energy, the CT energy for Eu^{3+}, and the centroid shift of Ce^{3+} 5d levels, leading to the optimal co-dopant lanthanoid ions, Sm^{3+} and Tm^{3+}, to obtain Ce^{3+} PersL at ambient temperature. The electron trap depths for Tm^{3+} and Sm^{3+} ions were estimated to be 0.726 and 1.04 eV, respectively. The prepared $YSiO_2N:Ce^{3+}$-Ln^{3+} (*Ln* = Sm or Tm) samples enhanced the Ce^{3+} blue PersL at 30 s after the excitation ceased by 2–3 times. The thermoluminescence (TL) glow curves of the Ln^{3+} co-doped samples showed additional glow peaks related to *Ln*-traps and enhanced the TL intensity related to intrinsic defects. The TL glow curve analyses with the initial rise method combined with the thermal cleaning and trap density methods revealed that the *Ln*-traps located below the CB have a distribution with ~0.25 eV width, whose centers were similar to the predicted trap depth by the constructed VRBE diagram.

In Chapter 8, the influence of the anion variation on Eu^{3+}: ^5D_J luminescence in the isostructural YO*X* (*X* = Cl or Br) hosts, yet with the different coordination environment, was investigated from the spectroscopic perspective. For Eu^{3+} ions in the YOCl host incorporated in the nine-fold monocapped square antiprism polyhedra $[YO_4Cl_5]$ with noncentrosymmetric C_{4v} symmetry, the Judd-Ofelt Ω_2 parameter of the YOCl:Eu^{3+} **was 8.**81 × 10^{-20} cm^2, comparable to the Eu^{3+}-doped oxides Y_2O_3 or YVO_4. The Ω_4 parameter also took a large value, 11.4 × 10^{-20} cm^2. On the other hand, the YOBr host consisted of the eight-fold distorted square antiprism $[YO_4Br_4]$ with C_{4v} symmetry due to the large separation of two [Br-Y-O-Y-Br] sheets attributed to the covalency of Br. The Ω_2 parameter of the YOBr:Eu^{3+} was relatively small, 2.72 × 10^{-20} cm^2, because of the structural similarity to the eight-fold regular square antiprism with D_4 symmetry. The Ω_4 parameter was also significantly large, 13.1 × 10^{-20} cm^2, due to the strongly covalent environment $[Eu^{3+}O_4Br_4]$. The CT band energies E^{CT} for the YOCl:Eu^{3+} and YOBr:Eu^{3+} were estimated to be 38163 cm^{-1} and 36686 cm^{-1}, respectively. The smaller E^{CT} for the YOBr:Eu^{3+}

resulted in the low thermal activation energy of the $^5D_0$ luminescence quenching. The difference in the relaxation processes of excited electrons between the CT and 4f-4f transitions made the precise assignment of complicated spectral structures possible. The large offset of the CT states in the configuration coordinate diagram for the YO*X*: Eu^{3+} caused thermally unstable and inefficient Eu^{3+} luminescence with the CT transition. It was revealed that the Judd-Ofelt intensity parameters Ω_t are significantly affected by the geometry of coordination polyhedra and the bonding character between Eu^{3+} ions and coordinating anions. The mixed-anion materials with the regular square antiprism-like local geometry have the great potential to show the intense $^5D_0 \rightarrow {}^7F_4$ luminescence located at ~700 nm, which is desirable as a fluorescence probe in biological applications.

In Chapter 9, the square pyramidal $[WO_5]^{4-}$ cluster in the oxychloride $Ca_3WO_5Cl_2$ showed the cyan CT luminescence between W 5d and O 2p orbitals. Compared with the blue CT luminescence of the $[WO_6]^{6-}$ octahedron in the oxide Ca_3WO_6, this cyan CT luminescence showed the higher absorption and lower luminescence energies. Because these characteristics of the $[WO_5]^{4-}$ square pyramid were not explained by the simple molecular orbital diagram for O_h symmetry, the *ab initio* calculations with the discrete-variational Xα (DV-Xα) and DV multi-electron (DVME) methods were performed to discuss the luminescence properties of the $Ca_3WO_5Cl_2$. Both the one- and multi-electron calculations revealed that the $[WO_5]^{4-}$ square pyramid took the larger CT energy due to not the crystal field splitting but the Madelung potential related to the existence of Cl^- ions in a lattice. However, since the *ab initio* molecular orbital and configuration interaction calculation cannot take the structural relaxation of the excited states into account, the redshift of the CT luminescence for the $[WO_5]^{4-}$ cluster could not be understood by these *ab initio* calculation results. Supposing that the CT excited states of the $[WO_5]^{4-}$ cluster took the larger offset in the qualitative configurational coordinate diagram, the redshift and the lower quenching temperature of the CT luminescence for the $[WO_5]^{4-}$ square pyramid were accounted for. The results in this study are expected to promote research on the CT luminescence of tungstates in a variety of material groups including mixed-anion compounds.

In Chapter 10, for the expansion of the possibility of the prospective dosimetric material, Ce^{3+} and Li^{+} co-doped MgB_4O_7, the glass-ceramic (GC) samples of MgB_4O_7:Ce^{3+}-Li^{+} were successfully synthesized by ceramming a magnesium borate glass with the composition of $25MgO\text{-}72B_2O_3\text{-}3Li_2O\text{-}0.3Ce^{3+}$ at 600, 650, 700, 750, 800, and 850 °C. It was confirmed by X-ray diffraction that the obtained GC samples had the MgB_4O_7 crystals as the main phase with a small amount of impurity $Mg_2B_2O_5$ phase. The GC samples showed a typical blue PL band due to the Ce^{3+} 5d → 4f transition under UV illumination, whose peak was redshifted from the peak in the as-made glass. For the GC samples, the Ce^{3+} radioluminescence bands under X-ray irradiation were narrower than the PL bands because the Ce^{3+} ions in the MgB_4O_7 phase were selectively excited. In the TL glow curves after β-ray irradiation, the GC samples showed two TL glow peaks at ~100 °C and ~220 °C. Due to the presence of the shallow electron traps, the fading of TL and optically stimulated luminescence (OSL) took place. Considering the fading ratio of the OSL intensity stimulated by a blue LED, GC750 and GC800 showed good stability for the radiation dose storage. These results show that GC750 and GC800 have the potential to be an excellent material for dosimetry if the influence of shallow traps can be reduced either during the synthesis process or by application of a pre-heating before the OSL readout.

Through a series of studies in this dissertation, the luminescent properties of some oxynitrides and oxyhalides were characterized, and the relationships between these properties and the physical and chemical features of mixed-anion coordination were discussed. In the discipline of luminescent materials, some mixed-anion compounds have been familiar to researchers and utilized for practical applications. However, to achieve the revolutionary materials, the systematical work on luminescence in minor compounds, such as oxyhydrides and oxysulfides, is required. Besides, new mixed-anion-type materials, such as oxygen-free compounds and compounds with more than two kinds of anions, are emerging. Further materials exploration and spectroscopic investigation will be performed by a high-throughput searching with machine learning and cutting-edge techniques (*e.g.,* high-resolution time-resolved spectroscopy or characterization of tiny particles in μm). The results are expected to promote more active research as a pioneer of work on the mixed-anion phosphors.

Figure and Table Captions

Figures

Chapter 1

Chapter 2

Chapter 3

Chapter 4

Chapter 5

Chapter 6

Chapter 7

Chapter 8

Chapter 9

Chapter 10

Tables

Chapter 2

Chapter 3

Chapter 4

Chapter 7

Chapter 8

Chapter 9

Chapter 10

Appendix A
List of Experimental Judd-Ofelt Intensity Parameters $\Omega_{\check{a}}$ for Eu^{3+}-Doped Inorganic Crystals

In this appendix, the Judd-Ofelt intensity parameters Ω_λ (λ = 2, 4, 6) of a variety of Eu^{3+}-doped inorganic-crystalline materials, obtained based on spectroscopic experiments, are collected and listed. As explained in Chapter 2, the spontaneous emission rate of 4f-4f transition for lanthanoid ions depends on the Ω_λ parameters, which are specific to the compounds, in particular, the site-symmetry around Ln^{3+} ions. The Ω_λ parameters vary from the Ln^{3+} species; *i.e.,* the Ω_λ parameters for Eu^{3+} and other Ln^{3+} ions, such as Tm^{3+} and Yb^{3+} ions, should be different because they depend on the expansion of 4f electron clouds (see section 2.1.3.2). All the data were extracted from the literature in the reference list. The Ω_λ parameters in this list were obtained without any consideration about the *J*-mixing between the adjacent levels. In order to compare the effect of the intrinsic local environment, the values of the samples with high crystallinity and low Eu^{3+}-concentration are collected. The sample forms are shown as far as possible (the term of NPs means nanoparticles).

Table A. Judd-Ofelt intensity parameters Ω_λ (λ = 2, 4, 6) for various Eu^{3+}-doped crystalline materials

host	categories	form	site-sym.	Ω_2 (10^{-20} cm^2)	Ω_4 (10^{-20} cm^2)	Ω_6 (10^{-20} cm^2)	ref.
Solution	–	–	–	1.62	5.65	5.02	[1]
Y_2O_3	RE_2O_3	particles (μm)	C_2 / S_6	9.86	2.23	< 0.32	[2]
Y_2O_3	RE_2O_3	particles (μm)	C_2 / S_6	9.9	3.4	–	[3]
Gd_2O_3	RE_2O_3	NPs (15 nm)	C_2 / S_6	5.61	1.57	< 0.5	[4]
Gd_2O_3	RE_2O_3	NPs (23 nm)	C_2 / S_6	2.5	1.08	< 0.5	[4]
Gd_2O_3	RE_2O_3	NPs (135 nm)	C_2 / S_6	5.28	1.66	< 0.5	[4]
Gd_2O_3:Li	RE_2O_3	films on Al_2O_3	C_2 / S_6	14.7	3.82	–	[5]
Gd_2O_3:Li	RE_2O_3	films on Si	C_2 / S_6	9.77	2.85	–	[5]
Gd_2O_3:Li	RE_2O_3	films on quartz	C_2 / S_6	8.28	4.11	–	[5]
Gd_2O_3	RE_2O_3	nanorods	C_2 / S_6	10.7	1.81	0.175	[6]
Gd_2O_3	RE_2O_3	NPs (42.3 nm)	C_2 / S_6	15.6	1.42	–	[7]
$(Lu_{0.25}Gd_{0.75})_2O_3$	RE_2O_3	NPs (31.5 nm)	C_2 / S_6	13.6	0.84	–	[7]
$(Lu_{0.5}Gd_{0.5})_2O_3$	RE_2O_3	NPs (25.6 nm)	C_2 / S_6	13.27	1.22	–	[7]
$(Lu_{0.75}Gd_{0.25})_2O_3$	RE_2O_3	NPs (24.2 nm)	C_2 / S_6	11.3	1.06	–	[7]
Lu_2O_3	RE_2O_3	NPs (26.6 nm)	C_2 / S_6	12.2	1.2	–	[7]
Lu_2O_3	RE_2O_3	bulk	C_2 / S_6	6.14	1.71	–	[8]
Lu_2O_3	RE_2O_3	NPs (50 nm)	C_2 / S_6	9.07	2.6	–	[8]
Lu_2O_3	RE_2O_3	nanorods	C_2 / S_6	9.21	2.62	–	[9]
YVO_4	vanadates	particles (μm)	D_{2d}	7.49	0.47	–	[10]
$YV_{0.95}P_{0.05}O_4$	vanadates/phosphates	particles (μm)	D_{2d}	7.66	0.49	–	[10]
$YV_{0.5}P_{0.5}O_4$	vanadates/phosphates	particles (μm)	D_{2d}	4.47	0.35	–	[10]
$YV_{0.05}P_{0.95}O_4$	vanadates/phosphates	particles (μm)	D_{2d}	1.42	0.36	–	[10]
YPO_4	phosphates	particles (μm)	D_{2d}	0.78	0.38	–	[10]
$NaMg(PO_3)_3$	phosphates	–	C_3 / S_6	2.09	4.24	–	[11]
$KLa(PO_3)_4$	phosphates	–	C_1	2.27	3.21	–	[12]
$LiGd_5P_2O_{13}$	phosphates	–	C_s	8.79	6.54	–	[13]
$KCaBO_3$	borates	–	C_1	4.62	2.08	1.77	[14]
α-$Y_2Si_2O_7$	silicates	–	C_1	3.95	7.22	–	[15]
y-$Y_2Si_2O_7$	silicates	–	C_i	3.69	2.79	–	[15]

Table A. Judd-Ofelt intensity parameters Ω_λ (λ = 2, 4, 6) for various Eu^{3+}-doped crystalline materials (*Continued*)

host	categories	form	site-sym.	Ω_2 (10^{-20} cm^2)	Ω_4 (10^{-20} cm^2)	Ω_6 (10^{-20} cm^2)	ref.
$CaSiO_3$	silicates	–	C_i / C_1 / C_2	1.72	2.59	–	[15]
Sr_2SiO_4	silicates	–	C_1 (CN 10)	1.4	0.49	–	[16]
Sr_2SiO_4	silicates	–	C_1 (CN 9)	8.75	14.7	–	[16]
Zn_2SiO_4	silicates	Bulk (microwave)	C_1	6.82	4.38	–	[17]
Zn_2SiO_4	silicates	Bulk (electric furnace)	C_1	6.3	4.13	–	[17]
$Ca_2YSc_2GaSi_2O_{12}$	silicates (garnets)	–	D_2	2.21	2.89	2.26	[18]
$Y_3Al_5O_{12}$	aluminates (garnets)	–	D_2	0.99	2.69	–	[19]
$YAlO_3$	aluminates (perovskites)	single-crystal	C_s	2.66	6.33	0.8	[20]
$GdAlO_3$	aluminates (perovskites)	particle (μm)	C_s	1.84	2.23	–	[21]
$LaAlO_3$	aluminates (perovskites)	NPs (~27nm)	D_3	8.01	4.89	–	[22]
$ZnAl_2O_4$	aluminates	NPs (100–150nm)	distorted D_{3d}	5.28	2.64	–	[23]
$Sr_2SAl_2SiO_7$	aluminosilicates	–	C_s	3.6	1.68	1.78	[24]
NaAlSiO4	aluminosilicates	Bulk	C_{4v}	5.89	3.19	–	[25]
$Y_2Mg_2Al_2Si_2O_{12}$	aluminosilicates	Bulk	C_2	1.62	2.73	–	[19]
$CaTiO_3$	oxides (perovskites)	particle (μm)	C_s	8.73	0.48	–	[26]
$BaTiO_3$	oxides (perovskites)	nonocrystals (31nm)	C_{4v}	1.11	0.28	–	[27]
$BaTiO_3$	oxides (perovskites)	nonocrystals (37.5nm)	C_{4v}	0.18	0.07	–	[27]
$CaZrO_3$	oxides (perovskites)	NPs (~40nm)	C_s	1.52	0.74	–	[28]
$CaHfO_3$	oxides (perovskites)	–	C_s	4.98	1.55	–	[29]
$LiLaMgWO_6$	oxides (perovskites)	–	C_2	11.2	1.16	–	[30]
$Li_3La_3W2O_{12}$	oxides (perovskites)	–	C_1	11.5	1.16	–	[31]
$Lu_2Ti_2O_7$	oxides (pyrochlore)	particle (μm)	D_{3d}	4.68	2.53	–	[32]
$NaGdTiO_4$	oxides	–	C_s	6.02	1.51	0.37	[33]
$CaMoO_4$	oxides	particle (μm)	S_4	4.55	0.78	–	[34]
Y_2MoO_6	oxides	particle (μm)	C_1 / C_2	4.44	1.53	–	[35]
Gd_2MoO_6	oxides	particle (μm)	C_1 / C_2	5.01	1.64	–	[35]
La_2MoO_6	oxides	particle (μm)	C_2	5.81	2.1	–	[35]
Bi_2MoO_6	oxides	particle (μm)	C_1	3.45	1.81	–	[35]
$Y_2(MoO_4)_3$	oxides	microcrystal	C_1	8.9	0.54	–	[36]

Table A. Judd-Ofelt intensity parameters Ω_λ (λ = 2, 4, 6) for various Eu^{3+}-doped crystalline materials (*Continued*)

host	categories	form	site-sym.	Ω_2 (10^{-20} cm^2)	Ω_4 (10^{-20} cm^2)	Ω_6 (10^{-20} cm^2)	ref.
$YNbO_4$	oxides	–	C_2	6.94	5.00	–	[21]
$PbNb_2O_6$	oxides	particle (μm)	C_s	1.76	2.55	–	[37]
$CaWO_4$	oxides	particle (μm)	S_4	8.18	–	–	[34]
$NaY(WO_4)_2$	oxides	microcrystal	S_4	8.61	1.12	0.47	[38]
$LiGd(WO_4)_2$	oxides	–	S_4	7.26	2.69	–	[39]
TiO_2 (anatase)	oxides	NPs (~10 nm)	D_{2d}	8.70	3.36	–	[40]
ZrO_2	oxides	nanocrystals (45.8 nm)	C_1	4.92	4.11	–	[21]
ZnO (A site)	oxides	NPs (11 nm)	C_1	9.59	8.11	< 0.25	[41]
ZnO (B site)	oxides	NPs (11 nm)	C_s / C_1	21.5	2.30	< 0.25	[41]
In_2O_3	oxides	NPs (15–20 nm)	C_2	14.46	3.92	0.29	[42]
$Ba_5Gd_8Zn_4O_{21}$	oxides	–	C_s	12.7	4.50	5.4	[43]
$Ba_2GdV_3O_{11}$	oxides	NPs (30–50 nm)	C_1	3.48	0.11	–	[44]
LaF_3	fluorides	–	C_{2v}	1.19	1.16	0.39	[45]
CaF_2	fluorides	NPs (60 nm)	O_h	0.73	2.53	–	[46]
CdF_2	fluorides	single-crystal	O_h	0.59	1.12	0.31	[47]
$NaGdF_4$	fluorides	NPs (~14nm)	distorted D_{3h}	2.33	2.62	–	[48]
$NaBiF_4$	fluorides	NPs (50–100 nm)	S_6	2.96	1.36	–	[49]
$NaYF_4$	fluorides	nanocrystals (~700 nm)	O_h	1.78	1.59	–	[50]
$NaYF_4$	fluorides	–	O_h	2.97	2.85	–	[21]
LaOF	oxyhalides	–	C_{3v}	11.1	1.53	–	[51]
LaOF	oxyhalides	–	C_{3v}	5.20	1.10	–	[52]
LaOCl	oxyhalides	–	C_{4v}	3.5	2.57	–	[53]
GdOCl	oxyhalides	–	C_{4v}	3.53	1.99	–	[53]
YOCl	oxyhalides	–	C_{4v}	8.81	11.4	0.982	[54]
YOBr	oxyhalides	–	C_{4v}	2.72	13.1	2.66	[54]
BiOF	oxyhalides	–	C_{4v}	0.88	0.57	–	[55]
BiOCl	oxyhalides	–	C_{4v}	1.42	0.69	–	[56]
BiOBr	oxyhalides	–	C_{4v}	1.62	3.16	–	[55]
Lu_2O_2S	oxysulfides	–	C_1	4.02	2.54	–	[9]

Table A. Judd-Ofelt intensity parameters Ω_λ (λ = 2, 4, 6) for various Eu^{3+}-doped crystalline materials (*Continued*)

host	categories	form	site-sym.	Ω_2 (10^{-20} cm^2)	Ω_4 (10^{-20} cm^2)	Ω_6 (10^{-20} cm^2)	ref.
Y_2O_2S	oxysulfides	–	C_1	13.0	10.2	–	[57]
$YSiO_2N$	oxynitrides	–	C_1 / C_2	15.1	5.22	13.1	[58]
$YSiO_2N$	oxynitrides	–	C_i	0.554	0.57	1.07	[58]

References

[1] K. Binnemans, K. Van Herck, C. Görller-Walrand, "Influence of dipicolinate ligands on the spectroscopic properties of europium(III) in solution". *Chem. Phys. Lett.* **266** (1997) 297–302.

[2] M.J. Weber, "Radiative and multiphonon relaxation of rare-earth ions in Y_2O_3". *Phys. Rev.* **171** (1968) 283–291.

[3] Ž. Antić, R. Krsmanović, V. Đorđević, T. Dramićanin, M.D. Dramićanin, "Optical properties of Y_2O_3:Eu^{3+} red emitting phosphor obtained via spray pyrolysis". *Acta Phys. Pol. A.* 116 (2009) 622–624.

[4] C. Liu, J. Liu, K. Dou, "Judd-Ofelt intensity parameters and spectral properties of Gd_2O_3:Eu^{3+} nanocrystals". *J. Phys. Chem. B.* **110** (2006) 20277–20281.

[5] G. Rajan, K.G. Gopchandran, "Effect of substrates on the photoemission properties of Li doped Gd_2O_3:Eu^{3+} nanocrystalline films". *Opt. Mater.* **33** (2011) 494–500.

[6] L. Liu, X. Chen, "Energy levels, fluorescence lifetime and Judd–Ofelt parameters of Eu^{3+} in Gd_2O_3 nanocrystals". *Nanotechnology.* **18** (2007) 255704 (8p).

[7] R.M. Krsmanović Whiffen, Ž. Antić, A. Speghini, M.G. Brik, B. Bártová, M. Bettinelli, M.D. Dramićanin, "Structural and spectroscopic studies of Eu^{3+} doped Lu_2O_3–Gd_2O_3 solid solutions". *Opt. Mater.* **36** (2014) 1083–1091.

[8] J.C. Boyer, F. Vetrone, J.A. Capobianco, A. Speghini, M. Bettinelli, "Variation of Fluorescence Lifetimes and Judd-Ofelt Parameters between Eu^{3+} Doped Bulk and Nanocrystalline Cubic Lu_2O_3". *J. Phys. Chem. B.* **108** (2004) 20137–20143.

[9] Z. Wang, B. Qian, H. Wang, D. Wang, H. Zou, Y. Song, X. Zhou, Y. Sheng, "The synthesis and luminescence properties of Lu_2O_3:Eu^{3+} rods and its comparative analysis with Lu_2O_2S:Eu^{3+} rods". *Opt. Mater.* **109** (2020) 110355 (8p).

[10] G. Pan, H. Song, Q. Dai, R. Qin, X. Bai, B. Dong, L. Fan, F. Wang, "Microstructure and optical

properties of Eu^{3+} activated $YV_{1-x}P_xO_4$ phosphors". *J. Appl. Phys*. **104** (2008) 084910 (9p).

[11] Z. Guo, Z. Zhu, X. Zhang, L. Zhou, "Photoluminescent properties and Judd-Ofelt analysis of Eu^{3+}-doped $NaMg(PO_3)_3$ red phosphor". *J. Lumin.* **202** (2018) 484–488.

[12] M. Ferhi, C. Bouzidi, K. Horchani-Naifer, H. Elhouichet, M. Ferid, "Judd-Ofelt analysis of spectroscopic properties of Eu^{3+} doped $KLa(PO_3)_4$". *J. Lumin*. **157** (2015) 21–27.

[13] Z. Wu, B. Chen, X. Li, J. Sun, J. Zhang, H. Zhong, H. Zheng, L. Tong, X. Zhang, H. Xia, "Calcination temperature optimization, energy transfer mechanism and fluorescence temperature dependence of $KLa(MoO_4)_2$:Eu^{3+} phosphors". *J. Phys. Chem. Solids.* **88** (2016) 96–103.

[14] A. Amarnath Reddy, S. Das, S. Ahmad, S. Surendra Babu, J.M.F. Ferreira, G. Vijaya Prakash, "Influence of the annealing temperatures on the photoluminescence of $KCaBO_3$:Eu^{3+} phosphor". *RSC Adv.* **2** (2012) 8768–8776.

[15] Y. Kitagawa, J. Ueda, M.G. Brik, S. Tanabe, "Intense hypersensitive luminescence of Eu^{3+}-doped $YSiO_2N$ oxynitride with near-UV excitation". *Opt. Mater.* **83** (2018) 111–117.

[16] S.K. Gupta, M. Mohapatra, S. Kaity, V. Natarajan, S.V. Godbole, "Structure and site selective luminescence of sol–gel derived Eu:Sr_2SiO_4". *J. Lumin.* **132** (2012) 1329–1338.

[17] L. Đačanin, S.R. Lukić, D.M. Petrović, M. Nikolić, Dramićanin, "Judd–Ofelt analysis of luminescence emission from Zn_2SiO_4:Eu^{3+} nanoparticles obtained by a polymer-assisted sol–gel method". *Physica B: Condens. Matter.* **406** (2011) 2319–2322.

[18] P. Loiko, N. Khaidukov, A. Volokitina, I. Zhidkova, E. Vilejshikova, A. Novichkov, V. Aseev, J.M. Serres, X. Mateos, K. Yumashev, "Luminescence peculiarities of Eu^{3+} ions in multicomponent $Ca_2YSc_2GaSi_2O_{12}$ garnet". *Dyes Pigm.* **150** (2018) 158–164.

[19] X. Zhang, T. Shen, D. Kan, D. Zhang, R. Dong, Z. An, Y. Song, K. Zheng, Y. Sheng, Z. Shi, H. Zou, "Study on the Local Structure and Luminescence Properties of a $Y_2Mg_2Al_2Si_2O_{12}$:Eu^{3+} Red Phosphor for White-Light-Emitting Diodes". *Inorg. Chem*. **59** (2020) 9927–9937.

[20] M.J. Weber, T.E. Varitimos, B.H. Matsinger, "Optical Intensities of Rare-Earth Ions in Yttrium Orthoaluminate". *Phys. Rev. B* **8** (1973) 47–53.

[21] A. Ćirić, S. Stojadinović, M.G. Brik, M.D. Dramićanin, "Judd-Ofelt parametrization from emission spectra: The case study of the Eu^{3+} $^5D_1$ emitting level". *Chem. Phys.* **528** (2020) 110513 (7p).

[22] T. Manohar, R. Naik, S.C. Prashantha, H. Nagabhushana, S.C. Sharma, H.P. Nagaswarupa, K.S. Anantharaju, C. Pratapkumar, H.B. Premkumar, "Photoluminescence and Judd–Ofelt analysis of Eu^{3+} doped $LaAlO_3$ nanophosphors for WLEDs". *Dyes Pigm.* **122** (2015) 22–30.

[23] M. Kumar, T.K. Seshagiri, M. Mohapatra, V. Natarajan, S.V. Godbole, "Synthesis, characterization

and studies of radiative properties on Eu^{3+}-doped $ZnAl_2O_4$". *J. Lumin.* **132** (2012) 2810–2816.

[24] H. Van Tuyen, D.T. Tien, N.M. Son, D. Van Phan, "Judd–Ofelt Parameters of Eu^{3+} and Energy Transfer of Ce^{3+}/Eu^{3+} in $Sr_2Al_2SiO_7$ Materials". *J. Electron. Mater.* **48** (2019) 7799–7805.

[25] R. Shukla, S.K. Gupta, H. Yadav, P. Ranjane, R.M. Kadam, S.N. Achary, A.K. Tyagi, "A carnegieite type red emitting $NaAlSiO_4:Eu^{3+}$ phosphor: Concentration dependent time resolved photoluminescence and Judd-Ofelt analysis". *J. Lumin.* **209** (2019) 283–290.

[26] S. Som, A.K. Kunti, V. Kumar, V. Kumar, S. Dutta, M. Chowdhury, S.K. Sharma, J.J. Terblans, H.C. Swart, "Defect correlated fluorescent quenching and electron phonon coupling in the spectral transition of Eu^{3+} in $CaTiO_3$ for red emission in display application". *J. Appl. Phys.* **115** (2014) 193101 (14p).

[27] D. Hreniak, W. Strek, J. Amami, Y. Guyot, G. Boulon, C. Goutaudier, R. Pazik, "The size-effect on luminescence properties of $BaTiO_3:Eu^{3+}$ nanocrystallites prepared by the sol–gel method". *J. Alloys Compd.* **380** (2004) 348–351.

[28] S.G. Prasanna Kumar, R. Hari Krishna, N. Kottam, P. Krishna Murthy, C. Manjunatha, R. Preetham, C. Shivakumara, T. Thomas, "Understanding the photoluminescence behaviour in nano $CaZrO_3:Eu^{3+}$ pigments by Judd-Ofelt intensity parameters". *Dyes Pigm.* **150** (2018) 306–314.

[29] S. Jang, H. Kim, S.W. Wi, H. Lim, J.-S. Chung, Y. Nah, D.H. Kim, Y.S. Lee, "Structural and luminescent properties of Eu-ion-doped $CaHfO_3$". *J. Lumin.* **226** (2020) 117490 (7p).

[30] L. Li, W. Chang, W. Chen, Z. Feng, C. Zhao, P. Jiang, Y. Wang, X. Zhou, A. Suchocki, "Double perovskite $LiLaMgWO_6:Eu^{3+}$ novel red-emitting phosphors for solid sate lighting: Synthesis, structure and photoluminescent properties". *Ceram. Int.* **43** (2017) 2720–2729.

[31] S. Wang, Y. Xu, T. Chen, W. Jiang, J. Liu, X. Zhang, W. Jiang, L. Wang, "Enhanced red emission of Eu^{3+}-activated phosphors via the special design in A-sites of double perovskite structure". *Opt. Laser Technol.* **134** (2021) 106603 (11p).

[32] K. Vuković, S. Ćulubrk, M. Sekulić, M.D. Dramićanin, "Analysis of luminescence of Eu^{3+} doped $Lu_2Ti_2O_7$ powders with Judd-Ofelt theory". *J. Res. Phys.* **38–39** (2015) 23–32.

[33] X. Li, B. Chen, R. Shen, H. Zhong, L. Cheng, J. Sun, J. Zhang, H. Zhong, Y. Tian, G. Du, "Fluorescence quenching of ^5D_J (J = 1, 2 and 3) levels and Judd–Ofelt analysis of Eu^{3+} in $NaGdTiO_4$ phosphors". *J. Phys. D Appl. Phys.* **44** (2011) 335403 (6p).

[34] F. Lei, B. Yan, "Hydrothermal synthesis and luminescence of $CaMO_4:RE^{3+}$ (M=W, Mo; RE=Eu, Tb) submicro-phosphors". *J. Solid State Chem.* **181** (2008) 855–862.

[35] B. Han, B. Liu, J. Zhang, P. Li, H. Shi, "Comparative Photoluminescence Properties and Judd–Ofelt

Analysis of Eu^{3+} Ion-Activated Metal Molybdate Phosphors $A_2MoO_6:Eu^{3+}$ (A = La, Y, Gd and Bi)". *J. Electron. Mater.* **46** (2017) 4039–4046.

[36] Y. Tian, X. Qi, X. Wu, R. Hua, B. Chen, "Luminescent Properties of $Y_2(MoO_4)_3:Eu^{3+}$ Red Phosphors with Flowerlike Shape Prepared via Coprecipitation Method". *J. Phys. Chem. C.* **113** (2009) 10767–10772.

[37] M. İlhan, İ.Ç. Keskin, "Evaluation of structural behaviour, radioluminescence, Judd-Ofelt analysis and thermoluminescence kinetic parameters of Eu^{3+} doped TTB–type lead metaniobate phosphor". *Physica B: Condens. Matter.* **585** (2020) 412106 (9p).

[38] Y. Tian, B. Chen, R. Hua, N. Yu, B. Liu, J. Sun, L. Cheng, H. Zhong, X. Li, J. Zhang, B. Tian, H. Zhong, "Self-assembled 3D flower-shaped $NaY(WO_4)_2:Eu^{3+}$ microarchitectures: Microwave-assisted hydrothermal synthesis, growth mechanism and luminescent properties". *Cryst. Eng. Comm.* **14** (2012) 1760–1769.

[39] D.L. Shruthi, A.J. Reddy, G.N.A. Kumar, C.K. Jayasankar, "Judd Ofelt theoretical analysis, Photoluminescence properties of Eu^{3+}activated $LiGd(WO_4)_2$ phosphors". *J. Lumin.* **222** (2020) 117167 (14p).

[40] M.G. Brik, Ž.M. Antic, K. Vukovic, M.D. Dramicanin, "Judd–Ofelt Analysis of Eu^{3+} Emission in TiO_2 Anatase Nanoparticles". *Mater. Trans.* **56** (2015) 1416–1418.

[41] Y. Liu, W. Luo, R. Li, G. Liu, M.R. Antonio, X. Chen, "Optical spectroscopy of Eu^{3+} doped ZnO nanocrystals". *J. Phys. Chem. C.* **112** (2008) 686–694.

[42] Q. Xiao, Y. Liu, L. Liu, R. Li, W. Luo, X. Chen, "Eu^{3+}-Doped In_2O_3 Nanophosphors: Electronic Structure and Optical Characterization". *J. Phys. Chem. C.* **114** (2010) 9314–9321.

[43] B. Tian, B. Chen, Y. Tian, X. Li, J. Zhang, J. Sun, H. Zhong, L. Cheng, S. Fu, H. Zhong, Y. Wang, X. Zhang, H. Xia, R. Hua, "Excitation pathway and temperature dependent luminescence in color tunable $Ba_5Gd_8Zn_4O_{21}:Eu^{3+}$ phosphors". *J. Mater. Chem.* **1** (2013) 2338–2344.

[44] J. Dalal, M. Dalal, S. Devi, P. Dhankhar, A. Hooda, A. Khatkar, V.B. Taxak, S.P. Khatkar, "Structural and Judd-Ofelt intensity parameters of a down-converting $Ba_2GdV_3O_{11}:Eu^{3+}$ nanophosphors". *Mater. Chem. Phys*. **243** (2020) 122631.

[45] H.M. Crosswhite, H.W. Moos, "Optical Properties of Ions in Crystals". (John Wiley & Sons, New York, 1967)

[46] E. Cantelar, J.A. Sanz-García, A. Sanz-Martín, J.E. Muñoz Santiuste, F. Cussó, "Structural, photoluminescent properties and Judd-Ofelt analysis of Eu^{3+}-activated CaF_2 nanocubes". *J. Alloys Compd.* **813** (2020) 152194 (9p).

[47] H. Boubekri, M. Diaf, L. Guerbous, J.P. Jouart, "Luminescence properties of Eu^{3+} doped CdF_2 single crystals". *Opt. Mater.* **78** (2018) 21–26.

[48] A. Bednarkiewicz, A. Mech, M. Karbowiak, W. Stręk, "Spectral properties of Eu^{3+} doped $NaGdF_4$ nanocrystals". *J. Lumin.* **114** (2005) 247–254.

[49] P. Du, X. Huang, J.S. Yu, "Facile synthesis of bifunctional Eu^{3+}-activated $NaBiF_4$ red-emitting nanoparticles for simultaneous white light-emitting diodes and field emission displays". *Chem. Eng. J.* **337** (2018) 91–100.

[50] P. Du, J.S. Yu, "Facile hydrothermal synthesis of Eu^{3+}-activated $NaYF_4$ nanocrystals and their Judd-Ofelt analysis, photoluminescence and cathodoluminescence properties". *Curr. Appl. Phys*. **17** (2017) 1662–1669.

[51] N. Dhananjaya, C. Shivakumara, R. Saraf, H. Nagabhushana, "Red-emitting LaOF:Eu^{3+} phosphors: Synthesis, structure and their Judd–Ofelt analysis for LED applications". *Mater. Res. Bull.* **75** (2016) 100–109.

[52] N. Rakov, J. de A.B. Barbosa, R.B. Guimarães, G.S. Maciel, "Spectroscopic properties of Eu^{3+}- and Eu^{3+}:Yb^{3+}-doped LaOF crystalline powders prepared by combustion synthesis". *J. Alloys Compd.* **534** (2012) 32–36.

[53] N. Dhananjaya, C. Shivakumara, R. Saraf, S. Behera, H. Nagabhushana, "Comparative study of Eu^{3+}-activated LnOCl (Ln=La and Gd) phosphors and their Judd-Ofelt analysis". *J. Rare Earths*. **33** (2015) 946–953.

[54] Y. Kitagawa, J. Ueda, K. Arai, H. Kageyama, S. Tanabe, "Difference of Eu^{3+} luminescent properties in YOCl and YOBr oxyhalide hosts". *J. Appl. Phys.* **129** (2021) 183104 (11p).

[55] R. Saraf, C. Shivakumara, S. Behera, N. Dhananjaya, H. Nagabhushana, "Synthesis of Eu^{3+}-activated BiOF and BiOBr phosphors: photoluminescence, Judd–Ofelt analysis and photocatalytic properties". *RSC Adv.* **5** (2015) 9241–9254.

[56] R. Saraf, C. Shivakumara, S. Behera, H. Nagabhushana, N. Dhananjaya, "Photoluminescence, photocatalysis and Judd–Ofelt analysis of Eu^{3+} -activated layered BiOCl phosphors". *RSC Adv.* **5** (2015) 4109–4120.

[57] O.J. Sovers, M. Ogawa, T. Yoshioka, "Detailed branching ratios for M_2O_2S:Eu^{3+}, Tb^{3+} and Pr^{3+} fluorescence from Judd-Ofelt intensity theory". *J. Lumin.* **18–19** (1979) 336–340.

[58] Y. Kitagawa, J. Ueda, K. Fujii, M. Yashima, S. Funahashi, T. Nakanishi, T. Takeda, N. Hirosaki, K. Hongo, R. Maezono, S. Tanabe, "Site-Selective Eu^{3+} Luminescence in the Monoclinic Phase of $YSiO_2N$". *Chem. Mater.* **33** (2021) 8873–8885.

Appendix B
Useful Data for Eu^{3+}: 4f-4f Transition

Here, the 4f energy levels structures and the squared reduced matrix elements (RMEs) of 4f-4f transition for Eu^{3+} are summarized to utilize the practical experimental studies. The 4f energy levels in the free-ion state and a coordination polyhedron (C_2 symmetry of Y_2O_3 and D_{2d} symmetry of YVO_4) are useful to assignment for the transition observed in spectra at the visible region and discussion on the degree of crystal field splitting (*i.e.,* Stark splitting). By referring to the RMEs, one can discuss the transition probability between some two levels, $^{2S+1}L_J$ and $^{2S'+1}L'_{J'}$. Further important data is summarized in the review papers [1,2].

Table B.1. Crystal field splitting of $^{2S+1}L_J$ manifolds of Eu^{3+} ions

$^{2S+1}L_J$	Free ion [1,3]	Y_2O_3 (C_2-site) [4]	YVO_4 (D_{2d}-site) [4]
$^7F_0$	0	0	0
$^7F_1$	379	199, 359, 543	337, 376
$^7F_2$	1043	859, 906, 949, 1379	936, 985, 1038, 1116
$^7F_3$	1896	1847, 1867, 1907, 2008, 2021, 2130, 2160	1854, 1873, 1903, 1904, 1957
$^7F_4$	2869	2668, 2800, 2846, 3015, 3080, 3119, 3163, 3178, 3190	2700, 2830, 2867, 2879, 2923, 2988, 3063
$^7F_5$	3912	3755, 3825, 3904, 3938, 4019, 4062, 4127, 4158, 4227, 4291	3750, 3800, 3870, 3915, 3928, 3949, 4065
$^7F_6$	4992	4589, 4611, 4791, 4812, 4925, 4960, 5032, 5045, 5271, 5314, 5459, 5636	4867, 4916, 4947, 5050, 5053, 5071
$^5D_0$	17227	17216	17183
$^5D_1$	18973	18930, 18954, 18992	18932, 18941
$^5D_2$	21445	21355, 21357, 21396, 21487, 21503	21407, 21419, 21462, 21473
$^5D_3$	24335	24258, 24267, 24284, 24330, 24354	24271

Table B.2. Squared reduced matrix elements $|\langle 4f^6[\alpha' S' L']J' || U^{\lambda} || 4f^6[\alpha SL]J\rangle|^2$ (λ = 2, 4, 6) for intermaniford transition of $^{2S'+1}L'_{J'} \rightarrow {}^{2S+1}L_J$ for Eu^{3+} ions[a] [4,5]

$^{2S'+1}L'_{J'}$	→	$^{2S+1}L_J$	$\lvert\langle\lvert\lvert U^2\rvert\rvert\rangle\rvert^2$	$\lvert\langle\lvert\lvert U^4\rvert\rvert\rangle\rvert^2$	$\lvert\langle\lvert\lvert U^6\rvert\rvert\rangle\rvert^2$
$^7F_1$	→	$^7F_0$	0	0	0
$^7F_2$	→	$^7F_0$	0.1374	0	0
		$^7F_1$	0.0518	0	0
$^7F_3$	→	$^7F_0$	0	0	0
		$^7F_1$	0.2092	0.1281	0
		$^7F_2$	0.1863	0.2124	0
$^7F_4$	→	$^7F_0$	0	0.1402	0
		$^7F_1$	0	0.1741	0
		$^7F_2$	0.2226	0.0062	0.0329
		$^7F_3$	0.3880	0.1352	0.1588
$^7F_5$	→	$^7F_0$	0	0	0
		$^7F_1$	0	0.1192	0.0544
		$^7F_2$	0	0.3153	0.2089
		$^7F_3$	0.1754	0.2527	0.3836
		$^7F_4$	0.5684	0.0128	0.4412
$^7F_6$	→	$^7F_0$	0	0	0.1450
		$^7F_1$	0	0	0.3774
		$^7F_2$	0	0.0477	0.4696
		$^7F_3$	0	0.2310	0.4135
		$^7F_4$	0.0856	0.5145	0.2691
		$^7F_5$	0.5410	0.6451	0.1213
$^5D_0$	→	$^7F_0$	0	0	0
		$^7F_1$	0	0	0
		$^7F_2$	0.0032	0	0
		$^7F_3$	0	0	0
		$^7F_4$	0	0.0023	0

Table B.2. Squared reduced matrix elements $|\langle 4f^6[\alpha' S' L']J'||U^{\lambda}||4f^6[\alpha SL]J\rangle|^2$ (λ = 2, 4, 6) for intermaniford transition of $^{2S'+1}L'_{J'} \rightarrow {}^{2S+1}L_J$ for Eu^{3+} ions[a] [4,5] (*Continued*)

$^{2S'+1}L'_{J'}$	→	$^{2S+1}L_J$	$\|\langle\|\|U^2\|\|\rangle\|^2$	$\|\langle\|\|U^4\|\|\rangle\|^2$	$\|\langle\|\|U^6\|\|\rangle\|^2$
$^5D_0$	→	$^7F_5$	0	0	0
		$^7F_6$	0	0	0.0005*
$^5D_1$	→	$^7F_0$	0	0	0
		$^7F_1$	0.0025	0	0
		$^7F_2$	0.0009*	0	0
		$^7F_3$	0.0038	0.0019	0
		$^7F_4$	0	0.0028	0
		$^7F_5$	0	0.0009*	0.00005*
		$^7F_6$	0	0	0.0006*
		$^5D_0$	0	0	0
$^5D_2$	→	$^7F_0$	0.0009*	0	0
		$^7F_1$	0.0002*	0	0
		$^7F_2$	0.0018	0.0015	0
		$^7F_3$	0.0023	0.0026	0
		$^7F_4$	0.0020	0.0003	0.0040
		$^7F_5$	0	0.0016	0.00002*
		$^7F_6$	0	0.00002*	0.0002
		$^5D_0$	0.0142	0	0
		$^5D_1$	0.0122	0	0

[a]The values marked with asterisk * are taken from the reference [3].

References

[1] K. Binnemans, "Interpretation of europium(III) spectra". *Coord. Chem. Rev.* 295 (2015) 1–45.

[2] P.A. Tanner, "Some misconceptions concerning the electronic spectra of tri-positive europium and cerium". *Chem. Soc. Rev.* 42 (2013) 5090–5101.

[3] K. Binnemans, "A comparative spectroscopic study of Eu^{3+} in crystalline host matrices". *Bull. Soc. Chim. Belg.* 105 (1996) 793–798.

[4] A.A. Kaminskii, "Crystalline Lasers: Physical Processes and Operating Schemes". (CRC Press, Boca Raton, 1996)

[5] W.T. Carnall, H. Crosswhite, H.M. Crosswhite, "Energy level structure and transition probabilities in the spectra of the trivalent lanthanides in LaF_3". (Argonne National Laboratory, Argonne, 1978)

List of Publication

Chapter 3

Y. Kitagawa, J. Ueda, M.G. Brik, S. Tanabe,

"Intense hypersensitive luminescence of Eu^{3+}-doped $YSiO_2N$ oxynitride with near-UV excitation"

Optical Materials **83** (2018) 111–117.

Chapter 4

Y. Kitagawa, J. Ueda, K. Fujii, M. Yashima, S. Funahashi, T. Nakanishi, T. Takeda, N. Hirosaki, K. Hongo, R. Maezono, S. Tanabe,

"Site-Selective Eu^{3+} Luminescence in the Monoclinic Phase of $YSiO_2N$"

Chemistry of Materials **33** (2021) 8873–8885.

Chapter 5

Y. Kitagawa, J. Ueda, J. Xu, T. Nakanishi, T. Takeda, N. Hirosaki, S. Tanabe,

"Deep-red to near-infrared luminescence from Eu^{2+}-trapped exciton states in $YSiO_2N$"

Physical Chemistry Chemical Physics (2022) *accepted.*

Chapter 6

Y. Kitagawa, J. Ueda, S. Tanabe,

"Time-resolved and temperature-dependent spectroscopy for blue luminescence of monoclinic $YSiO_2N:Ce^{3+}$ phosphor"

Journal of Luminescence, under review.

Chapter 7

Y. Kitagawa, J. Ueda, S. Tanabe,

"Blue persistent phosphor of $YSiO_2N:Ce^{3+}$ developed by co-doping Sm^{3+} or Tm^{3+} ions and thermoluminescence analysis of their trap distributions"

Physica Status Solidi A (2022) *in press.*

Chapter 8

Y. Kitagawa, J. Ueda, K. Arai, H. Kageyama, S. Tanabe,

"Difference of Eu^{3+} luminescent properties in YOCl and YOBr oxyhalide hosts"

Journal of Applied Physics **33** [9] (2021) 183014 (11p).

Chapter 9

Y. Kitagawa, S. Takemura, D. Hirai, Z. Hiroi, K. Ogasawara, J. Ueda, S. Tanabe,

"Characterization of Charge Transfer Luminescence of $[WO_6]^{6-}$ Octahedron and $[WO_5]^{4-}$ Square Pyramid with *Ab initio* Energy Level Calculation"

Inorganic Chemistry, under review.

Chapter 10

Y. Kitagawa, E.G. Yukihara, S. Tanabe,

"Development of Ce^{3+} and Li^{+} co-doped magnesium borate glass ceramics for optically stimulated luminescence dosimetry"

Journal of Luminescence **232**, (2021) 117847 (8p).

Other Publications as a Co-author

Y. Masubuchi, S. Nishitani, A. Hosono, **Y. Kitagawa**, J. Ueda, S. Tanabe, H. Yamane, M. Higuchi, S. Kikkawa,
"Red-emission over a wide range of wavelength at various temperatures from tetragonal $BaCN_2:Eu^{2+}$"
Journal of Materials Chemistry C **6** (2018) 6370–6377.

G. Guelou, M. Martirossyan, K. Ogata, I. Ohkubo,Y. Kakefuda, N. Kawamoto, **Y. Kitagawa**,
J. Ueda, S. Tanabe, K. Maeda, K. Nakamura, T. Aizawa, T. Mori,
"Rapid deposition and thermoelectric properties of ytterbium boride thin films using
hybrid physical chemical vapor deposition"
Materialia **1** (2018) 244–248.

Y. Tsuchiya, Z. Wei, T. Broux, C. Tassel, H. Ubukata, **Y. Kitagawa**, J. Ueda, S. Tanabe, H. Kageyama,
"Formation of $PbCl_2$-type AHF (A = Ca, Sr, Ba) with partial anion order at high pressure"
Dalton Transaction **50** (2021) 8385–8391.

Reviews

北川裕貴，上田純平，田部勢津久，
「近紫外励起可能な高輝度赤色蛍光を示す Eu3+賦活酸窒化物蛍光体の創製」
『化学工業（特集/ 新たな希土類研究と応用）』**70**[7] (2019) 37–43.

Achievements

Presentation (*International Conference*)

1. Y. Kitagawa, J. Ueda, S. Tanabe, "Fabrication and Optical Properties of Eu^{3+}-doped $YSiO_2N$ Oxynitride Red Phosphor", *9th International Symposium of Nitrides (ISNT2017) & 5th International Symposium on SiAlONs and Non-oxides (ISSNOX5)* (Sapporo, Aug 27-30, 2017) **Oral.**

2. Y. Kitagawa, J. Ueda, M.G. Brik, S. Tanabe, "Intense Red Luminescence by Near-UV Excitation in $YSiO_2N:Eu^{3+}$", *Glass and Optical Materials Division (GOMD) Meeting* (Texas, May 20-24, 2018) **Oral.**

3. Y. Kitagawa, E.G. Yukihara, S. Tanabe, "Preparation and Luminescence Characteristics of Ce^{3+}-Li^{+} Co-doped Magnesium Borate Glass Ceramics for Dosimetry", *25th Int'l Congress on Glass* (Boston, June 9-14, 2019) **Oral.**

4. Y. Kitagawa, J. Ueda, S. Tanabe, "Anion-substitution Effect on Eu^{3+} luminescence in YO*X* (*X* = Cl or Br)", *The 13th Pacific Rim Conference of Ceramic Societies (PACRIM13)* (Okinawa, 10/27-11/1, 2019) **Oral.**

5. Y. Kitagawa, J. Ueda, M. G. Brik, S. Tanabe, "Intense hypersensitive luminescence of Eu^{3+} in distorted sites with mixed-anion coordination excitable by near-UV", *Phosphor Safari 2019* (Xiamen, 11/14-11/17, 2019) Poster.

6. Y. Kitagawa, "Introduction of our group's research on functional luminescent materials", *Virtual Student Exchange Program Meeting* (Online, Aug 27-28, 2020) **Invited.**

7. S. Tanabe, **Y. Kitagawa**, J. Ueda, "Mixed-anion compounds giving unique luminescence characteristics in rare-earths", *19th International Conference on Luminescence* (*ICL2020*) (Online, Jul 26-30, 2021) **Invited.**

8. **Y. Kitagawa**, J. Ueda, D. Hirai, S. Takemura, K. Ogasawara, S. Tanabe, "Characterization of charge transfer luminescence of $[WO_5]^{4-}$ square pyramid in $Ca_3WO_5Cl_2$ with *ab initio* energy level calculation", *International Conference of Mixed-Anion Compounds* (*ICMAC*) (Kobe, 12/7–10, 2021) Poster.

Presentation (*Domestic Conference in Japan*)

1. ○**北川 裕貴**, 上田 純平, 田部 勢津久,「長残光発現に向けた希土類イオン添加 $YSiO_2N$ の VRBE(Vacuum Referred Binding Energy)ダイアグラムの構築」, 日本セラミックス協会 2017 年年会 (東京, 3/17-19, 2017), **口頭発表.**

2. ○**北川 裕貴** , 上田 純平, 田部 勢津久,「$YSiO_2N$ における Eu^{3+}イオンの赤色発光増強と真空基準結合エネルギーダイアグラムの構築」, 複合アニオン化合物の創製と新機能」キックオフミーティング (福岡, 5/29, 2017), ポスター発表.

3. ○**北川 裕貴**, 上田 純平, 田部 勢津久,「Fabrication and Optical Properties of Eu^{3+}-doped $YSiO_2N$ Oxynitride Red Phosphor」, 第 49 回日本セラミックス協会ガラス部会夏季若手セミナー（小樽, 8/20-22, 2017）, ポスター発表.

4. ○**北川 裕貴**, 上田 純平, 田部 勢津久,「キャリアトラップエンジニアリングによる Ce^{3+}添加 $YSiO_2N$ 長残光蛍光体の開発」, 日本セラミックス協会 第 30 回秋季シンポジウム (神戸大, 9/19-21, 2017), **口頭発表.**

5. ○**北川 裕貴**, 上田 純平, Mikhail Brik, 田部 勢津久,「近紫外励起可能な Eu^{3+}添加 $YSiO_2N$ 酸窒化物の Judd-Ofelt 理論に基づく蛍光特性評価」, 第 65 回 応用物理学会 春季学術講演会 (東京, 3/17-20, 2018), **口頭発表.**

6. ○**北川 裕貴**, 上田 純平, 田部 勢津久,「$YSiO_2N$ が有する低/高対称性 Y^{3+}サイト中における Eu^{3+}の $^5D_0 \rightarrow {}^7F_2$ 電気双極子遷移確率の評価」, 第 80 回応用物理学会秋季学術講演会 (札幌, 9/18-21, 2019), **口頭発表.**

7. ○華 瀚森, **北川 裕貴**, 上田 純平, 田部 勢津久, 鱒渕 友治,「Eu^{2+}イオンの 5d-4f 発光エネルギーの圧力依存性と体積弾性率との相関」, 第 60 回ガラスおよびフォトニクス材料討論会 (大阪, 12/4-5, 2019).

8. ○**北川 裕貴**, 上田 純平, 田部 勢津久,「$YSiO_2N$ が有する低/高対称性 Y^{3+}サイトにおける Eu^{3+} 赤色発光機構の考察」, 第 67 回応用物理学会春季学術講演会 (東京, 3/12-15, 2020)→開催中止, **講演奨励賞受賞講演.**

9. ○**北川 裕貴**, 上田 純平, 田部 勢津久,「酸窒化物蛍光体 $YSiO_2N:Eu^{3+}$における局所構造の反転中心の有無がもたらす特異な蛍光特性についての考察」, 第 14 回 物性科学領域横断研究会 (オンライン, 12/4-5, 2020), **口頭発表.**

10. ○**北川 裕貴**, 上田 純平, 田部 勢津久,「PbClF 型構造を有する Eu^{3+}添加酸ハロゲン化物における Judd-Ofelt 強度パラメータ Ω と局所配位環境の相関」, 第 11 回フォトニクスのための材料研究会 (オンライン, 3/30, 2021), **招待講演.**

11. ○**北川 裕貴**，上田 純平，平井 大悟郎，田部 勢津久，「酸塩化物 $Ca_3WO_5Cl_2$ における電荷移動遷移発光の物性評価」，日本セラミックス協会 第 34 回秋季シンポジウム（オンライン，9/1-3，2021），**口頭発表.**

Academic Funding

1. 平成 31–令和 3 年度
   日本学術振興会 科学研究費助成事業（特別研究員奨励費, DC1）
   研究課題: 『価電子帯制御に基づく新規光機能性複合アニオン材料の創製』
   代表者，310 万円.

Awards

1. 『**優秀ポスター賞**』，新学術領域「複合アニオン化合物の創製と新機能」キックオフミーティングポスターセッション，福岡，平成 29 年 5 月.
2. 『**優秀発表賞**』， 第 49 回日本セラミックス協会ガラス部会夏季若手セミナー，北海道，平成 29 年 8 月.
3. 『**Best Experimental Performance Award**』, 1st North American Summer School on Photonic Materials (NASSPM), Quebec, June (2019).
4. 『**Excellent Presentation Award**』, Phosphor Safari 2019, Xiamen, November (2019).
5. 『**講演奨励賞**』，第 80 回応用物理学会秋季学術講演会，令和 2 年 3 月.
6. 『**優秀発表賞**』，第34回日本セラミックス協会秋季シンポジウム，令和3年9月.

Acknowledgements

This dissertation was written based on the work done at Kyoto University, Japan, where I have worked for almost six years since April 2016. During this time, many people supported and encouraged me in a variety of aspects, and I would like to express my deep gratitude to all of them.

First of all, I would like to express my most sincere gratitude to my supervisor, Professor Setsuhisa Tanabe, for his constant support, sincere encouragement, and critical advice on my research problems. His deep insight into materials science and his research philosophy are always a guide for my study and inspire my motivation to study various topics. He provided a lot of variable academic/non-academic opportunities, cultivating my research, thinking, and language skills.

I am especially obliged to Assistant Professor Jumpei Ueda for daily fruitful discussions on research. His deep insight not only into optical physics but also into general materials science and engineering always helps me to investigate and discuss the physical properties of mixed-anion phosphors. It is definitely fortunate for me to spend my first carrier as a scientist with him, stimulating my scientific motivation.

I would like to express my gratitude to Professor Mikhail G. Brik in the University of Tartu (Estonia), who was a visiting professor at Kyoto University in 2017–2018, for the impressive lecture course on theoretical backgrounds of spectroscopy, the detailed instruction of the Judd-Ofelt analysis for Eu^{3+}-doped materials, and the supervision of my first paper as a co-author. I am sincerely honored that I studied under his supervision. I also would like to thank Associate Professor Sebastian Mahlik in the University of Gdańsk (Poland), who was a visiting professor at Kyoto University in 2019, for the excellent lecture about quantum physics and the daily fruitful discussion on luminescence in solids. I also would like to thank Professor Angela Seddon in the University of Nottingham (the United Kingdom), who was a visiting professor at Kyoto University in 2020, for constructive and critical comments for my research presentation.

I would like to express my appreciation to Professor Katsuhisa Tanaka and Assistant

Professor Shunsuke Murai in the Graduate School of Engineering at Kyoto University for the fruitful discussion on my research in every mid-term joint research seminar. I would also like to thank all members of the Takana Laboratory for being in a state of friendly rivalry.

I would like to express my gratitude to my senior researcher in the Tanabe Laboratory: Dr. Jian Xu in the International Center for Young Scientists (ICYS) at the National Institute for Materials Science (NIMS), for his excellent instruction and recommendation for the research topics and daily scientific chat before and after in NIMS. I sincerely respect him as a great young scientist and always imitate his research attitudes; Dr. Michele Back in Ca' Foscari University of Venice (Italy), for many valuable discussions on the scientific and non-scientific matter. The two years when he stayed at Kyoto University encouraged my research attitudes; Dr. Kazuki Asami, who is an alumnus of the Tanabe Laboratory, for kind consideration for me and instruction of research not only on luminescent materials but also on general materials science. He always encouraged me and tackled difficulties together so that I could get over them; Dr. Haipeng Ji in Zhengzhou University (China) and Dr. Ruilin Zheng, who is a JSPS fellow in Kyoto University, for fruitful discussion and some advice for my work.

I would like to thank Mr. Masami Hasumoto, who is a technical staff in the UVSOR-III facility at Institute for Molecular Science, Japan, for helping me with VUV measurements. I would also thank Dr. Tsutomu Kiyomura, who is a technical researcher for the "Nanotechnology Platform" Program at Kyoto University Microstructural Characterization Platform, for helping with STEM and EDX measurements.

I would like to express my gratitude to Professor Eduardo G. Yukihara in the Paul Scherrer Institute (Switzerland) for measurements of dosimetric properties of my glass-ceramic samples and many suggestions about writing and summarizing a research article.

I would like to thank Professor Hiroshi Kageyama in Graduate School of Engineering at Kyoto University, who leads the JSPS research project of "Mixed-Anion," for providing valuable opportunities to interact with many young scientists and students all over Japan and promotion of many collaborations with researchers in various fields of materials science. I would also like to thank Mr. Kazunari Arai, who is a Ph.D. student in the Kageyama Laboratory at Kyoto

University, for measurements of synchrotron X-ray diffraction at Spring-8.

I would like to thank Professor Masatomo Yashima in the Tokyo Institute of Technology for many constructive comments and advice on the results of crystal structure analysis. I would also like to thank Assistant Professor Kotaro Fujii in the Tokyo Institute of Technology for measurements of neutron diffraction at J-PARC and for instructing how to perform Rietveld refinement and check the validity of refinement results.

I would like to thank Professor Ryo Maezono and Associate Professor Kenta Hongo in the Japan Advanced Institute of Science and Technology (JAIST) for providing opportunities for me to learn how to perform the *ab initio* calculation. I would also like to thank Dr. Keishu Utimura, who was a Ph.D. student in the Maezono Laboratory at JAIST, for showing me the detailed way to calculate with various packages, such as CASTEP, VASP, QUANTUM ESPRESSO, and Phonopy, and for providing a lot of advice on computational techniques.

I would like to express my gratitude to Dr. Shiro Funahash in NIMS for measurements of single-crystal X-ray diffraction. His contribution finally led me to the solution on the monoclinic structure of $YSiO_2N$, which had puzzled me for almost five years. I would like to thank Dr. Takayuki Nakanishi in NIMS for providing the opportunity for collaboration to analyze the crystal structure of $YSiO_2N$. I would like to thank Dr. Takashi Takeda and Dr. Naoto Hirosaki in NIMS for proving some comments and suggestions for my research. I would also like to thank Dr. Hiroyo Segawa in NIMS for XAS measurements at Photon Factory.

I would like to express my deep appreciation to Dr. Shota Takemura in NIMS for the *ab initio* molecular-orbital and configuration-interaction calculation with DV-Xα and DVME methods and for fruitful discussion on the correlation between spectroscopic results and calculated energy level diagrams. I would like to thank Professor Kazuyoshi Ogasawara in Kwansei Gakuin University for providing the computational program for the DVME calculation.

I would like to thank Assistant Professor Daigorou Hirai in the University of Tokyo for preparing various single-crystal samples and fruitful discussions at some Mixed-Anion meetings.

I would like to thank short-visiting researchers, Dr. Morgan Pellerin and Dr. Victor

Castaing from the PSL Research University (France), Dr. Tadeusz Lesniewski from the University of Gdańsk (Poland), and Mr. Thom Snoeren from Utrecht University (Nederland). Their visiting stimulated and motivated my research attitudes.

I would like to thank other members and previous members of the Tanabe Laboratory; Ms. Maki Kubo and Ms. Ayumi Katayama, for so much support for our comfortable research environments, indirectly leading to my a lot of experimental results; Mr. Atsushi Hoshino, Mr. Ryomei Maki, Mr. Shun Miyano, and Mr. Kotaro Yasuda, for a lot of kind words of concern for me before and after their graduation; Mr. Daisuke Murata, Mr. Masaya Harada, and Mr. Takayuki Tokunaga, for their teaching basic knowledge about luminescent materials and the way to use experimental equipment; Mr. Hiroshi Nambu, for the cooperation in two years of the master's course as peers; Mr. Shogo Tanaka, Mr. Hansen Hua, Mr. Kenta Kusuki, Mr. Gaku Goto, Mr. Qixuan Zhang, Ms. Qiping Du, Mr. Jiyao Li, Mr. Eishi Kanai, Mr. Shunsuke Kozuka, and Mr. Tomoaki Minowa, for many enjoyable and inspiring moments we together with.

I would like to offer my special thanks to all my friends whom I met at Kyoto University. They always encouraged me and have been emotional support. Especially, I would like to thank Mr. Shimpei Naniwa in the Yoshida laboratory at Kyoto University. I am very proud of these nine years, in which we have devoted ourselves diligently to studying chemistry at the Faculty of Integrated Human Studies and Graduate School of Human and Environmental Studies. I also would like to express my deepest appreciation to Dr. Takuya Maeda in Cornell University. He always demonstrates an exemplary way of being an excellent researcher and provides enormous advice on the Ph.D. life as a senior researcher and a good friend.

Finally, I sincerely wish to thank my parents, Masayuki Kitagawa and Miho Kitagawa, for their understanding, support, and heartfelt encouragement during my whole student life at Kyoto University.

Yuuki KITAGAWA

January 17th, 2022, in Kyoto

※著作権等

"Intense hypersensitive luminescence of Eu^{3+}-doped $YSiO_2N$ oxynitride with near-UV excitation" Y. Kitagawa, J. Ueda, M.G. Brik, S. Tanabe ("*Optical Materials*" September 2018. Volume 83. pp. 111-117). doi: 10.1016/j.optmat.2018.05.039.

"Site-Selective Eu^{3+} Luminescence in the Monoclinic Phase of $YSiO_2N$" Y. Kitagawa, J. Ueda, K. Fujii, M. Yashima, S. Funahashi, T. Nakanishi, T. Takeda, N. Hirosaki, K. Hongo, R. Maezono, S. Tanabe ("*Chemistry of Materials*" November 2021, Volume 33, Issue 22, pp. 8873–8885). doi: 10.1021/acs.chemmater.1c03139.

“Deep-red to near-infrared luminescence from Eu^{2+}-trapped exciton state in $YSiO_2N$” Y. Kitagawa, J. Ueda, J. Xu, T. Nakanishi, T. Takeda, N. Hirosaki, S. Tanabe (“*Physical Chemistry Chemical Physics*” January 2022, in press). doi: 10.1039/D1CP05242J

“Blue persistent phosphor of $YSiO_2N:Ce^{3+}$ developed by co-doping Sm^{3+} or Tm^{3+} ions and thermoluminescence analysis of their trap distributions” Y. Kitagawa, J. Ueda, S. Tanabe (“*Physica Status Solidi A*, December 2021, in press). doi: 10.1002/pssa.202100670

"Difference of Eu^{3+} luminescent properties in YOCl and YOBr oxyhalide hosts" Y. Kitagawa, J. Ueda, K. Arai, H. Kageyama, S. Tanabe ("*Journal of Aplied Physics*" May 2021, Volume 129, Issue 18, 183104 (11p)). doi: 10.1063/5.0049826.

"Development of Ce^{3+} and Li^{+} co-doped magnesium borate glass ceramics for optically stimulated luminescence dosimetry" Y. Kitagawa, E.G. Yukihara, S. Tanabe ("*Journal of Luminescence*" April 2021 Volume 232, 117847 (8p)). doi: 10.1016/j.jlumin.2020.117847.